



City Research Online

City, University of London Institutional Repository

Citation: Armakolas, I. (2018). Cavitation erosion fracture mechanisms and their detection in ship rudders. (Unpublished Doctoral thesis, City, University of London)

This is the accepted version of the paper.

This version of the publication may differ from the final published version.

Permanent repository link: <https://openaccess.city.ac.uk/id/eprint/21028/>

Link to published version:

Copyright: City Research Online aims to make research outputs of City, University of London available to a wider audience. Copyright and Moral Rights remain with the author(s) and/or copyright holders. URLs from City Research Online may be freely distributed and linked to.

Reuse: Copies of full items can be used for personal research or study, educational, or not-for-profit purposes without prior permission or charge. Provided that the authors, title and full bibliographic details are credited, a hyperlink and/or URL is given for the original metadata page and the content is not changed in any way.



CITY
UNIVERSITY OF LONDON
— EST 1894 —

School of Mathematics, Computer Science & Engineering

Cavitation Erosion Fracture Mechanisms and their Detection in Ship Rudders

Ioannis Armakolas (MEng)

This thesis is submitted for the fulfilment of the requirements for the degree of
Doctor of Philosophy

February 2018

Table of Contents

List of Figures	7
List of Tables	17
Acknowledgements	19
Declaration	21
Abstract	23
Nomenclature	25
Chapter 1	29
Introduction	29
1.1 Motivation	29
1.2 Present study	32
Chapter 2	35
Literature Review	35
2.1 Introduction	35
2.2 Cavitation experienced by ship propellers	35
2.3 Cavitation experienced by rudders and the propeller – rudder interaction	41
2.4 Cavitation physics	44
2.5 Cavitation erosion	51
2.6 Acoustic emissions and non – destructive testing techniques (NDT) for damage evaluation	65
2.7 Summary of literature review	68
Chapter 3	71
Experimental Procedure and Conditions	71
3.1 Introduction	71
3.2 Experimental test rig	71
3.3 Experimental procedure and conditions	78
Chapter 4	81
Mass Loss Results	81
4.1 Introduction	81
4.2 Test rig evaluation	82
4.3 Correlation with the ‘T. O. Erosion study’	91
4.4 The effect of cathodic protection	94
4.5 Mass loss measurements on various alloys and coatings	100
4.6 Summary and discussion	118

Chapter 5	127
Microscopic Examination	127
5.1 Introduction	127
5.2 The digital optical microscope - Procedure	127
5.3 Optical microscopic observations	129
5.4 Fractography	151
5.5 Fractography - Procedure	157
5.6 Fractography - Results	158
5.7 Summary and discussion	173
Chapter 6	177
Acoustic Emissions due to Cavitation Erosion	177
6.1 Introduction	177
6.2 Acoustic emission and sound propagation theory	177
6.3 Acoustic emission sensing equipment	189
6.4 Tests prior to the acoustic measurements	192
6.5 Various test rig configurations, acoustic sensors and signal capturing method -Details 193	
6.6 Cavitation related acoustic emissions (grade DH36 steel) - Results	195
6.7 Cavitation related acoustic emissions (all alloys) - Comparison	218
6.8 Conversion of acoustic emissions into stress- Principles	222
6.9 Conversion of acoustic emissions to stress- Procedure and results- Grade DH36 steel ..	224
6.10 Conversion of acoustic emissions to stress – Results – Cupronickel 70-30 and stainless steel 254	232
6.11 Fibre Bragg grating sensors (FBG) – Basic theory and applications	236
6.12 Fibre Bragg grating sensors(FBG) – Preliminary tests	238
6.13 Fibre Bragg grating sensors (FBG) – Acoustic emission tests	241
6.14 Correlation of fracture toughness with erosion	244
6.15 Summary and discussion	246
Chapter 7	249
Acoustic Emission Measurements on Model Ship Rudders	249
7.1 Introduction	249
7.2 Experimental test rig	249
7.3. Experimental procedure: Acoustic emission measurements and the triangulation source location technique	254
7.4 Acoustic emission– Cavitation erosion correlation measurements	259
7.5 Acoustic emission – Cavitation erosion source location measurements - Piezoelectric and fibre Bragg grating sensor based systems	263

7.6 Double size model rudder– Exploration of possible scale effects.....	265
7.7 Summary and discussion	273
Chapter 8	275
Conclusions & Recommendations for Future Work	275
8.1 Introduction	275
8.2 Conclusions	276
8.3 Recommendations for future work.....	280
References	283
Appendix A	305
A.1 Case study: Acoustic emission (AE) hull structural monitoring.....	305
A.2 Procedure and equipment.....	305
A.3 Indicative results	307
Appendix B	309
B.1 The metal magnetic memory (MMM) method	309
B.2 Experimental procedure and testing.....	310
B.3 Cavitation erosion evaluation by means of the metal magnetic memory (MMM) method	311
Appendix C	313
C.1 The triangulation technique by Tobias – The operating sound field	313
Appendix D	317
D.1 The triangulation technique – Source location measurements – Piezoelectric sensors ..	317
D.2 The triangulation technique– Source location measurements– Fibre Bragg grating sensors	334
Appendix E	351
E.1 Case study: Cavitation erosion and impact testing on the Metaline 785 protective coating	351
E.2 Experimental procedure and conditions - Erosion.....	351
E.3 Results and discussion - Erosion	352
E.4 Conclusion - Erosion	356
E.5 Impact testing	357
E.6 Impact testing - Results	357
Appendix F.....	361
F.1 Three dimensional microscopic images of cavitation erosion pits.....	361
Appendix G.....	381
G.1 Measurement uncertainty analysis.....	381

List of Figures

Figure 1.1: Turbinia vessel at speed in 1894 (Source: Tyne & Wear Museums)	30
Figure 1.2: Cavitation tunnel owned by Mitsubishi Heavy Industries (Source: Mitsubishi Heavy Industries Mechatronics Systems, LTD.)	31
Figure 2.1: Different forms of cavitation, as there are experienced by a ship propeller (Source: Wijngaarden, 2012)	36
Figure 2.2: Tip and hub vortex cavitation (Source: SVA Potsdam GmbH, n.d)	37
Figure 2.3: Evidence of sheet (blue arrow) and blade root (red arrow) cavitation (Source: Carlton, n.d.)	38
Figure 2.4: Cloud (blue arrow), sheet (red arrow) and tip vortex (green arrow) cavitation (Source: Carlton, n.d.)	38
Figure 2.5: Full – scale cavitating sheet and vortex cavitation of an LNG ship propeller (Source: Carlton, 2012)	39
Figure 2.6: Evidence of cavitation induced erosion, on the propeller of a small personal watercraft (Source: Wikimedia Commons, 2006)	39
Figure 2.7: Propeller – Hull vortex cavitation emanating from a podded propulsion unit (Source: Carlton, 2012)	40
Figure 2.8: Semi – balanced rudder (Source: Marine Insight, 2017)	41
Figure 2.9: Rudder – propeller interaction (Source: SVA Potsdam GmbH, n.d)	42
Figure 2.10: Cavitation induced erosion on the rudder of the Finnkraft vessel (Source: Carlton, n.d)	43
Figure 2.11: Harvey’s nucleation model (Source: Carlton, 2012)	46
Figure 2.12: Computed bubble collapse. Left – In contact with wall, Right – At a distance (Source: Plesset and Chapman, 1971)	49
Figure 2.13: Successive bubble shapes during collapse, near a solid wall – rigid boundary (Source: Blake and Gibson, 2017).	50
Figure 2.14: Shock wave generation during bubble collapse filmed at 100 million frames per second. Time is noted on the upper left corner of each shot (Source: Lindau and Lauterborn, 2003)	53
Figure 2.15: Liquid jet formation during bubble collapse filmed at 75000 frames per second (Source: Lauterborn and Bolle, 1975)	54
Figure 2.16: Erosion pattern of an aluminium specimen for a distance $\gamma = 0.69$ (Source: Philipp and Lauterborn, 1998)	56
Figure 2.17: Consecutive frames showing the collapse of cloud cavitation in the vicinity of a hydrofoil (Source: Reisman et al., 1998)	57
Figure 2.18: The basis of the Fortes – Patella model (Source: Fortes – Patella et al., 2004)	58
Figure 2.19: Orange peeling erosion pattern (Source Legi – Grenoble, n.d.)	62
Figure 2.20: Oxide induced colour – tinting marks on grade DH36 steel (Source: Carlton, 2012)	63
Figure 3.1: Test rig – Perspex water tank	72
Figure 3.2: Test rig – Plastic base (bridge)	73
Figure 3.3: Hielscher UIP1000hd ultrasonic transducer and sonotrode (Source: Hielscher - Ultrasound Technology, n.d.)	74
Figure 3.4: Test rig – Plastic base (bridge) inside the water tank with sonotrode on the top	75
Figure 3.5: Test rig and water recirculation system	76

Figure 3.6: VersaSTAT 3 potentiostat/galvanostat. RE = Reference Electrode, WE = Working electrode, CE = Counter electrode	77
Figure 4.1: Mass loss of grade DH36 steel (25 mm) for a 50% (500W) power output.....	82
Figure 4.2: Rate of mass loss of grade DH36 steel (25 mm) at a 50% (500W) power output....	83
Figure 4.3: Mass loss of grade DH36 steel (25 mm) for a 75% (750W) power output.....	84
Figure 4.4: Rate of mass loss of grade DH36 steel (25 mm) for a 75% (750W) power output. ..	84
Figure 4.5: Mass loss of grade DH36 steel (50 mm) for a 75% (750W) power output.....	85
Figure 4.6: Rate of mass loss of grade DH36 steel (50 mm) for a 75% (750W) power output. ..	85
Figure 4.7: CFD simulation of sonotrode operation (Source: Carlton, n.d.)	86
Figure 4.8: Mass loss of grade DH36 steel (50 mm) from BAE Systems for a 75% (750W) power output.....	88
Figure 4.9: Rate of mass loss of grade DH36 steel (50 mm) from BAE Systems for a 75% (750W) power output.....	88
Figure 4.10: Initial surface roughness.....	89
Figure 4.11: Progression of erosion for Grade DH36 steel.....	90
Figure 4.12: Mass loss comparison between the ‘T.O. Erosion study’ and the present study....	91
Figure 4.13: Rate of mass loss comparison between the ‘T.O. Erosion study’ and the present study.....	92
Figure 4.14: Mass loss comparison between the ‘T.O. Erosion study’ and the present study - Two suppliers are considered for the present study.	93
Figure 4.15: Rate of mass loss comparison between the ‘T.O. Erosion study’ and the present study - Two suppliers are considered for the present study.	93
Figure 4.16: Mass loss of grade DH36 steel (50 mm) at a 75% (750W) power setting and under a -790 mV CP.....	95
Figure 4.17: Rate of mass loss of grade DH36 steel (50 mm) at a 75% (750W) power setting and under a -790 mV CP.....	96
Figure 4.18: Mass loss of grade DH36 steel (50 mm) at a 75% (750W) power setting and under a -790 mV CP. Present vs ‘T.O. Erosion study’.....	97
Figure 4.19: Rate of mass loss of grade DH36 steel (50 mm) at a 75% (750W) power setting and under a -790 mV CP. Present vs ‘T.O. Erosion study’.	97
Figure 4.20: Mass loss of grade DH36 steel (50 mm) at a 75% (750W) power setting and under different CP potentials.....	98
Figure 4.21: Rate of mass loss of grade DH36 steel (50 mm) at a 75% (750W) power setting and under different CP potentials.....	99
Figure 4.22: Total mass loss versus different working potentials for grade DH36 steel.....	99
Figure 4.23: Mass loss of stainless steel 254 at a 75% (750W) power setting and under a -790 mV CP.....	102
Figure 4.24: Rate of mass loss of stainless steel 254 (50 mm) at a 75% (750W) power setting and under a -790 mV CP.....	102
Figure 4.25: Progression of erosion for stainless steel 254.....	103
Figure 4.26: Mass loss of cupronickel 70-30 at a 75% (750W) power setting and under a -790 mV CP.....	104
Figure 4.27: Rate of mass loss of cupronickel 70-30 at a 75% (750W) power setting and under a -790 mV CP.....	104
Figure 4.28: Progression of erosion for cupronickel 70-30.....	105
Figure 4.29: Mass loss of I coating at a 75% (750W) power setting and under a -790 mV CP.....	106

Figure 4.30: Rate of mass loss of I coating at a 75% (750W) power setting and under a -790 mV CP.....	106
Figure 4.31: Progression of erosion for I coating.....	107
Figure 4.32: Mass loss of P coating at a 75% (750W) power setting and under a -790 mV CP.	108
Figure 4.33: Rate of mass loss of P coating at a 75% (750W) power setting and under a -790 mV CP.....	108
Figure 4.34: Progression of erosion for P coating.....	109
Figure 4.35: Mass loss of A coating at a 75% (750W) power setting and under a -790 mV CP.	110
Figure 4.36: Rate of mass loss of A coating at a 75% (750W) power setting and under a -790 mV CP.....	110
Figure 4.37: Progression of erosion for A coating.....	111
Figure 4.38: Mass loss of Double coating at a 75% (750W) power setting and under a -790 mV CP.....	112
Figure 4.39: Rate of mass loss of Double coating at a 75% (750W) power setting and under a -790 mV CP.	112
Figure 4.40: Progression of erosion for Double coating.....	113
Figure 4.41: Mass loss of R coating at a 75% (750W) power setting and under a -790 mV CP.	114
Figure 4.42: Rate of mass loss of R coating at a 75% (750W) power setting and under a -790 mV CP.....	114
Figure 4.43: Mass loss of B coating at a 75% (750W) power setting and under a -790 mV CP.	115
Figure 4.44: Rate of mass loss of B coating at a 75% (750W) power setting and under a -790 mV CP.....	116
Figure 4.45: Erosion bump of B coating.	117
Figure 4.46: Mass loss of C coating at a 75% (750W) power setting and under a -790 mV CP.	117
Figure 4.47: Rate of mass loss of C coating at a 75% (750W) power setting and under a -790 mV CP.....	118
Figure 4.48: Mass loss comparison - Virgin alloys.....	119
Figure 4.49: Rate of mass loss comparison – Virgin alloys.....	119
Figure 4.50: Mass loss comparison – Protective coatings.....	120
Figure 4.51: Rate of mass loss comparison – Protective coatings.....	120
Figure 4.52: Mass loss comparison – Protective coatings (except I, Double).....	121
Figure 4.53: Rate of mass loss comparison – Protective coatings (except I, Double).....	121
Figure 4.54: Mass loss comparison – All specimens.....	122
Figure 4.55: Rate of mass loss comparison – All specimens.	122
Figure 4.56: Mass loss comparison – All specimens (except I, Double).....	123
Figure 4.57: Rate of mass loss comparison – All specimens (except I, Double).....	123
Figure 5.1: Keyence VHX-700F digital optical microscope and Z500R lens (x500-5000).	128
Figure 5.2: Microscopic appearance of cavitation - induced erosion for Grade DH36 steel (x500).....	129
Figure 5.3: 3D illustration of erosion pit (1). Grade DH36 steel.....	130
Figure 5.4: 3D illustration of erosion pit (1). Grade DH36 steel – Colour contour.....	130

Figure 5.5: Microscopic appearance of cavitation - induced erosion for stainless steel 254 (x500).	131
Figure 5.6: 3D illustration of erosion pit (1). Stainless steel 254.	132
Figure 5.7: 3D illustration of erosion pit (1). Stainless steel 254 – Colour contour.	132
Figure 5.8: Microscopic appearance of cavitation - induced erosion for cupronickel 70-30 (x500).	133
Figure 5.9: 3D illustration of erosion pit (1). Cupronickel 70-30.	134
Figure 5.10: 3D illustration of erosion pit (1). Cupronickel 70-30 – Colour contour.	134
Figure 5.11: Microscopic appearance of cavitation related erosion for I coating (x500).	136
Figure 5.12: 3D illustration of erosion pit (1). I coating.	137
Figure 5.13: 3D illustration of erosion pit (1). I coating – Colour contour.	137
Figure 5.14: Microscopic appearance of cavitation - induced erosion for P coating (x500).	138
Figure 5.15: 3D illustration of erosion pit (1). P coating.	139
Figure 5.16: 3D illustration of erosion pit (1). P coating – Colour contour.	139
Figure 5.17: Microscopic appearance of cavitation - induced erosion for the A coating (x500).	140
Figure 5.18: 3D illustration of erosion pit (1). A coating.	141
Figure 5.19: 3D illustration of erosion pit (1). A coating – Colour contour.	141
Figure 5.20: Microscopic appearance of cavitation - induced erosion for Double coating (x500).	142
Figure 5.21: 3D illustration of erosion pit (1). Double coating.	143
Figure 5.22: 3D illustration of erosion pit (1). Double coating – Colour contour.	143
Figure 5.23: Microscopic appearance of cavitation related erosion for R coating (x500).	144
Figure 5.24: 3D illustration of erosion pit (1). R coating.	145
Figure 5.25: 3D illustration of erosion pit (1). R coating – Colour contour.	145
Figure 5.26: Microscopic appearance of, cavitation – induced, erosion for B coating (x500).	146
Figure 5.27: 3D illustration of erosion pit (1). B coating.	147
Figure 5.28: 3D illustration of erosion pit (1). B coating – Colour contour.	147
Figure 5.29: Microscopic appearance of, cavitation – induced, erosion for C coating (x500).	148
Figure 5.30: 3D illustration of erosion pit (1). C coating.	149
Figure 5.31: 3D illustration of erosion pit (1). C coating – Colour contour.	149
Figure 5.32: Left – Ductile failure, Right – Brittle failure. (Source: University of Southampton).	151
Figure 5.33: Ductile – brittle transition	152
Figure 5.34: Scanning electron microscope (SEM) fractograph of ductile fracture dimples in low carbon steel. (Source: ASM International, 1992).	153
Figure 5.35: Intergranular and Transgranular fracture. (Source, GO-TECH, n.d.).	154
Figure 5.36: Scanning electron microscope (SEM) image of carbon steel. Left – Transgranular fracture, Right – Intergranular fracture. (Source: ASM International, 1992).	154
Figure 5.37: Combination of ductile dimples and transgranular fracture in carbon steel. (Source: CITIMETAL GROUP CORP., n.d.).	155
Figure 5.38: Stress – Strain Curve. Left (fcc), Right (bcc – stainless steel 254, cupronickel 70-30).	156
Figure 5.39: Eroded surface of grade DH36 steel.	158
Figure 5.40: Microscopic images of non-eroded (Top) and eroded (Bottom) grade DH36 steel. Arrows: Green – Intergranular, Blue – Transgranular, Red – Ductile.	159

Figure 5.41: SEM image of an eroded (5h) grade DH36 steel specimen. Arrows: Green – Intergranular, Blue – Transgranular, Red – Ductile.....	160
Figure 5.42: Erosion progression for grade DH36 steel. SEM images. Top-0.5h, Middle 2.5h, Bottom-5h. Arrows: Green – Intergranular, Blue – Transgranular, Red – Ductile.	161
Figure 5.43: Rate of mass loss of Grade DH36 steel.	162
Figure 5.44: Eroded surface of stainless steel 254.....	163
Figure 5.45: Microscopic images of non-eroded (Top) and eroded (Bottom) stainless steel 254. Arrows: Green – Intergranular, Blue – Transgranular, Red – Ductile.	164
Figure 5.46: SEM image of an eroded (5h) stainless steel 254 specimen. Arrows: Green – Intergranular, Blue – Transgranular, Red – Ductile.....	165
Figure 5.47: Erosion progression for stainless steel 254. SEM images. Top-0.5h, Middle 2.5h, Bottom-5h. Arrows: Green – Intergranular, Blue – Transgranular, Red – Ductile.	166
Figure 5.48: Rate of mass loss of stainless steel 254.....	167
Figure 5.49: Eroded surface of cupronickel 70-30.....	168
Figure 5.50: Microscopic images of non-eroded (Top) and eroded (Bottom) cupronickel 70-30. Arrows: Green – Intergranular, Blue – Transgranular, Red – Ductile.	169
Figure 5.51: SEM image of an eroded (5h) cupronickel 70-30 specimen. Arrows: Green – Intergranular, Blue – Transgranular, Red – Ductile.....	170
Figure 5.52: Erosion progression for cupronickel 70-30. SEM images. Top-0.5h, Middle 2.5h, Bottom-5h. Arrows: Green – Intergranular, Blue – Transgranular, Red – Ductile.	171
Figure 5.53: Rate of mass loss of cupronickel 70-30.	172
Figure 6.1: Crack propagation modes (Source: NPTEL).....	179
Figure 6.2: The propagation of a longitudinal wave in air (Source: Antonine-Education, n.d.)	182
Figure 6.3: Transverse and longitudinal waves (Source: Saada, 1993).....	185
Figure 6.4: Asymmetric and symmetric Lamb waves (Source: NDT Resource centre, n.d.) ...	186
Figure 6.5: Lamb waves - Dispersion curves for a 5mm thick steel plate.	187
Figure 6.6: Lamb waves - Dispersion curves for a 1mm thick steel plate.	188
Figure 6.7: The arrival of the S0 and A0 modes at a distant acoustic sensor.....	188
Figure 6.8: Acoustic emission sensing system – Illustration.....	189
Figure 6.9: Acoustic emission sensing system	189
Figure 6.10: Acoustic sensor mounted on the test plate – specimen.....	190
Figure 6.11: Top– PVDF and brass sensor, Bottom – Brass and aluminum Sensor along with its piezoelectric crystal sitting in its case.....	191
Figure 6.12: Mass loss of grade DH36 steel for various test rig configurations	192
Figure 6.13: AE Distribution (4mm–5%, 3mm–5%, 2mm–5% and 1mm–5%).....	195
Figure 6.14: AE Distribution (1mm–5%, 1mm–10%, 1mm–20% and 1mm–30%)	196
Figure 6.15: AE Distribution (1mm–30%, 1mm–40%, 1mm–50% and 1mm–75%)	196
Figure 6.16: AE Distribution (4mm–5%, 3mm–5%, 2mm–5% and 1mm–5%).....	197
Figure 6.17: AE Distribution (1mm–5%, 1mm–10%, 1mm–20% and 1mm–30%)	197
Figure 6.18: AE Distribution (1mm–30%, 1mm–40%, 1mm–50% and 1mm–75%)	198
Figure 6.19: AE Distribution (4mm–5%, 3mm–5%, 2mm–5% and 1mm–5%).....	198
Figure 6.20: AE Distribution (1mm–5%, 1mm–10%, 1mm–20% and 1mm–30%)	199
Figure 6.21: AE Distribution (1mm–30%, 1mm–40%, 1mm–50% and 1mm–75%)	199
Figure 6.22: AE Distribution (4mm–5%, 3mm–5%, 2mm–5% and 1mm–5%).....	200
Figure 6.23: AE Distribution (1mm–5%, 1mm–10%, 1mm–20% and 1mm–30%)	200

Figure 6.24: AE Distribution (1mm–30%, 1mm–40%, 1mm–50% and 1mm–75%).....	201
Figure 6.25: AE Distribution (4mm–5%, 3mm–5%, 2mm–5% and 1mm–5%).....	201
Figure 6.26: AE Distribution (1mm–5%, 1mm–10%, 1mm–20% and 1mm–30%).....	202
Figure 6.27: AE Distribution (1mm–30%, 1mm–40%, 1mm–50% and 1mm–75%).....	202
Figure 6.28: AE Distribution (4mm–5%, 3mm–5%, 2mm–5% and 1mm–5%).....	203
Figure 6.29: AE Distribution (1mm–5%, 1mm–10%, 1mm–20% and 1mm–30%).....	203
Figure 6.30: AE Distribution (1mm–30%, 1mm–40%, 1mm–50% and 1mm–75%).....	204
Figure 6.31: AE Distribution (4mm–5%, 3mm–5%, 2mm–5% and 1mm–5%).....	204
Figure 6.32: AE Distribution (1mm–5%, 1mm–10%, 1mm–20% and 1mm–30%).....	205
Figure 6.33: AE Distribution (1mm–30%, 1mm–40%, 1mm–50% and 1mm–75%).....	205
Figure 6.34: AE Distribution (4mm–5%, 3mm–5%, 2mm–5% and 1mm–5%).....	206
Figure 6.35: AE Distribution (1mm–5%, 1mm–10%, 1mm–20% and 1mm–30%).....	206
Figure 6.36: AE Distribution (1mm–30%, 1mm–40%, 1mm–50% and 1mm–75%).....	207
Figure 6.37: AE Distribution (4mm–5%, 3mm–5%, 2mm–5% and 1mm–5%).....	207
Figure 6.38: AE Distribution (1mm–5%, 1mm–10%, 1mm–20% and 1mm–30%).....	208
Figure 6.39: AE Distribution (1mm–30%, 1mm–40%, 1mm–50% and 1mm–75%).....	208
Figure 6.40: AE Distribution (4mm–5%, 3mm–5%, 2mm–5% and 1mm–5%).....	210
Figure 6.41: AE Distribution (1mm–5%, 1mm–10%, 1mm–20% and 1mm–30%).....	211
Figure 6.42: AE Distribution (1mm–30%, 1mm–40%, 1mm–50% and 1mm–75%).....	211
Figure 6.43: FFT – Aluminium Sensor – DH36 steel (4mm-5%, 3mm-5%, 1mm-5%, 1mm-50%).....	212
Figure 6.44: AE Distribution (4mm–5%, 3mm–5%, 2mm–5% and 1mm–5%).....	212
Figure 6.45: AE Distribution (1mm–5%, 1mm–10%, 1mm–20% and 1mm–30%).....	213
Figure 6.46: AE Distribution (1mm–30%, 1mm–40%, 1mm–50% and 1mm–75%).....	213
Figure 6.47: FFT – Brass Sensor – DH36 steel (4mm-5%, 3mm-5%, 1mm-5%, 1mm-50%)..	214
Figure 6.48: AE Distribution (4mm–5%, 3mm–5%, 2mm–5% and 1mm–5%).....	214
Figure 6.49: AE Distribution (1mm–5%, 1mm–10%, 1mm–20% and 1mm–30%).....	215
Figure 6.50: AE Distribution (1mm–30%, 1mm–40%, 1mm–50% and 1mm–75%).....	215
Figure 6.51: FFT – PVDF Sensor – DH36 steel (4mm-5%, 3mm-5%, 1mm-5%, 1mm-50%).	216
Figure 6.52: Mass loss of cupronickel 70 -30 for various test rig configurations.....	218
Figure 6.53: Mass loss of stainless steel 254 for various test rig configurations	219
Figure 6.54: AE Distribution - Grade DH36 steel	220
Figure 6.55: AE Distribution – Cupronickel 70-30.....	221
Figure 6.56: AE Distribution – Stainless steel 254.....	221
Figure 6.57: Stress distribution for grade DH36 steel. Aluminium sensor (LPD).....	226
Figure 6.58: Stress distribution for grade DH36 steel. Brass sensor (LPD).....	227
Figure 6.59: Stress distribution for grade DH36 steel. PVDF sensor (LPD).....	227
Figure 6.60: Induced stress distribution for grade DH36 steel. Aluminium sensor (TO)	229
Figure 6.61: Induced stress distribution for grade DH36 steel. Brass sensor (TO).....	229
Figure 6.62: Induced stress distribution for grade DH36 steel. PVDF sensor (TO).....	230
Figure 6.63: Induced stress distribution for cupronickel 70-30. Aluminium sensor (LPD)	233
Figure 6.64: Induced stress distribution for stainless steel 254. Aluminium sensor (LPD).....	235
Figure 6.65: The operation of a fibre Bragg grating sensor. (Source: National Instruments – NI, n.d.)	237
Figure 6.66: Left – Attached FBG sensors layout, Right – Test rig.	239
Figure 6.67: SM130 Optical Sensor Interrogator unit. (Source: Micron Optics, n.d.).....	239

Figure 6.68: Visualised wavelength shift of the sensors for different sonotrode positions. Top (Left – Right), Bottom – Centre.....	240
Figure 6.69: Fibre Bragg grating (FBG) – based acoustic emission sensing system.....	241
Figure 6.70: FFT – FBG sensor – DH36 steel (4mm-5%, 3mm-5%, 1mm-5%, 1mm-50%)	242
Figure 6.71: FFT comparison of different piezoelectric sensors.	243
Figure 6.72: Fracture toughness vs Mass loss.....	245
Figure 6.73: Fracture toughness vs Average pit depth.....	245
Figure 6.74: Fracture toughness vs Average pit volume	246
Figure 7.1: Half-rudder model. Top-exterior, bottom-interior.....	250
Figure 7.2: Hielscher UP200Ht ultrasonic transducer and sonotrode (Source: Hielscher - Ultrasound Technology, n.d.).....	251
Figure 7.3: UIP1000hd ultrasonic transducer mounted onto the adjustable base inside the water tank.....	252
Figure 7.4: Half-rudder model positioned inside the water tank.....	253
Figure 7.5: Top – Rudder with acoustic sensor (Drawing) – Rudder with acoustic sensor position marked by red square (Image).....	255
Figure 7.6: Rudder with acoustic sensor (Drawing). Different sonotrode locations (P1,P2,P3).	255
Figure 7.7: Top – Location of the four acoustic sensors (drawing). Middle – Location of the four acoustic sensors (image). Bottom – Mounted acoustic sensors (image).....	257
Figure 7.8: Coordinates of different sensors and sonotrode placements on the half rudder model.....	259
Figure 7.9: Different sonotrode placements (P1, P2, P3) and the centrally located piezoelectric sensor.	260
Figure 7.10: Acoustic Power (dB) distribution curves for different sonotrode placements and various test rig configurations with regards to the rudder as well as the small rectangular specimen (Grade DH36 steel).	261
Figure 7.11: Stress (MPa) distribution curves for different sonotrode placements and test rig configurations as well as the small rectangular specimen (Grade DH36 steel).....	262
Figure 7.12: Double size half-rudder model. Top-exterior, bottom-interior.....	266
Figure 7.13: Double size half-rudder model ‘hanged’ into the plastic water tank. The mounted probe of the UIP1000hd ultrasonic transducer can also be seen.....	267
Figure 7.14: Double size rudder with acoustic sensor (Drawing). Different sonotrode locations (P1,P2,P3).....	268
Figure 7.15: Double size rudder. Acoustic power (dB) distribution results for various sonotrode placements (P1, P2, P3) and test rig configurations.....	268
Figure 7.16: Double size rudder. Stress distribution for sonotrode placements P1, P2, P3.....	270
Figure 7.17: Coordinates of sensors and sonotrode placements on the double size rudder.....	272
Figure 7.18: Full scale ship rudder – Property of BAE Systems.....	274
Figure A1: Top -Two acoustic sensors along with their preamplifiers installed at crucial points of the ship structure. Bottom – BALRUE Data Acquisition Unit and Laptop.....	306
Figure A2: Gauge length strain extensometers installed at crucial points of the ship structure.	307
Figure A3: Strain – Stress response of four gauge length strain extensometers during sea trials.	308
Figure C1: Acoustic emission source location at the intersection of three circles. Rudder.	313
Figure D1: Sonotrode placement (0, 10) – Piezoelectric sensor based system.....	317

Figure D2: Filtered waveforms from all piezoelectric sensors (0, 10)	318
Figure D3: Sonotrode placement (0, 13) – Piezoelectric sensor based system	319
Figure D4: Filtered waveforms from all piezoelectric sensors (0, 13)	319
Figure D5: Sonotrode placement (0, 16) – Piezoelectric sensor based system	320
Figure D6: Filtered waveforms from all piezoelectric sensors (0, 16)	321
Figure D7: Sonotrode placement (0, 19) – Piezoelectric sensor based system	322
Figure D8: Filtered waveforms from all piezoelectric sensors (0, 19)	322
Figure D9: Sonotrode placement (0, 22) – Piezoelectric sensor based system	323
Figure D10: Filtered waveforms from all piezoelectric sensors (0, 22)	324
Figure D11: Sonotrode placement (6.5, 16) – Piezoelectric sensor based system	325
Figure D12: Filtered waveforms from all piezoelectric sensors (6.5, 16)	325
Figure D13: Sonotrode placement (13, 16) – Piezoelectric sensor based system	326
Figure D14: Filtered waveforms from all piezoelectric sensors (13, 16)	327
Figure D15: Sonotrode placement (3.2, 8) – Piezoelectric sensor based system	328
Figure D16: Filtered waveforms from all piezoelectric sensors (3.2, 8)	328
Figure D17: Sonotrode placement (3.2, 24) – Piezoelectric sensor based system	329
Figure D18: Filtered waveforms from all piezoelectric sensors (3.2, 24)	330
Figure D19: Sonotrode placement (9.8, 8) – Piezoelectric sensor based system	331
Figure D20: Filtered waveforms from all piezoelectric sensors (9.8, 8)	331
Figure D21: Sonotrode placement (9.8, 24) – Piezoelectric sensor based system	332
Figure D22: Filtered waveforms from all piezoelectric sensors (9.8, 24)	333
Figure D23: Sonotrode placement (0, 10) – FBG sensor based system	334
Figure D24: Filtered waveforms from all FBG sensors (0, 10)	335
Figure D25: Sonotrode placement (0, 13) – FBG sensor based system	336
Figure D26: Filtered waveforms from all FBG sensors (0, 13)	336
Figure D27: Sonotrode placement (0, 16) – FBG sensor based system	337
Figure D28: Filtered waveforms from all FBG sensors (0, 16)	338
Figure D29: Sonotrode placement (0, 19) – FBG sensor based system	339
Figure D30: Filtered waveforms from all FBG sensors (0, 19)	339
Figure D31: Sonotrode placement (0, 22) – FBG sensor based system	340
Figure D32: Filtered waveforms from all FBG sensors (0, 22)	341
Figure D33: Sonotrode placement (6.5, 16) – FBG sensor based system	342
Figure D34: Filtered waveforms from all FBG sensors (6.5, 16)	342
Figure D35: Sonotrode placement (13, 16) – FBG sensor based system	343
Figure D36: Filtered waveforms from all FBG sensors (13, 16)	344
Figure D37: Sonotrode placement (3.2, 8) – FBG sensor based system	345
Figure D38: Filtered waveforms from all FBG sensors (3.2, 8)	345
Figure D39: Sonotrode placement (3.2, 24) – FBG sensor based system	346
Figure D40: Filtered waveforms from all FBG sensors (3.2, 24)	347
Figure D41: Sonotrode placement (9.8, 8) – FBG sensor based system	348
Figure D42: Filtered waveforms from all FBG sensors (9.8, 8)	348
Figure D43: Sonotrode placement (9.8, 24) – FBG sensor based system	349
Figure D44: Filtered waveforms from all FBG sensors (9.8, 24)	350
Figure E1: Test rig and water recirculation system	352
Figure E2: Mass loss comparison between the MetaLine 785 and coatings from another supplier – Best coatings	353

Figure E3: Mass loss comparison between the MetaLine 785 and coatings from another supplier – All coatings	353
Figure E4: Erosion progress. From left to right: 0h-2h-5h	354
Figure E5: Distinctive bump at 100x (Left)-3D representation of the identified erosion pit on the bump at x500(Right)-Optical Microscopy	354
Figure E6: Erosion pattern after 5h of cavitation at 100x. From left to right: Metaline-A-B. Optical microscopy	355
Figure E7: Cross-like feature at the top of the distinctive bump	355
Figure E8: Erosion progress during the extended exposure. From left to right: 7h-15h-25h ..	356
Figure E9: 1Kg steel ball and the three coatings – From left to right- Metaline, R and C.....	357
Figure E10: From left to right – Metaline, R and C coatings before impact.	358
Figure E11: From left to right – Metaline, R and C coatings after impact.....	358
Figure E12: From left to right – Metaline, R and C coatings after impact (20x).....	358
Figure E13: From top to bottom – Metaline, R and C coatings after impact (3D).....	359
Figure E14: Mass loss due to steel ball impact.....	360
Figure E15: Mass loss comparison. Steel ball impact – Cavitation.....	360
Figure F1: 3D illustration of erosion pit (2). Grade DH36 steel.	360
Figure F2: 3D illustration of erosion pit (2). Grade DH36 steel – Colour contour.	360
Figure F3: 3D illustration of erosion pit (3). Grade DH36 steel.	360
Figure F4: 3D illustration of erosion pit (3). Grade DH36 steel – Colour contour.	360
Figure F5: 3D illustration of erosion pit (2). Stainless steel 254.	360
Figure F6: 3D illustration of erosion pit (2). Stainless steel 254 – Colour contour.	360
Figure F7: 3D illustration of erosion pit (3). Stainless steel 254.	360
Figure F8: 3D illustration of erosion pit (3). Stainless steel 254 – Colour contour.	360
Figure F9: 3D illustration of erosion pit (2). Cupronickel 70-30.	360
Figure F10: 3D illustration of erosion pit (2). Cupronickel 70-30 – Colour contour.	360
Figure F11: 3D illustration of erosion pit (3). Cupronickel 70-30.	360
Figure F12: 3D illustration of erosion pit (3). Cupronickel 70-30 – Colour contour.	360
Figure F13: 3D illustration of erosion pit (2). I coating.....	360
Figure F14: 3D illustration of erosion pit (2). I coating – Colour contour.....	360
Figure F15: 3D illustration of erosion pit (3). I coating.....	360
Figure F16: 3D illustration of erosion pit (3). I coating – Colour contour.....	360
Figure F17: 3D illustration of erosion pit (2). P coating.....	360
Figure F18: 3D illustration of erosion pit (2). P coating – Colour contour.....	360
Figure F19: 3D illustration of erosion pit (3). P coating.....	360
Figure F20: 3D illustration of erosion pit (3). P coating – Colour contour.....	360
Figure F21: 3D illustration of erosion pit (2). A coating.....	360
Figure F22: 3D illustration of erosion pit (2). A coating – Colour contour.....	360
Figure F23: 3D illustration of erosion pit (3). A coating.....	360
Figure F24: 3D illustration of erosion pit (3). A coating – Colour contour.....	360
Figure F25: 3D illustration of erosion pit (2). Double coating.....	360
Figure F26: 3D illustration of erosion pit (2). Double coating – Colour contour.....	360
Figure F27: 3D illustration of erosion pit (3). Double coating.....	360
Figure F28: 3D illustration of erosion pit (3). Double coating – Colour contour.....	360
Figure F29: 3D illustration of erosion pit (2). R coating.....	360
Figure F30: 3D illustration of erosion pit (2). R coating – Colour contour.....	360

Figure F31: 3D illustration of erosion pit (3). R coating.....	360
Figure F32: 3D illustration of erosion pit (3). R coating – Colour contour.....	360
Figure F33: 3D illustration of erosion pit (2). B coating.....	360
Figure F34: 3D illustration of erosion pit (2). B coating – Colour contour.....	360
Figure F35: 3D illustration of erosion pit (3). B coating.....	360
Figure F36: 3D illustration of erosion pit (3). B coating – Colour contour.....	360
Figure F37: 3D illustration of erosion pit (2). C coating.....	360
Figure F38: 3D illustration of erosion pit (2). C coating – Colour contour.....	360
Figure F39: 3D illustration of erosion pit (3). C coating.....	360
Figure F40: 3D illustration of erosion pit (3). C coating – Colour contour.....	360

List of Tables

Table 3.1: Tap water chemical analysis	79
Table 5.1: Characteristics of the three base alloys - Microscopy	135
Table 5.2: Fracture mechanics attributes of the examined alloys	175
Table 6.1: Fracture toughness values of the three examined alloys	244
Table 7.1: Source location measurements – Half rudder model.....	264
Table 7.2: Source location measurements – Double size half rudder model.....	272
Table D1: Results chart (0, 10) – Piezoelectric sensor based system.....	318
Table D2: Results chart (0, 13) – Piezoelectric sensor based system.....	320
Table D3: Results chart (0, 16) – Piezoelectric sensor based system.....	321
Table D4: Results chart (0, 19) – Piezoelectric sensor based system.....	323
Table D5: Results chart (0, 22) – Piezoelectric sensor based system.....	324
Table D6: Results chart (6.5, 16) – Piezoelectric sensor based system.....	326
Table D7: Results chart (13, 16) – Piezoelectric sensor based system.....	327
Table D8: Results chart (3.2, 8) – Piezoelectric sensor based system.....	329
Table D9: Results chart (3.2, 24) – Piezoelectric sensor based system.....	330
Table D10: Results chart (9.8, 8) – Piezoelectric sensor based system.....	332
Table D11: Results chart (9.8, 24) – Piezoelectric sensor based system.....	333
Table D12: Results chart (0, 10) – FBG sensor based system.....	335
Table D13: Results chart (0, 13) – FBG sensor based system.....	337
Table D14: Results chart (0, 16) – FBG sensor based system.....	338
Table D15: Results chart (0, 19) – FBG sensor based system.....	340
Table D16: Results chart (0, 22) – FBG sensor based system.....	341
Table D17: Results chart (6.5, 16) – FBG sensor based system.....	343
Table D18: Results chart (13, 16) – FBG sensor based system.....	344
Table D19: Results chart (3.2, 8) – FBG sensor based system.....	346
Table D20: Results chart (3.2, 24) – FBG sensor based system.....	347
Table D21: Results chart (9.8, 8) – FBG sensor based system.....	349
Table D22: Results chart (9.8, 24) – FBG sensor based system.....	350

Acknowledgements

Firstly, I would like to thank my supervisor Professor John S. Carlton, for his thoughtful guidance and support throughout this study, both from a scientific and personal point of view. Apart from his constructive insights, he always had the way of motivating me towards the completion of this project, especially during hard times, something that I will always be grateful for. I would also wish to thank my second supervisor Professor Manolis Gavaises as well as Professor Dinos Arcoumanis for always being on my side whenever I asked for their input or help.

Moreover, I would like to thank Professor Tong Sun and her laboratory staff for our productive cooperation through these years as well as their willingness on assisting me even in matters outside the main scope of our work. The same applies for my friend and colleague Mr. Miodrag Vidakovic, with whom we went through and successfully completed a quite demanding project.

In addition, I would like to thank all of my colleagues for their support and assistance throughout these years, and especially Saeed, Giannis, Elena and Elham. I would also like to thank Mr Jim Hooker from the technical staff for being exceptionally supportive and proactive (many thanks for the ear protection!) in some cases.

Of course, I am especially grateful to Dr Leonard Rogers for his continuous support throughout my study as well as the opportunity he gave me to work with him on a very important international project. His expertise in the NDT field is unmatched and I am grateful for having the opportunity to work with him. I would also like to thank BAE Systems and especially Dr Caroline Voong and Dr Malcolm Robb for actively supporting my work. The same applies for the Lloyd's Register Foundation which supported me financially through my PhD.

Last but not least, I would like to thank my family and friends for supporting me through this quest, although this period has been exceptionally demanding for them. Love you all and will always be grateful for your support.

Ioannis Armakolas

February 2018

Declaration

I hereby declare that the presented work in this thesis is my own or was developed in a joint effort with other members of the research group as it is stated and referenced in the text accordingly!

I grant powers of discretion to the University Librarian to allow this thesis to be copied in whole or in part without further reference to me. This permission covers only single copies made for study purposes, subject to normal conditions of acknowledgement.

London, _____

(Ioannis Armakolas)

Abstract

The phenomenon of cavitation is of great importance when ship propellers and rudders are considered, as it can often be the cause of vibrations, noise, reduced efficiency and even erosion in some instances. The underlying fracture mechanisms of erosion, however, have not been fully understood yet.

As such, this study aims to expand our knowledge regarding the fracture mechanisms of common shipbuilding alloys and explore whether cavitation erosion can be monitored, by using the relevant quantitative and qualitative data. As such, an experimental test rig was built, based on the induction of cavitation by ultrasonic means, in order for a series of tests, including mass loss and acoustic emission measurements as well as microscopic observations to be conducted. Due to the interest of BAE Systems, a number of protective coatings were also examined under an analogous context.

Specimens were initially exposed to ultrasonically induced cavitation under identical experimental conditions. Mass loss was periodically measured thus materials were categorized in that respect while the positive effect of cathodic protection on the resulting erosion was confirmed. Examination through optical and scanning electron microscopes was also conducted thus the fracture mechanisms and macroscopic characteristics of cavitation erosion were identified, for each of the examined materials. Results showed that, erosion initiates through plastic deformation (orange peeling) before proceeding into ductile and brittle, due to work hardening, fracture, whereas the extent and crack propagation characteristics of each phase, depend on the material's mechanical properties and crystalline structure.

Acoustic emissions were also examined, with the aim of, characterizing the materials and potentially be utilized for erosion monitoring. Upon the successful establishment of acoustic thresholds for cavitation erosion, in the case of small specimens, a small model rudder was also examined under an analogous context, although in that instance, cavitation localization was also considered, through a triangulation source location technique. In that instance, cavitation induced erosion, was effectively monitored and characterized both in terms of intensity and location. A model rudder twice as large as the small one was also examined in order for any possible scale effects to be identified. Cavitation induced erosion, was again effectively monitored, both in terms of intensity and location, although results indicated that the method should be optimized, with respect to the parameter of size.

As such, the future researcher could further promote the evolvement of the aforementioned ship rudder monitoring system, by means of optimizing the analytical procedures in order to overcome any possible scale effects, further adapting the characteristics of the system to match the size of the objects to be monitored and eventually lead to the full – scale application of the system. The conduction of sea trials would also be of great benefit and importance towards the direction of forming a solid cavitation erosion monitoring system.

Nomenclature

Abbreviations

3D	Three - dimensional
AE	Acoustic emission
BCC	Body – centred cubic
CP	Cathodic protection
DAQ	Data acquisition
DBTT	Ductile – brittle transition temperature
FBG	Fibre Bragg grating
FCC	Face – centred cubic
FFT	Fast Fourier transform
LPD	Logarithmic peak detector
MFL	Magnetic flux leakage
MMM	Metal magnetic memory
NDT	Non – destructive testing
PHV	Propeller – hull vortex cavitation
PVDF	Polyvinylidene fluoride
RMF	Residual magnetic field
SEM	Scanning electron microscope

Roman Symbols

A	Constant of the logarithmic peak detector	-
B	Constant of the logarithmic peak detector	-
C	Characteristic conversion constant of the logarithmic unit	-
Ca	Cavitation number	-
c	Speed of sound	m/s
c_g	Group velocity	m/s
c_l	Speed of longitudinal sound waves	m/s
c_p	Phase speed	m
C_p	Specific heat at constant pressure	J/(Kg*K)
c_R	Rayleigh wave speed	m/s
c_t	Speed of transverse (shear) sound waves	m/s
C_v	Specific heat at constant volume	J/(Kg*K)
d	Plate thickness	m

D_t	Diameter of transducer	m
E	Young's modulus	Pa
e	Vapour pressure of the fluid	Pa
f	Frequency	Hz
G	Shear modulus	Pa
G_c	Critical strain energy release rate	J/m ²
H	Residual magnetic field	A/m
K_B	Bulk modulus	Pa
K_i	Magnetic field gradient	T
K_I	Stress intensity factor	Pa*m ^{0.5}
K_s	Applied stress / generated electric charge coefficient	-
M	Magnification factor	-
M	Plane wave modulus	Pa
m_{current}	Current mass of specimen after cavitation exposure	g
m_{initial}	Initial mass of specimen before cavitation exposure	g
M_m	Molar mass	Kg/mol
M_s	Momentum	N*s
N	Near field length	m
n	Quantity	mol
N₁₀₀	Number of grains per square inch at a x100 magnification	-
N₅₀₀	Number of grains per square inch at a x500 magnification	-
n_{ASTM}	ASTM grain size	-
n_{eff}	Effective refractive index of fibre Bragg grating	-
p	Pressure	Pa
P_∞	Pressure infinitely far from the bubble	Pa
P_g	Pressure of non – condensable gas in the bubble	Pa
p_l	Pressure of surrounding liquid	Pa
p_r	Reference pressure	Pa
p_v	Gas or vapour pressure inside a bubble	Pa
R	Bubble radius	m
r	Distance from crack tip	m
R_{cl}	Shear to bulk modulus ratio	-
R_{max}	Maximum bubble radius	m
s	Distance between bubble centre and surface	m
S	Surface tension	N/m
S_s	Surface energy	J/m ²

T	Temperature	K
t	Time	s
U	Total strain energy	J
U_r	Radial component of velocity	ω
U_x	Axial component of velocity	m/s
u	Velocity of fluid	m/s
v	Poisson's ratio	-
V	Voltage	V
V_r	Input voltage of the preamplifier	V
V_v	Volume	m ³
x	Coordinates – x axis	-
X	Logarithmically converted amplitude	V
Y	Amplitude of sound wave	dB
y	Coordinates – y axis	-
z	Coordinates – z axis	-

Greek Symbols

α	Width of crack	m
α_{FBG}	Linear thermal coefficient of the fibre	-
β	Fluid – material transmission factor	J/mm ³
γ	A material's surface energy density	J/m ²
γ_b	Free energy of the grain boundary	KJ/mol
γ_h	Ratio of specific heats	-
γ_r	Bubble centre to surface distance / Bubble's max radius	-
γ_s	Free energy of surface exposed by transgranular fracture	KJ/mol
δ_i	Time difference – Triangulation technique	s
η	Bubble's max radius / Distance from free surface	-
η*	Transmission efficiency	-
Λ	Grating period	nm
λ	Wavelength	m
λ_B	Bragg wavelength	nm
λ_k	Distance between two inspection points – MMM	m
λ_L	Lame constant	-
λ_w	Wavelength of sound wave	m
μ	Lame constant	-

μ_L	Dynamic viscosity of liquid	Pa*s
ξ	Thermos – optic coefficient	-
ρ	Density of medium	Kg/m ³
ρ_e	Effective photo - elastic	
σ_c	Critical stress	Pa
τ	Rayleigh collapse time	s
ω	Circular frequency	Hz

Chapter 1

Introduction

1.1 Motivation

Ships play a dominant role in the global trade and transport, as the Earth's surface is mostly covered by water, and they carry about 95% of goods at some point in their lifecycle. Nevertheless, some of their main mechanical devices and components, such as propellers and rudders, can be subject to significant deterioration due to the often-harsh operating conditions. Corrosion and erosion are mainly accountable, the former being caused by the electrochemical interaction between the mechanical components and the seawater in way that an electrochemical cell is formed and the latter from phenomena such as cavitation.

Cavitation is a general fluid dynamics phenomenon and can be defined as the rapid formation, growth and subsequent collapse of very small bubbles or cavities that contain vapour gas or air, within a liquid, in extremely small intervals of time, due to large pressure or velocity variations. Such conditions are commonly apparent in the operation of mechanical devices oriented towards the induction of momentum into liquids such as propellers, turbines and pumps as well as in components such as ship rudders and stabilizers. As a result, the operation of those mechanical devices and components is commonly affected by cavitation and its non-desirable effects.

Most importantly cavitation is commonly related to the deterioration of the exposed components and devices, as the continuous exposure of a solid material in shock waves of severe amplitude, due to cavitation induced bubble collapsing, can result into significant erosion (Preece, 1970; Arndt, 1981). This form of damage is widely known as cavitation erosion. In addition to erosion, the presence of significant noise as well as vibrations originating from the exposed components and devices is often reported by ship owners and operators.

The physical phenomenon of cavitation was first mentioned by Euler (1756) who observed a loss of performance in water wheels, whereas the first attempt to describe and analyse the underlying dynamics governing cavitation was made by Besant (1859) in the middle of the 19th century. A little more than a decade later, Reynolds (1873) published a paper where the over-speeding effect of cavitation on propellers was discussed thus he raised awareness

regarding the relation of the phenomenon to the marine industry. What he particularly observed was that, the rotational speed of the propeller shaft would rise significantly in the presence of cavitation of considerable intensity. The same over-speeding effect was noted by Sir Charles Parsons in 1894, in his experimental steam turbine propelled vessel called Turbinia (Carlton, 2012) which can be seen in Figure 1.1. Following Besant's work, a significant effort oriented towards the suggestion of a basic cavitation mechanism was undertaken by Rayleigh (1917) in his analysis of an isolated spherical void collapse in an incompressible liquid, followed by Parsons and Cook (1919).



Figure 1.1: Turbinia vessel at speed in 1894 (Source: Tyne & Wear Museums)

Sir Parson's preliminary observations lead him to build an enclosed circulating channel in order for small propellers of a diameter of 2 inches to be examined with regards to cavitation. This tunnel and a subsequent one built at Wallsend were the precursors of the larger tunnels that were built in Europe and America during the 1920s while even larger and modernized cavitation testing facilities were constructed around the world, in the years after. Observation techniques have also evolved through the years, with the introduction of borescope methods and the induction of faster and more light-sensitive cameras, that replaced traditional methods such as the observation of full-scale cavitation by means of windows cut into the ship's hull. In addition to the theoretical and experimental study of cavitation from a hydrodynamic point of view, research is also conducted in the field of materials science by means of extensive laboratory testing, using accelerated erosion tests for instance, in order for the resistance of a new material against cavitation induced erosion to be examined.

An example of a modern 49m long cavitation tunnel, owned by Mitsubishi Heavy Industries can be seen in Figure 1.2.



Figure 1.2: Cavitation tunnel owned by Mitsubishi Heavy Industries (Source: Mitsubishi Heavy Industries Mechatronics Systems, LTD.)

In general, cavitation is a non-desirable phenomenon, yet it has been used productively in a number of applications. In wastewater treatment for instance cavitation can be used for the destruction or removal of complex organic chemicals, particles and pollutants (Gogate, 2002). In this case cavitation, can be induced either acoustically by means of ultrasonic irradiation (Pandit and Moholkar, 1996) or hydrodynamically (Gogate and Pandit, 2001).

More recently, the induction of cavitation by means of laser beams or streams of protons has been suggested, although it has not yet been applied in large scale applications mainly due to complexity and cost related issues (Ozonek, 2012).

In addition to wastewater applications, the use of cavitation as means of water ballast treatment for the removal of invasive non-indigenous organisms that would had otherwise been transferred from an aquatic environment to another is also considered (Cvetkovic et al., 2015).

In the medical area, shock wave lithotripsy is gaining significant acceptance as a treatment choice for kidney stones (Williams et al., 1988) while evidence suggests that cavitation bubble collapse might be the dominant mechanism (Sass et al., 1992; Zhong et al., 1997; Zhu et al., 2002).

Acoustic cavitation has also been used in sonoporation, which is the process by which, a cell's plasma membrane permeability is modified to allow the uptake of genes or macromolecular drugs into the cell nuclei (Wu, 2006; Lentacker et al., 2014).

Hydrodynamic as well as acoustic cavitation has even been tested as means of biodiesel production with promising results (Kelkar et al., 2008; Pal et al., 2009; Pai et al., 2010; Ghayal et al., 2013).

1.2 Present study

Despite the numerous efforts, the way cavitation induced erosion acts, has not been adequately clarified yet, especially in relation to the properties of the affected materials. Furthermore, a methodology by means of which, the cavitation induced erosion of the affected components, could be directly monitored, has not been effectively implemented till this point. In contrast, the results of cavitation induced erosion, are mostly to be noticed indirectly, either through a loss of performance and efficiency or during an inspection.

As such, the main aim of this study is to approach and study the phenomenon of cavitation induced erosion in relation to some common shipbuilding materials such as grade DH36 steel, stainless steel and cupronickel, both from a quantitative and qualitative point of view. Towards that direction, specimens made from those materials are to be exposed to ultrasonically induced cavitation for a prolonged period of time, under experimental conditions that have been found, from previous studies, to maximize the resulting erosion rate. At the same time, a series of macroscopic and microscopic observations as well as a number of measurements relating to the effects of cavitation on the examined materials, will take place. An identical procedure will also be followed for a number of protective coatings supplied by BAE Systems.

Materials will initially be examined macroscopically. In particular, a series of mass loss measurements will be conducted in order for the effects of cavitation to be documented in a quantitative way as well as for the various erosion phases of each one of the examined materials to be identified. Additionally, the emerging erosion patterns on the eroded surfaces will be observed and studied macroscopically whereas the potential effects of cathodic protection on the resulting erosion rate are also to be examined. At the end of this phase, a preliminary hypothesis and comparison regarding the resistance of various shipbuilding materials against ultrasonically induced cavitation will be conducted.

The next phase of this study is oriented towards the microscopic exploration of the fractography of the eroded materials. Towards that direction, a series of observations will be

conducted through the lens of a digital optical microscope, in order for an initial estimation regarding the governing fracture mechanisms and patterns for each of the examined materials to be made. Those estimations will then be evaluated at a later stage by means of a scanning electron microscope (SEM). The potential correlation between the different phases of cavitation erosion, in terms of the already measured mass loss, and the observed fracture mechanisms of each of the materials will finally be explored and a relevant hypothesis will be composed.

Following the initial mass loss measurements and the subsequent microscopic observations, the acoustic emissions of each of the examined materials due to cavitation activity and erosion will then be measured and studied. Due to the high frequency nature of acoustic emissions however, specialized hardware will be designed and manufactured, such as custom piezoelectric transducers and fibre Bragg grating sensors which are essentially optical strain sensors. At the end of this phase the possible connection between cavitation erosion in terms of the already measured mass loss, the governing fracture mechanisms and the measured acoustic emissions will be investigated.

Finally, an investigation regarding the creation and development of a cavitation erosion monitoring system, based on the resulting acoustic emissions, will be conducted. Towards that direction, acoustic emission measurements will be conducted for a variety of experimental conditions, resulting into “non-erosive” and “erosive” cavitation, always in terms of the measured mass loss with the purpose of establishing acoustic ‘erosion’ thresholds for each one of the examined materials. Investigations will initiate by means of conducting tests on small specimens before the monitoring system eventually gets tested on rudder models of various sizes. In addition to the assessment of cavitation erosion intensity, damage localization techniques such as acoustic triangulation by means of an array of multiple acoustic sensors will also be examined.

Chapter 2

Literature Review

2.1 Introduction

The following literature review provides an overview of research, oriented towards the study of cavitation, both in relation to the underlying physics and its immediate effects, such as the erosion of the affected components. In this context, the induction of cavitation through the operation of ship propellers and rudders is initially discussed while some common experimental techniques that are utilized for investigative purposes are mentioned. Afterwards, the review focuses on cavitation itself and as such the first attempts to describe the phenomenon, both from a theoretical and practical point of view, are discussed, followed by some main findings and observations relating to the underlying physics. The cavitation induced erosion of materials is then discussed and as such studies oriented towards the investigation of the underlying mechanisms of erosion are presented along with the most important theoretical and experimental findings. Research relating to the acoustic emissions of materials due to erosion or fracture in general is eventually presented and discussed, along with studies oriented towards the application of non-destructive testing techniques (NDT), both in an experimental and practical context.

2.2 Cavitation experienced by ship propellers

A propeller produces thrust in order to move the ship across water, by means of developing suction over the backs and pressure over the face of its blades. Cavitation in the form of bubbles or cavities may occur, when the absolute pressure on the suction side falls below the vapour pressure of the water medium. Cavitation bubbles are usually unstable and tend to collapse violently while the radiated pressure waves can result into a series of undesired phenomena such as a significant amount of vibrations and noise as well as erosion.

Propellers may experience various forms of cavitation, depending on the operating conditions, the position of the ship and the design of the propeller itself. These are graphically illustrated in Figure 2.1 while the most common forms that can be observed in model as well as full scale propellers are further discussed (Newton, 1961; Carlton, 2012).

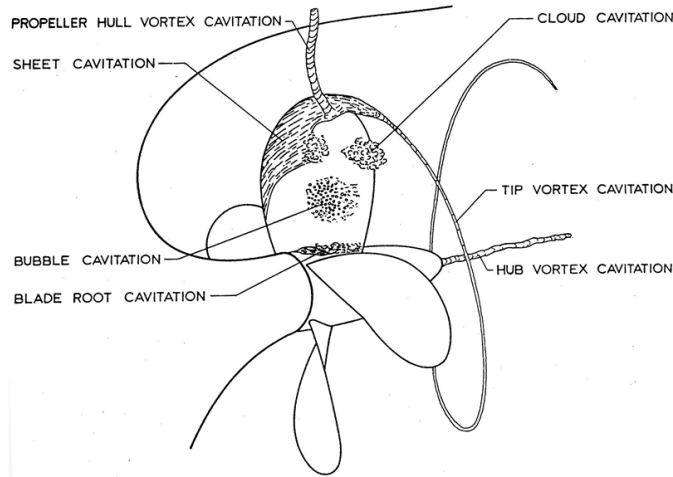


Figure 2.1: Different forms of cavitation, as they are experienced by a ship propeller (Source: Wijngaarden, 2012)

Tip vortex cavitation occurs at the tip of the propeller blade and can be initially observed at some distance behind the blade tips, thus it is said to be ‘unattached’. The vortex eventually becomes stronger and gets attached to the tip of the blade either when the blade loading increases or the cavitation number decreases. Cavitation number is a dimensional number, that is used in flow calculations and can be defined as follows:

$$Ca = \frac{p_0 - e}{\frac{1}{2}\rho u^2} \quad (2.1)$$

where p_0 is the reference pressure, e is the vapor pressure of the fluid, ρ is the density of the fluid and u its velocity.

Conversely, the hub vortex is created by a combination of vortices originating from the root of each blade and it is very likely to cavitate in the presence of a converging propeller cone. Hub vortex cavitation has the appearance of a rope of which the strands correspond to the number of blades of the propellers. A combination of tip and hub vortex cavitation can be seen in Figure 2.2:



Figure 2.2: Tip and hub vortex cavitation (Source: SVA Potsdam GmbH, n.d)

Cavitation can also be observed in the form of sheet, bubble and cloud cavitation. Sheet cavitation occurs at the leading edges of the propeller blades, either at the face or back surfaces, depending on the incidence angles.

In particular, sheet cavitation will develop at the back or suction side of the blade for positive incidence angles whereas it may initially appear at the face or pressure side of the blade for negative incidence angles. It is primarily caused by the large suction pressures that are apparent near the leading edge of the propeller blade, and may extend all over its surface, if the cavitation number decreases or the angle of incidence increases. Although sheet cavitation is generally stable, an occasional instability that can be observed in some instances, may cause propeller erosion.

The occurrence of sheet cavitation can be seen in Figure 2.3. Evidence of blade root cavitation is also apparent.

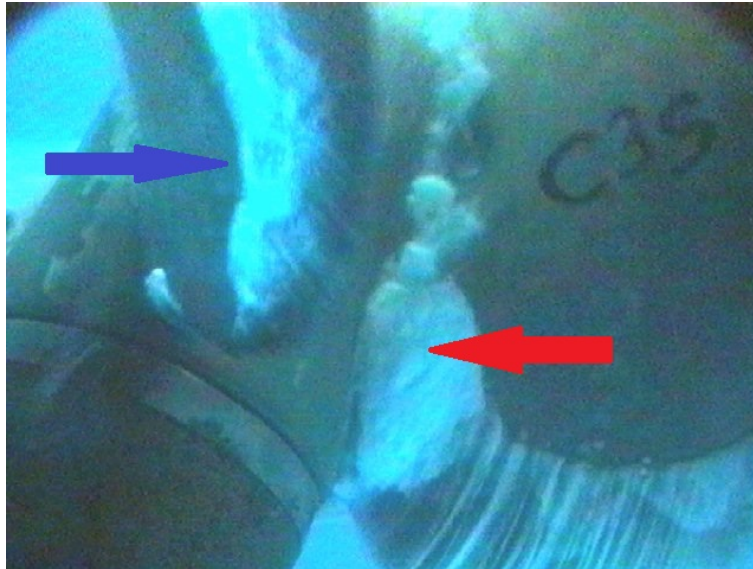


Figure 2.3: Evidence of sheet (blue arrow) and blade root (red arrow) cavitation (Source: Carlton, n.d.)

Conversely, bubble cavitation may be observed at the mid-chord region of the propeller blade if the section's camber line is too high, and it is mainly induced by the high suction pressures that are apparent in that area whereas it is generally characterized by the presence of large bubbles. Finally, cloud cavitation, which is considered to be particularly dangerous when it comes to propeller erosion, essentially consists of numerous very small bubbles and is usually found behind strongly developed and stable sheet cavities.

The presence of cloud cavitation is evident in Figure 2.4 along with other forms of cavitation such as sheet and tip vortex.

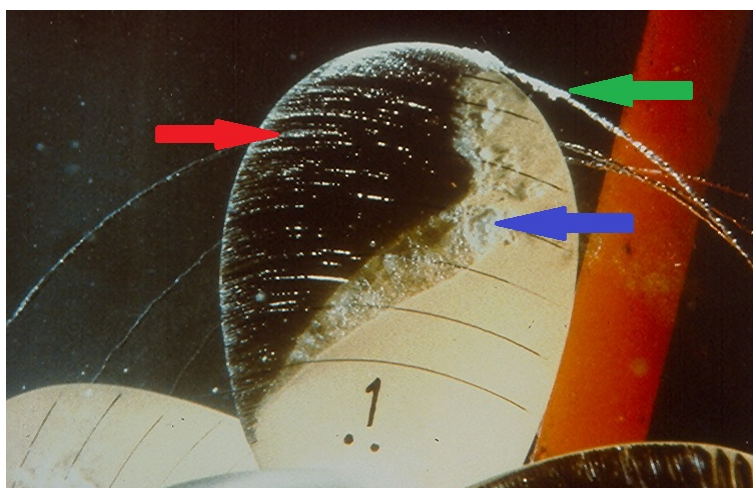


Figure 2.4: Cloud (blue arrow), sheet (red arrow) and tip vortex (green arrow) cavitation (Source: Carlton, n.d.)

Experiments have shown that the initiation of cloud cavitation is essentially triggered by the penetration of an attached sheet cavity by a re-entrant jet. This results into the formation of the bubbly cloud, which is then convected downstream (Kawanami et al., 1997).

The full – scale cavitating sheet and vortex cavitation, of an LNG ship propeller, can be seen in Figure 2.5:



Figure 2.5: Full – scale cavitating sheet and vortex cavitation of an LNG ship propeller (Source: Carlton, 2012).

Evidence of cavitation induced erosion on a small propeller can be seen in Figure 2.6:

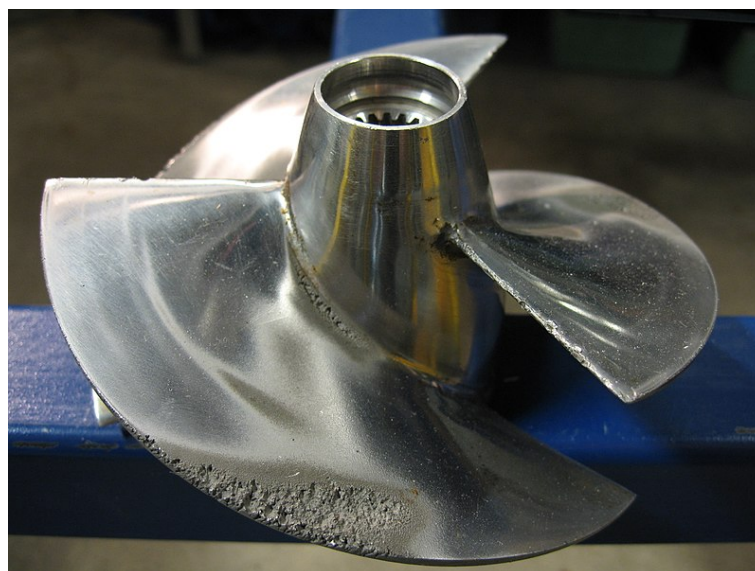


Figure 2.6: Evidence of cavitation induced erosion, on the propeller of a small personal watercraft (Source: Wikimedia Commons, 2006)

Finally, the propeller- hull vortex cavitation (PHV) may be observed in the form of cavitating vortices, extending from the propeller to the hull. The occurrence of the propeller – hull vortex cavitation phenomenon, can be seen in Figure 2.7:

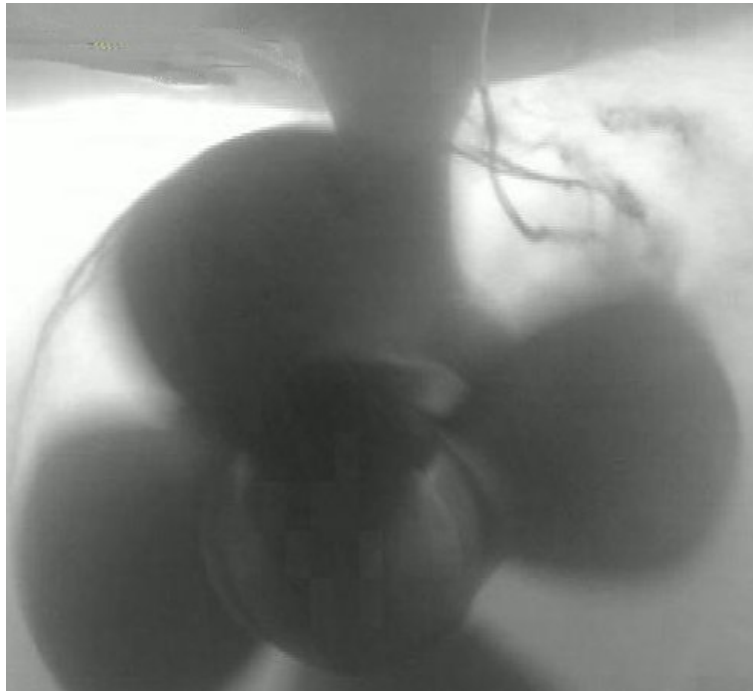


Figure 2.7: Propeller – Hull vortex cavitation emanating from a podded propulsion unit (Source: Carlton, 2012)

Common indicators of the presence of PHV cavitation in ships are vibrations and noise that can easily be heard from within the ship's hull. It was first reported by Huse (1971), who showed that PHV cavitation is stronger for small tip clearances and low advance coefficients. Certain hypotheses regarding the inception of PHV have been proposed, yet the one based on the “pirouette” effect is the most likely to be correct according to Huse, as it manages to explain many features of PHV. In particular, it is believed that, in high loading conditions, the propeller becomes starved of water, as the axial velocity that is induced by the propeller becomes equal to the inflow velocity. As a result, a stagnation point is created just above the propeller, at the hull plate, which then has to draw water from astern, leading to the creation of a streamline connecting the hull with the propeller. It is noteworthy that in the case of ducted propellers, Gent and Kooji (1976) and Kooji and Berg (1977) concluded that PHV is induced by the clearance between the hull and the duct as well as the relative position of the propeller blades.

2.3 Cavitation experienced by rudders and the propeller – rudder interaction

Rudders can be categorized into balanced and unbalanced variants with the former being fixed to the rudder shaft at the top of their plate and the latter having the shaft fixed along the length of their plate. Another category of rudders, called semi – balanced are commonly used in modern ships and are characterized by being partly balanced and partly unbalanced with regards to the position of the shaft.

An example of a semi – balanced ship rudder can be seen in Figure 2.8:

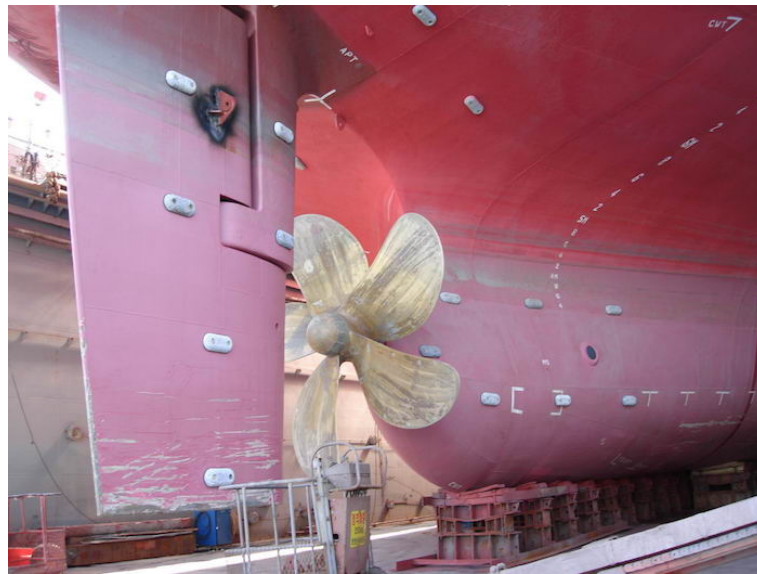


Figure 2.8: Semi – balanced rudder (Source: Marine Insight, 2017)

Rudders are the means of manoeuvring and control for ships whilst they also provide directional stability through the forces that are generated on their sides. They are usually positioned behind the flow field of the propeller, in an effort of enhancing their effectiveness thus they also suffer from the effects of cavitation mostly due to their hydrodynamic interaction with the propeller.

The interaction of a rudder with the tip vortex that is generated by the preceding propeller can be seen in Figure 2.9:

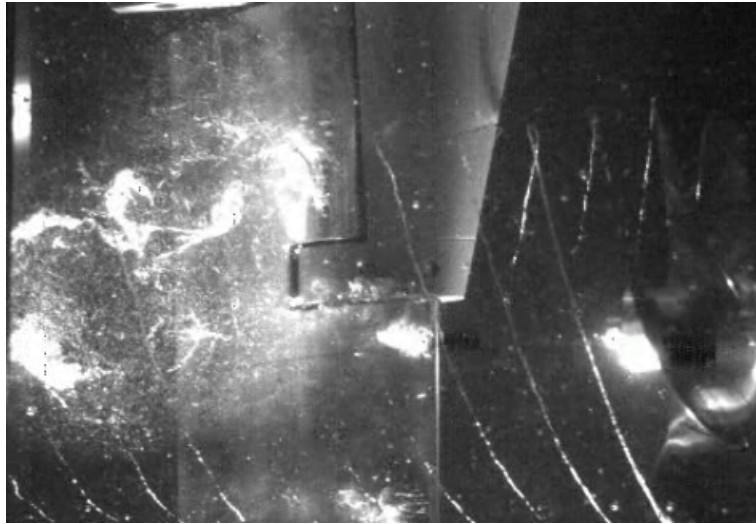


Figure 2.9: Rudder – propeller interaction (Source: SVA Potsdam GmbH, n.d)

Cavitation in rudders is mostly evident in two regions, namely the leading edge of the rudder as well the gap between its movable and fixed portion (Oh et al., 2012).

It is noteworthy that, in sea trials conducted by the U.S. Navy with a ship equipped with twin screws and rudders, it was found that rudders would experience extreme cavitation-induced erosion on their outboard surface, when speeds exceeded 23 knots, even in mild sea conditions and when course keeping manoeuvres were only performed. The inner surface of the rudders in contrast would experience no erosion at all whereas these observations were confirmed through dry dock inspection. This was due to the fact that the propellers were rotating in outboard directions and as such the rudders experienced the slipstream on their outboard surface (Shen et al. 1997a).

The presence of cavitation induced erosion on a full – scale ship rudder can be seen in Figure 2.10:



Figure 2.10: Cavitation induced erosion on the rudder of the Finnkraft vessel (Source: Carlton, n.d)

The theoretical aspects of the propeller – rudder interaction have been thoroughly investigated through the years. Tsakonas et al. (1975) stated that the rudder – propeller interaction is mainly governed by loading effects. Moriyama and Yamazaki (1981) managed to calculate the forces acting on a rudder by means of an analytical method while some years later Zhu and Dong (1986) developed a theoretical method by means of which the hydrodynamic interaction of propellers and rudders could be predicted. The approach from Tamashima et al. (1993) treated the propeller as an actuator disc and made use of a panel method to calculate the resulting forces on the rudder while at the same time Li (1994) developed a linear method, that allowed for calculations regarding the propeller rudder interaction to be made in relation to experimental results.

Han et al. (1999) made use of a boundary element method (BEM), in order to develop a numerical technique oriented towards the analysis of the propeller-rudder hydrodynamic interaction while results obtained through this method were successfully compared to experimental findings. In the following years, he and his colleagues developed a vortex lattice and surface panel method oriented towards the investigation of the flow around propellers and horn-type rudders, respectively (Han et al., 2001) whereas they compared their results to experimental measurements conducted at the Samsung Ship Model Basin (SSMB).

The propeller – rudder interaction has also been explored from a practical point of view by means of experiments conducted in wind tunnels (Molland, 1981; Molland and Turnock, 1991) where it was found that by increasing the propeller thrust loading the rudder side force

also increases. It was also found that for constant rpm, the presence of the rudder may affect the propeller's developed thrust and torque. Stierman (1989) showed, by means of experiments conducted in a towing basin with three propellers of varying pitch ratios and two rudders located at varying positions, that rudders can experience positive thrust at low advance ratios. Later on, Kracht (1992) characterized the propeller – rudder interaction by means of conducting lift, drag and cavitation measurements in towing basins for a variety of rudder configurations. In addition, Shen et al. (1997b) demonstrated that the presence of a hull can considerably affect the propeller – rudder interaction, though a series of theoretical and experimental measurements.

More recently, Kinnas et al. (2007) predicted the occurrence of sheet cavitation on rudders with respect to propeller effects, tunnel walls and time, by means of a vortex lattice method coupled with a finite volume method and a boundary element method. Rhee and Kim (2008) evaluated a new rudder system, that makes use of cam devices which effectively close the gap between the horn and the movable wing parts and it is oriented towards lift augmentation and cavitation suppression, by means of a three-dimensional flow analysis. It is noteworthy that, due to promising results the authors suggested that the utilization of the new rudder system should be investigated and considered further. At the same time, Paeik et al. (2008) managed to successfully visualize the flow characteristics around the gap of semi – balanced rudder by making use of particle image velocimetry (PIV) visualization and pressure measurements, in tests that were performed in a cavitation tunnel.

2.4 Cavitation physics

The process leading to cavitation has many similarities with the well-known phenomenon of a liquid that boils at a lower temperature as the altitude increases. With regards to cavitation, however, the dissolved air or nuclei tend to form cavities or bubbles containing gas or vapour, at the areas of the liquid where pressure drops below the vaporisation point at a constant temperature. When pressure rises again, these cavities collapse and as a result a series of undesired effects may occur. In the case of ship propellers for instance, such operational conditions are common, especially at the suction sides of the blades where cavitation mostly occurs, thus a number of undesired effects such as erosion as well as vibrations and noise are frequently observed.

Bubble collapsing due to cavitation is accompanied by a number of phenomena, such as fast emitting shock waves, high speed water jets and even light. With regards to the latter, light can sometimes be seen emitting from a cavitating liquid, in a phenomenon called

sonoluminescence, which can be ascribed to the extremely high temperatures resulting from the adiabatic compression of the trapped gas within the collapsing bubbles (Carlton, 2012). In particular, temperatures of the order of 100.000K have been suggested with regard to the surrounding fluid. Wheeler (1960) suggested that, conditions favourable to the initiation of chemical reactions between water and metal are induced by cavitation and thus estimated that the surface of an affected solid material may experience temperatures of the order of 500-800 °C, through the interpretation of monochrome and colour photomicrographs, showing the form and texture of the resulting indentations.

Definition of cavitation as a boiling phenomenon caused by low pressure, although accurate, misses a crucial factor, namely the ability of a liquid to withstand large tensions, a parameter closely related to the liquid's capacity of withstanding pressures beyond its vapour point without boiling. This factor mainly depends on the purity of the liquid, in the sense that an increased amount of dissolved air, microscopic gas bubbles or nuclei for instance, can significantly affect the ability of a liquid to withstand tensions. In this case cavitation, could even occur for pressures lower than the normal vapour point of liquid. It should be noted that the term nuclei refers to clusters of gas of sufficient size to allow subsequent growth when pressure drops. Conversely, in ideal conditions, where water could be considered as completely pure, it would withstand very large tensions without undergoing cavitation. In such a case for instance, values of the order of ≈ 140 MPa at 25 °C were obtained experimentally by isochoric cooling of ultra-pure water (Zheng, 1991). Nevertheless, in typical conditions, the tensile strength of water is very low and the highest value ever obtained is 27.7 MPa as it was measured by Briggs (1950).

Cavitation inception can occur either by entrained or stationary nuclei that are harboured in small wall crevices and although the former is supposed to be the case for ship propellers, the parameter of stationary nuclei is also important. It should be noted that, the nuclei must be able to withstand large pressure variations without collapsing otherwise they would dissolve into the liquid and, therefore, the required 'weak spots' for cavitation inception would not exist. As such, the surface tension must balance the pressure forces as follows:

$$p_v - p_l = \frac{2S}{R} \quad (2.2)$$

where p_v stands for the gas or vapour pressure inside the bubble, p_l for the pressure of the surrounding liquid, S for the surface tension and R for the bubble radius.

According to equation (2.2), nuclei gas would diffuse into the liquid, when either very small bubbles or large pressure variations would be the case. Nevertheless, they continue to exist in equilibrium with the surrounding liquid in such conditions thus several stabilisation models have been proposed by several researchers in an attempt of describing the observed behaviour.

Harvey et al. (1947), for instance, suggested that gas pockets positioned in hydrophobic crevices of solid surfaces act as cavitation nuclei. He proved that these gas pockets could exist in equilibrium with the surrounding fluid, under the right conditions, however, these pockets would grow in size to form bubbles and eventually get entrained by the fluid, as a response to a rapid pressure reduction. The basis of this mechanism can be seen in the Figure 2.11:

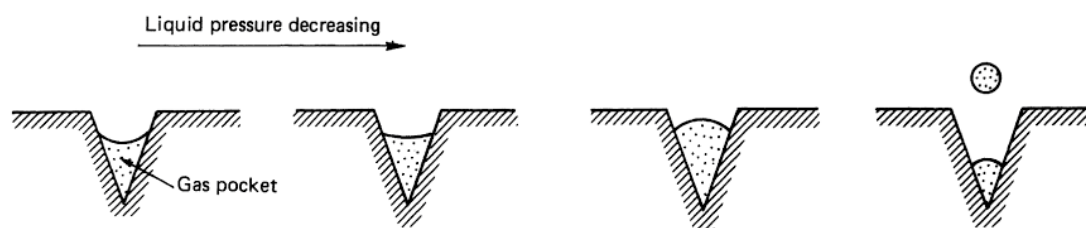


Figure 2.11: Harvey's nucleation model (Source: Carlton, 2012)

The Harvey model of stationary nuclei can successfully explain some observed phenomena, such as the rise of the tensile strength at pressurisation, yet it fails to offer an explanation for some others. For instance, it fails to explain why although water exhibits its maximum strength at 10°C, that strength drops when the temperature approaches 0°C, as it was found by Briggs (1950) in his experiments with ultra-pure water and Keller (1982) with ordinary tap water, at stress levels two orders of magnitude lower for the latter in relation to the former.

Another model of nucleation by Fox & Herzfeld (1954) suggested that free gas bubbles in a liquid could be stabilised by a skin of organic molecules such as fatty acids. In this case, the size of the bubble normally increases when it passes through the low-pressure areas of the liquid whereas the skin is supposed to prevent the gas from diffusing into the liquid, below a minimum bubble size, and due to the pressure difference between the liquid and the interior of the bubble. It is noteworthy that, although the proposed organic skin would dissolve in liquids containing alcohol and tetrachloride, cavitation may still be observed in such cases. This model was later revised by Yount (1972 and 1982) in his Varying-Permeability model, where he assumed that the bubble gas pressure is in balance with the gas pressure in the liquid due to a skin formed by surface-active molecules, and as such no collapsing occurs. In his unwetted mote model Plesset (1963) suggested that bubble nucleation is possible without the

presence of gases or vapour other than the ones dissolved in the liquid whereas motes would provide the necessary ‘weak spots’ in the liquid, where tensile failure would easily occur at low pressures. Moreover, Johnson & Cooke (1981) proved that, gas bubbles in seawater can be protected and stabilised by a skin of substances, at atmospheric pressure, therefore, their presence in such conditions is possible. In this case, Yount’s model provides a logical explanation regarding their stabilisation.

The earliest attempt to describe and analyse the dynamics governing the growth and collapse of a bubble in a continuous liquid was made by Besant (1859), even though cavitation damage on machinery was misunderstood till the early-1900s. Lord Rayleigh (1917) undertook a significant effort in the field of cavitation and bubble dynamics research, with his analysis of an isolated spherical void collapse in an incompressible liquid. He suggested a basic mechanism that would explain the relationship between a collapsing bubble and the observed damage of the affected solid surfaces, although he noted that cavitation damage may not be the sole attribute to this cause.

From an analytical point of view, the dynamics of gas, vapour or gas-vapour bubbles in a liquid can be effectively described by means of the Rayleigh - Plesset equation (Franc & Michel, 2004):

$$R \left(\frac{d^2R}{dt^2} \right) + \frac{3}{2} \left(\frac{dR}{dt} \right)^2 = \frac{1}{\rho_L} \left(p_g + p_v - p_\infty - \frac{4\mu_L}{R} \frac{dR}{dt} - \frac{2S}{R} \right) \quad (2.3)$$

where R is the bubble radius, t is time, ρ_L , μ_L and S are the density, the dynamic viscosity and the surface tension of the liquid respectively, p_g is the pressure of the non-condensable gas in the bubble, p_v is the vapour pressure, and p_∞ is the pressure infinitely far from the bubble. It should be noted that the Rayleigh-Plesset equation is based on the simple Rayleigh equation with the addition of the $-\frac{4\mu_L}{R} \frac{dR}{dt}$ parameter, in the instance of a viscous liquid.

At equilibrium, the Rayleigh – Plesset equation is simplified as follows:

$$p_g + p_v = p_\infty + \frac{2S}{R} \quad (2.4)$$

Supposing that a bubble exists in equilibrium with the surrounding liquid under a pressure p_v , and at $t=0$ a higher-pressure p_∞ is applied, then the bubble would collapse in a characteristic time τ , namely the Rayleigh collapse time, whereas the effects of viscosity, surface tension

and non-condensable gas are not considered. Based on those assumptions, the Rayleigh-Plesset equation is integrated as follows:

$$\left(\frac{dR}{dt}\right)^2 = \frac{2(p_\infty - p_v)}{3\rho} \left[\left(\frac{R_o}{R}\right)^3 - 1 \right] \quad (2.5)$$

Integration of equation (2.4) within a range from 0 to R_o would give:

$$\tau = 0.915R_o \sqrt{\frac{\rho}{p_\infty - p_v}} \quad (2.6)$$

The values of τ that are obtained by means of equation (2.6) are in good agreement with experimental findings regarding various initial bubble diameters, ranging from approximately one micrometer to one meter. For instance, a bubble with an initial radius of 1cm would collapse in approximately 1ms, under an external pressure of 1bar, in water.

The Rayleigh-Plesset model manages to illustrate the behaviour of the first bubble collapse effectively. It also shows that almost infinite pressures and velocities occur towards the end of the collapse, a consideration that could partly explain the erosion of the affected materials. Nevertheless, it does not provide any information about the subsequent rebounds and collapses that occur in various situations, whereas it is based on some ideal conditions. The bubble's shape for instance is assumed to be symmetrically spherical whereas the parameters of non-condensable gas, surface tension, gravity, heat exchange, compressibility, inertia forces and flow turbulence are ignored.

In real conditions, however, the dynamics of bubble collapsing can be influenced by gravity, compressibility, pressure gradients, as well as any flow turbulence. In addition, the presence of a surface, either free or solid, near the bubble can significantly affect its symmetry and behaviour during the collapse. Several researchers have taken these parameters into consideration in order to achieve a more realistic description of the phenomenon.

Plesset and Chapman (1971), for instance, studied the behaviour of a collapsing bubble near a wall for a variety of distances. They found that, when a bubble collapses near a solid wall, its shape tends to flatten close to the wall and a hollow is created on the opposite side whereas a re-entrant jet, directed towards the wall, is also created. The high-velocity jet then pierces the bubble and strikes the surface. Mitchell and Hammit (1973) held a similar research yet they also considered the parameters of pressure gradient and relative velocity in addition to wall proximity. Nevertheless, their approach was based on the use of spherical coordinates whereas

Plesset and Chapman's research was based on the use of cylindrical ones, which allowed them to study the micro-jet formation in a much deeper level.

The results of Plesset and Chapman's computations regarding an initially spherical bubble collapsing near a wall can be seen in Figure 2.12. It should be noted that two cases are presented, either with the bubble in contact with the solid wall or at a distance of half the bubble's radius. In the case of the former, the creation of a microjet directed towards the solid wall can be seen.

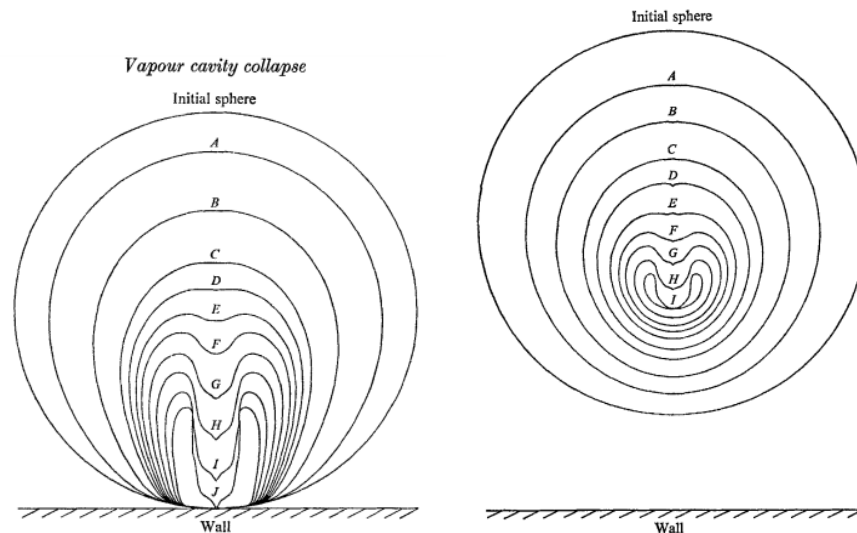


Figure 2.12: Computed bubble collapse. Left – In contact with wall, Right – At a distance (Source: Plesset and Chapman, 1971)

A contrasting behavior can be observed in the presence of a free surface. In that instance, the re-entrant jet is rather directed towards the bubble center instead of the free surface whereas the development of a counter jet, directed towards the free surface, can be observed afterwards. Chahine (1982) found that, this behavior mainly depends on the value of η , namely the ratio of the bubble's maximum radius to the initial distance of its center from the free surface. When $\eta < 0.3$ for instance, the free surface is not significantly disturbed whereas for larger values a strong disturbance from a counter jet is to be expected. In the case where a bubble moves between two walls, it would subsequently split into two symmetrical bubbles whereas a re-entrant jet, directed towards each one of the walls, would then be emitted from the corresponding bubbles. This behavior was confirmed by Plesset and Chapman (1971) as well as from Blake and Gibson (1981 and 1987).

Blake and Gibson (1987), conducted an analysis of the re-entrant jet by means of calculating the momentum of the bubble. What they found was that, a positive momentum relates to the

induction of a re-entrant jet directed towards the wall whereas a negative one has the opposite effect. They also found that, the momentum in the case of a solid wall and a free surface, is positive and negative, respectively. According to their analysis then, the jet is directed towards the surface, in the presence of a solid wall, whereas in the case of a free surface it is directed towards the bubble. Their findings are in good agreement with the aforementioned observations that were made from other researchers.

Some theoretical calculations from Blake and Gibson (1987), in the case of a bubble collapse near a solid wall, can be seen in Figure 2.13, in the form of successive bubble shapes.

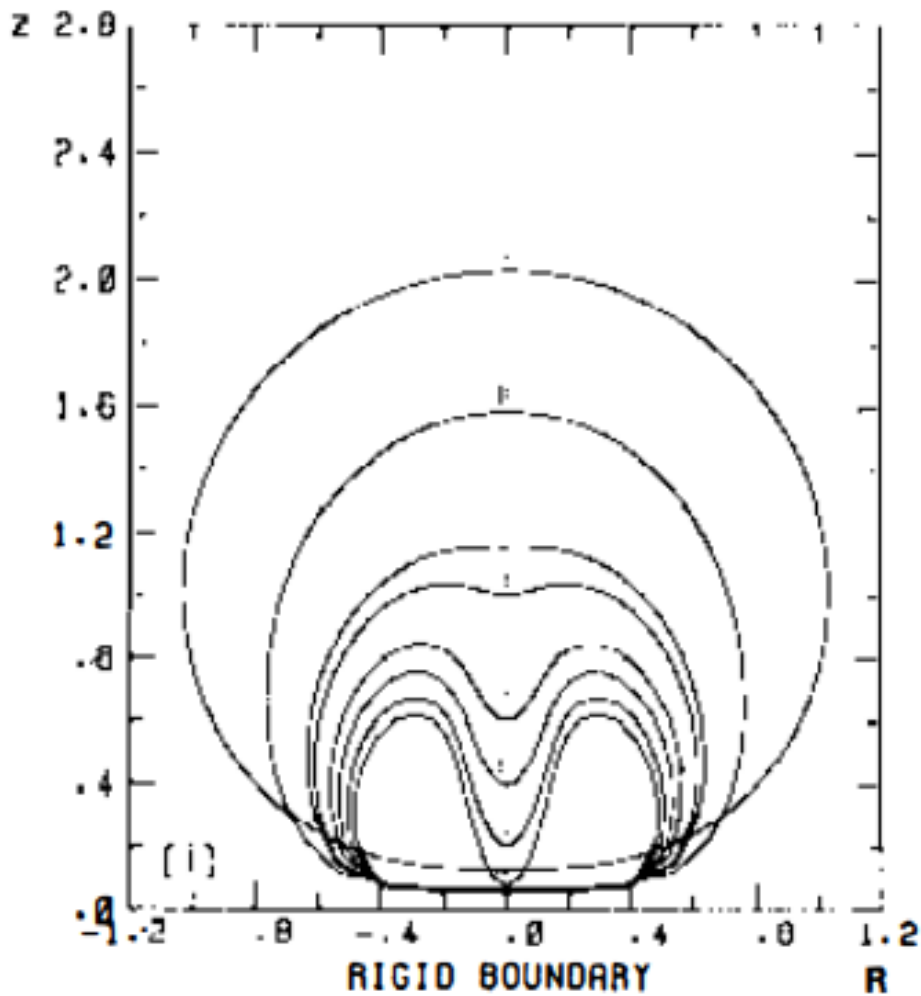


Figure 2.13: Successive bubble shapes during collapse, near a solid wall – rigid boundary (Source: Blake and Gibson, 1987).

It should be noted that their approach considers the presence of a bubble near a plane boundary with a unit vector x , where the flow is considered to be axisymmetric. The momentum can then be calculated by means of the following equation:

$$M_S = \int_0^t F_{px} dt \quad (2.7)$$

where $F_{px} = \pi\rho \int_{r=0}^{\infty} r(u_r^2 - u_x^2) dr$

and u_x and u_r are the axial and radial components of the velocity, respectively.

Finally, the parameter of compressibility, in general, appears to be related, to the velocity of the collapse. The quasi-acoustic solution from Herring (1941) and Trilling (1952) as well as the approach from Gilmore (1952), are two significant numerical solutions that also take into account the parameter of the compressibility of the liquid, nevertheless, they both lead to a different variant of the Rayleigh-Plesset equation. It is noteworthy that, both solutions do not give any information about the very last stages of the collapse that often lead to rebounds and new collapses. Those stages were studied by Plesset and Hickling (1964) who offered the first numerical solution that could describe both the collapse and the upcoming rebound, while including the compressibility parameter. It should also be noted that their solution was essentially based on the Gilmore approach and their results clearly demonstrated the emission of a pressure wave propagating outwards at the instant of the rebound.

2.5 Cavitation erosion

Cavities tend to collapse violently and rapidly when the pressure conditions allow them to do so, and as a result the released energy, can induce significant erosion to the affected solid materials. The magnitude of the released energy ranges from an a few hundred to a 1000 MPa, a value considerably high when compared to the ultimate strength of most of the affected materials (Preece and Vyas, 1976; Hammit and De, 1982; Brunton 1970). Nevertheless, the way the released energy acts, as an erosive factor, as well as its connection with the mechanical properties of the material is not well understood yet although bubble, cloud and vortex cavitation structures are believed to be more prone to cause erosion rather than the more stable sheet cavitation.

A series of phenomena are believed to be the main cause of erosion. These include (Franc and Michel, 2004):

- a) Bubble collapse and rebound where high instantaneous pressures and temperatures are generated from the collapse.
- b) Micro-jet formation where due to the presence of a flat solid surface near the bubble collapse, a high-speed liquid jet is developed towards that direction.

- c) Clouds of micro bubbles collapsing and generating cascade of implosions. In this case the amplitudes of the resulting pressure waves also increase.
- d) Cavitating vortices that also generate cascade of implosions. These are characterised by a long duration of loading time.

The high-pressure shock waves that are emitted from a rebounding bubble are considered to be one of the primary causes of erosion, especially when they occur in a short distance from the solid surface. Rayleigh (1917) first mentioned the emission of high-pressure waves in his theoretical work regarding a spherical cavity in an infinite liquid followed by Parsons and Cook (1919). The presence of shock waves was later confirmed experimentally by Harrison (1952) and Sutton (1957) by means of measuring the impact stresses at the exposed solid surfaces. At the same time Guth (1954) managed to visualize the resulting shock wave using a schlieren technique. Hickling and Plesset (1964) and Ivany (1965) evaluated these observations through their numerical analyses in the following years whereas Fujikawa and Akamatsu (1980) measured pressures of the order of 100 MPa with a duration of 1 μ s.

Recent studies with high-speed photography from Philipp and Lauterborn (1998) and Lindau and Lauterborn (2003) have also shown that high-pressure waves are emitted from a collapsing spherical bubble. In particular minimum bubble radiuses of less than 36 μ m were found leading to the hypothesis that even higher pressures may exist inside a bubble. Nevertheless, the presence of a solid boundary appears to be affecting the symmetry of the bubble and as a result the shock waves are expected to attenuate as it was found by Benjamin and Ellis (1966). Consequently, some researchers proposed that the shock wave hypothesis cannot fully explain the severity of cavitation related erosion (Knapp et al., 1970).

Photographic evidence of the generation of a high – pressure shock wave is presented in Figure 2.14:

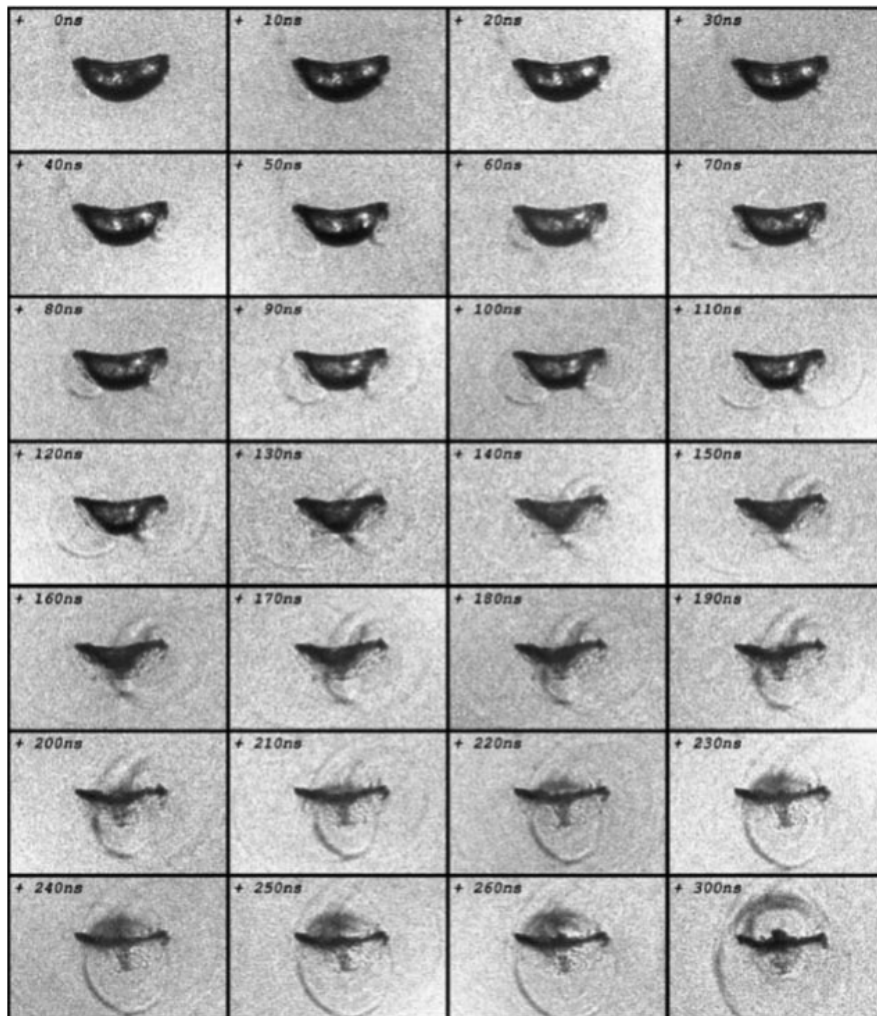


Figure 2.14: Shock wave generation during bubble collapse filmed at 100 million frames per second. Time is noted on the upper left corner of each shot (Source: Lindau and Lauterborn, 2003)

The presence of a solid boundary near the bubble can affect its symmetry and lead to an asymmetrical collapse and the inception of another interesting phenomenon. In particular, a liquid jet directed towards the solid surface, would be induced under those conditions. Kornfeld and Suvorov (1944) first suggested the presence of a liquid jet motivated by the observation of asymmetries on the bubble surface during the collapse phase. The liquid jet formation was later experimentally confirmed by Naude and Ellis (1961) and Benjamin and Ellis (1966).

High-speed photography studies by Shutler and Mesler (1965), Ivany et al. (1966), Plesset and Chapman (1969), Mitchell and Hammitt (1970) and Lauterborn and Bolle (1975) also demonstrated that a high-speed liquid jet passes through the interior of the cavity before complete closure. It should be noted that the liquid jet can cause high water hammer pressures of short duration on the surface mainly due to its high velocity. In particular, a velocity of the

order of 100 m/s may be expected as it was reported by Vogel et al. (1989) leading to maximum water hammer pressures of the order of 450 MPa.

Photographic evidence relating to the formation of a liquid jet during bubble collapse is presented in Figure 2.15. In particular, the liquid jet is evident in the form of thin black line, connecting the bubble and the flat surface.

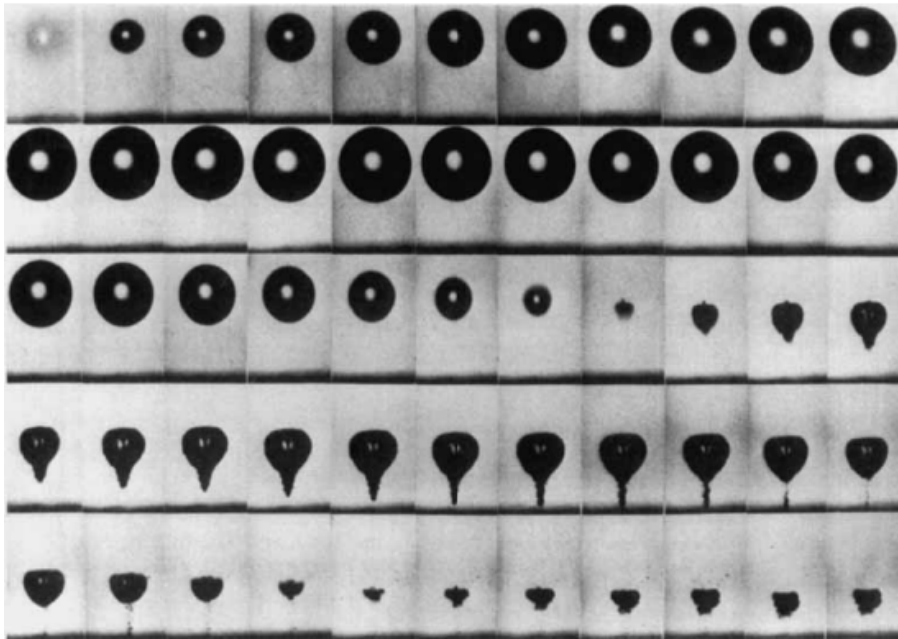


Figure 2.15: Liquid jet formation during bubble collapse filmed at 75000 frames per second (Source: Lauterborn and Bolle, 1975)

Although shock waves and liquid jets are considered to play a major role in the resulting erosion their contribution strongly depends on the distance of the collapse from the solid surface as well as the radius of the bubble. In particular, it was suggested by Tulin (1969) that the jet impact on the exposed surface might be enhanced by shock waves from nearby collapsing cavities. Kling and Hammitt (1972) found evidence of both shock wave and liquid jet impacts on the surface of an aluminium alloy exposed to spark-induced cavitation, by examining the resulting erosion pits. Ellis and Starrett (1979) demonstrated with the aid of high frame rate photography that, for laser induced cavitation liquid jets contribute more than shock waves, in the resulting erosion of the exposed surface. The simultaneous presence of shock waves and liquid jets was later confirmed by Shima et. al (1981), while they also investigated how the bubble radius as well as the parameter of the distance from the exposed solid surface can affect the collapse and implosion mechanism. In particular, they found that both mechanisms co-exist within a specific range of distances, whereas each of them is dominant within others.

Philipp and Lauterborn (1998) managed to examine the erosion mechanism more effectively, by means of a combination of high-speed photography and interferometric analysis of damaged patterns. Based on the dimensionless distance $\gamma_r = s/R_{\max}$, where s is the distance between the bubble centre and the surface and R_{\max} is the maximum bubble radius, they managed to classify the erosion patterns in relation to the parameter of distance from the collapse. Damage was observed only in the cases where that distance was less than twice the bubble maximum radius ($\gamma_r < 2$) whereas the resulting damage pattern was essentially a combination of shock wave, liquid jet and toroidal vortex structure impacts. They also found that the toroidal structure, in particular, gets formed when the jet hits the surface.

More specifically the contribution of the liquid jet was very small for distances $\gamma_r > 0.7$ whereas for $\gamma_r = 3.0$ the jet velocity was found to be of the order of 138 m/s (the maximum value that was obtained), although the impact velocity was significantly lower. It was also found that for $\gamma_r > 1$ the impact velocity was lower than 25 m/s corresponding to a water hammer pressure of the order of 34 MPa. According to the authors this behaviour can be attributed to the water layer that lies between the collapse point and the surface, acting as a barrier that may significantly reduce the jet velocity and attenuate the water hammer pressure originating from the jet. Nevertheless, when $\gamma_r < 1$ the jet hits the surface directly with an impact velocity of 83m/s corresponding to a 110 MPa water hammer pressure, and therefore damage can be observed in that instance. It is also noteworthy that, according to the researchers, the erosion patterns were only dependent on the distance γ_r whereas an increase in terms of bubble population number only amplified the intensity of the patterns, with their shape essentially remaining unaffected. Moreover, a change with regards to the radius of the bubble resulted into a change in the erosion pattern radius too. It should be noted that the researchers also managed to visualise through photographs the procedure by means of which a bubble is subjected to several collapses, each one closer to the affected surface. As such they managed to explain the fact that, even from great distances the affected surface is subject to high pressures and temperatures whereas in the case where $\gamma_r < 1$ the first collapse dominates the erosion process.

The erosion pattern, of one of the aluminium specimens that were utilized in this study, is presented in Figure 2.16, at a distance $\gamma_r = 0.69$, for which high water hammer pressures are expected.

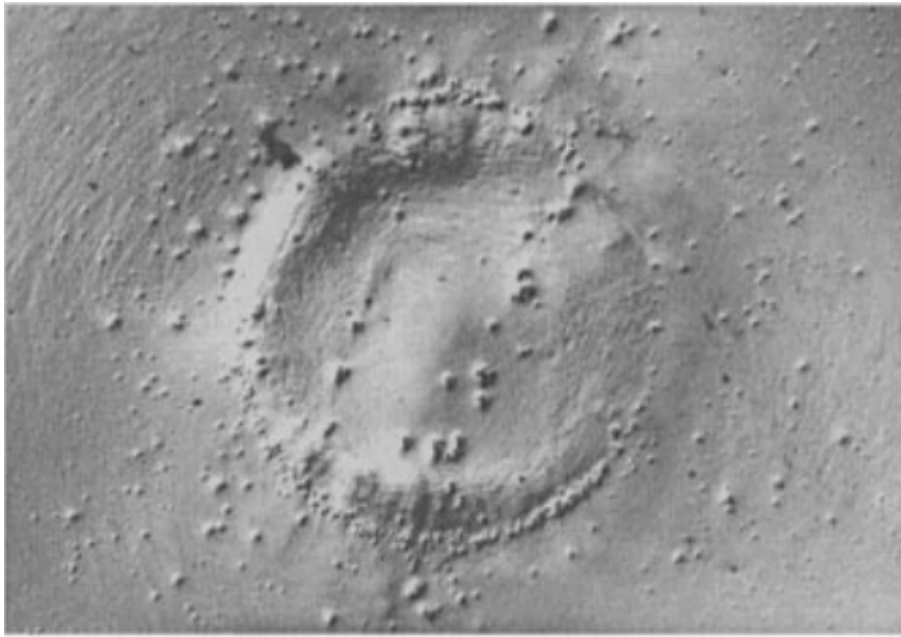


Figure 2.16: Erosion pattern of an aluminium specimen for a distance $\gamma = 0.69$ (Source: Philipp and Lauterborn, 1998)

In most industrial and marine applications, however, cavitation bubbles grow and collapse in clusters and as such the duration of the pressure pulses as well as the resulting pressure levels are even higher (Morch, 1977). The first attempt to analyse the behaviour of collective collapses in clouds of bubbles was made by van Wijngaarden (1964) followed by Hansson and Morch (1979 and 1980) for a unidimensional array of spherically identical bubbles. It was found that the collapse of the cluster initiates at the cluster boundary due to the hydrostatic pressure and spreads towards the centre of the cluster. Vyas and Preece (1974) suggested that the collapse of the cluster is triggered by the pressure waves of the first collapses and as a result a single high-intensity shock wave is formed and directed towards the solid surface. Brunton (1979), however, found that erosion is mostly due to the collapse of multiple individual bubbles rather than a single high-intensity shock wave. The cumulative effect of the bubble cloud in relation to the collapse of individual bubbles was later studied by Chahine (1982) and Chahine and Maryland (1982) who found that this phenomenon results into greater erosion damage. Tomita and Shima (1986) later showed that cascades of implosions characterize bubble clouds. In particular, collective collapses are following the initial collapse of a single bubble close to a solid wall. Due to the presence of the solid wall, however, the collapse is asymmetric and a micro-jet is created which pierces the bubble. This behaviour leads to the formation of a vapour torus that often splits into several small bubbles which then collapse collectively. Cascades of implosions characterize collective collapses, for which it is believed that the pressure wave emitted by the collapse and rebound of a single bubble can

amplify the collapse velocities of the surrounding bubbles and as a result the amplitude of the pressure waves related to those collapses increases too. Reisman et al. (1998) showed that the shock wave, which propagates inward, may strengthen considerably near the cloud centre due to geometric focusing, therefore, the erosive potential of the total collapse could also increase. Photographic evidence of cloud cavitation collapsing, from this study is presented in Figure 2.17:

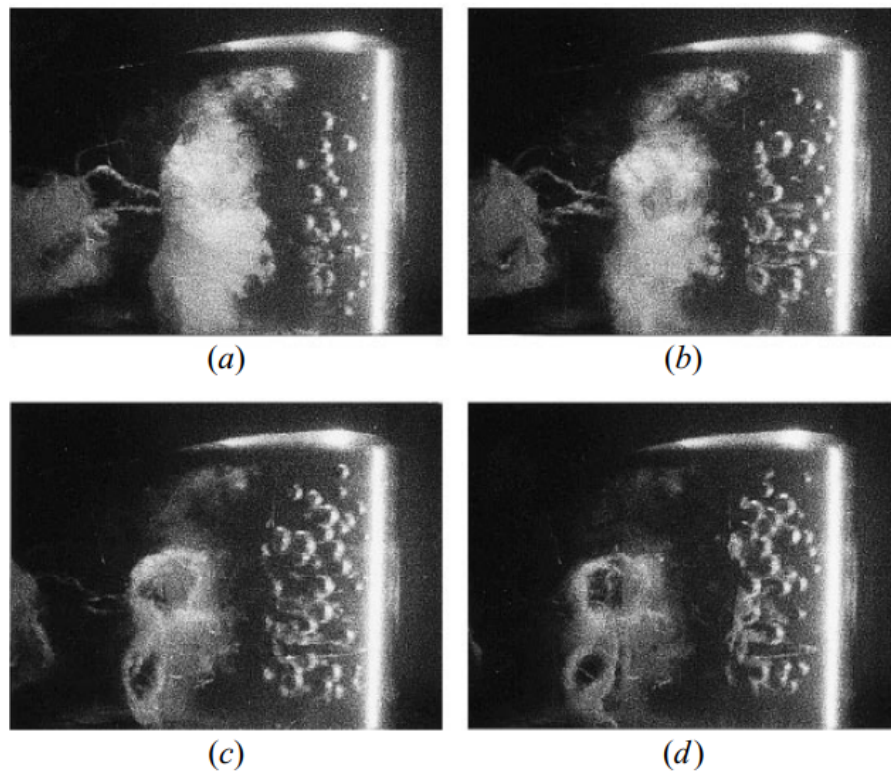


Figure 2.17: Consecutive frames showing the collapse of cloud cavitation in the vicinity of a hydrofoil (Source: Reisman et al., 1998)

Cavitating vortices appear in shear flows such as in the wakes of bluff bodies and in the break up region of shed sheet cavitation and they are considered to be highly erosive mainly due to two main factors. Firstly, the formation of foamy clouds at the end of the collapse in which cascade mechanisms may be observed and then the rather long loading time, often reaching values of the order of $10\mu\text{s}$, whereas the pressure waves derived from bubble or cloud collapses can last for about $1\mu\text{s}$. The amplitude of those pressure waves is sometimes higher than 100MPa and in conjunction with the long loading times, this can lead into the induction of significant erosion in machinery (Oba, 1994).

Recent studies by Bark et al. (2004) and Fortes-Patella et al. (2004) contributed significantly towards the understanding of the underlying physics of cavitation erosion. Bark et al. (2004), in particular, published the EROCAV observation handbook in which they gave a list of

(macroscopic) hydrodynamic mechanisms that could lead to erosion. Their main hypothesis is that a very high proportion of the collapse energy of a large cavity can be focused into a small region of the solid surface and cause significant erosion, under specific geometries. Fortes-Patella et al. (2004) suggested that the potential power of macro cavities could be converted into collapsing clouds of micro bubbles and shock waves that can cause significant erosion on the solid surface. Their model essentially provides the mechanisms by means of which the energy cascade of cavitation can be converted into an erosion damage rate and is based on a series of energy transformations. This is graphically illustrated in Figure 2.18:

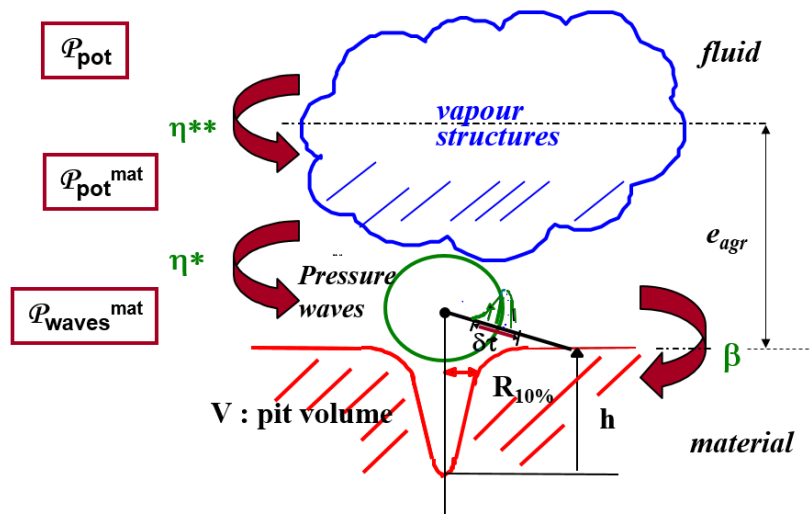


Figure 2.18: The basis of the Fortes – Patella model (Source: Fortes – Patella et al., 2004)

In that instance, the P_{pot} , P_{pot}^{mat} and P_{waves}^{mat} parameters stand for the potential power of the vapour structure, the flow aggressiveness potential and the pressure wave power, respectively. In addition, the η^{**} and η^* parameters represent transmission efficiencies whereas the β parameter stands for the fluid – material transmission factor.

In contrast to the research trend for cavitation erosion throughout the years, a number of researchers (Krenn, 1949; Petracchi, 1949; Taylor, 1979) proposed that the nature of erosion is mainly electrochemical. Previous observations of eroded dielectric materials, however, such as glass and quartz had already shown that erosion damage could not be solely attributed to electrochemical phenomena (Fottinger, 1926; Schroter, 1932). Similar results were obtained for materials such as stainless steel, tungsten and carbides in the case where erosion was induced chemically inert liquids (Wheeler, 1960). Plesset (1960), Leith and Thompson (1960) and Eisenberg et al. (1965) confirmed by means of experiments, that cavitation erosion is due

to a combination of mechanical and chemical factors, which was similar to what Glikman (1962) proposed. The synergistic action of electrochemical and mechanical factors in cavitation erosion was further investigated in the following years by numerous researchers (Hoar and Scully, 1964; Gina and Messino, 1969; Preece and Vyas, 1974; Goebel et al., 1974). What those researchers found was that, hydrogen embrittlement and chemical dissolution in corrosive media as well as the removal of the protective oxide film due to mechanical factors are the dominant mechanisms with regard to the synergistic electrochemical and mechanical processes. The quantitative contribution of electrochemical parameters in the resulting cavitation erosion was investigated and calculated by a number of researchers using specialized experimental techniques (Jesnitzer et al., 1979; Ashworth et al., 1979; Chincholle, 1980; Chincholle and Sinomeau, 1982).

In any case, the dominant opinion nowadays, is that erosion and corrosion act in a synergistic way (Zhao et al., 2016). Due to the suspected and experimentally confirmed synergistic action of electrochemical and mechanical factors, the effect of an applied anodic or cathodic current for reduction of cavitation damage was also investigated by a number of researchers (Derendovski, 1968; Von Altof et al., 1973; Simoneau et al., 1981) through the years. According to their research, cathodic protection is the preferable method due to the presence of cushioning hydrogen bubbles above the surface of the exposed material. The amount of the required applied current, however, depends on the polarization curve of the metal to be protected (Fontana, 1967).

Some materials may fail rapidly under the presence of continuous cavitation implosions. In contrast, materials such as nickel aluminium bronze (Ni-Al-Bronze) can often retain their form for a long period of time under cavitation attack. Nevertheless, their surface will at some point begin getting deformed and modified microscopically without any loss of material whilst it will also experience a degree of work hardening due to cavitation bubble collapse. This will make the material more brittle and prone to produce cracks a fact that may eventually lead to mass loss. In any case, parameters such as the energy transfer ratio as well as the type and severity of cavitation severity should be considered if one was to characterize a material's response against cavitation.

Erosion rate versus time curves obtained from laboratory tests indicate four distinct erosion phases (Karimi and Martin, 1986):

- a) The Initial phase or incubation period where permanent deformation and local displacement of micro particles may occur along with the development of cracks for brittle materials. No mass loss is observed during this period whereas the hydrodynamic impacts may produce several pits on the material's surface.
- b) The Accumulation or acceleration phase where an increased loss of mass is experienced by the material due to progressive work hardening and crack development all over the surface of the material.
- c) Steady state phase where a local equilibrium between the surface and the erosive effect of the collapsing bubbles is finally established. This is the phase where the mass loss rate of the affected material, tends to adopt a linear behaviour and become steady.
- d) The deceleration phase where the newly formed rough surface, essentially reduces the collapsing pressure of the bubbles, by means of cushioning effects and as a result the erosion rate also decreases.

Thiruvendagam and Preiser (1964) stated that the incubation and accumulation period are related to the surface characteristics of the specimen. Other researchers correlated the length of the incubation period with parameters such as hardness (Hobbs and Brunton, 1965) and endurance limit (Mathieson and Hobbs, 1960). Plesset and Devine (1966) and Hobbs (1967) demonstrated by means of photographs that during the during the steady state and deceleration phases, the accumulation between the fluid and the eroded surface, may result into a reduction of the bubble cloud collapsing intensity.

In general, the progress of cavitation erosion as well as its intensity can be evaluated by means of different ways. The weight measurement of the material before and after cavitation exposure, for instance, is a common practice. Another method lies on the study of the fractography of the eroded surface of a variety of materials and has been utilized by a number of researchers though the years (Preece, 1980; Hackworth, 1979; Okada and Hammitt, 1981; Hoss et al., 1980), although they all considered especially advanced states of erosion. As a result, the eroded surfaces of different materials revealed common fracture characteristics, thus a clear distinction between them could not be made. As such, several definitions are available for the intensity of the cavitation related erosion:

- Pitting rate: pit density per unit time and unit surface area.
- The total mass loss rate dm/dt .
- The total volume loss rate dV/dt .
- M DPR, the mean depth of penetration rate: The volume loss rate per unit surface area as suggested by Kato.

The aggressiveness of the flow, in terms of the intensity of the resulting cavitation erosion, can also be evaluated either by means of conducting pitting tests or direct measurements of the resulting impact forces (Franc and Michel, 2004) Pitting tests can be conducted during the incubation period where pits do not overlap. In this case, valuable information regarding the cavitation aggressiveness can be obtained by the density as well as the total number of pits. Microscopic and laser techniques can also be utilized for surface measuring purposes. In general, erosion pits are mostly found to be circular and with diameter of the order of some micrometres to one millimetre. Nevertheless, pitting tests can only give an estimation of the impact forces in relation to the yield strength of the examined material. In contrast, suitable transducers, in the sense that their size and shape will not affect the cavitation flow, can be placed on the exposed solid surface and directly measure the impact forces. The transducers must be of a high natural frequency of the order of MHz and well calibrated whereas they must also be durable in order to be capable of withstanding the forces they are meant to count.

Acoustic and electro-chemical methods may also be utilized for the evaluation of the aggressiveness of the cavitation flow. Despite the ease of use for the former and the fact that it is a non-invasive method, it is often difficult to distinguish the erosive from the non-erosive forms of cavitation. The latter is based upon the measurement of the current, generated by the re-passivation of the eroded surface, by an electrode positioned where erosion is expected to occur. The resulting signal is proportional to the mass loss rate.

Some materials will only experience the first stages of erosion known as orange peeling where the surface essentially experiences plastic deformation and as such it closely resembles the appearance of the surface of an orange, and may only erode a little further in the duration of a propeller's life for instance, whereas others will stop eroding when a critical depth is reached. In other cases, the first stages will progress to light erosion and finally to the complete penetration of the propeller blade. These processes will in some cases only take a few hours to fully develop, whereas in others they could take months and even years. The appearance of the orange peeling erosion pattern can be seen in Figure 2.19:

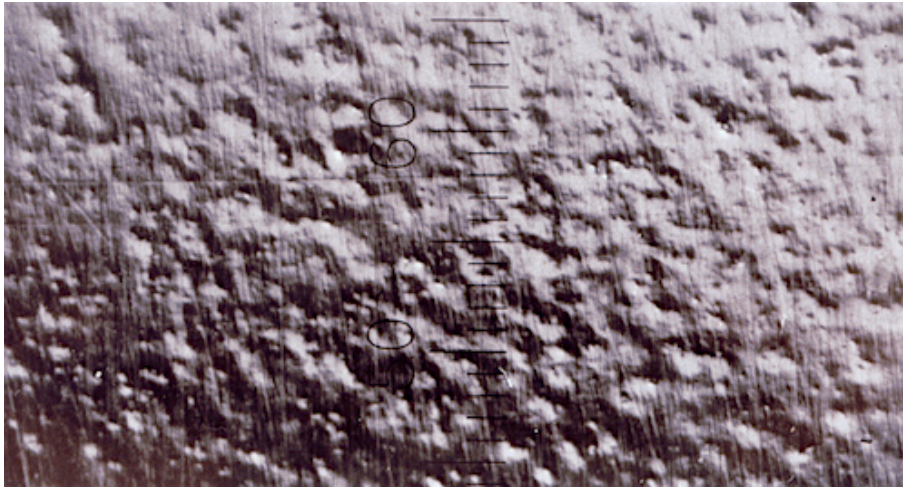


Figure 2.19: Orange peeling erosion pattern (Source Legi – Grenoble, n.d.)

The cavitation erosion resistance of a material can be completely different from another one as it mainly depends on its mechanical properties (hardness, brittle, ductile etc.) as well as the physical properties of the medium (temperature, flow velocity, pressure etc.). Common industrial alloys such as stainless steels (Heathcock et al., 1982; Hansson et al., 1978; Wade and Preece, 1978), cast irons (Iwai et al., 1983; Okada et al., 1983), aluminium alloys (Vaidya and Preece, 1978; He and Hammitt, 1982; Hansson and Morch, 1978) and copper alloys (Dakshinamoorthy, 1975; Wright and Mikkola, 1976) have been thoroughly investigated with regard to their resistance against cavitation erosion. Straight correlation between a material's properties and the rate of cavitation related erosion has not been achieved yet, however, despite the numerous efforts. It is noteworthy that Thomas and Brunton (1970) attempted and managed to correlate fatigue with the erosion rate in the case of ductile materials such as copper brass and mild steel.

With regards to the physical properties there is a general tendency for the erosion rate to increase when the parameters of temperature, velocity and pressure rise, up to a point above which the erosion rate decreases again. It is also noteworthy that, in grade DH36 steel that was subjected to cavitation erosion, oxide induced colour-tinting marks were observed (Carlton, 2012). These can be seen in Figure 2.20:



Figure 2.20: Oxide induced colour – tinting marks on grade DH36 steel (Source: Carlton, 2012)

Considering that the temperature of the surrounding water is of the order of 20 °C, it follows that these points must have been subjected to extremely high local temperatures of the order of more than 300 °C. This observation tends to support the opinion that high amounts of energy are released, in areas where cavitation activity is present.

Cavitation erosion can be restricted either through the improvement of the hydrodynamic field in order to eliminate the phenomenon as much as possible or by means of using more resistant materials. Elimination is almost impossible as cavitation inception is a very complex phenomenon which is not fully understood yet depending not only on the hydrodynamic design of a propeller, for instance, but also in the wake field, the interaction between the propeller and the hull, the position of the ship, the loading, the physical properties of the surrounding water etc.

Therefore, most of the efforts have mostly focused towards the improvement of the resistance of the materials against cavitation induced erosion by means of the following methods:

- a) Surface hardening techniques: Wade and Preece (1978) found that a martensitic structure exhibits a significantly improved erosion resistance in comparison to the ferrite phase. This can be achieved by means of heat treatment as it was the case for the AISI 1080 steel that was examined. Heathcock et al. (1982) demonstrated that the erosion resistance of ferritic stainless steels can also be improved by means of heat treatment for temperatures higher than 700 °C, where a duplex microstructure is obtained containing both ferrite and low carbon martensite phases. Ion implantation (Hu et al., 1980; Preece and Kaufmann, 1982), and mechanical hardening (Fanty, n.d.) techniques have also been studied extensively, both leading into improved erosion resistance through the induction of compressive stress on the surface of metals, although by different means. The induction of compressive stress by means of cold work has also been reported (Gould, 1970). Erosion resistance has also been improved by means of laser surface alloying in the case of FeCoCrAlCu high – entropy alloy (Zhang et al., 2015a) and the application of a Co-Pd film by means of electroplating in 316L stainless steel (Li, S.R. et al., 2015) while the Hastelloy C-2176, which is essentially a NiMoCr with the addition of tungsten on its surface exhibited an erosion incubation period three times longer than the one of 316L stainless steel (Li, Z. et al., 2015). High-velocity oxygen -fuel (HVOF) spraying (Hong et al., 2016) and plasma transferred arc (PTA) welding (Wang et al., 2016) techniques have also been examined on steels with protective coatings on their surface and were found to be beneficial with regard to cavitation erosion.
- b) Application of protective coatings: Both soft and hard coatings may be applied on metals (Bowden and Field, 1964; Matthewson, 1979). Elastomers and polymers for the former and hard metallic layers for the latter are commonly utilized. In recent years, in situ production of ceramic particle reinforced coatings, such as TiB₂/Fe, has been reported (Du et al., 2008a) which were found to offer excellent wear resistance (Du et al., 2008b; Qu et al., 2015). Moreover, tungsten carbide (WC) ceramic particles are commonly used in Ni and Co based composite coatings as they were found to offer excellent wear resistance due to their high hardness (Sharma, 2012; Paul et al., 2013).
- c) Cathodic or anodic protection: As it was previously mentioned in this chapter.

In most cases, these methods can be effectively utilized for the improvement of the erosion resistance of many materials by extending the so-called incubation period. Nevertheless, further research would be required, if one would wish to improve the cavitation erosion resistance of all available materials. In this case, an analytical calculation of the cavitation related erosion of a material, would be based on an equation consisting of parameters such as:

- The type of cavitation experienced.
- The way the released energy erodes the material.
- The material's strength as well as its mechanical properties.
- The existence as well as the extend of the basic phases of cavitation induced erosion.
- The amount of energy released by the collapsing of the cavities.
- The distance of the collapsing point from the material's surface.
- The exposure time of the material's surface to the collapsing bubbles.
- The bubble collapse rate.

2.6 Acoustic emissions and non – destructive testing techniques (NDT) for damage evaluation

Metals absorb and release strain energy due to stress. Acoustic emissions can be defined as the rapid release of that energy in the form of strain waves. The amplitude of those waves is directly related to the severity of the underlying fracture event, therefore they have attracted a lot of interest throughout the years, for structural monitoring purposes. Cavitation erosion can be regarded as one of those cases where the exposed metal is subjected to stress and as a result it emits acoustic emissions, corresponding to erosion induced fracture events within its structure. As such, the study of cavitation erosion induced acoustic emissions is closely related to the field of fracture mechanics which is concerned with the propagation of cracks in materials.

Griffith (1921), who is often regarded as the father of fracture mechanics, was the first to suggest a thermodynamic approach to analyze crack propagation based on an earlier study from Inglis (1913), although his work was not initially considered to be relevant to engineering matters. Numerous incidents during World War II, such as the fracture of steel bridges in Belgium (Shank, 1954) as well as the structural issues the Liberty ships suffered from (Biggs, 1960), however, resulted into the formation of committees that commenced metallurgical investigations relating to the observed issues. It was during that period when Griffith's theory attracted attention with Irwin (1957) further advancing his model by replacing the

thermodynamic surface energy parameter with the strain energy release rate G_c , while Wells (1956) first introduced the first fracture test that was capable of fully simulating a welded plate structure, with various version of the test being adopted all over the globe. Those approaches are analyzed in more detail in *Chapter 6*.

The first report of acoustic emissions, in relation to the induction of stress onto a metal, was made by Portevin and Le Chatelier (1923). In particular, they reported small sharp noises, originating from aluminium alloys undergoing extended deformation. Those noises were accompanied by the appearance of striations on the surface of the samples, thus they were directly associated to the induced stress. The phenomenon of acoustic emissions was further investigated by Kaiser (1953) who reported faint noises at low stress levels for a variety of metals such as zinc, steel, aluminium and copper. An even more detailed description of emissions originating from a metal due to stress was given a few years later by Schofield (1958), who amplified the acoustic signals, drove them through a loudspeaker and described them as of giving the impression of particles of metal colliding. He also observed that the frequency of those sounds-signals varied with regards to the condition of the material. Acoustic emissions of high frequency were acquired just before the material fractures, for instance, whereas low frequency signals were acquired just after the initial fracture events.

The use of acoustic emissions as means of structural health monitoring, for internal flaws and cracks, attracted much interest in the following years (Dunegan, 1968; Pollock, 1968; Votava and Jax, 1979). The non-destructive nature of the method as well as the ability to monitor structures remotely and accurately contributed to the continuous interest from the industry. With regard to cavitation erosion, several researchers have managed to establish a relationship between the resulting erosion rate and the acoustic power of the cavitation related noise (Hammitt, 1978; Hammitt and De, 1979). In particular, they proposed a relation of the form:

$$\text{Erosion rate} = K (\text{acoustic power})^{1/n}$$

with K being a constant of proportionality, relating to test facility parameters.

Acoustic emissions have also been utilized for acoustic source localization purposes. The procedure is essentially based on an array of at least three sensors, mounted on the structure to be examined, while the time delay with regard to the arrival of the acoustic waves at each one of the sensors is recorded. In the case of isotropic and homogeneous plates, a triangulation technique can then be applied in order for the position of the source of the acoustic event to be derived analytically, as it was initially proposed by Tobias (1976). An analogous effort to

derive an analytical source location method, although for anisotropic plates, was later made by Sachse and Sancar (1986). More recently, several source location optimization techniques have been developed both for the cases of isotropic (Liang et al., 2013; McLaskey et al., 2010; He et al., 2012) and anisotropic plates (Nakatani et al., 2012; Kundu et al., 2007; Hajzargerbashi et al., 2011; Koabaz et al., 2012). With regards to complex structures, methods such as source localization by time reversal (Ing et al., 2005; Ribay et al., 2007) and source localization by means of an array of densely distributed sensors (Trace and Chang, 1996; Lin, 1998) have been proposed and developed.

Acoustic emissions are measured by means of ultrasonic transducers which are usually made by piezoelectric materials. The piezoelectric effect is the ability of some materials to produce an electrical charge in response to an applied mechanical stress (Gautschi, 2002). Piezoelectricity was first observed experimentally back in the 19th century by the brothers Curie (1880), who managed to measure the produced electrical charge while at the same time they demonstrated that this charge was proportional to the applied mechanical pressure. It was Lippman (1881), who predicted, based on the thermodynamic theory, that a converse piezoelectric effect should also occur, thus a piezoelectric element would exhibit mechanical strain under the influence of an electrical field. This prediction was experimentally confirmed, later that year, by the Curie brothers. The basic theory regarding piezoelectricity was formulated towards the end of the 19th century by Voigt (1890) and was widely utilized until 1951 when a more modern theory regarding piezoelectric materials was considered initially by Laval (1951) and later on by Joel and Wooster (1961). In practical terms and for acoustic monitoring purposes, ultrasonic transducers made from piezoelectric materials can be used either actively, where the sensors would generate ultrasonic signals (Giurgiutiu, 2003), or passively, where the sensors would measure ultrasonic signals generated by the structure itself, due to internal fracture events (Mal et al., 2003).

In the last two decades, another type of transducers, namely the fiber Bragg gratings (FBGs), have made their appearance. FBGs are essentially optical fibers that reflect a specific wavelength of light and transmit all others, thus any induced mechanical strain would cause a reflected-wavelength shift than can be measured (Othonos and Kalli, 1999; Kashyap, 2010). FBGs have shown a great potential for applications relating to harsh environments, either in the field of biomechanics or engineering. This is due to their immunity to electromagnetic interference (EMI), small size and cost as well as chemical inertness (Grattan and Sun, 2000; Mihailov, 2012).

Another means of condition monitoring relies on the residual magnetic field (RMF) of ferromagnetic materials. The residual magnetic field (RMF) of a ferromagnetic material can be influenced by stress, magnetic field and temperature (Craik and Wood, 1970). In particular, the effect of stress is called the magneto-mechanical effect or inverse magneto-strictive effect (Cullity and Graham, 2009). Traditional monitoring methods based on the RMF, such as the magnetic flux leakage method (MFL) require the presence of a strong artificial field on the examined objects and as a result are incapable of detecting early mechanical degradation. This is because the strong artificial magnetic field tends to re-orient the magnetic field of the examined material, thus any information, related to micro-defects and internal stresses, that would normally influence the residual magnetic field, is eliminated. Nevertheless, the magnetic flux leakage method (MFL) has been extensively used for monitoring and inspection purposes on pipelines, rail tracks and other steel structures (Shannon et al., 1988; Khalid, 1999; Hwang et al., 2000; Pohl et al., 2004).

A more recent method, namely the metal magnetic memory method (MMM), was introduced in 1998 (Doubov, 1998). In contrast to MFL methods the metal magnetic memory (MMM) method takes advantage of Earth's own magnetic field (about 40 A/m), instead of an artificial one, thus any changes of the residual magnetic field of the material due to mechanical degradation can be directly identified. It should also be noted that, any changes with regards to the residual magnetic field of a material due to external loads and subsequently internal micro-damage are permanent, thus the exposed structures can be inspected even when the load is removed.

The metal magnetic memory method (MMM) received extensive interest in the following years (Doubov and Vlasov, 2004; Ren et al., 2001; Roskosz and Gawrilenko, 2008; Wang et al., 2011), due to its unique characteristics. Nevertheless, the MMM method is fairly new, thus the underlying mechanisms have not been fully understood yet, especially with regards to plastic deformation and the corresponding change of the residual magnetic field.

2.7 Summary of literature review

A wide range of studies, relevant to the topics with which this thesis is concerned, have been reviewed in *Chapter 2*. Those topics include the immediate effects of cavitation such as the resulting erosion of the affected material for instance, as well as the non-destructive techniques (NDT) that can be utilized for erosion monitoring purposes and as such a great part of this literature review is mainly concerned with studies relevant to those areas. In addition, a considerable amount of literature, related to the study of cavitation as a physical phenomenon,

is also presented in order to offer a more comprehensive perspective of the examined subject, to the reader.

Cavitation, as a physical phenomenon, had not been studied until the middle of the 19th century when a considerable effort, oriented towards the understanding of the governing dynamics, was undertaken. Further study was commenced in the beginning of the 20th century, and resulted into a more comprehensive understanding of the underlying physical mechanisms leading to cavitation. These essentially consist of large pressure and velocity variations leading to the inception and subsequent collapse of cavities containing air or vapour within a liquid. Recent technological advancements such as high-speed photography have allowed for the phenomenon to be directly and accurately visualized, an element of great importance to any researcher concerned with cavitation, especially in conjunction with a variety of numerical simulation techniques.

The large pressure and velocity variations that are required for cavitation inception are commonly apparent in ship components such as propellers and rudders. With regards to the operating conditions it has been found that cavitation can either develop on the back (suction) or face side of the blades as well as in the tip and hub regions of the propeller. Moreover, an additional type of cavitation called propeller – hull vortex cavitation (PHV), extending from the propeller to the hull of the ship, is also likely to be experienced in the form of noise as well as vibrations, although it does not generally result into the induction of erosion. The operation of the ship propeller is also very likely to influence the rudder of the ship which is usually positioned in the way of the propeller flow. As such the so-called propeller - rudder interaction could induce cavitation related issues not only to the source (propeller) but to the rudder as well.

It is apparent that the phenomenon of cavitation has been of great importance to the industry not only due to the unpleasant noise and vibrations it causes but also due to the resulting erosion and loss of efficiency that has been reported in some cases. As such a large amount of studies have been concerned with cavitation related erosion, in an effort of understanding the underlying mechanisms. Although the ultimate nature of the cavitation erosion mechanism is still debatable several phenomena such as bubble collapse and rebound, micro jet formation, clouds of collapsing micro bubbles and cavitation vortices are considered to be the dominant candidates. What most researchers agree about, however, is that, the generated pressures, when a bubble collapses, are considerably high in terms of amplitude and as such the erosion of an affected materials is well justified. A considerable amount of research has also been conducted

in the field of materials science, in relation to cavitation induced erosion. As such a large variety of materials, including metals and alloys as well as composites, have been studied in this context, however, direct correlation between cavitation related erosion and the properties of the exposed materials has not yet been achieved apart from a few isolated cases.

Finally, with regard to non-destructive monitoring techniques, researchers have been mostly concerned with the use of acoustic emissions, which have been utilized both in the laboratory and the field for more than 50 years, with good results. Acoustic emission based NDT techniques however have mostly been used in static structures, for structural health monitoring, and have not been utilized as much for cavitation erosion monitoring purposes. This would require additional research due to the complexity of the acoustic emission spectrum related to cavitation erosion. Nevertheless, advanced hardware such as, highly sensitive acoustic sensors, optical sensors, modern signal capturing devices as well as the relevant software and some promising NDT techniques such as the metal magnetic memory method (MMM) could be of great assistance towards that direction as it has been demonstrated through the relevant studies and applications.

It appears that although considerable efforts have been undertaken in a variety of fields, there are still matters that can be further explored, such as the erosion resistance of materials, that are commonly used, in cavitation prone applications, as well as the utilization of non-destructive techniques for cavitation erosion monitoring and localization purposes, in consideration of components such as rudders. This is the context through which this study will proceed.

Chapter 3

Experimental Procedure and Conditions

3.1 Introduction

The components which consist the basis of the ultrasonic cavitation test rig are presented and discussed in *Chapter 3* along with the corresponding experimental procedures and conditions. It should be noted that, any instrumentation and underlying theory matters relating to the specialized components which were used in experimental procedures such as the microscopic observations and the study of acoustic emissions will be presented and discussed in *Chapter 5* and *6*, respectively.

The main aim of this study commanded that, the examined specimens, would be exposed to a cavitating liquid medium (water), thus an appropriate test rig was built, essentially consisting of a water tank, a base plate (bridge) on which specimens were mounted and an ultrasonic cavitation excitation source in the form of an ultrasonic transducer.

In addition to those basic components, specialized equipment such as an accurate mass balance for mass loss measurements, an impressed current unit (potentiostat/galvanostat) for cathodic protection measurements as well as a water recirculation system to keep the water temperature steady, were also utilized.

3.2 Experimental test rig

A rectangular and open on the top water tank (390mm x 255mm x 275mm, L x W x H), made from Perspex, was utilized in these series of experiments whilst two types of square specimens with a side length of 25 and 50 mm, respectively and a thickness of 5mm were examined.

Each specimen was firmly positioned at the bottom of the water tank onto an appropriate base plate (bridge), also made from Perspex, in order for any potential galvanic corrosion issues to be avoided.

The water tank and the probe of the ultrasonic transducer (sonotrode) which is positioned just above the submerged specimen, can be seen in Figure 3.1:

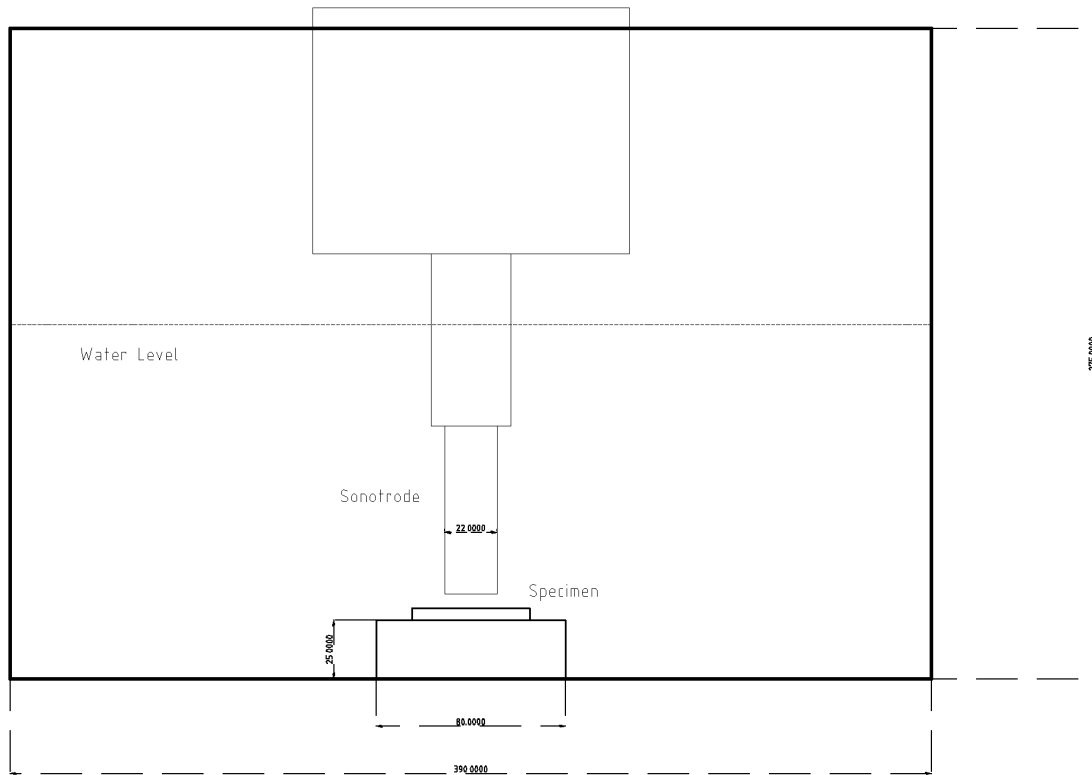


Figure 3.1: Test rig – Perspex water tank

The bridge, on which the 50mm - side specimens were mounted, has a side length of 80mm and a height of 25mm. In addition, the bridge has a square recess on the top with a 50.5 mm side length, leaving a 25 μ m gap on each side, and a depth of 0.5mm, such as each specimen can be mounted on it, properly. Moreover, each specimen as well as the bridge have got markings to ensure correct fitment, in addition to two small brackets with screws that hold the specimen in position while some space for optical or acoustic sensors is available at the bottom of the bridge in the form of a tunnel (80mm x 60mm x15 mm, L x W x H). It should be noted that the bridge is firmly placed onto a rectangular piece of thin plastic, which is glued at the bottom of the tank.

An almost identical, but half-size, with regards to its side length, model of the bridge was also built to accommodate the 25mm specimens. The half-size bridge (40mm x 25mm, L x H) has also got a recess on the top of it, with a side length of 25.5mm, leaving a 25 μ m gap on each side and a depth of 0.5mm. The large plastic base (bridge) on which a steel specimen is firmly mounted can be seen in Figure 3.2:

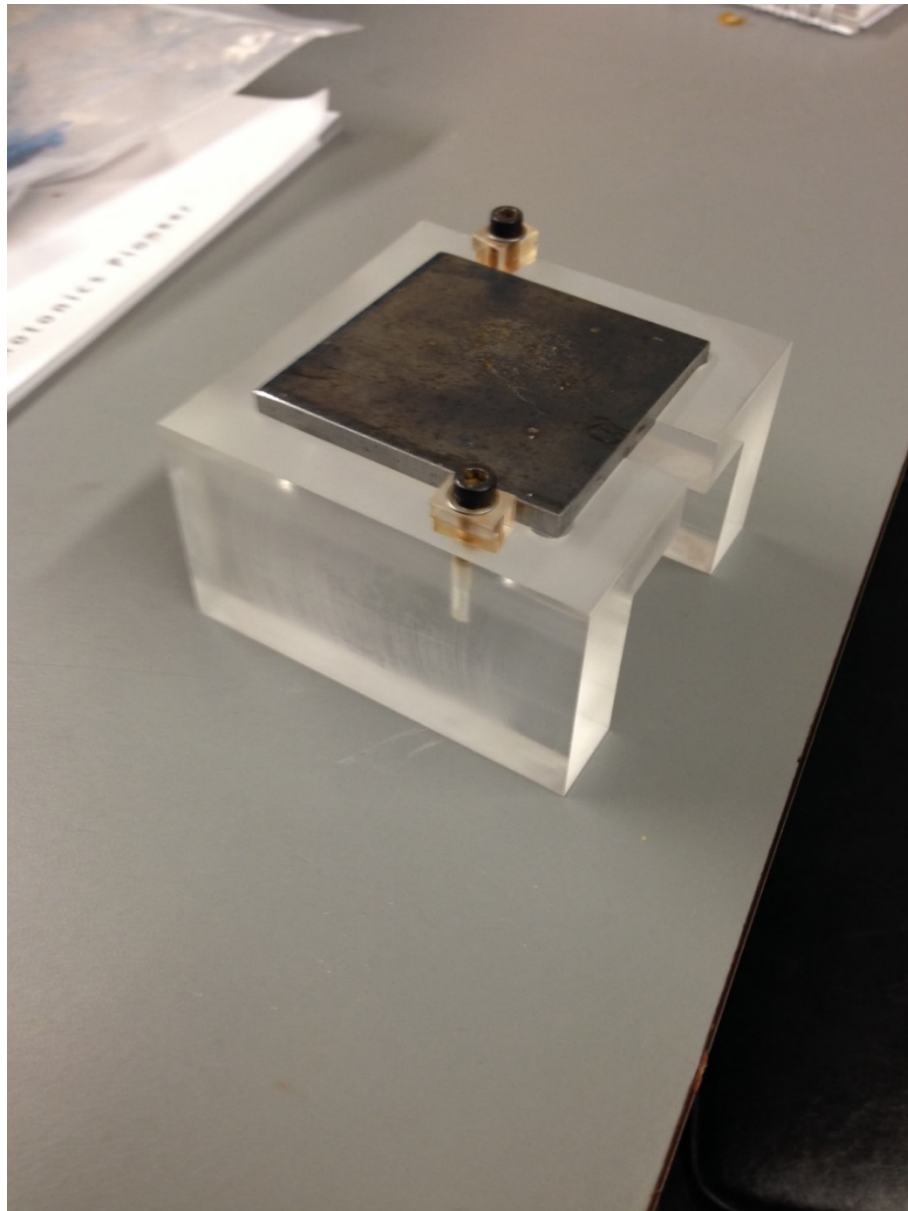


Figure 3.2: Test rig – Plastic base (bridge)

The plastic tank was normally filled with fresh tap water, for which a chemical analysis report is provided at the end of this chapter, while cavitation was induced by means of a vibrating device, namely the Hielsher UIP1000hd ultrasonic transducer, which was mounted on an adjustable yet firm base. As such the probe tip (sonotrode) of the ultrasonic transducer was positioned just above the surface of the specimen at a predetermined distance. The ultrasonic transducer and the probe tip (sonotrode) can be seen in Figure 3.3:



Figure 3.3: Hielscher UIP1000hd ultrasonic transducer and sonotrode (Source: Hielscher - Ultrasound Technology, n.d.)

The operating principle of the ultrasonic transducer is based on the reversed piezoelectric effect thus longitudinal mechanical oscillations are generated by electric stimulation. The frequency of those mechanical oscillations is set at 20 ± 1 kHz while the power output of the ultrasonic transducer can be adjusted all over the range between 5 and 100% of its maximum power output which is 1000W. The titanium made sonotrode or probe tip is mounted on the horn of the ultrasonic transducer where it functions as a $\lambda/2$ (2nd axial mode) oscillator (with λ standing for wavelength) while the maximum amplitude of the generated longitudinal mechanical oscillations is 150 μ m. Mechanical oscillations of that extent transmit pressure fluctuations into the water, of sufficient amplitude to induce cavitation, via the front face of the sonotrode (tip). As such significant erosion, can be induced on the surface of a specimen placed relatively close to the sonotrode tip as well as to the sonotrode itself which, under normal operating conditions would require refurbishment or replacement, frequently. Even so only a slight amount of refurbishment is attainable without heavily influencing the operational characteristics of the sonotrode, thus utilization of a new piece is often required.

The intensity of the ultrasonically induced cavitation, is essentially dependent upon the diameter of the sonotrode, the gap between the sonotrode tip and the specimen as well as the power output of the device.

For the demands of this research, it was decided that a titanium made cylindrical sonotrode with a tip diameter of 22mm should be utilized as the source of ultrasonically induced cavitation, since an identical arrangement produced satisfactory results in an earlier relevant study from a technical organization, which cannot be named in this thesis due to confidentiality issues. From this point onward this earlier study will be referred as ‘T. O. Erosion study’ with T.O. standing for ‘Technical Organization’.

Similarly, the gap between the sonotrode tip and the specimen was also chosen based on the findings of the ‘T. O. Erosion study’ and was set at 1mm. The gap between the sonotrode tip and the specimen was measured every single time the specimen was placed into the tank again by means of a feeler gauge in order to ensure that it is positioned in the same relative location. Figure 3.4 shows the sonotrode tip of the ultrasonic transducer mounted just above an exposed specimen. Cavitation is slightly visible, in the form of foamy water, in the area between the sonotrode tip and the specimen.

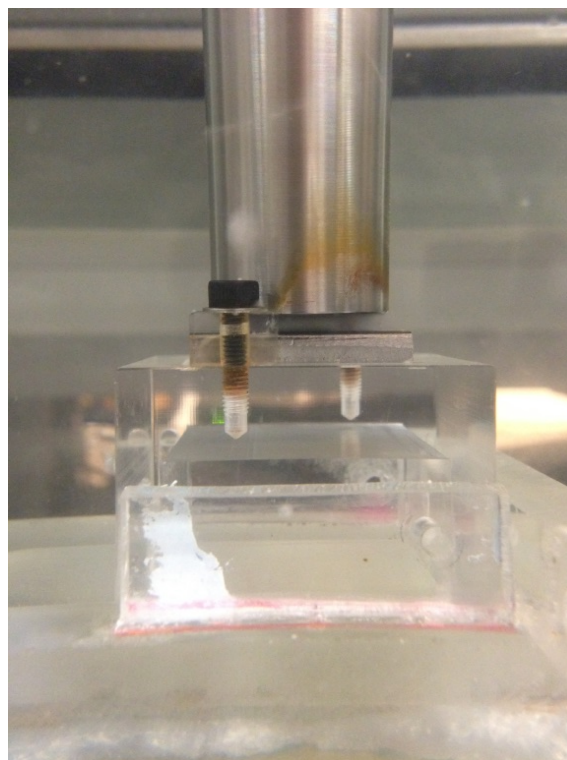


Figure 3.4: Test rig – Plastic base (bridge) inside the water tank with sonotrode on the top

A noteworthy side effect triggered by the utilization of ultrasonically induced cavitation is that, a significant amount of energy is transmitted by the vibrating sonotrode into the water and as a result the temperature gradually rises. As a preventive measure, a simple water recirculation system was built, with the purpose of maintaining the temperature steady at 25 ± 2 °C.

More specifically, water is circulated by means of a small submersible pump (flow rate 20ml/s) placed into an additional reservoir near the main tank through two small hoses (10mm diameter). The first hose supplies and the other one discharges water, in and out of the main tank, respectively, thus the temperature is kept relatively steady and any excessive heat generated from the operation of the sonotrode gets removed, whilst the desired water level (7cm above the specimen's surface) is maintained. The main tank and the water recirculation system is presented in Figure 3.5:

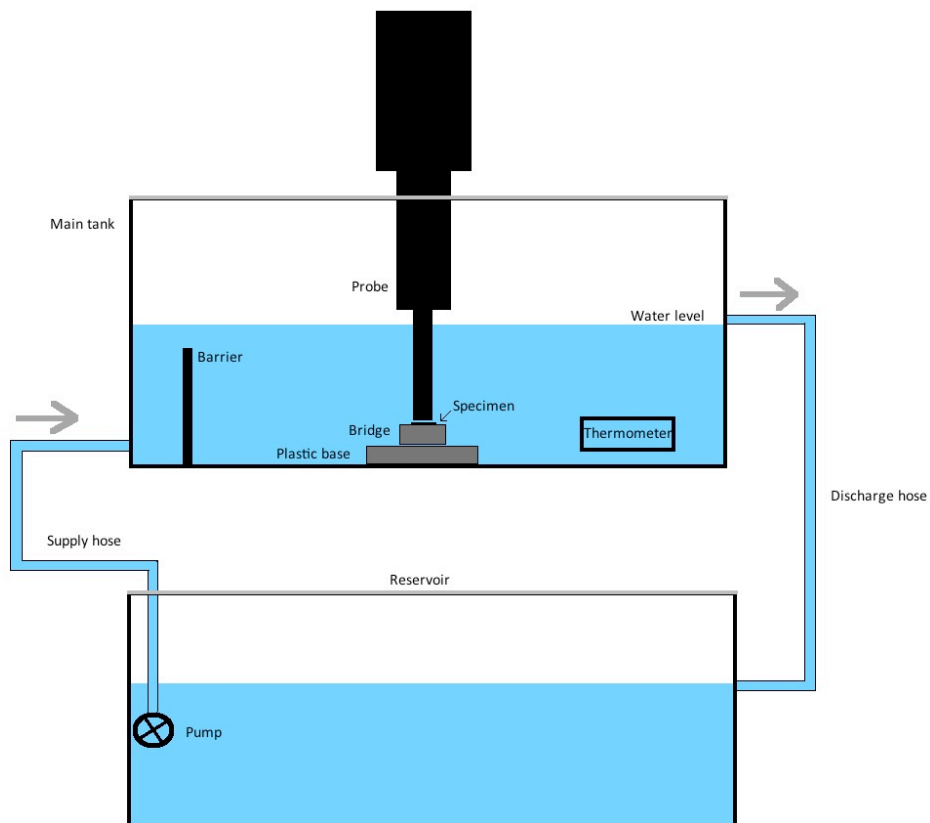


Figure 3.5: Test rig and water recirculation system

The discharge hose is connected to the main tank, though a hole located just above the desired water level, thus it also acts as a level controller in addition to its main purpose which is to transfer water from the main tank into the additional reservoir with the aid of gravity. In contrast, the supply hose is connected to the main tank through an additional hole located on the opposite side of the tank and at a lower height whilst it operates with the aid of the submersible pump. This arrangement was mainly chosen with the purpose of eliminating any potential flow disturbances in the vicinity of the specimen and towards that direction a small barrier was also placed nearby the supply hose. In order to ensure that the water temperature is kept within the desired range, a submersible thermometer is conveniently located into the tank, thus temperature readings can also be taken while the test rig is operating. Minor corrections regarding the flow of water, could then be made if it is so required.

Cathodic protection was also applied on most specimens as it was found to be beneficial, with regards to cavitation induced mass loss, in the ‘T. O. Erosion study’. The VersaSTAT 3 potentiostat/galvanostat is used in this study, consisting of three electrodes (working, counter, reference) and a main unit. The main unit adjusts the output of the counter electrode as required in order for the desired potential to be established on the working electrode (specimen). The working potential is then measured with regards to the saturated calomel reference electrode. Cathodic (protective) reactions occur on the working specimen under the appropriate potential, thus it gets electrochemically protected, whereas the anode (counter electrode) corrodes. A schematic showing the operation of a three-electrodes potentiostat can be seen in Figure 3.6:

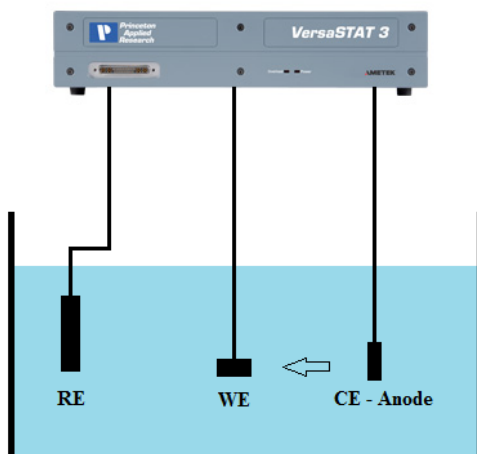


Figure 3.6: VersaSTAT 3 potentiostat/galvanostat. RE = Reference Electrode, WE = Working electrode, CE = Counter electrode

3.3 Experimental procedure and conditions

Results from the ‘T. O. Erosion study’ dictated that, when the gap between the sonotrode tip and the specimen is adjusted at 1mm, cavitation of sufficient intensity to cause significant erosion is induced whereas at the same time the sonotrode tip does not become eroded excessively. The same applies for a sonotrode power output of 75% (750W) and as such these were the experimental conditions that were selected to be applied in all cases.

It should be noted that, later in this research, a variety of power outputs and gaps are also considered and examined, in addition to the optimal ones, with the purpose of identifying the conditions for which cavitation ceases to be ‘erosive’ and establish acoustic erosion thresholds. More details regarding this procedure, however, will be given in *Chapter 6*.

Cathodic protection was also applied on most specimens as it was found to be beneficial, with regards to the cavitation induced erosion - mass loss, in the ‘T. O. Erosion study’. In an analogous context, a working potential of -790 mV was applied, as it was found to minimize mass loss, due to the optimal amount of cathodic (protective) reactions occurring on the surface of the specimens. Various electric potentials, however, were also examined for investigative reasons. The relevant results are presented in *Chapter 4*.

The cavitation induced erosion – mass loss of each one of the examined specimens was periodically measured every half an hour, by means of a Mettler AE160 mass balance. The particular mass balance has a resolution of 0.1 mg and a weight range of 0-162g. The weight accuracy of the mass balance was evaluated, by means of measuring the mass of a virgin specimen twenty times and then calculating the mean value of those measurements as well as the relevant standard deviation. The relevant calculations are presented in *Appendix G*.

In addition, a chemical analysis report of the tap water that was used for these series of measurements is provided in Table 3.1:

Parameter	Mean Value
Conductivity (20 °C)	604.67 μ S/cm
Hardness (Total) as CaCO ₃	259.5 mg/l
Turbidity	0.072 FTU
Total Organic Carbon as C	2.071 mg/l
Hydrogen Ion	7.75 pH
Aluminium as Al	4.825 mg/l
Chloride as Cl	48.748 mg/l
Iron as Fe	2.969 mg/l
Lead as Pb	0.225 mg/l
Mercury as Hg	<0.09 mg/l
Nickel as Ni	1.338 mg/l

Table 3.1: Tap water chemical analysis

It should be noted that prior to normal testing, experimental conditions from the ‘T. O. Erosion study’ were evaluated and correlated to the present test rig, as a sort of investigation on whether they would have the desired effects on the examined specimens or not, always in terms of the resulting cavitation related erosion – mass loss.

Following the preliminary investigation, each specimen was then exposed to cavitation generated by the sonotrode, which was operating at a 75% (750W) power output setting and was placed at a distance of 1mm from the surface of the specimen, for a period of five hours and under the application of cathodic protection (-790 mV) while mass loss measurements were taken every thirty minutes. As it was previously noted, a variety of experimental conditions, relating to the power output of the sonotrode and the cathodic protection potential, were also examined mainly for investigative and comparison reasons and will be presented accordingly.

A variety of alloys and protective coatings were examined with regards to their response against ultrasonically induced cavitation. These include:

- Grade DH36 steel
- Stainless steel 254
- Cupronickel 70-30
- Protective coatings on grade DH36 steel

More details regarding the alloys and the protective coatings that were examined will be given in the next chapter – *Chapter 4* along with the relevant experimental results.

Chapter 4

Mass Loss Results

4.1 Introduction

Mass loss results relating to specimens exposed to ultrasonically induced cavitation are presented in this chapter. Initially, the efficiency of the test rig was evaluated on small steel specimens in the sense that a correlation with the ‘T. O. Erosion study’ was conducted under identical experimental conditions. Afterwards, the effect of cathodic protection was examined and eventually measurements were conducted on multiple specimens made from a variety of different materials and coatings.

The majority of specimens were exposed to ultrasonically induced cavitation for a period of five hours whilst mass loss measurements were conducted every thirty minutes. Comparison graphs were plotted, showing the progression of mass loss over time as well as its first derivative, the rate of mass loss for each of the examined materials and coatings. Mass loss can be defined as follows:

$$\Delta m = m_{\text{initial}} - m_{\text{current}} \quad (4.1)$$

where m_{initial} is the initial mass of the specimen before cavitation exposure and m_{current} is the current mass of the specimen, after a specific period of cavitation exposure. Similarly, the rate of mass loss, when intervals of thirty minutes are considered, can be defined as follows:

$$\frac{\Delta m}{\Delta t} = \frac{m_t - m_{t-1}}{30} \quad (4.2)$$

where m_t is the current mass loss at time t and m_{t-1} is the mass loss that was measured thirty minutes before, at an earlier time $t-1$.

It should be noted that, in the majority of cases, five specimens from each one of the examined materials were tested, in order for any possible issues with regards to the composition or properties of an individual specimen as well as the operation of the experimental test rig to be excluded and as such to produce more accurate results. In addition the measurement uncertainty was calculated, through the procedure that is presented in *Appendix G*, and was found to be $\pm 0.00002\text{g}$ (95% confidence level), applicable to all mass loss measurements.

4.2 Test rig evaluation

The experimental test rig, was initially evaluated, by means of testing eighteen specimens, made by grade DH36 steel, which was supplied from two different sources. In addition to the parameter of the supplier, two sonotrode power outputs and specimen sizes were also examined. The gap between the sonotrode tip and each specimen was set at 1 mm in all cases. More specifically, the following were tested:

- Two 25 mm side length grade DH36 steel specimens at a 50% (500W) power setting. *Four hours of cavitation exposure.*
- Six 25 mm side length grade DH36 steel specimens at a 75% (750W) power setting. *Five hours of cavitation exposure.*
- Five 50 mm side length grade DH36 steel specimens at a 75% (750W) power setting. *Five hours of cavitation exposure.*
- Five 50 mm side length grade DH36 steel specimens supplied by BAE systems at a 75% (750W) power setting. *Five hours of cavitation exposure.*

Figures 4.1 and 4.2 show the mass loss and rate of mass loss of the 25 mm side length, grade DH36 steel specimens for a 50% (500W) sonotrode power output:

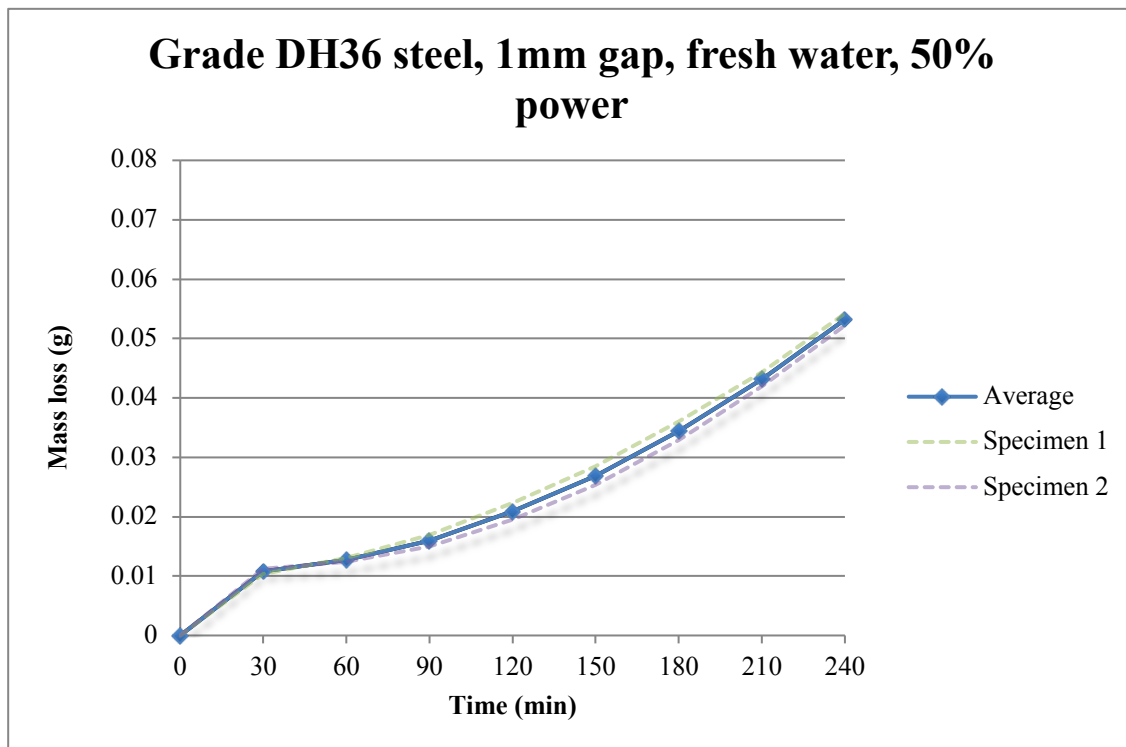


Figure 4.1: Mass loss of grade DH36 steel (25 mm) for a 50% (500W) power output.

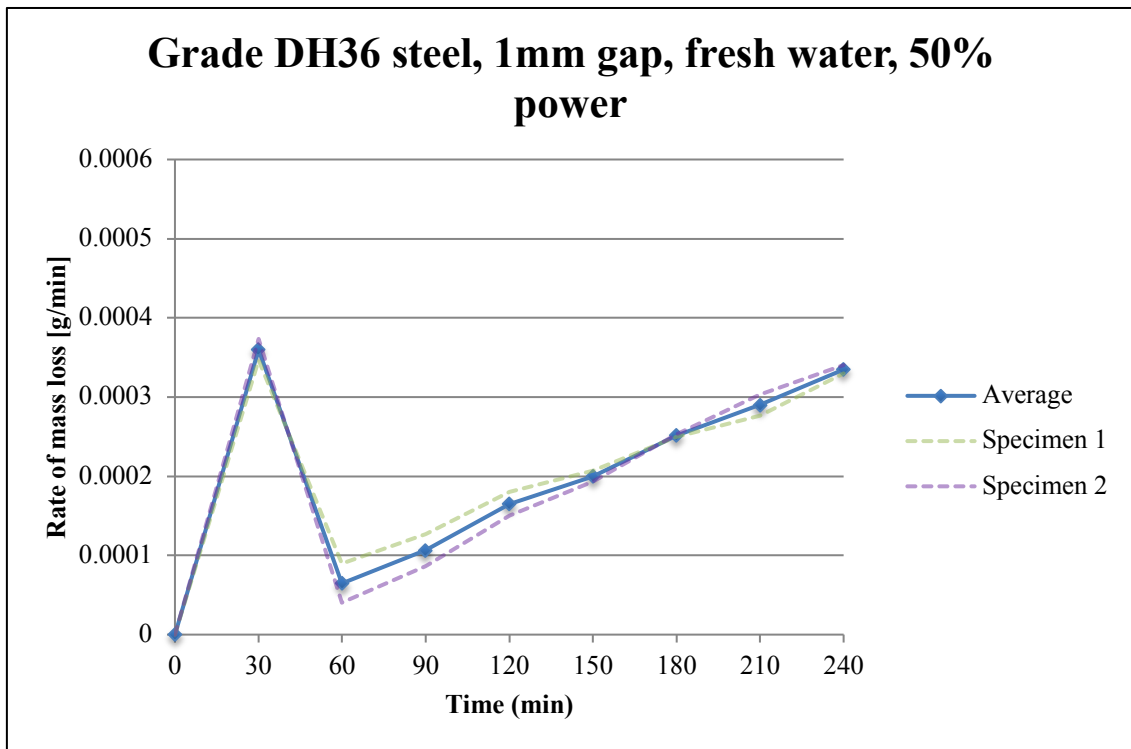


Figure 4.2: Rate of mass loss of grade DH36 steel (25 mm) at a 50% (500W) power output.

Preliminary experiments conducted with the 25 mm side length Grade DH36 steel specimens, showed that the test rig is capable of inflicting a measurable amount of cavitation related erosion, even when an average power output (50% - 500W) is considered. More specifically, an average total mass loss of 0.058g was experienced by the specimens after four hours of cavitation exposure.

It is noteworthy that, the rate of mass loss reaches its peak value during the first thirty minutes of cavitation exposure, before it decreases considerably after one hour, although it was expected that, no mass loss would occur during this initial or incubation period apart from some plastic deformation (orange peeling). This behaviour can be attributed to a stress amplifying parameter such as the presence of notches on the virgin surface, a hypothesis which will be further explored by means of surface roughness measurements, whereas the subsequent decrease of mass loss is due to the progressive work hardening of the attacked surface. Past that point, the surface of each specimen becomes fails uniformly at a low yet slightly increasing rate while specimens appear to remain at this ‘steady – state’ stage for the remaining three hours of exposure.

Mass loss and rate of mass loss results for both the 25mm and 50mm side length grade DH36 steel specimens, at a 75% (750W) power setting, are presented in Figures 4.3, 4.4, 4.5 and 4.6:

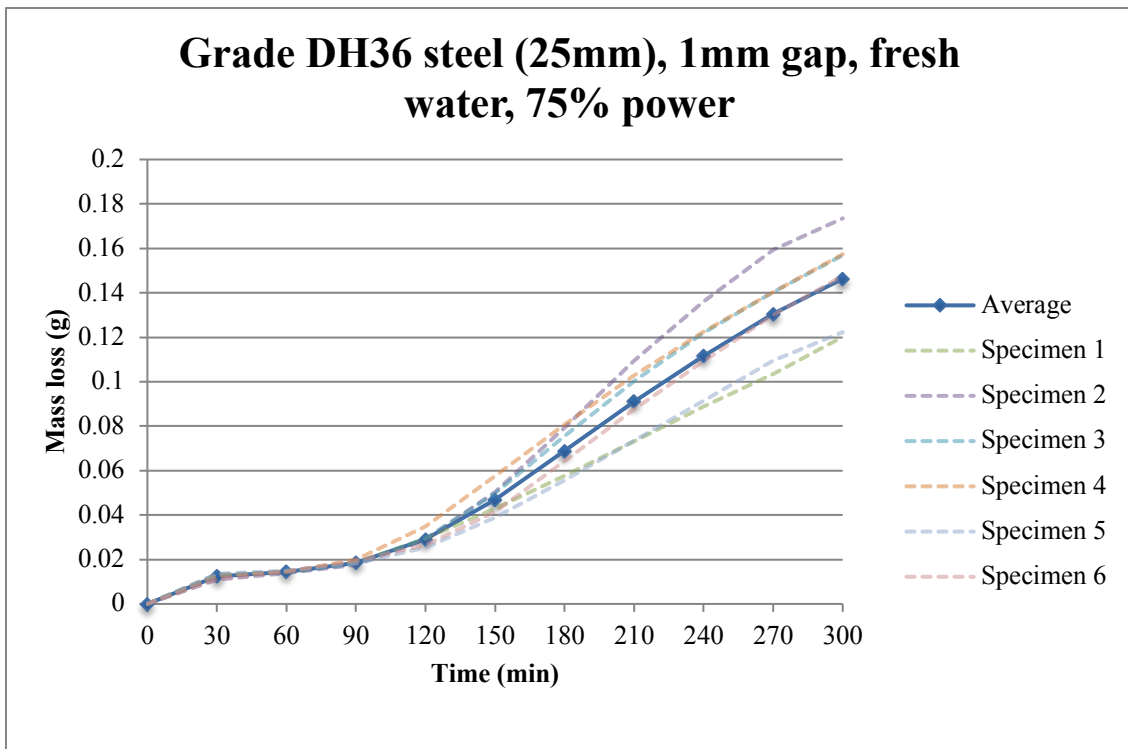


Figure 4.3: Mass loss of grade DH36 steel (25 mm) for a 75% (750W) power output.

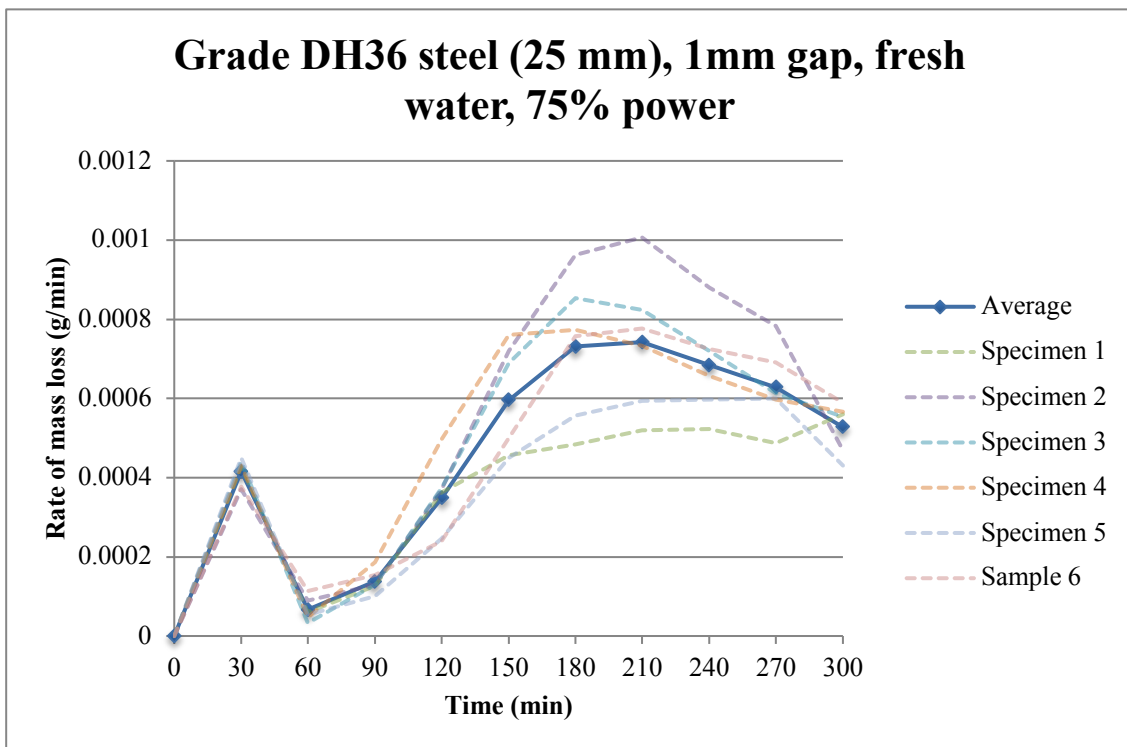


Figure 4.4: Rate of mass loss of grade DH36 steel (25 mm) for a 75% (750W) power output.

Similarly, for the 50 mm side length grade DH36 steel specimens:

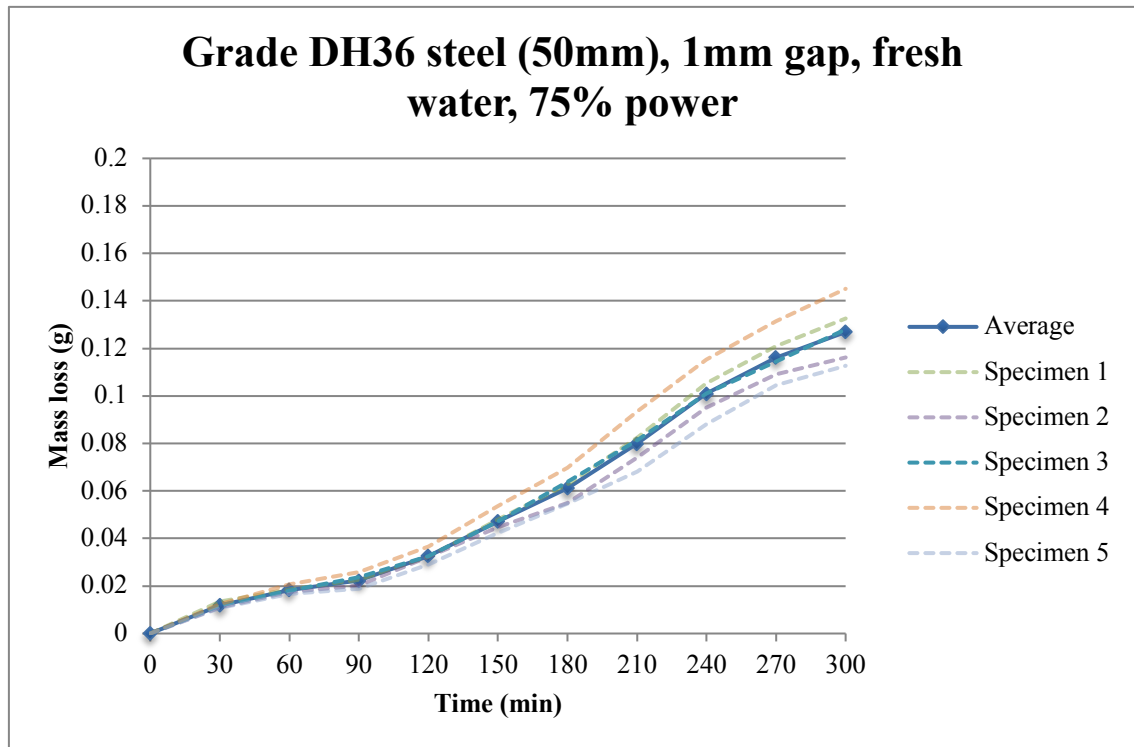


Figure 4.5: Mass loss of grade DH36 steel (50 mm) for a 75% (750W) power output.

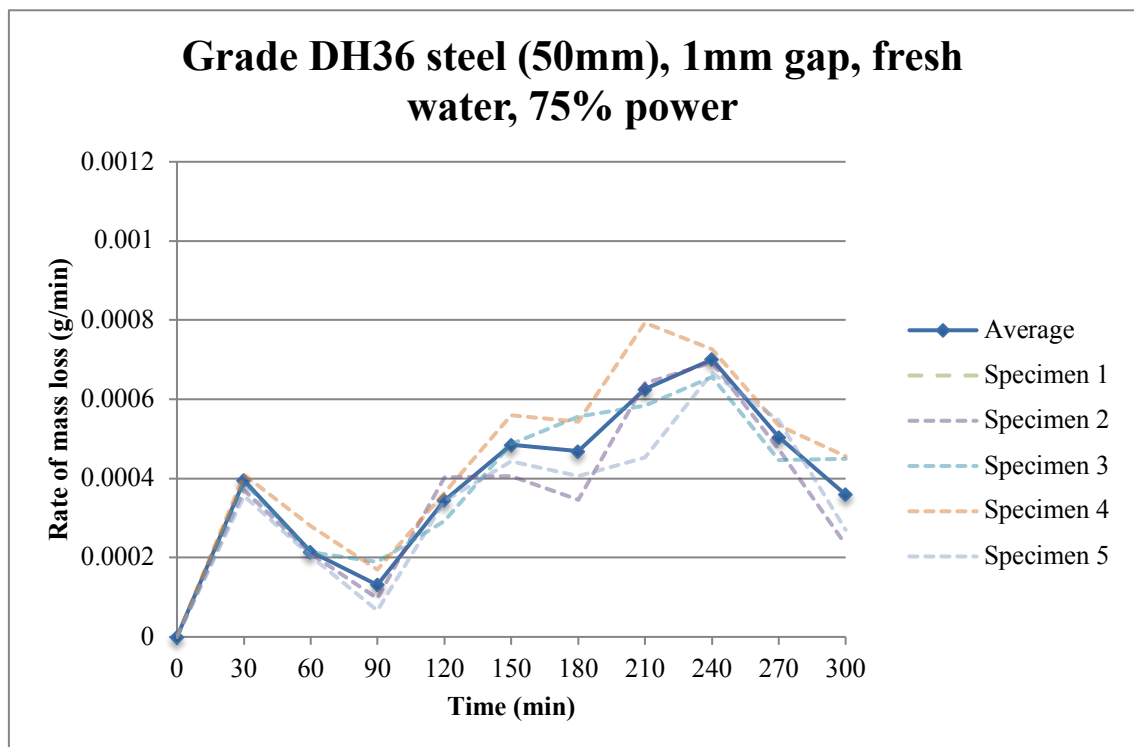


Figure 4.6: Rate of mass loss of grade DH36 steel (50 mm) for a 75% (750W) power output.

It appears from the results that, when the power output of the sonotrode is amplified, the average total mass loss increases. This is because the energy transfers between the sonotrode and the material, and hence damage, increase with the amplification of the power output of the instrument. More specifically, the total average mass loss ranged from 0.14 g for the 25 mm side length specimens to 0.13 g for the 50 mm side length specimens.

The measured difference between the two specimen sizes, although small, can be attributed to dissimilar cavitation flow characteristics relating to their different side length and relevant exposed surface area. In particular, the side length of the smallest specimens (25 mm) is comparable to the diameter of the sonotrode tip (22 mm) whereas with regards to the large ones, their side length (50 mm) is more than two times the diameter of the sonotrode tip. It can be seen in Figure 4.7, where a CFD simulation of the sonotrode operation is presented, that a flow turbulence occurs at its edge, thus the smaller specimens are prone to experience edge effects. As such, an increased amount of erosion would be expected in that instance, which is indeed the case.

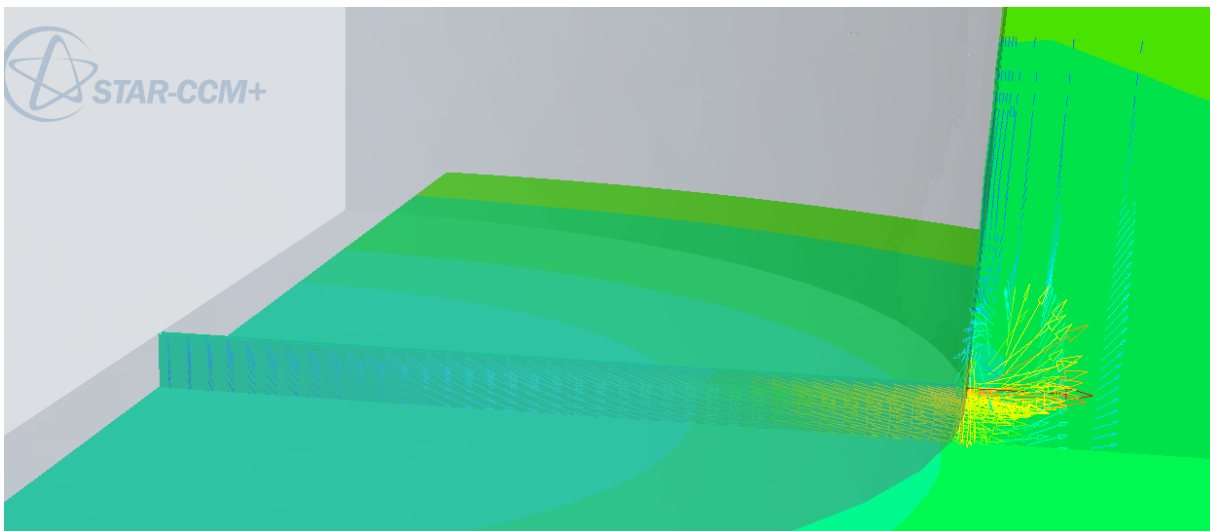


Figure 4.7: CFD simulation of sonotrode operation (Source: Carlton, n.d.)

With regards to their rate of mass loss, however, both types of specimens share a similarly high initial rate of mass loss, of the order of 0.0004 g/min, which is comparable to the rate of mass loss that was measured when a 50% (500W) power output was applied, thus 0.00038 g/min. Past the initial peak, the rate of mass loss decreases significantly, before it rises up again until three and a half to four hours. Interestingly the rate of mass loss then decreases significantly and afterwards rises again before it stabilizes and decreases. Some small discrepancies that may be observed can again be attributed to the parameter of specimen size.

Again, this behaviour is in contrast with what was essentially expected, in the sense that, in many cases cavitation initiates in the form of plastic deformation (orange peeling) with no apparent mass loss, a phase called the incubation period. The parameter of stress amplifying notches is again believed to be the cause, a hypothesis which will be examined towards the end of this sub-chapter. Past that point and due to the expansion of work hardening effects, the rate of mass loss then reduces significantly, only for a short period though, after which the rate of mass loss increases again and the specimens appear to be going through an accumulation phase before eventually entering a steady state phase and a deceleration phase one hour before the end of the exposure. It appears from the results that, the increased erosive potential of the 75% (750W) setting, leads into the deterioration of the work hardened upper layers of the surface in a short period of time ranging from half to one hour, whereas the newly exposed deeper layers of the surface have to go through the aforementioned phases again.

It should be noted that all grade DH36 steel specimens that have been presented so far were provided by the same supplier. From this point, onwards, however, all materials that are going to be presented, including grade DH36 steel, were supplied by BAE Systems.

Figures 4.8 and 4.9 show the mass loss and rate of mass loss of 50mm side length grade DH36 steel specimens, supplied by BAE Systems for a 75% (750W) power output:

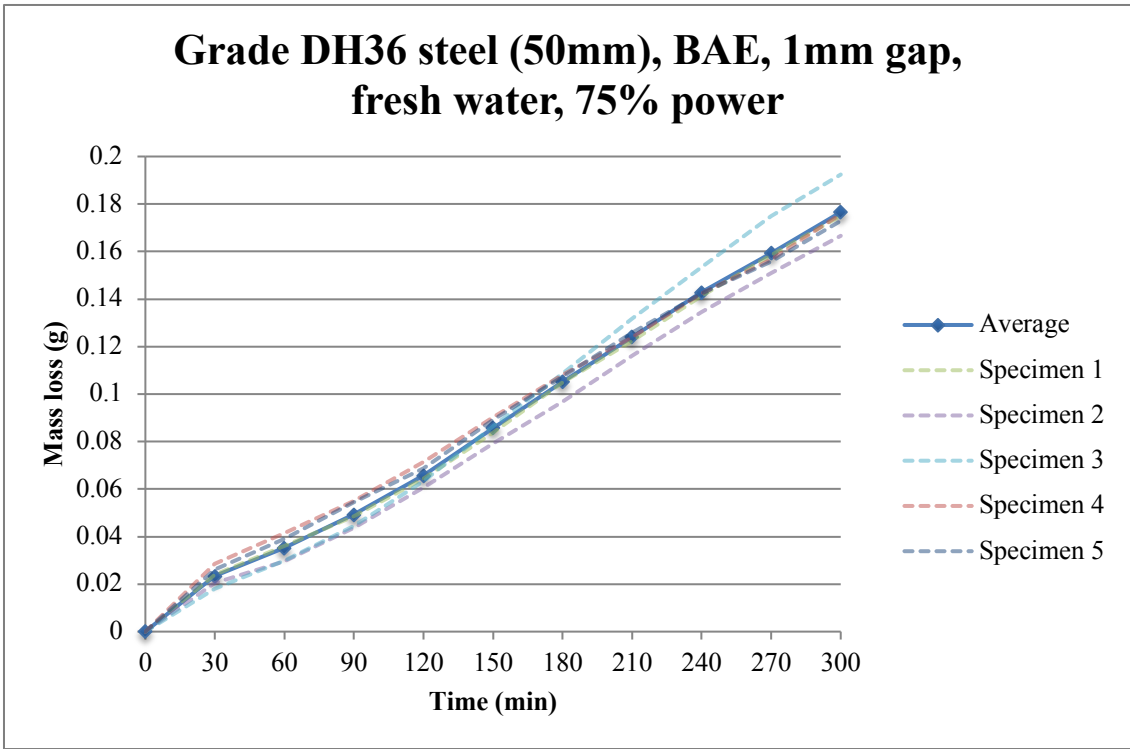


Figure 4.8: Mass loss of grade DH36 steel (50 mm) from BAE Systems for a 75% (750W) power output.

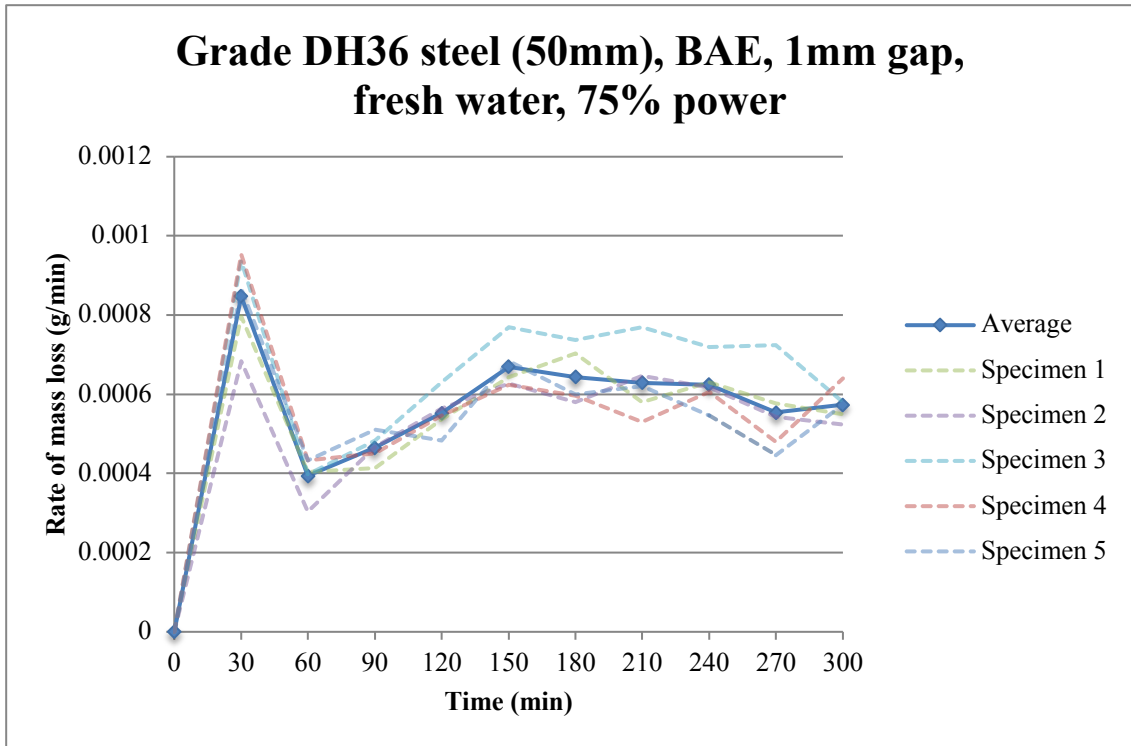


Figure 4.9: Rate of mass loss of grade DH36 steel (50 mm) from BAE Systems for a 75% (750W) power output.

For specimens provided by BAE Systems, the average total mass loss was higher in comparison to the ones provided by the other supplier, at 0.18g. As for the rate of mass loss, the peak value that was measured was almost twice the initial rate of specimens provided by the other supplier, at 0.00008 g/min after thirty minutes. Afterwards the rate of mass loss sharply decreases before it stabilizes and slightly decreases towards the end of the exposure. Again, the high initial rate of mass loss can be attributed to a stress amplifying parameter, such as the presence of notches due to a rough virgin surface. From that point onwards and due to the extension of work hardening effects the rate of mass loss decreases thus the specimens are going through the steady state phase, during which they fail uniformly, before eventually entering the deceleration period thirty minutes before the end of the exposure.

Although the ‘steadier’ behaviour that was observed, with regard to the rate of mass loss, can be attributed to the internal condition of the alloys (flaws and cracks) or a slightly dissimilar chemical composition, within the material standard, a hypothesis relating to the initial surface roughness was formed with regard to the initial peak of mass loss and the observed differences between suppliers. As such, an exploration was conducted, for specimens provided by both the first supplier and BAE Systems (as received and polished). An average initial surface roughness value for the specimens of the ‘T. O. Erosion study’ is also provided. Results, as measured by use of a Mitutoyo SJ-310 roughness tester are presented in Figure 4.10:

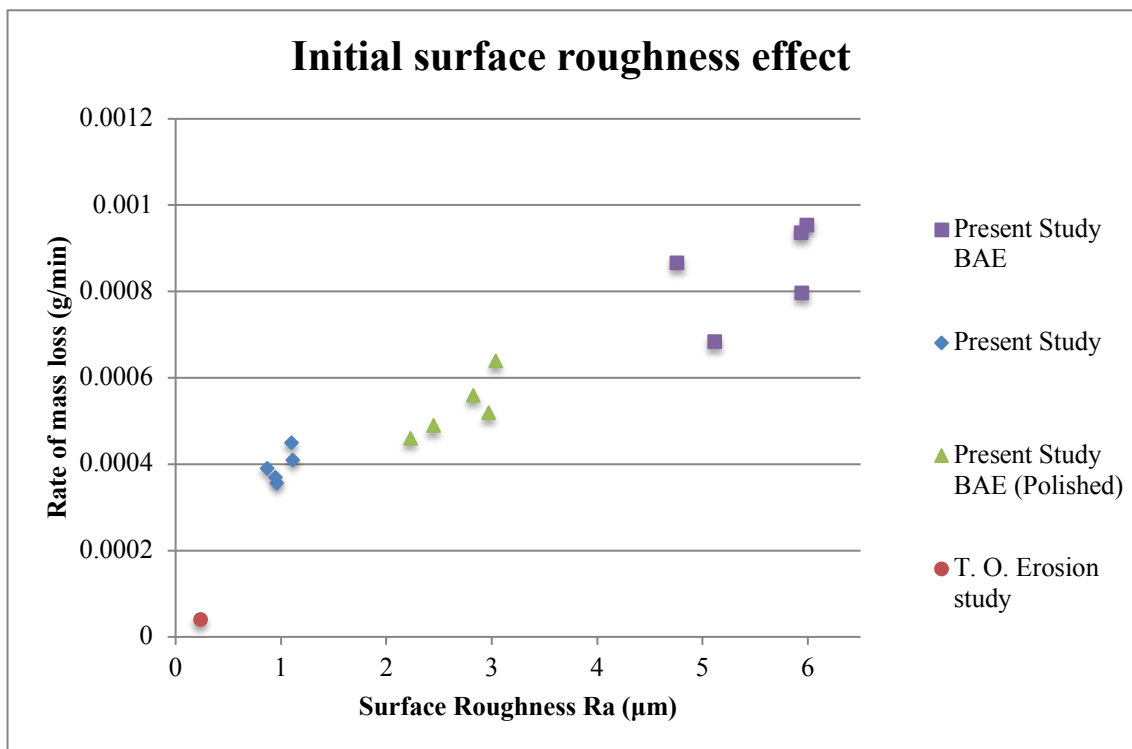


Figure 4.10: Initial surface roughness.

A connection between the initial surface roughness and the rate of mass loss may be observed. This is due to the presence of notches on the rougher surfaces, that act as stress concentrators and result into an increased amount of damage – mass loss. This hypothesis may also explain why the average rate of mass loss of specimens with dissimilar initial surface roughness becomes almost identical further into the procedure, despite the initial differences, whereas an analogous degree of erosion can be observed for all specimens towards the end of the exposure. The progression of the macroscopic appearance of erosion in the case of grade DH36 steel is presented in Figure 4.11:

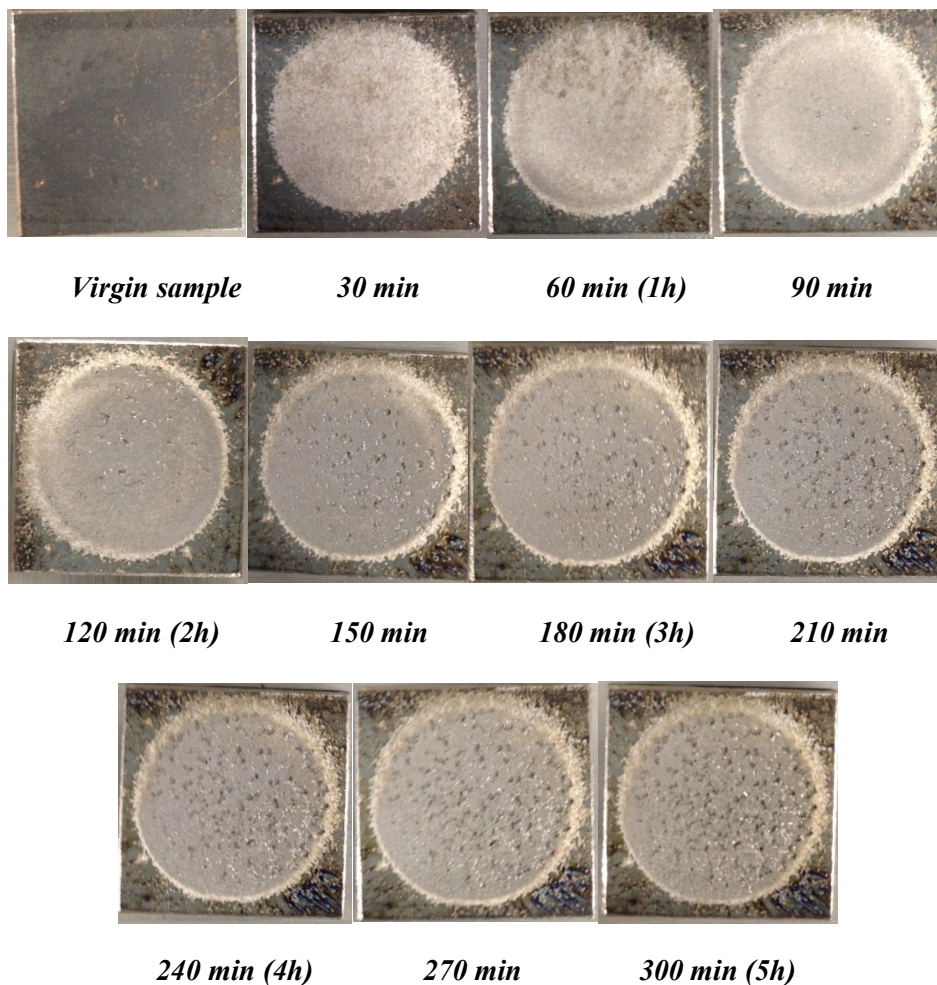


Figure 4.11: Progression of erosion for Grade DH36 steel.

It can be seen that the exposed surface gets eroded progressively, with only a few deep pits appearing after two hours of cavitation exposure, whereas their number increases for the rest of the exposure before they eventually dominate the erosion pattern. As such, a significantly eroded and rough surface can be observed at the end of the exposure, the shape of which is identical to the sonotrode tip, thus it is circular with a diameter of 22 mm.

4.3 Correlation with the ‘T. O. Erosion study’

The proposed experimental procedure and conditions were essentially based on the findings of the ‘T. O. Erosion study’ that was also concerned with ultrasonically induced cavitation erosion. As such, an attempt to correlate the preliminary results of the current research with the ‘T. O. Erosion study’, under identical experimental conditions, was made.

The common ground between the two studies, in this comparison, was the use of grade DH36 steel specimens, which were examined in two different sizes (25 mm and 50 mm side length) and were exposed to cavitation under two different sonotrode power outputs (50% - 500W and 75% - 750W). In both cases, specimens were exposed to ultrasonically induced cavitation for a period of four and five hours, with respect to their size, whilst mass loss measurements were taken every thirty minutes. Results were plotted onto mass loss and rate of mass loss comparison graphs whereas it should be noted that only the average mass loss values were plotted in this case, to make reading of the results easier.

A graphic comparison between grade DH36 steel specimens with a side length of 25 mm, from the ‘T. O. Erosion study’ and the present study, in terms of cavitation induced mass loss, is presented in Figures 4.12 and 4.13:

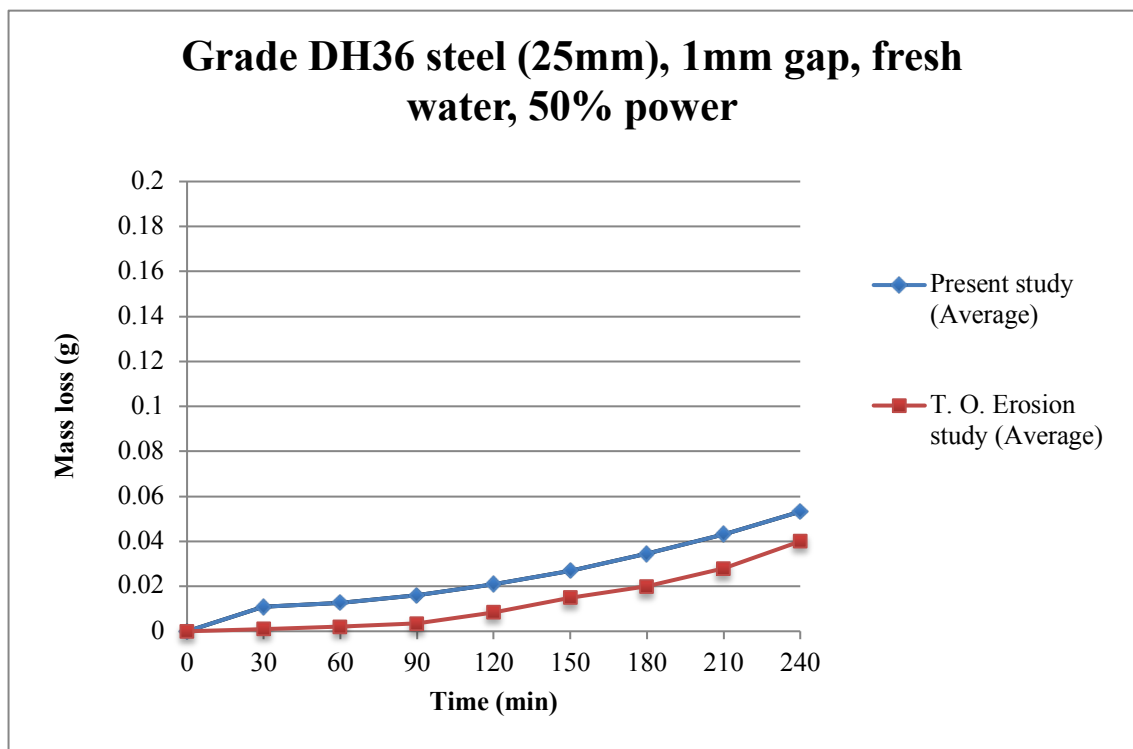


Figure 4.12: Mass loss comparison between the ‘T. O. Erosion study’ and the present study.

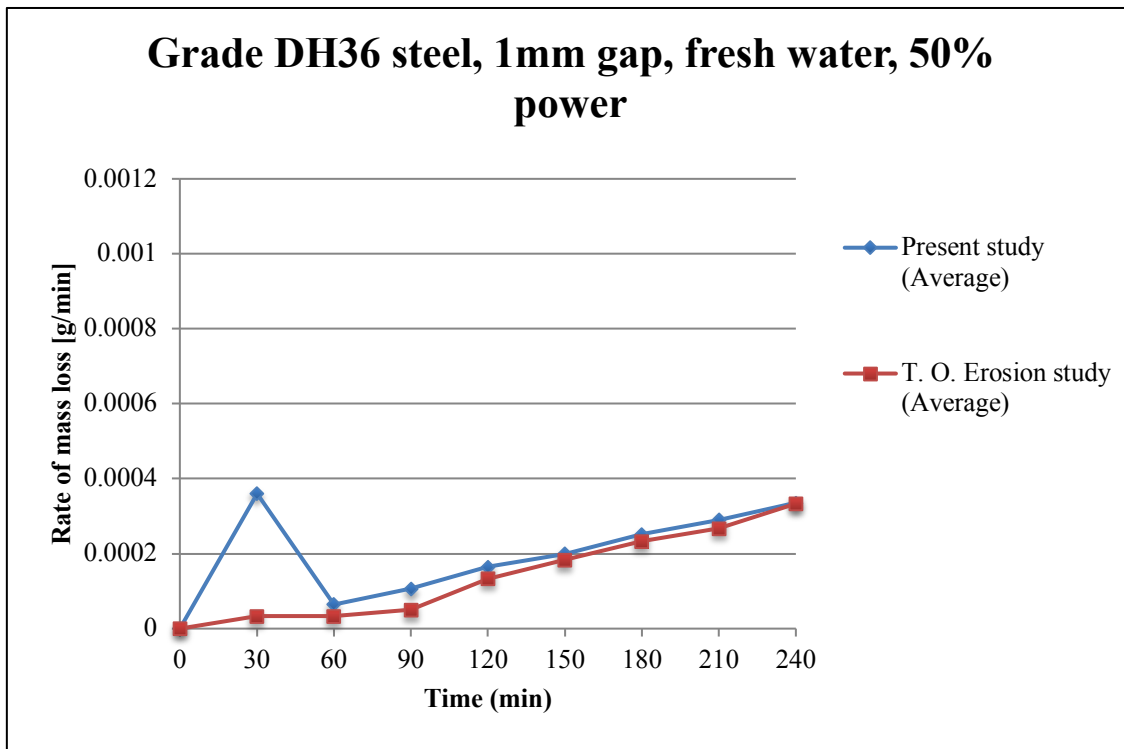


Figure 4.13: Rate of mass loss comparison between the ‘T. O. Erosion study’ and the present study.

Mass loss curves from the ‘T. O. Erosion study’ and the present study are similar, although in the case of the latter, specimens appear to be losing more mass during the first thirty minutes of the exposure, leading to a final mass loss difference of 0.01g between the two studies.

It can be seen that, the mass loss rate of the specimens of the present study is significantly higher compared to the earlier one, for the first thirty minutes of the exposure, whereas beyond that point, curves are similar. Considering that, all specimens were made from grade DH36 steel, that difference could be attributed to the higher initial surface roughness of the specimens of the present study or a slightly different chemical composition, within the material standard, and internal condition (flaws and cracks). The fact that, specimens from both studies behave in an identical way past the one hour mark, however, indicates that the parameter of the initial surface roughness is possibly the major difference between the two batches of specimens. This hypothesis is in good agreement with the data of Figure 4.9 where it can be seen that, the lower the initial surface roughness, the higher the initial resistance of steel against erosion. In this context, specimens from the ‘T. O. Erosion study’ were relatively smoother compared to the present one whereas their initial rate of mass loss was also lower.

Results from specimens, with a side length of 50 mm, from two different suppliers were also compared to the ‘T. O. Erosion study’ and are presented in Figures 4.14 and 4.15:

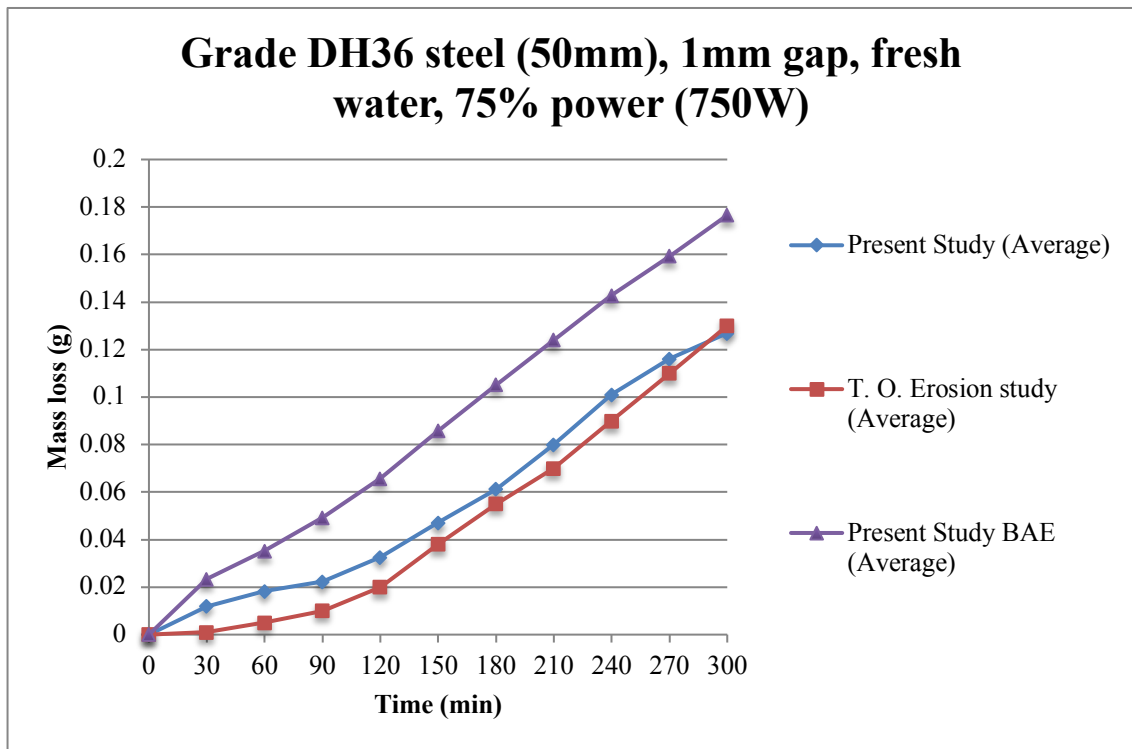


Figure 4.14: Mass loss comparison between the ‘T. O. Erosion study’ and the present study - Two suppliers are considered for the present study.

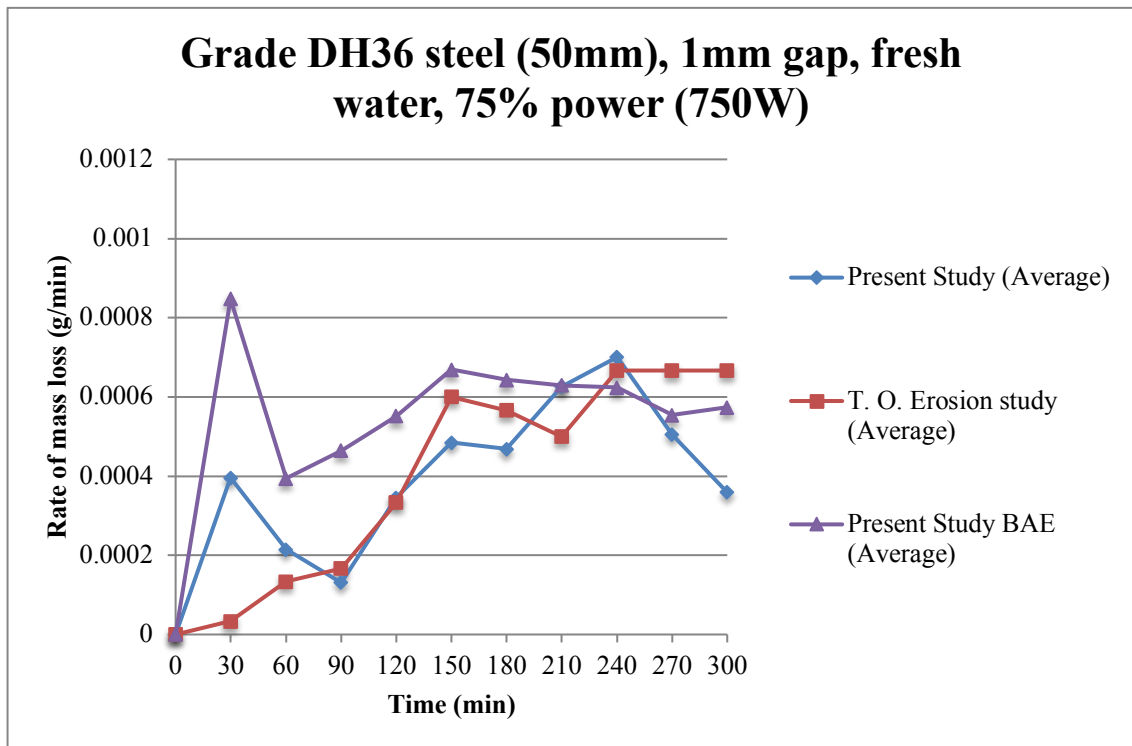


Figure 4.15: Rate of mass loss comparison between the ‘T. O. Erosion study’ and the present study - Two suppliers are considered for the present study.

In the case of the 50 mm specimens from the first supplier, the average total mass loss was identical to the ‘T. O. Erosion study’, at 0.13g, whereas the appearance of the mass loss curves

was analogous. Nevertheless, the initial mass loss rate of specimens from the present study was again higher in comparison to the earlier one, a behaviour that can again be attributed to the higher initial surface roughness of the specimens of the present study, in favour of the parameters of a possibly slightly different chemical composition or condition. This hypothesis is again in good agreement with the data of Figure 4.9, where it can be seen that the smoother the initial surface, the higher the resistance of steel against erosion.

A similar behaviour can be observed in the case of specimens provided by BAE Systems. In that instance the initial rate of mass loss is even higher compared to the other two cases whereas past the point it tends to stabilize. This behaviour can again be attributed to the initial surface roughness of specimens provided by BAE Systems, which was the highest amongst the examined specimens, although the parameter of a slightly different chemical composition, within the material standard, and condition could also explain some discrepancies with regards to the progression of erosion past the initial stages.

Nevertheless, correlation with the ‘T. O. Erosion study’ is considered to be successful, in the sense that the progression of mass loss, in terms of the measured rate, as well as the resulting total mass loss are similar and comparable in all cases, apart from the initial rate of mass loss which is believed to be influenced by the parameter of surface roughness. In fact, those two factors were successfully correlated for four different cases, in the previous sub-chapter, including specimens from both the ‘T. O. Erosion study’ and the present study.

4.4 The effect of cathodic protection

The effect of cathodic protection was also examined by means of an immersed current unit with three electrodes. A working potential of -790 mV was chosen, as it was found to be beneficial in the ‘T. O. Erosion study’, with regards to the resulting erosion - mass loss. In all cases, mass loss and mass loss rate curves for specimens without any cathodic protection were also plotted for comparison reasons. In addition, a comparison with results from the ‘T. O. Erosion study’ was also conducted for correlation purposes. Working potentials around the optimal value of -790 mV were also tested whereas their effect in terms of mass loss is presented and discussed at the end of this sub-chapter.

In this context, cathodic protection was applied on thirteen 50 mm side length grade DH36 steel specimens. More specifically:

- Five 50 mm side length grade DH36 steel specimens supplied by BAE Systems at a 75% (750W) power setting, with CP (-790 mV). *Five hours of cavitation exposure.*

- Two 50 mm side length grade DH36 steel specimens supplied by BAE Systems at a 75% (750W) power setting, with CP (-250 mV). *Five hours of cavitation exposure.*
- Two 50 mm side length grade DH36 steel specimens supplied by BAE Systems at a 75% (750W) power setting, with CP (-500 mV). *Five hours of cavitation exposure.*
- Two 50 mm side length grade DH36 steel specimens supplied by BAE Systems at a 75% (750W) power setting, with CP (-1000 mV). *Five hours of cavitation exposure.*
- Two 50 mm side length grade DH36 steel specimens supplied by BAE Systems at a 75% (750W) power setting, with CP (-1250 mV). *Five hours of cavitation exposure.*

The average mass loss and rate of mass loss, for a working potential of -790 mV, is presented in Figures 4.16 and 4.17. An average mass loss curve for specimens without cathodic protection (CP) is also provided for comparison reasons.

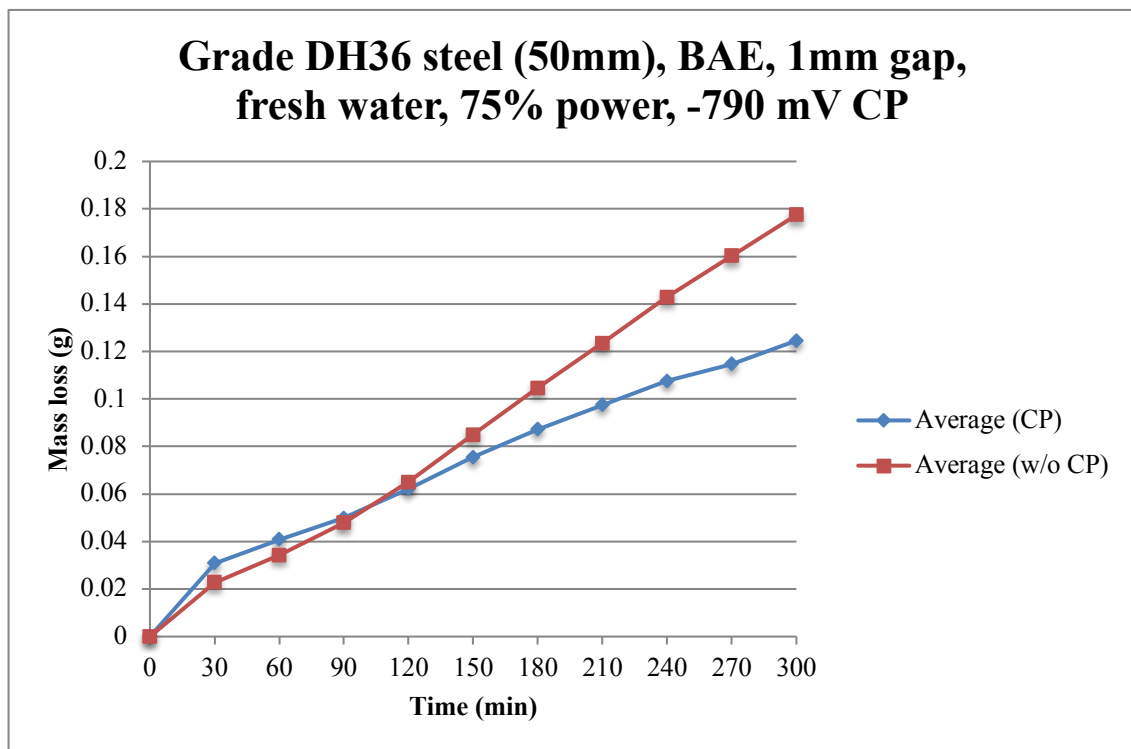


Figure 4.16: Mass loss of grade DH36 steel (50 mm) at a 75% (750W) power setting and under a -790 mV CP.

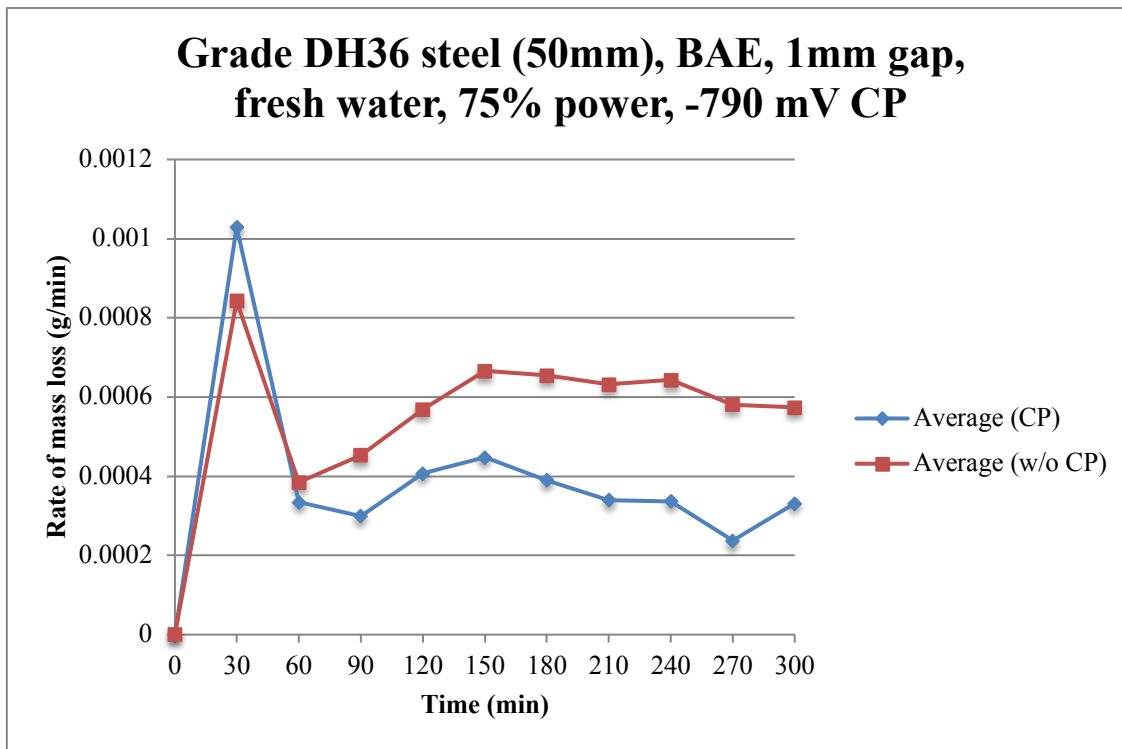


Figure 4.17: Rate of mass loss of grade DH36 steel (50 mm) at a 75% (750W) power setting and under a -790 mV CP.

It can be clearly seen that, a working potential of -790 mV CP, significantly improved the behaviour of the specimens against ultrasonically induced cavitation, in terms of the resulting erosion - mass loss. In particular, there was a reduction of the cavitation related mass loss of the order of 0.06g, thus the total mass loss was 0.12g instead of 0.18g.

The effect of cathodic protection can be seen more clearly in the rate of mass loss curves. Apart from a slight advantage in favour of the specimens without cathodic protection (CP) in the initial rate of mass loss, which is due to a small delay of the system on establishing the appropriate working potential thus resulting into slightly non – favourable conditions, the rate is considerably lower for the protected specimens for the rest of the exposure period. As a result, the total mass loss of the protected specimens is significantly lower. This is because erosion is essentially a function of mechanical and electrochemical parameters, thus when cathodic (protective) reactions occur at the protected specimen the electrochemical aspect of the damage attenuates and as a result mass loss decreases.

A similar behaviour was observed in the ‘T. O. Erosion study’, of which the experimental conditions were utilized. Mass loss and mass loss rate results from both studies, with and without cathodic protection are presented in Figures 4.18 and 4.19:

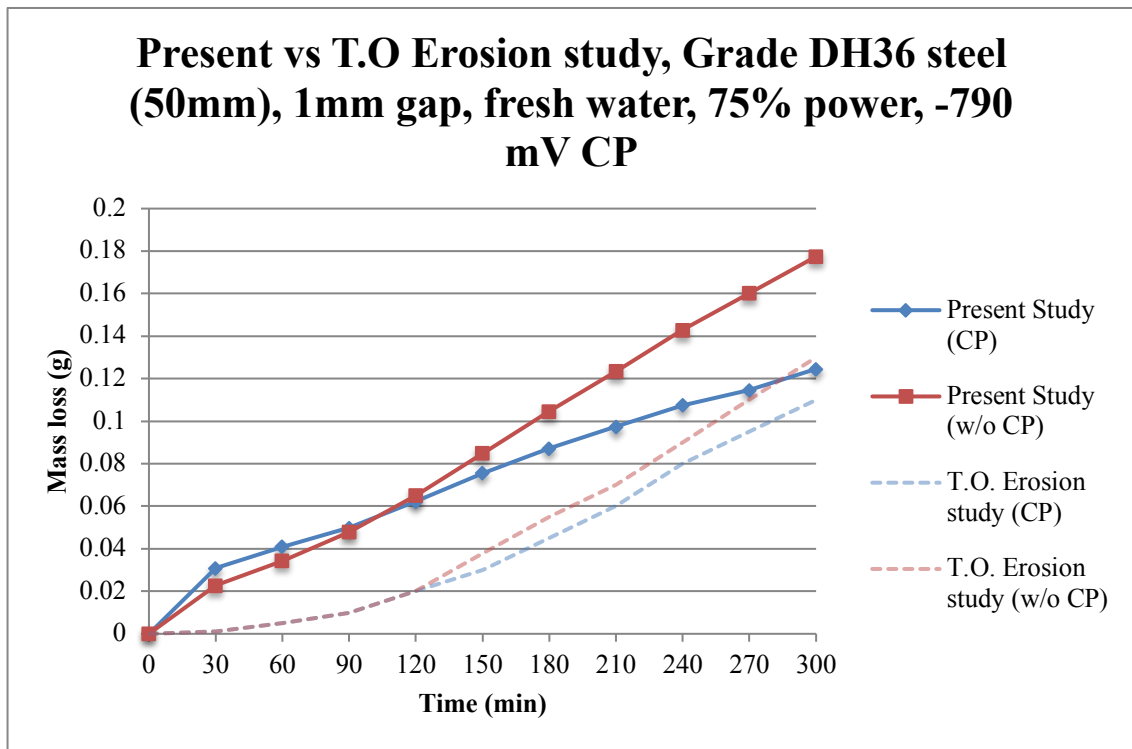


Figure 4.18: Mass loss of grade DH36 steel (50 mm) at a 75% (750W) power setting and under a -790 mV CP. Present vs ‘T.O. Erosion study’.

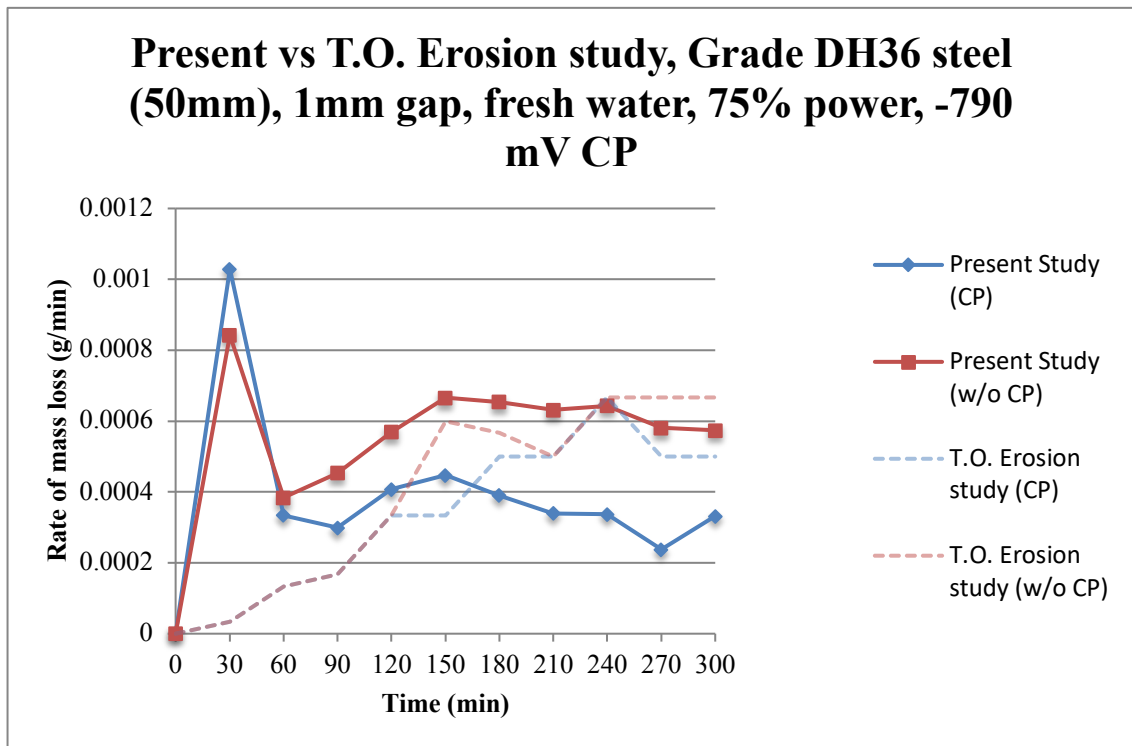


Figure 4.19: Rate of mass loss of grade DH36 steel (50 mm) at a 75% (750W) power setting and under a -790 mV CP. Present vs ‘T.O. Erosion study’.

Similarly, results from the ‘T. O. Erosion study’ indicate that, there was an improvement in terms of cavitation related mass loss, when cathodic protection was applied, as the

electrochemical aspect of erosion was limited. That difference, however, was of the order of 0.02g instead of 0.06g. This is also reflected in the rate of mass loss curves (CP and w/o CP) which are less dispersed, with respect to each other, in the ‘T. O. Erosion study’ and imply a smaller mass loss difference. This behaviour can again be attributed to the dissimilar initial surface roughness of the two batches of specimens as well as a slightly different composition, within the material standard, of the otherwise identical materials or even different conditions, similarly to the hypothesis that was formed for the initial correlation measurements of the previous sub-chapter. It is also noteworthy that the rate of mass loss curves (CP and w/o CP) from the ‘T. O. Erosion study’ almost match for the first two hours of cavitation, thus the effect of cathodic protection is more pronounced past the initial phases. This was also confirmed by the present study, for which the rate of mass loss curves (CP and w/o CP) are more dispersed with respect to each other past those phases. This is because the newly exposed material is more susceptible to electrochemical damage in comparison to the work-hardened, by the earlier phases, surface.

Mass loss and rate of mass loss results for different potentials are presented in Figures 4.20, 4.21 and 4.22:

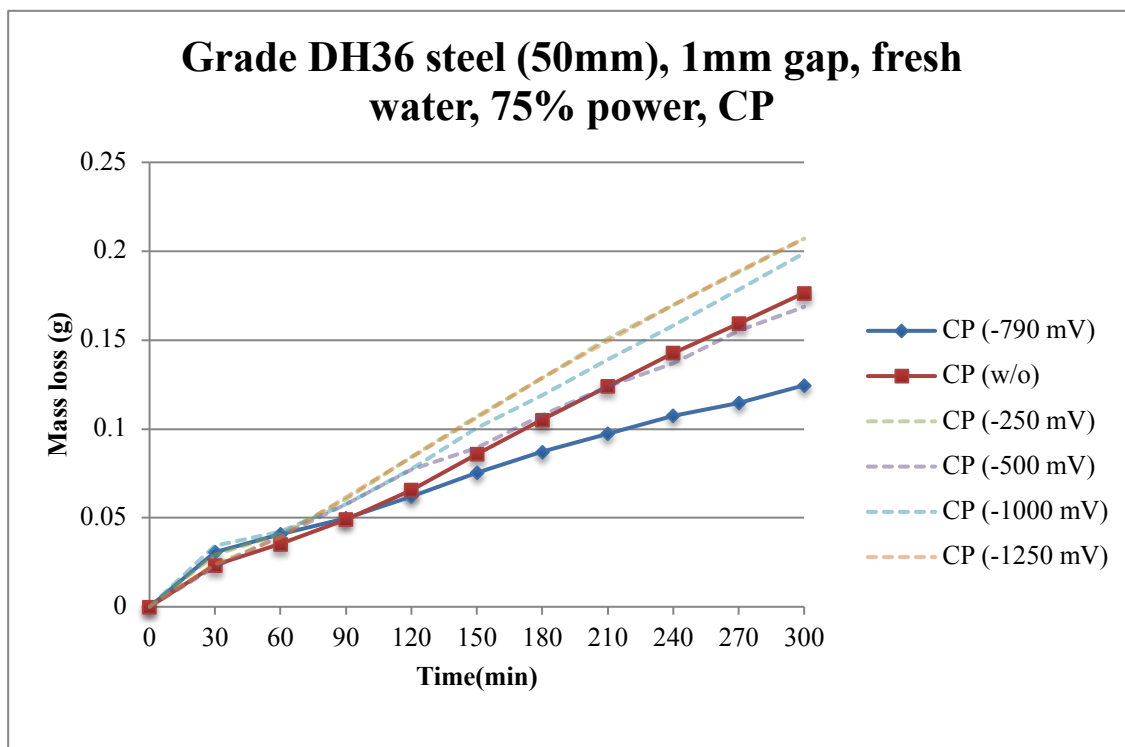


Figure 4.20: Mass loss of grade DH36 steel (50 mm) at a 75% (750W) power setting and under different CP potentials.

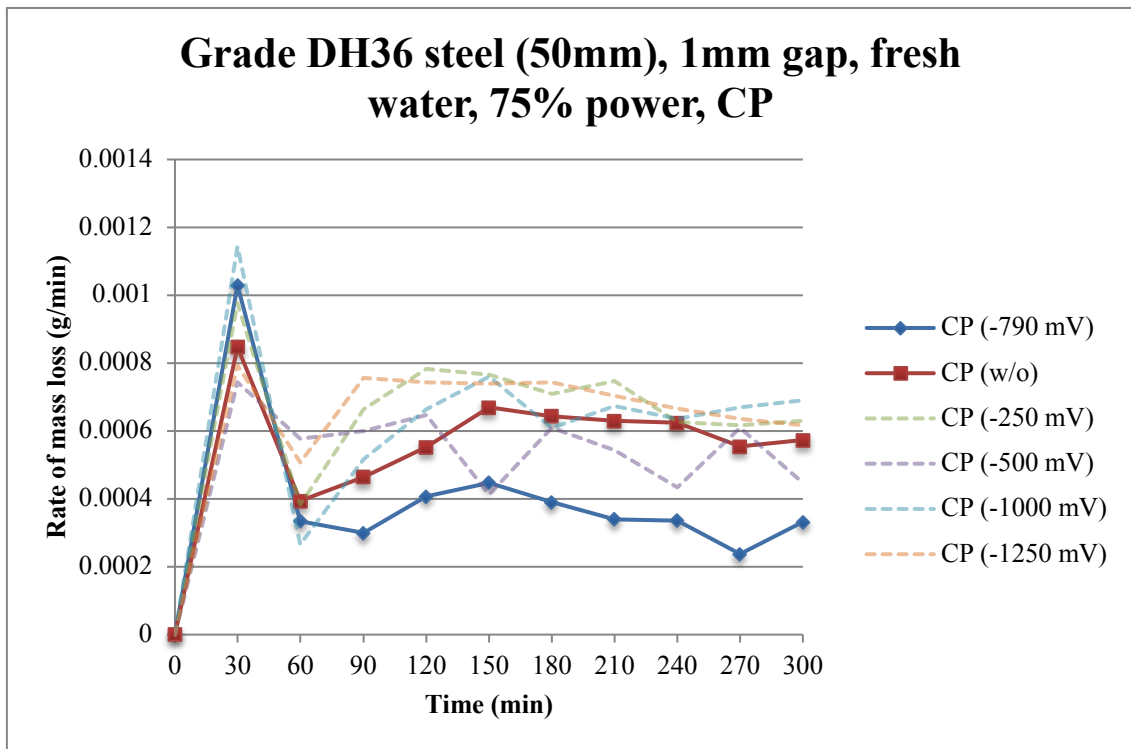


Figure 4.21: Rate of mass loss of grade DH36 steel (50 mm) at a 75% (750W) power setting and under different CP potentials.

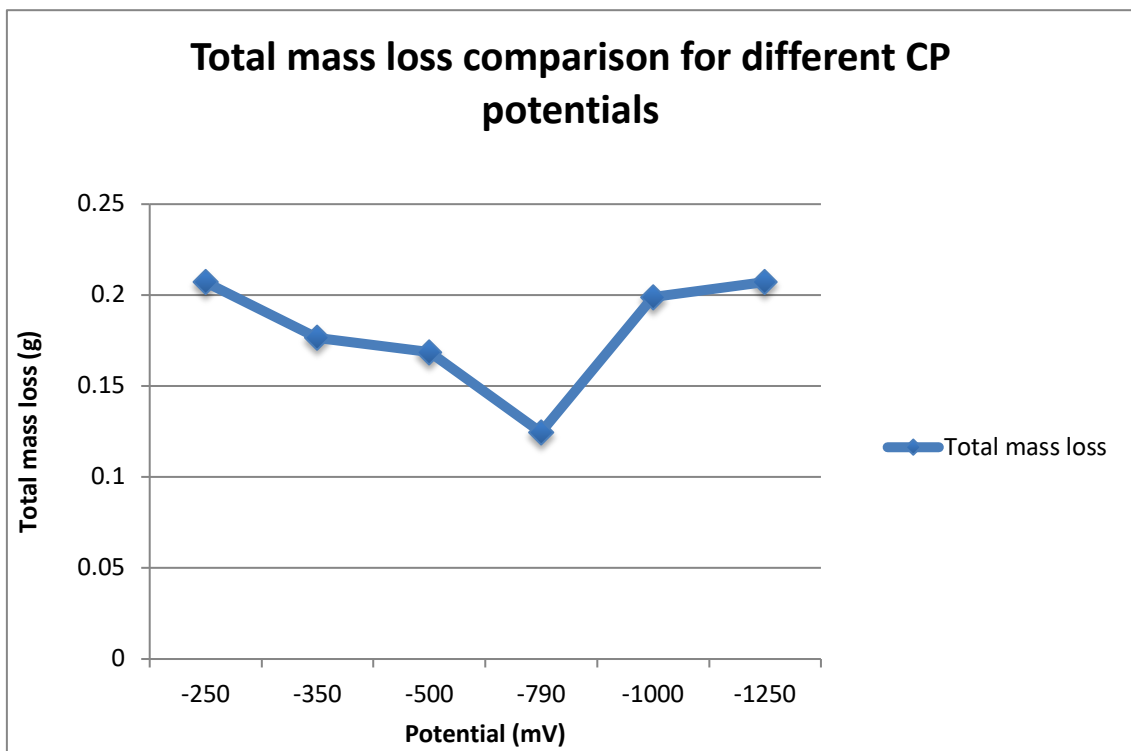


Figure 4.22: Total mass loss versus different working potentials for grade DH36 steel.

The beneficial effect of the -790 mV potential can be seen in the presented mass loss graphs. In particular, the more positive -500 mV working potential, failed to improve the resistance of the specimens against cavitation, in terms of the resulting mass loss, whereas the even more

positive-250 mV working potential further impaired the resistance of the specimens against cavitation and as a result mass loss was even higher than the non-protected specimens. This was also the case for the more negative -1000 mV and -1250 mV working potentials.

This behaviour can be ascribed to the electric potential of grade DH36 steel in fresh water which is -350 mV, when exposed to cavitation. Anything more positive than this value (-250 mV) leads to a positive current on the working sample and anodic reactions, thus the alloy loses electrons and corrodes whereas more negative values (-500 mV, -790 mV), lead to an influx of electrons. These electrons then react with the surrounding water and dissolved oxygen, to form hydroxyl ions, thus the working sample is electrochemically protected. Extremely negative values (-1000 mV, -1250 mV), however, lead to the embrittlement of the sample due to excessive hydrogen production from the cathodic reaction, thus mass loss increases, whereas in the presence of an insufficient negative potential (-500 mV), the occurring cathodic reactions are not sufficient to prevent partial oxidation and corrosion of the protected material.

4.5 Mass loss measurements on various alloys and coatings

Mass loss measurements were also conducted on specimens made from other alloys. The experimental conditions were kept identical to the tests which were conducted on grade DH36 steel, mainly for comparison reasons and as such, the gap between the sonotrode tip and each specimen was set at 1mm while the power output of the ultrasonic transducer was adjusted at 75% (750W). In this context, all specimens were exposed to ultrasonically induced cavitation for a period of five hours while their mass loss was measured every thirty minutes.

The additional alloys that were tested are the following:

- Stainless steel 254
- Cupronickel 70-30

While the study of protective coatings was not the main thrust of this study, the opportunity was taken to add these to the measurement file due to interest of BAE Systems in this matter. As such, a number of protective coatings that were applied on base specimens, made from grade DH36 steel, were also tested, under identical experimental conditions. Their commercial names will not be presented, by request of BAE Systems, thus they will be characterized by means of a single capital letter. The same applies for the composition of those coatings, thus only brief details will be given. The protective coatings that were tested are the following:

- I coating
- P coating
- A coating
- Double coating
- R coating
- B coating
- C coating

Similarly to their commercial names, detailed information regarding the composition of those coatings cannot be given, however, it can be noted that they essentially consist of a polyester base which is reinforced, in some cases, by additional components.

In addition to the aforementioned experimental conditions, cathodic protection was also utilized in all cases. In particular, a working potential of -790 mV was applied on all specimens, as it was found to improve the resistance of grade DH36 steel, which was the reference metal in this study, against ultrasonically induced cavitation, in terms of the resulting erosion – mass loss.

It should be noted that, although the optimal working potential for stainless steel 254 and cupronickel 70-30 is possibly different, it was decided that the conditions of this study should be adjusted with respect to the reference metal, namely the grade DH36 steel. In addition, grade DH36 steel is more likely to corrode in comparison to the other two alloys, as it is implied by the relevant anodic index, thus it was thought that its protection is of major importance in the case where a common application of those alloys is considered. This is the context under which, the -790 mV working potential was applied on the other alloys as well. With regards to the protective coatings, these were applied on base specimens, made from grade DH36 steel, thus it was decided that a -790 mV working potential should be applied in that instance too, although it would not necessarily improve the resistance of their coatings themselves.

Mass loss and rate of mass loss results for each one of the additional alloys and protective coatings are presented below. Moreover, the progression of erosion in thirty min intervals, is also presented, in the form of macroscopic pictures.

Mass loss and rate of mass loss results for stainless steel 254 are presented in Figures 4.23 and 4.24. It should be noted that the average surface roughness of the stainless steel 254 specimens was 5.12 μm .

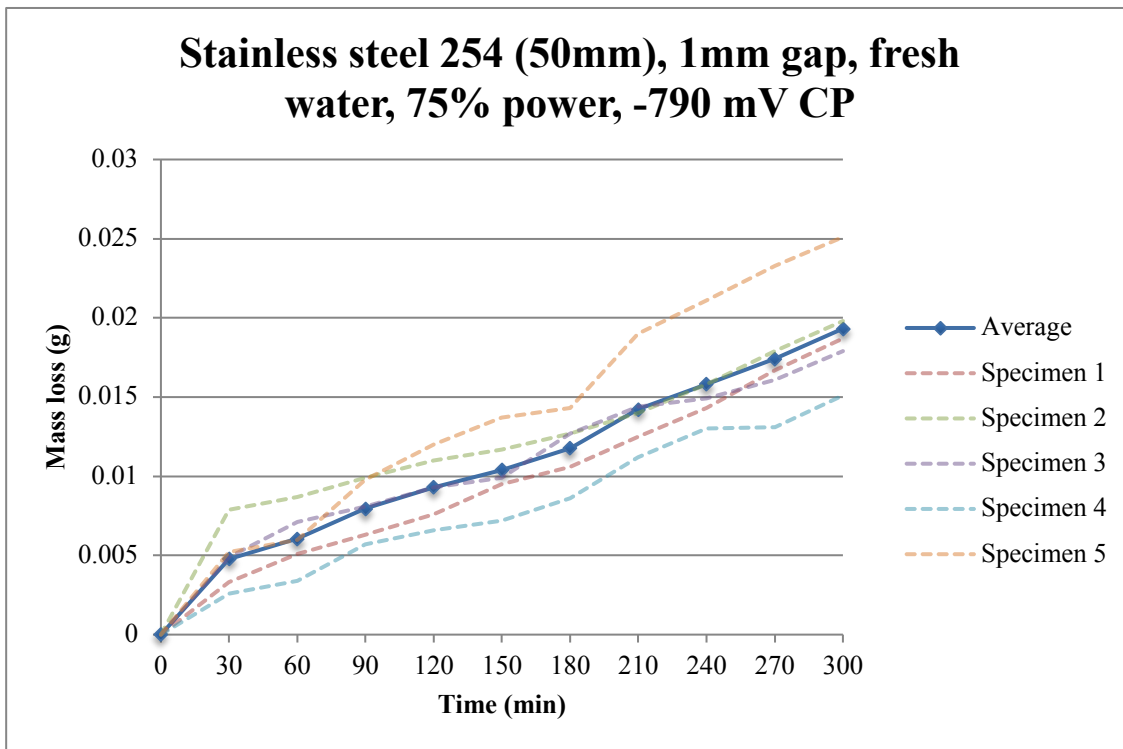


Figure 4.23: Mass loss of stainless steel 254 at a 75% (750W) power setting and under a -790 mV CP.

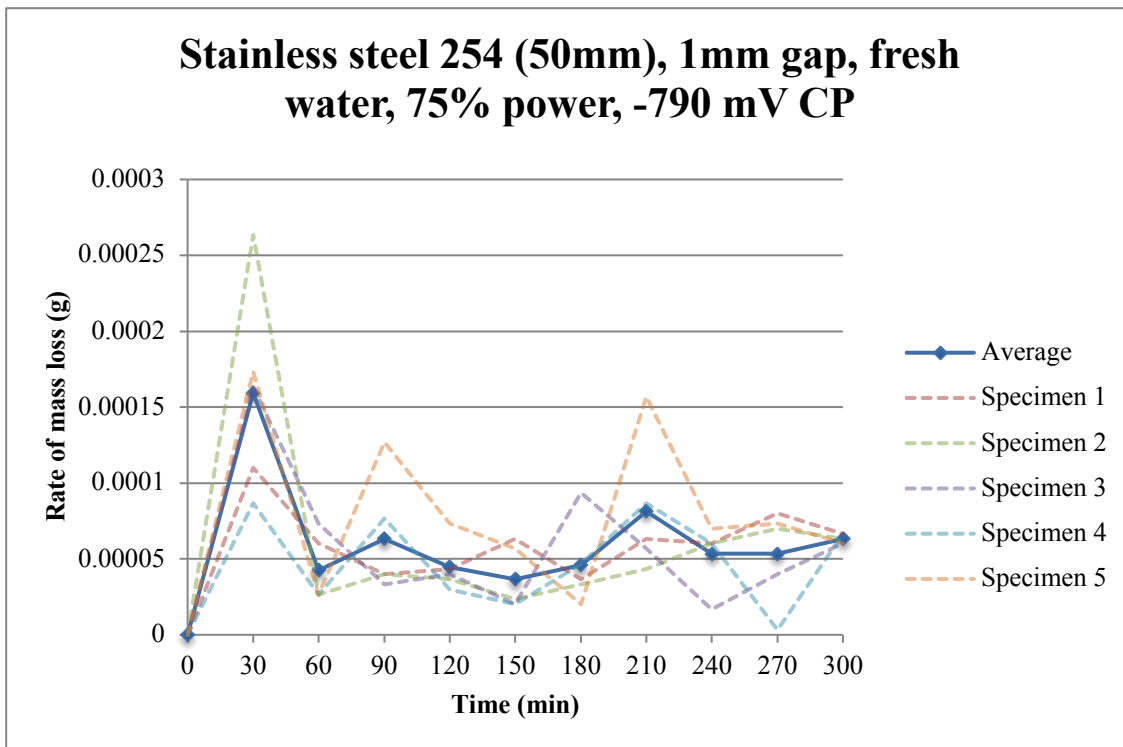


Figure 4.24: Rate of mass loss of stainless steel 254 (50 mm) at a 75% (750W) power setting and under a -790 mV CP.

The total mass loss of stainless steel 254, after five hours of cavitation exposure, was of the order of 0.02g. In comparison to grade DH36 steel, there is a 0.1g difference, 0.02g against

0.12g. Similarly to grade DH36 steel, the rate of mass loss of stainless steel 254 peaks just after thirty minutes of cavitation exposure, whereas the subsequent progressive work hardening results into its rate to decrease significantly and remain steady at approximately 0.00005 g/min for the rest of the procedure.

The progression of the macroscopic appearance of erosion for stainless steel 254 is presented in Figure 4.25:

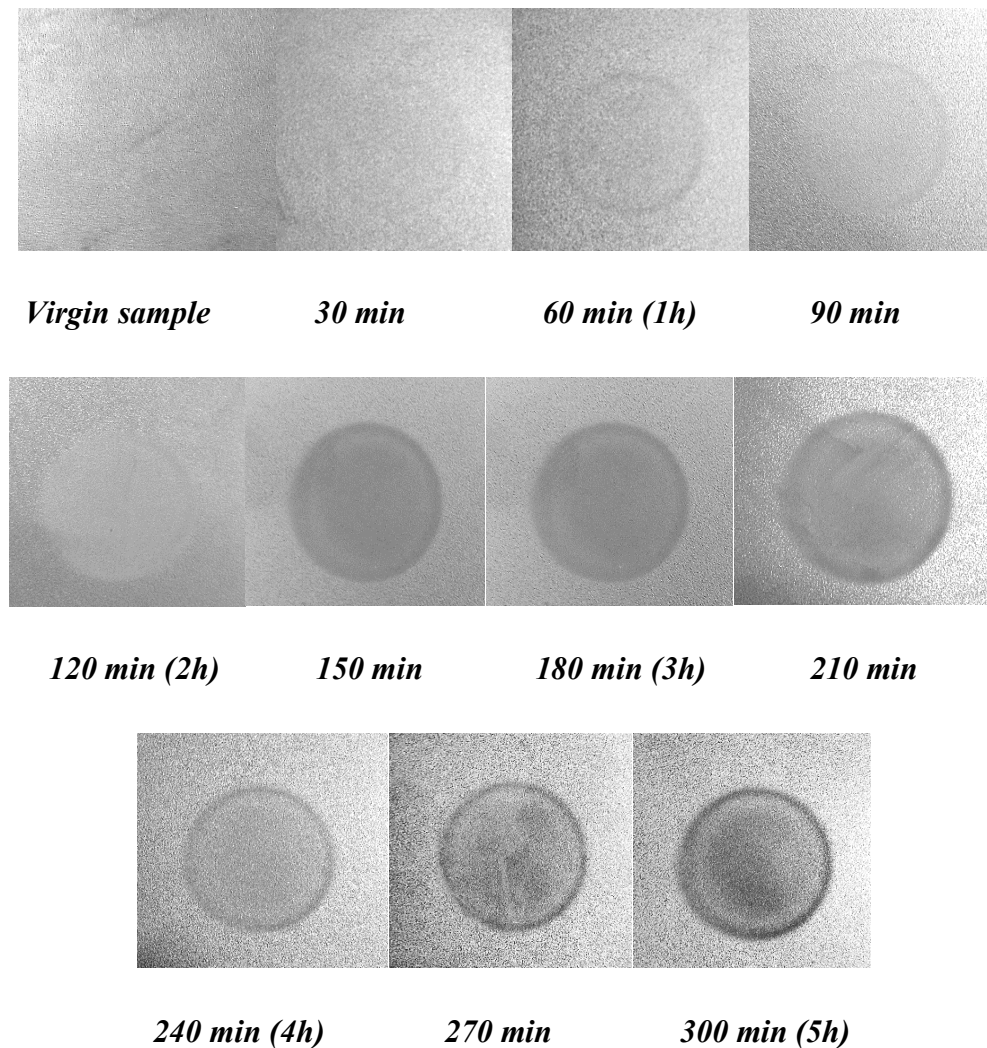


Figure 4.25: Progression of erosion for stainless steel 254.

Mass loss and rate of mass loss results for cupronickel 70-30 are presented in Figures 4.26 and 4.27. In that instance the average surface roughness was of the order of 10.22 μm .

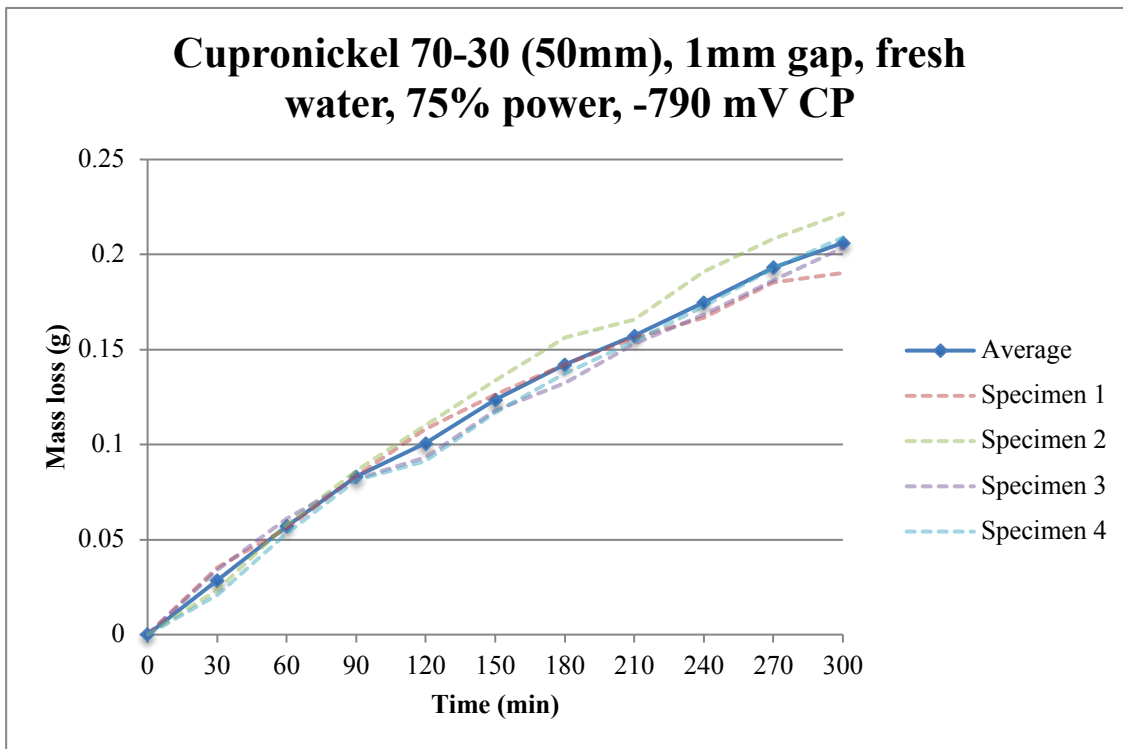


Figure 4.26: Mass loss of cupronickel 70-30 at a 75% (750W) power setting and under a -790 mV CP.

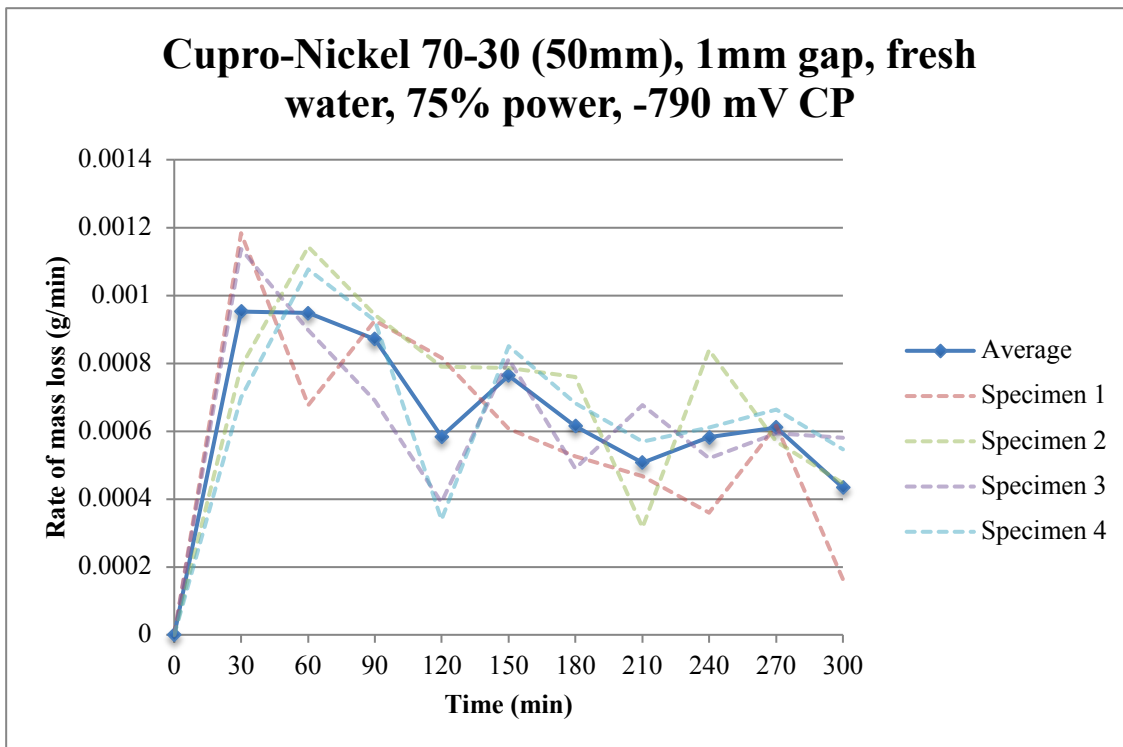


Figure 4.27: Rate of mass loss of cupronickel 70-30 at a 75% (750W) power setting and under a -790 mV CP.

The total mass loss of cupronickel 70-30, after five hours of cavitation exposure, was of the order of 0.2g, approximately 0.08g higher than the mass loss of grade DH36 steel and ten

times the mass loss of stainless steel 254. The rate of mass loss of cupronickel 70-30 peaks after thirty minutes of exposure, similarly to the other alloys, however, it remains at that peak value for more than an additional thirty minutes, before it decreases progressively towards the end of the exposure. The progression of work hardening effects appears to be slower in that instance possibly due to the more ductile nature of this alloy in comparison to the other two.

The progression of the macroscopic appearance of erosion for cupronickel 70-30 is presented in Figure 4.28:

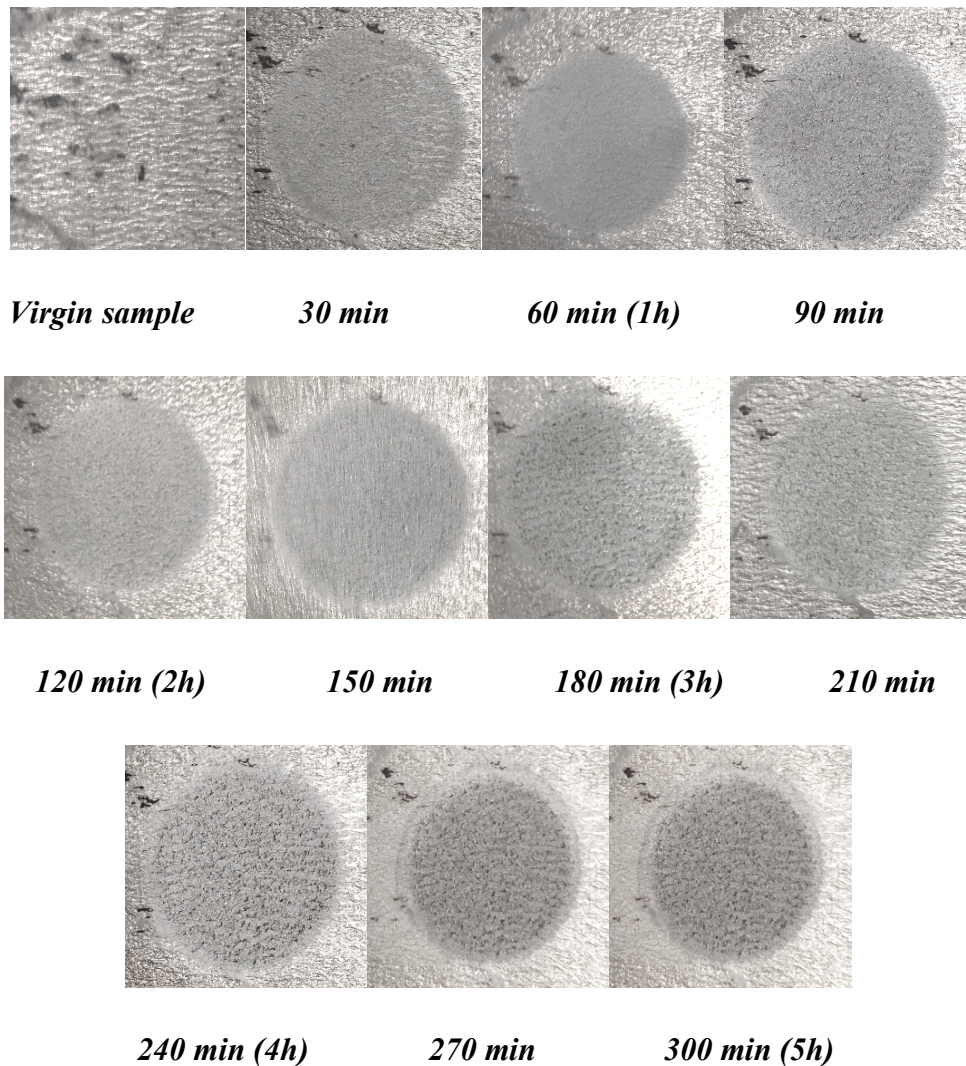


Figure 4.28: Progression of erosion for cupronickel 70-30.

Mass loss and rate of mass loss results for the I coating are presented in Figures 4.29 and 4.30:

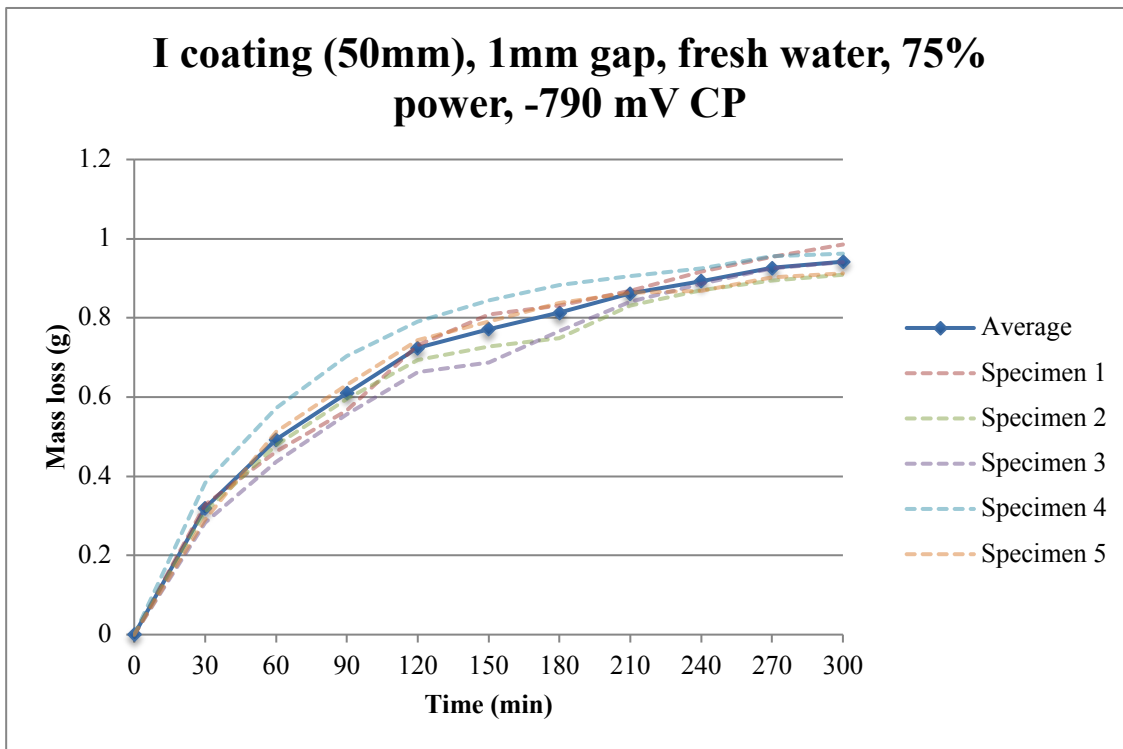


Figure 4.29: Mass loss of I coating at a 75% (750W) power setting and under a -790 mV CP.

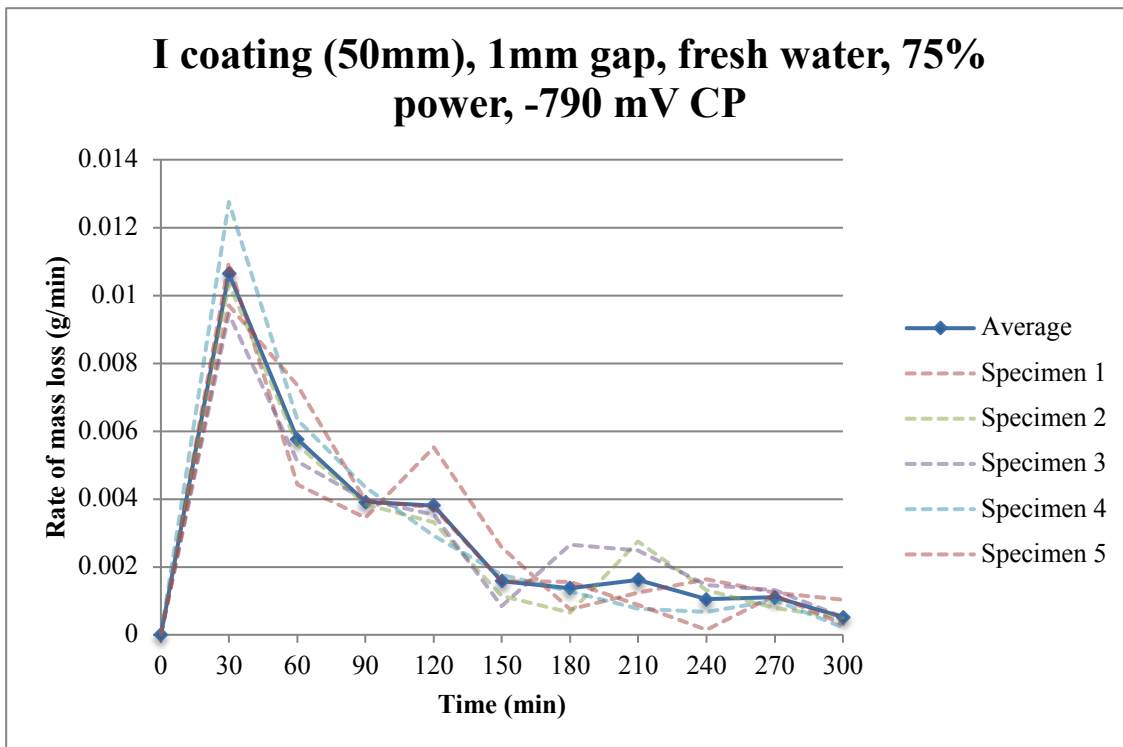


Figure 4.30: Rate of mass loss of I coating at a 75% (750W) power setting and under a -790 mV CP.

The total mass loss of the I coating was of the order of 1g after five hours of cavitation exposure. It should be noted, however, that the coating itself got destroyed just after two hours

of cavitation exposure thus the very high mass loss that was measured mostly relates to the erosion of the coating and not the protected grade DH36 steel, which only got exposed to cavitation after that point. This behaviour is represented in the measured rate of mass loss, which is very high for the first two hours, due to the erosion of the coating, before it decreases significantly and becomes steady for the rest of the procedure. Moreover, from this point to end of the exposure, the rate of mass loss is comparable to the non-protected grade DH36 steel.

The progression of the macroscopic appearance of erosion for the I coating is presented in Figure 4.31:

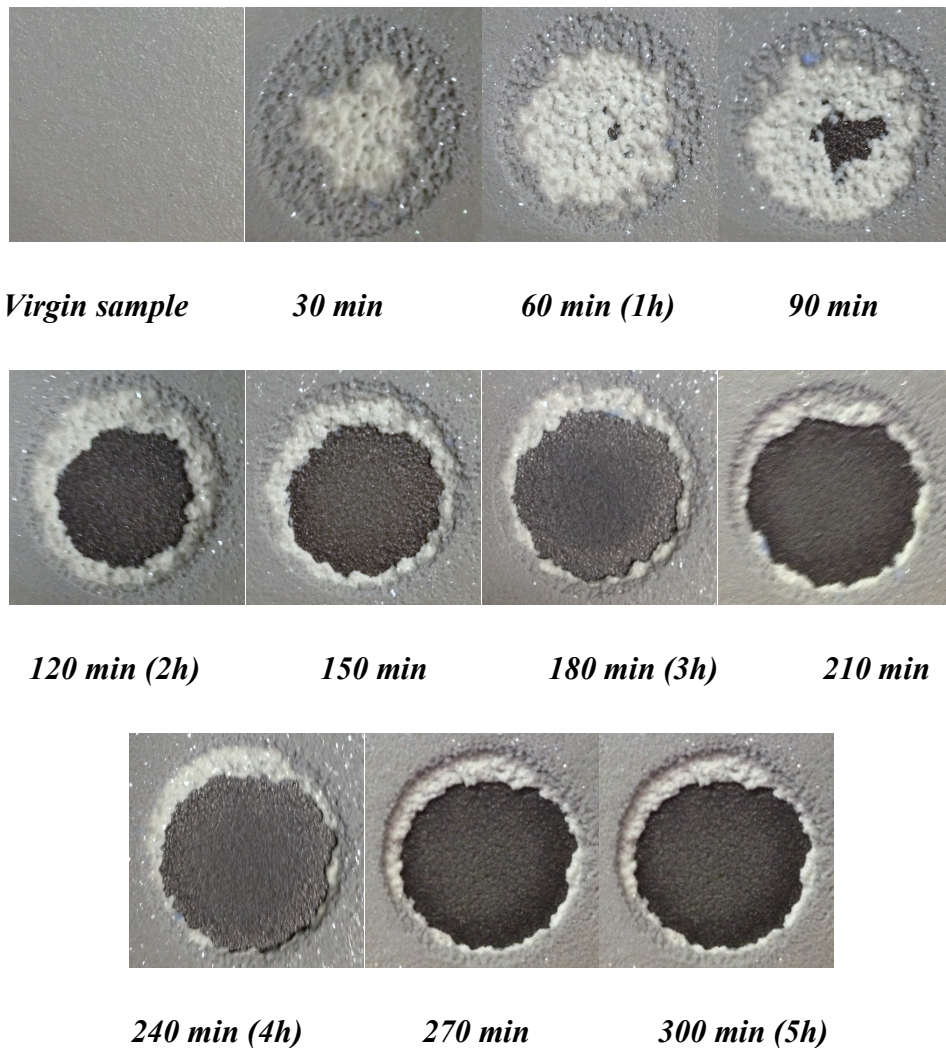


Figure 4.31: Progression of erosion for I coating.

Mass loss and rate of mass loss results for P coating are presented in Figures 4.32 and 4.33:

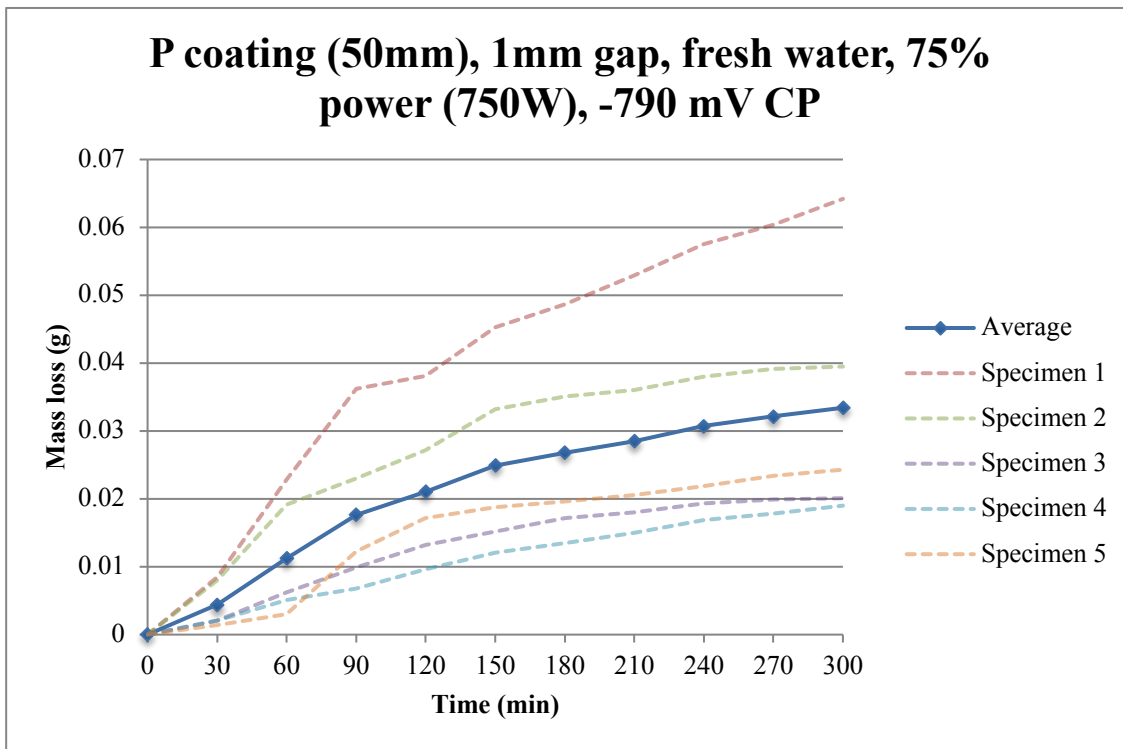


Figure 4.32: Mass loss of P coating at a 75% (750W) power setting and under a -790 mV CP.

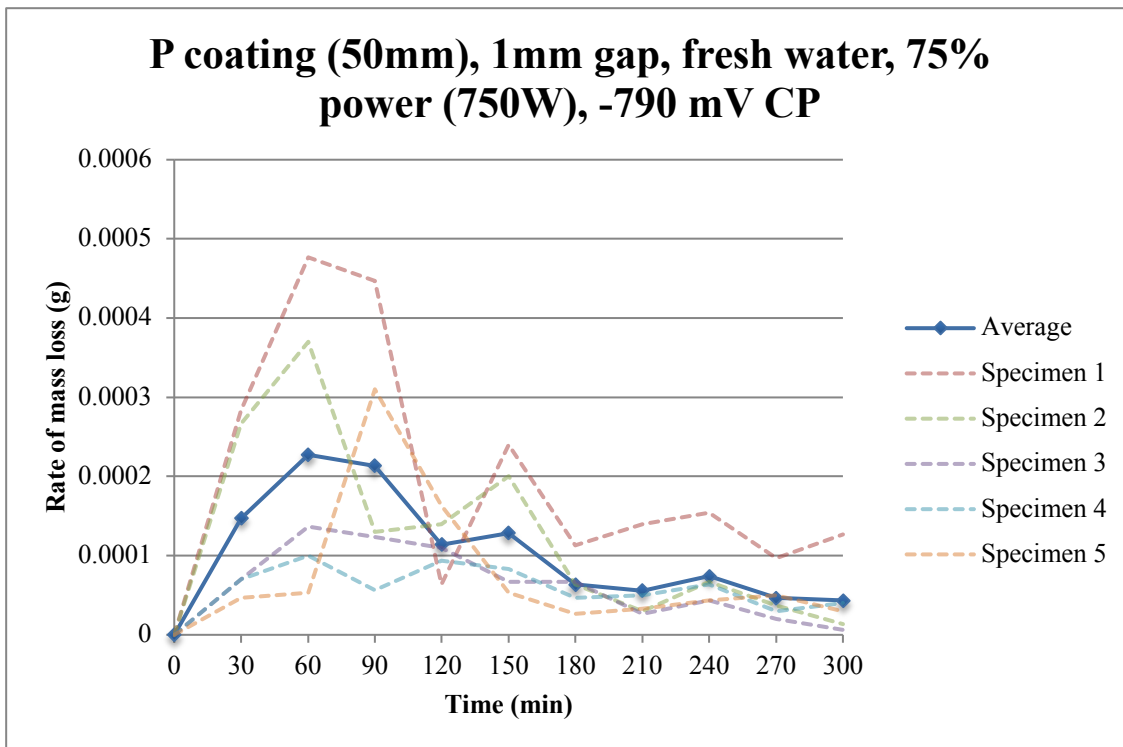


Figure 4.33: Rate of mass loss of P coating at a 75% (750W) power setting and under a -790 mV CP.

The total mass loss of the P coating, was of the order of 0.03g after five hours of cavitation exposure. The mass loss rate peaks after one hour into the procedure before it gradually decreases and stabilizes, after approximately three hours of cavitation exposure.

It is also noteworthy that a high deviation between different specimens was observed, in terms of mass loss and mass loss rate. This behaviour can be attributed to the dissimilar characteristics of the surface of each specimen, in the sense that unevenly distributed bumps and cavities could be observed on each one of them. As such dissimilar flow characteristics, would be applicable for each of the specimens, resulting into cavitation of varying erosive potential.

The progression of the macroscopic appearance of erosion for P coating is presented in Figure 4.34:

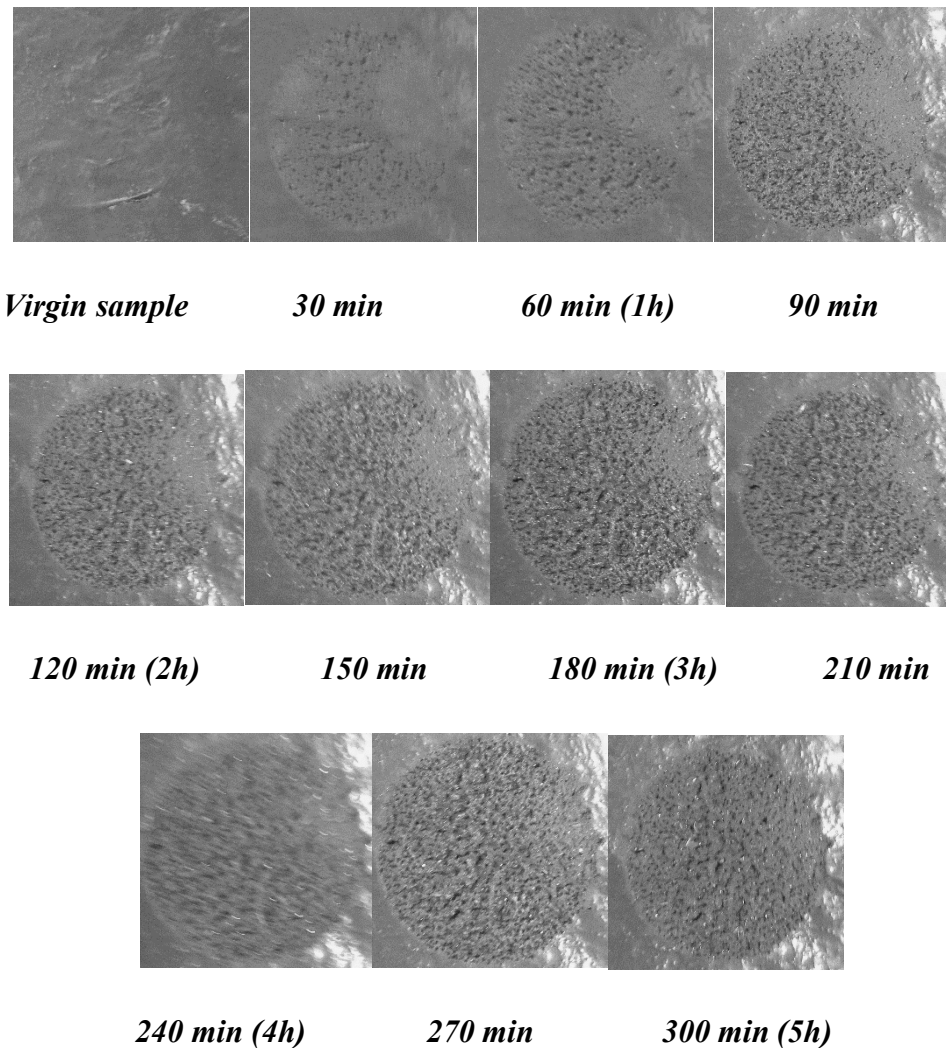


Figure 4.34: Progression of erosion for P coating.

Mass loss and rate of mass loss results for A coating are presented in Figures 4.35 and 4.36:

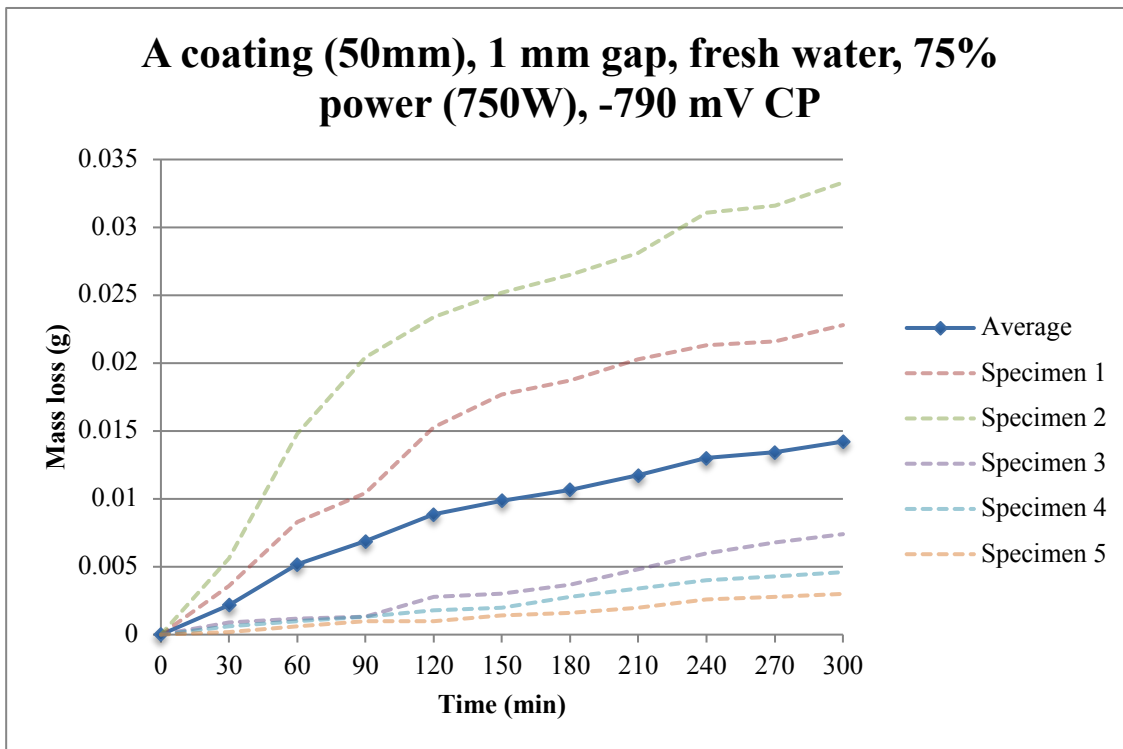


Figure 4.35: Mass loss of A coating at a 75% (750W) power setting and under a -790 mV CP.

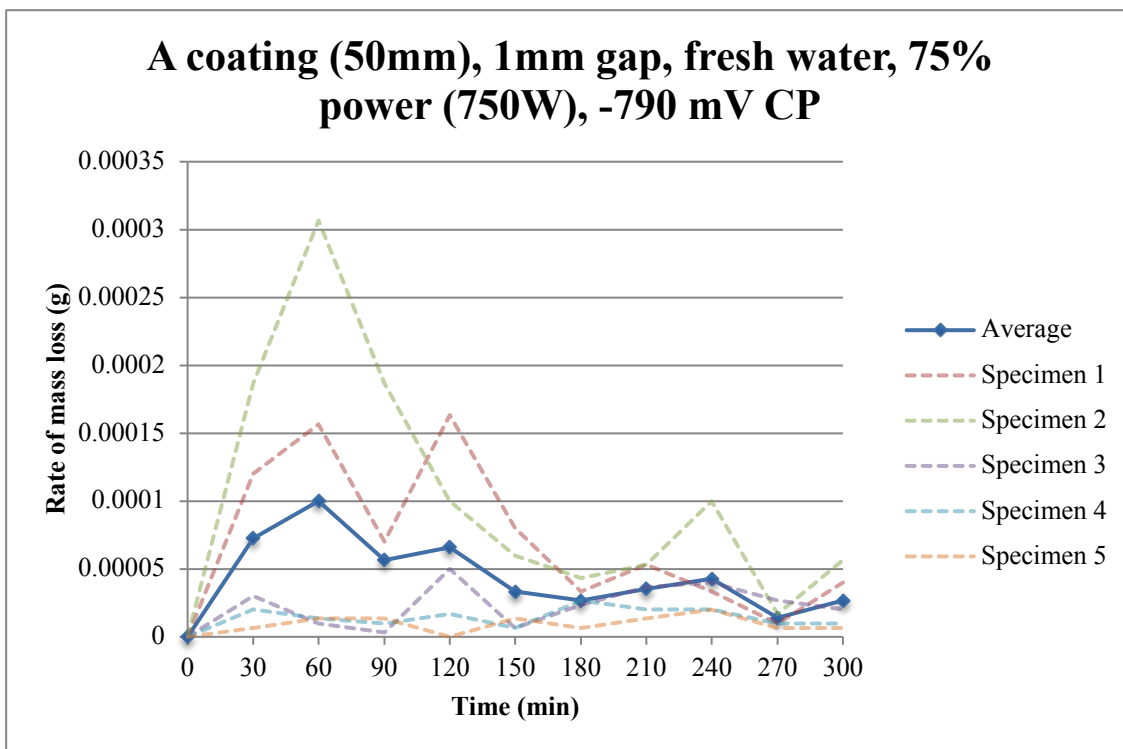


Figure 4.36: Rate of mass loss of A coating at a 75% (750W) power setting and under a -790 mV CP.

The total mass loss of the A coating was of the order of 0.015 g after five hours of cavitation exposure. The corresponding rate of mass loss peaks after thirty minutes into the procedure before it decreases and stabilizes towards the end of the exposure.

Similarly to the P coating, the unevenly coated surfaces of the specimens, resulted into highly dispersed results. Again, this behaviour can be attributed to the manifestation of cavitation erosion of varying intensity, due to dissimilar flow characteristics, for each one of the specimens.

The progression of the macroscopic appearance of erosion of the A coating is presented in Figure 4.37:

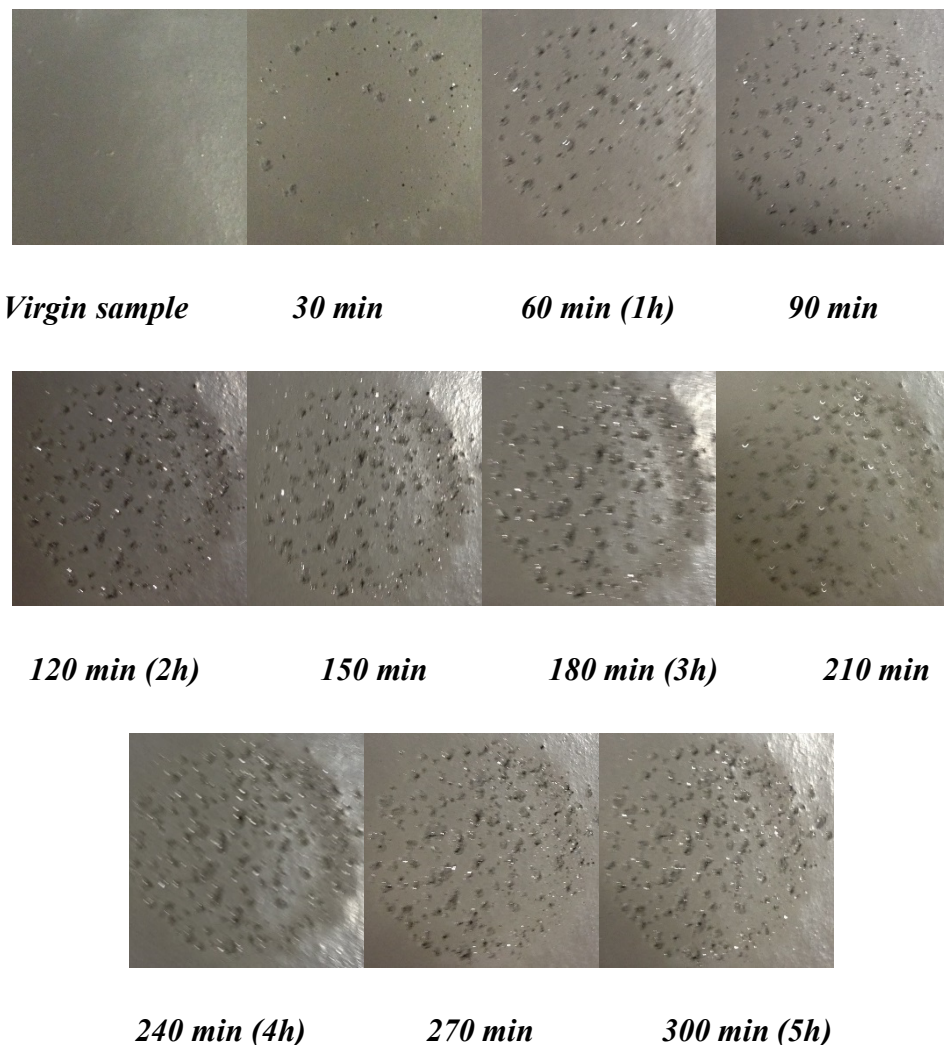


Figure 4.37: Progression of erosion for A coating.

Mass loss and rate of mass loss results for Double coating are presented in Figures 4.38 and 4.39:

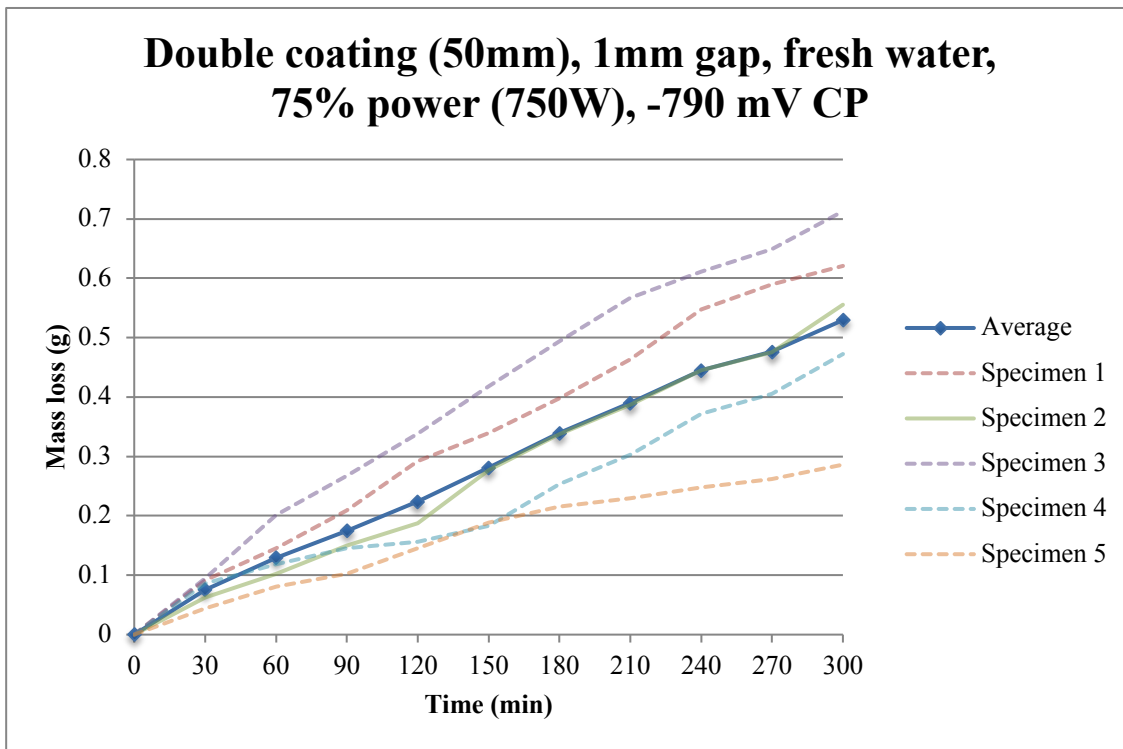


Figure 4.38: Mass loss of Double coating at a 75% (750W) power setting and under a -790 mV CP.

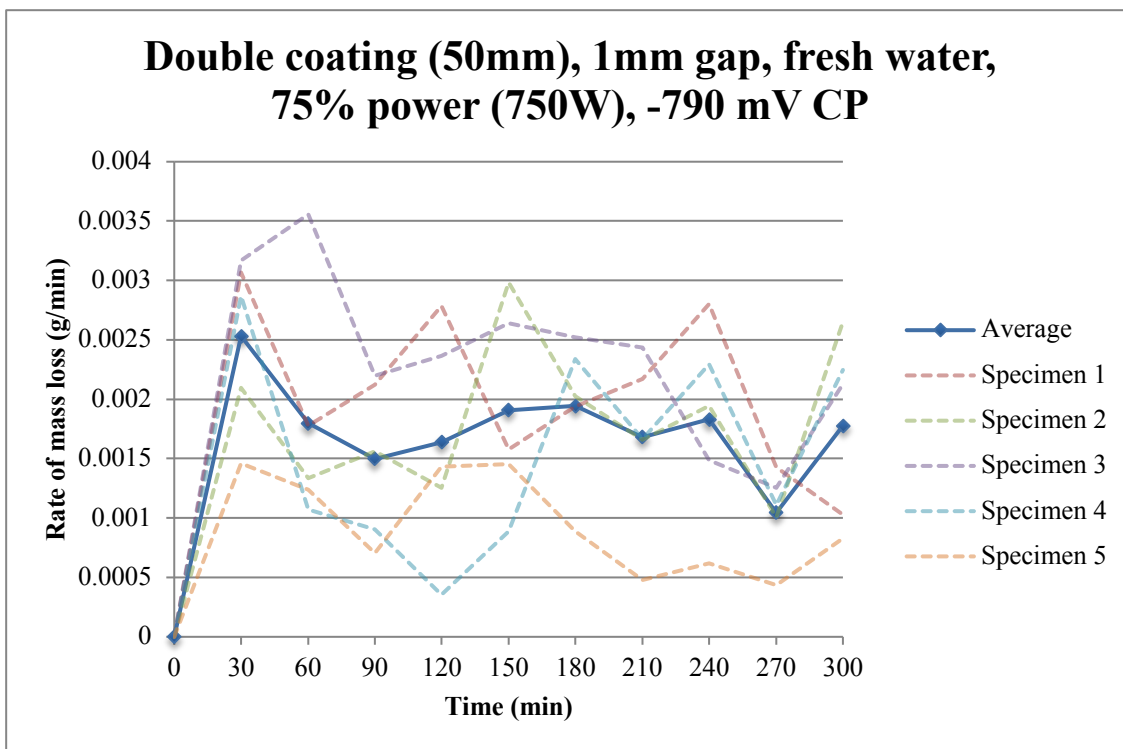


Figure 4.39: Rate of mass loss of Double coating at a 75% (750W) power setting and under a -790 mV CP.

The total mass loss of the Double coating was of the order of 0.5g, after five hours of cavitation exposure. Double coating exhibited a similar to the I coating behaviour, in the sense that the

severe mass loss which was observed was mostly due to the coating itself and not the protected grade DH36 steel. The coating was not completely destroyed, however, in this case thus the protected material was not completely exposed to cavitation, a condition that was the case for the I coating. The rate of mass loss peaked after thirty minutes of cavitation exposure before it decreases and stabilizes for the rest of the exposure.

The progression of the macroscopic appearance of erosion for Double coating is presented in Figure 4.40:

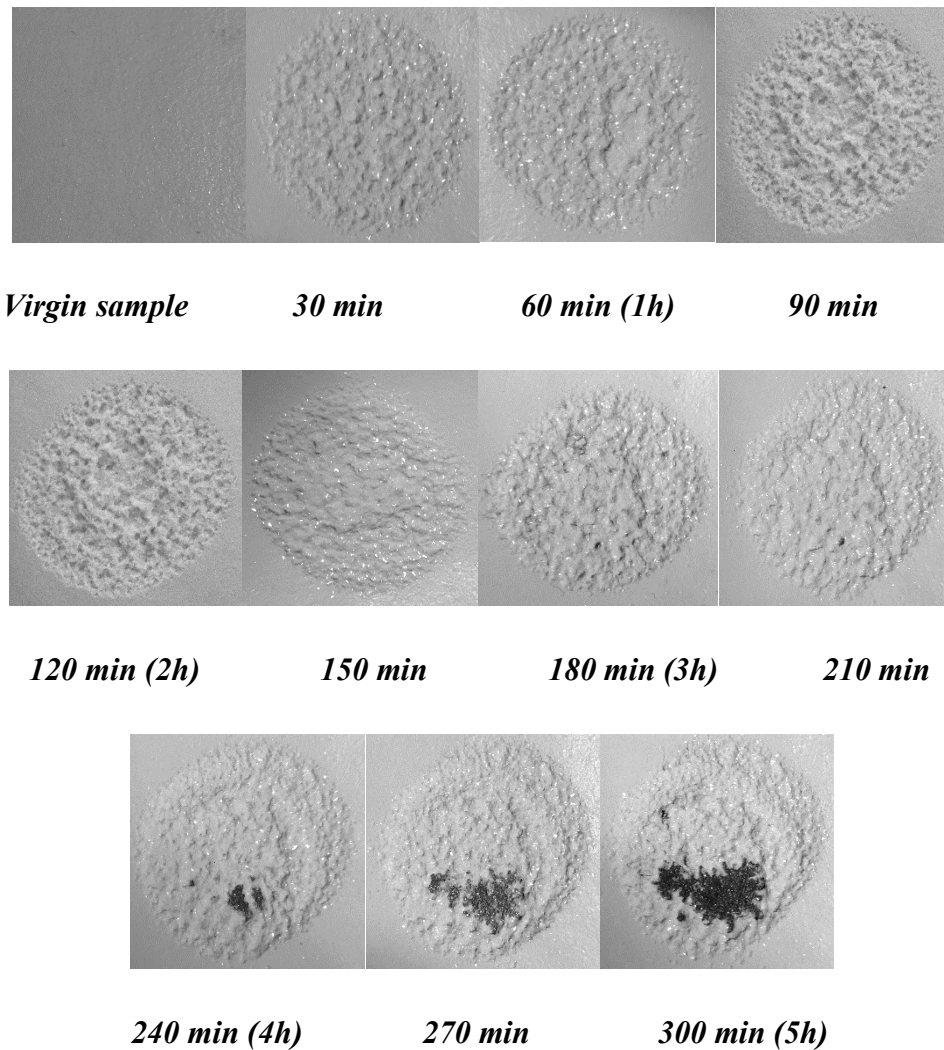


Figure 4.40: Progression of erosion for Double coating.

Mass loss and rate of mass loss results for R coating are presented in Figures 4.41 and 4.42:

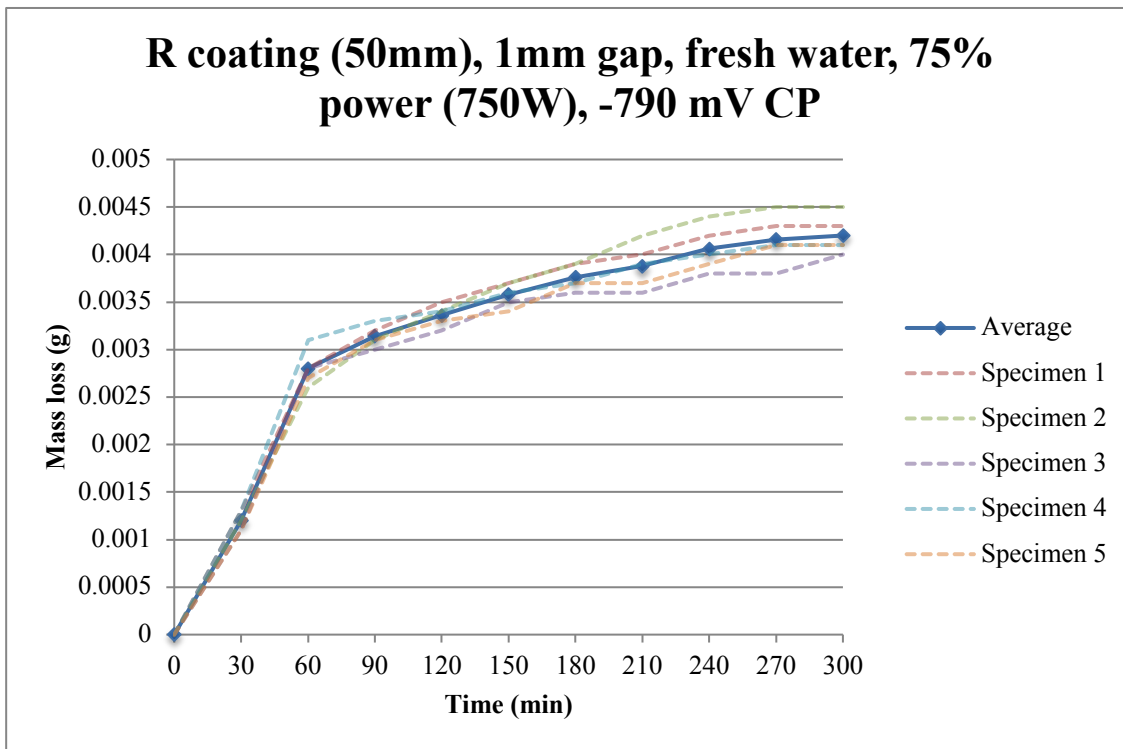


Figure 4.41: Mass loss of R coating at a 75% (750W) power setting and under a -790 mV CP.

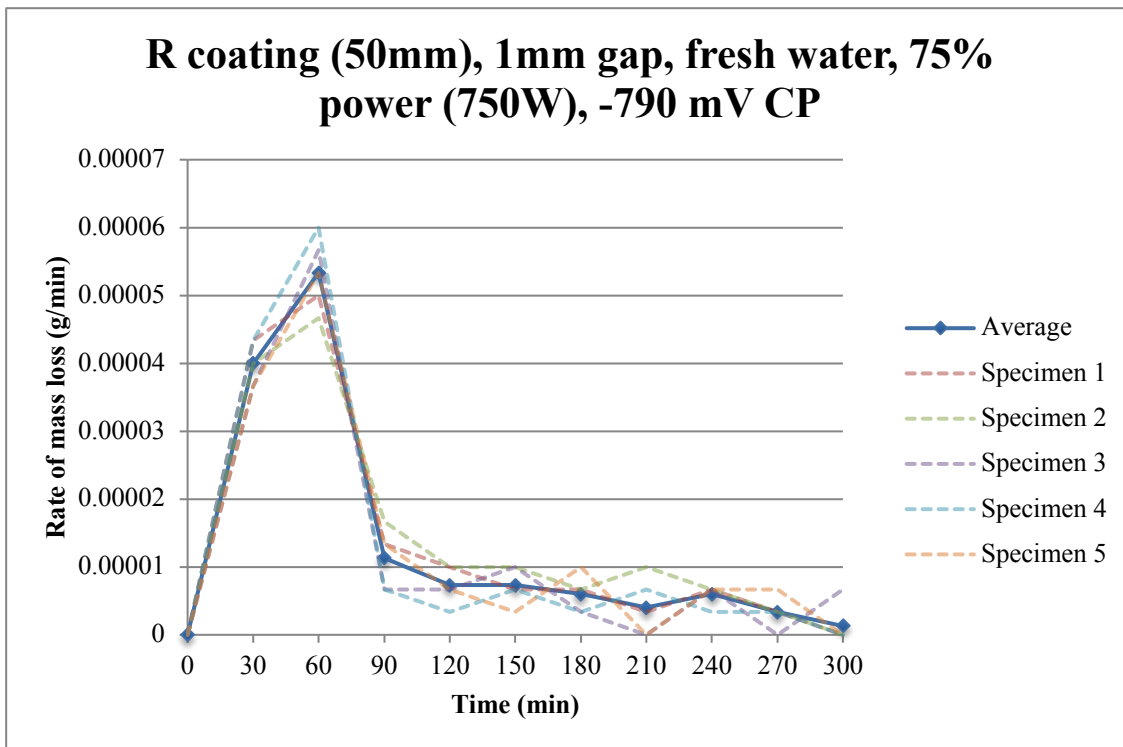


Figure 4.42: Rate of mass loss of R coating at a 75% (750W) power setting and under a -790 mV CP.

The total mass loss of the R coating was of the order of 0.004g, after five hours of cavitation exposure. The corresponding rate of mass loss peaks after one hour into the procedure before it decreases significantly and almost reaches zero towards the end of the exposure.

This behaviour implies a considerable amount of initial work hardening whereas it is also noteworthy, that the presence of the R coating resulted into a much more silent operation of the ultrasonic transducer. The manifestation of a cushioning effect could possibly be the cause of the observed behaviour, whereas this could also explain the excellent behaviour of the R coating in terms of cavitation related mass loss, especially when compared to the other metals and protective coatings.

The macroscopic appearance of the surface of R coating, remained unaffected during the procedure and as such no pictures will be presented at this point. The microscopic appearance of the R coating, however, will be examined in *Chapter 5*

Mass loss and rate of mass loss results for the B coating are presented in Figures 4.43 and 4.44:

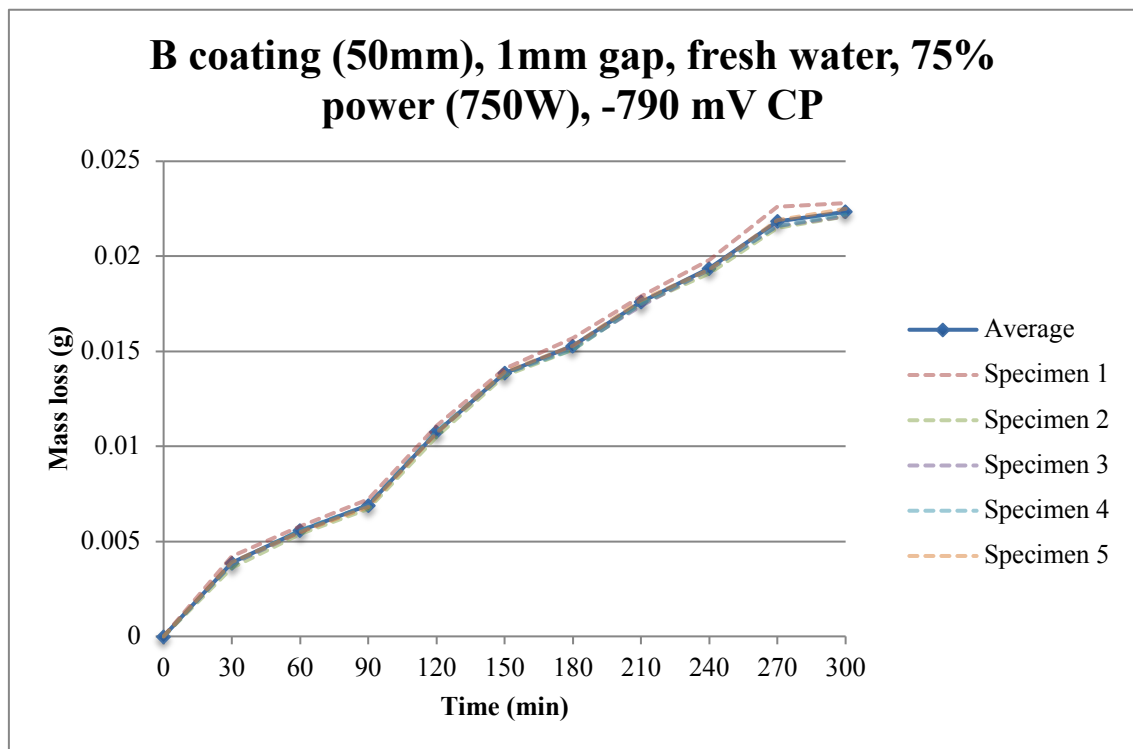


Figure 4.43: Mass loss of B coating at a 75% (750W) power setting and under a -790 mV CP.

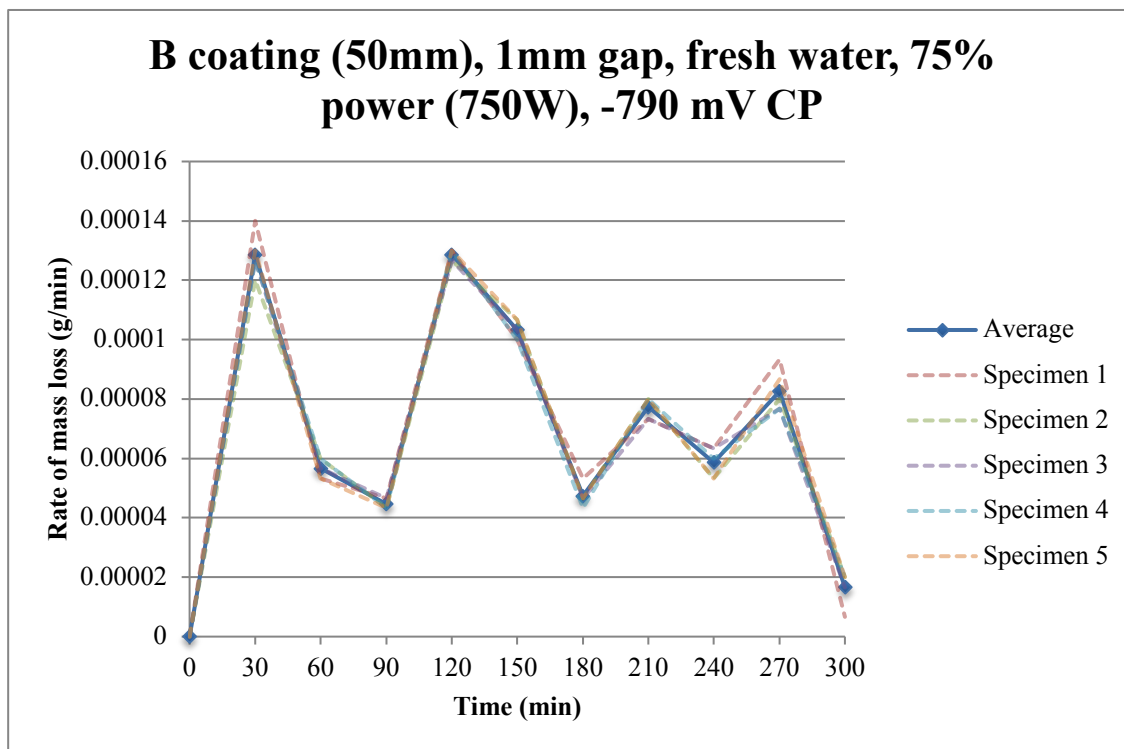


Figure 4.44: Rate of mass loss of B coating at a 75% (750W) power setting and under a -790 mV CP.

The total mass loss of the B coating was of the order of 0.022g after five hours of cavitation exposure. The rate of mass loss peaks two times into the procedure, after thirty minutes and two hours, respectively, and then fluctuates before decreasing considerably towards the end of the exposure.

The macroscopic appearance of the B coating, remained unaffected throughout the procedure, apart from a distinctive bump that appeared after thirty minutes of cavitation exposure, possibly due to local temperature effects, and is probably related to the first mass loss rate peak. The appearance of that bump remained unchanged for the rest of the cavitation exposure apart from a rip on the side that cannot be seen in the macroscopic pictures and is possibly related to the second mass loss rate peak, in the sense that both appeared after two hours into the procedure. As such, a single macroscopic picture showing the erosion bump will only be presented here whereas the microscopic appearance of the B coating will be further examined in *Chapter 5*.

Figure 4.45 shows the macroscopic appearance of the erosion bump of the B coating after five (5) hours of cavitation exposure:



Figure 4.45: Erosion bump of B coating.

Mass loss and rate of mass loss results for C coating are presented in Figures 4.46 and 4.47:

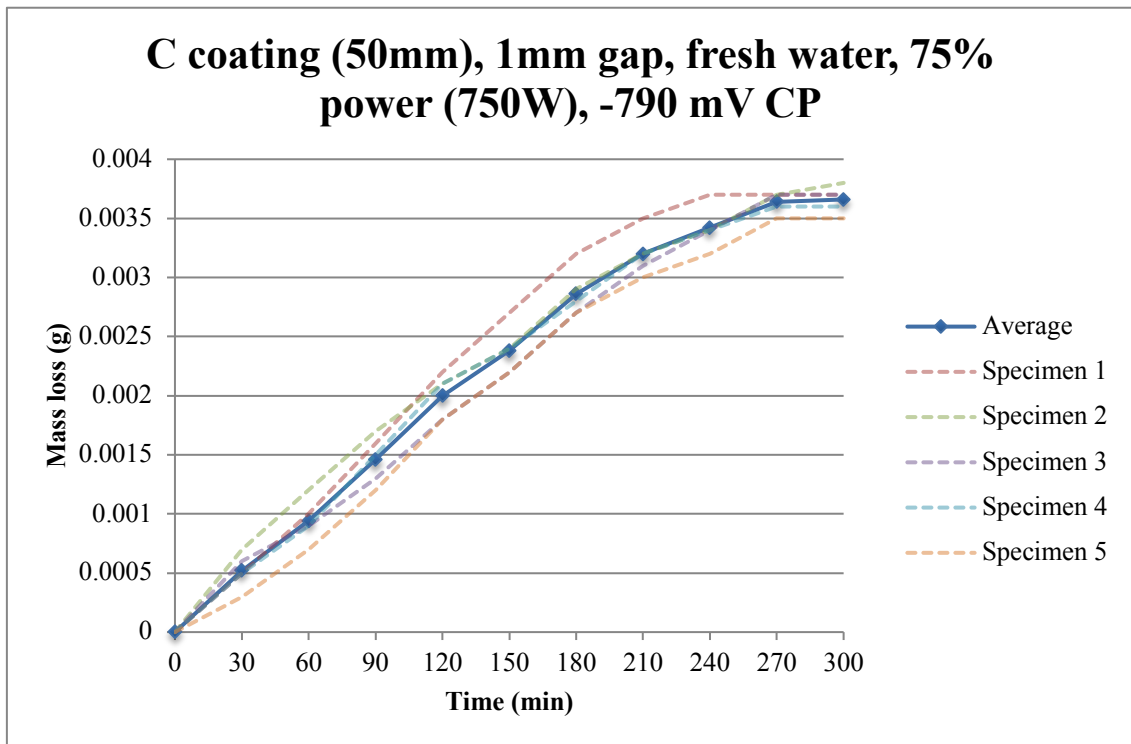


Figure 4.46: Mass loss of C coating at a 75% (750W) power setting and under a -790 mV CP.

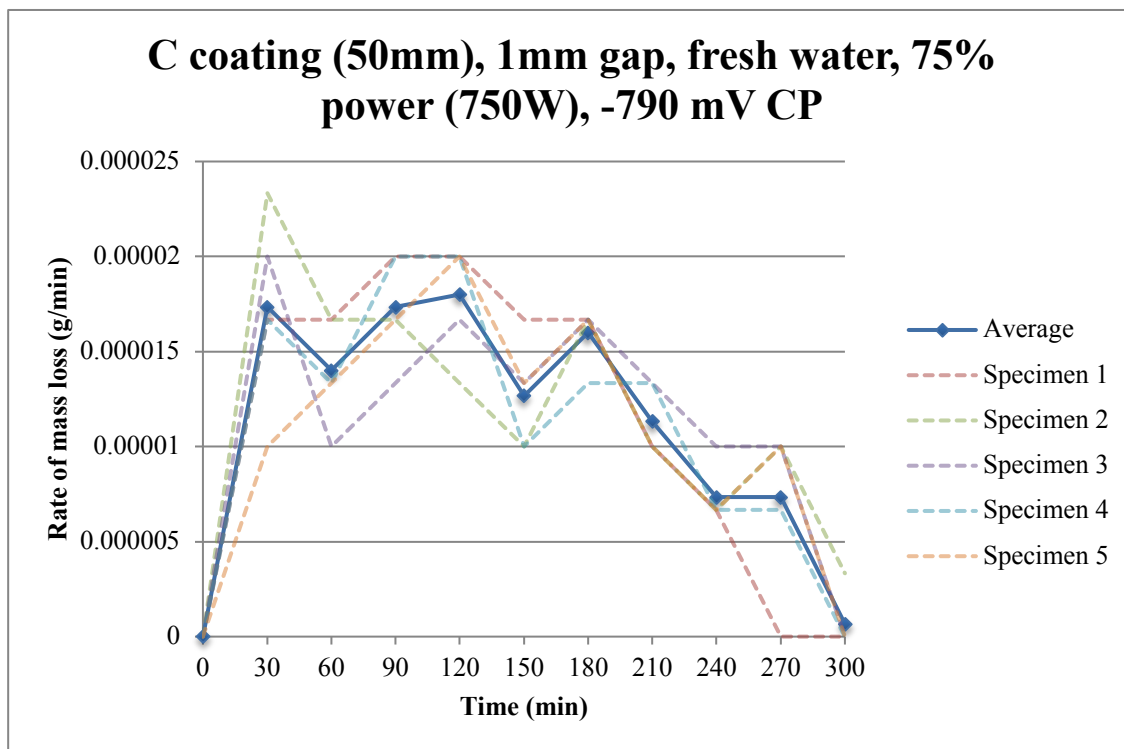


Figure 4.47: Rate of mass loss of C coating at a 75% (750W) power setting and under a -790 mV CP

The total mass of for the C coating was of the order of 0.0036g, after five hours of cavitation exposure. This was the lowest mass loss that was measured among the examined alloys and coatings and it is only comparable to the R coating which performed slightly worse in that respect. The rate of mass loss peaks multiple times throughout the procedure and tends to become zero towards the end of it, implying a progressive work hardening of the exposed material.

Moreover, and similarly to the R coating, the presence of the C coating resulted into a more silent operation of the ultrasonic transducer, again suggesting a cushioning effect from its surface.

As for the macroscopic appearance of the eroded surface, it remained unaffected throughout the procedure and as such no pictures will be presented in this chapter. The microscopic appearance of the C coating, however, will be examined in *Chapter 5*.

4.6 Summary and discussion

All mass loss tests are summarized and discussed in this sub-chapter. Results are presented in the form of collective comparison graphs.

Mass loss and mass loss rate results for the three alloys that were tested are presented in Figures 4.48 and 4.49:

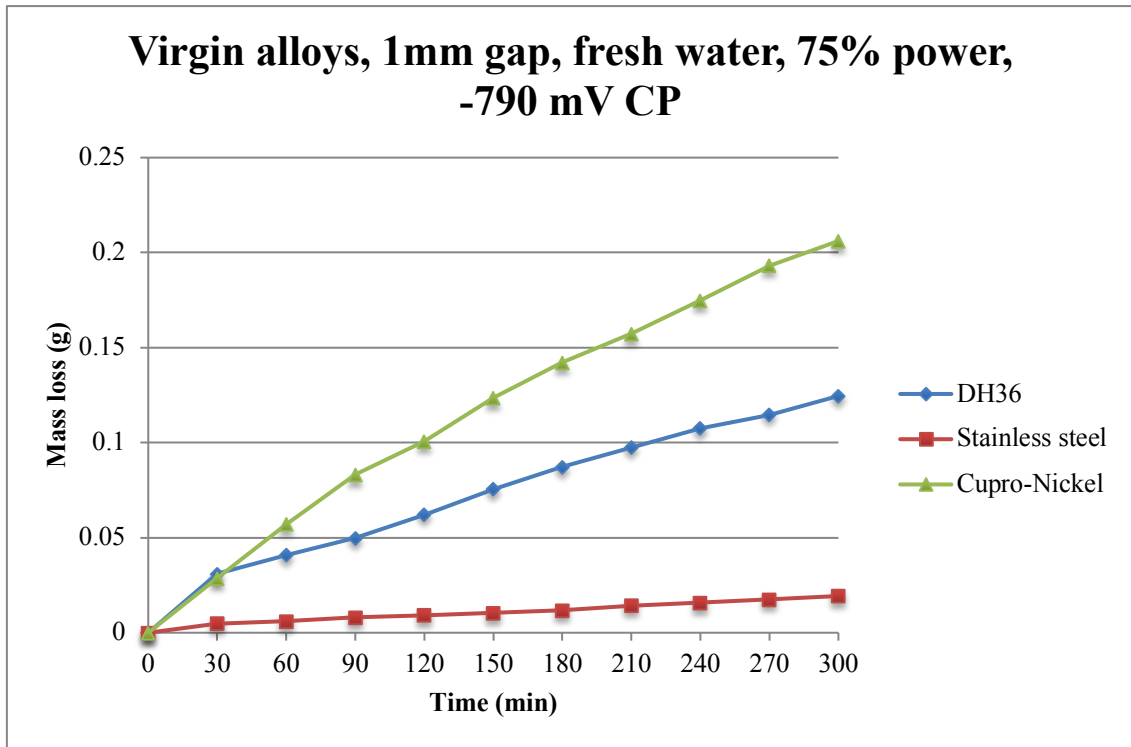


Figure 4.48: Mass loss comparison - Virgin alloys.

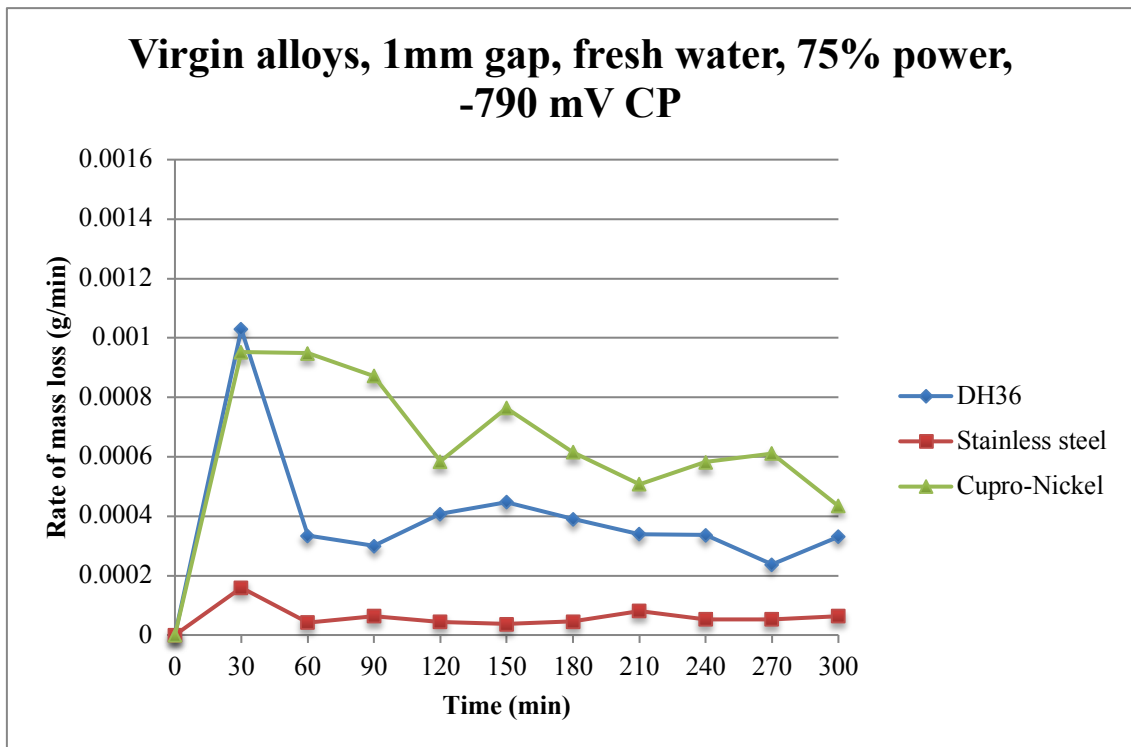


Figure 4.49: Rate of mass loss comparison – Virgin alloys.

Mass loss and mass loss rate results for the protective coatings that were tested are presented in Figures 4.50 and 4.51:

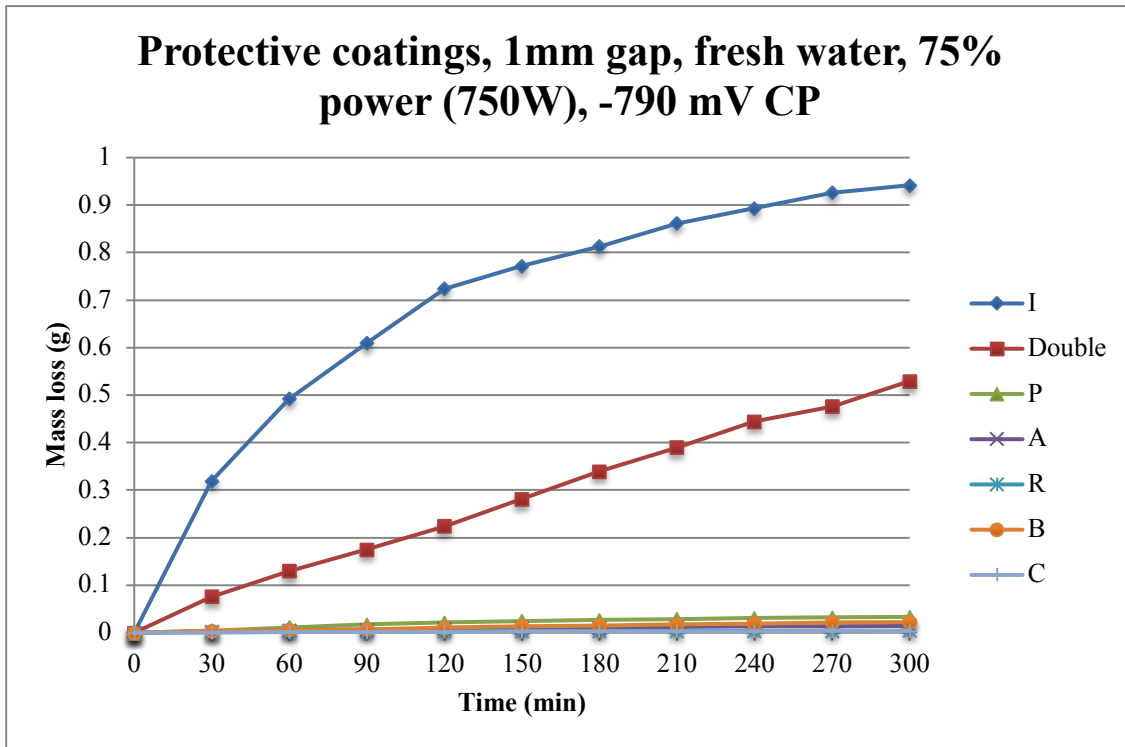


Figure 4.50: Mass loss comparison – Protective coatings.

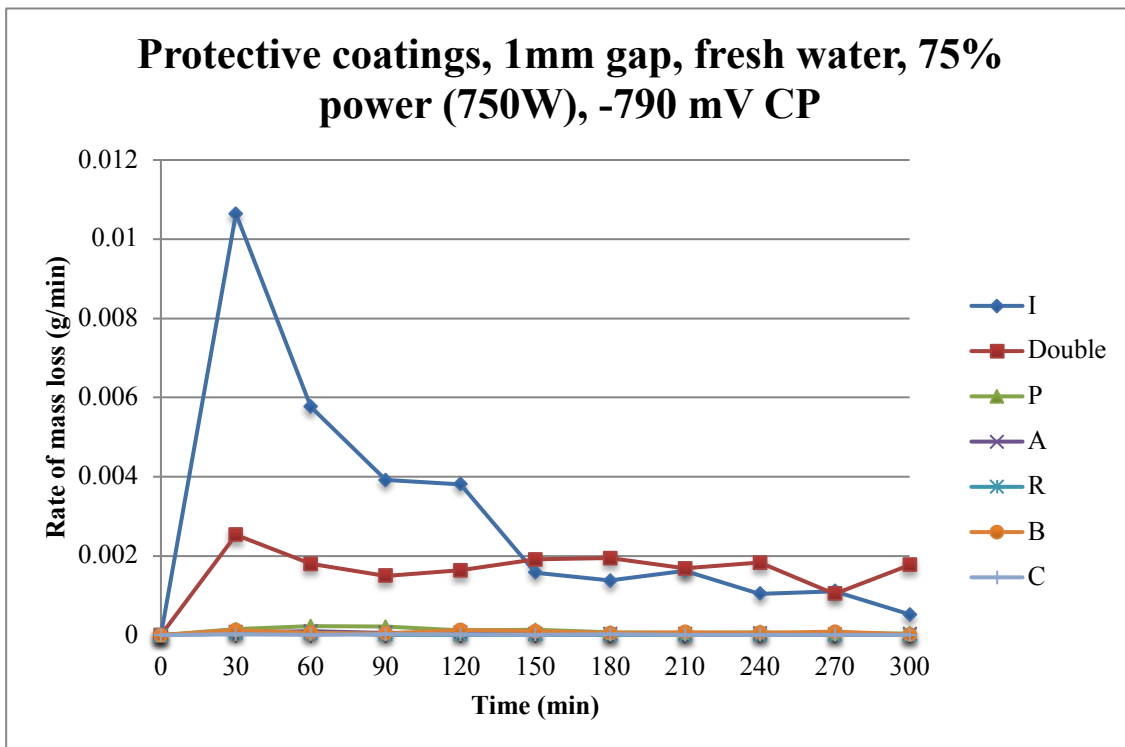


Figure 4.51: Rate of mass loss comparison – Protective coatings.

Results for the protective coatings are also presented on a different scale, oriented towards the lower end of the mass loss spectrum, in Figures 4.52 and 4.53:

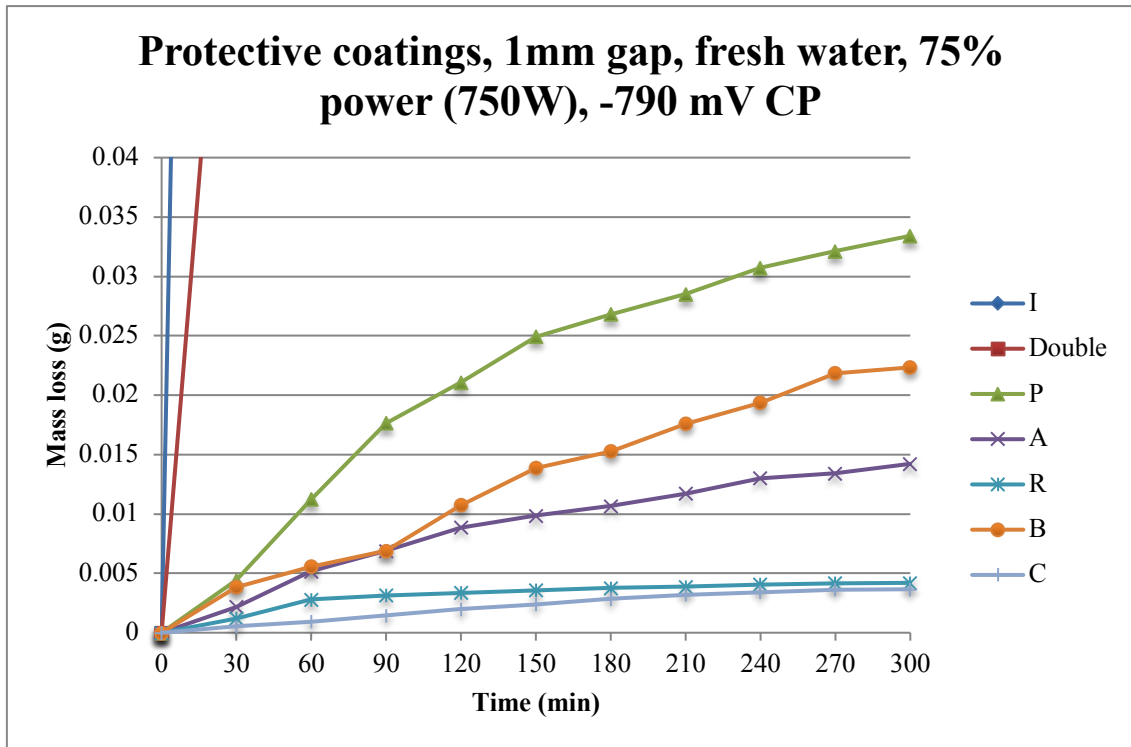


Figure 4.52: Mass loss comparison – Protective coatings (except I, Double).

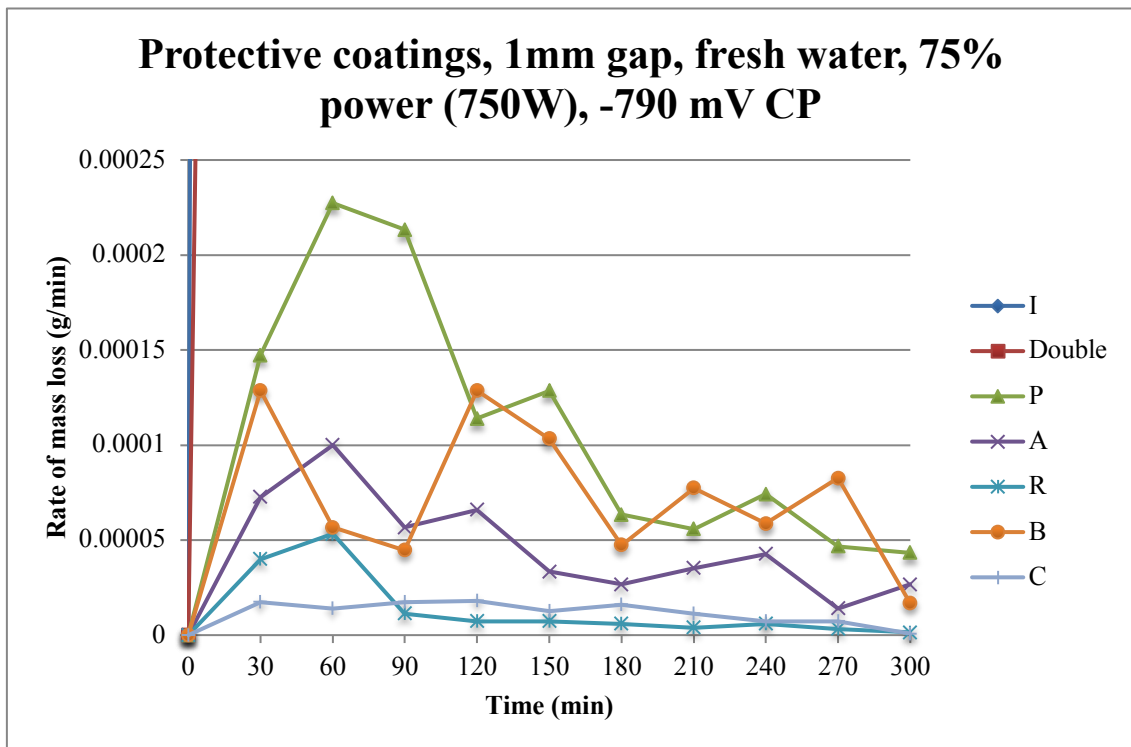


Figure 4.53: Rate of mass loss comparison – Protective coatings (except I, Double).

Mass loss and mass loss rate results for all specimens are presented in Figures 4.54 and 4.55:

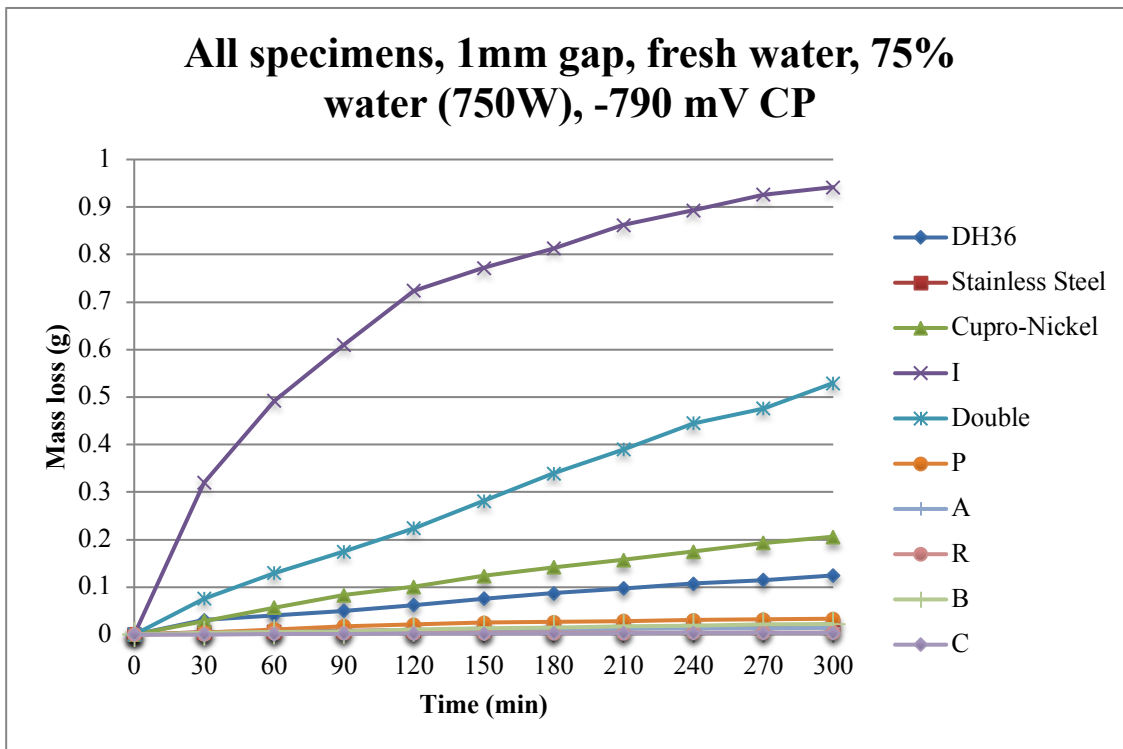


Figure 4.54: Mass loss comparison – All specimens.

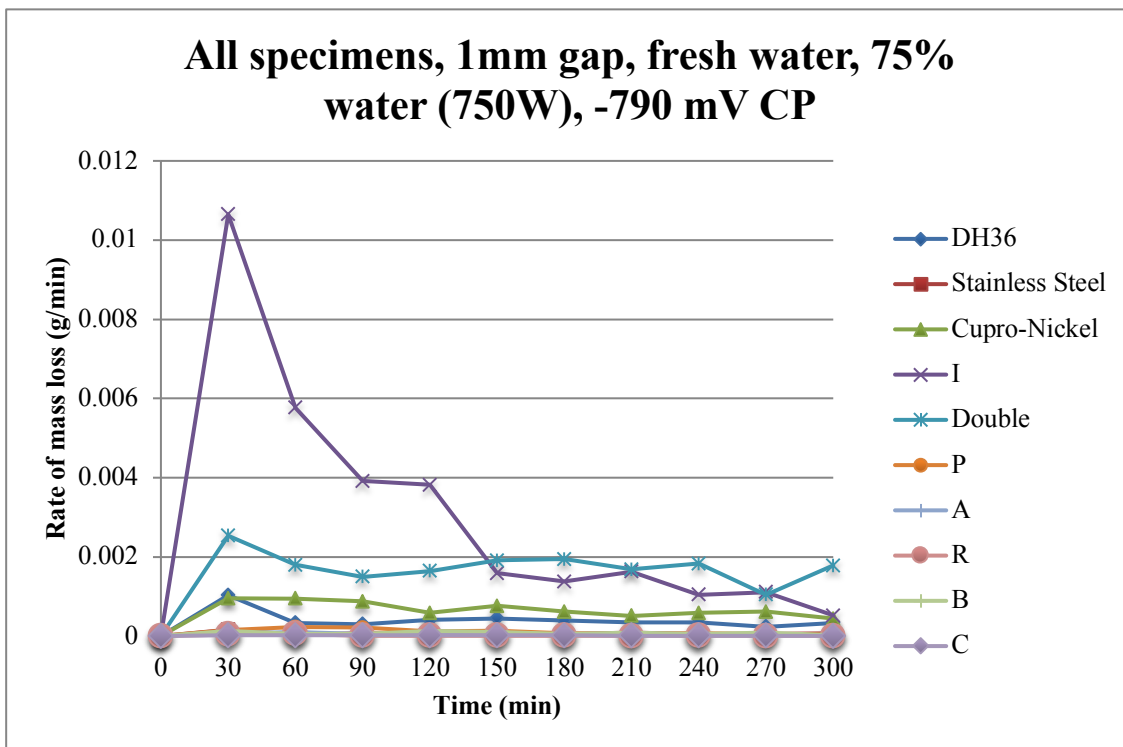


Figure 4.55: Rate of mass loss comparison – All specimens.

Results for all specimens are also presented on a different scale, oriented towards the lower end of the mass loss spectrum, in Figures 4.56 and 4.57:

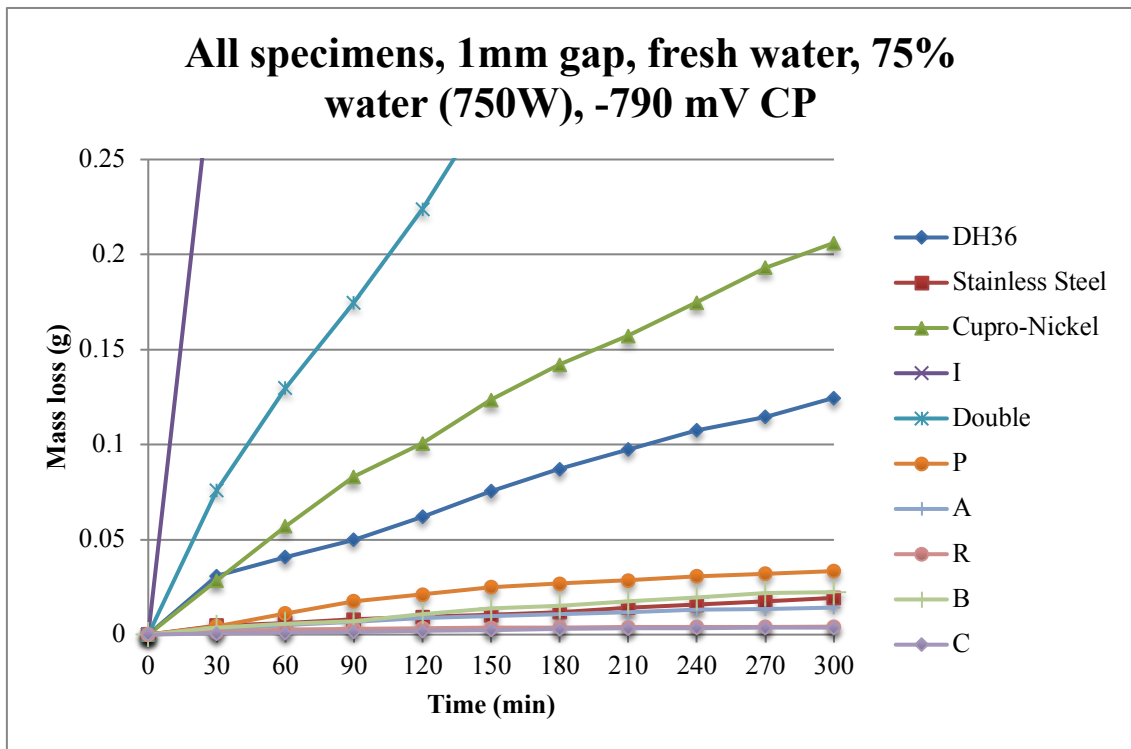


Figure 4.56: Mass loss comparison – All specimens (except I, Double).

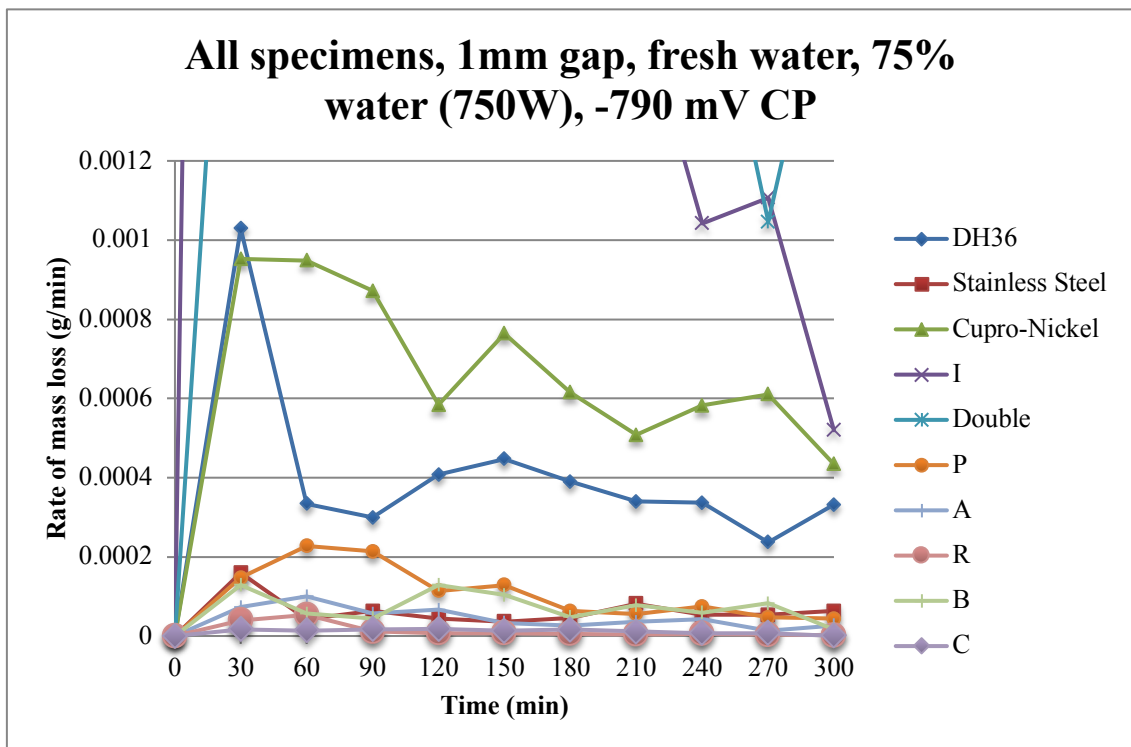


Figure 4.57: Rate of mass loss comparison – All specimens (except I, Double).

Firstly, it should be noted that all results were several orders of magnitude above the estimated measurement uncertainty (95% confidence level) of $\pm 0.00002\text{g}$, thus they are considered to be accurate and representative of the true condition of the exposed materials.

With regard to the virgin alloys, the best behaviour in terms of resistance against cavitation induced erosion – mass loss was exhibited by stainless steel 254 with an average total of 0.02g, followed by grade DH36 steel with 0.12g and finally by cupronickel 70-30 with 0.20g. Interestingly, grade DH36 steel and cupronickel 70-30 exhibited an identical initial rate of mass loss (0.001 g/min) for the first thirty minutes of cavitation exposure. Nonetheless, the rate of mass loss for grade DH36 steel decreased significantly and stabilized at a lower level compared to cupronickel 70-30 for the rest of the procedure, thus resulting into a reduced amount of total mass loss for the former in comparison to the latter. Stainless steel 254 exhibited a similar to the grade DH36 steel behaviour, with its rate of mass loss reaching its peak (0.0001 g/min) thirty minutes into the procedure, before decreasing and stabilizing, although on a much smaller extent compared to the other two virgin alloys. Consequently, this had a profound effect on its total mass loss, which was significantly lower compared to grade DH36 steel and cupronickel 70-30.

It appears that in the case of cupronickel 70 – 30 work hardening progressed slowly and was accompanied by a considerable amount of mass loss before leading to a relatively steady state phase towards the end of the exposure, whereas in the case of the other alloys the effects of work hardening became immediately apparent and resulted into them becoming more resistant against cavitation thus they reached a relatively steady state phase sooner. Those differences can be attributed to the dissimilar mechanical properties of the examined alloys as there appears to be a connection with regard to the progression as well as the extent of mass loss. In particular cupronickel 70-30, which was the alloy that exhibited the highest mass loss throughout the exposure, has a yield strength of 130 MPa and an ultimate strength of 350 MPa, whereas the relevant values for DH36 steel, which was slightly more resistant than cupronickel in that respect, and stainless steel 254, which exhibited the lowest mass loss, are 350 (yield)-490 (ultimate) MPa, and 310 (yield) – 690 (ultimate) MPa, respectively. As such the beneficial effects of work hardening became immediately apparent in the case of the more resistant materials, according to their properties, whereas the opposite was the case for the more ductile in nature and less resistant cupronickel. That matter, however, will be further explored by means of microscopic and fractographic investigation in *Chapter 5* as for instance, the large differences between grade DH36 steel and stainless steel 254, with regard to the measured mass loss, imply that, apart from the mechanical properties of the examined alloys, some microscopic characteristics such as, their crystalline structure and grain size, may also be of significance when cavitation erosion resistance is considered.

Protective coatings, can be ranked into three groups characterized by similar compositions and resistance against ultrasonically induced cavitation erosion – mass loss. The first group would consist of C and R coatings, which exhibited the best behaviour in terms of cavitation erosion resistance, with a total mass loss of 0.0036g and 0.0041g respectively. The second group would consist of the A, B and P coatings, which are of similar composition and exhibited a cavitation related mass loss of the order of 0.015g, 0.023g and 0.032g respectively. The last group would consist of the I and Double coatings, with a total mass loss of 0.92g and 0.52g respectively. It should be noted that with regards to the last group both coatings got heavily eroded up to the point where the protected metal surface was finally exposed. This behaviour was more pronounced in the case of the I coating, which totally collapsed after three hours of cavitation exposure and as a result the protected alloy was eventually exposed to cavitation. It should also be noted that in some cases (A, P and Double coating), results between specimens varied significantly, a behaviour that can be attributed to the uneven application of the coatings on the base plate.

Again, differences can be attributed to the dissimilar structure and mechanical properties of the examined coatings. In general, mass loss results indicate that the use of protective coatings against ultrasonically induced cavitation erosion – mass loss, could be of benefit for the protected alloys. In some cases, however, the coating collapsed and as a result the protected alloy was eventually exposed to cavitation.

Chapter 5

Microscopic Examination

5.1 Introduction

In addition to mass loss measurements and macroscopic observations, specimens were also examined under the lens of a digital optical microscope. As such, microscopic images of the eroded surfaces as well as 3D representations of cavitation induced erosion pits are initially presented. Erosion pits are then characterized with regards to their depth, volume and unique shape for each one of the examined alloys whereas protective coatings are also considered. Finally, the three alloys (Grade DH36 steel, stainless steel 254, cupronickel 70-30) are examined by means of a scanning electron microscope (SEM) and are characterized in terms of the governing fracture mechanisms, relating to cavitation induced erosion.

5.2 The digital optical microscope - Procedure

A Keyence VHX-700F digital optical microscope was utilized in this study. In conjunction with the Z500R lens, this unit is capable of capturing microscopic images for a variety of magnifications ranging from 500 to 5000. In addition, the unit is capable of composing accurate 3D representations of the examined surfaces, by gradually adjusting its focus inwards or outwards while taking multiple snapshots of the surface. Moreover, a real-time depth and volume analysis can be performed by the microscope by means of the same focus adjusting technique in conjunction with the relevant software package.

For the purpose of this study, all specimens were examined under the microscope lens at the minimum magnification of x500 which was sufficient in order for, cavitation induced erosion patterns and pits, to be adequately identified and characterized.

All three alloys as well as the seven protective coatings, which were previously exposed to ultrasonically induced cavitation, were examined. These are the following:

- Grade DH36 steel
- Stainless steel 254
- Cupronickel 70-30
- I coating
- P coating

- A coating
- Double coating
- R coating
- B coating
- C coating

The main unit of the digital optical microscope, the lens as well as the adjustable base can be seen in Figure 5.1:



Figure 5.1: Keyence VHX-700F digital optical microscope and Z500R lens (x500-5000).

5.3 Optical microscopic observations

A general microscopic image, showing the cavitation induced erosion pattern, along with two types of 3D illustrations, either with a colour contour or not, of a characteristic erosion pit are presented for each one of the examined alloys. Additional 3D illustrations of cavitation erosion pits are provided in *Appendix F*.

The erosion pits of each material are then characterized with regards to their average measured depth, volume and shape, whereas a short discussion on the findings is conducted at the end of this sub - chapter.

Grade DH36 steel

The microscopic appearance of the eroded surface of grade DH36 steel is presented in Figure 5.2.

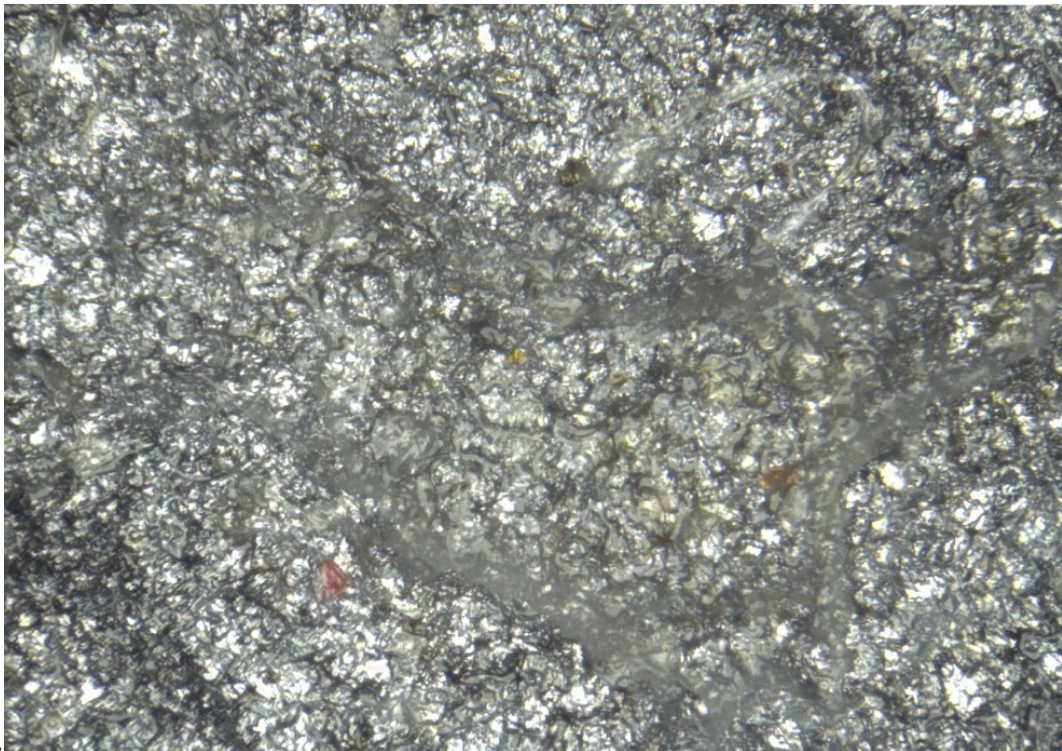


Figure 5.2: Microscopic appearance of cavitation - induced erosion for Grade DH36 steel (x500).

3D illustrations of a, characteristic cavitation - induced, erosion pit for grade DH36 steel are presented in Figures 5.3 and 5.4:

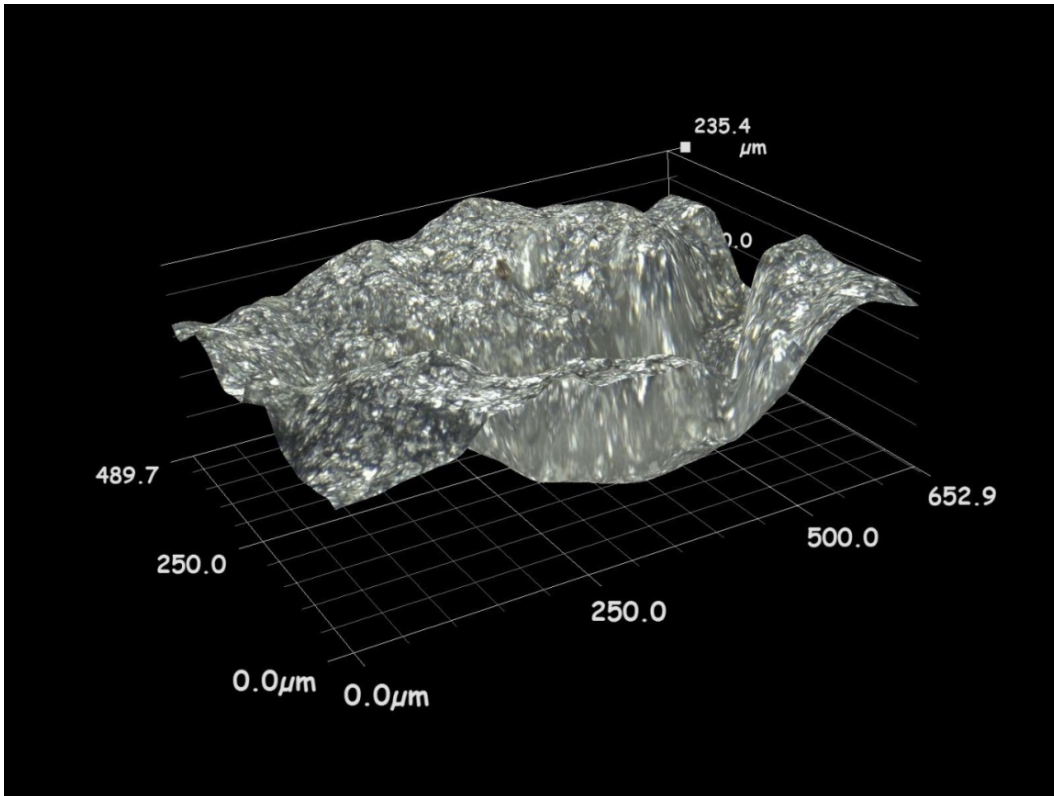


Figure 5.3: 3D illustration of erosion pit (1). Grade DH36 steel.

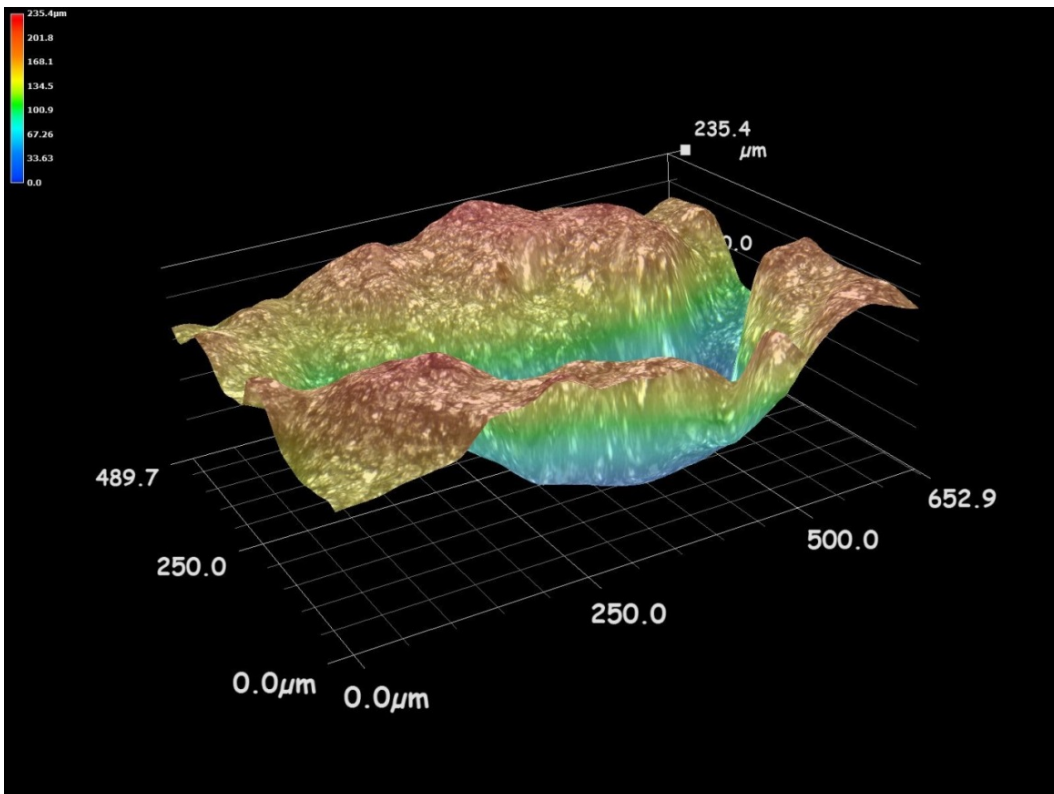


Figure 5.4: 3D illustration of erosion pit (1). Grade DH36 steel – Colour contour.

The shiny appearance of the eroded surface is indicative of mainly brittle fracture and the presence of distinctive facets and edges further enhances this assumption. A large amount of irregularly shaped, cavitation induced, erosion pits can be also be found on the surface of grade DH36 steel, with an average depth of several hundreds μm . Those pits are densely distributed all over the eroded surface while some of them appear to be joined together. They are all characterized by steep slopes of varying length, in proportion to their depth. It is also noteworthy that the erosion pattern on the surface of grade DH36 steel is circular with a diameter of approximately 22 μm , similarly to the cavitation inducing sonotrode tip.

The measured depths of three characteristic erosion pits are 235.4, 354.7 and 317.3 μm , respectively, thus the average depth in that instance would be 302.4 μm . An erosion pit with a depth analogous to the average value would have a volume of approximately 8 mm^3 , as it was measured through the digital microscope.

Stainless steel 254

The microscopic appearance of the eroded surface of stainless steel is presented in Figure 5.5:

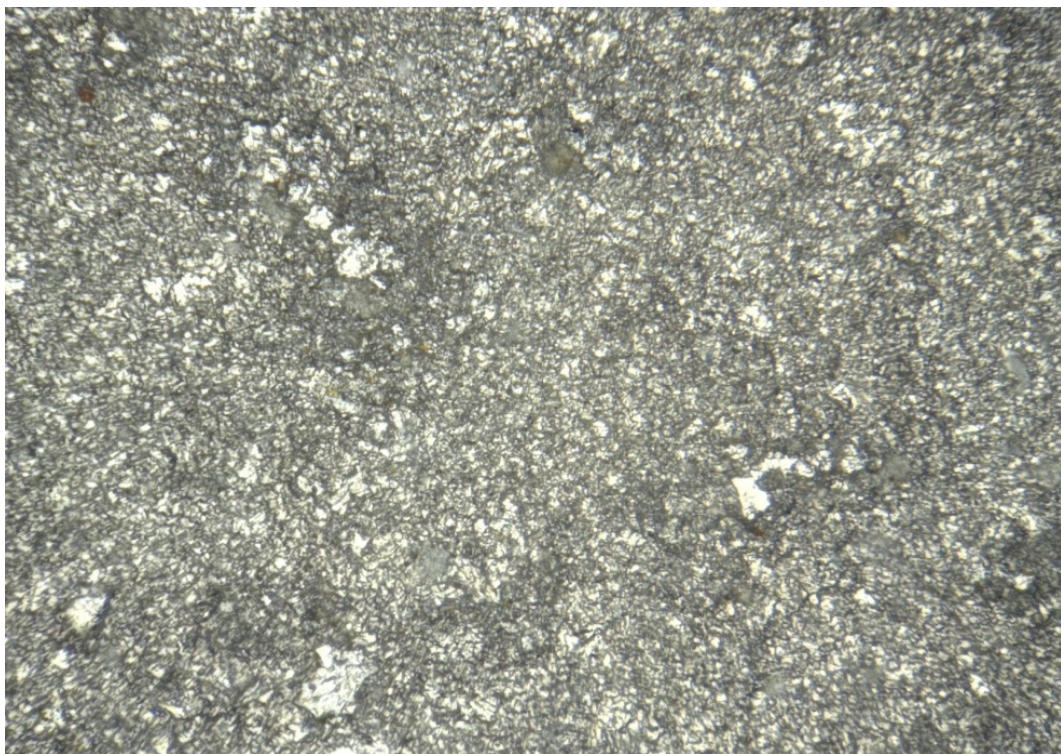


Figure 5.5: Microscopic appearance of cavitation - induced erosion for stainless steel 254 (x500).

3D illustrations of a characteristic, cavitation - induced, erosion pit for stainless steel 254 are presented in Figures 5.6 and 5.7:

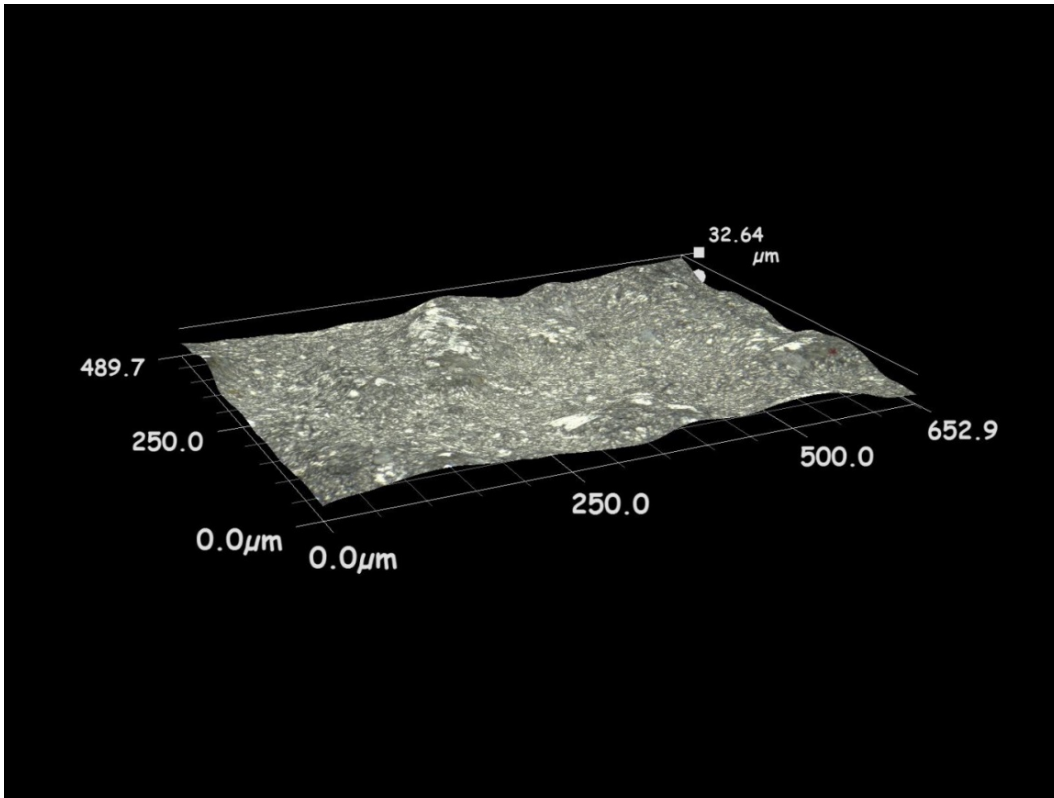


Figure 5.6: 3D illustration of erosion pit (1). Stainless steel 254.

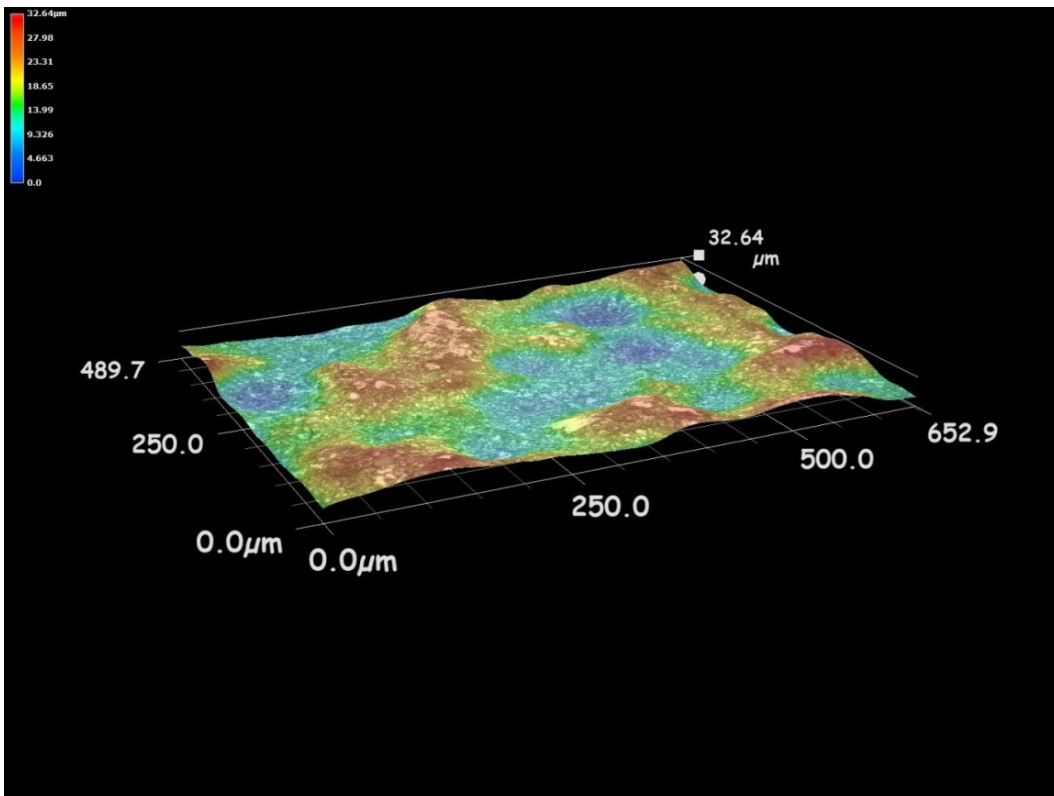


Figure 5.7: 3D illustration of erosion pit (1). Stainless steel 254 – Colour contour.

The shiny appearance of the surface of stainless steel, along with the presence of distinctive facets, indicates the presence of brittle fracture, similar to grade DH36. steel. A large amount of densely distributed circular pits can also be found on the surface of stainless steel 254, with an average depth of the order of several tens μm . It is noteworthy that, only a few of them appear to be joined together, whereas in all examined cases they are evenly distributed, circular in shape and relatively shallow. It should also be noted that multiple pits can be seen on each representation due to their small diameter. The erosion pattern of stainless steel 254 is again circular with a diameter of 22 mm, similarly to the cavitation inducing sonotrode tip.

The depths of the three circular erosion pits that were examined are 32.64, 35.32 and 40.17 μm , respectively, thus the average depth in that instance would be 36 μm . For an erosion pit with a depth analogous to the average value the corresponding measured volume is 2 mm^3 .

Cupronickel 70-30

The microscopic appearance of the eroded surface of cupronickel 70-30 is presented in Figure 5.8:

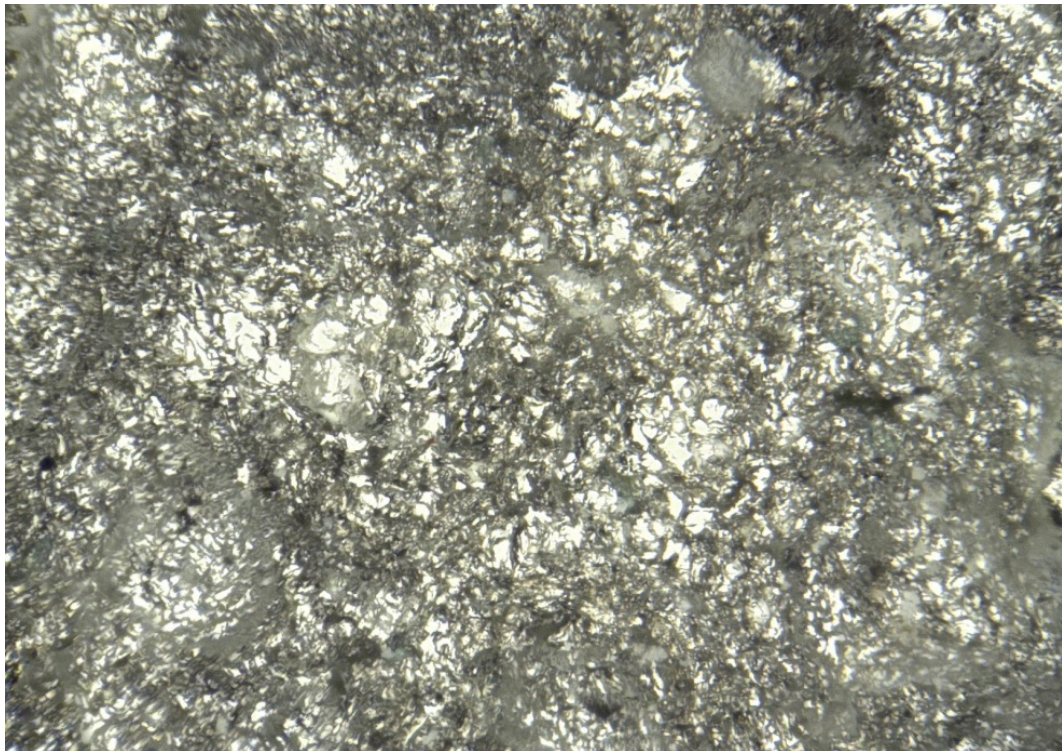


Figure 5.8: Microscopic appearance of cavitation - induced erosion for cupronickel 70-30 (x500).

3D illustrations of a characteristic, cavitation - induced, erosion pit for cupronickel 70-30 are presented in Figures 5.9 and 5.10:

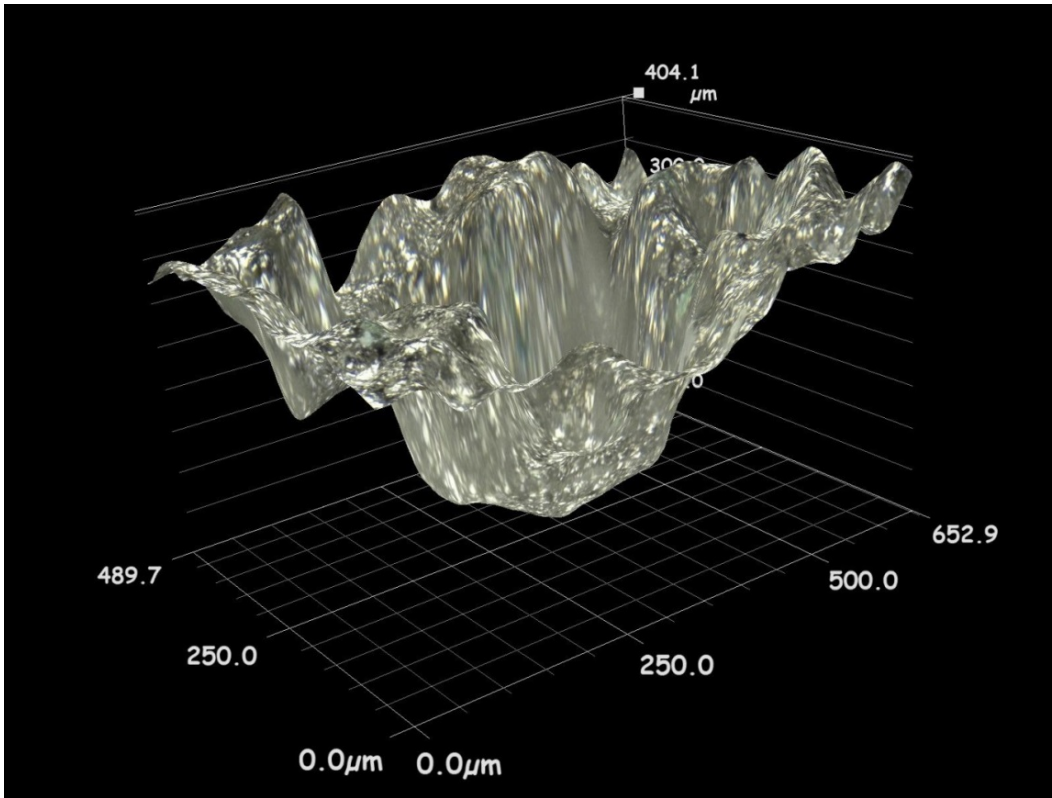


Figure 5.9: 3D illustration of erosion pit (1). Cupronickel 70-30.

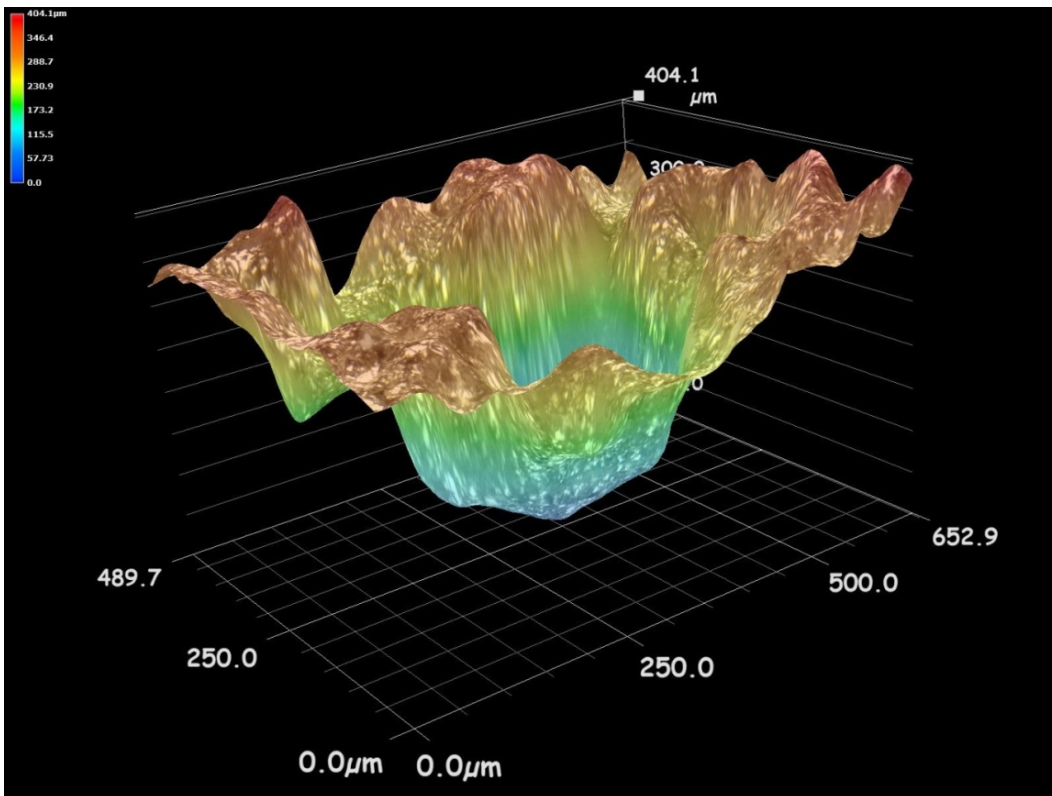


Figure 5.10: 3D illustration of erosion pit (1). Cupronickel 70-30 – Colour contour.

In that instance, the shiny appearance of the surface, in addition to a large amount of facets, also indicates the presence of mainly brittle fracture. Nevertheless, elements that closely resemble ductile dimples, may be observed in some areas, thus indicating the presence of ductile fracture too. The shape of the, cavitation induced, erosion pits that can be found on the surface of cupronickel 70-30 is asymmetrical and sharp towards the bottom whereas the average depth is of the order of several hundreds μm . It is also noteworthy that the majority of those pits appear to be joined together, possibly due to the severity of the cavitation induced erosion. It should be noted that all examined pits are characterized by steep slopes of varying length, in proportion to their depth, similarly to grade DH36 steel. Again, the eroded area is circular with a diameter of 22 mm, similarly to the cavitation inducing sonotrode tip.

The examined erosion pits are irregularly shaped with a depth of 404.1, 346.4 and 344.8 μm , respectively, thus the average depth in that instance would be 365.1 μm . For an erosion pit with a depth analogous to the average value the corresponding measured volume is 12 mm^3 .

Results regarding the three base alloys are summarized in Table 5.1:

	Grade DH36 steel	Stainless steel 254	Cupronickel 70 - 30
Mass loss	0.12 g	0.02 g	0.20 g
Pit depth (Average)	302.4 μm	36 μm	365.1 μm
Pit volume (Average)	8 mm^3	2 mm^3	12 mm^3
Shape	Irregular and characterized by steep slopes	Circular	Irregular and characterized by steep slopes

Table 5.1: Characteristics of the three base alloys - Microscopy

Further to the three base alloys, namely the grade DH36 steel, stainless steel 254 and cupronickel 70 – 30, all seven protective coatings were also examined, as it was the case in *Chapter 4*. This is due to the interest of BAE Systems, however, they do not form part of the main scope of this thesis.

Nevertheless, they are presented in a similar, to the base alloys, layout, thus a general microscopic image of the erosion pattern along with the representation of three erosion pits are given for each proactive coating. The depths of the erosion pits were also measured and are given below.

I coating

The microscopic appearance of the eroded surface of I coating is presented in Figure 5.11:

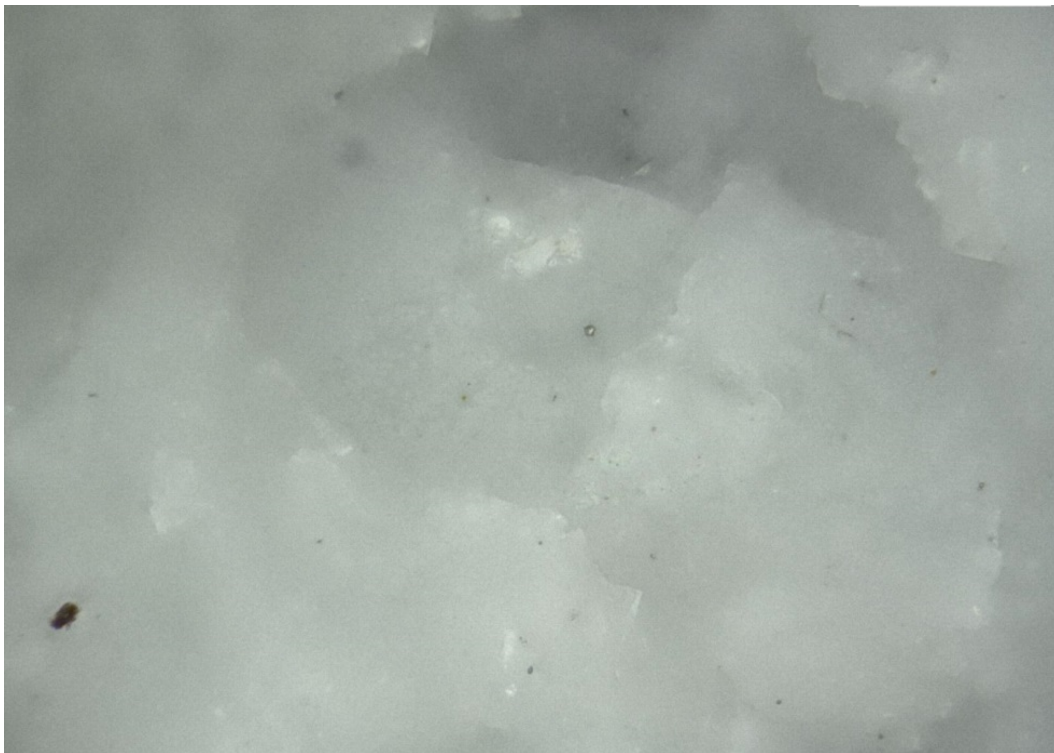


Figure 5.11: Microscopic appearance of cavitation related erosion for I coating (x500).

3D illustrations of a characteristic cavitation - induced, erosion pit for the I coating are presented in Figures 5.12 and 5.13:

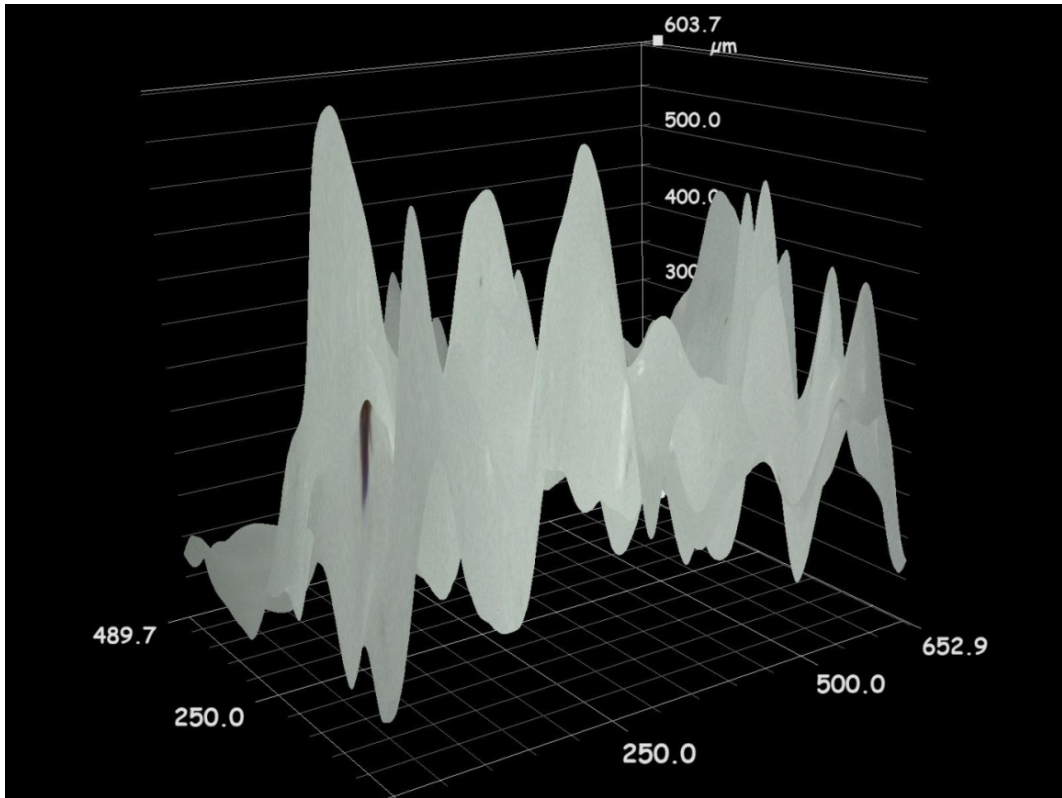


Figure 5.12: 3D illustration of erosion pit (1). I coating.

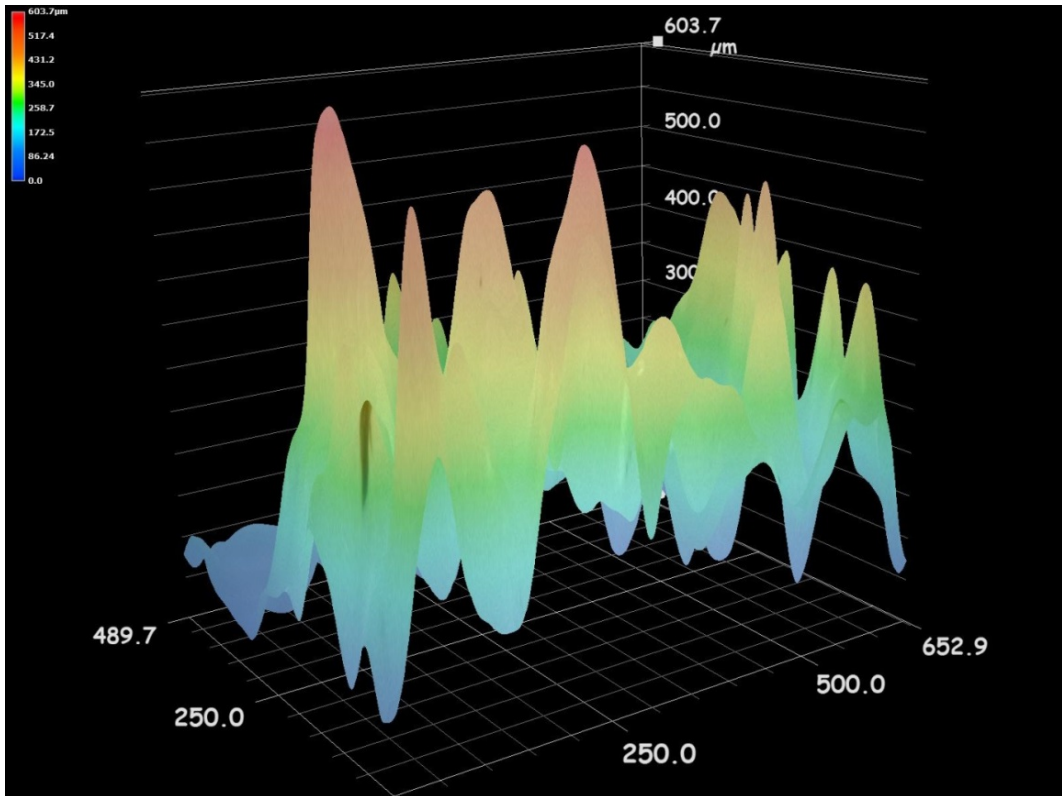


Figure 5.13: 3D illustration of erosion pit (1). I coating – Colour contour.

The I coating exhibited the highest mass loss due to cavitation, in comparison to the other alloys and protective coatings. This behaviour was also reflected in the appearance of the resulting erosion pattern, which was mainly circular with a diameter of 22 mm, corresponding to the cavitation inducing sonotrode tip.

It is noteworthy that, apart from a 2mm wide region located at the outer edges of the circular erosion pattern the coating was totally eroded, thus the protected metal was eventually exposed. In addition, any pits located within the boundaries of the 2mm wide region appear to be joined together whilst their shape could be described as rough and uneven. Moreover, their depths are of the order of several hundreds μm .

In particular, the depths of the three examined pits, located within the 2mm wide region of the circular pattern, are 603.7, 510 and 358.1 μm , respectively.

P coating

The microscopic appearance of the eroded surface of P coating is presented in *Figure 5.14*:



Figure 5.14: Microscopic appearance of cavitation - induced erosion for P coating (x500).

3D illustrations of a characteristic, cavitation – induced, erosion pit for the P coating are presented in Figures 5.15 and 5.16:

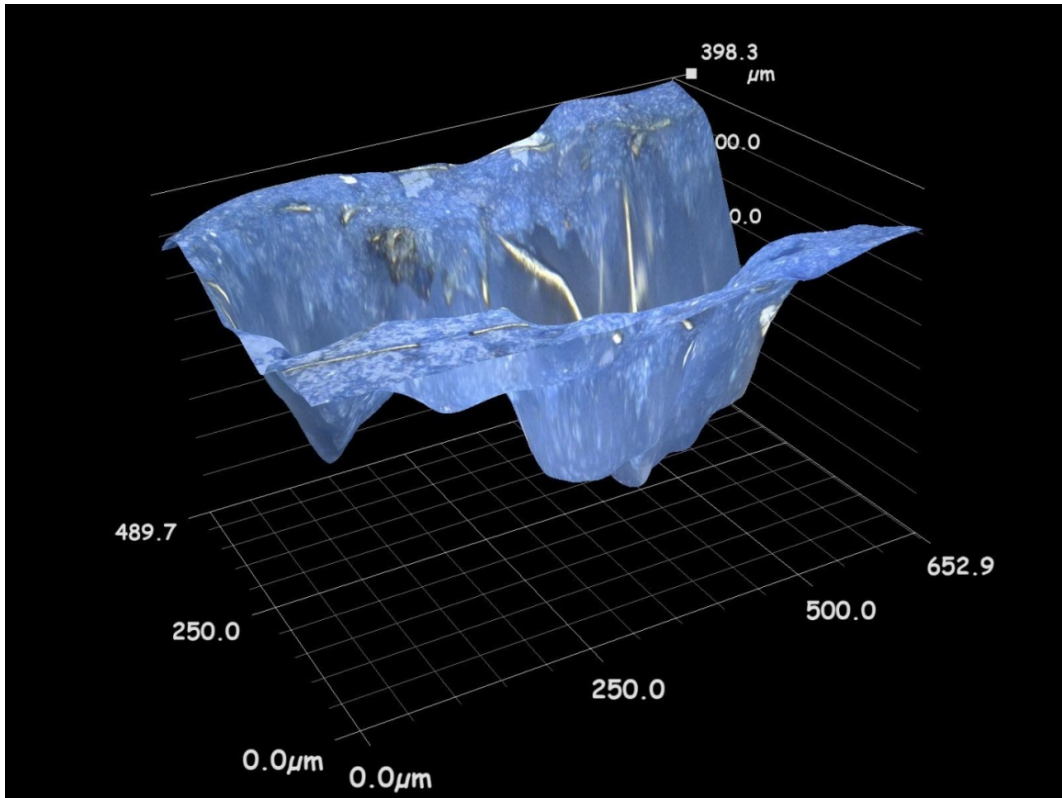


Figure 5.15: 3D illustration of erosion pit (1). P coating.

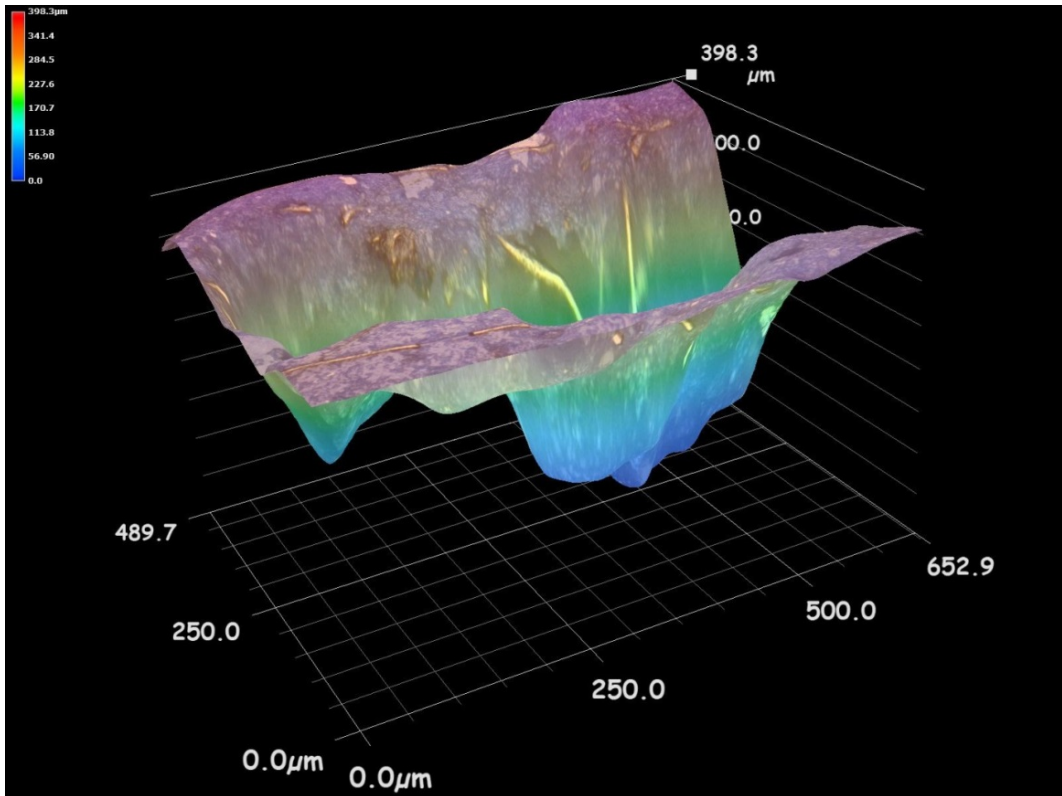


Figure 5.16: 3D illustration of erosion pit (1). P coating – Colour contour.

Cavitation - induced erosion pits, are densely distributed all over the surface of P coating with some of them even appearing to be joined together. Their shape is mainly irregular, although many of them appear to be exhibiting an analogous erosion pattern, in the form of well- defined hollows. They also seem to be more densely distributed towards the centre of the erosion pattern.

It should be noted that the erosion pattern is mainly circular with a diameter of 22 mm, similarly to the tip of the cavitation inducing sonotrode and the erosion pattern of the other examined materials.

The depths of the three examined erosion pits are 398.3, 336.4 and 331.6 μm , respectively.

A coating

The microscopic appearance of the eroded surface of A coating is presented in Figure 5.17:



Figure 5.17: Microscopic appearance of cavitation - induced erosion for the A coating (x500).

3D illustrations of a characteristic, cavitation – induced, erosion pit for the A coating are presented in Figures 5.18 and 5.19:

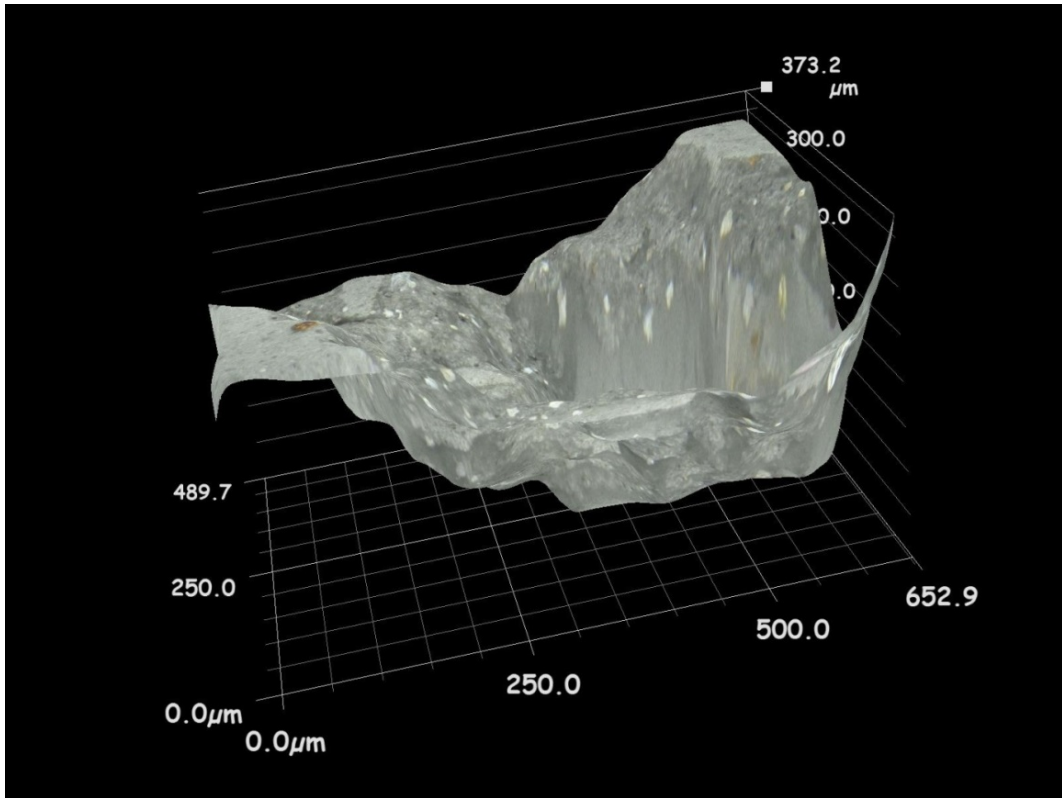


Figure 5.18: 3D illustration of erosion pit (1). A coating.

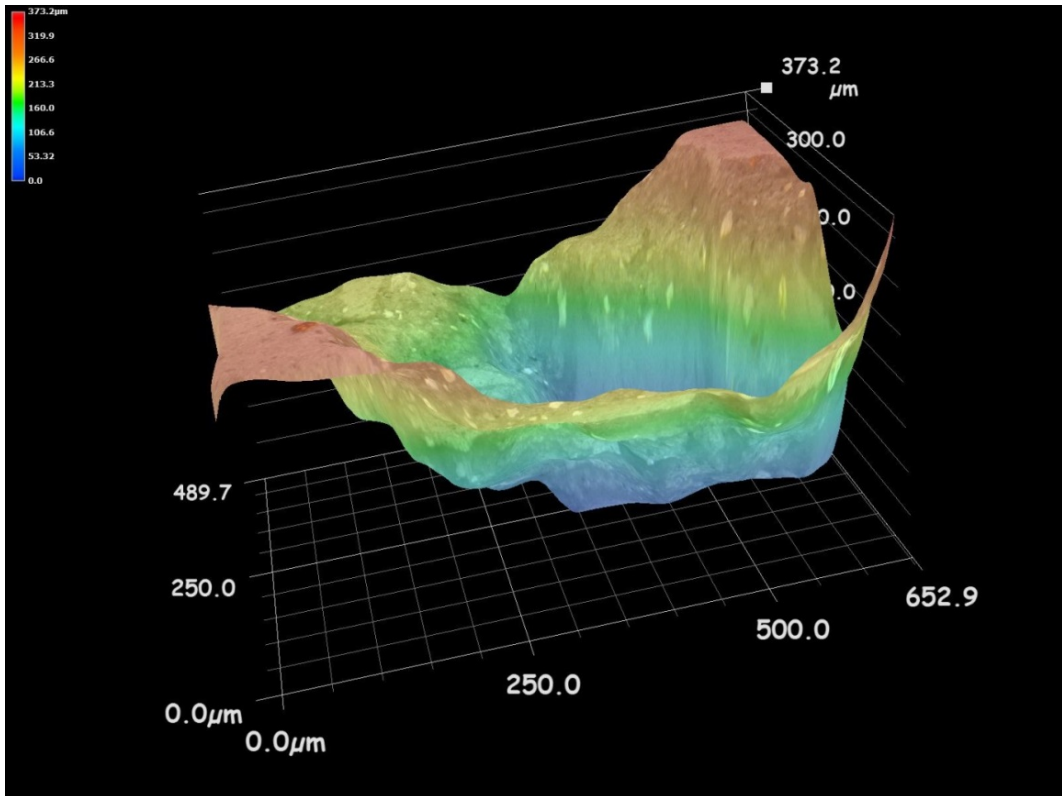


Figure 5.19: 3D illustration of erosion pit (1). A coating – Colour contour.

The appearance of the eroded surface of A coating is in many terms similar to the P coating. As such, erosion pits are densely distributed, especially towards the centre of the erosion pattern, whilst their shape is mostly irregular, with some of them closely resembling well-defined hollows. It is also noteworthy that, some of the pits appear to be joined together, similarly to the P coating.

The shape of the erosion pattern is again circular, whilst its diameter corresponds to the 22 mm diameter of the cavitation inducing sonotrode tip, similarly to the other examined materials.

The depths of the three examined erosion pits are 373.2, 349 and 376 μm , respectively.

Double coating

The microscopic appearance of the eroded surface of Double coating is presented in Figure 5.20:

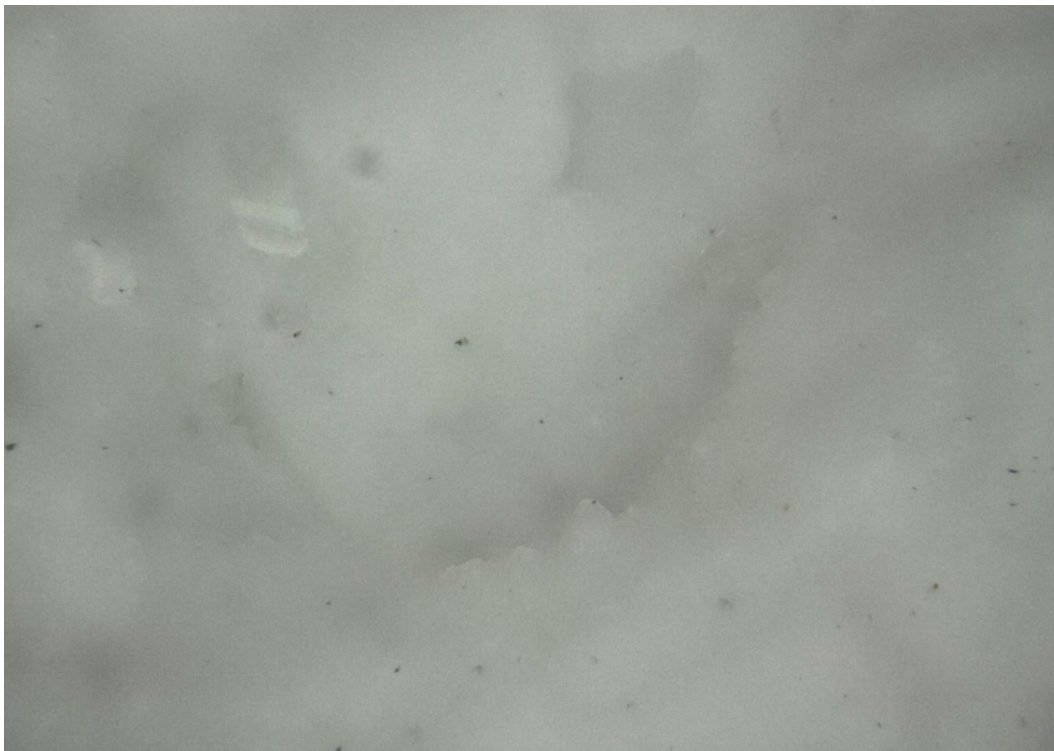


Figure 5.20: Microscopic appearance of cavitation - induced erosion for Double coating (x500).

3D illustrations of a characteristic, cavitation – induced, erosion pit for the Double coating are presented in Figures 5.21 and 5.22:

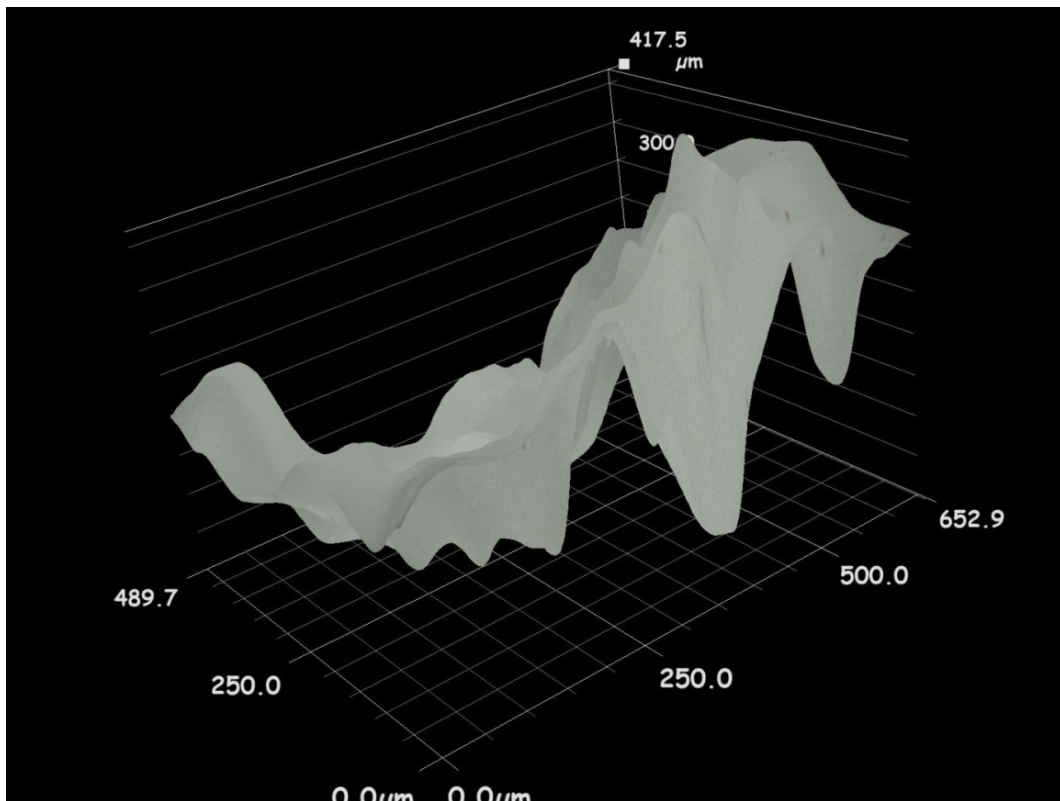


Figure 5.21: 3D illustration of erosion pit (1). Double coating.

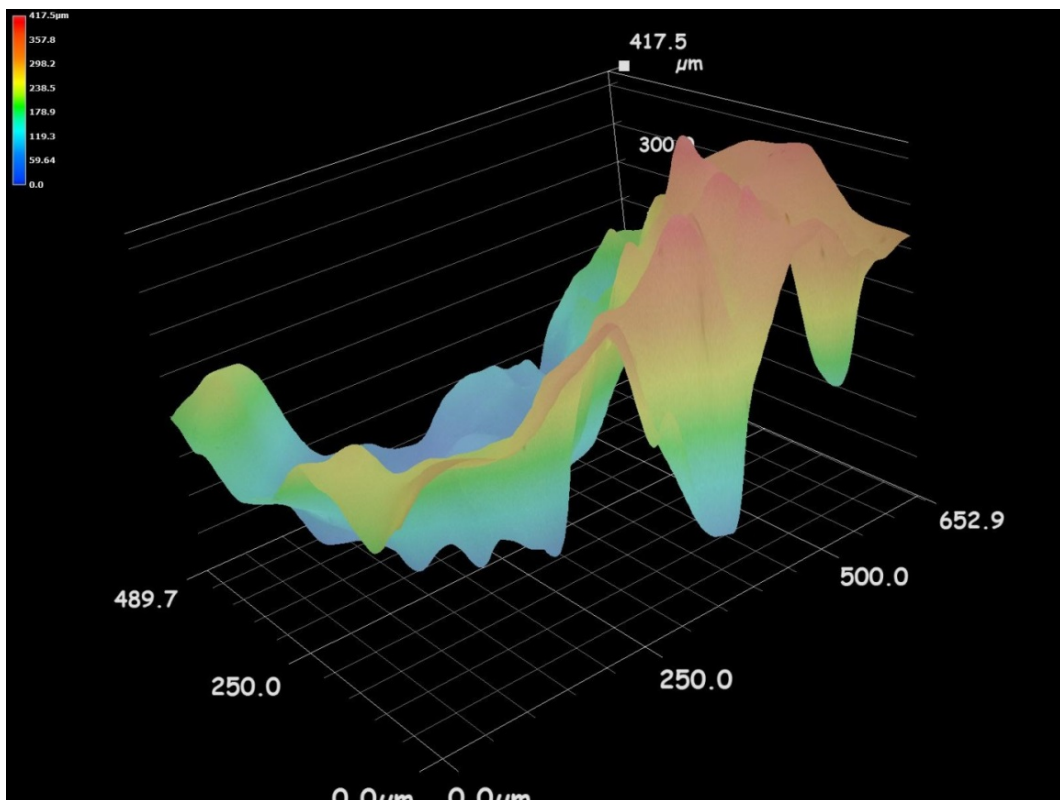


Figure 5.22: 3D illustration of erosion pit (1). Double coating – Colour contour.

The shape of the eroded area of the Double coating was circular with dimensions similar to the cavitation inducing sonotrode tip, therefore its diameter was 22mm. The coating was

almost completely eroded towards the centre of the erosion pattern thus the protected metal was eventually exposed to cavitation in that region. In contrast, many joined pits were identified at the edges of the circular pattern. This behaviour could possibly explain the very high mass loss that was measured, which was the highest besides the I coating.

It should be noted that the examined pits were sharp and irregularly shaped, with an average depth of the order of several hundreds of μm .

In particular, the depths of the three examined erosion pits, located at the edges of the circular erosion pattern, are 417.5, 426.2 and 538.9 μm , respectively.

R coating

The microscopic appearance of the eroded surface of R coating is presented in Figure 5.23:



Figure 5.23: Microscopic appearance of cavitation related erosion for R coating (x500).

3D illustrations of a characteristic, cavitation – induced, erosion pit for the R coating are presented in Figures 5.24 and 5.25:

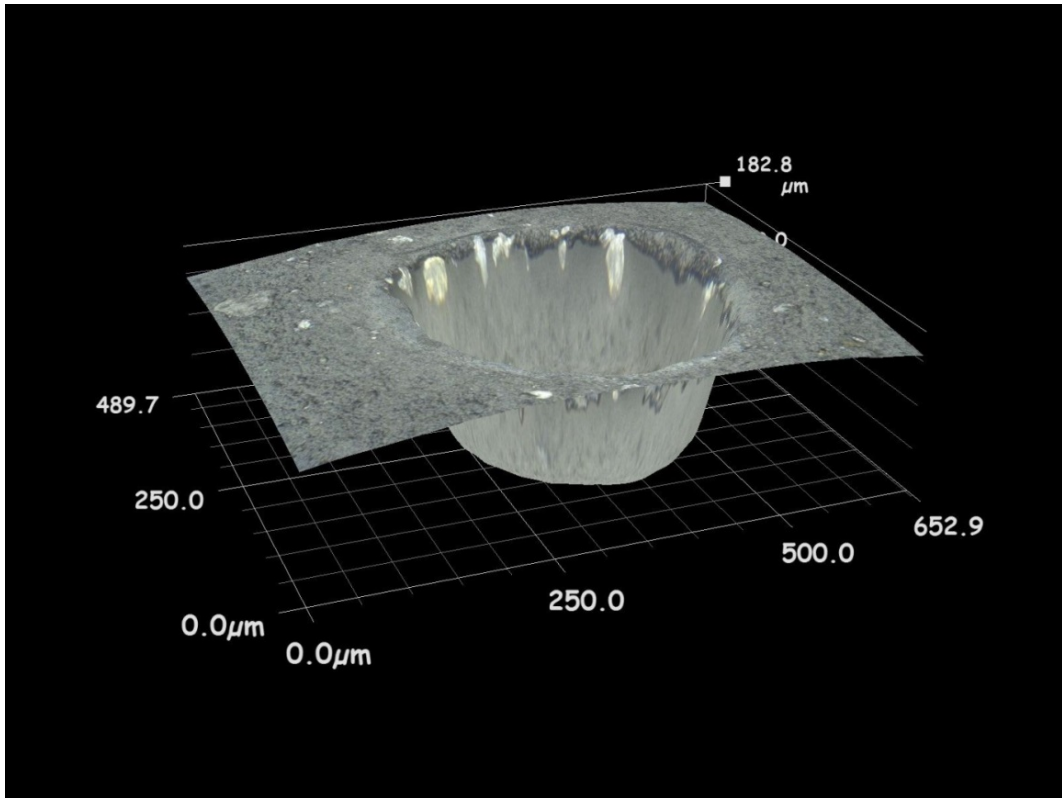


Figure 5.24: 3D illustration of erosion pit (1). R coating.

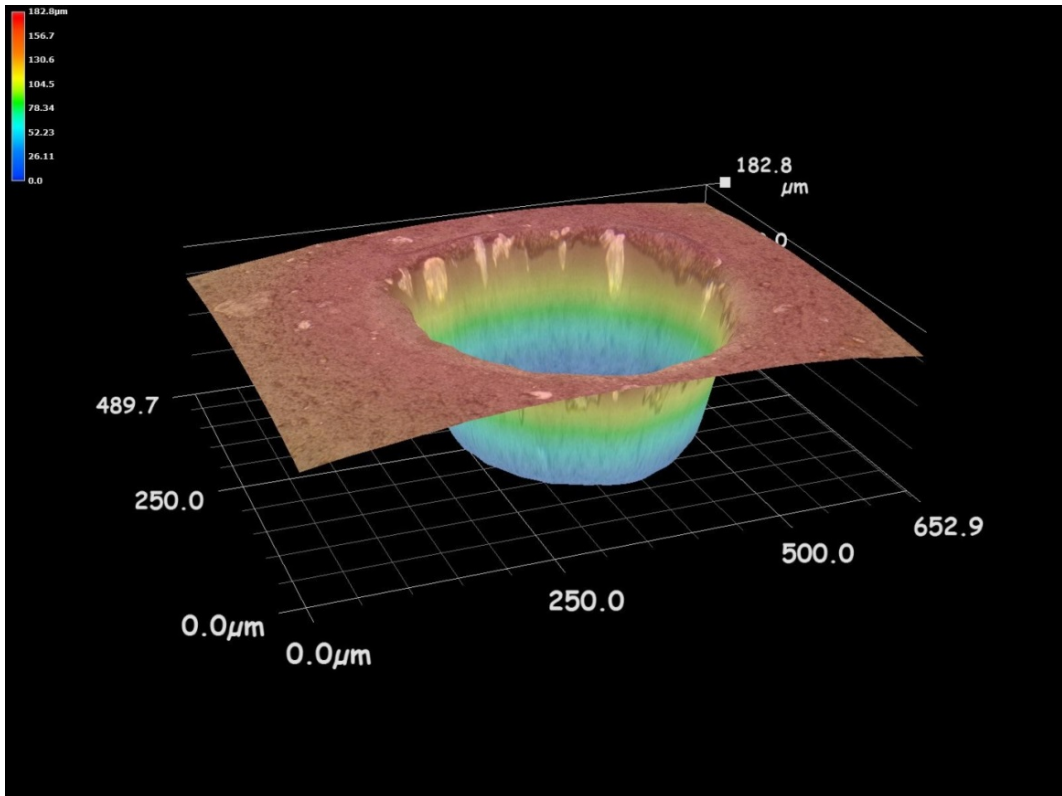


Figure 5.25: 3D illustration of erosion pit (1). R coating – Colour contour.

R coating exhibited the second lowest loss of mass due to cavitation erosion, besides the C coating. As such, no erosion pattern could be identified on its surface, besides a few scattered erosion pits, detectable only under the microscope lens. The shape of those pits was mainly circular with a depth of the order of several hundreds of microns.

It should also be noted that, although a circular slight discoloration of a diameter similar to the sonotrode tip, thus 22 mm, was observed macroscopically, no microscopic characteristics relating to this discoloration could be identified.

The depths of the three examined erosion pits are 182.8, 141.7 and 148.5 μm , respectively.

B coating

The microscopic appearance of the eroded surface of B coating is presented in Figure 5.26:

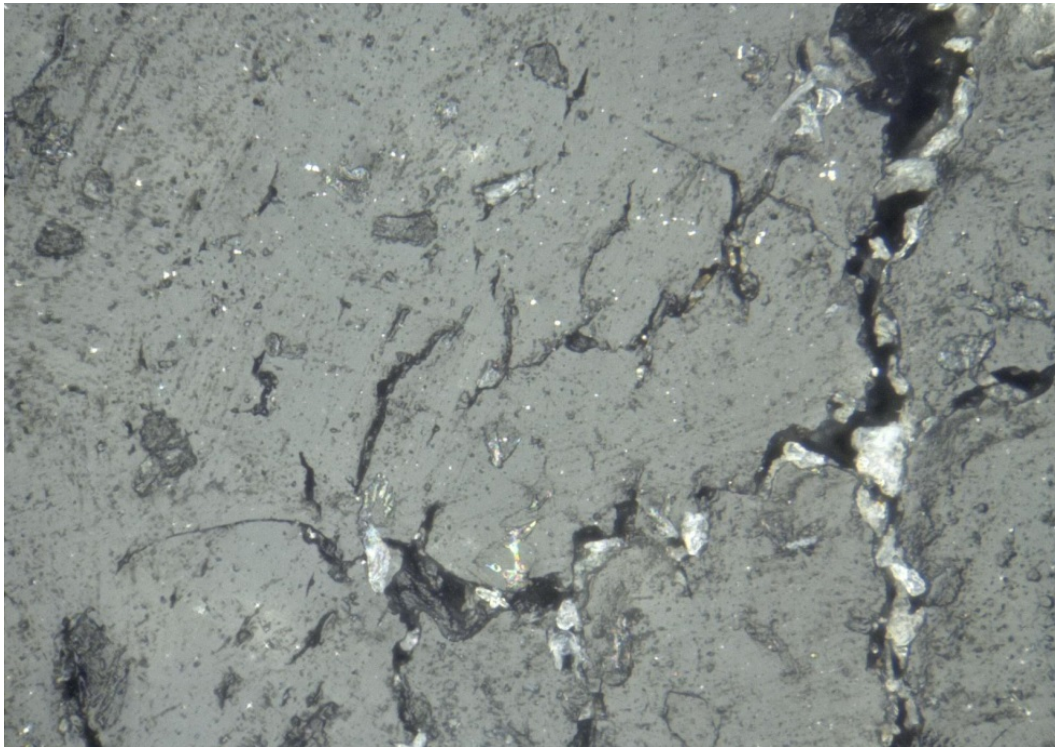


Figure 5.26: Microscopic appearance of, cavitation – induced, erosion for B coating (x500).

3D illustrations of a characteristic, cavitation – induced, erosion pit for the B coating are presented in Figures 5.27 and 5.28:

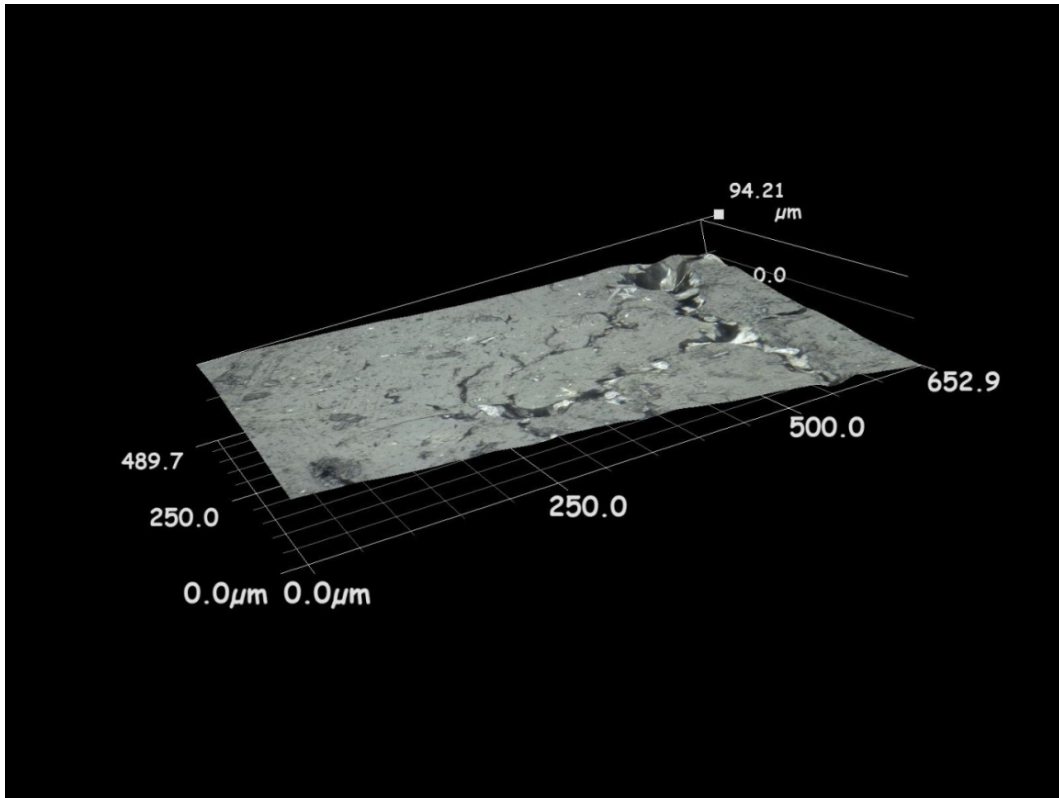


Figure 5.27: 3D illustration of erosion pit (1). B coating.

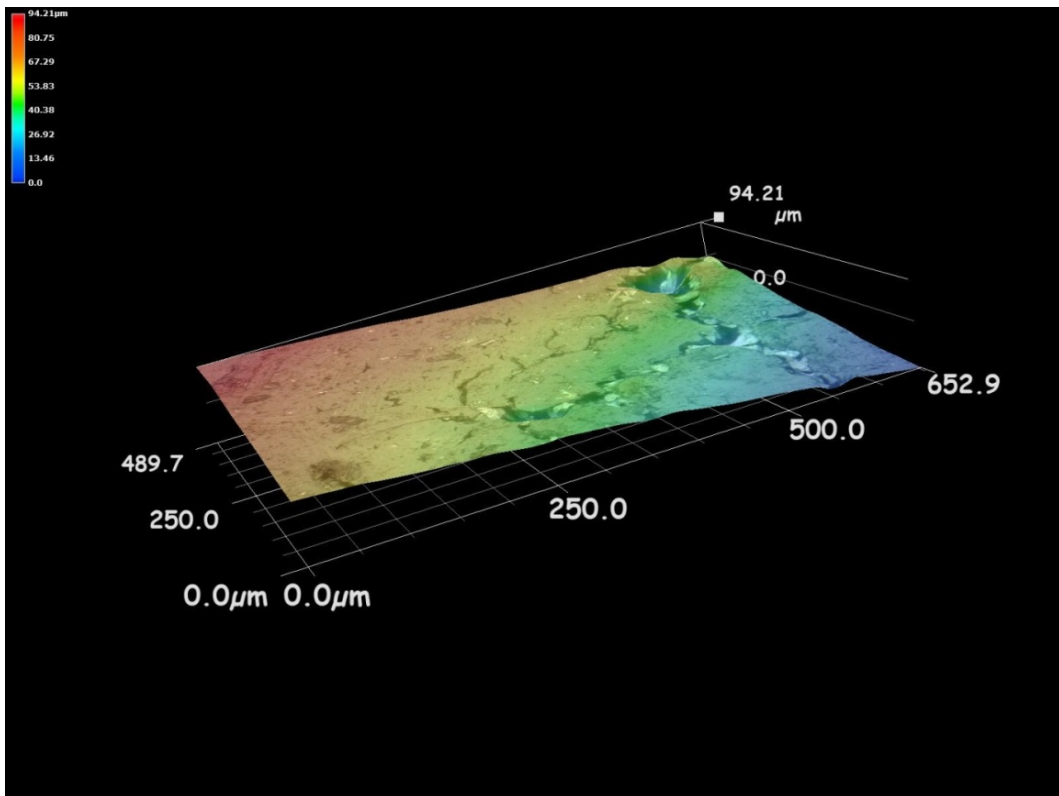


Figure 5.28: 3D illustration of erosion pit (1). B coating – Colour contour.

The B coating exhibited a unique behaviour in the sense that, a large circular bump of a diameter of 11mm emerged at the centre of its surface. The coating on the bump, however,

appeared to be rather deformed instead of eroded, possibly due to local temperature effects relating to cavitation activity.

More specifically, the coating at the deformed region became soft and was bent inwards. As such, cracks emerged and propagated at the edges of the bump resulting into the formation of joined cracks-pits.

The depths of three examined pit-cracks are of 94.21, 36.55 and 105 μm , respectively.

C coating

The microscopic appearance of the eroded surface of C coating is presented in Figure 5.29:

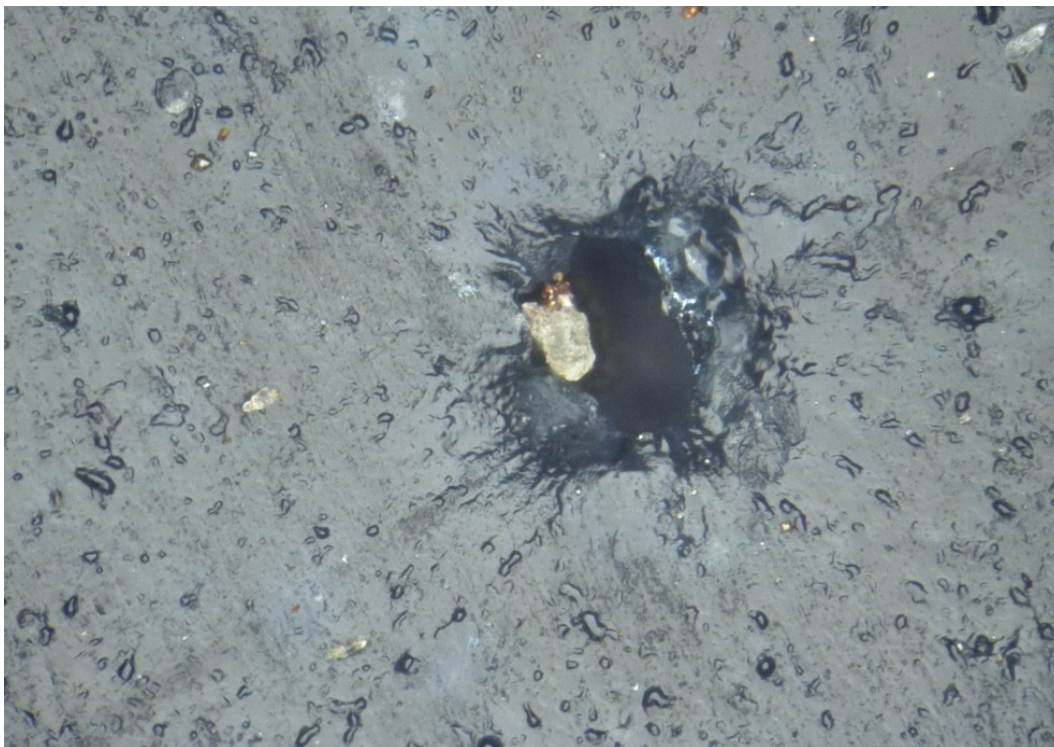


Figure 5.29: Microscopic appearance of, cavitation – induced, erosion for C coating (x500).

3D illustrations of a characteristic, cavitation – induced, erosion pit for the C coating are presented in Figures 5.30 and 5.31:

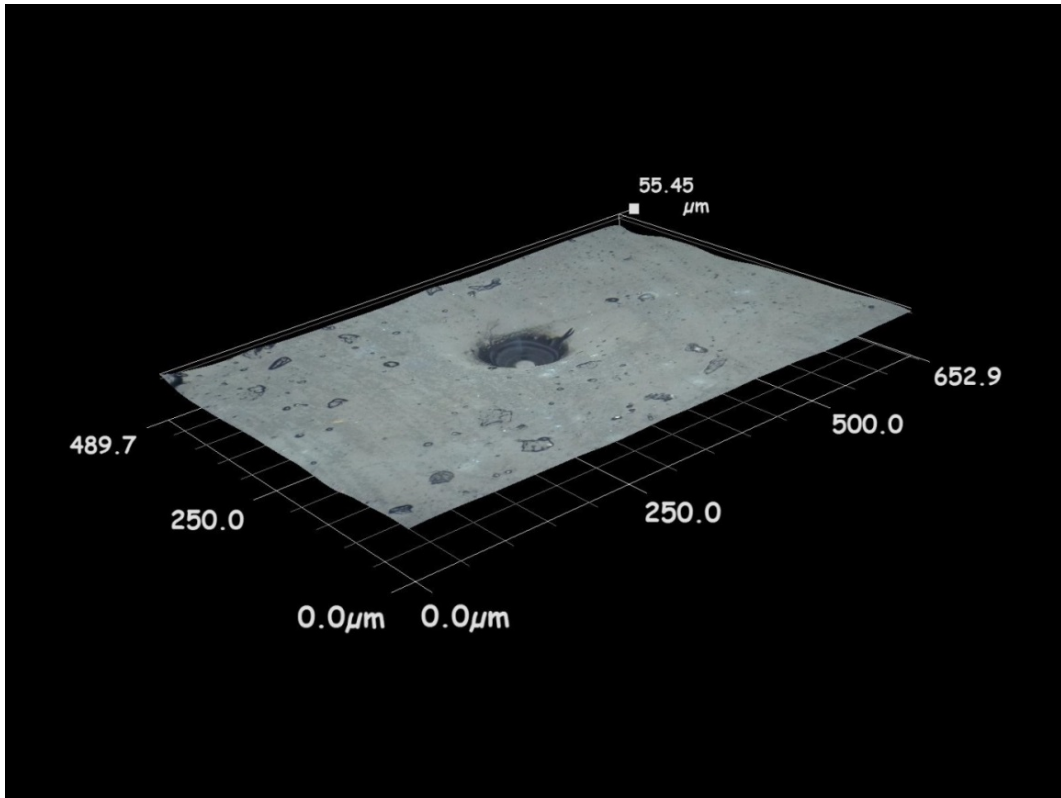


Figure 5.30: 3D illustration of erosion pit (1). C coating.

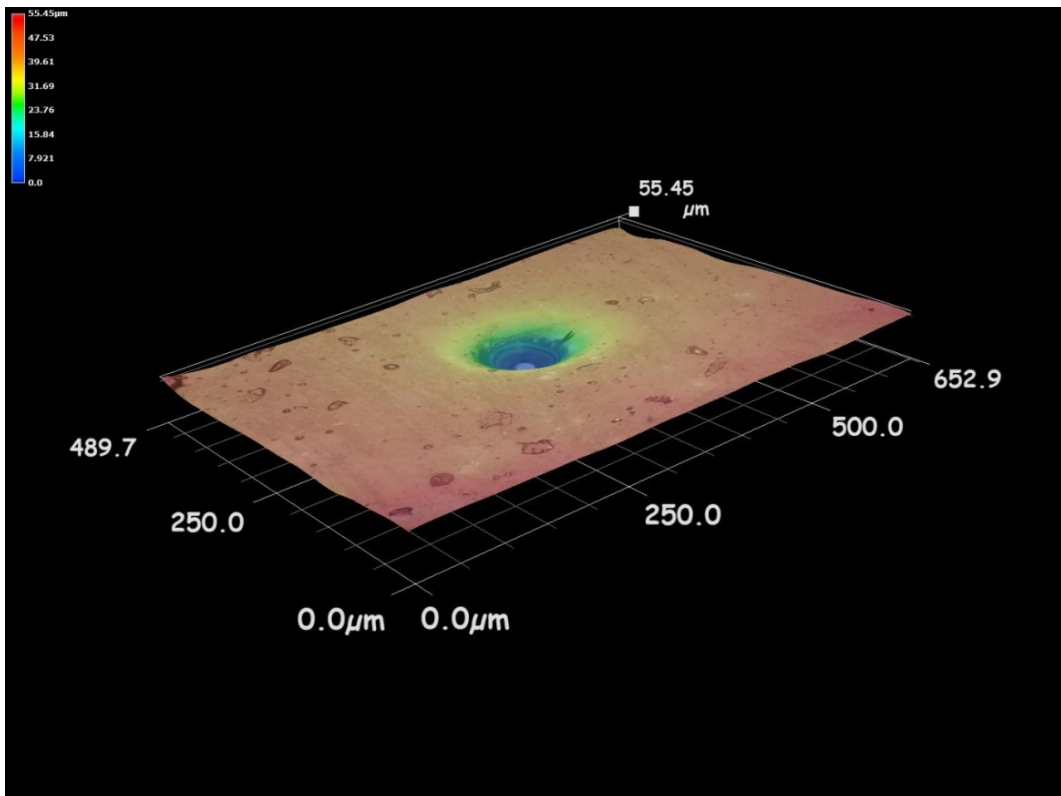


Figure 5.31: 3D illustration of erosion pit (1). C coating – Colour contour.

C coating exhibited the lowest mass loss due to cavitation erosion and this was reflected in the microscopic appearance of its eroded surface. As such, only a few scattered erosion pits could

be identified under the microscope lens. It should also be noted that no definite erosion pattern could be identified either macroscopically or microscopically, in contrast to the other examined materials, apart from the R coating which exhibited an analogous behaviour with regards to mass loss.

The shape of those erosion pits ranged from circular to mainly circular with irregular edges whereas their average depth was of the order of several tens of μm .

The depths of the three examined erosion pits are 55.45, 44.33 and 63.78 μm , respectively.

Discussion on the findings

Preliminary observations indicate that, the appearance of the eroded surfaces of all alloys and coatings is in good agreement with the cavitation induced mass loss.

For instance, the eroded surface of cupronickel 70-30, which was the alloy that exhibited the highest amount of mass loss, was rough. In addition, its densely distributed erosion pits were sharp and deep whilst some of them were even joined together towards the centre of the eroded region. Analogous remarks apply for grade DH36 steel, although to a much lesser extent, as one would expect from the corresponding cavitation induced mass loss, which was lower than cupronickel 70-30. Erosion features on the surface of stainless steel 254 were even smoother in the sense that, only some densely distributed yet shallow cavities could be identified. These remarks are in good agreement with its behaviour in terms of, cavitation induced erosion - mass loss, which was significantly lower than the other two alloys.

Only a few scattered erosion pits could be identified on the surfaces of R and C coatings, which exhibited the best behaviour in terms of resistance against cavitation induced erosion – mass loss between all coatings. In contrast, the Double and I coatings, which exhibited the highest mass loss between all coatings, totally collapsed by cavitation, especially towards the centre of the relevant eroded regions whereas some deep and sharp erosion pits could be observed at the boundaries of these areas. As for the A and P coatings, which in terms of mass loss lie between the aforementioned groups of coatings, they both exhibited a large amount of irregularly shaped, mildly deep erosion pits mostly located towards the centre of their erosion pattern. Finally, the B coating displayed a unique behaviour, in the sense that a distinctive bump appeared at the centre of its surface, possibly due to local temperature effects.

5.4 Fractography

Fracture can be defined as the separation of a body due to an applied stress. Stress essentially induces or amplifies cracks which then propagate inside the material and can eventually lead to failure. Of the many types of fracture, two are of major interest here (Knott, 1973):

- **Ductile:** The application of stress induces cracks that propagate slowly and are accompanied by the plastic deformation of the material. In many cases of ductile fracture cracks resist further propagation unless the applied stress increases.
- **Brittle:** Cracks propagate rapidly and are accompanied by minimal or zero deformation of the material. In brittle fracture, rapid crack propagation may continue even when the applied stress remains constant.

In addition to the aforementioned major types of fracture, the phenomenon of creep might also be of concern in some cases. Creep can be defined as the time – dependent deformation of a material due to an applied stress, usually occurring at high temperatures, resulting into an increase in length that can affect the performance of the affected component and cause failure. Considering, however, that creep normally does not become important until 40% of the melting temperature is reached, which is of the order of 1400 °C for all the examined alloys, it is likely to be a secondary influence compared to cavitation induced brittle and ductile fracture. Nevertheless, those temperatures may be reached instantaneously when bubbles collapse, as the colour tinting marks that have been observed suggest (see Figure 2.20, *Chapter 2*).

The difference between ductile and brittle fracture can be seen in Figure 5.32:

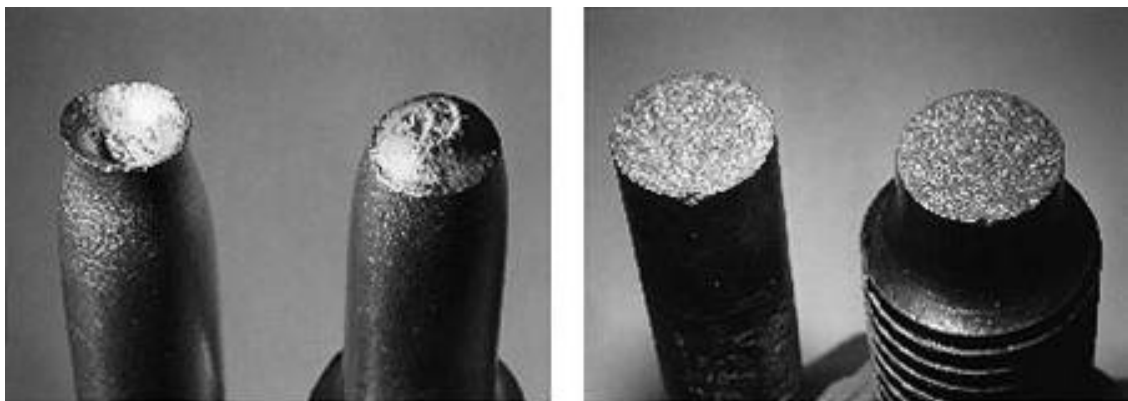


Figure 5.32: Left – Ductile failure, Right – Brittle failure. (Source: University of Southampton).

Typically, bcc (body-centred cubic) metals such as iron and steel alloys, exhibit brittle fracture below a critical temperature, called the ductile – brittle transition temperature (DBTT), whereas above this temperature a ductile behaviour is to be expected (Argon, 2001). Considering that ships may experience polar water temperatures, the parameter of DBTT should be taken into account, especially when cavitation induced loading that could result in rudder erosion is considered. This phenomenon is illustrated in Figure 5.33:

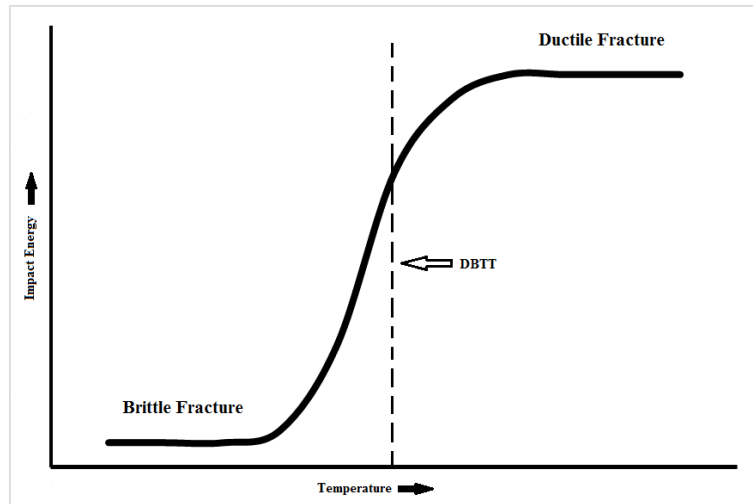


Figure 5.33: Ductile – brittle transition

In contrast, fcc (face-centred cubic) metals and alloys, such as copper, aluminium, nickel and austenitic steels exhibit ductile behaviour mainly due to the high number of slip systems in their crystals. In alloys, however, the presence of different atoms significantly affects the critical stress that is required for slip and cleavage and as a result a considerable loss of ductility may occur whereas the way cracks propagate would also be affected.

On a macroscopic level, ductile fracture surfaces appear to be rough (orange peeling) and exhibit large necking regions, whereas brittle fracture surfaces are relatively flat and are characterized by a crystallized appearance. On a microscopic level, ductile fracture surfaces also appear to be rough and are characterized by the presence of numerous microvoids and dimples. Those microvoids are the basis of the mechanism behind ductile fracture, called microvoid coalescence, and nucleate when stress is applied before they expand into larger cavities – cracks and cause fracture (Benzerga and Leblond, 2010).

The microscopic appearance of microvoids and dimples, when examined by means of a scanning electron microscope, can be seen in Figure 5.34:

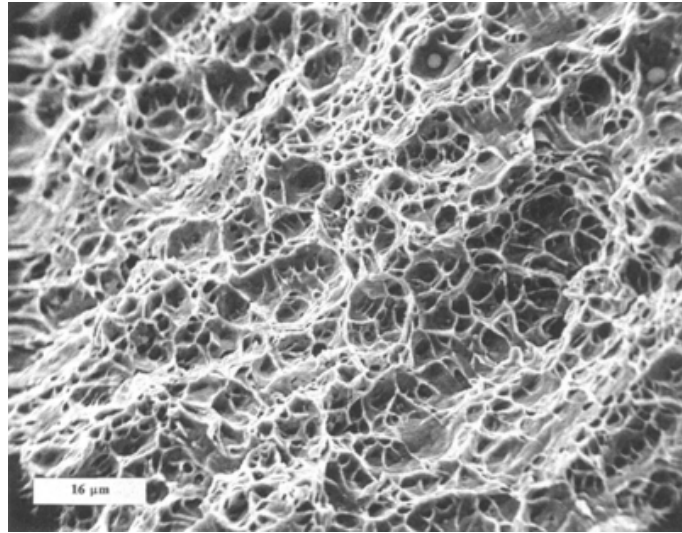


Figure 5.34: Scanning electron microscope (SEM) fractograph of ductile fracture dimples in low carbon steel. (Source: ASM International, 1992).

Brittle fracture, is characterized by two main types of crack propagation (Pineau et al., 2016):

- **Cleavage or transgranular fracture:** In this case, cracks propagate through the grains of the material along low-index crystallographic planes. Considering that alloys are essentially polycrystalline and contain grain boundaries, dislocations and other imperfections, however, cracks change direction from grain to grain due to the different orientation of atoms on each one of them. This results into a bumpy and edgy granular pattern whilst patterns of ridges caused by the alternating direction of cracks can also be observed by means of a scanning electron microscope.
- **Intergranular fracture:** In this case cracks propagate through the grain boundaries of the material and as a result, the appearance of the surface is characterized by edges and facets often resembling the actual shape of the grains. Intergranular fracture occurs when the phases in the grain boundaries are weakened or embrittled.

The difference between transgranular and intergranular fracture is illustrated in Figures 5.35 and 5.36:

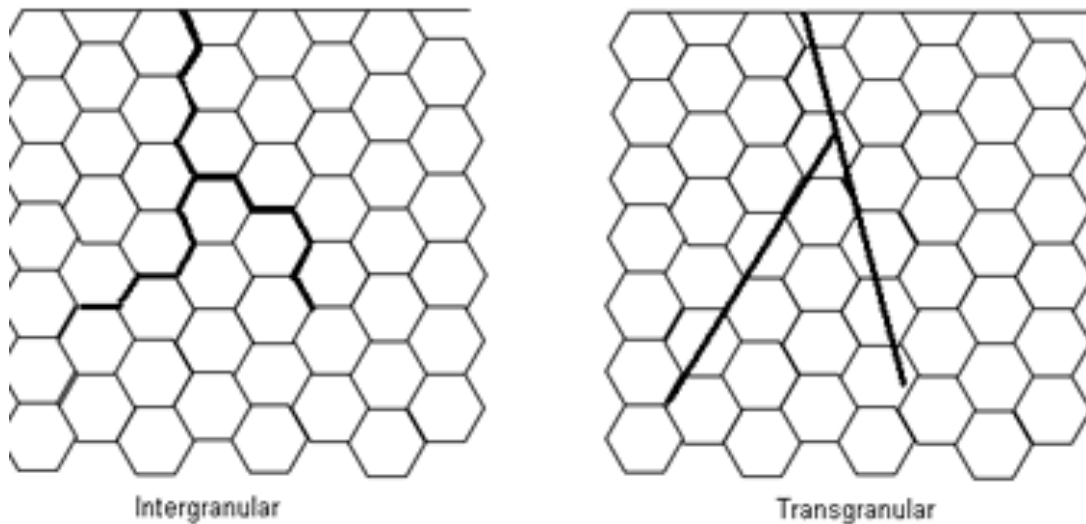


Figure 5.35: Intergranular and Transgranular fracture. (Source, GO-TECH, n.d.).

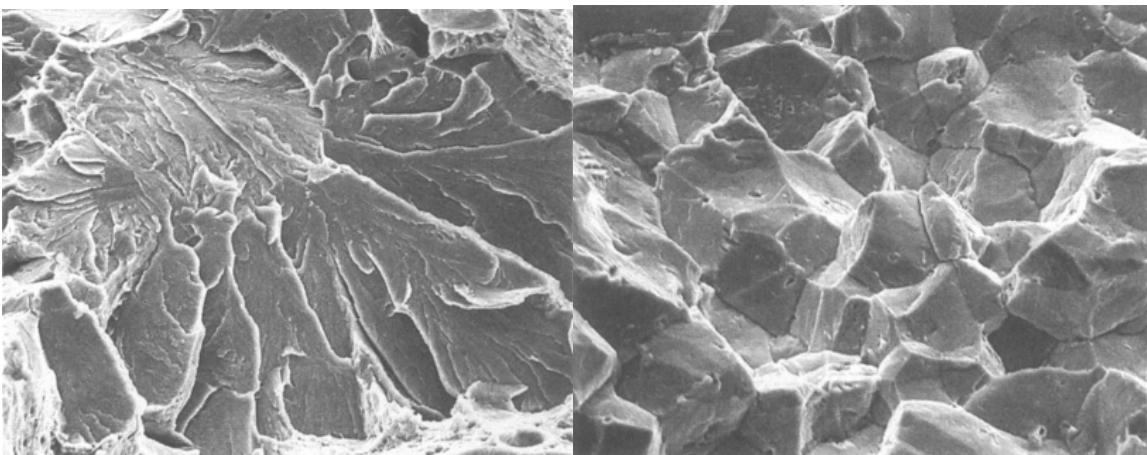


Figure 5.36: Scanning electron microscope (SEM) image of carbon steel. Left – Transgranular fracture, Right – Intergranular fracture. (Source: ASM International, 1992).

Commonly, examination of alloys that have failed from brittle fracture, reveals fractions of transgranular fracture as well as evidence of ductile fracture. The basis of this behaviour lies on the orientation of the grains in the sense that those oriented favourably to the axis of loading exhibit ductile behaviour, whereas those oriented unfavourably respond in a transgranular way. This process is called quasi-cleavage fracture.

In this case, the appearance of the affected surface would exhibit transgranular characteristics (ridges, bumpy edges) as well as signs of ductile fracture (dimples). A combination of transgranular fracture and ductile dimples can be seen in Figure 5.37:

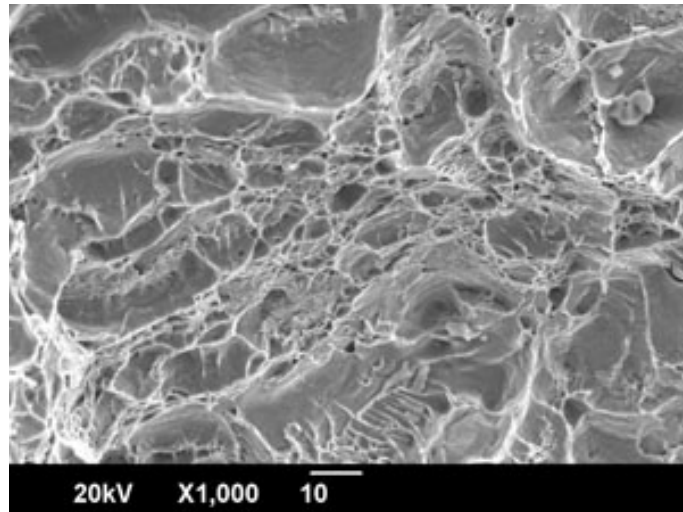


Figure 5.37: Combination of ductile dimples and transgranular fracture in carbon steel. (Source: CITIMETAL GROUP CORP., n.d.).

Brittle intergranular fracture is common in polycrystalline alloys and can be mainly attributed to weakened grain boundaries. Factors that weaken grain boundaries include the presence of impurities (Seah, 1980), the embrittlement of the material due to high concentrations of phosphorus and carbon as well as the absorption of hydrogen from the atmosphere (Krauss, 2000). The presence of large grains also favours intergranular fracture and further enhances the effects of those factors along with the continuous application of stress at elevated temperatures (creep). Moreover, intergranular fracture may be caused by ductile micro-voids. In this case the ductility of the boundaries is lower than the grains and as a result micro-voids develop and expand inside the grain boundaries, thus leading to intergranular fracture. In contrast, transgranular fracture usually occurs over low index crystallographic planes. As such, transgranular fracture is mostly to be found in BCC metals, such as iron and steel alloys whereas intergranular fracture mostly occurs in FCC metals such as copper, aluminium, nickel and austenitic steels (Liu, 2005).

It was suggested that transgranular fracture would evolve into intergranular fracture for values of the ratio R_{CI} lower than 1, with that ratio being defined as follows (Francois et al., 2013):

$$R_{CI} = 1.20 - \frac{\gamma_b}{2\gamma_s} \quad (5.1)$$

where γ_b is the free energy of the grain boundary per unit area and γ_s the free energy of a surface exposed by transgranular fracture. It has been found that in the case of pure metals, γ_b and γ_s correlate with the shear modulus G and bulk modulus K_B , respectively, thus the relevant R_{CI} ratios could be effectively calculated (Cottrell, 1989).

In practice, both brittle and ductile types of fracture appear either as a combination or as the evolution of one mode to another. In this case a microscopic examination of the fractured surface would be required and traces of both types of fracture as well as the relevant propagation modes would be identified. This is due to the nature of alloys, as they contain many types of grains, each one of which has its own properties and orientation, favouring specific modes of crack propagation. It may also be the result of cold work hardening, where initial plastic deformation, essentially strengthens the material by inducing more dislocations of atoms, which then interact and become pinned. As such, the material strengthens and behaves in a brittle way. In a typical stress – strain curve (left side of Figure 5.38) for a bcc alloy (steel) the region between the yield point (Y), or the point where the material ceases to behave elastically and plastically deforms, and the point where the material fractures, is where work hardening takes place. It should be noted, however, that even before the material plastically deforms, an amount of work hardening is still taking place, although to a much lesser extent. It should be noted that analogous remarks apply for fcc alloys (cupronickel 70-30, stainless steel 254), although in this case the yield point is not as profound.

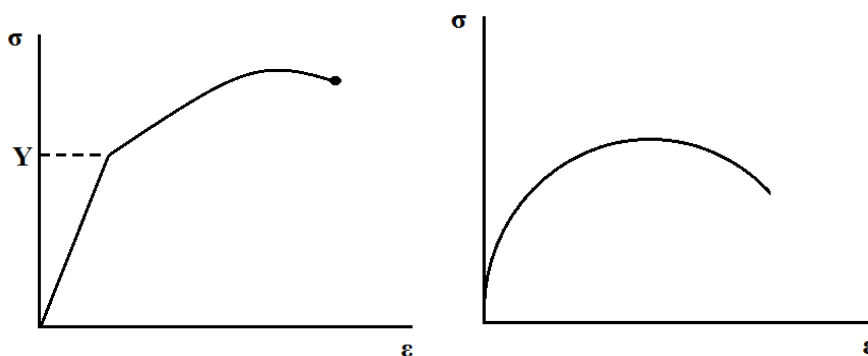


Figure 5.38: Stress – Strain Curve. Left (fcc), Right (bcc – stainless steel 254, cupronickel 70-30)

Nevertheless, to effectively define the fracture modes involved in failure, a material must be examined both macroscopically and microscopically. As such, an initial estimation regarding the dominant fracture type can be made by means of macroscopic observation. The propagation of cracks can then be traced through the microscope. Conventional optical microscopes cannot focus on the entire surface at high magnification settings, nevertheless an initial estimation can be made. Further investigation, however, would require the use of a scanning electron microscope which can effectively focus on the entire examined area at very high magnification settings.

5.5 Fractography - Procedure

A preliminary estimation regarding the governing fracture type was made, for each one of the examined alloys, based on the macroscopic appearance of the relevant erosion patterns. Microscopic examination then revealed specific crack propagation paths as well as distinctive characteristics.

Towards that direction, some unique features of each alloy, such as grain size and shape were also examined microscopically. Grain size has a significant effect on the mechanical properties of a metal and in general, the smaller the grain size the higher the strength of the metal. Moreover, as the grain size of the metal decreases its ductility decreases too.

As such, all alloys were prepared following a common procedure for metallographic examination, including fine grinding, polishing and chemical etching stages. Although an identical grinding and polishing procedure was followed for all alloys, different etching agents were utilized for each one of them. Grade DH36 steel was etched by means of Nital, which is a solution of alcohol and nitric acid, whereas stainless steel 254 was etched with HCl, namely hydrochloric acid, and cupronickel 70.30 with FeCl_3 , namely ferric chloride, respectively.

Following the metallographic preparation of each alloy, microscopic images were taken and grains were counted manually. It should be noted that those pictures are presented in the following sub-chapter. A quantity that characterizes grain size, namely the ASTM grain size number, was then calculated by means of the following equation, for each alloy:

$$N_{100} = 2^{n_{ASTM}-1} \quad (5.2)$$

where N_{100} is the number of grains per square inch at a x100 magnification and n_{ASTM} is the ASTM grain size number. It should be noted that the smallest possible magnification for this optical microscope was x500 thus the grains per square inch number N_{500} was converted to the N_{100} number by means of the following equation which includes the magnification factor (M):

$$N_{100} = \left(\frac{M}{100}\right)^2 \times N_{500} \quad (5.3)$$

Microscopic images of both eroded and non-eroded specimens, were then compared for each one of the examined alloys. In particular, any distinctive features of the eroded surfaces were compared to the non-eroded grain structure, which was revealed through metallographic preparation, under a magnification of x500. An estimation regarding the governing fracture mechanism was then made, based on the macroscopic and microscopic findings.

The three alloys, were finally examined by means of a scanning electron microscope (SEM) in order for the initial estimations regarding the governing fracture types to be either confirmed or reconsidered accordingly. In addition to specimens exposed to cavitation for five hours, specimens exposed for half an hour as well as two and a half hours were also examined in order for the progression of erosion to be studied in terms of the governing fracture mechanisms of each stage.

5.6 Fractography - Results

Results are categorized and discussed for each one of the examined alloys, on a basis of macroscopic, microscopic and SEM findings.

DH36 steel

The macroscopic erosion pattern of grade DH36 steel after five hours of cavitation exposure is presented in Figure 5.39:



Figure 5.39: Eroded surface of grade DH36 steel.

The homogenous and crystallized macroscopic appearance of the eroded surface of grade DH36 steel is characteristic of brittle fracture.

The microscopic appearance of both the non-eroded surface, as it was revealed through metallographic preparation, and eroded surface of grade DH36 steel after five hours of cavitation exposure is presented in Figure 5.40 at a magnification of x500. A scaled mesh (100 μ m) was used in both images for comparison reasons.

The calculated ASTM grain size number of Grade DH36 steel is 12 corresponding to a very fine structure and a mean grain diameter ranging from 5.6-8 μm .

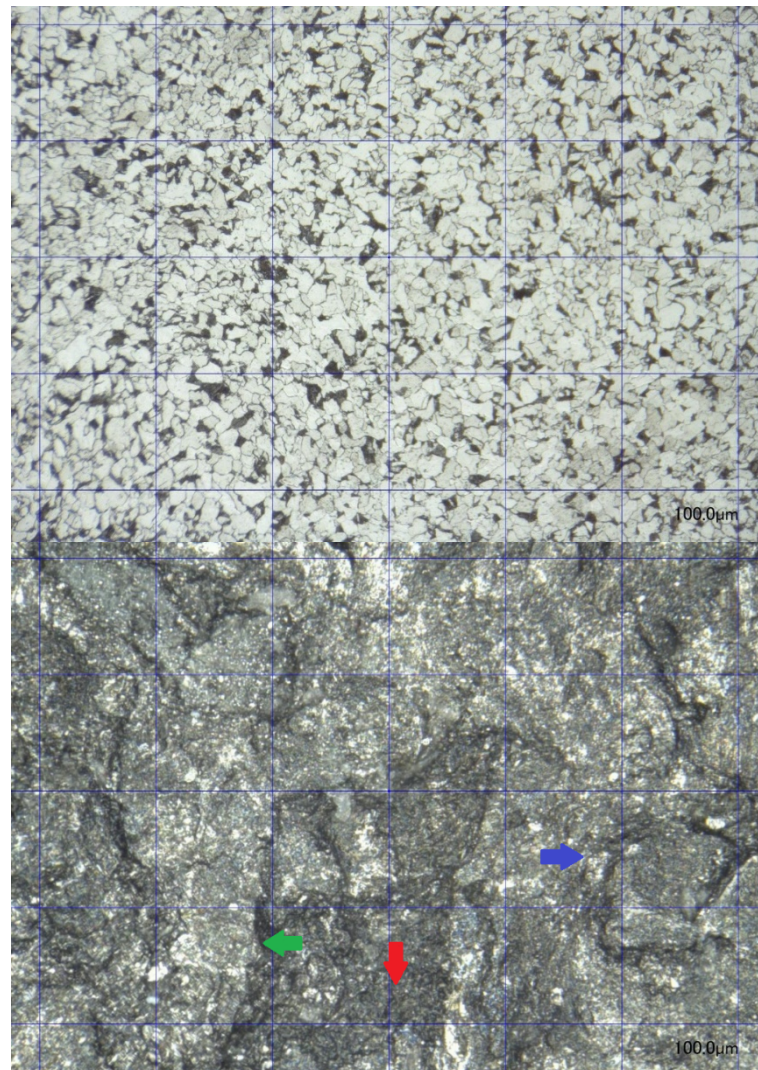


Figure 5.40: Microscopic images of non-eroded (Top) and eroded (Bottom) grade DH36 steel. Arrows: Green – Intergranular, Blue – Transgranular, Red – Ductile.

Further examination under the microscope, revealed a significant number of well-defined facets and nearly straight edges, which are usually signs of brittle intergranular fracture, as well as regions with a bumpy and granular appearance, a characteristic of transgranular fracture. In comparison with the individual grains, those well-defined facets and nearly straight edges appear to be following the grain boundaries, although favourably orientated grains would present a similar pattern in the case of transgranular fracture. This is due to the fact that cracks in transgranular fracture propagate through the atoms of the grains. In this case and due to the length of those nearly straight edges and the relatively small size of the grains, transgranular fracture appears to be the dominant crack propagation type at these regions. In contrast, intergranular fracture is apparent at the smaller and sharper features of the fracture

pattern, which with regards to size are comparable to the grains. Finally, a considerable number of ductile dimples can be observed, implying an amount of initial plastic deformation and ductile fracture.

Grade DH36 steel specimens were also examined by means of a scanning electron microscope (SEM) in order for the estimations regarding the dominant fracture mechanisms to be validated. The SEM image of an eroded (5h) grade DH36 steel specimen is presented in Figure 5.41:

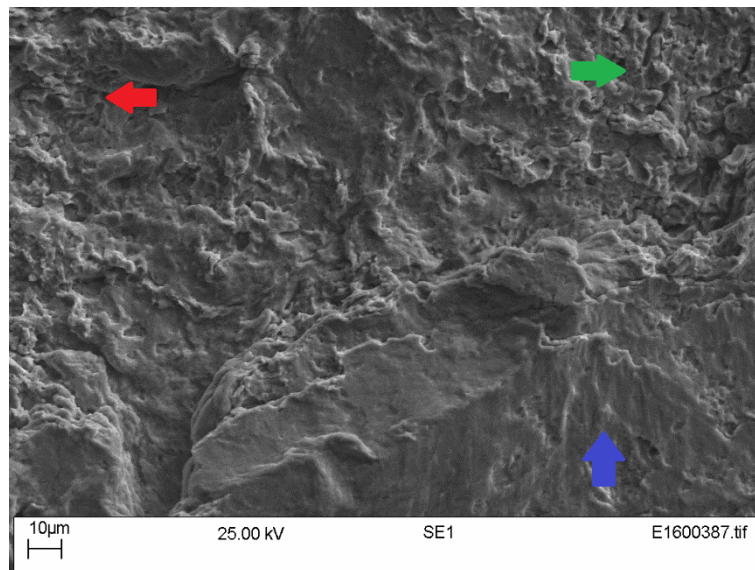


Figure 5.41: SEM image of an eroded (5h) grade DH36 steel specimen. Arrows: Green – Intergranular, Blue – Transgranular, Red – Ductile.

Similarly to the optical microscopy pictures, the eroded surface is characterized by a combination of mainly transgranular and to a lesser extent intergranular brittle fracture as well as by a considerable amount of ductile dimples. More specifically, it appears that some features that were initially attributed to intergranular fracture, such as straight edges and well-defined large facets, were indeed caused by transgranular fracture. These regions, when observed through the SEM, are characterized by ridges and smooth bumps, which are common signs of transgranular fracture. In contrast, some small and well-defined facets, of size comparable to the actual grains of the metal, imply the presence of intergranular fracture in those regions. Finally, a considerable amount of small ductile dimples is apparent at some regions, marking the occurrence of ductile fracture. Erosion progression (0.5h, 2.5h and 5h) for grade DH36 steel is presented in Figure 5.42:

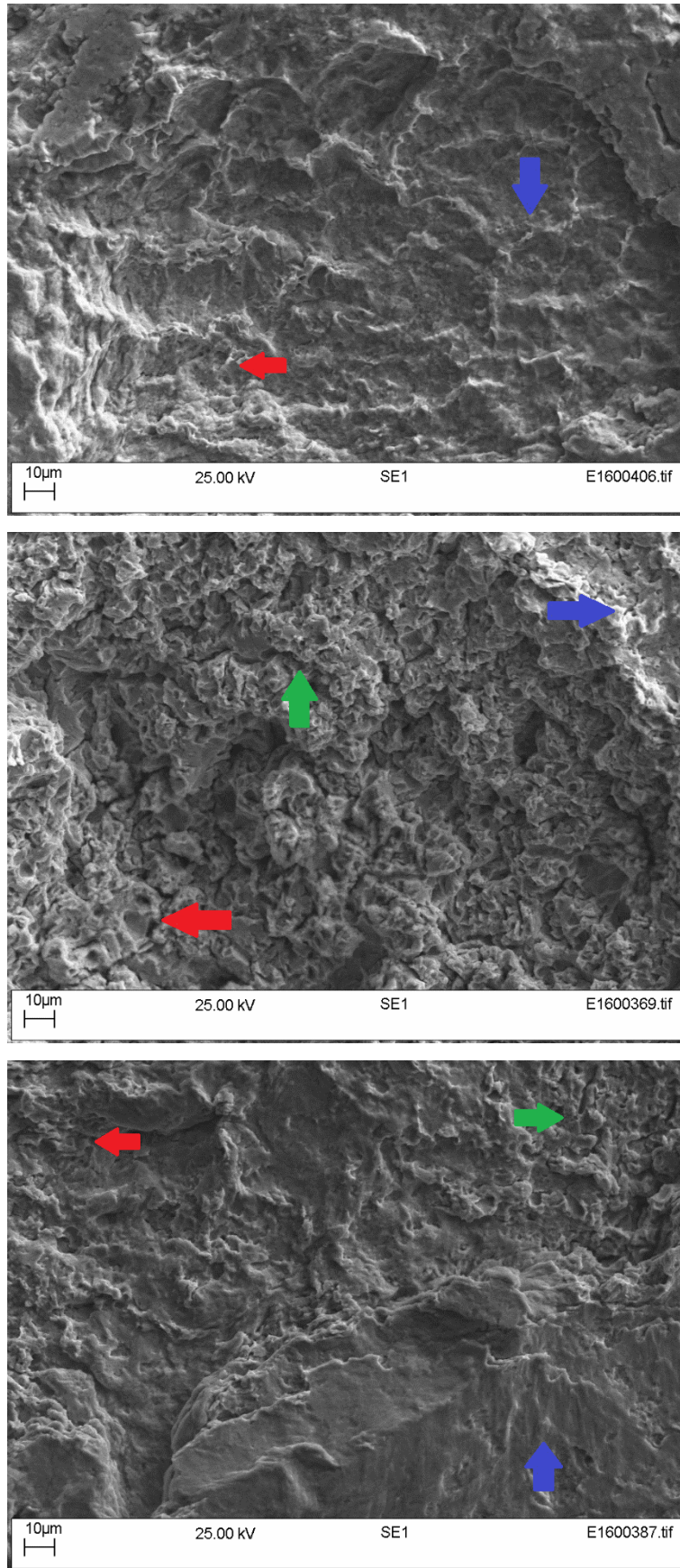


Figure 5.42: Erosion progression for grade DH36 steel. SEM images. Top-0.5h, Middle 2.5h, Bottom-5h. Arrows: Green – Intergranular, Blue – Transgranular, Red – Ductile.

In the case of grade DH36 steel, erosion initially appears (0.5h) in the form of ductile and to a lesser extent transgranular brittle fracture. These are characterized by large ductile dimples for the former, which are apparent all over the surface, and small ridges for the latter, respectively. The next stage (2.5h) is mostly characterized by well-defined facets of size comparable to the grains of the metal as well as by a considerable amount of small ductile dimples. These imply that at this stage (2.5h) erosion is essentially a combination of intergranular brittle and ductile fracture. Signs of transgranular fracture are still apparent in the form of ridges and smooth bumps, although to a much lesser extent compared to the earlier stage (0.5h). This behaviour could possibly explain why the appearance of the surface at the final stage (5h) is essentially a combination of the three fracture modes, namely transgranular and intergranular brittle fracture as well as ductile fracture, although it appears that the transgranular mode of brittle fracture is more dominant.

The erosion progression of grade DH36 steel can also be explained by its rate of mass loss due to ultrasonically induced cavitation erosion, which is presented in Figure 5.43:

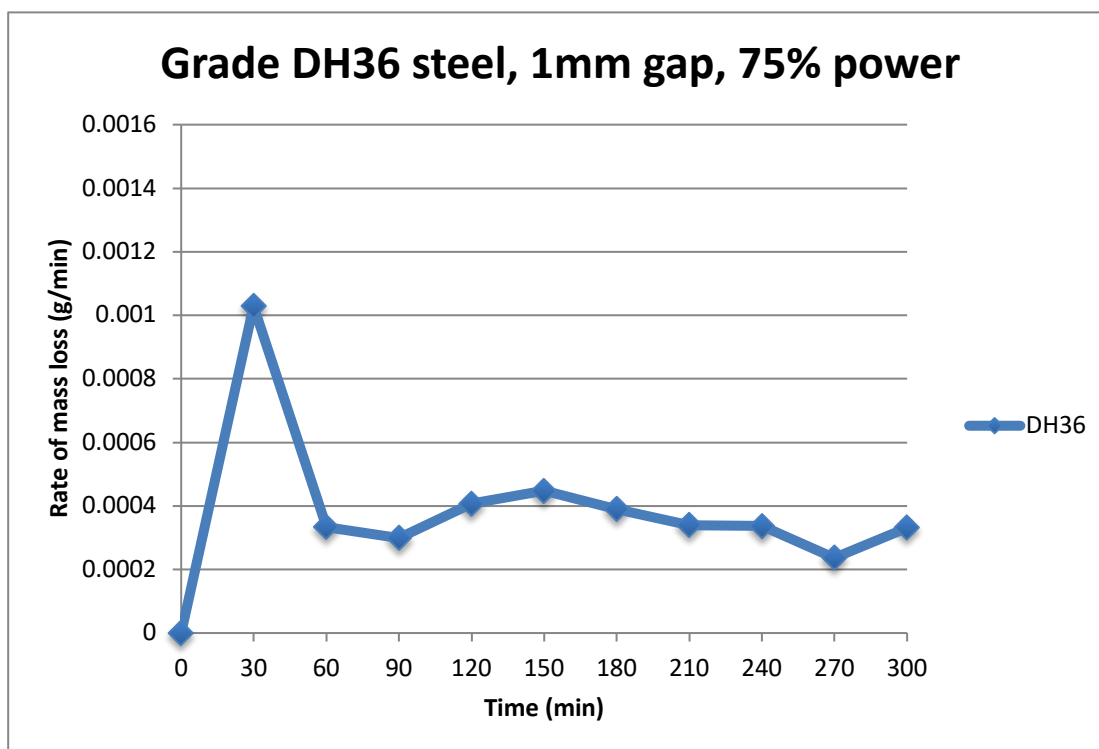


Figure 5.43: Rate of mass loss of Grade DH36 steel.

The behaviour of grade DH36 steel is characterized by an initial period of increased mass loss for the first 0.5h which is related to ductile fracture and gradual work hardening. In fact, examination through the SEM, revealed signs of ductile fracture for the first 0.5h as well as some signs of transgranular fracture, which can be attributed to work hardening. The next

stage (2.5h) is characterized by a more stable and reduced rate of mass loss, relating to brittle fracture. This behaviour can also be observed through the SEM, where signs of significant intergranular fracture are mostly apparent along with a small amount of ductile fracture. The latter relates to the slightly increasing rate of mass loss, which implies that a small amount of ductile fracture and work hardening is still taking place. Finally, the rate of mass loss steadies and decreases with time resulting into a surface (5h) that is mostly characterized by two modes of brittle fracture (intergranular and transgranular) as it can be seen in the SEM images.

Stainless steel 254

The macroscopic erosion pattern of stainless steel 254 after five hours of cavitation exposure is presented in Figure 5.44:

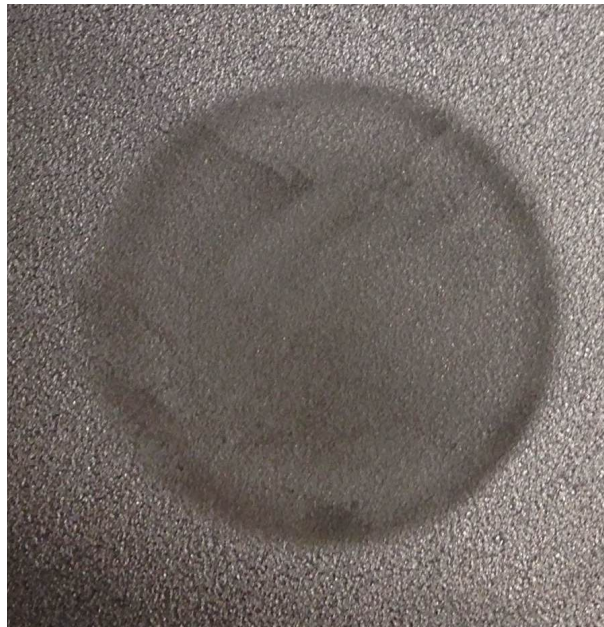


Figure 5.44: Eroded surface of stainless steel 254.

The macroscopic appearance of stainless steel 254 is represented by a smooth and homogenous erosion pattern, characteristic of brittle fracture. The microscopic appearance of both the non-eroded surface, revealed through metallographic preparation, and eroded surface of stainless steel 254 after five hours of cavitation exposure is presented in Figure 5.45 at a magnification of x500. A scaled mesh (100 μ m) was used in both images for comparison reasons.

The calculated ASTM grain size number of stainless steel 254 was of the order of 6 corresponding to a medium structure and a mean grain diameter ranging from 32-45 μ m.

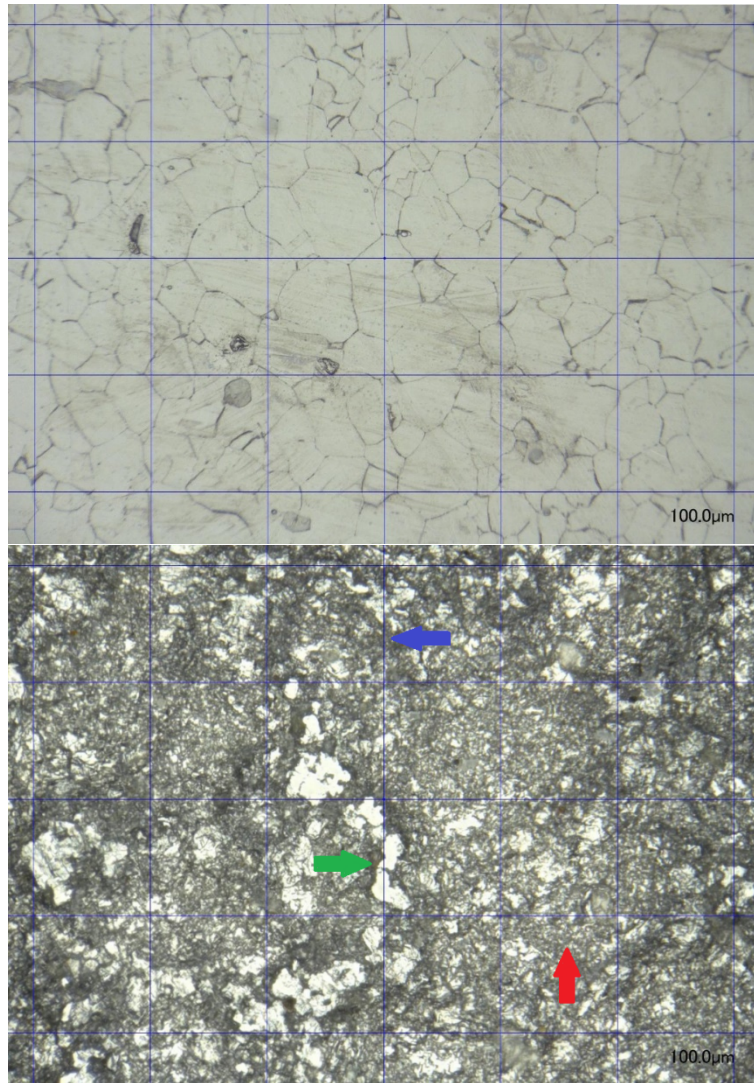


Figure 5.45: Microscopic images of non-eroded (Top) and eroded (Bottom) stainless steel 254. Arrows: Green – Intergranular, Blue – Transgranular, Red – Ductile.

Further investigation under the microscope lens revealed a granular and slightly bumpy surface, as well as a significant amount of distinctive reflective facets. These characteristics imply brittle fracture and more specifically a combination of transgranular and intergranular fracture. In particular, the size of those distinctive facets is comparable to the size of the individual grains of the metal, as it can be seen in Figure 5.45. This implies that cracks propagated through the grain boundaries at these regions in an intergranular way and as a result the more erosion-resistant grains remained on the surface. This is due to the different nature of grains as stainless steel 254 is essentially an alloy. In contrast, the edgy and significantly smaller bumps, which are spread all over the surface, imply crack propagation through the grains (transgranular). There are also regions where some ductile dimples can be observed, implying a small amount of initial plastic deformation and ductile fracture. The SEM image of the eroded (5h) stainless steel 254 specimen is presented in Figure 5.46:

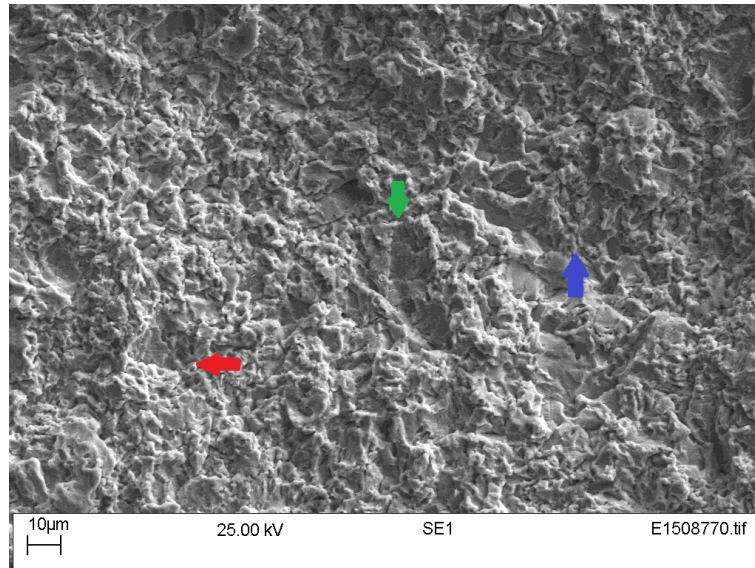


Figure 5.46: SEM image of an eroded (5h) stainless steel 254 specimen. Arrows: Green – Intergranular, Blue – Transgranular, Red – Ductile.

The appearance of the eroded surface is characteristic of mainly transgranular brittle fracture. A considerable amount of intergranular brittle fracture can also be observed in the form of facets, due to cracks propagating through the grain boundaries at some regions. Finally, the presence of ductile fracture, although not easily identifiable in the previous optical microscopy picture, is evident through the small ductile dimples that can be observed in some regions of the examined surface. Observations made by means of the SEM are in good agreement with the initial estimations made through the digital optical microscope images.

The progression of erosion over the period of 5h was also investigated. SEM pictures of stainless steel 254 specimens, for an exposure period of 0.5h, 2,5h and 5h are presented in Figure 5.47:

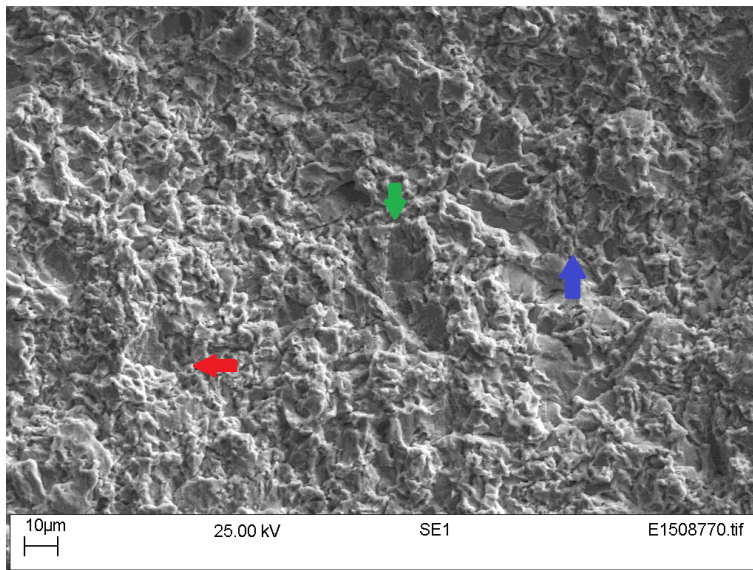
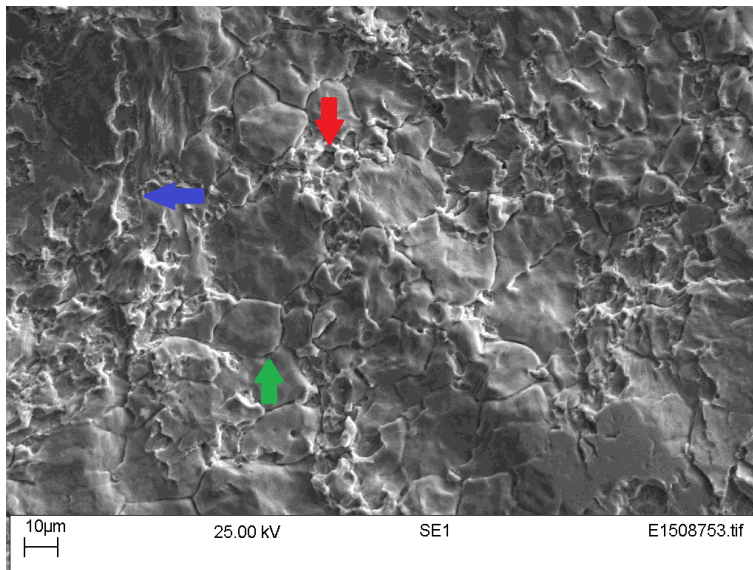
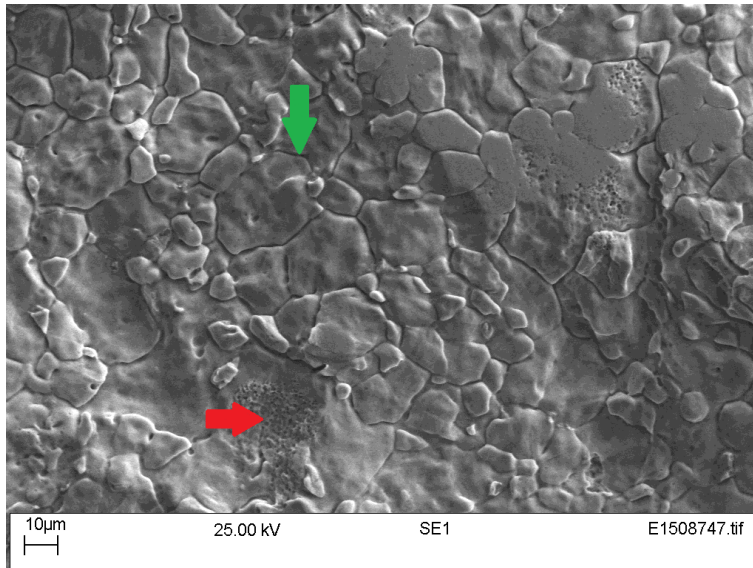


Figure 5.47: Erosion progression for stainless steel 254. SEM images. Top-0.5h, Middle 2.5h, Bottom-5h. Arrows: Green – Intergranular, Blue – Transgranular, Red – Ductile.

It appears that in the case of stainless steel 254 erosion initiates in the form of intergranular brittle fracture, as it can be seen in Figure 5.47. More specifically, well defined facets of size comparable to the actual grains of the metal are apparent all over the surface. Additionally, areas containing small ductile dimples may be observed, marking the occurrence of ductile fracture during the initial stages of erosion. The next image (2.5h) shows that just after the initial stage, erosion proceeds in a transgranular way and in the form of small bumps, whereas evidence of a considerable amount of intergranular fracture is still apparent. A small amount of ductile dimples can still be observed although they only represent small regions of the fracture pattern and could be remains from the initial erosion stages. This leads to the final fracture pattern (5h) which is essentially a combination of mostly transgranular brittle fracture from the latter stages of erosion and intergranular brittle fracture from the earlier stages. Evidence of the initial ductile fracture can still be seen in the form of small ductile dimples.

Erosion progression by means of different fracture mechanisms is in good agreement with the measured rate of mass loss, which is presented in Figure 5.48:

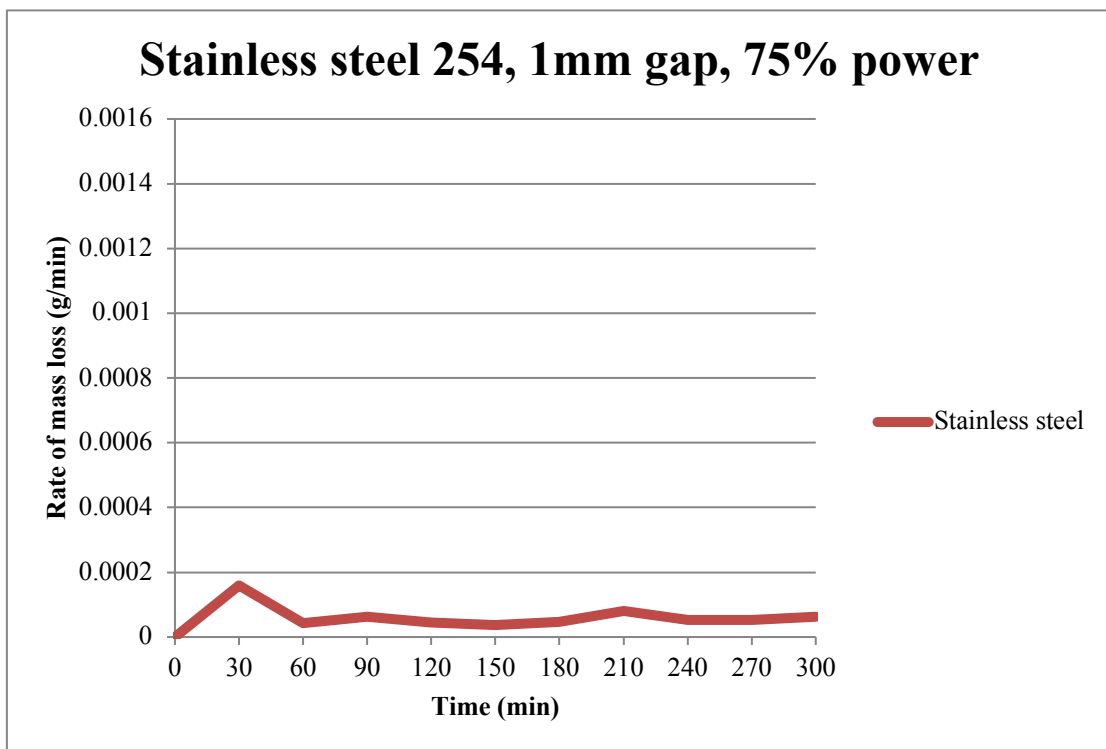


Figure 5.48: Rate of mass loss of stainless steel 254.

The peak of the rate of mass loss after 30 minutes of cavitation exposure implies a small yet measurable amount of ductile fracture and work hardening. This is in good agreement with the SEM observations where a small amount of ductile dimples was observed along with mostly intergranular brittle fracture. The rate of mass loss after the first 30 minutes, however,

can be almost represented with a straight line, implying that erosion progressed almost steadily, which is a characteristic of brittle fracture. Mass loss results are again in good agreement with the SEM images, in the sense that after the first 30 minutes, erosion progressed in a brittle and transgranular way.

Cupronickel 70-30

The macroscopic erosion pattern of cupronickel 70-30 after five hours of cavitation exposure is presented in Figure 5.49:



Figure 5.49: Eroded surface of cupronickel 70-30.

The bumpy and granular appearance of the surface implies the presence of brittle fracture along with a significant amount of initial ductile fracture. The microscopic appearance of both the non-eroded surface, revealed through metallographic preparation, and eroded surface of cupronickel 70-30 after five hours of cavitation exposure is presented in Figure 5.50 at a magnification of x500. A scaled mesh (100 μ m) was used in both images for comparison reasons.

The calculated ASTM grain size number of cupronickel 70-30 was 7 corresponding to a fine structure and a grain diameter ranging from 22-32 μ m.

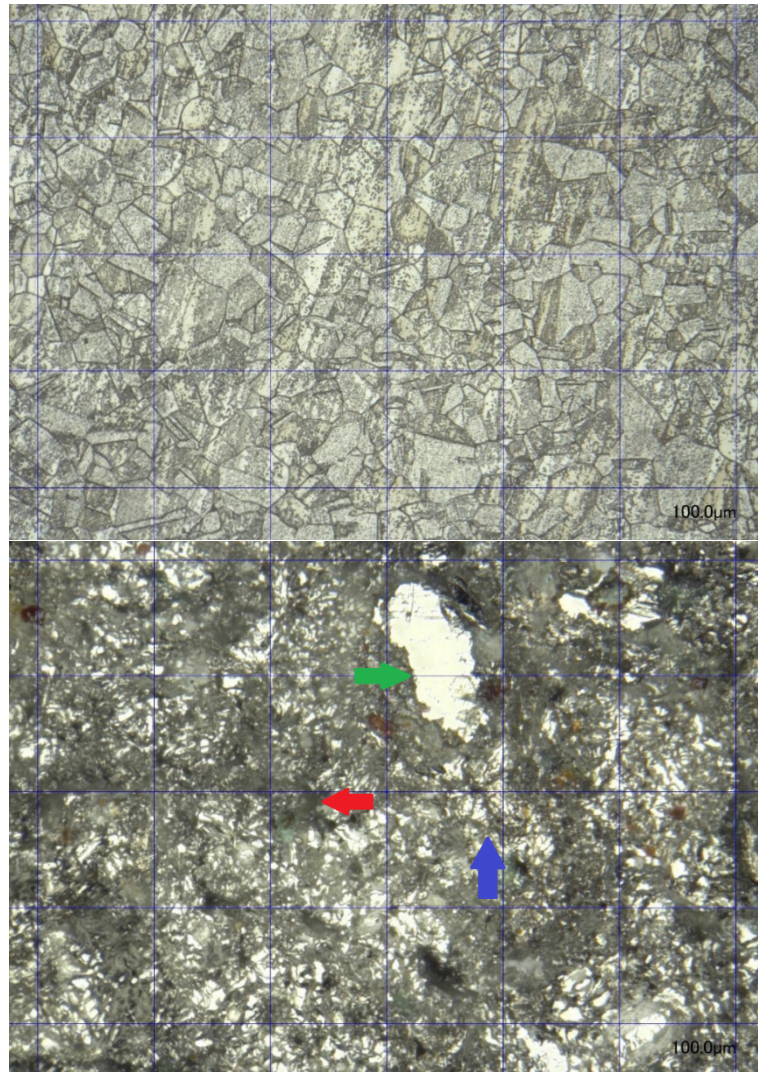


Figure 5.50: Microscopic images of non-eroded (Top) and eroded (Bottom) cupronickel 70-30. Arrows: Green – Intergranular, Blue – Transgranular, Red – Ductile.

Microscopic examination revealed a shiny and reflective surface, representative of significant intergranular brittle fracture. The jagged appearance of the surface further enhances this hypothesis. Additionally, the size of those reflective facets is comparable to the actual grains of the alloy, which implies that cracks propagated through the grain boundaries at these regions and as a result the more erosion-resistant grains remained on the surface. Nevertheless, those facets are not as well defined as in stainless steel 254 for instance, thus it appears that a significant amount of transgranular fracture has also taken place at the same regions. Multiple ductile dimples are also apparent, implying a considerable amount of initial plastic deformation and ductile fracture.

The validity of the assumptions relating to the governing fracture mechanisms was examined by means of a scanning electron microscope (SEM). The SEM image of the eroded (5h) cupronickel 70-30 specimen is presented in Figure 5.51:

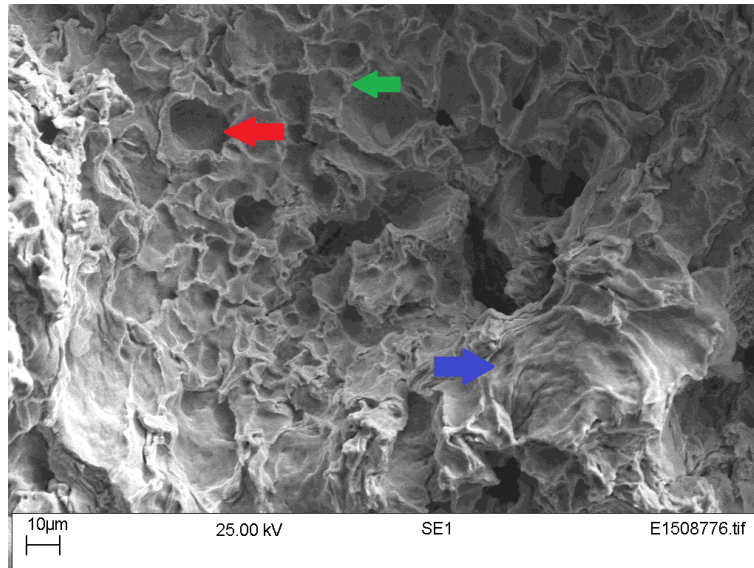


Figure 5.51: SEM image of an eroded (5h) cupronickel 70-30 specimen. Arrows: Green – Intergranular, Blue – Transgranular, Red – Ductile.

Examination of the eroded surface revealed a significant amount of ductile dimples and therefore ductile fracture. Signs of considerable transgranular fracture are also apparent at specific regions of the erosion pattern in the form of ridges. These observations are in good agreement with the initial estimations made through the optical microscopic pictures. It is noteworthy however, that signs of intergranular fracture are not as apparent in the SEM image in comparison to the optical microscopic image. It should also be noted that in the case of the optical image facets are not as well defined as in stainless steel 254 for instance. The appearance of those facets could have been affected by the already confirmed presence of significant transgranular fracture. Examination of the erosion progress (0.5h, 2.5h, 5h) can possibly reveal the presence of such mechanisms.

Erosion progression for cupronickel 70-30 for three different exposure periods (0.5h, 2.5h, 5h) is presented in Figure 5.52:

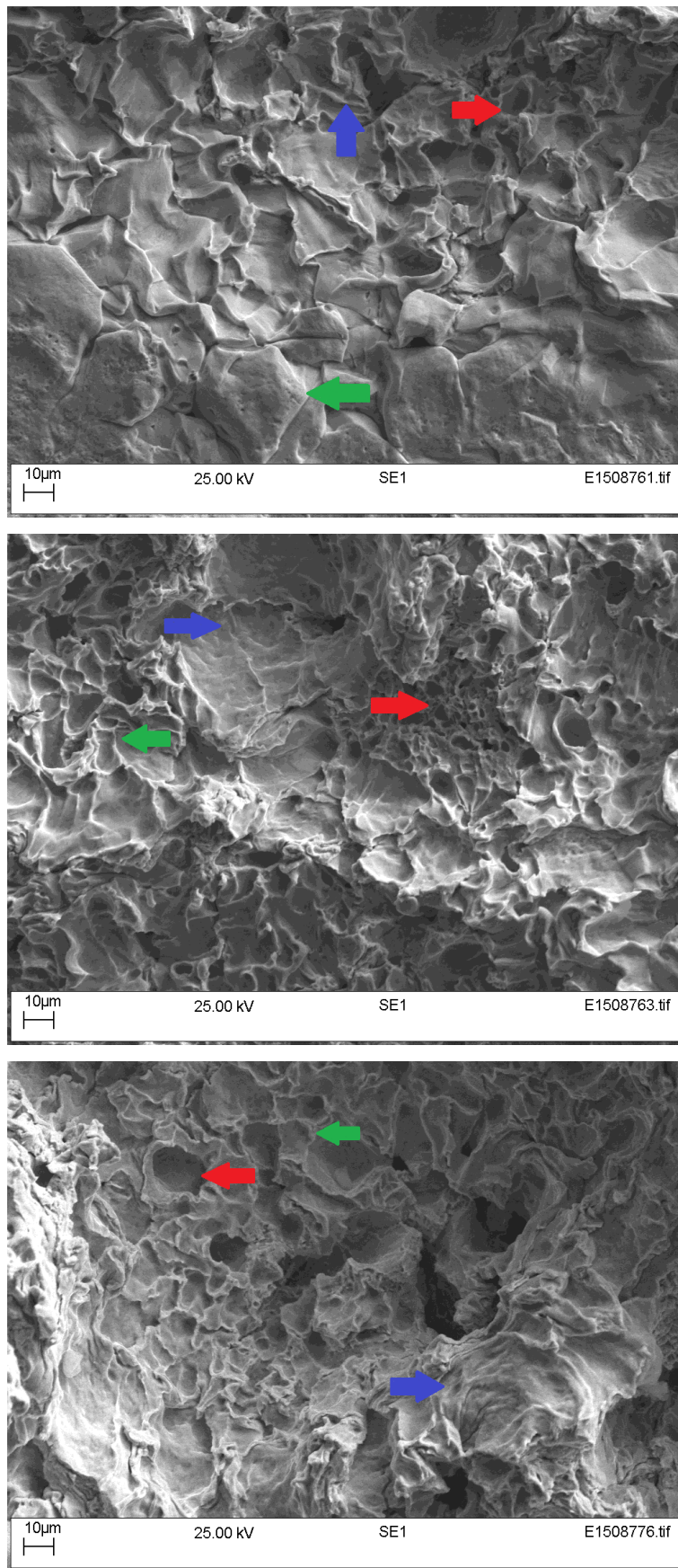


Figure 5.52: Erosion progression for cupronickel 70-30. SEM images. Top-0.5h, Middle 2.5h, Bottom-5h. Arrows: Green – Intergranular, Blue – Transgranular, Red – Ductile.

The initial stages of erosion (0.5h) for cupronickel 70-30 are characterized by a combination of well-defined facets, of size comparable to the grains of the alloy, caused by intergranular fracture, as well as a significant amount of dimples relating to ductile fracture. A small amount of transgranular fracture can also be observed at some regions in the form of small ridges. The next stages of erosion (2.5h) are characterized by a combination of brittle transgranular and ductile fracture (ridges and dimples) with only a few signs of intergranular fracture. A similar behaviour can be observed at the latter stages of erosion (5h) hence a combination of transgranular fracture and ductile fracture (ridges and dimples). This behaviour could possibly explain why signs of intergranular fracture are only apparent on the optical microscopy image and not as much on the more detailed SEM image (5h). Erosion initiates by means of ductile fracture before progressing in the form of intergranular brittle fracture, whereas at the next stages fracture appears to be progressing in a brittle and transgranular way, thus the initially formed well-defined grains and facets are affected.

The behaviour of cupronickel 70-30 in terms of the governing fracture mechanisms and erosion progression can also be explained by its rate of mass loss through the five hours period, which is presented in Figure 5.53:

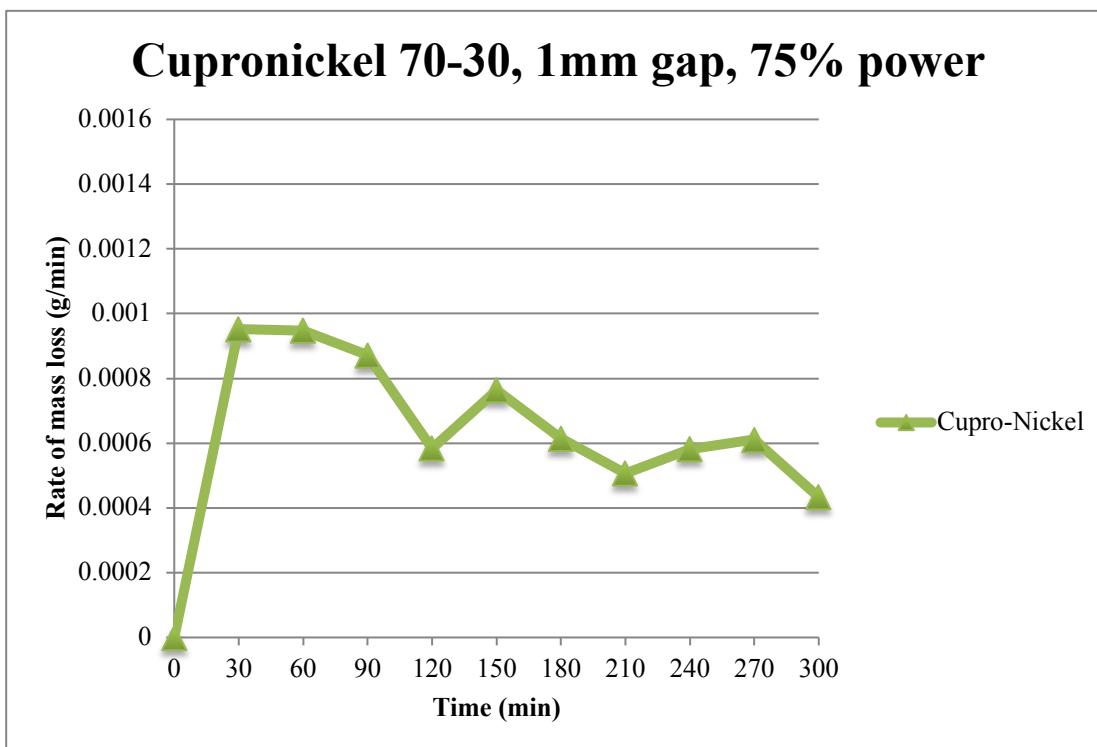


Figure 5.53: Rate of mass loss of cupronickel 70-30.

It appears from the results that, the high initial rate of mass loss (0.5h) relates to a significant amount of ductile fracture and work hardening. In fact, the appearance of the surface at the initial stages of erosion is characterized by ductile fracture (dimples) as well as signs of intergranular fracture, related to work hardening. The next stages (2.5h and 5h) are also characterized by high rates of mass loss and gradual work hardening, although to a much lesser extent. This behaviour is also apparent in the SEM pictures (2.5h and 5h), where the erosion pattern is basically a combination of ductile and transgranular brittle fracture in both cases. Results are again in good agreement with the SEM observations.

5.7 Summary and discussion

The preliminary macroscopic and microscopic examination that was conducted on all alloys indicated that the appearance of the surface, in terms of pit density and depth is analogous to the resulting mass loss. Further examination of the three alloys (grade DH36 steel, stainless steel 254, cupronickel 70-30) by both optical and scanning electron microscopic means illuminated some unique fractographic characteristics relating to cavitation induced erosion.

For instance, erosion appears to initiate in the form of plastic deformation and ductile fracture, before gradually progressing into brittle fracture due to work hardening, for all alloys. The extent of the initial plastic deformation and ductile fracture, however, is more profound in the case of cupronickel 70-30, a behaviour that was actually expected, as face-centred cubic (fcc) metals and alloys such as copper and nickel are essentially ductile in nature. This is also in good agreement with its mechanical properties in the sense that, it has the lowest yield strength, namely 130 MPa in contrast to 350 MPa and 310 MPa, for grade DH36 steel and stainless steel 254, respectively. Moreover, in the case of cupronickel signs of ductile fracture were even apparent in advanced stages of erosion also, despite the ongoing severe brittle fracture. This is because, being the weaker alloy compared to the other two, with an ultimate strength of 350 MPa in contrast to 490 MPa and 690 MPa for grade DH36 steel and stainless steel 254, respectively, cupronickel 70 – 30 suffered from the deterioration of its work hardened upper surface by means of brittle fracture. As such, the newly exposed layers of its surface had to go through the same work hardening procedure again, thus an extent of ductile fracture was apparent throughout the procedure. This behaviour can be also seen through its measured rate of mass loss where despite the initial work hardening the rate remains at high levels and only slightly decreases towards the end of the exposure.

In contrast, the work hardening process in the case of stainless steel 254 which is an austenitic steel and is also considered to be ductile in nature, resulted into a significantly lower mass loss

throughout the procedure from mainly brittle fracture. This is because the work hardened and embrittled stainless steel 254, being considerably stronger than cupronickel 70 – 30, retained the upper layers of its surface whereas only a small amount of mass was lost by means of brittle fracture. Grade DH36 steel, although body-centred cubic (bcc) in nature, exhibited a ductile behaviour in the beginning too, before progressing into brittle fracture. In that instance, however, it appears that some parts of the surface deteriorated, thus the newly exposed layers at those points, had to go through the same work hardening procedure. Nevertheless, this phenomenon was not as extended as in the case of cupronickel 70 - 30, a behaviour which is in good agreement with the mechanical properties of grade DH36 steel, in the sense it is stronger than cupronickel 70 – 30, whereas its rate of mass loss is also lower.

Intergranular brittle fracture appears to be the dominant initial mode of crack propagation for stainless steel 254 and cupronickel 70-30, which is in good agreement with what was expected, as both of them are face-centred cubic (fcc) alloys and are essentially supposed to behave as such. In addition, they both consist of relatively large grains in comparison to grade DH36 steel thus they are more prone to intergranular brittle fracture. In contrast grade DH36 steel initially exhibited transgranular brittle fracture, a behaviour which is in good agreement again with what was expected, considering that this alloy is essentially body-centred cubic (bcc) and is supposed to exhibit transgranular fracture. In addition, the size of its grains is considerably smaller in comparison to the other alloys, thus it is more prone to exhibit transgranular fracture.

What is noteworthy, however, is that in the case of fcc alloys (stainless steel 254, cupronickel 70-30), the initial intergranular fracture evolves into transgranular whereas the opposite is the case for the bcc alloy (grade DH36 steel). It appears that in the case of the former, the gradual work hardening of the alloys in conjunction with the depletion of possible crack propagation paths between the grains, result into crack propagation through the grains themselves. In the case of grade DH36 steel, however, the appearance of intergranular fracture further into the exposure, is possibly related to micro-voids contained within the boundaries which act as nuclei as erosion progresses.

The most significant attributes with regard to effects of erosion, in terms of fracture mechanics, on the examined alloys are summarized in Table 5.2:

	Grade DH36 steel	Stainless steel 254	Cupronickel 70 - 30
Structure	bcc	fcc	fcc
Yield - Ultimate strength	350 - 490	310 - 690	130 - 350
Mass loss	0.12 g	0.02 g	0.20 g
Erosion (0.5h)	Ductile > Transgranular brittle	Intergranular brittle > Ductile	Ductile > Intergranular brittle > Transgranular brittle
Erosion (2.5h)	Transgranular brittle > > Ductile	Transgranular brittle > Intergranular brittle > Ductile	Transgranular brittle > Ductile > Intergranular brittle
Erosion (5h)	Transgranular brittle > > Intergranular brittle > > Ductile	Transgranular brittle > Intergranular brittle > Ductile	Transgranular brittle > Ductile

Table 5.2: Fracture mechanics attributes of the examined alloys

Reading through Table 5.2, one may see, that all alloys behaved in accordance with their properties whilst the same applies for the measured mass loss, which in terms of rate can be correlated to the different fracture mechanisms that were observed at each erosion stage. For instance, high initial mass loss rates were accompanied by mostly ductile fracture (orange peeling) whereas reduced rates were related to the gradual work hardening and the resulting brittle fracture. It is noteworthy that the extent of the initial ductile fracture is analogous to the initial mass loss rate, in the sense, that cupronickel 70-30 exhibited the highest amount of initial mass loss rate and ductile fracture, followed by grade DH36 steel and stainless steel 254. Interestingly, an analogous connection applies when one wishes to examine the

aforementioned alloys with regards to their yield and ultimate strength. In particular, the highest the yield and ultimate strength, the lowest the resulting mass loss and the extent of ductile fracture.

As such, it appears that, although the way cavitation induced erosion acts is still debatable, the systematic study of the relevant qualitative and quantitative data, can reveal some major underlying fracture mechanisms, relating to this phenomenon. Apart from the characterization of the affected materials, in regards to cavitation induced erosion, which is of great importance from a practical way of view, such a technique could also be utilized in conjunction with other methods to further enhance our understanding regarding this phenomenon. These could be the study of cavitation induced erosion from a hydrodynamic point of view, as well as the utilization of computational techniques.

Nevertheless the future researcher could make use of this systematic approach for the evaluation of additional alloys that are used in shipbuilding, as well as protective coatings. It should also be noted that with regards to the latter, the relevant industry, has been increasingly keen on using them, wherever possible, during the last decade, thus the emergence of new materials, demands that their behaviour against cavitation induced erosion should also be evaluated.

Chapter 6

Acoustic Emissions due to Cavitation Erosion

6.1 Introduction

The use of acoustic emissions (AE) as means of cavitation erosion monitoring, initially with regards to small specimens made from grade DH36 steel, stainless steel 254 and cupronickel 70-30, is investigated and presented in *Chapter 6*, with the aim of being eventually utilized for ship rudders (*Chapter 7*). As such, the underlying theory behind acoustic emissions as well as some important details regarding the propagation of sound waves are initially presented, followed by a brief description of the specialized acoustic emissions equipment that was utilized for these series of tests. Preliminary measurements regarding the acoustic emissions of grade DH36 steel in relation to ultrasonically induced cavitation erosion are then presented for a variety of test rig configurations, sampling rates, signal capturing methods and piezoelectric sensors. In addition, the conversion of cavitation erosion related acoustic emissions into stress loading units for grade DH36 steel as well as for stainless steel 254 and cupronickel 70-30, is also investigated, by means of two different signal capturing methods and a variety of piezoelectric sensors.

The use of fibre Bragg grating (FBG) sensors, which are essentially tiny optical sensors, as means of acoustic emission monitoring, is also explored and presented in this chapter. Preliminary measurements conducted on a large steel plate, in order to explore whether cavitation activity can be identified or not by means of those sensors, are initially presented, followed by acoustic measurements conducted on small grade DH36 steel specimens. A short comparison between FBG and piezoelectric sensors is also conducted with respect to cavitation detection.

6.2 Acoustic emission and sound propagation theory

Acoustic emissions are essentially elastic stress waves, that are produced when metals absorb and release strain energy and stress. The mechanisms by means of which a metal undergoes such internal transformation, the result of which is the release of elastic stress waves - acoustic emissions, are the basis of fracture mechanics.

In particular, plastic deformation and crack growth are considered to be the primary sources of acoustic emissions (AE) in metals (Rogers, 2001). The plastic deformation of metals is a

non-linear permanent phenomenon whilst it has been demonstrated through studies that the dominant underlying mechanism is the dislocation of a row of atoms along a crystal slip plane (Fitzgerald, 1966; Scruby, 1984). On a micro-scale level, however, imperfections or cracks, of size comparable to the grains of the metal, are the basis of the underlying fracture mechanism.

Cracks in metals arise either at the time of manufacturing or during operation due to work induced stress. In general, the amplitude of the local stress must be higher than the yield strength of the metal in order for cracks to initiate and propagate as well as for plastic deformation to be induced. Nevertheless, cracks can propagate catastrophically when they reach a critical length, even when the applied stress is lower than the theoretical strength of the metal. Fracture mechanics provide the necessary tools, in the form of quantitative relations between the initial crack size, the material properties and the induced stress for crack propagation related calculations and subsequently fracture prediction.

The English aeronautical engineer Alan Griffith, often regarded as the founder of fracture mechanics, first suggested and then utilized a thermodynamic approach to analyse crack propagation (Griffith, 1921). His work was based on an earlier study by Inglis (1913), who calculated the stress concentrations around elliptical holes on glass, although his mathematical solution leads to infinite stresses at the tip of a perfectly sharp crack. Griffith concentrated into an energy-balance approach, instead. He used the mathematical result of Inglis and suggested that the change of the total energy of the plate due to the introduction of a crack is:

$$U + S_s = -\frac{\pi a^2 \sigma^2}{2E} + 2a\gamma \quad (6.1)$$

where, U is the total strain energy, S_s is the surface energy, a is the width of the crack, E is the Young's modulus of the material and γ is the material's surface energy density (J/m^2).

This relationship essentially implies that the energy supplied to drive the crack is equal to the energy required to separate the surfaces.

As the width of the crack a grows larger up to a critical point, the total energy of the system decreases. Beyond that critical point, crack propagation is rapid. For a given stress, the critical width of the crack a_c can be found by minimizing the energy in relation to the crack width:

$$\frac{\partial(U + S_s)}{\partial a} = 2\gamma - \frac{a_c^2 \pi \sigma}{E} = 0 \quad (6.2)$$

Additionally, the critical stress σ_c for which a crack with width α will propagate can be found by rewriting equation (6.2) as follows:

$$\sigma_c = \sqrt{\frac{2E\gamma}{\pi\alpha}} \quad (6.3)$$

Griffith's equation, predicts that small cracks are less damaging than large ones, a result which is in good agreement with experimental observations. Nevertheless, it is only applicable to very brittle materials such as glass whereas it fails to provide an accurate prediction with regards to fracture for more ductile materials.

Irwin (1957) suggested that the released strain energy from the propagation of cracks dissipates due to plastic flow near the crack tip. He thus introduced the parameter G_c , which is the critical strain energy release rate and replaced the thermodynamic surface energy in Griffith's equation by using the semi-inverse method (Westergaard, 1939):

$$\sigma_c = \sqrt{\frac{EG_c}{\pi\alpha}} \quad (6.4)$$

G_c is calculated experimentally during a fracture test. Consequently, for a given material with a crack of width a and an associated G_c value, the critical stress σ_c can be calculated. In addition, the critical width of a crack a_c can also be calculated for a known applied stress σ . It applies that when G is higher than G_c the crack will propagate. Conversely for values of G lower than G_c the crack will remain stable. When G is equal to G_c the system will settle on a metastable equilibrium.

The ways cracks propagate can be classified in three distinct modes:

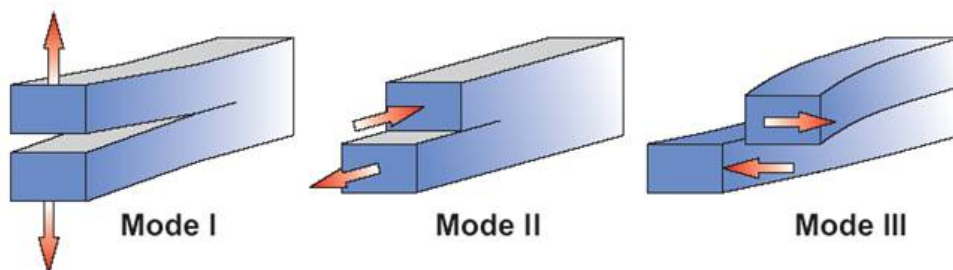


Figure 6.1: Crack propagation modes (Source: NPTEL)

In *mode I* (opening mode), tensile forces pull apart the crack in the y direction. In *mode II* (sliding or in-plane shear), the crack surfaces, slide over each other toward the x direction due

to shear forces parallel to the crack surface. Finally, in *mode III* (tearing or out of plane shear), shear forces parallel to the crack front pull apart the crack surfaces toward the z direction.

Mode I or opening mode is the most commonly encountered configuration in crack propagation. Due to the variety of loadings that may occur in engineering applications, however, a combination of the three propagation modes would possibly be observed. The contribution of the individual stress components for a mixed-mode crack propagation is given by equation (6.5):

$$\sigma_{ij} = \sigma_{ij}^I + \sigma_{ij}^{II} + \sigma_{ij}^{III} \quad (6.5)$$

where $i, j = x, y$ and *I, II, III* stand for the individual crack propagation modes.

The semi-inverse method developed by *Westergaard* 1939 shows the stresses for *mode I* (opening mode). Similar relations apply for modes *II* and *III*.

$$\begin{aligned} \sigma_x &= \frac{K_I}{\sqrt{2\pi r_c}} \cos \frac{\theta}{2} \left(1 - \sin \frac{\theta}{2} \sin \frac{3\theta}{2} \right) \\ \sigma_y &= \frac{K_I}{\sqrt{2\pi r_c}} \cos \frac{\theta}{2} \left(1 + \sin \frac{\theta}{2} \sin \frac{3\theta}{2} \right) \\ \tau_{xy} &= \frac{K_I}{\sqrt{2\pi r_c}} \cos \frac{\theta}{2} \cos \frac{3\theta}{2} \sin \frac{\theta}{2} \end{aligned} \quad (6.6)$$

where K_I is the stress intensity factor and r_c the distance from the crack tip. The second part of the equations, contain the angle θ , thus they indicate the angular dependence. The set of equations (6.6) can be rewritten in a simplified form:

$$\sigma \cong \frac{K}{\sqrt{2\pi r_c}} \quad (6.7)$$

It applies that the parameter K is linearly related to the stress σ as well as to the square root of a characteristic length associated with the crack width. In the case of mode *I*:

$$K_I = \sigma \sqrt{a} f(g) \quad (6.8)$$

where $f(g)$ relates to the crack and loading geometries. K_I for mode *I* can then be defined as a measure of material toughness. Its critical value represents the maximum stress that a material can withstand at a crack tip, namely its fracture toughness, whereas for higher values the crack

would propagate rapidly. The critical stress σ_c for a crack of length a and an already defined critical stress intensity factor K_{IC} would be:

$$\sigma_c \cong \frac{K_{IC}}{\sqrt{\pi a}} \quad (6.9)$$

Finally, it applies from equations (6.4) and (6.9) that:

$$K_{IC}^2 = EG_c \quad (6.10)$$

It should also be noted that, for a pure *mode II* loading of the crack it applies that:

$$K_{IIC} = \sqrt{\frac{3}{4}} K_{IC} \quad (6.11)$$

An investigation regarding the correlation of fracture toughness to the measured erosion - mass loss as well as other parameters is provided in *sub-chapter 6.14*.

In addition to crack inception theory, the study of cracks with regards to their relevant propagation characteristics is also of major importance, especially when one wishes to explore the phenomenon of acoustic emissions in more detail. The propagation of cracks in metals occurs in the form of elastic – stress waves, which are essentially sound waves, as sound is essentially a disturbance travelling through a medium. The simplest sound wave is the sine wave, although relatively rare to be found alone, as most sounds are combinations of multiple sine waves. A simple sound wave (sine) can be fully characterized by four fundamental features:

- *Speed (c)*: The speed by which the sound wave propagates through the medium.
- *Amplitude (Y)*: The maximum displacement of a vibrating molecule of the medium from its normal position, relating to the strength of the sound wave which is interpreted by the human ear as loudness. Because of its sinusoidal form the amplitude of a sound wave varies periodically from $-A$ to A , with $|A|$ being the maximum amplitude of the oscillation.
- *Wavelength (λ_w)*: The distance between two amplitude peaks (A) or crests ($-A$).
- *Frequency (f)*: The number of waves that pass from a fixed point every second (Hz). Frequency can be also calculated by means of equation (6.12):

$$f = \frac{1}{T} \quad (6.12)$$

where period T is the time required for a complete oscillation (sinusoidal) cycle. More specifically, T is the time required for a wavelength to pass a fixed point.

Speed, wavelength and frequency are related as follows:

$$c = f\lambda_w \quad (6.13)$$

In the case of air as well as in the bulk of liquids, sound is only transmitted in the form of longitudinal waves, also known as compression waves. In longitudinal waves the motion of the medium's particles is parallel and anti-parallel to the direction of the propagation of the wave. The propagation of a longitudinal wave in air is presented in Figure 6.2:

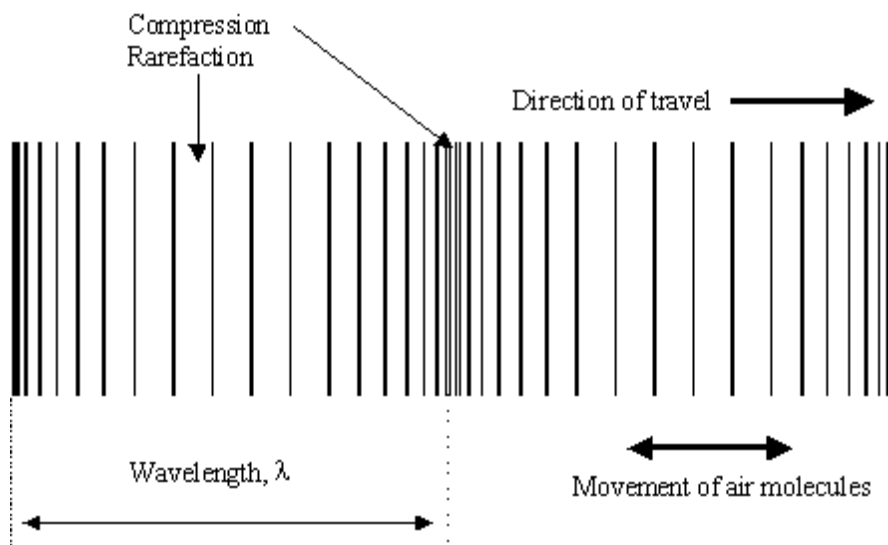


Figure 6.2: The propagation of a longitudinal wave in air (Source: Antonine-Education, n.d.)

In addition to equation (6.13), the speed of sound in liquids and gases can also be calculated by means of equation (6.14) (Timoshenko and Goodier, 1970):

$$c = \sqrt{\frac{K_B}{\rho}} \quad (6.14)$$

where c is the speed of sound, K_B is the bulk modulus of the medium (stiffness coefficient) and ρ is the density of the medium. For ideal gases the speed equation is transformed as follows:

$$K_B = \gamma_h p \quad (6.15)$$

where γ_h is the ratio of specific heats and p is pressure:

$$\gamma_h = \frac{C_p}{C_v} \quad (6.16)$$

$$p = \frac{nR_g T}{V_v} \quad \text{and} \quad = \frac{nM_m}{V_v}$$

Here n stands for moles, $R_g = 8.3 \text{ J mol}^{-1} \text{ K}^{-1}$ is the gas constant, T stands for temperature in Kelvin, M_m stands for the molar mass in Kg mol^{-1} and V_v stands for volume.

The combination of equations (6.14), (6.15) and (6.16), leads to equation (6.17):

$$c = \sqrt{\frac{\gamma_h R_g T}{M_m}} \quad (6.17)$$

Equation (16) is valid for ideal gases, however, minor corrections are required for real gases.

In contrast to gases and liquids, multiple modes of sound propagation are possible in the case of solids. The four primary ones are (Han, 2007):

- *Longitudinal waves*: Similarly to liquids and gases the sound waves of this category oscillate in the direction (parallel and anti-parallel) of propagation. In seismology, these waves are called P (Primary) waves.
- *Transverse(Shear) waves*: In this case waves oscillate toward a direction perpendicular to the direction of propagation. They propagate slower than longitudinal waves whereas they can only be found in solids. In seismology, these waves are called S (Shear) waves.
- *Surface (Rayleigh) waves*: These waves are essentially a combination of a longitudinal and transverse motion, resulting into an elliptic orbit motion. They propagate near the surface of thick solids whilst they are slightly slower than shear waves. They penetrate the solid to a depth of one wavelength and due to their sensitivity are often used for the detection of surface defects.
- *Plate (Lamb) waves*: Plate waves, also known as guided Lamb waves, result from the conversion between Longitudinal and Shear waves. Guided Lamb waves are complex vibrational waves that propagate through the entire thickness of a thin solid (plate).

The speed of longitudinal sound waves is proportional to the Young's modulus (E) of the medium in which they propagate and can be calculated by means of equation (6.18) (Andrews, 2007):

$$c_l = \sqrt{\frac{E}{\rho}} \quad (6.18)$$

The speed of transverse (Shear) sound waves is proportional to the Shear Modulus (G) of the medium in which they propagate and can be calculated by means of equation (6.19):

$$c_t = \sqrt{\frac{G}{\rho}} \quad (6.19)$$

In the case of perfectly elastic isotropic materials, E (Young's modulus) and G (Shear modulus), remain constant towards all directions thus equations (6.17) and (6.18) can be rewritten in a different form, by making use of the Lamé constants λ_L and μ . Moreover, for thin plates, E can be referred as M , namely the plane wave modulus (Timoshenko and Goodier, 1970). In addition, G can be replaced with the Lamé constant μ (Saada, 1993).

In this context the Lamé constants are related to E and G as well as to the Poisson's ratio ν as follows (Timoshenko and Goodier, 1970):

$$E = M = \lambda_L + 2\mu \quad (6.20)$$

$$G = \mu = \frac{E}{2(1 + \nu)}$$

$$\lambda = \frac{E \nu}{(1 + \nu)(1 - 2\nu)}$$

Equations (6.18) and (6.19) can then be rewritten as follows:

$$c_l = \sqrt{\frac{\lambda_L + 2\mu}{\rho}} \quad (6.21)$$

$$c_t = \sqrt{\frac{\mu}{\rho}} \quad (6.22)$$

It can be seen that either way, the speed of longitudinal and transverse waves, depends solely upon the properties of the medium in which they propagate. Moreover, it follows that the ratio of the speeds of the longitudinal and transverse sound waves will be unique and constant for each solid as it can be seen through equation (6.23):

$$\frac{c_l}{c_t} = \sqrt{\frac{\lambda_L + 2\mu}{\mu}} \quad (6.23)$$

The main difference between longitudinal and transverse waves, in terms of the direction of oscillation, is illustrated in Figure 6.3. In particular, black arrows stand for the direction of oscillation whereas the red arrows stand for the direction of propagation.

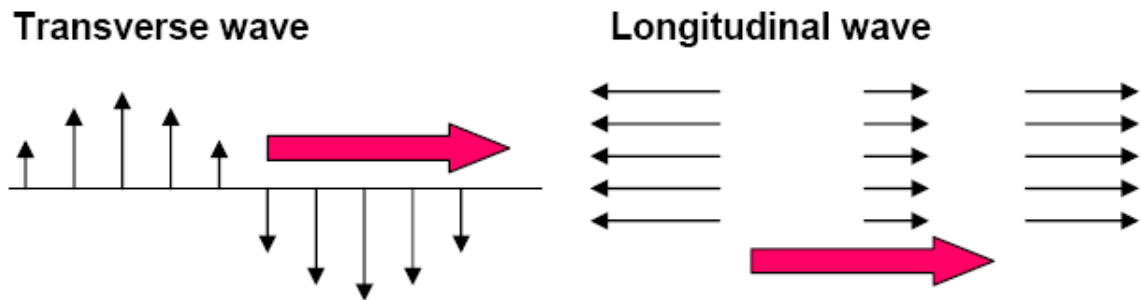


Figure 6.3: Transverse and longitudinal waves (Source: Saada, 1993)

With regards to Rayleigh or surface waves, which contain both longitudinal and transverse oscillations and propagate near the surface of thick solids, their speed can be approximated by means of equation (6.24) (Bergmann, 1948):

$$\frac{c_R}{c_t} = \frac{0.87 + 1.12 \nu}{1 + \nu} \quad (6.24)$$

where c_R stands for the Rayleigh wave speed, c_t stands for the transverse wave speed and ν stands for Poisson's ratio. It should be noted that this approximation is only accurate for linear elastic materials with positive Poisson's ratios.

In the case of thin plates with parallel free boundaries, longitudinal and transverse waves are combined into guided Lamb waves. Lamb waves are highly dispersive as their speed depends not only upon the properties of the medium in which they propagate but on frequency as well. In addition, Lamb waves propagate in two distinct forms known as symmetric and anti-symmetric. The two modes of propagation are presented in Figure 6.4:

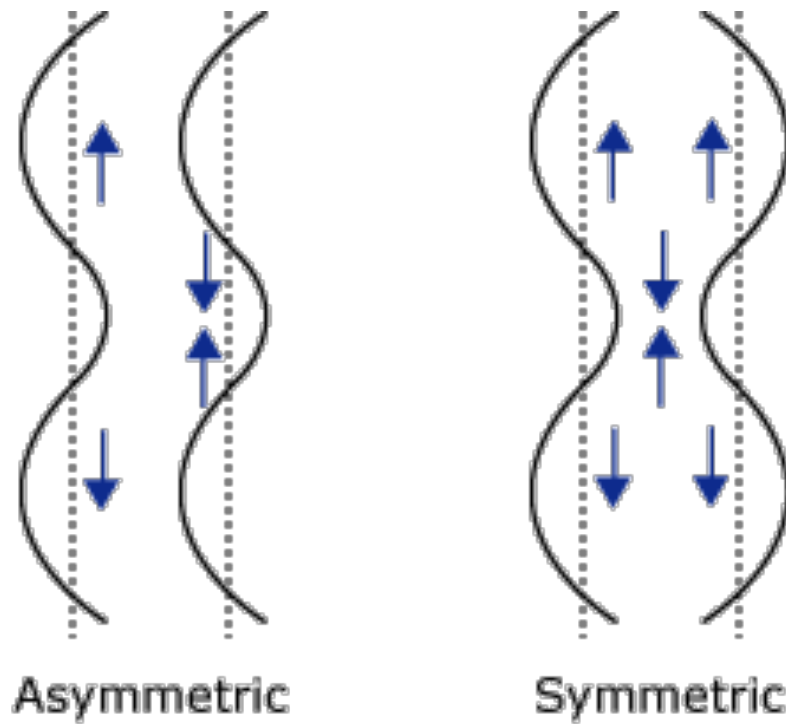


Figure 6.4: Asymmetric and symmetric Lamb waves (Source: NDT Resource centre, n.d.)

Lamb waves are described by means of dispersion equations (6.25) and (6.26) (Rose, 1999):

Symmetric modes:

$$\frac{\tan(qd)}{\tan(pd)} = -\frac{4k^2qp}{(k^2 - q^2)^2} \quad (6.25)$$

Anti-symmetric modes:

$$\frac{\tan(qd)}{\tan(pd)} = -\frac{(k^2 - q^2)^2}{4k^2qp} \quad (6.26)$$

where:

$$q^2 = \frac{\omega^2}{c_t^2} - k^2 \quad (6.27)$$

$$p^2 = \frac{\omega^2}{c_l^2} - k^2$$

$$k = \frac{\omega}{c_p}$$

Here, d , k , c_l , c_t , c_p and ω stand for the plate thickness, wavenumber, longitudinal wave speed, transverse wave speed, phase speed and circular frequency, respectively.

The speed of a propagating guided Lamb wave (phase) c_p can be calculated by means of equations (6.25) and (6.26) as a function of frequency. In the case of multiple guided Lamb waves interacting and propagating as a group their velocity c_g , which is different than the phase velocity c_p of each phase, can be calculated by means of equation (6.28) (Rose, 1999):

$$c_g = c_p^2 \left[c_p - (f d) \frac{d c_p}{d(f d)} \right]^{-1} \quad (6.28)$$

where d stands for the plate thickness and f stands for frequency.

The solution of the dispersion equations leads to a set of wave dispersion curves that can then be plotted on a graph. The dispersion curves ($c_p - f$) that were obtained through the LAMSS Waveform Revealer 3.0 software, for two steel plates of different thickness, are presented in Figures 6.5 and 6.6:

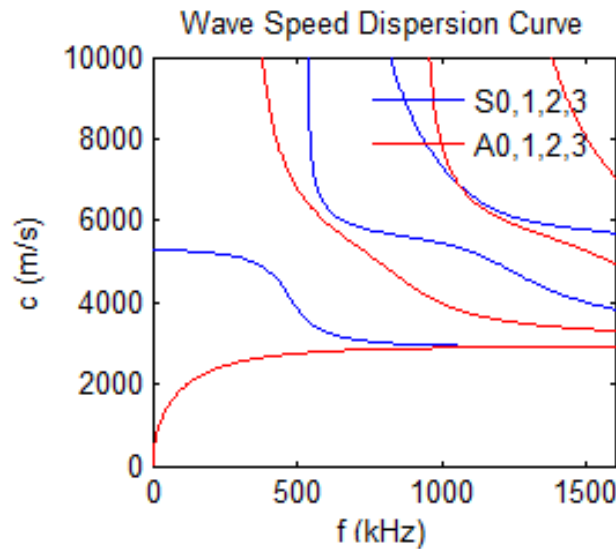


Figure 6.5: Lamb waves - Dispersion curves for a 5mm thick steel plate.

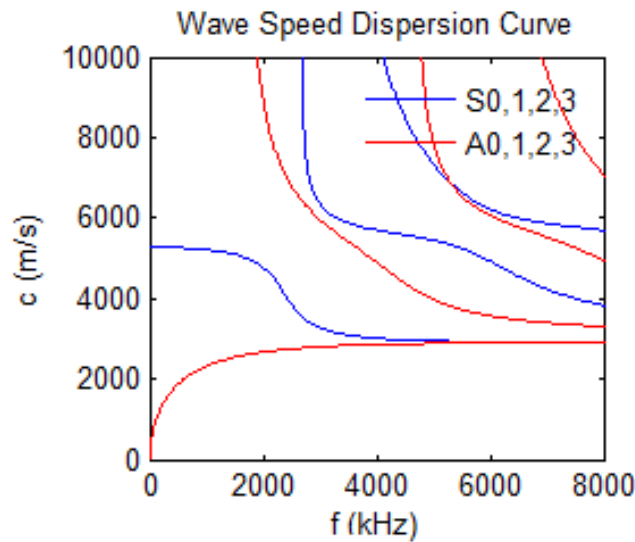


Figure 6.6: Lamb waves - Dispersion curves for a 1mm thick steel plate.

It can be seen that for a given frequency, the amount of possible propagation modes increases with thickness. Furthermore, and for frequencies below 500 kHz, only two propagation modes are present, namely the S0 (symmetric) and A0 (antisymmetric). S0 mode is considerably faster than A0, thus it would be the first to be captured by an acoustic sensor, in the case of acoustic emission monitoring.

This can be seen in Figure 6.7, where the response of a piezoelectric sensor due to an acoustic event on a plate is represented. It should be noted that the X axis represents the time of arrival, whereas the Y axis shows the amplitude of the acoustic emission signal. Here the S0 mode is the first to arrive at the sensor, followed by A0, 60 μ s later:

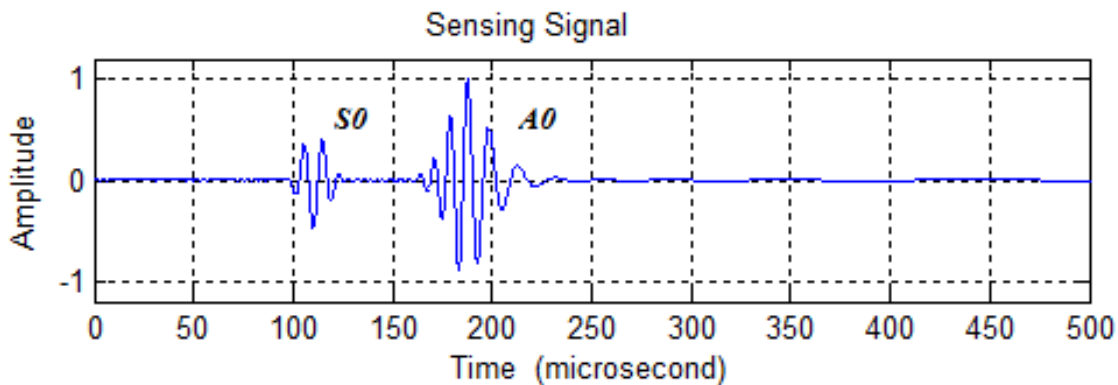


Figure 6.7: The arrival of the S0 and A0 modes at a distant acoustic sensor.

Lamb waves tend to attenuate when the plate is surrounded by liquid and as a result the dispersion curves can differ significantly. S0 and A0 modes however are not very dispersive in low frequencies and tend to be non-dispersive as frequency increases, thus they are ideal for the acoustic testing of plates under most conditions.

6.3 Acoustic emission sensing equipment

A suitable sensing system had to be utilized, for acoustic emissions to be properly captured and processed. In its most basic form, such a system would consist of an acoustic sensor, a signal amplifier and a processing unit, either in the form of a computer or an oscilloscope. The operation of the acoustic sensor would be based on the piezoelectric effect, thus any induced mechanical stress would result into a measurable amount of electric charge. The generated electric charge would then be amplified, captured and eventually get processed by either a computer or oscilloscope.

These are the principles upon which, the acoustic emission sensing system that was utilized for the purposes of this study, was built. The sensing system is illustrated in Figures 6.8 and 6.9:

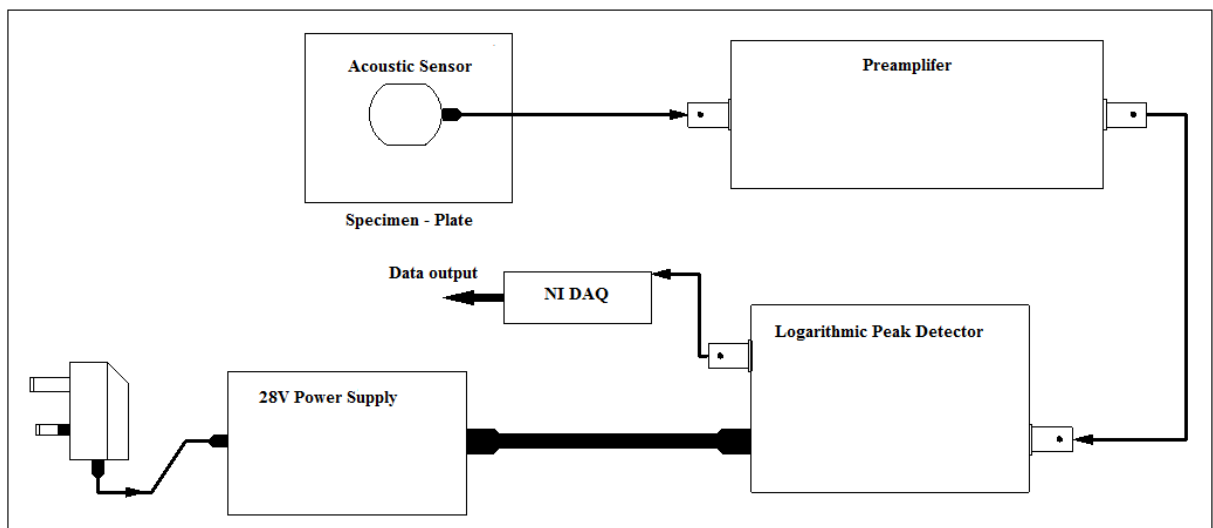


Figure 6.8: Acoustic emission sensing system – Illustration.

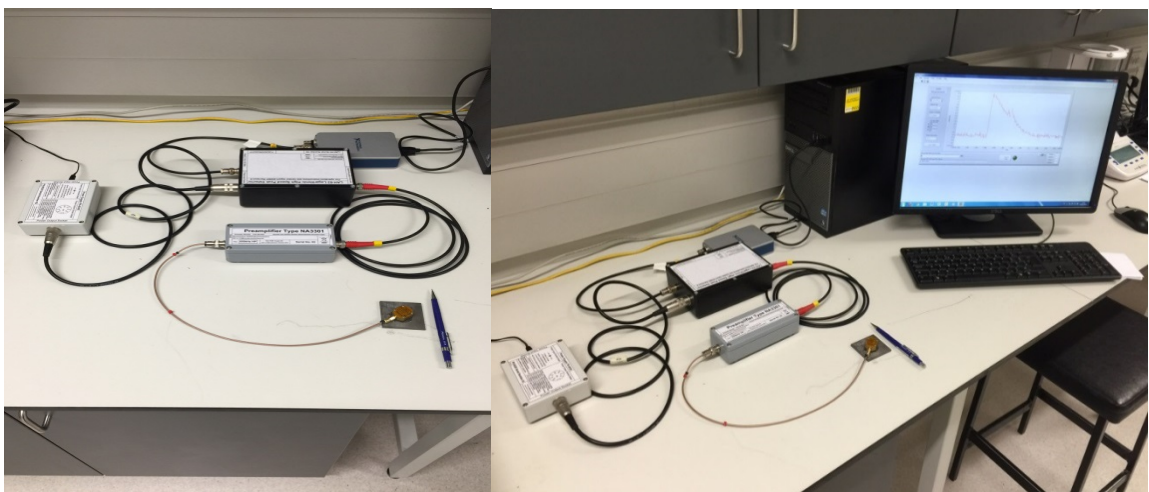


Figure 6.9: Acoustic emission sensing system

In particular, the acoustic emission sensing system that was built consists of the following:

- Acoustic – Piezoelectric Sensors
- 40dB Signal Attenuator
- 40dB Preamplifier with an 850 kHz High – Pass filter
- Logarithmic Peak Detector (LPD)
- NI DAQ (Data Acquisition System)
- Computer

Three acoustic – piezoelectric sensors, with different nominal frequencies were utilized in this study. Nominal frequency can be defined as the desired centre frequency of the piezoelectric crystal. In particular, the acoustic – piezoelectric sensors that were utilized along with the relevant nominal frequencies are the following:

- Piezoelectric element in aluminium case – 600 kHz
- Piezoelectric element in brass case – 150 kHz
- PVDF film in brass case – 2 MHz

Each of the acoustic sensors was mounted on the opposite to the exposed side of the test plates – specimens, on a designated area. This arrangement can be seen in Figure 6.10:

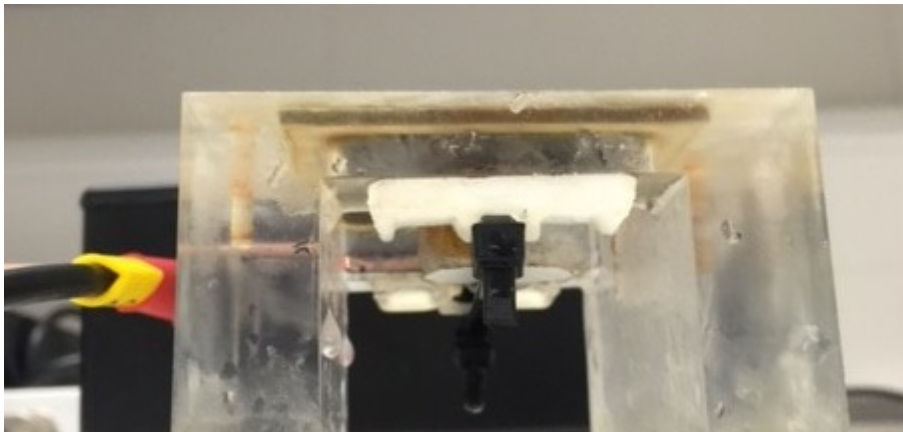


Figure 6.10: Acoustic sensor mounted on the test plate – specimen.

The acoustic sensors that were utilized can be seen in more detail in Figure 6.11. The piezoelectric crystal of the aluminium sensor can also be seen.



Figure 6.11: Top– PVDF and brass sensor, Bottom – Brass and aluminum Sensor along with its piezoelectric crystal sitting in its case

All acoustic sensors were driven by the 40dB preamplifier, which was powered by a 28V power supply, whilst their signal was attenuated by means of the 40dB attenuator. The resulting acoustic signals were then passed through the logarithmic peak detector (LPD). The logarithmic peak detector essentially tracks the peaks (maximum amplitude) of the acoustic signal – waveform and holds them for an adjustable time frame ranging from 40 μ s to 1ms. As such, only signals related to major energy releasing events, instead of the whole waveform, are identified and captured whereas through the logarithmic conversion these events are instantly transformed into acoustic power units. The optimized signal from the logarithmic peak detector is driven through the NI DAQ at a sampling rate of 100 kHz to a computer, where it can be further processed.

For comparison reasons, pre – LPD raw acoustic signals were also monitored at a high sampling rate through a Tektronix oscilloscope without the presence of either the LPD or the NI DAQ.

In all cases the measurement uncertainty is also presented, which was calculated through the procedure that was described in *Appendix G*, for a 95% confidence level.

6.4 Tests prior to the acoustic measurements

A series of tests were conducted prior to the acoustic measurements. These were similar to the mass loss measurements, in the sense that specimens were exposed to ultrasonically induced cavitation for a predetermined period of time. In this case, however, various test rig configurations were examined in order to find the transition point between non-erosive and erosive cavitation, always in terms of the resulting mass loss. Moreover, all test rig configurations leading to erosive cavitation were characterized in terms of intensity.

As such, tests were conducted on grade DH36 steel specimens, exposed to ultrasonically induced cavitation for a period of two hours, whereas mass loss measurements were conducted every thirty minutes in order for cavitation to be characterized in terms of erosion-mass loss. Results are presented in Figure 6.12:

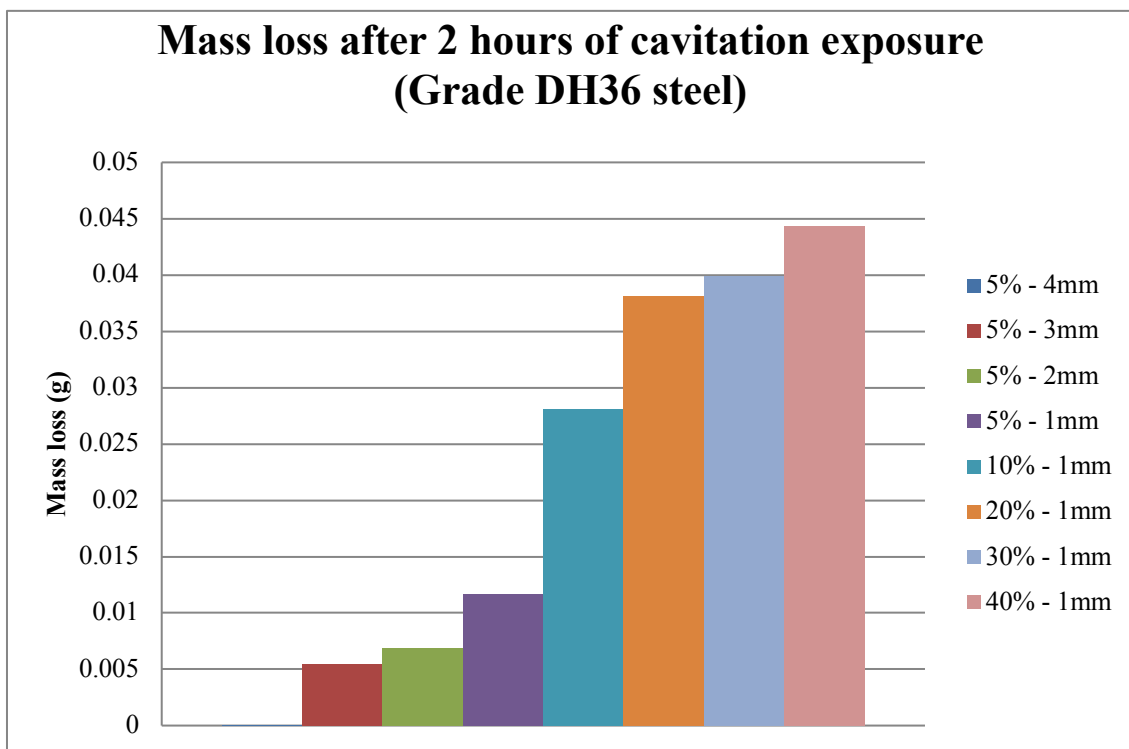


Figure 6.12: Mass loss of grade DH36 steel for various test rig configurations

It can be seen that cavitation ceases to be erosive for a power setting of 5% (50W) and a gap, between the specimen and the sonotrode tip, of the order of 4mm. By gradually reducing the gap and then increasing the power output of the sonotrode, cavitation becomes increasingly erosive as it can be seen in Figure 6.12. As a result, a cavitation erosion threshold was established (4mm-5%) for this particular test rig and material (grade DH36 steel).

6.5 Various test rig configurations, acoustic sensors and signal capturing method - Details

Cavitation related acoustic emissions originating from grade DH36 steel are initially examined. Specimens are exposed to ultrasonically induced cavitation under various test rig configurations, as per the procedure described in *subchapter 6.4*.

In particular, the various test rig configurations that were examined, in terms of the power output of the sonotrode and the gap between the sonotrode tip and the specimen, are:

- 75% (750W) sonotrode power output and 1 mm gap
- 50% (500W) sonotrode power output and 1 mm gap
- 40% (400W) sonotrode power output and 1 mm gap
- 30% (300W) sonotrode power output and 1 mm gap
- 20% (200W) sonotrode power output and 1 mm gap
- 10% (100W) sonotrode power output and 1 mm gap
- 5% (50W) sonotrode power output and 1 mm gap
- 5% (50W) sonotrode power output and 2 mm gap
- 5% (50W) sonotrode power output and 3 mm gap
- 5% (50W) sonotrode power output and 4 mm gap (non – erosive configuration)

The acoustic emissions of the exposed grade DH36 steel specimens, in relation to each one of the aforementioned test rig configurations, were captured by means of three different acoustic sensors (aluminium, brass, PVDF) and will be presented in *sub-chapter 6.6*. Moreover, various sampling rates as well as two different sensing systems are examined.

More specifically the different sensing configurations that are utilized are the following:

1. Logarithmic peak detector and NI DAQ sensing system (LPD)

Aluminium sensor:

- 100 kHz sampling rate and 40 μ s hold time frame. 2.5s – 250000 Data points duration
- 25 kHz sampling rate and 40 μ s hold time frame. 10s – 250000 Data points duration
- 1.25 kHz sampling rate and 1 ms hold time frame. 200s – 250000 Data points duration

Brass sensor:

- *100 kHz sampling rate and 40 μs hold time frame. 2.5s – 250000 Data points duration*
- *25 kHz sampling rate and 40 μs hold time frame. 10s – 250000 Data points duration*
- *1.25 kHz sampling rate and 1 ms hold time frame. 200s – 250000 Data points duration*

PVDF sensor:

- *100 kHz sampling rate and 40 μs hold time frame. 2.5s – 250000 Data points duration*
- *25 kHz sampling rate and 40 μs hold time frame. 10s – 250000 Data points duration*
- *1.25 kHz sampling rate and 1 ms hold time frame. 200s – 250000 Data points duration*

2. Tektronix oscilloscope based sensing system (TO)

All sensors (Aluminum, Brass, PVDF). 0.04s – 1250000 Data points duration

31.3 MHz sampling rate - Raw acoustic waveform obtained

Acoustic emissions obtained through the two different sensing systems, in the form of electric signals, were further processed by means of an Excel-based software. Processed acoustic data was then plotted onto distribution graphs, categorized accordingly with regards to the signal capturing method and the sensor type as well as the different test rig configurations.

In particular, the sonotrode was operated for five minutes, prior to each acoustic measurement, in order for a local equilibrium to be established. Acoustic emissions captured in the form of electric signals were then converted into acoustic power units (dB) by means of the linear equation (6.29), provided by the manufacturer of the logarithmic peak detector and NI DAQ sensing system:

$$Y = 44.035X - 9.7032 \quad (6.29)$$

where Y represents the acoustic emission signal in terms of acoustic power units (dB) and X represents the acoustic signal in terms of voltage (V).

In the case of the Tektronix oscilloscope, however, the logarithmic equation (6.30) was utilized for the conversion of raw electric signals into acoustic power units:

$$Y = 20 \log_{10} \frac{V_2}{V_1} \quad (6.30)$$

where Y represents the acoustic emission signal in terms of acoustic power units (dB), V_2 stands for the acoustic emission signal in terms of Voltage (V) and V_1 stands for the reference input voltage of the preamplifier.

In the case of the Tektronix oscilloscope-based system, a fast Fourier transform (FFT) analysis was also performed with regards to the raw acoustic signals in order for any identifiable resonances to be documented. Results are presented in the following subchapter.

6.6 Cavitation related acoustic emissions (grade DH36 steel) - Results

1. Logarithmic Peak Detector and NI DAQ sensing system (LPD)

Aluminium sensor (± 0.007 dB) – 100 kHz – 40 μ s. Figures 6.13, 6.14 and 6.15.

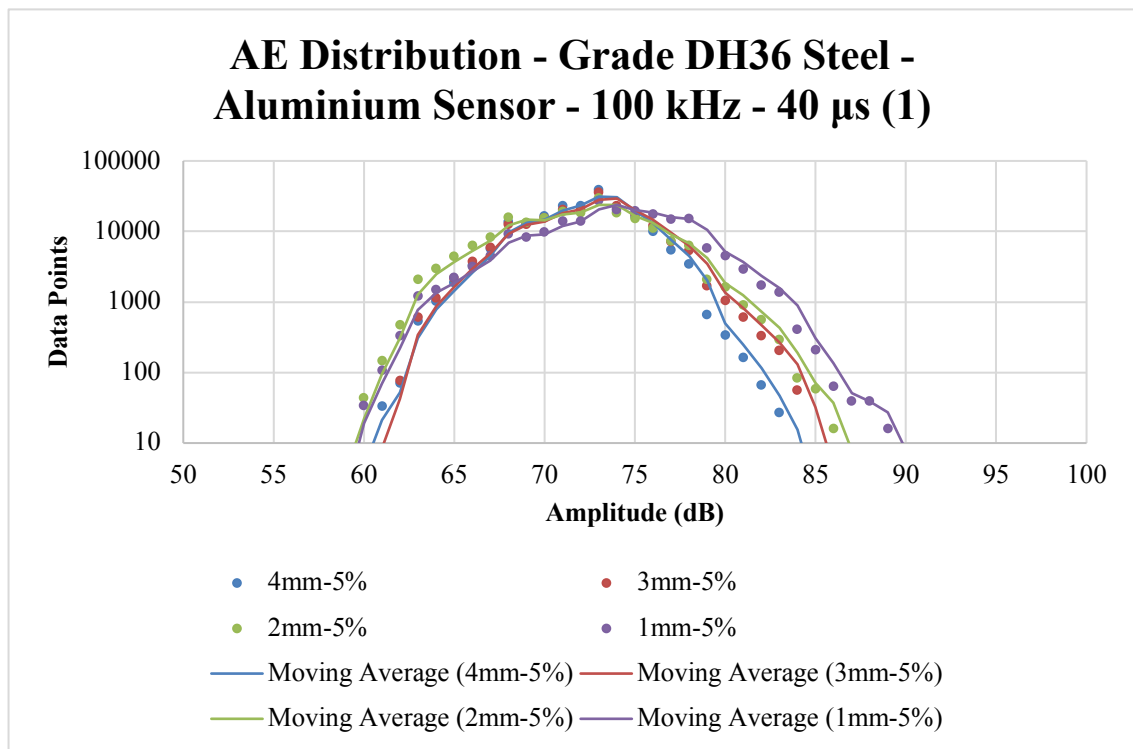


Figure 6.13: AE Distribution (4mm–5%, 3mm–5%, 2mm–5% and 1mm–5%)

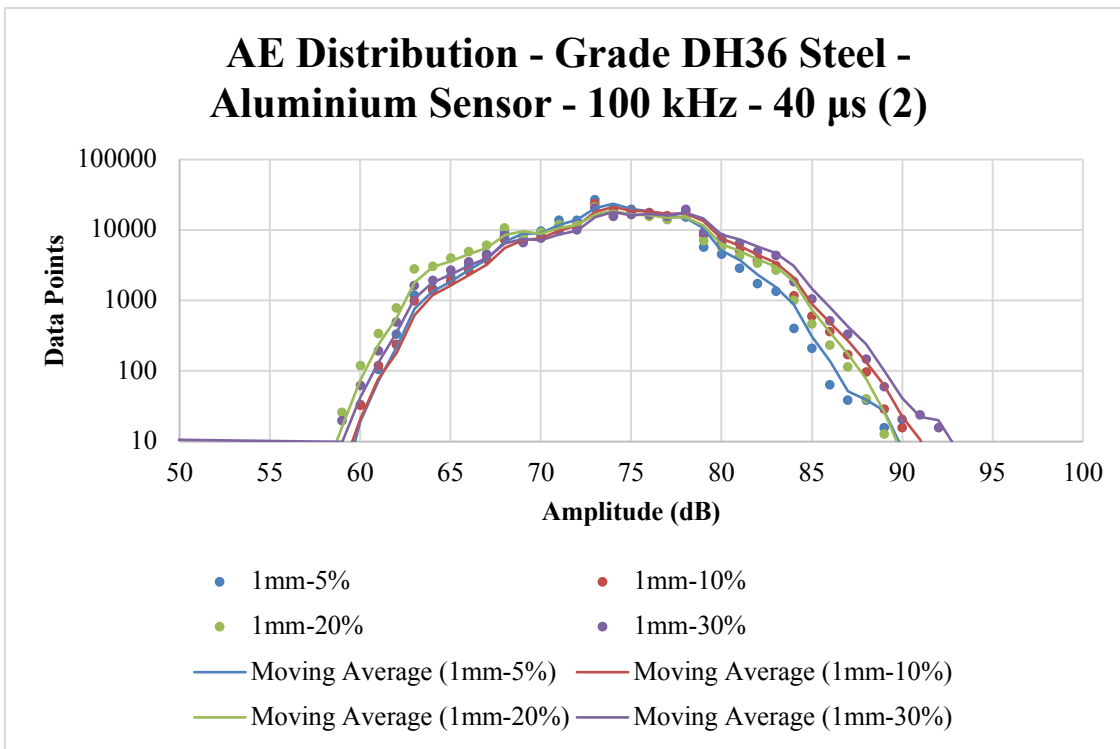


Figure 6.14: AE Distribution (1mm-5%, 1mm-10%, 1mm-20% and 1mm-30%)

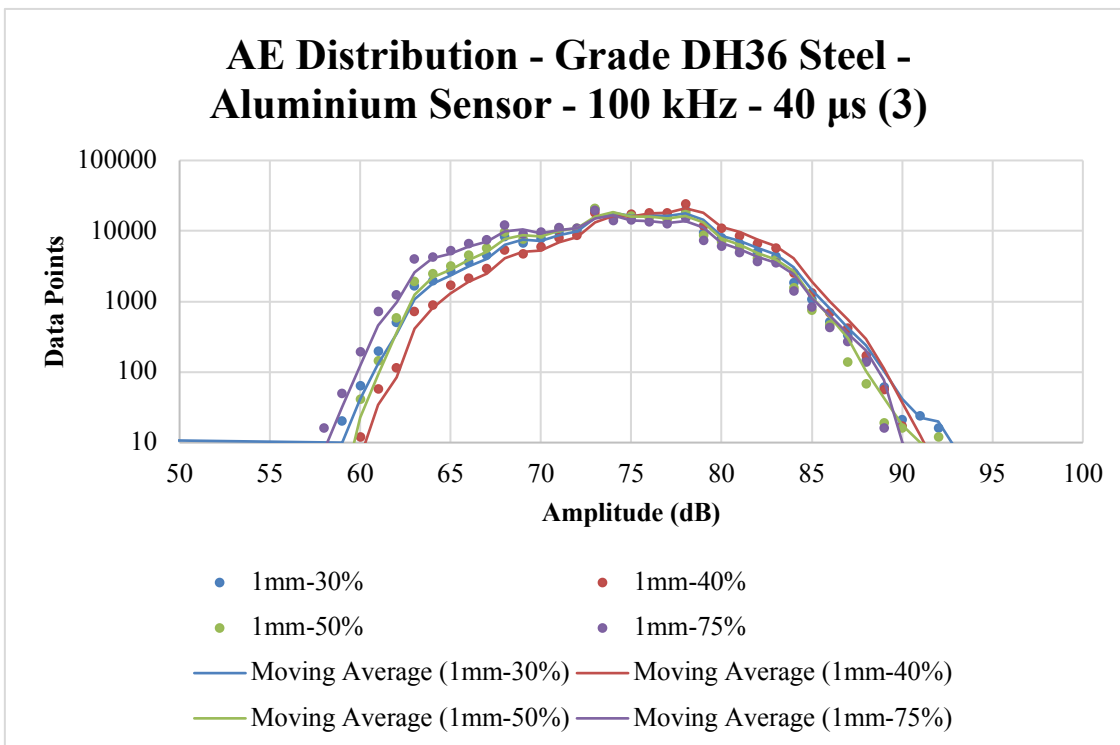


Figure 6.15: AE Distribution (1mm-30%, 1mm-40%, 1mm-50% and 1mm-75%)

Aluminium sensor (± 0.007 dB) – 25 kHz – 40 μ s. Figures 6.16, 6.17 and 6.18.

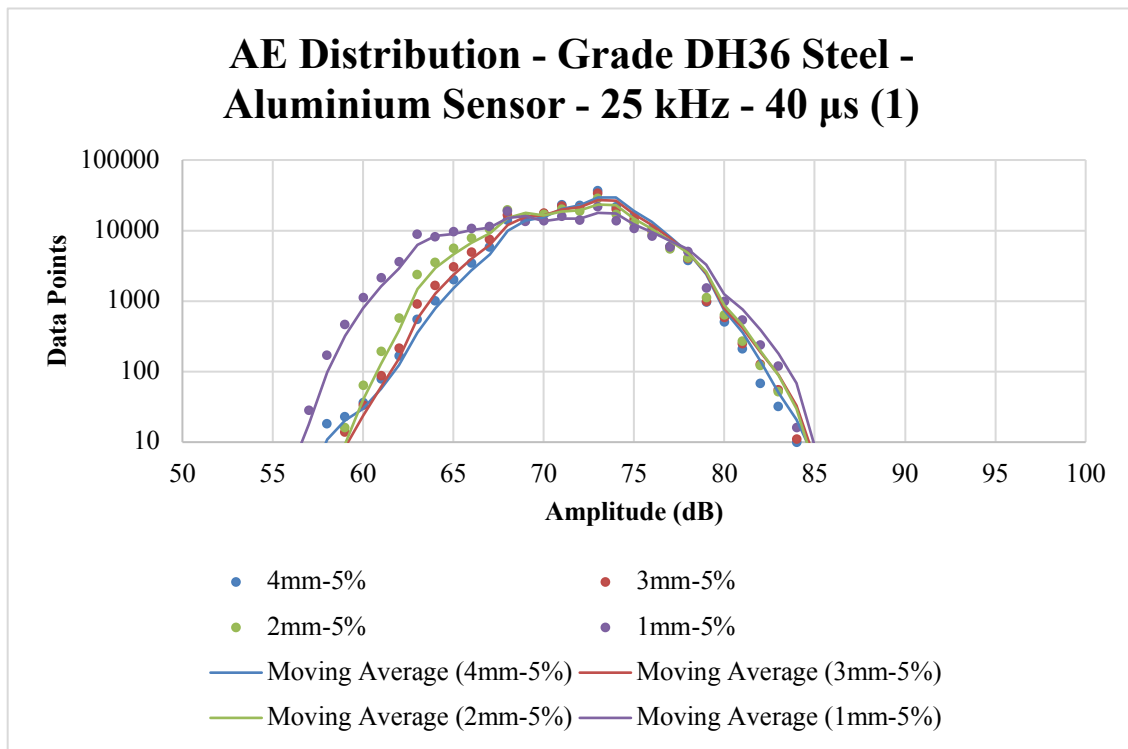


Figure 6.16: AE Distribution (4mm-5%, 3mm-5%, 2mm-5% and 1mm-5%)

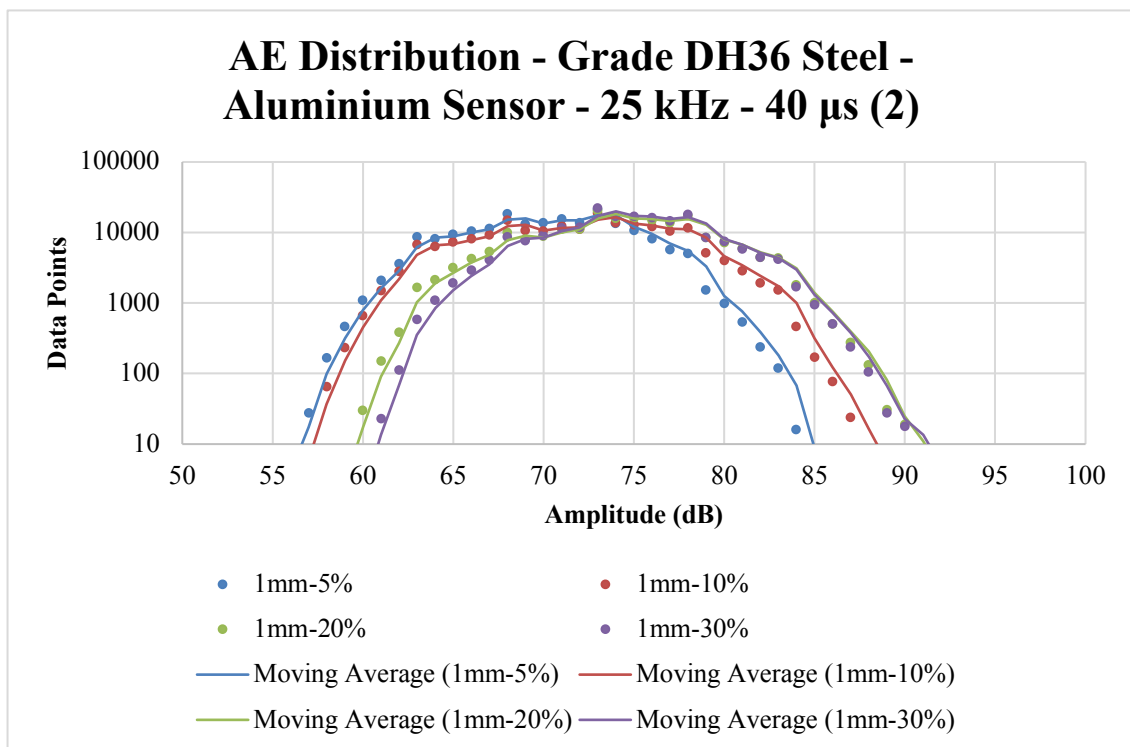


Figure 6.17: AE Distribution (1mm-5%, 1mm-10%, 1mm-20% and 1mm-30%)

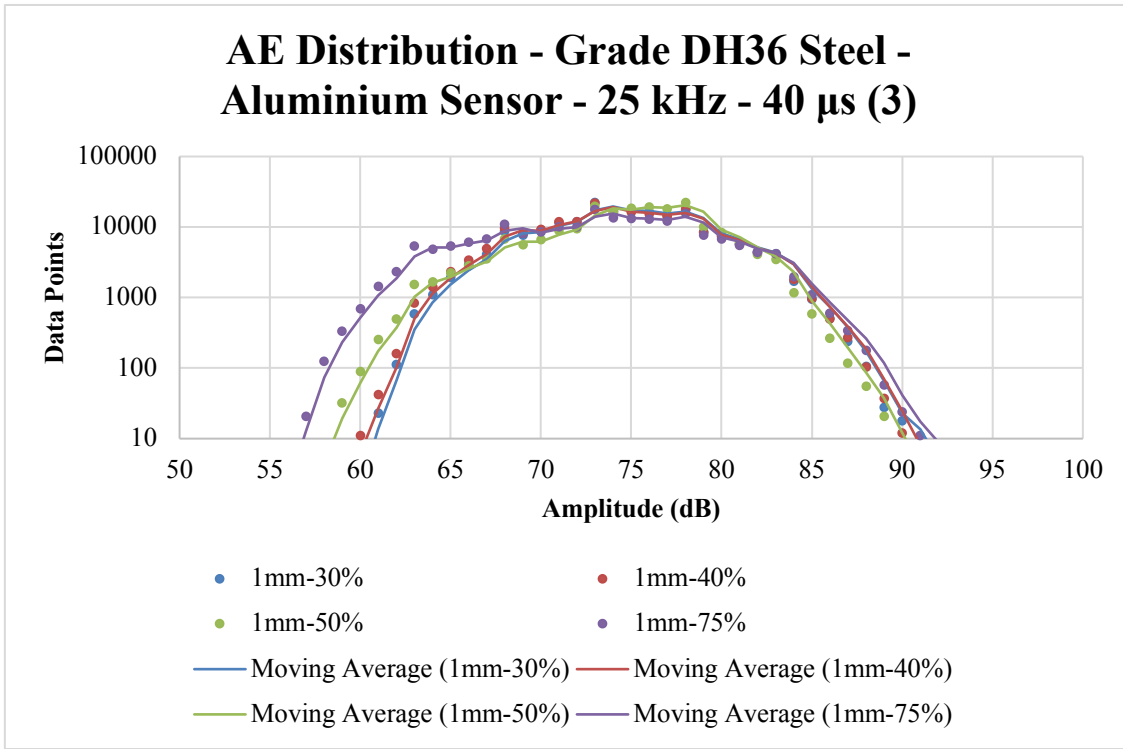


Figure 6.18: AE Distribution (1mm–30%, 1mm–40%, 1mm–50% and 1mm–75%)

Aluminium sensor (± 0.007 dB) – 1.25kHz – 1 ms. Figures 6.19, 6.20 and 6.21.

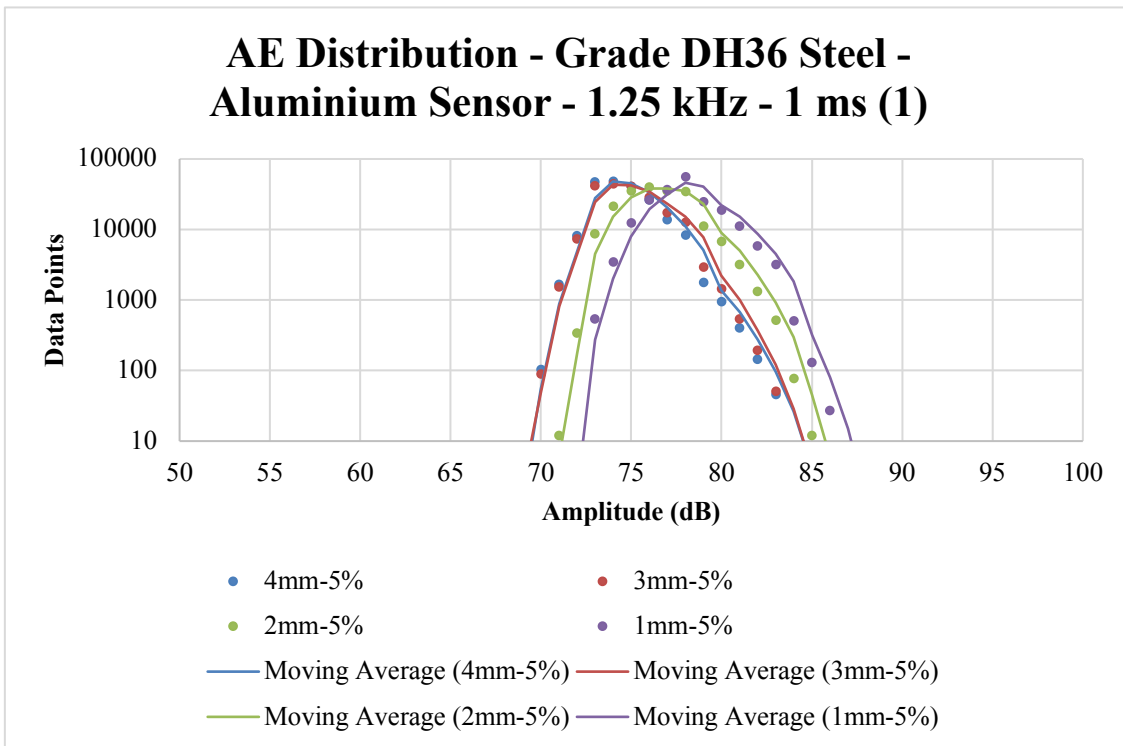


Figure 6.19: AE Distribution (4mm–5%, 3mm–5%, 2mm–5% and 1mm–5%)

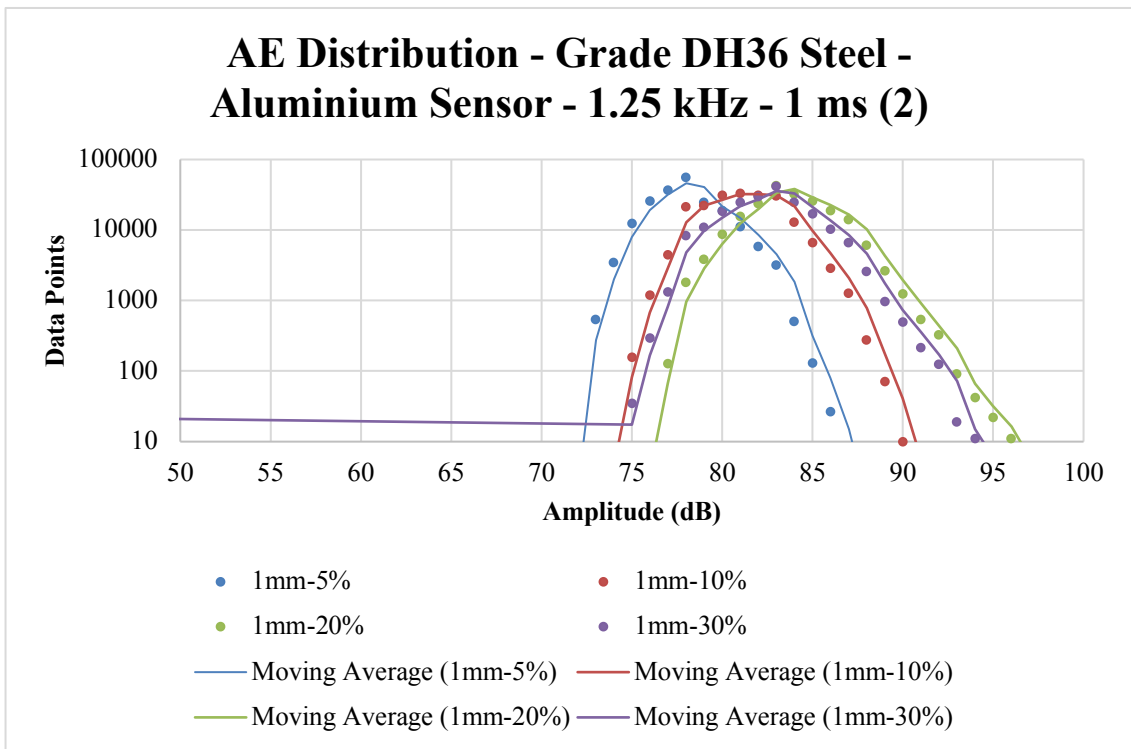


Figure 6.20: AE Distribution (1mm-5%, 1mm-10%, 1mm-20% and 1mm-30%)

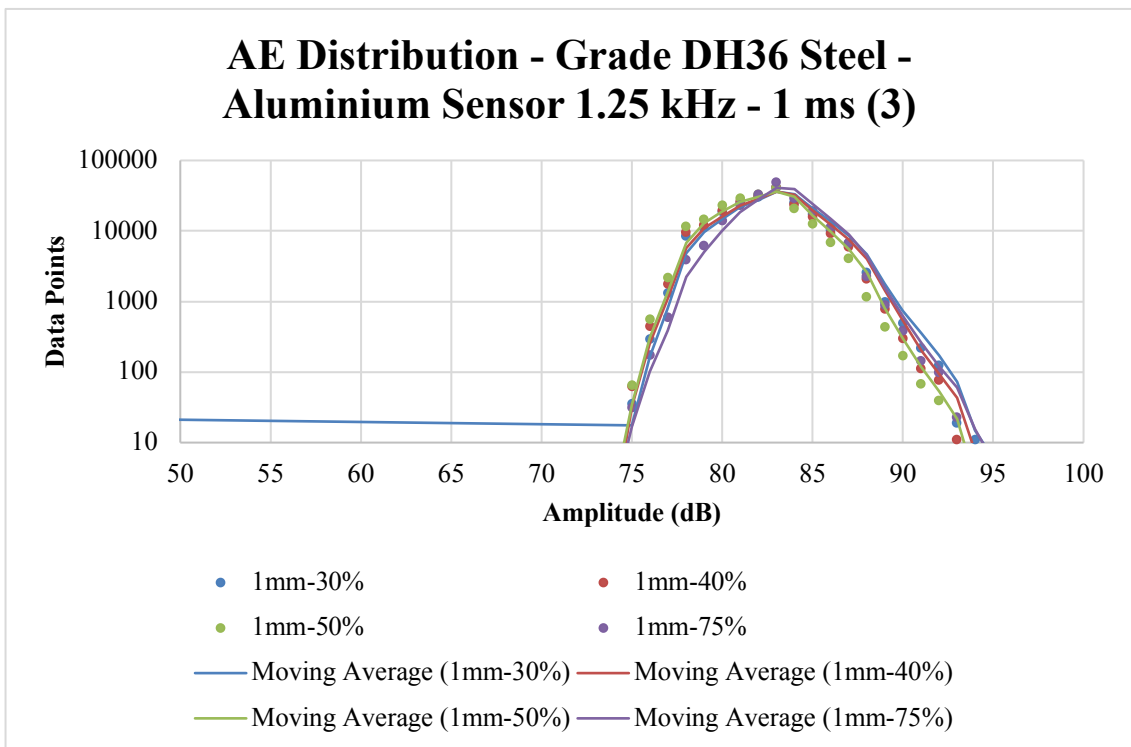


Figure 6.21: AE Distribution (1mm-30%, 1mm-40%, 1mm-50% and 1mm-75%)

Brass sensor (± 0.001 dB) – 100 kHz – 40 μ s. Figures 6.22, 6.23 and 6.24.

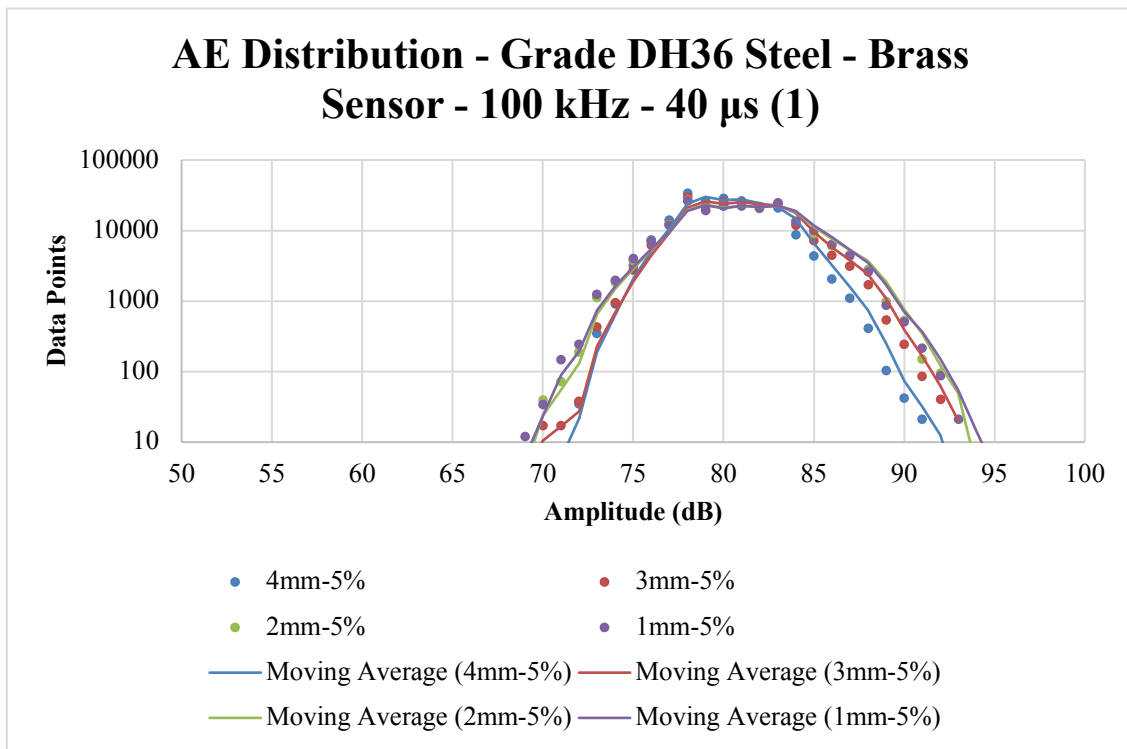


Figure 6.22: AE Distribution (4mm–5%, 3mm–5%, 2mm–5% and 1mm–5%)

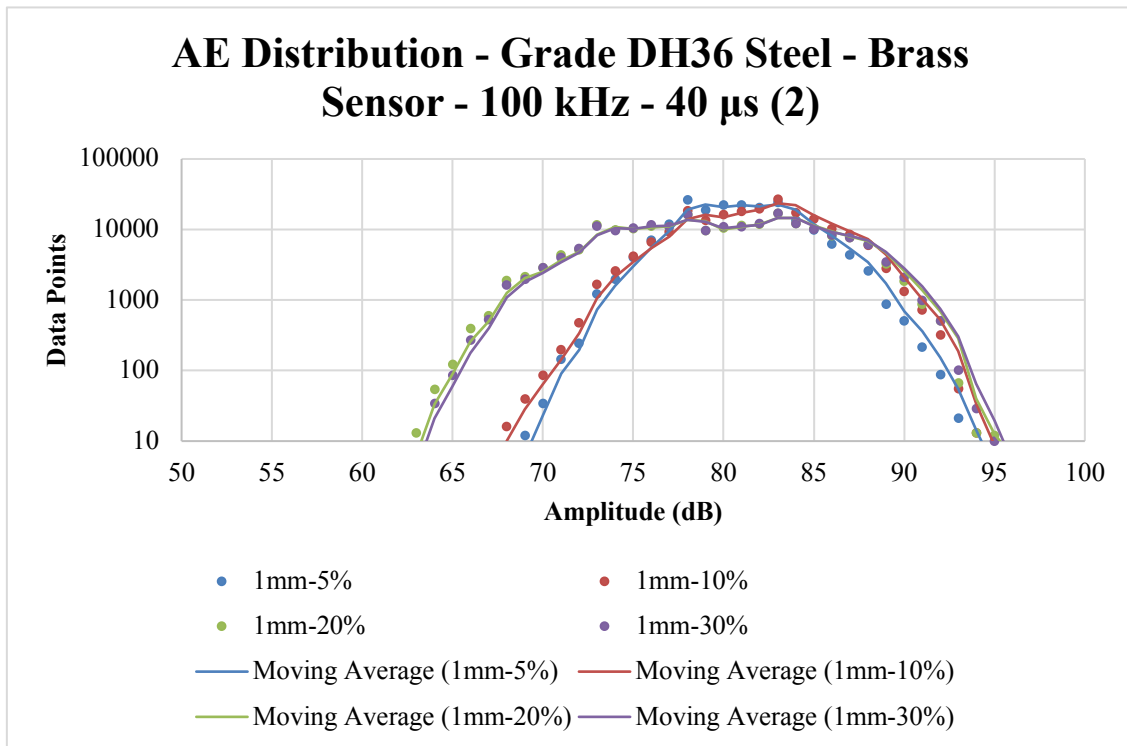


Figure 6.23: AE Distribution (1mm–5%, 1mm–10%, 1mm–20% and 1mm–30%)

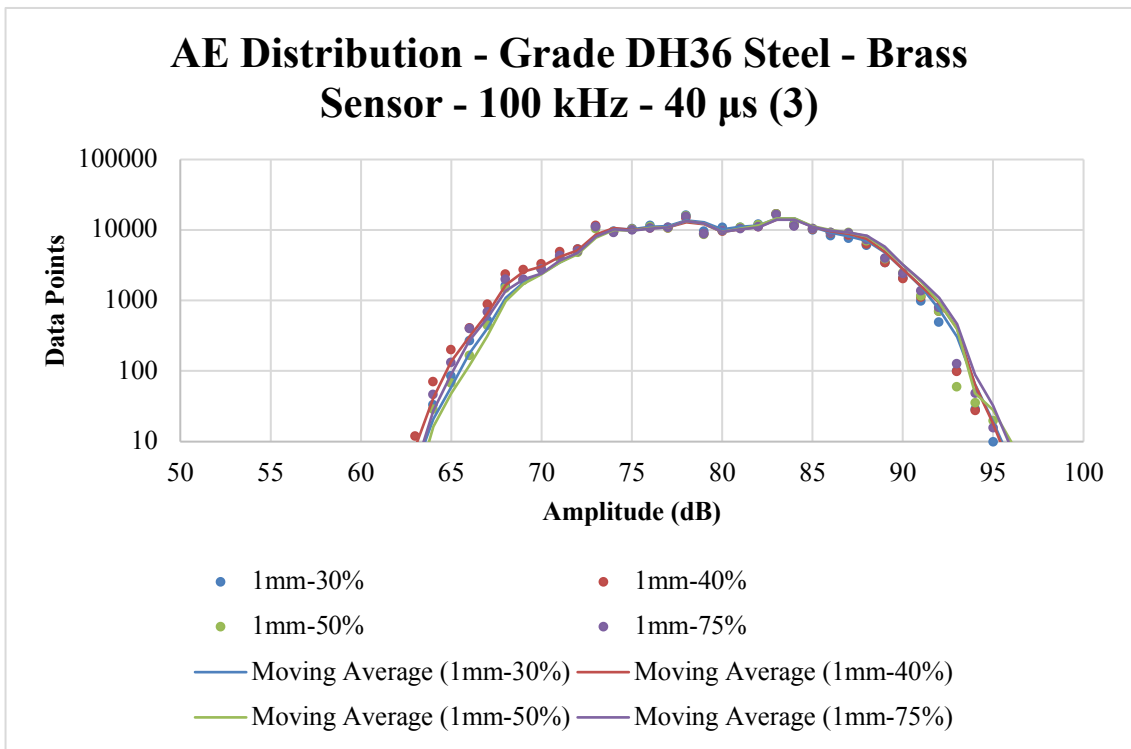


Figure 6.24: AE Distribution (1mm–30%, 1mm–40%, 1mm–50% and 1mm–75%)

Brass sensor (± 0.001 dB) – 25 kHz – 40 μ s. Figures 6.25, 6.26 and 6.27.

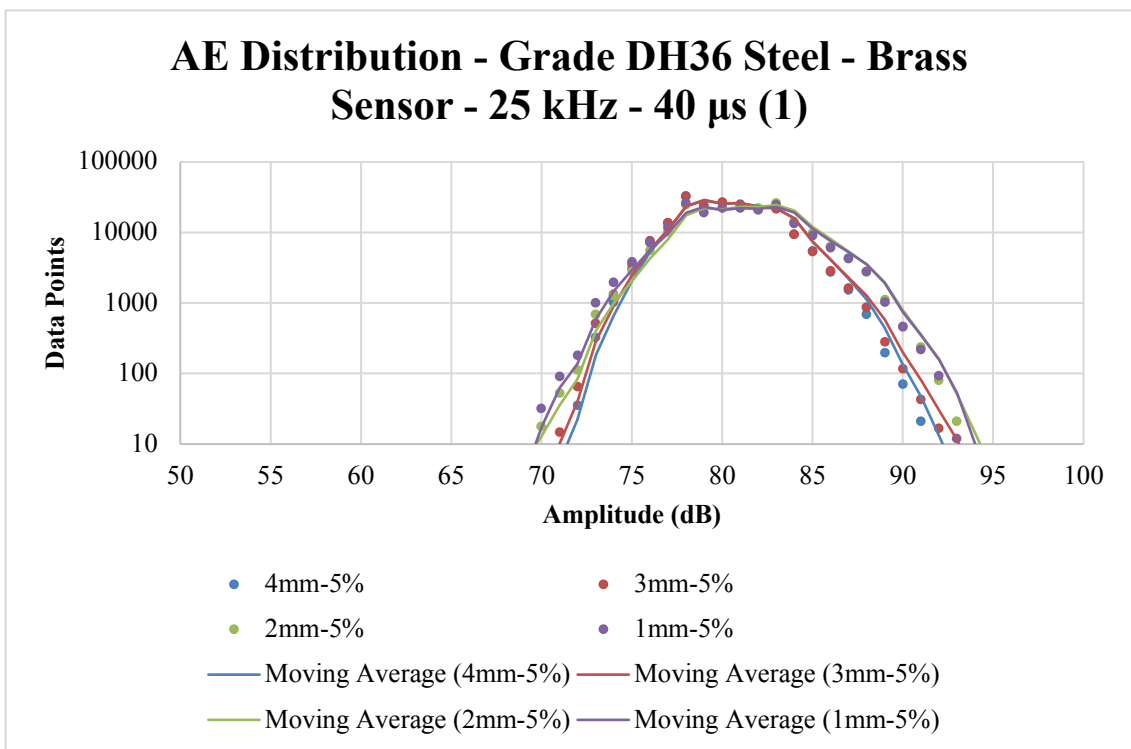


Figure 6.25: AE Distribution (4mm–5%, 3mm–5%, 2mm–5% and 1mm–5%)

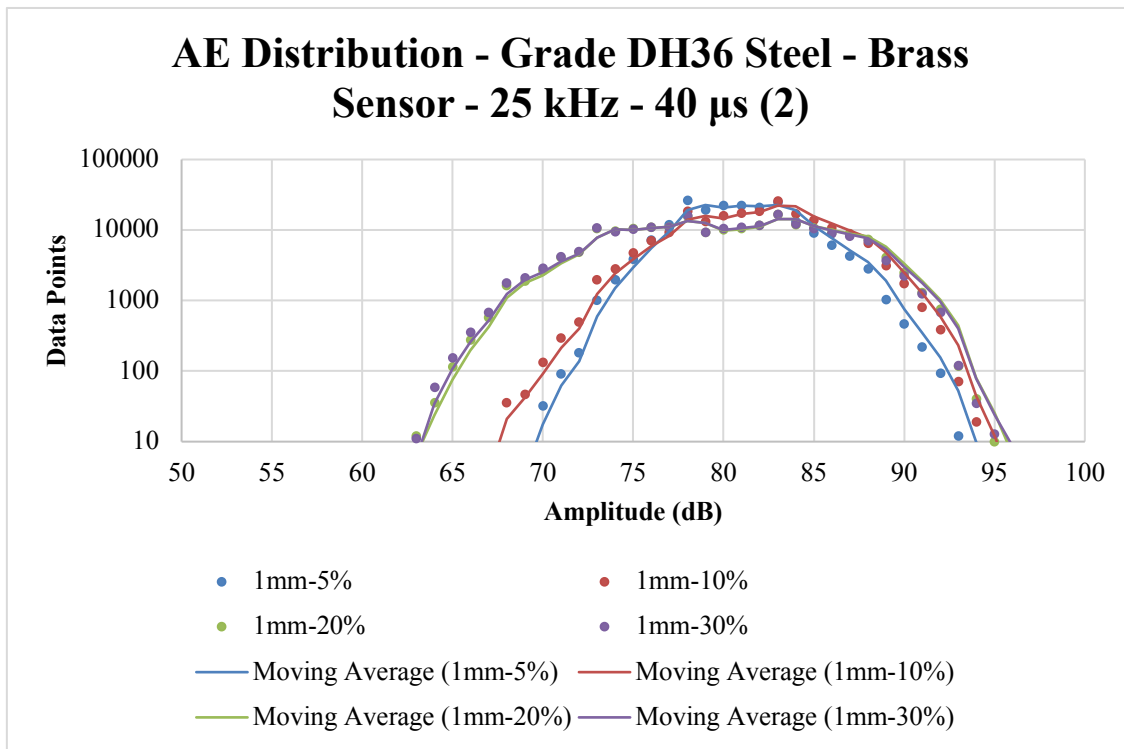


Figure 6.26: AE Distribution (1mm-5%, 1mm-10%, 1mm-20% and 1mm-30%)

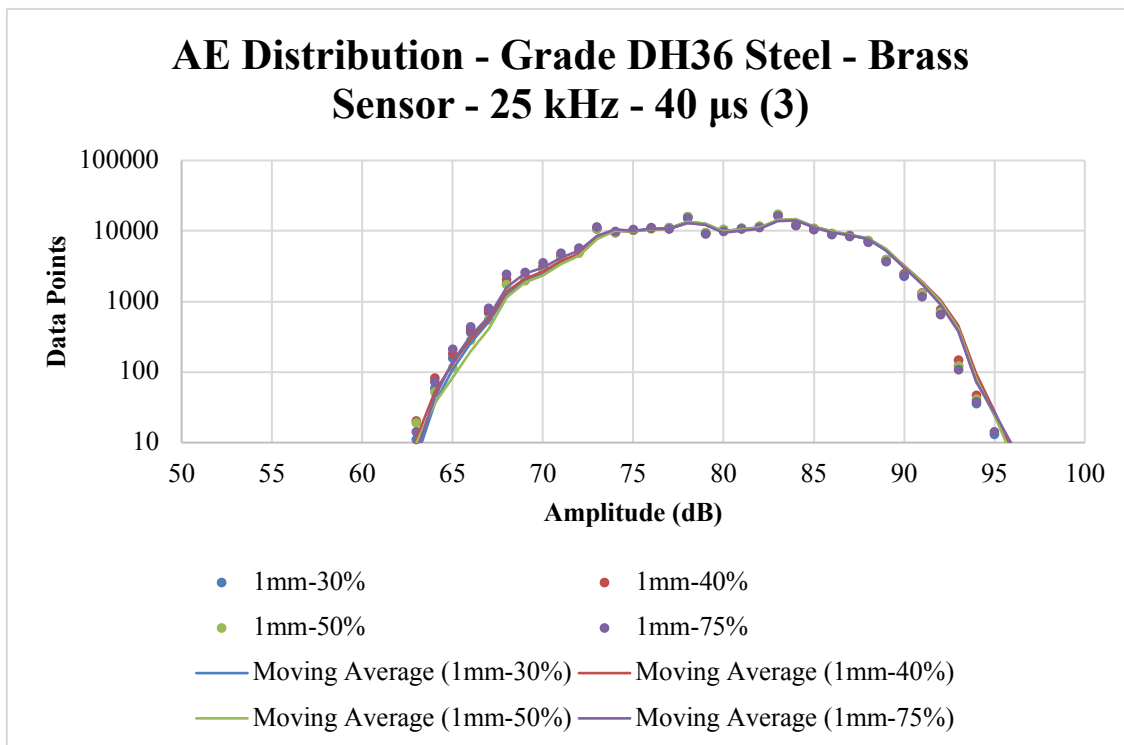


Figure 6.27: AE Distribution (1mm-30%, 1mm-40%, 1mm-50% and 1mm-75%)

Brass sensor (± 0.001 dB) – 1.25 kHz – 1 ms. Figures 6.28, 6.29 and 6.30.

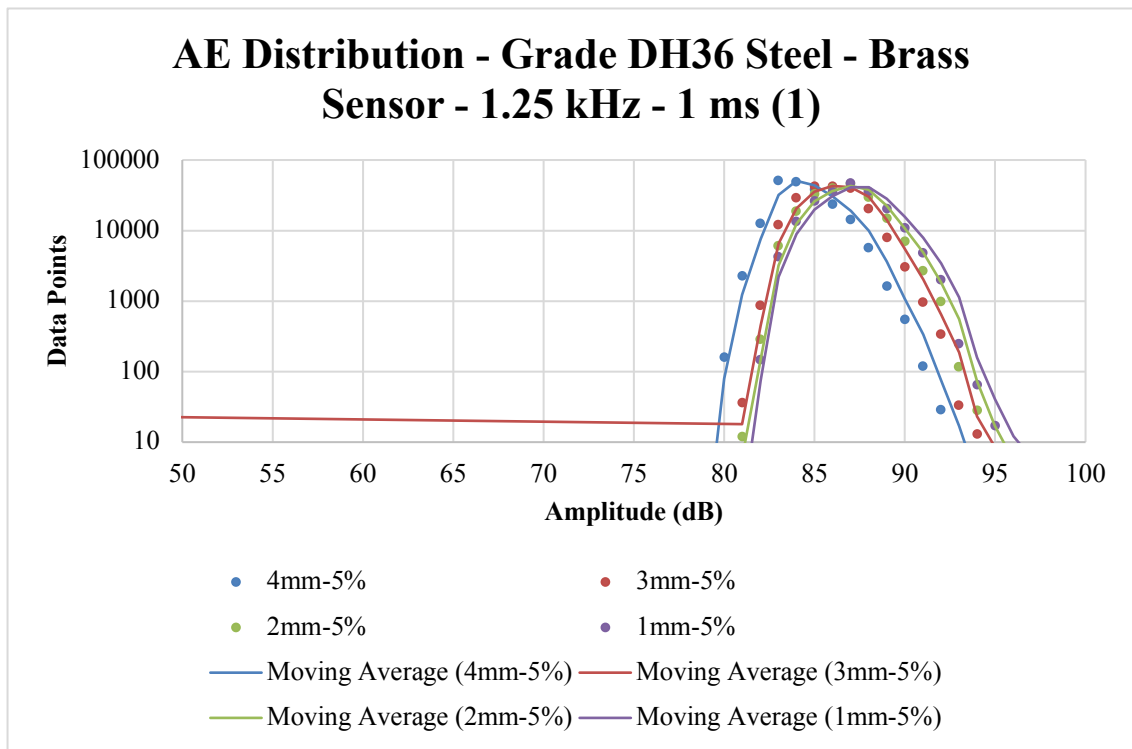


Figure 6.28: AE Distribution (4mm–5%, 3mm–5%, 2mm–5% and 1mm–5%)

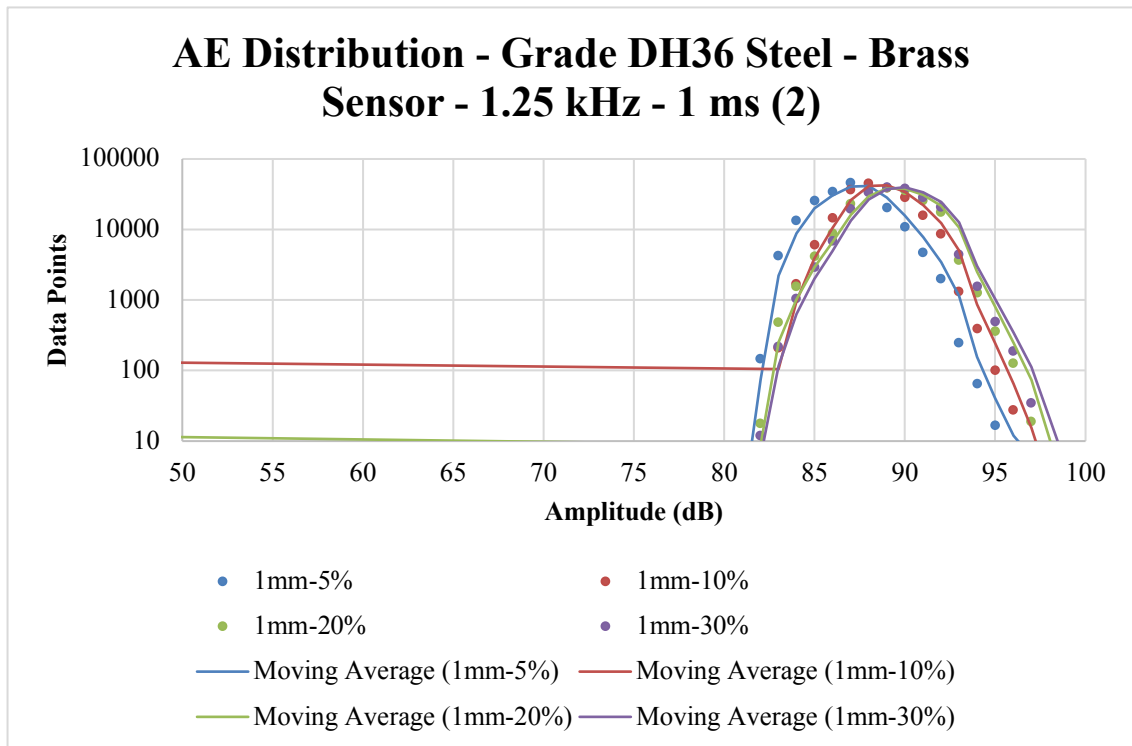


Figure 6.29: AE Distribution (1mm–5%, 1mm–10%, 1mm–20% and 1mm–30%)

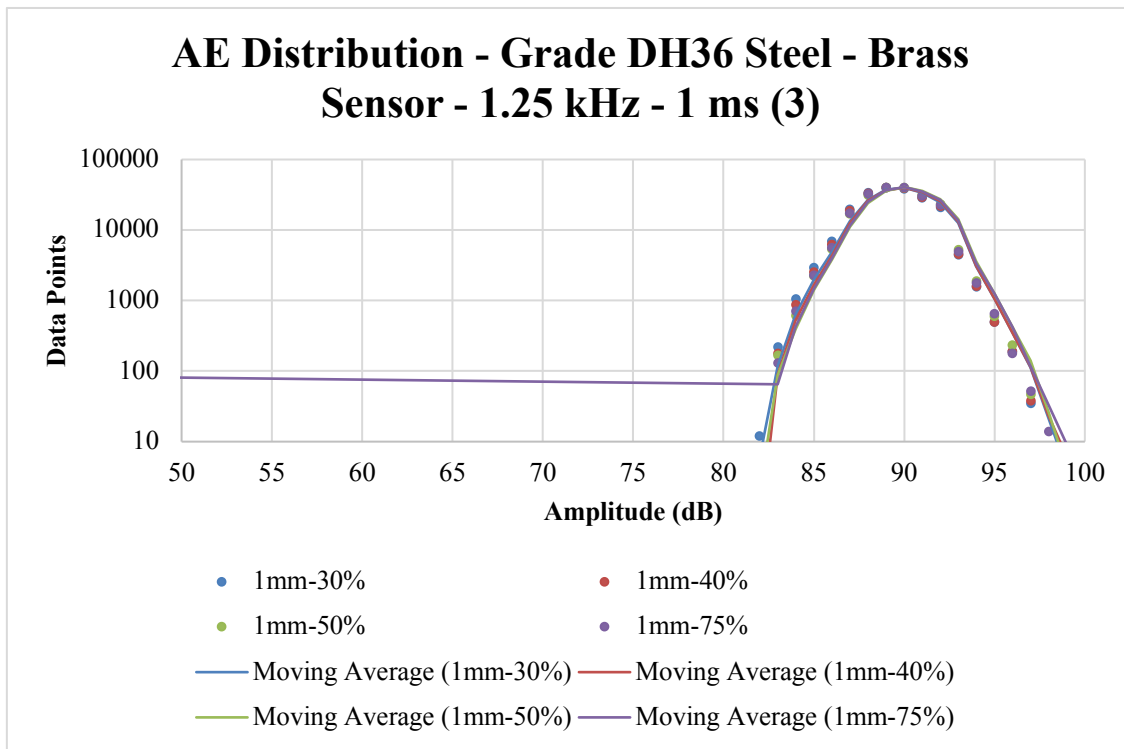


Figure 6.30: AE Distribution (1mm–30%, 1mm–40%, 1mm–50% and 1mm–75%)

PVDF sensor (± 0.016 dB) – 100 kHz – 40 μ s. Figures 6.31, 6.32 and 6.33.

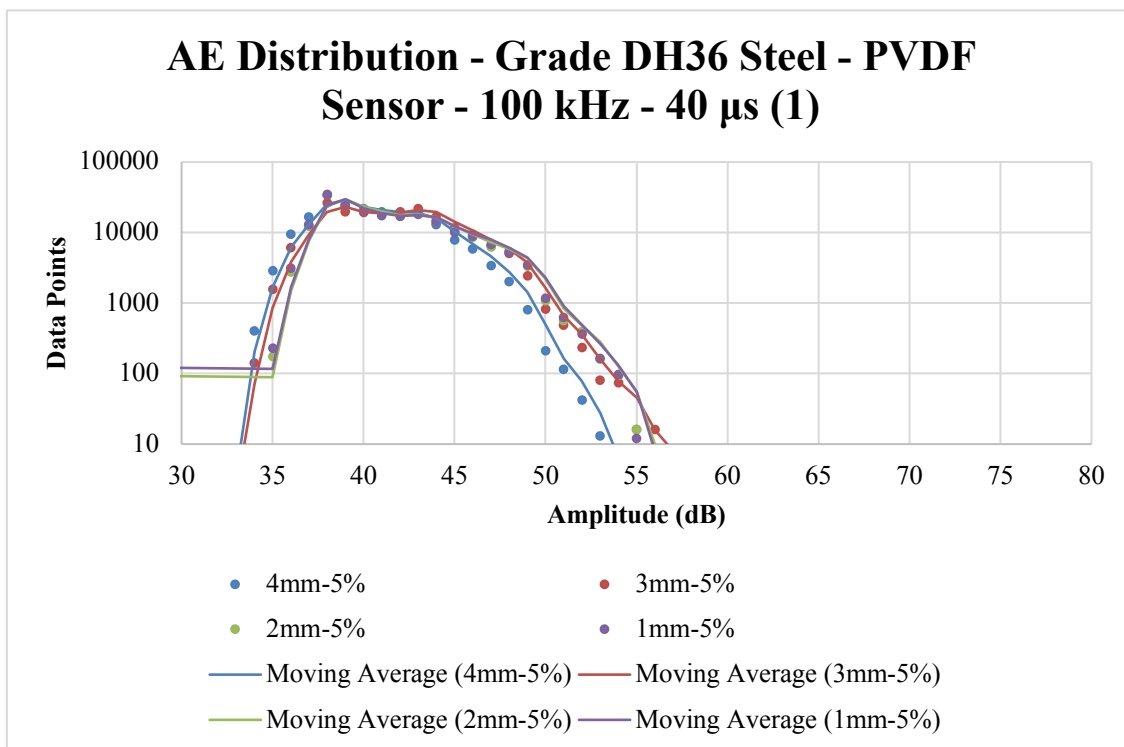


Figure 6.31: AE Distribution (4mm–5%, 3mm–5%, 2mm–5% and 1mm–5%)

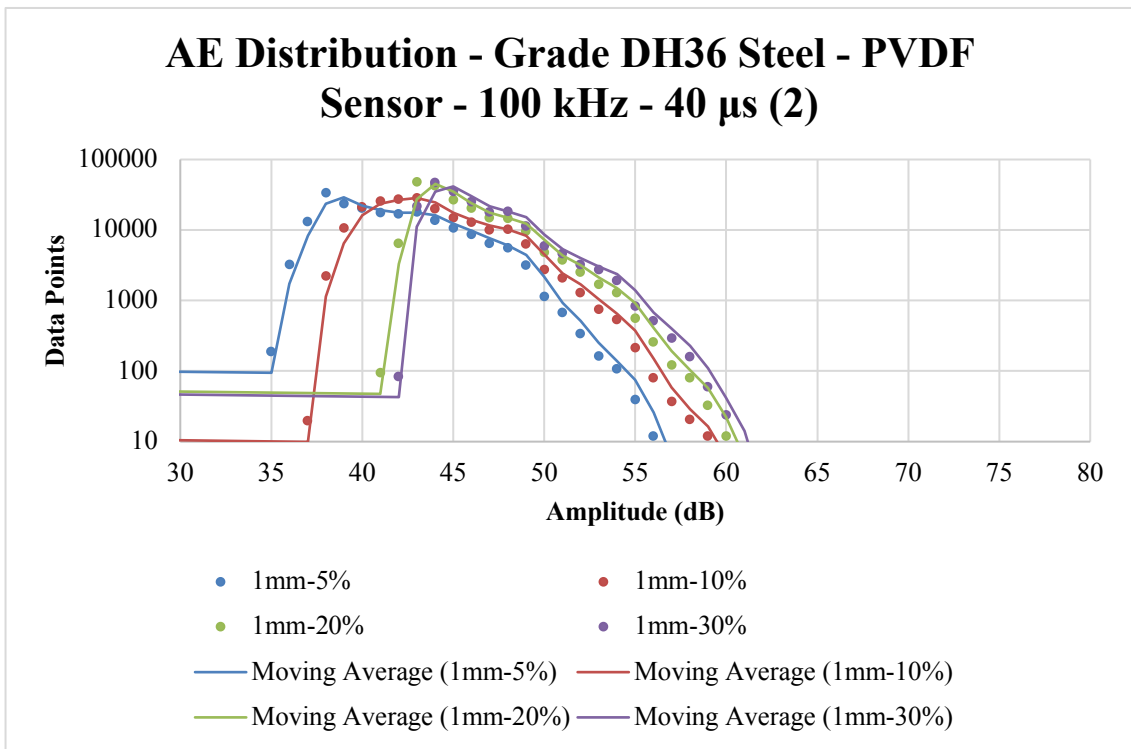


Figure 6.32: AE Distribution (1mm–5%, 1mm–10%, 1mm–20% and 1mm–30%)

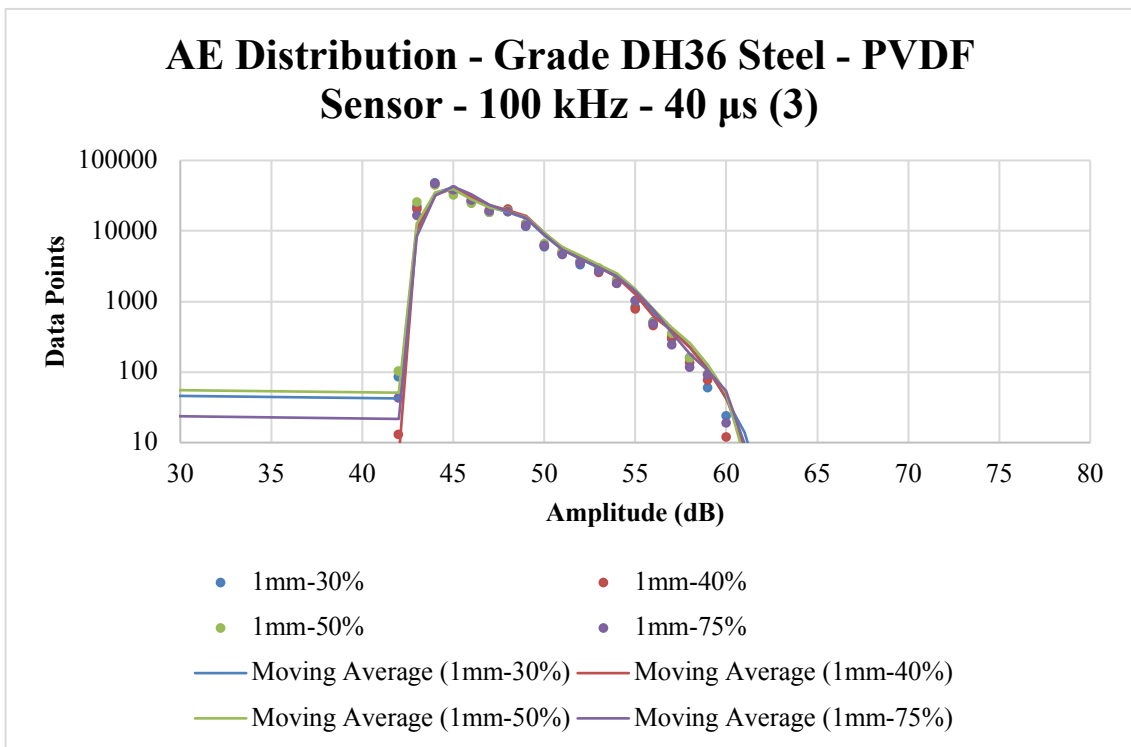


Figure 6.33: AE Distribution (1mm–30%, 1mm–40%, 1mm–50% and 1mm–75%)

PVDF sensor (± 0.016 dB) – 25 kHz – 40 μ s. Figures 6.34, 6.35 and 6.36.

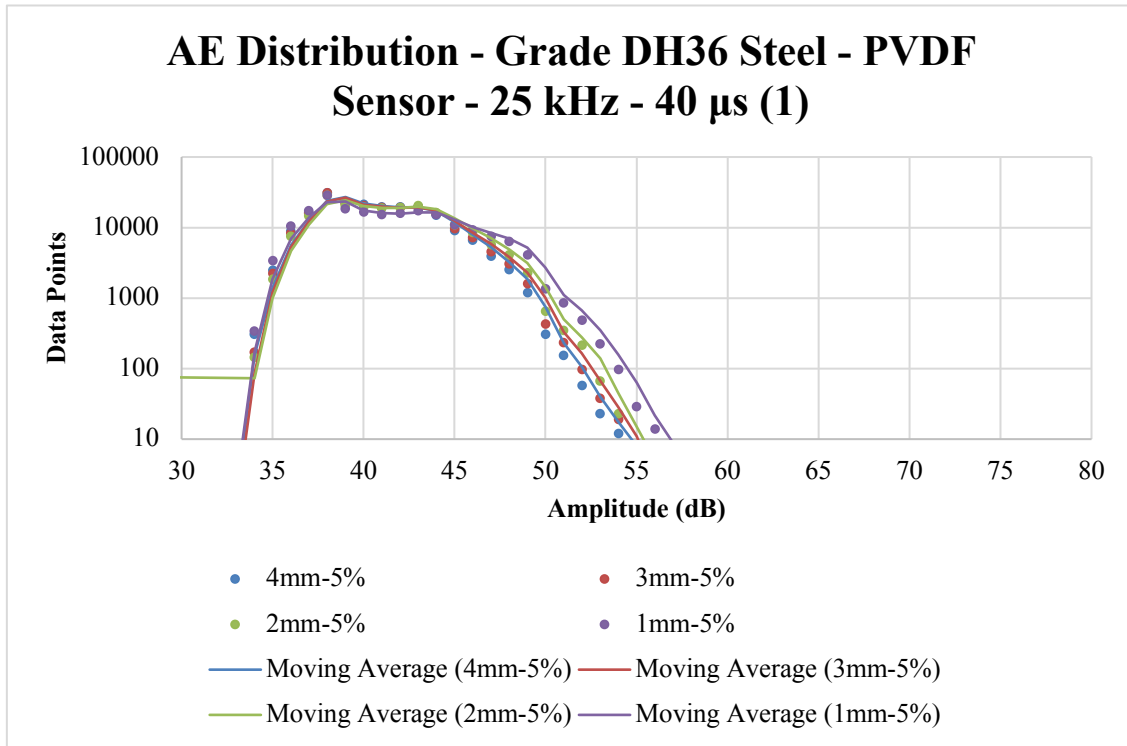


Figure 6.34: AE Distribution (4mm–5%, 3mm–5%, 2mm–5% and 1mm–5%)

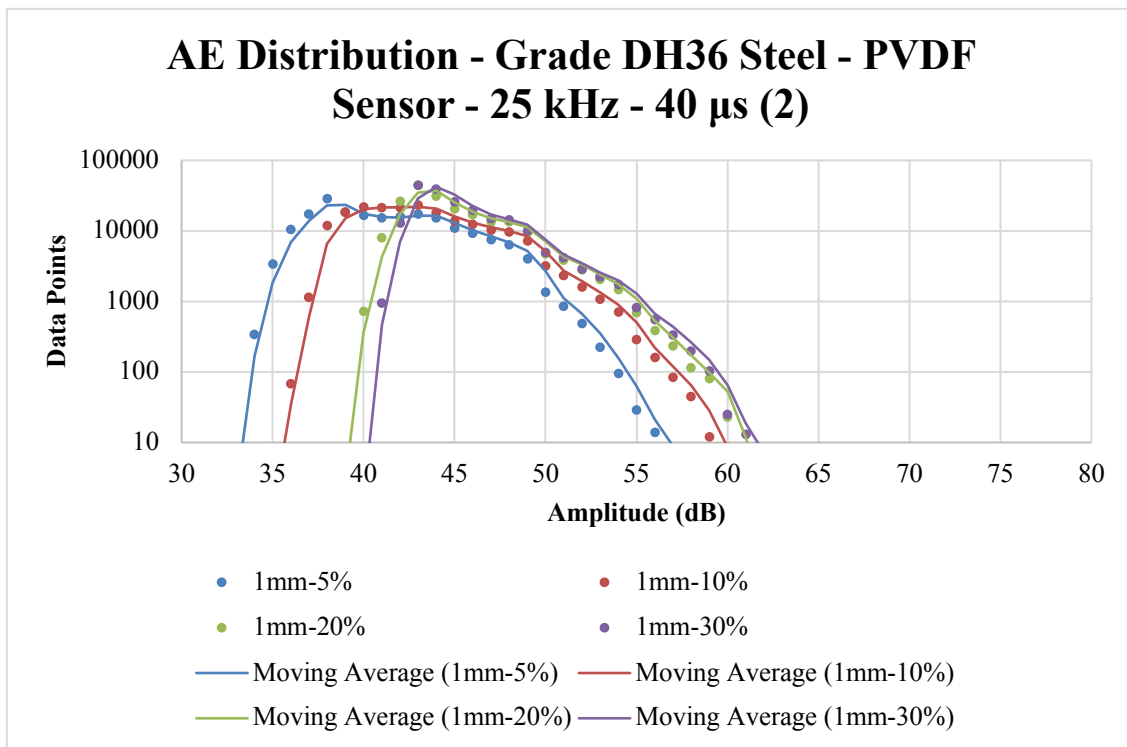


Figure 6.35: AE Distribution (1mm–5%, 1mm–10%, 1mm–20% and 1mm–30%)

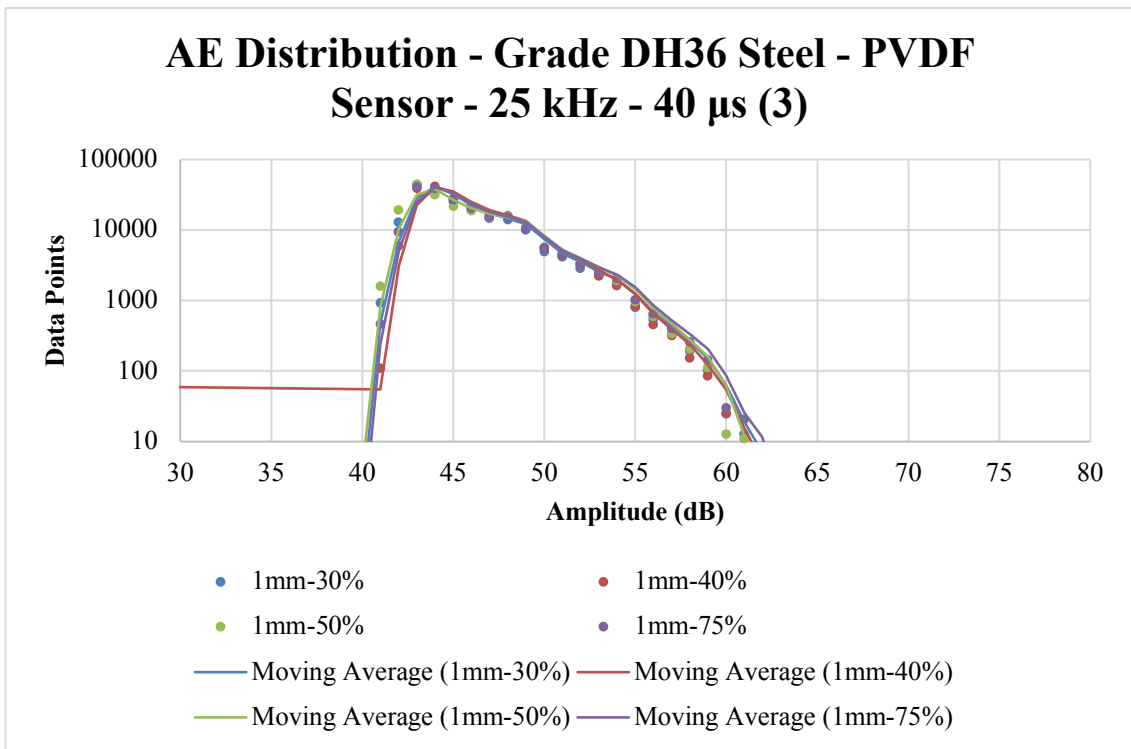


Figure 6.36: AE Distribution (1mm–30%, 1mm–40%, 1mm–50% and 1mm–75%)

PVDF sensor (± 0.016 dB) – 1.25 kHz – 1 ms. Figures 6.37, 6.38 and 6.39.

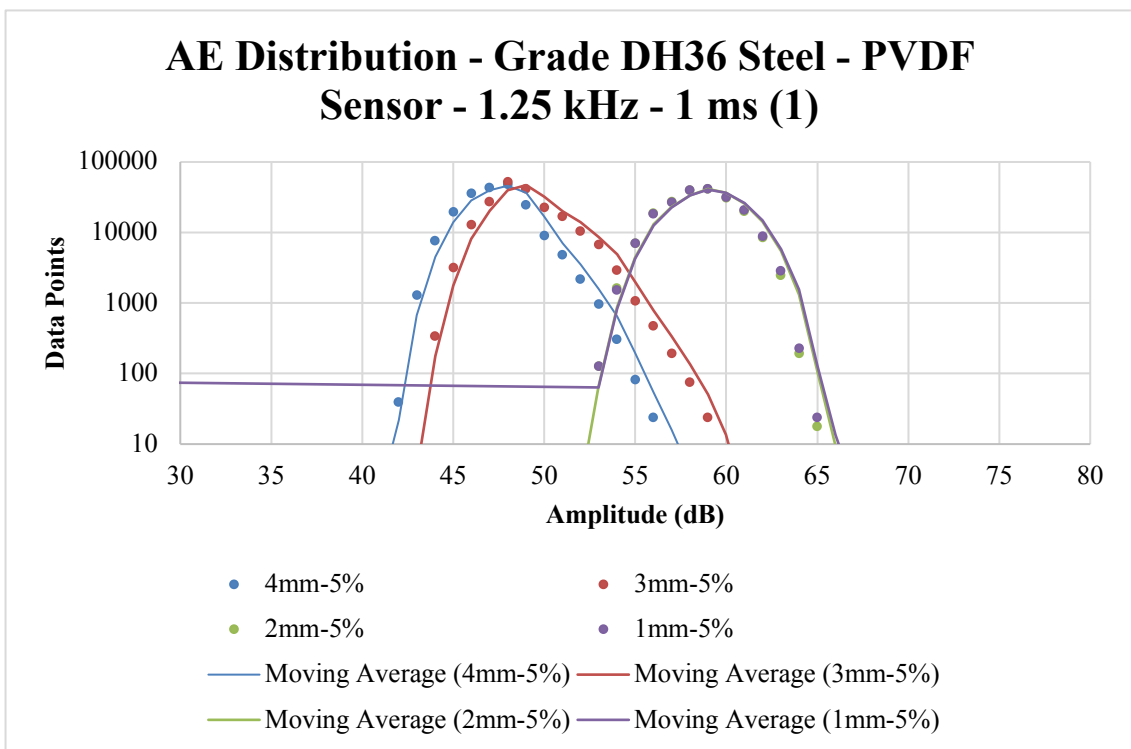


Figure 6.37: AE Distribution (4mm–5%, 3mm–5%, 2mm–5% and 1mm–5%)

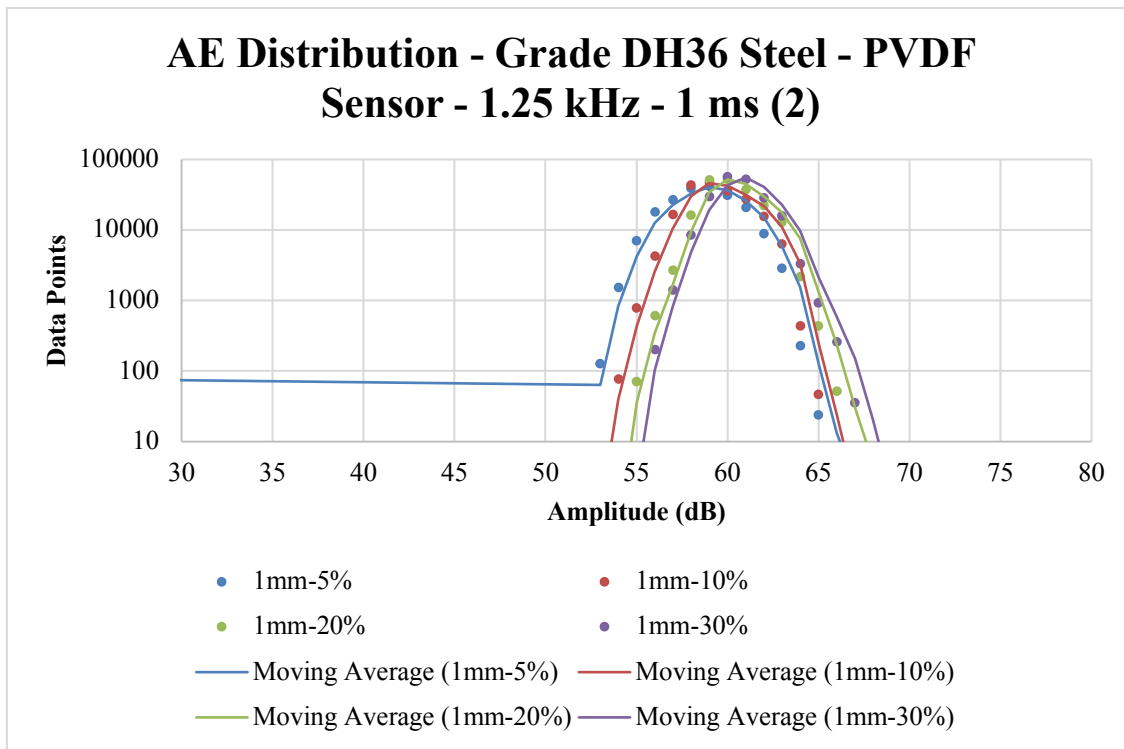


Figure 6.38: AE Distribution (1mm–5%, 1mm–10%, 1mm–20% and 1mm–30%)

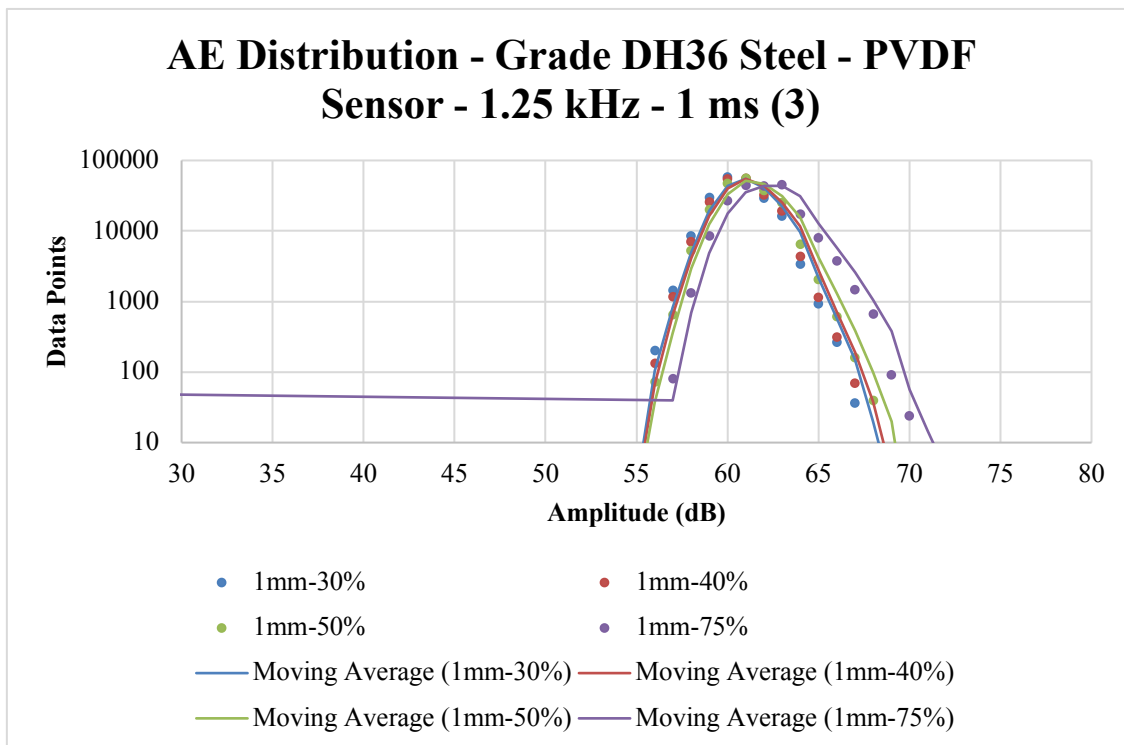


Figure 6.39: AE Distribution (1mm–30%, 1mm–40%, 1mm–50% and 1mm–75%)

Acoustic emissions captured by means of the logarithmic peak detector and the NI DAQ appear to exhibit analogous patterns with regards to the different test rig configurations and

the corresponding cavitation. In particular, the amplitudes of the measured acoustic emissions for power settings higher than 30% (300W) were of similar order, always with regards to a particular sensor and sampling rate. In contrast, the largest variations with regards to amplitude were measured for power settings ranging between 5% (50W) and 30% (300W) and a gap of 1mm, for all sensors and sampling rates. Finally, with regards to acoustic emissions related to the transition point between ‘non-erosive’ and ‘erosive’ cavitation, this is mostly evident when a sampling rate of 100 kHz is utilized, allowing for collapsing events that are directly related to the operating frequency (20 kHz) of the sonotrode to be captured whereas for lower rates some higher energy yet slower events become more evident and as a result curves come closer together. One of course should also consider the parameter of the sensor itself, as it appears that the characteristics of the aluminium sensor in conjunction with the appropriate sampling rate offer clearer resolution of the resulting signals in comparison to other sensors.

The key points regarding the behaviour of the acoustic sensors in conjunction with the logarithmic peak detector and the NI DAQ are the following:

Aluminium sensor with logarithmic peak detector and NI DAQ:

- AE amplitudes ranging between 55 and 98 dB.
- AE distribution curves are more dispersed for power settings ranging between 5% (50W) and 30% (300W). Dispersion is more pronounced for low sampling rates.
- The transition point between ‘non-erosive’ and ‘erosive’ cavitation is only detectable, in terms of AE, for a sampling rate of 100 kHz (85 dB). Lower sampling rates lead to almost identical distribution curves and amplitudes.

Brass sensor with logarithmic peak detector and NI DAQ:

- AE amplitudes ranging between 62 and 100 dB.
- AE distribution curves for power settings higher than 30% (300W) are almost identical to each other whereas they are not as dispersed as in the aluminium sensor case for instance, for power settings ranging between 5% (50W) and 30% (300W).
- The transition point between ‘non-erosive’ and ‘erosive’ cavitation is detectable for all sampling rates (93 to 96 dB), although in comparison to the aluminium sensor, distribution curves are not as dispersed and as such the transition point is not as apparent.

PVDF sensor with logarithmic peak detector and NI DAQ:

- AE amplitudes ranging between 32 and 70 dB.
- AE distribution curves for power settings higher than 30% (300W) are almost identical to each other, whereas they are more dispersed for power settings ranging between 5% (50W) and 30% (300W), similarly to the other sensors.
- The transition point between ‘non-erosive and ‘erosive’ cavitation is only detectable for sampling rates of 100 kHz and 1.25 kHz and is of the order of 57 and 60 dB, respectively. In the case of the former frequency, however, distributions curves are not as dispersed thus it is not clear whether the transition point corresponds to ‘light erosion’ or not.

2. Tektronix Oscilloscope based sensing system (TO)

Aluminum sensor (± 0.007 dB) – 31.3 MHz. Figures 6.40, 6.41, 6.42 and 6.43.

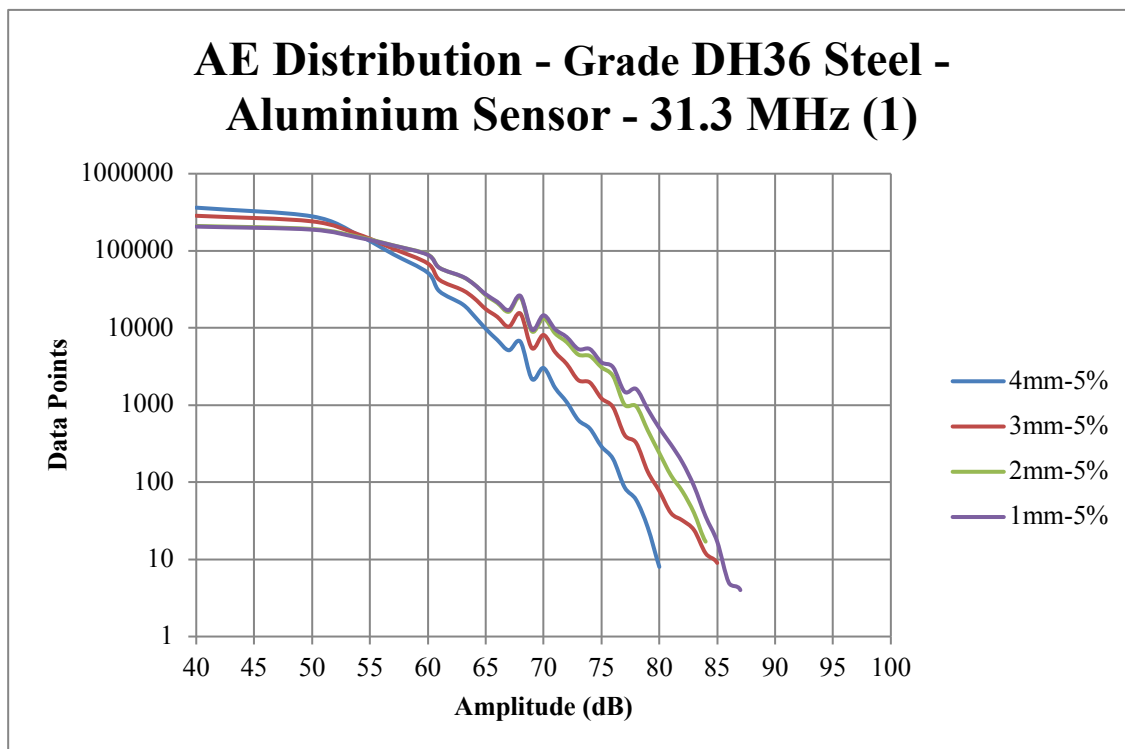


Figure 6.40: AE Distribution (4mm–5%, 3mm–5%, 2mm–5% and 1mm–5%)

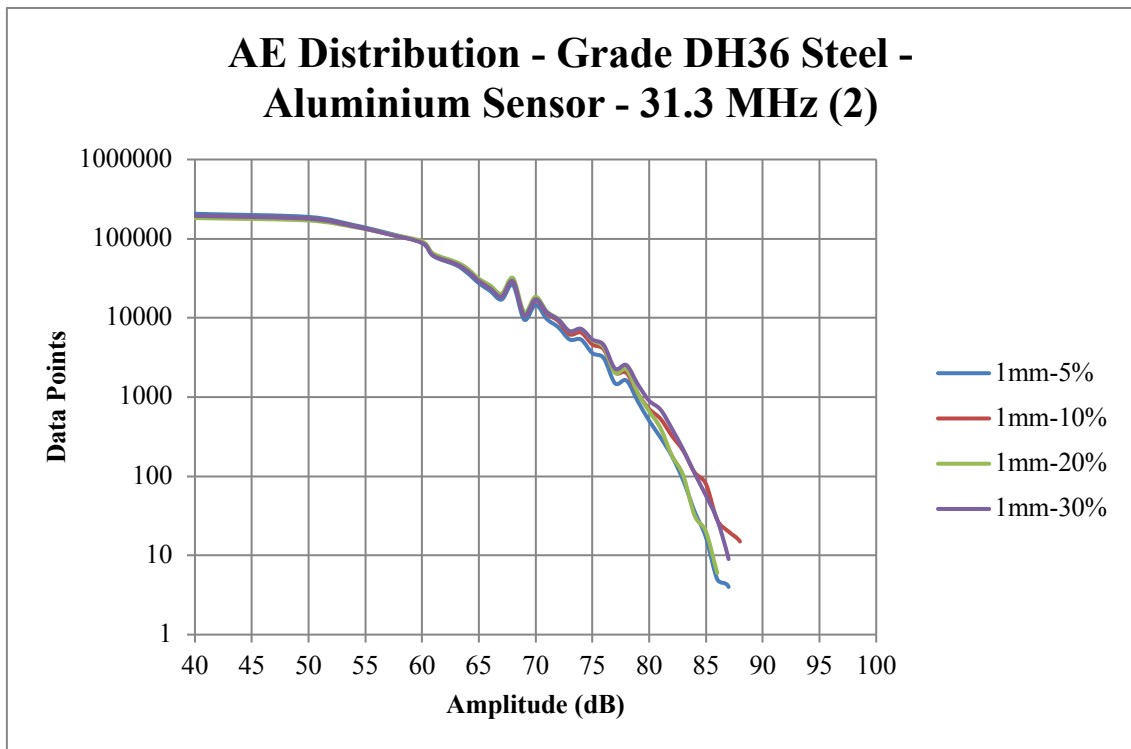


Figure 6.41: AE Distribution (1mm-5%, 1mm-10%, 1mm-20% and 1mm-30%)

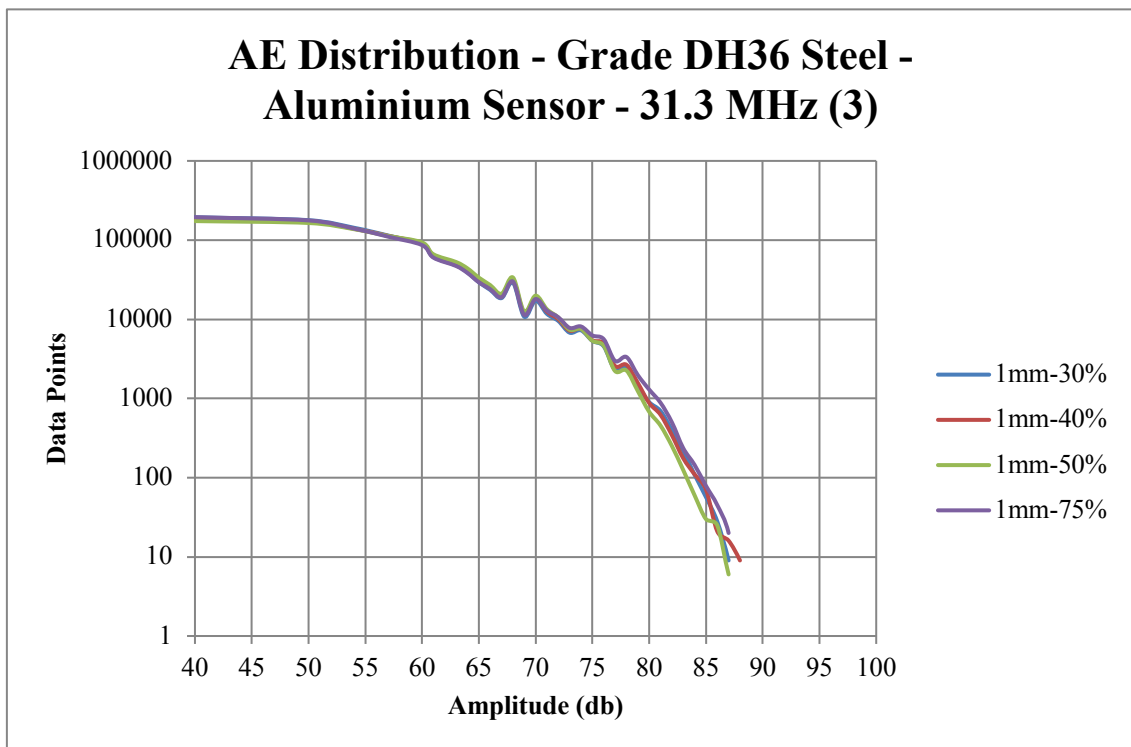


Figure 6.42: AE Distribution (1mm-30%, 1mm-40%, 1mm-50% and 1mm-75%)

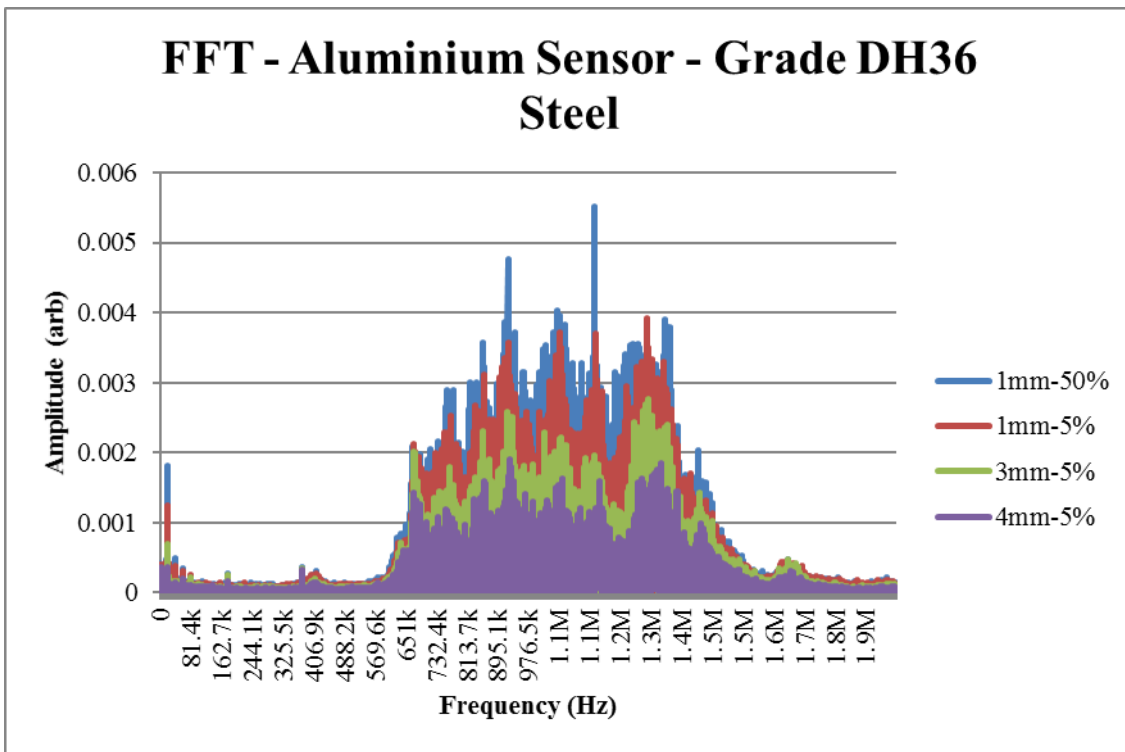


Figure 6.43: FFT – Aluminium Sensor – DH36 steel (4mm-5%, 3mm-5%, 1mm-5%, 1mm-50%).

Brass sensor (± 0.001 dB) – 31.3 MHz. Figures 6.44, 6.45, 6.46 and 6.47.

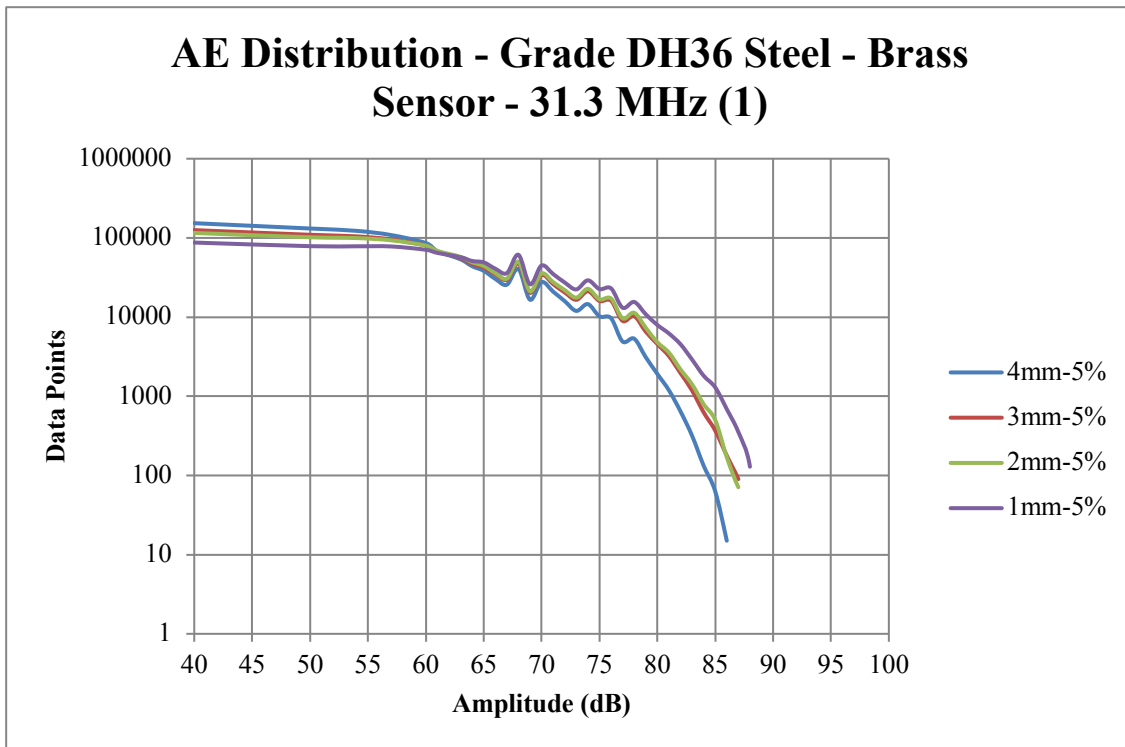


Figure 6.44: AE Distribution (4mm-5%, 3mm-5%, 2mm-5% and 1mm-5%)

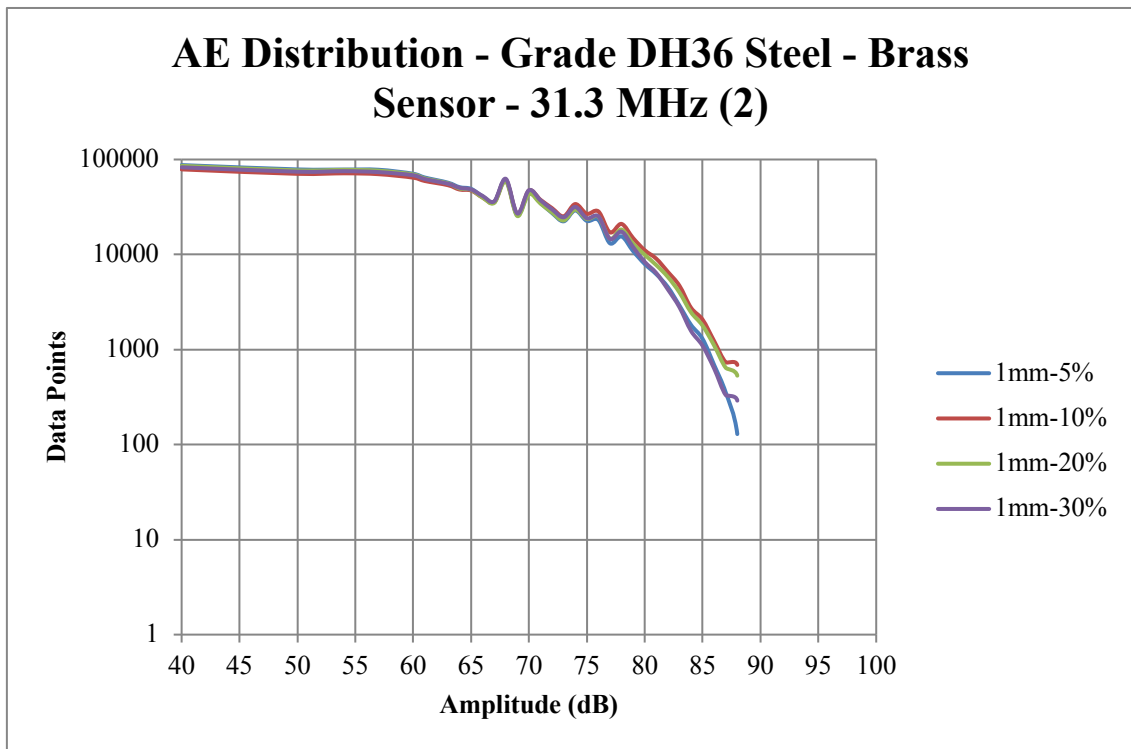


Figure 6.45: AE Distribution (1mm-5%, 1mm-10%, 1mm-20% and 1mm-30%)

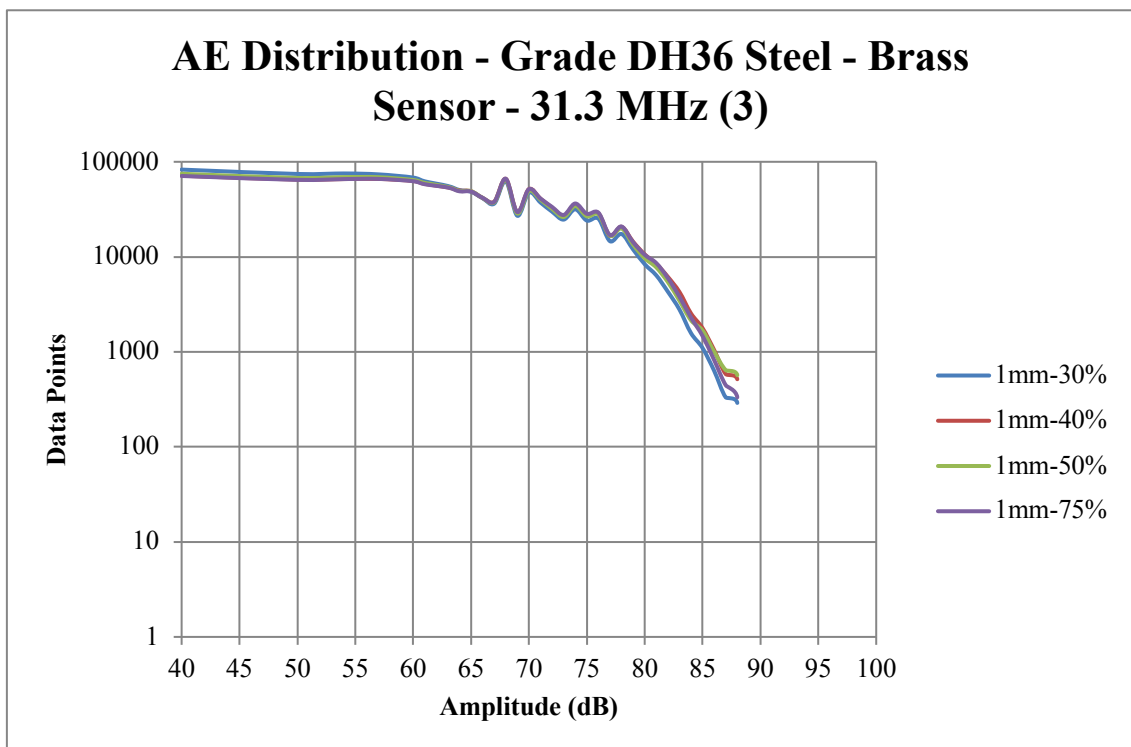


Figure 6.46: AE Distribution (1mm-30%, 1mm-40%, 1mm-50% and 1mm-75%)

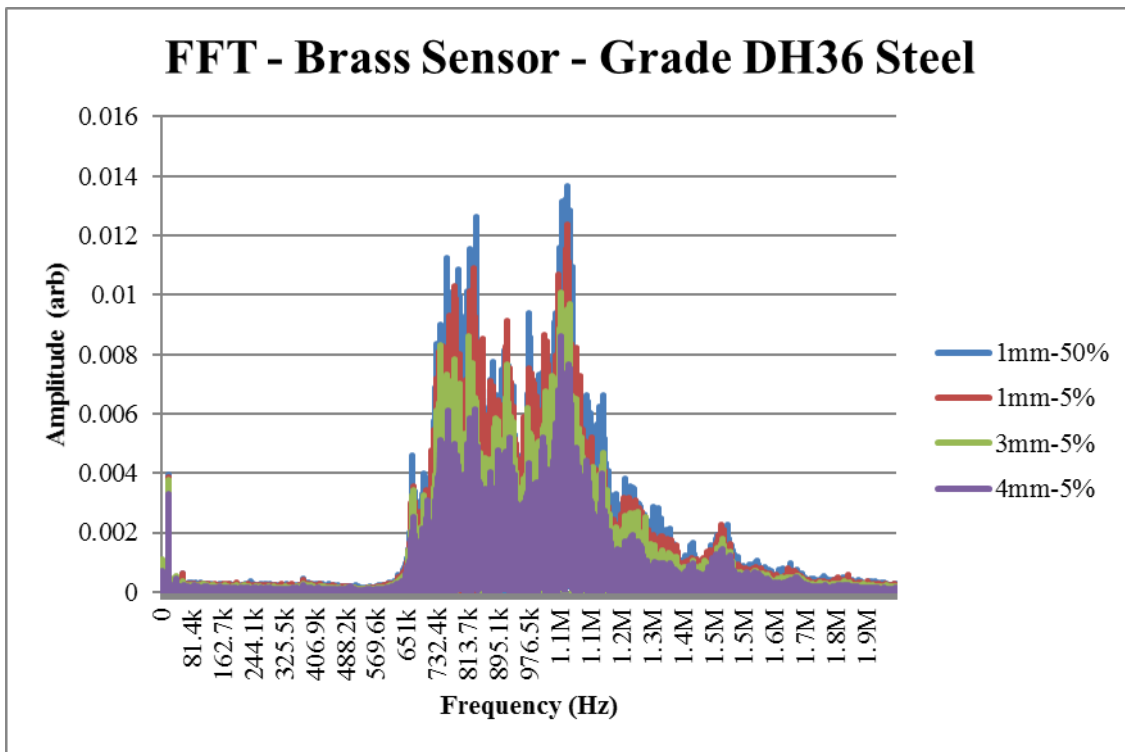


Figure 6.47: FFT – Brass Sensor – DH36 steel (4mm-5%, 3mm-5%, 1mm-5%, 1mm-50%).

PVDF sensor (± 0.016 dB) – 31.3 MHz. Figures 6.48, 6.49, 6.50 and 6.51.

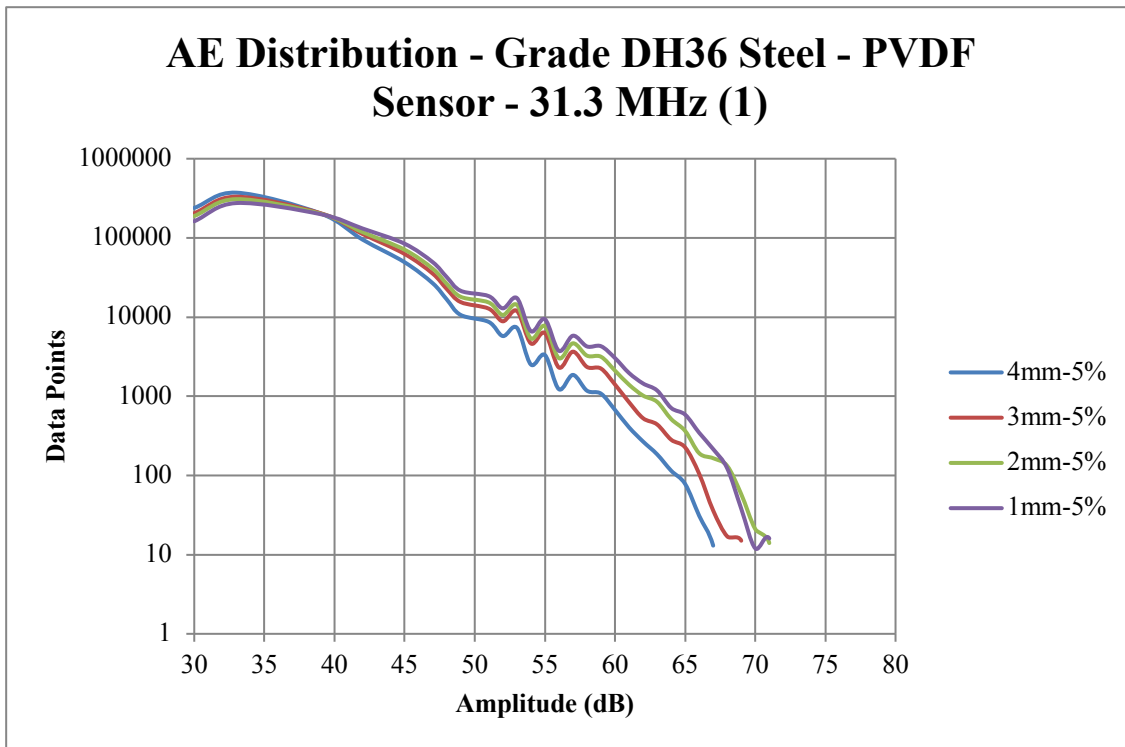


Figure 6.48: AE Distribution (4mm-5%, 3mm-5%, 2mm-5% and 1mm-5%)

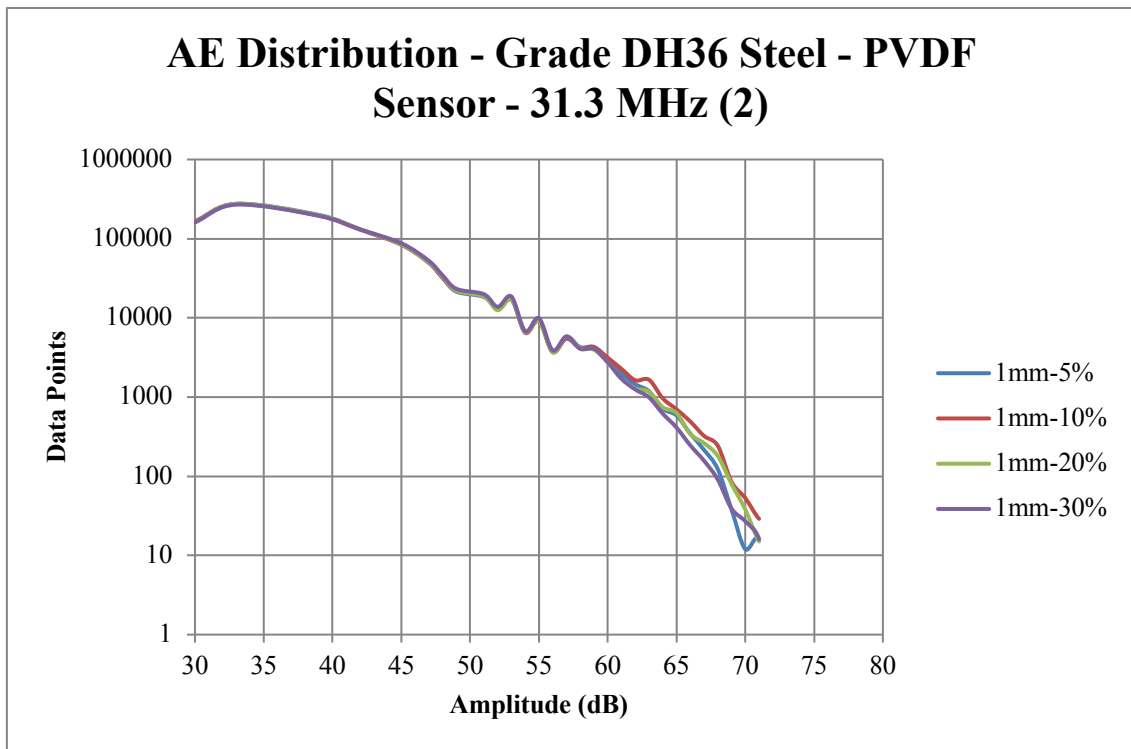


Figure 6.49: AE Distribution (1mm-5%, 1mm-10%, 1mm-20% and 1mm-30%)

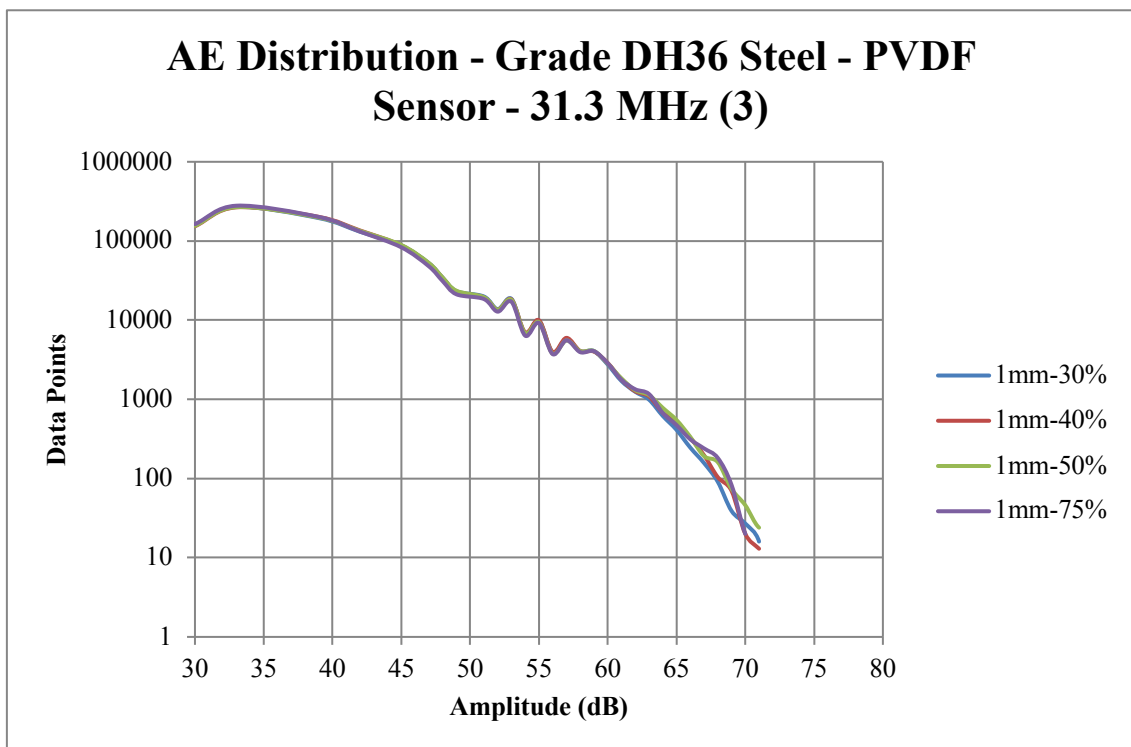


Figure 6.50: AE Distribution (1mm-30%, 1mm-40%, 1mm-50% and 1mm-75%)

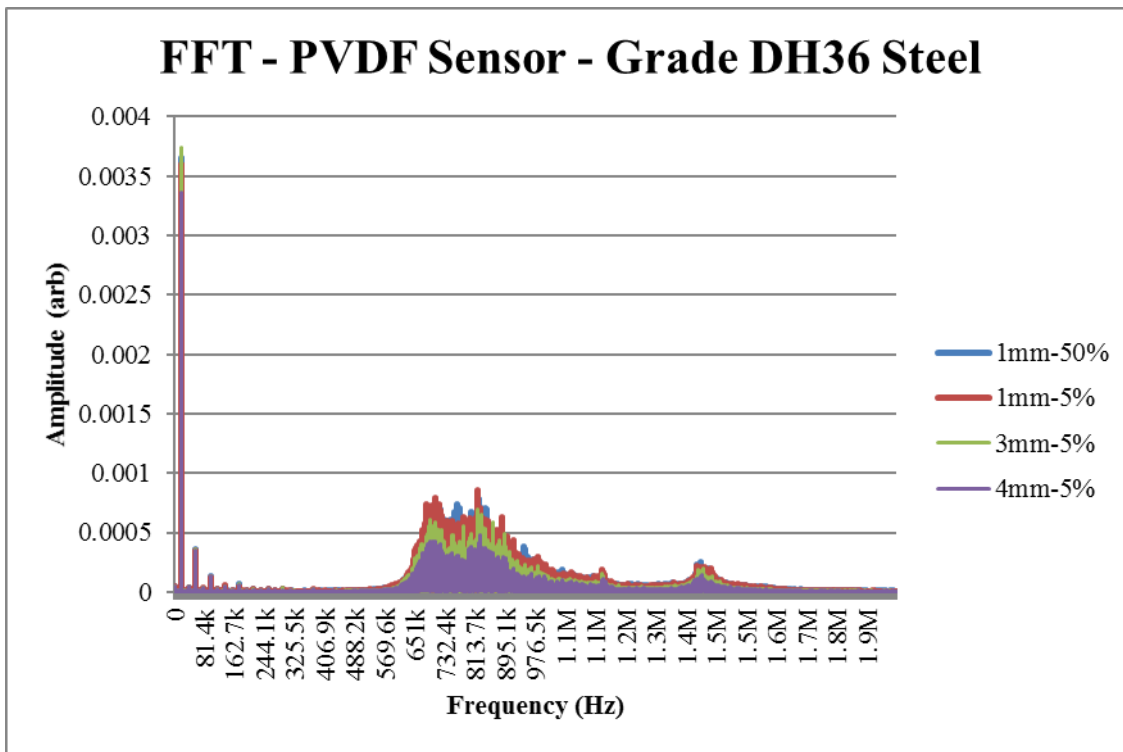


Figure 6.51: FFT – PVDF Sensor – DH36 steel (4mm-5%, 3mm-5%, 1mm-5%, 1mm-50%).

A different range of results was obtained, when acoustic emissions were captured by means of the Tektronix oscilloscope-based system at a sampling rate of 31.3 MHz. In this case, acoustic emission distribution curves are more dispersed for different gaps whereas they tend to come closer and become identical for a steady gap of 1mm and different power settings. This is due to the high sampling rate not allowing high energy collapsing events than normally appear at lower rates to be captured. It is also noteworthy that the transition point between ‘non-erosive’ and ‘erosive’ cavitation is evident for all sensors, although not as clearly as with the previous method. In addition, the appearance of the AE distributions is entirely different in comparison to the previous method (logarithmic peak detector and NI DAQ), mainly because they consist of raw acoustic signals instead of the waveform peaks solely. In terms of amplitudes, however, all sensors exhibited a similar to the previous method behaviour in the sense that the stronger acoustic signals were obtained when measurements were conducted with the brass sensor, followed by the aluminium sensor and finally the PVDF sensor.

The key points regarding the behaviour of the acoustic sensors in conjunction with the Tektronix oscilloscope, for a variety of test rig configurations, are the following:

Aluminium sensor with Tektronix oscilloscope:

- AE amplitudes ranging between 40 dB (preamplifier gain) and 88 dB.
- AE distribution curves are identical for different power settings and a steady gap (1mm). In contrast, AE distribution curves are more dispersed around the transition point between ‘non-erosive’ and ‘erosive’ cavitation.
- The transition point between ‘non-erosive’ and ‘erosive’ cavitation is of the order of 85 dB, similar to the value that was obtained with the previous method.

Brass sensor with Tektronix oscilloscope:

- AE amplitudes ranging between 40 dB (preamplifier gain) and 88 dB.
- AE distribution curves are similar to the aluminium sensor, thus they appear to be identical for different power settings and dispersed for different gaps.
- The transition point between ‘non-erosive’ and ‘erosive’ cavitation is 88 dB in contrast to the range of 93 - 96 dB that was obtained though the previous method.
- Interestingly, amplitudes would not change, above the transition point.

PVDF sensor with Tektronix oscilloscope:

- AE amplitudes ranging between 40 dB (Preamplifier gain) and 71 dB.
- Similarly to the other sensors, AE distribution curves are identical for different power settings and dispersed for different gaps.
- The transition point between ‘non-erosive’ and ‘erosive’ cavitation is 69 dB in contrast to the range of 57 to 60 dB that was obtained though the previous method.

Finally, a fast Fourier transform (FFT) analysis was performed on raw acoustic signals, that were obtained by means of all acoustic sensors in conjunction with the Tektronix oscilloscope. Results indicate that a 19.5 kHz resonance, along with its harmonics, is apparent in all cases and is possibly related to the ultrasonic transducer as it matches its operating frequency. Interestingly, the amplitude of that resonance varies with cavitation intensity.

Another interesting region of the FFT spectra lies between 600 kHz and 1.8 MHz. Resonances within that region are related to the sensors themselves and essentially consist of natural frequencies that are excited by cavitation activity. In addition, resonances within that region are further amplified by the preamplifier, of which the high-pass filter has a cut-off frequency of 850 kHz. Furthermore, and similarly to the 19.5 kHz resonance, the amplitude of those resonances appears to be directly influenced by the test rig configuration, hence the resulting cavitation intensity, although in this case amplitude differences are even higher.

Finally, it can be seen that the amplitudes of the recorded resonances on the FFT graphs vary with regards to the acoustic sensor type that was utilized. In this context, the strongest amplitudes were obtained for the brass sensor followed by the aluminium sensor and the PVDF sensor, similarly to the previously reported acoustic emissions measurements.

6.7 Cavitation related acoustic emissions (all alloys) - Comparison

Acoustic emission (AE) measurements were also conducted with regards to stainless steel 254 and cupronickel 70-30. Similarly to the tests that were conducted on grade DH36 steel, some preliminary mass loss measurements were conducted, in order for the transition point between ‘non-erosive’ and ‘erosive’ cavitation to be found for each of the examined alloys. Mass loss results for cupronickel 70-30 and stainless steel 254 can be seen in Figure 6.52 and 6.53:

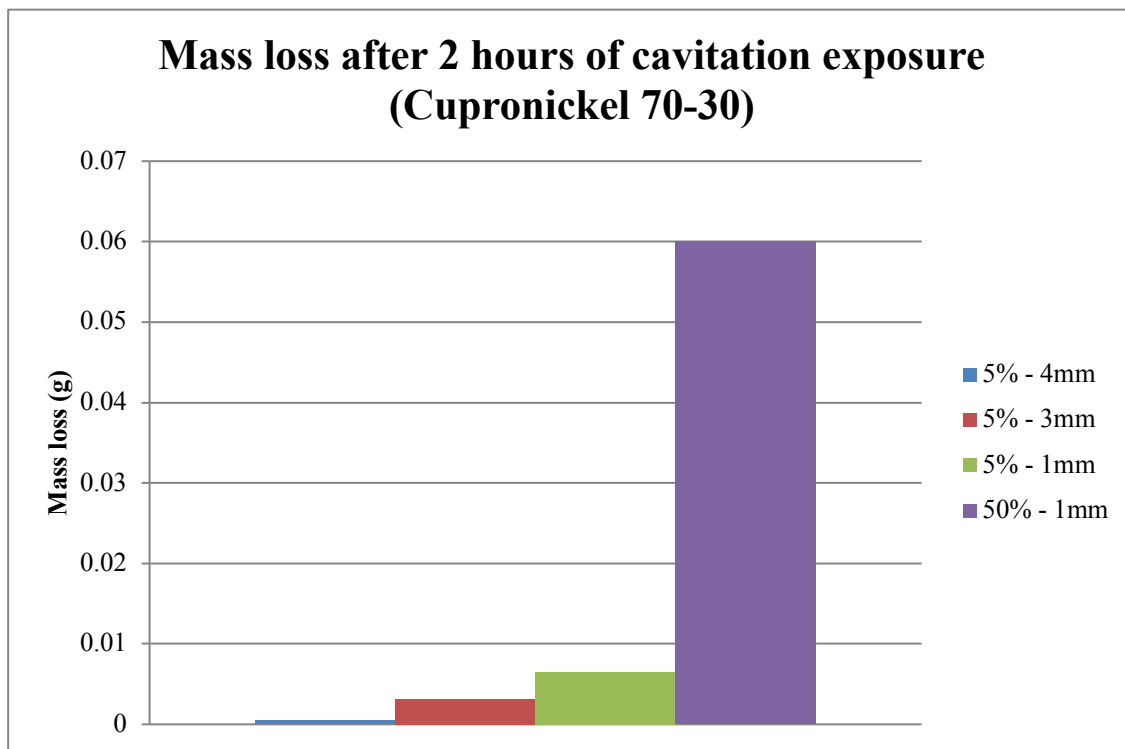


Figure 6.52: Mass loss of cupronickel 70 -30 for various test rig configurations

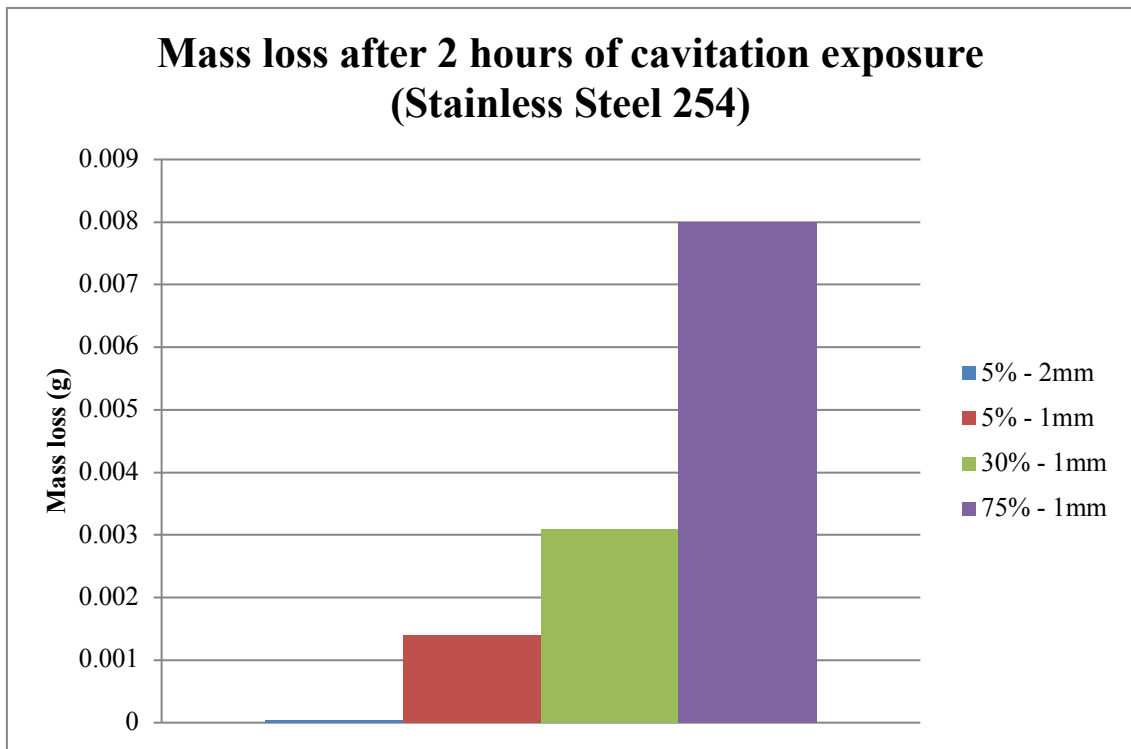


Figure 6.53: Mass loss of stainless steel 254 for various test rig configurations

The ultrasonic transducer was operated for a period of two hours and mass loss measurements were taken every thirty minutes thus it was found that the ‘non-erosive’ test rig configuration for cupronickel 70-30 and stainless steel 254 is 4mm - 5% (50W) and 2mm – 5% (50W), respectively. Moreover, it was found that the next, ‘slightly erosive’ configuration, for cupronickel 70-30 and stainless steel 254 is, 3mm – 5% (50W) and 1mm – 5% (50W), respectively. It should be noted, however, that in contrast to preliminary measurements conducted on grade DH36 steel, only four basic different test rig configurations corresponding to different erosion levels, ranging from ‘non-erosive’ to ‘highly erosive’, were examined in the case of cupronickel 70-30 and stainless steel 254, for ease of comparison.

As such, acoustic emission measurements were taken for each one of the examined alloys, with regards to those four different test rig configurations, resulting into the induction of cavitation of varying intensity (no-erosion, light erosion, medium erosion, high erosion). For comparison reasons, distribution graphs corresponding to the acoustic emissions of grade DH36 steel are also presented, however, in this case, only four different test rig configurations leading to analogous erosion levels are presented, similarly to the other alloys.

Measurements were conducted using the aluminium sensor as it was previously found to offer a clear resolution of the resulting acoustic emissions, especially around the transition point between ‘non-erosive’ and ‘slightly erosive’ cavitation. In contrast, the transition point, when

acoustic emissions were captured by means of the brass and PVDF sensor, was either not evident or rather difficult to be identified due to the indeterminate with respect to power settings appearance of the distribution curves. It should be noted that a sampling rate of 100 kHz would have to be utilized in the case of aluminium sensor, in order for the transition point to be identified whereas for all other sampling rates curves are identical, similarly to the other sensors. It appears that a sampling rate of 100 kHz allows for collapsing events directly related to the operating frequency of the sonotrode (20 kHz) to be identified and is a good match to the unique characteristics of the particular sensor in the sense that a clear resolution of the measured acoustic emissions is offered under those conditions.

Finally, with regards to the signal capturing system, acoustic emissions were captured by means of the logarithmic peak detector and NI DAQ the reason being that, only the peaks of the resulting waveform are captured and amplified this way, instead of the whole raw signal. The benefits of this method can be seen in the resolution of the resulting acoustic emission distribution curves which is much clearer in comparison to the Tektronix oscilloscope method. Comparative results for all alloys can be seen in Figures 6.54, 6.55 and 6.56 (± 0.007 dB at a 95 % confidence level):

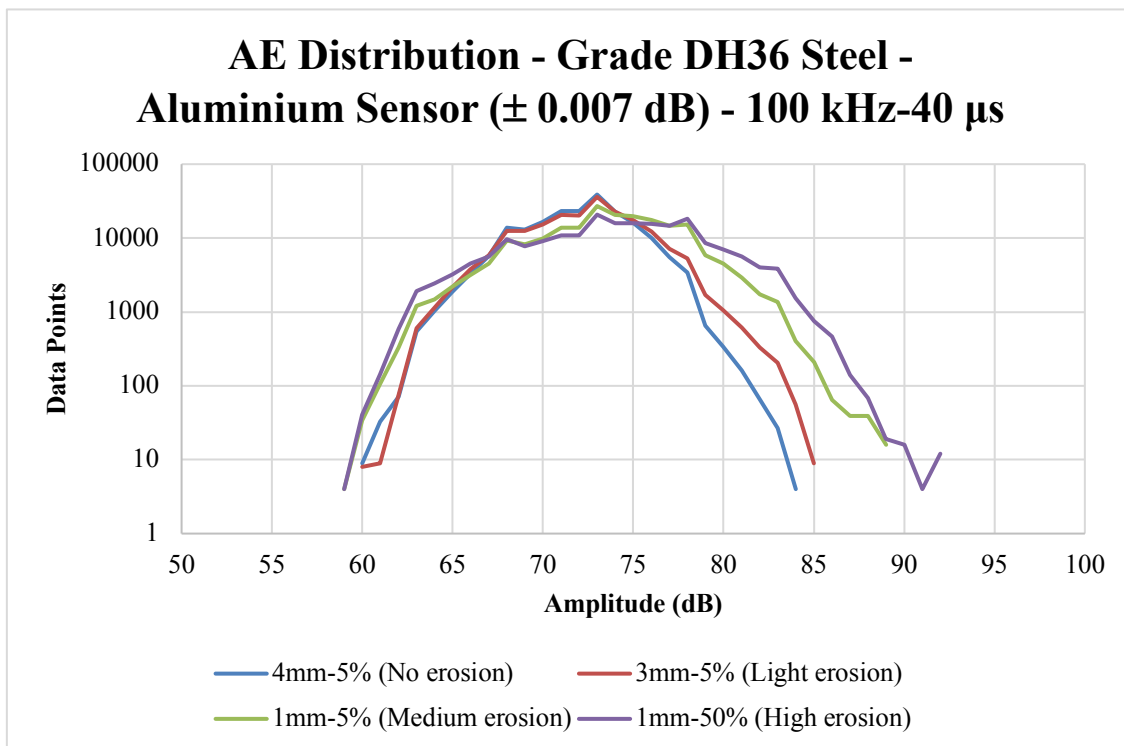


Figure 6.54: AE Distribution - Grade DH36 steel

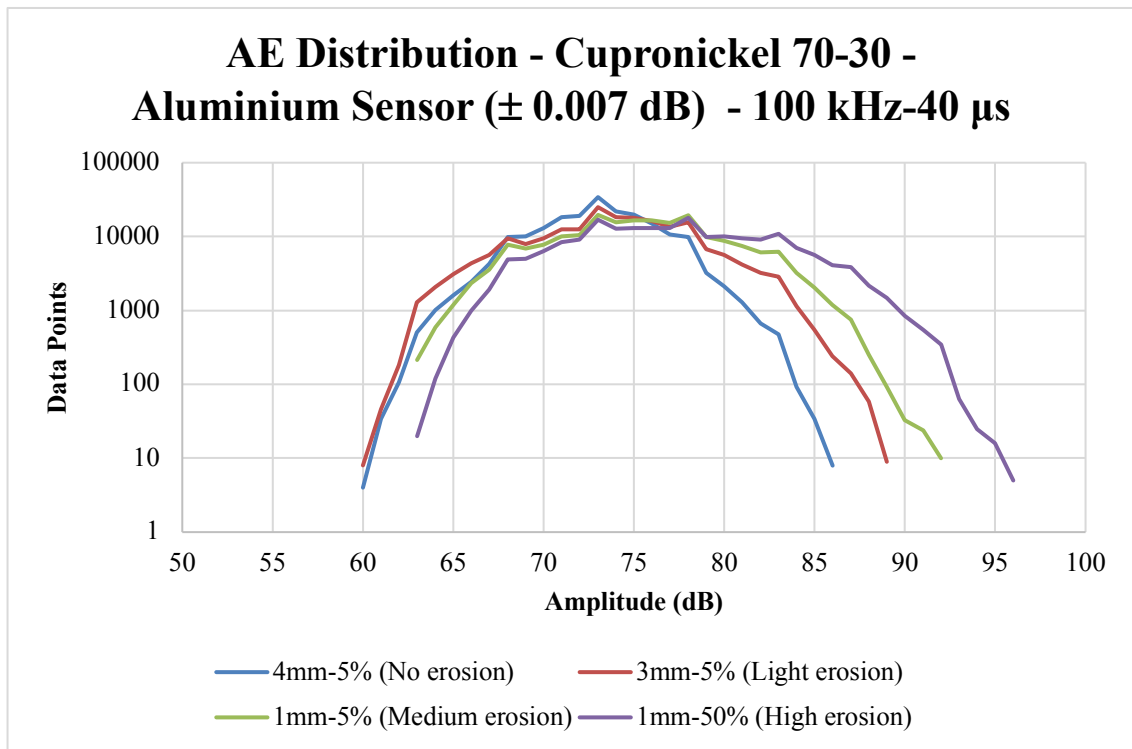


Figure 6.55: AE Distribution – Cupronickel 70-30

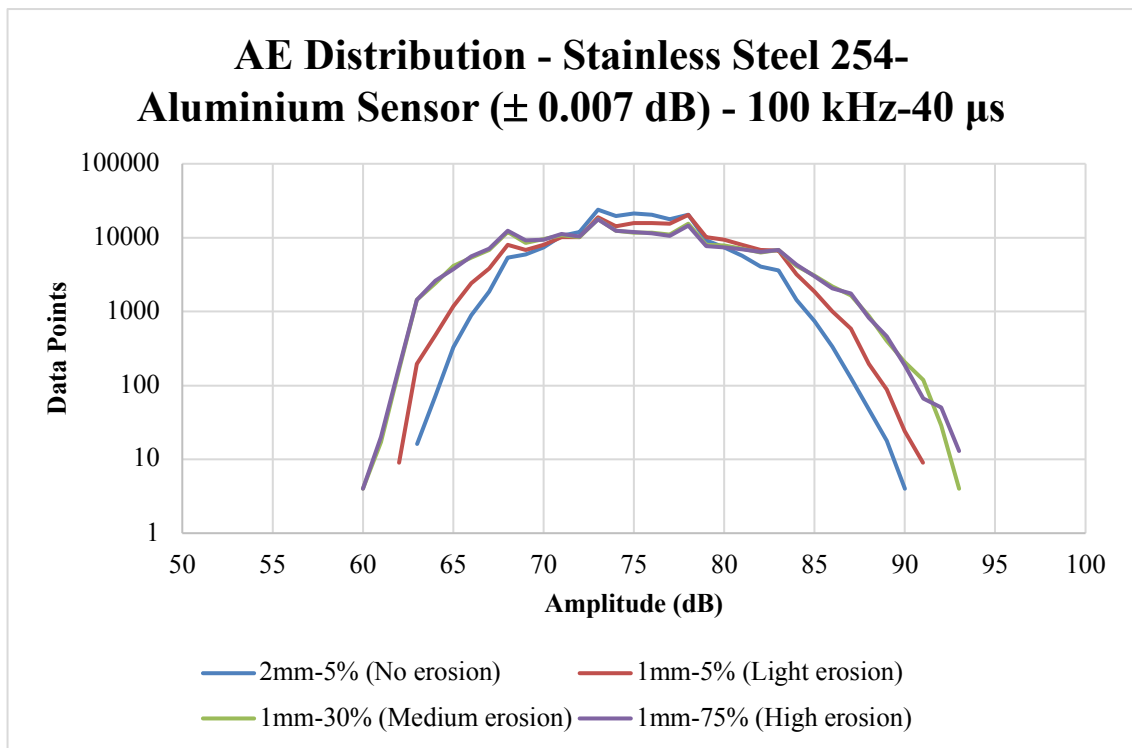


Figure 6.56: AE Distribution – Stainless steel 254

It appears that, the transition point between ‘non-erosive’ and ‘erosive’ cavitation can be clearly identified for all alloys. In particular, the transition point for grade DH36 steel is 85 dB, whereas the corresponding values for cupronickel 70-30 and stainless steel 254 are 89 and

91 dB, respectively. Moreover, the acoustic emission amplitude for the ‘non-erosive’ configuration, is of the order of 84 dB for grade DH36 steel, 86 dB for cupronickel 70-30 and 90 dB for stainless steel 254. Finally, it appears that, test rig configurations leading to cavitation of high intensity, are clearly represented by means of the relevant acoustic emission distribution curves, for all alloys.

The observed variations between different alloys, in terms of acoustic emission power, can be attributed to their dissimilar microscopic structure and mechanical properties. As such it appears that, for an acoustic sensing system to be properly calibrated and for acoustic emission measurements to be conducted accurately one has to consider not only the properties of the system, such as the acoustic sensor type and the sampling rate, but the properties of the material to be measured as well. Nevertheless, once an initial calibration, taking into consideration all parameters, has been made, the measured acoustic emissions can give valuable information with regards to cavitation intensity and even the resulting erosion, in the cases where the relevant data is available.

6.8 Conversion of acoustic emissions into stress- Principles

Acoustic emissions are defined as the elastic stress waves that, originate from rapid energy releasing events inside a material due to applied stress. Considering that the generated electric charge from a piezoelectric acoustic sensor, that is attached on the material, is proportional to the amplitude of those elastic waves and assuming that an initial calibration has been performed, by means of using a known load on the surface of the examined material, one can translate acoustic emission signals (voltage) into applied stress values. For materials of which the mechanical properties are known, the conversion of acoustic emissions into the corresponding applied stress values, can stand as a valuable tool for erosion estimation.

Acoustic sensors essentially consist of piezoelectric elements, thus any applied force or incoming stress wave results into the generation of electric charge. The amount of electric charge that is generated is strictly proportional to the applied force whereas the behaviour of the piezoelectric crystal is linear, thus when the input force is doubled the resulting electrical signal will also double. The ratio (output voltage) / (input force) can be defined as the sensitivity of the sensor which is constant for most piezoelectric elements with regards to a broad range of applied forces.

In order for the linear behaviour of the piezoelectric sensor to be utilized properly, however, an accurate initial calibration is required, for the sensitivity of the sensor in the specific

application to specified. This essentially consists of the relationship between the induced load – applied stress on the examined material, which is then released from it in the form of elastic stress waves, and the output voltage of the attached sensor, therefore a known load must be induced on the surface of the examined material.

One of the most common calibration methods is based on the fracture of a 0.5mm diameter 2H graphite lead on the surface of the examined material at an angle of 45° with the acoustic sensor attached on the opposite side. The pencil lead break is known as a Hsu – Nielsen source and is regarded as a fast, accurate and reproducible means of conducting initial calibration that is very representative of real AE sources. In particular, the pencil lead fracture induces rapid energy releasing events inside the material, due to the applied stress, which then excite the sensor and produce electric charge. The force required for the fracture of a 2mm long and 0.5 mm wide 2H graphite lead is 1 N and is regarded as a single H-N unit. Considering that the contact area at the tip of the pencil is approximately $2 \times 10^{-8} \text{ m}^2$, a single H-N unit equals to an induced mechanical stress of the order of approximately 0.05 GPa.

As such, during the initial calibration of each sensor using a Hsu – Nielsen source, the maximum amplitude of the resulting acoustic emission signal (voltage), related to the main energy releasing event, is noted and assigned to the already calculated applied stress (0.05 GPa). It should be noted that the resulting signal is composed of many different energy releasing events, as a result of the pencil induced stress, of which the amplitude is significantly lower than the main event's and as such they are neglected.

Cavitation is characterized by numerous imploding cavities that induce stress on the surface of the exposed material thus the generated acoustic emissions, in the form of electrical signals from the attached sensor, essentially represent energy releasing events from that material. These events are either the result of individually or collectively imploding cavities. Considering the numerous implosions that characterize cavitation, however, one can assume that each acquired voltage – energy releasing event is essentially induced by means of collectively collapsing cavities. Based on the linear behaviour of the piezoelectric element and considering that, the relationship between an applied stress on the surface that results into an event which then excites the sensor, and the acquired voltage, is known from the initial calibration, one can assign each captured voltage into a cavitation induced applied stress value.

Acoustic emission signals caused by cavitation, however, are much richer and denser compared to the ones from the initial calibration, due to the numerous imploding cavities on

the surface of the material inducing several energy releasing events inside the material. One could therefore describe cavitation impact as a series of numerous and in many cases simultaneous pencil lead fractures of different amplitudes, in the sense that the variety of the collapsing cavities in terms of impact force and contact area results into energy releasing events of varying amplitudes inside the material. Nevertheless, those acoustic emission signals will be translated into induced applied stresses but instead of examining each stress value individually, which was the case for the initial calibration, the distribution of them will be calculated and studied.

6.9 Conversion of acoustic emissions to stress- Procedure and results- Grade DH36 steel

Acoustic emission signals were captured by means of three different acoustic sensors, similarly to the former acoustic emission measurements. In particular, the following were utilized:

- Aluminium sensor
- Brass sensor
- PVDF sensor

Acoustic emission signals were captured by means of two sensing systems, namely:

- A logarithmic peak detector and a NI DAQ at a sampling rate of 100 kHz and a 40 μ s time hold frame, for which the transition point between ‘non-erosive’ and ‘erosive’ cavitation was identifiable for all acoustic sensors.
- A Tektronix oscilloscope at a sampling rate of 31.3 MHz.

All data was further processed and converted into the corresponding stress distributions by means of an Excel – based software. Results are presented below, categorized with regards to the sensing system and the sensor type.

1. Logarithmic Peak Detector and NI DAQ sensing system (LPD)

Four test rig configurations were examined as follows:

- 4mm gap and a 5% (50W) sonotrode power output – “No erosion” after 2 hours.
- 3mm gap and a 5% (50W) sonotrode power output – Light erosion after 2 hours.
- 1mm gap and a 5% (50W) sonotrode power output – Medium erosion after 2 hours.
- 1mm gap and a 50% (500W) sonotrode power output – High erosion after 2 hours.

The logarithmic peak detector essentially tracks the peaks (maximum amplitude) of the acoustic waveform and holds them for an adjustable time frame of 40 μ s to 1ms. As such, only the maximum amplitudes (peaks) related to energy releasing events, instead of the whole raw waveform, are identified and captured.

Due to the nature of the logarithmic peak detector, however, those amplitude peaks (voltages) are logarithmically converted inside the unit. This happens, so that signals can be converted into the relevant acoustic power (dB) units by means of the linear equation (6.29) that was mentioned in *sub-chapter 6.6*, as follows:

$$Y = 44.035X - 9.7032 \quad (6.29)$$

Which is an equation of the form:

$$Y = A X + B$$

where Y is the acoustic power (dB), X is the logarithmically converted amplitude (V) and A (= 44.035), B (= 9.7032) are constants provided by the initial calibration of the unit.

Conversion of voltages into stresses however, is based on the linear behavior of the piezoelectric elements. As such, only a linear range of amplitudes can be used for this conversion instead of the logarithmic output of the logarithmic peak detector. Therefore, the logarithmically converted range of peak amplitudes was converted to the equivalent linear one by means of equation (6.31) on which the unit's logarithmic conversion is based:

$$X = C \ln\left(\frac{V}{V_r}\right) \quad (6.31)$$

Or,

$$V = \exp\left(\frac{X}{C} + \ln V_r\right)$$

where X is the logarithmically converted amplitude, V is the raw linear amplitude, C the characteristic conversion constant of the unit that was calculated by measuring the signal before - after the logarithmic peak detector and V_r the input voltage of the preamplifier (0.0001 V).

By applying a load on the surface of one of the sensors, by means of a Hsu – Nielsen source, and by measuring the maximum amplitude of the resulting acoustic emission signal, before - after the logarithmic peak detector, the constant C was identified and was of the order of 0.25.

Afterwards, once peak acoustic emission signals from the logarithmic peak detector were converted into the corresponding linear values, they were further converted into stresses by means of the linear equation (6.32):

$$\sigma = K_s V \quad (6.32)$$

where K_s is the applied stress on the material's surface – generated electric charge coefficient of each sensor found from the initial calibration, V is the acquired linear peak voltage and σ is the corresponding applied stress. Initial calibration using the Hsu-Nielsen source (0.05 GPa stress pulse) provided the K_s constant for each one of the sensors.

A 100 KHz sampling rate and a 40 μ s time frame were chosen for this study, as these were the only DAQ settings for which the transition point between 'non-erosive' and erosive cavitation was identifiable for all sensors. Stress data were plotted onto amplitude distribution graphs, and are presented in Figures 6.57, 6.58 and 6.59. The measurement uncertainty, at a 95% confidence level, is also plotted onto the graphs.

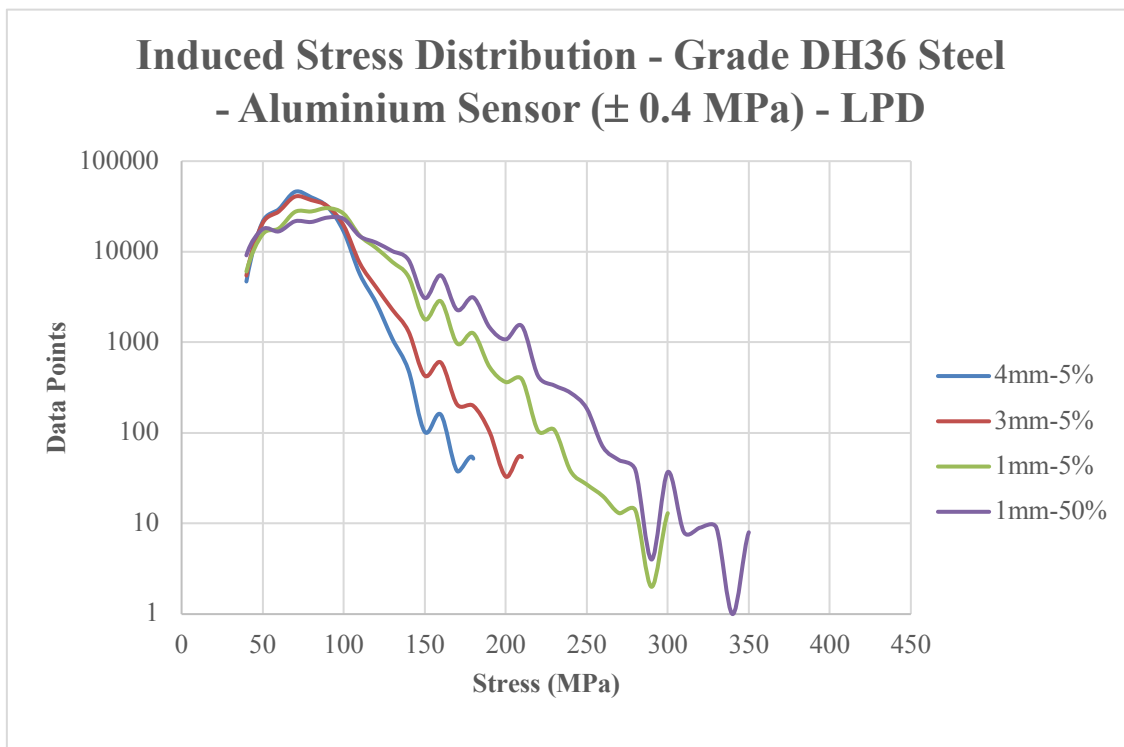


Figure 6.57: Stress distribution for grade DH36 steel. Aluminium sensor (LPD)

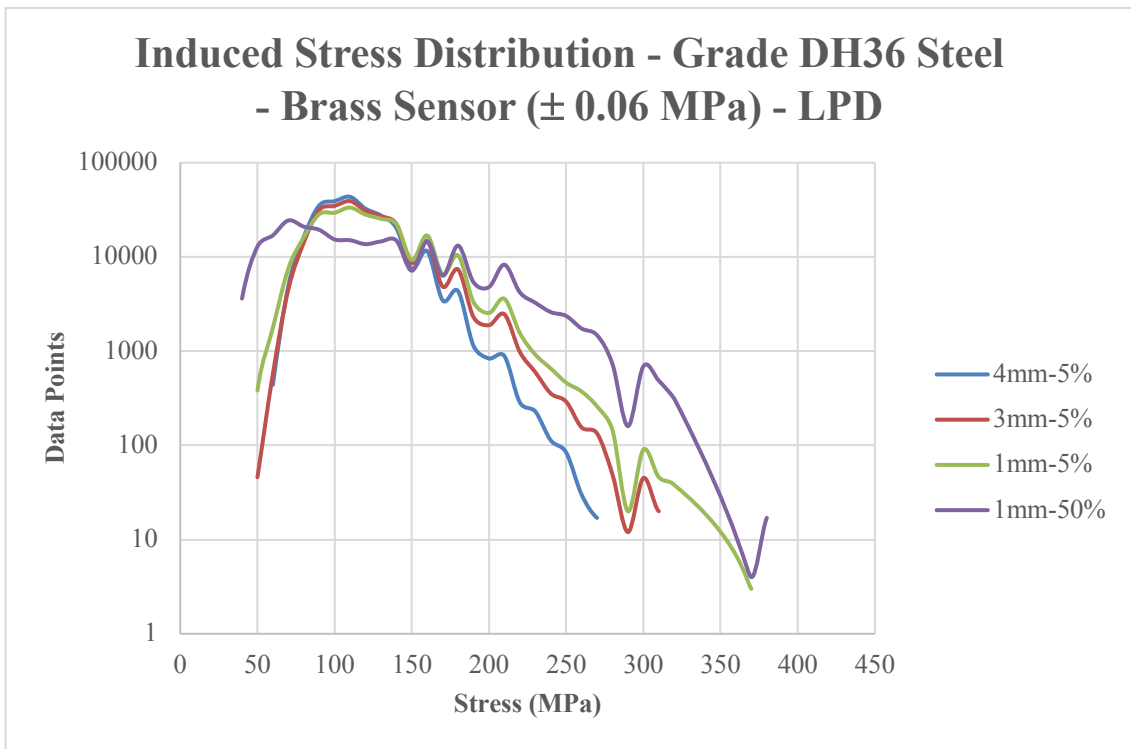


Figure 6.58: Stress distribution for grade DH36 steel. Brass sensor (LPD)

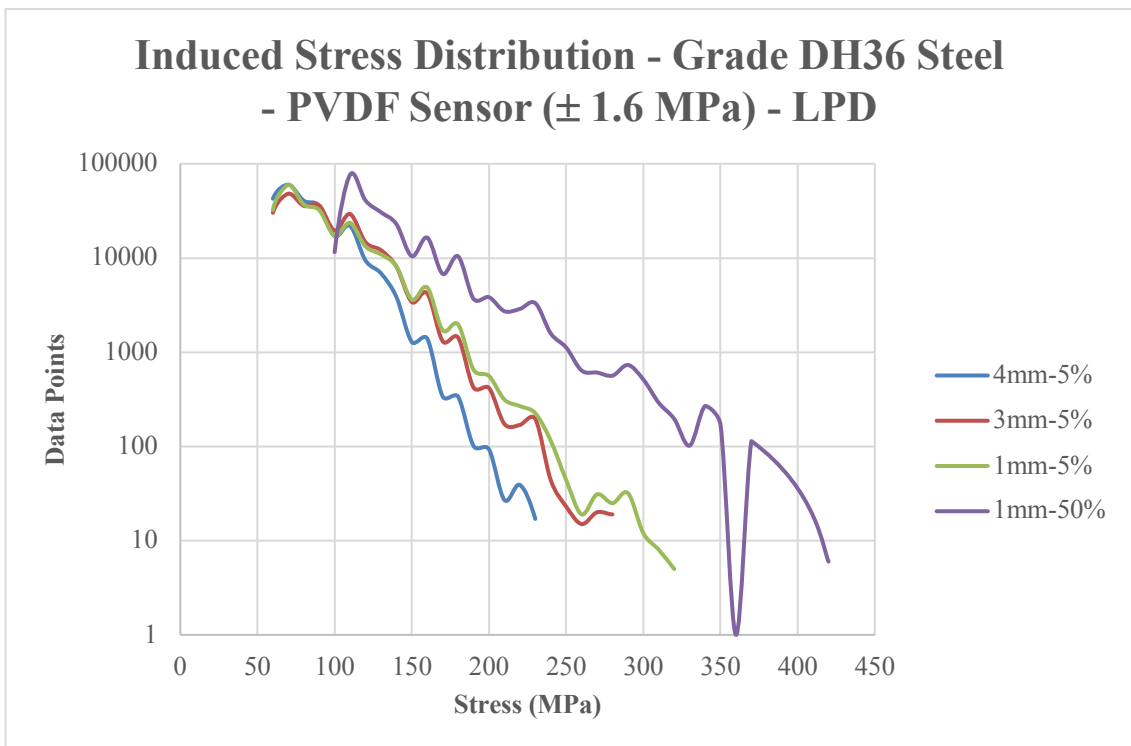


Figure 6.59: Stress distribution for grade DH36 steel. PVDF sensor (LPD)

2. Tektronix Oscilloscope based sensing system (TO)

Four different test rig configurations were also examined in the case of the Tektronix oscilloscope-based system as follows:

- 4mm gap and a 5% (50W) sonotrode power output – “No erosion” after 2 hours.
- 3mm gap and a 5% (50W) sonotrode power output – Light erosion after 2 hours.
- 1mm gap and a 5% (50W) sonotrode power output – Medium erosion after 2 hours.
- 1mm gap and a 50% (500W) sonotrode power output – High erosion after 2 hours.

In this case, however, only raw acoustic emission signals were captured. As such, considering the linear nature of the piezoelectric elements, no conversion similar to the one conducted for the logarithmic peak detector – based system was required. Linear raw acoustic signals were directly converted into stress by means of the linear equation (6.32):

$$\begin{aligned} \sigma \\ = K_s V \end{aligned} \tag{6.32}$$

where K_s is the applied stress on the material’s surface – generated electric charge coefficient of each sensor, V is the linear voltage and σ is the induced stress. Initial calibration using the Hsu-Nielsen source (0.05 GPa stress pulse) provided the K_s constant for each sensor.

Similarly to the previous method, applied stress values were plotted onto amplitude distribution graphs and are presented in Figures 6.60, 6.61 and 6.62, along with the measurement uncertainty at a 95% confidence level.

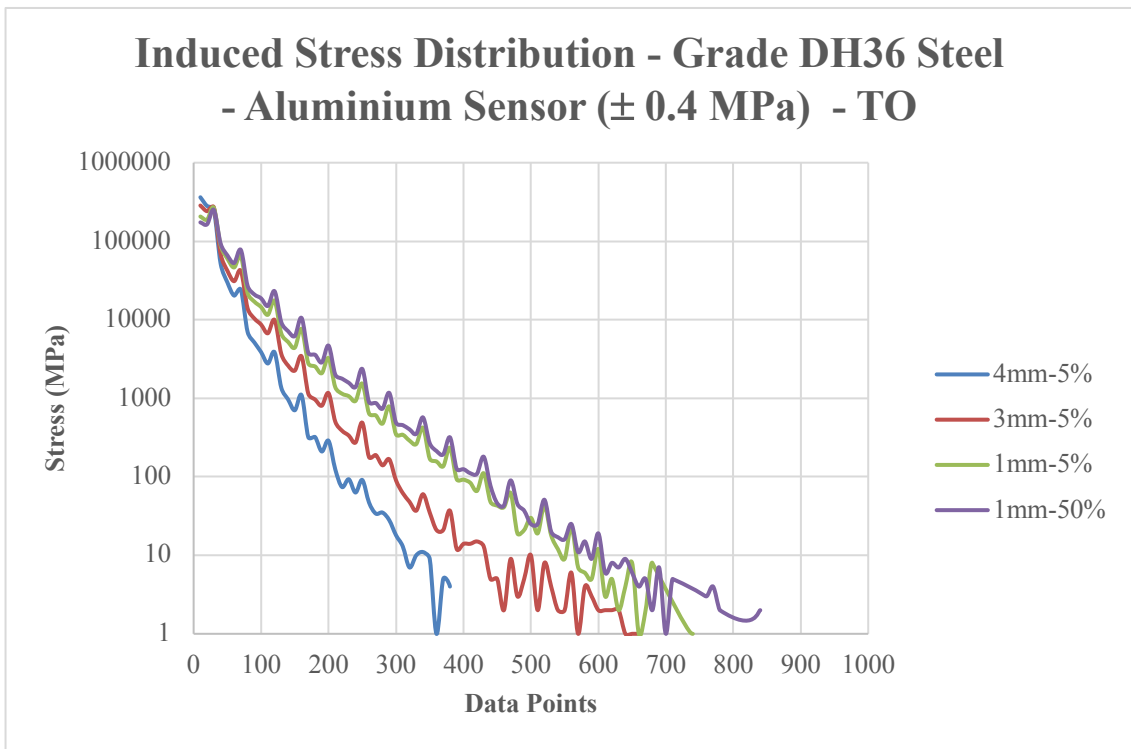


Figure 6.60: Induced stress distribution for grade DH36 steel. Aluminium sensor (TO)

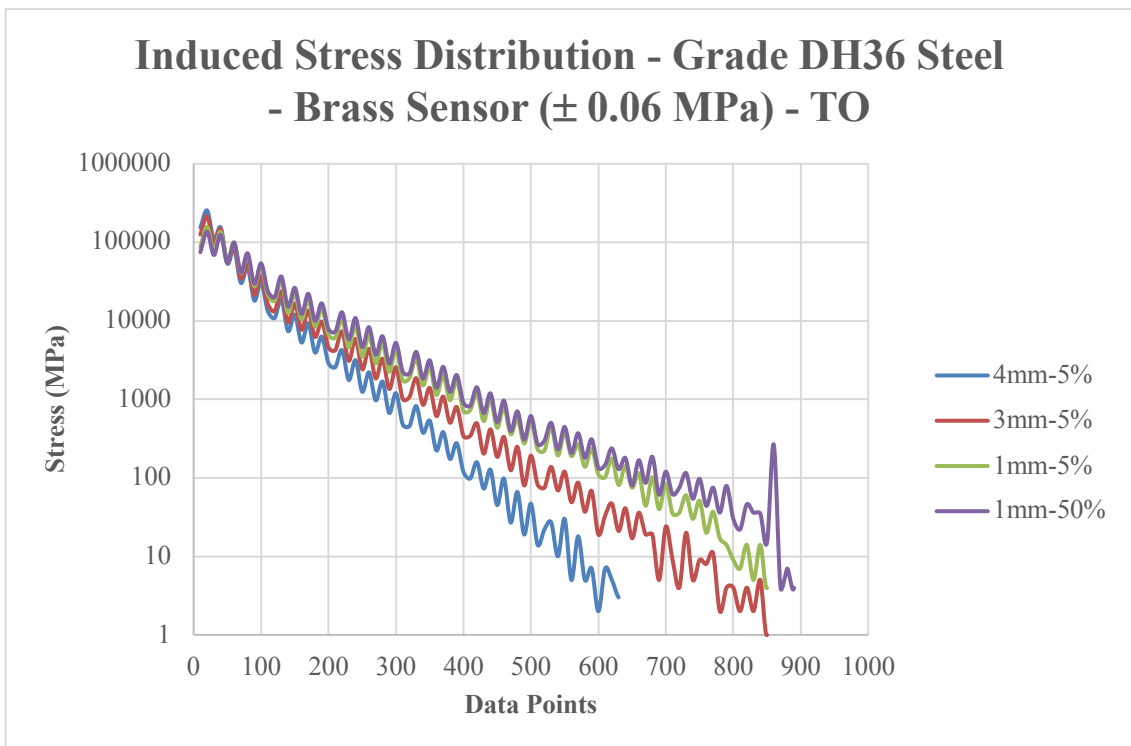


Figure 6.61: Induced stress distribution for grade DH36 steel. Brass sensor (TO)

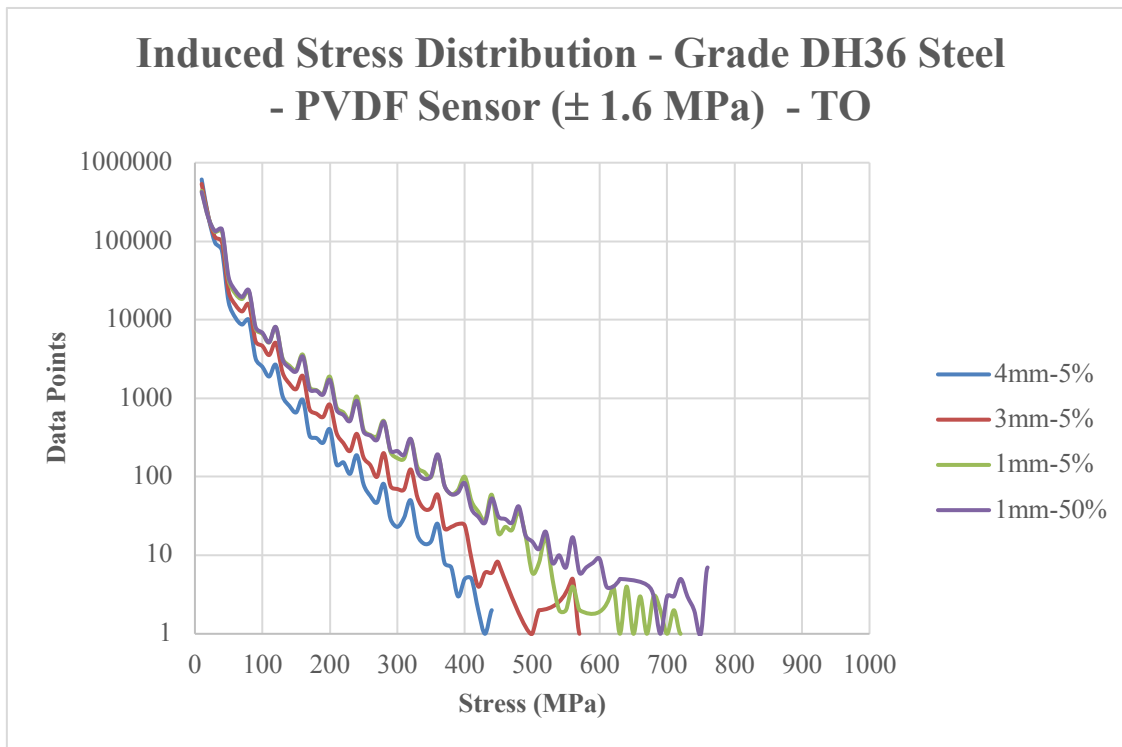


Figure 6.62: Induced stress distribution for grade DH36 steel. PVDF sensor (TO)

The importance of Figures 6.57 through to 6.62 is that they show that it is possible to distinguish between a cavitation scenario which is ‘non – erosive’ or erosive, similarly to the former acoustic power measurements. However, it appears from the results that the use of two different acoustic emission sensing systems – methods lead to a dissimilar range of stress distributions. Moreover, stress distribution data from the Tektronix oscilloscope method, was inconsistent between different sensors. Interestingly, distribution curves for the Tektronix oscilloscope – based system, appear to be following a sinusoidal pattern, whereas in the case of the logarithmic peak detector, curves are considerably smoother.

More specifically, stress values for the logarithmic peak detector – based system ranged from, 180-340 MPa for the aluminium sensor, 260-370 MPa for the Brass sensor and 240-420 MPa for the PVDF sensor. In this case, stress values are fairly close whilst all sensors appear to have essentially exhibited an almost linear behaviour with regards to the applied stresses.

In contrast, stress values obtained by means of the Tektronix oscilloscope – based system ranged from, 350-800 MPa for the aluminium sensor, 600-880 MPa for the brass sensor and 420-750 MPa for the PVDF sensor. Differences of that order, imply that the piezoelectric elements did not exhibit a linear behaviour with regards to the applied stresses, as it was expected. Considering that piezoelectric elements behave linearly for a broad range of frequencies and that each sensor was calibrated carefully by means of an identical source, it

was considered that such differences in the Tektronix oscilloscope – based system were due to the different characteristics of each piezoelectric element and the very high sampling rate. More specifically, it is a fact that the high natural frequencies of each sensor are excited by cavitation, thus the corresponding signals are essentially a combination of cavitation induced stress and resonances from each piezoelectric material. The use of a very high sampling frequency (31.3 MHz) in the oscilloscope method, therefore allowed for both types of signals to be captured.

According to the manufacturer of the sensors, strong high-frequency resonances were to be expected from the piezoelectric elements in the region between 600 kHz and 3 MHz. In addition, the High Pass filter of the preamplifier allowed for frequencies above 850 KHz to be further amplified. In fact, strong resonances in the region between 600 kHz and 1.2 MHz are apparent on all FFT graphs, of which the amplitude and specific frequencies depend on the sensor type. It should also be noted that those frequencies were apparent even when the sonotrode was not operating whilst their amplitude gradually increased with cavitation intensity. The latter also applies for the 19.5 kHz component and its related components.

It appears that signals obtained through the Tektronix oscilloscope – based system at a sampling rate of 31.3 MHz were essentially a combination of cavitation induced stresses and strong resonances from the sensors, as it can be seen in the FFT graphs in *sub-chapter 6.6*. This can explain why, although all sensors were calibrated with a known load, the resulting stress values varied significantly, thus their behaviour was not linear. It should also be noted that a 100 kHz sampling rate was also considered and tested with the Tektronix oscilloscope - based system, however the resulting signal was rather noisy and amplitude peaks could not be identified as accurately. As such it was decided that results obtained through the oscilloscope at very high sampling rates should be better utilized for fast Fourier transform (FFT) purposes.

Sensors exhibited a linear behaviour and stress values were almost identical, however, when acoustic emission signals were captured through the logarithmic peak detector at a sampling rate of 100 kHz. It can be seen in the FFT graphs of *sub-chapter 6.6* that for frequencies up to 100 kHz only the operating frequency of the sonotrode (19.5 kHz) along with its harmonics is apparent. As a result, stress distributions, in this case, are much more representative of cavitation induced loading, free of sensor related resonances. In addition, the behaviour of grade DH36 steel against cavitation, in terms of erosion, was in good agreement with the stress values obtained through the logarithmic peak detector in relation to its mechanical properties.

In particular, the yield strength of grade DH36 steel is 350 MPa whereas its ultimate strength ranges from 490-620 MPa, the former being the stress level at which the material starts to behave plastically and the latter the stress level at which the material will fail or fracture under quasi – steady conditions. Another important parameter is the endurance limit of the material, which is the cyclic stress that can be applied to the material without causing fatigue failure which in the case of grade DH36 steel is half its ultimate strength thus 245-310 MPa.

Results from the logarithmic peak detector – based system, indicate that stress values were just below the yield strength of DH36 steel (350 MPa), apart from the 1mm-50% configuration for which the obtained stresses were comparable (aluminium) or slightly exceeded this value (brass, PVDF). Moreover, results for all other test rig configurations including the ‘non erosive’ one, were comparable to the minimum endurance limit of steel (245 MPa). In particular stress values ranged from 180 to 260 MPa for the ‘non-erosive’ setting, whereas for the next ‘lightly erosive’ setting stress values ranged from 210 to 320 MPa, depending on the sensor type. Stress values generally increased with cavitation intensity whereas the maximum obtained stresses were of the order of 350 to 420 MPa. It should be noted that small variations between sensors indicate different sensitivity characteristics. Nevertheless, results are in good agreement with erosion - mass loss data, as well as the mechanical properties of the material whereas they also indicate the possible presence of fatigue failure in addition to plastic deformation and brittle fracture. In this context, the aluminium sensor appears to offer a clearer resolution of stress distribution curves in comparison to the brass and PVDF sensor.

6.10 Conversion of acoustic emissions to stress – Results – Cupronickel 70-30 and stainless steel 254

The acoustic emissions of cupronickel 70-30 and stainless steel 254 were also converted into stresses, by means of an identical to the grade DH36 steel, procedure. Acoustic emission signals were only captured through the logarithmic peak detector – based system, however, as it was previously shown by measurements conducted on grade DH36 steel, that a clear resolution of the resulting stress distribution curves is offered whereas the obtained stress values are consistent and in good agreement with the actual erosion of the material and its mechanical properties, especially in comparison to the Tektronix oscilloscope – based system. It should also be noted that in this case, only the aluminium sensor was utilized as it was found to offer a clearer resolution of the resulting distribution curves in comparison to the other two sensors.

Four test rig configurations were examined for cupronickel 70-30, as follows:

- 4mm gap and a 5% (50W) sonotrode power output – “No erosion” after 2 hours.
- 3mm gap and a 5% (50W) sonotrode power output – Light erosion after 2 hours.
- 1mm gap and a 5% (50W) sonotrode power output – Medium erosion after 2 hours.
- 1mm gap and a 50% (500W) sonotrode power output – High erosion after 2 hours.

In addition, four test rig configurations were examined for stainless steel 254, as follows:

- 2mm gap and a 5% (50W) sonotrode power output – “No erosion” after 2 hours.
- 1mm gap and a 5% (50W) sonotrode power output – Light erosion after 2 hours.
- 1mm gap and a 30% (50W) sonotrode power output – Medium erosion after 2 hours.
- 1mm gap and a 75% (500W) sonotrode power output – High erosion after 2 hours.

Acoustic emission signals were converted into stresses by means of the procedure described in *sub-chapter 6.9*. Results are again plotted onto comparative amplitude distribution graphs.

Stress distribution data for cupronickel 70-30 with regards to various test rig configurations is presented in Figure 6.63:

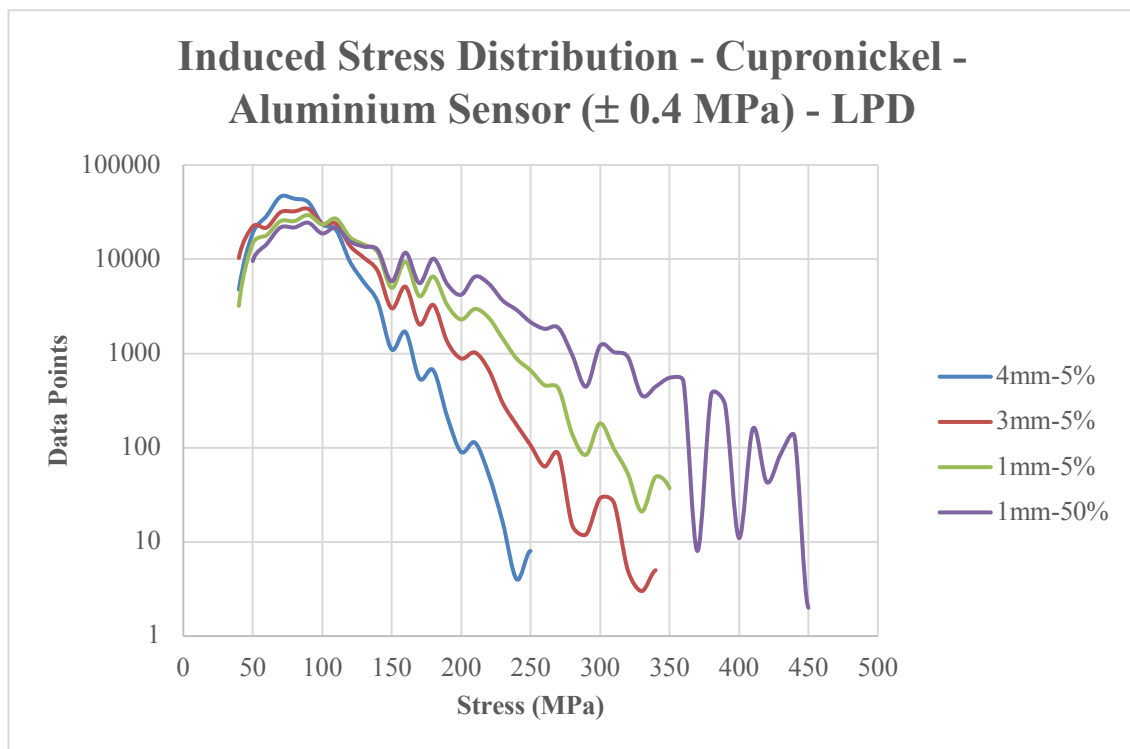


Figure 6.63: Induced stress distribution for cupronickel 70-30. Aluminium sensor (LPD)

The yield strength of cupronickel 70-30 is 130 MPa and its ultimate strength is 350 MPa. The endurance limit of copper alloys is approximately 0.4 times their ultimate strength, thus the relevant value in that case would be 140 MPa. It should be noted that this approximation is

optimal thus in general, real values could be even lower, mainly due to manufacturing flaws and cracks inside the material.

In this case, stress values for the non-erosive setting (4mm - 5%) are well above the theoretical yield strength of the material (130 MPa) and endurance limit (140 MPa). This implies that a considerable amount of plastic deformation took place, although it didn't result into measurable erosion – mass loss. In addition, fatigue fracture would possible occur if exposure was further prolonged, as the measured stresses are well above the endurance limit of the material. Stress values for the next 'light erosion' setting (3mm - 5%) are of the order of the ultimate strength (350 MPa) of the material. In this case, there was a small amount of measurable erosion – mass loss, thus a combination of plastic deformation and brittle fracture would be expected. The same applies for the next setting (1mm5%), for which the frequency of those stresses was even higher and as a result there was a considerable amount of measurable erosion. Finally, stresses were even higher for the last, most erosive, setting (1mm50%), implying the presence of significant brittle fracture in addition to plastic deformation.

It should be noted that in the case of cupronickel 70-30, the measured stresses were at least 100 MPa higher in comparison to grade DH36 steel, for all test rig configurations. Considering that, the induced cavitation forces were similar and that signals were captured by means of the same acoustic monitoring system, this difference could be attributed to the different structure of the materials. More specifically, it appears that the internal structure of cupronickel 70-30 'amplifies' the resulting stress waves, possibly due to internal flaws and specific structural characteristics. In particular, the ASTM grain size number of cupronickel 70-30 and grade DH36 steel is 7 and 12 respectively, suggesting a considerable difference with regards to the size of their grains and their boundaries. Subsequently the crack propagation paths and speeds would differ significantly, as well as the possible stress amplifying points. One should also consider the possible internal flaws and cracks inside the materials that act as stress concentrators and amplifiers. In general, however, results for cupronickel 70-30 are in good agreement with mass loss measurements and optical observations.

The stress distribution data of stainless steel 254 in relation to various test rig configurations is presented in Figure 6.64:

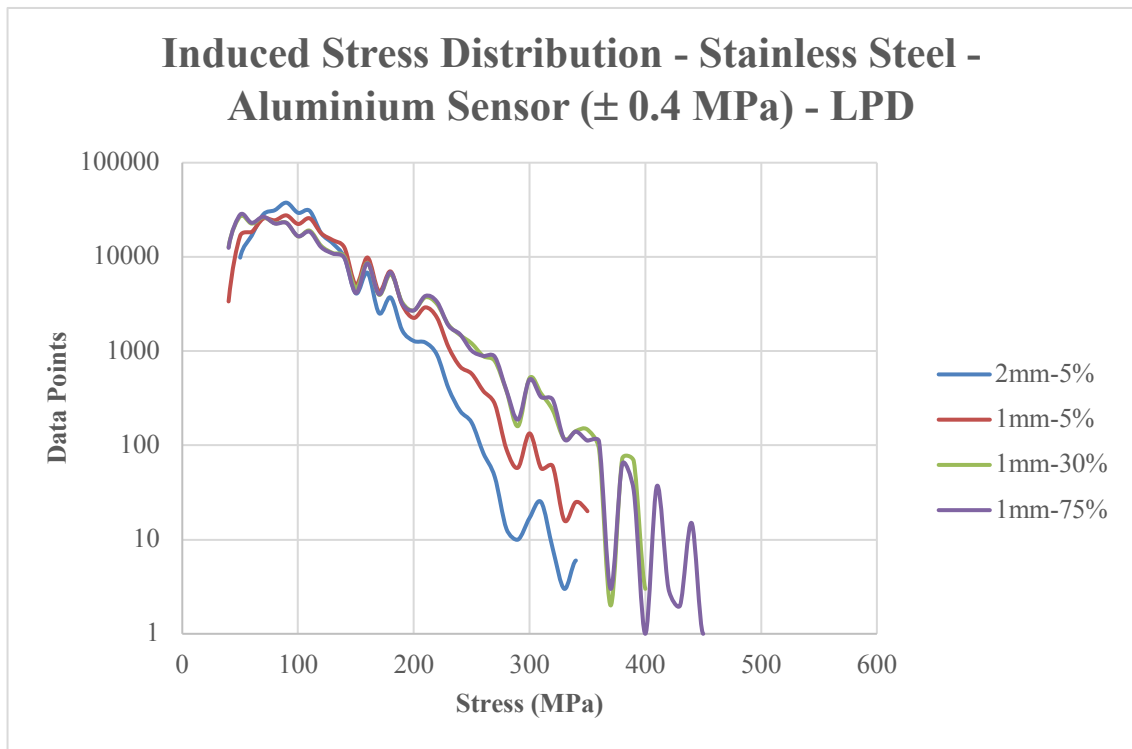


Figure 6.64: Induced stress distribution for stainless steel 254. Aluminium sensor (LPD)

The mechanical properties of stainless steel 254 suggest that it can withstand high loads before failing, especially when compared to the other two examined alloys and this was also confirmed by mass loss measurements and optical observations. In particular, the yield strength of stainless steel 254 is 310 MPa whereas its ultimate strength is 690 MPa. The endurance limit of stainless steel is approximately half its ultimate strength thus the relevant value would be 345 MPa. It should be noted again that these values are essentially theoretical whereas the real values could be even lower, mainly due to imperfections and internal flaws.

In the case of stainless steel 254, stress values for the non-erosive setting (2mm - 5%) were slightly above the yield strength of the material (345 MPa) and its endurance limit. This implies that although no erosion was apparent after two hours of exposure, both in visual and mass loss terms, the material would possibly fracture if exposed for a longer period. This could possibly be the case for the next light erosion setting (1mm - 5%) for which the amplitude of the resulting stresses was similar to the ‘no erosion’ setting, although at a higher frequency, thus light fatigue fracture could possibly be the cause of erosion. Stress values for the high intensity settings (1mm30% and 1mm75%) were well above the endurance limit of the material and its theoretical yield strength (415 MPa). This implies that a small amount of plastic deformation was possibly apparent in conjunction with fatigue and brittle, due to work – hardening, fracture.

It is noteworthy that again, the measured stresses were significantly higher than the ones measured for grade DH36 steel. Additionally, the amplitudes of those stresses were similar to cupronickel 70-30, although their behaviour in terms of erosion was dissimilar. This could again be attributed to the microscopic structure of the material as well as to presence of internal flaws and defects. In particular, the ASTM grain size number of stainless steel 254 is 6 thus comparable to cupronickel 70-30 (7), implying a similar structure in terms of grain size. On the other hand, the ASTM grain size number for grade DH36 steel is 12, representing a much smaller mean grain size.

It appears that there is a connection between the mean grain size and the resulting stresses. This could be due to different crack propagation paths, as significant differences in both the length and structure of the grain boundaries could result into the stress inside the materials to be either amplified or attenuated. The length and structure of the grain boundaries could also be related to manufacturing-induced internal flaws and cracks acting as stress amplifiers. Nevertheless, the actual behaviour of the materials under loading is in good agreement with their mechanical properties in the sense that although the internal structure of the materials in terms of grain size is possibly related to the amplitude of the resulting stresses, their behaviour under loading, in terms of erosion – mass loss, is dependent upon their mechanical properties (yield strength, endurance limit) and consequently their composition.

6.11 Fibre Bragg grating sensors (FBG) – Basic theory and applications

Fibre Bragg gratings (FBG) are essentially optical sensors that reflect a specific wavelength of light, called the Bragg wavelength, and transmit all others. This is achieved by means of creating periodic variations to the refractive index of the fibre core (Meltz et al., 1989). In particular, the reflected Bragg wavelength is defined as follows:

$$\lambda_B = 2n_{eff}\Lambda \quad (6.33)$$

where λ_B stands for the Bragg wavelength, n_{eff} is the effective refractive index of the FBG and Λ is the grating period.

The operation of a fibre Bragg grating optical sensor (FBG) can be seen in Figure 6.65:

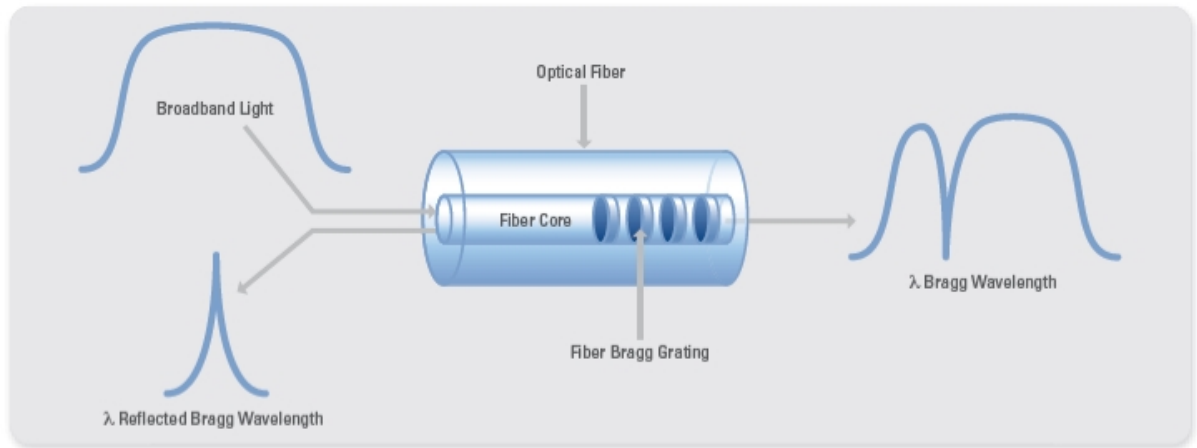


Figure 6.65: The operation of a fibre Bragg grating sensor. (Source: National Instruments – NI, n.d.)

The Bragg wavelength shift is the result of a strain and temperature change, as it can be seen in equation (6.34):

$$\frac{\Delta\lambda_B}{\lambda_B} = (\alpha_{FBG} + \xi)\Delta T + (1 - \rho_e)\Delta\varepsilon \quad (6.34)$$

where:

- $\Delta\varepsilon$ is the change in strain.
- ΔT is the change in temperature.
- α_{FBG} is the linear thermal coefficient of the fibre.
- ξ is the thermos-optic coefficient.
- ρ_e is the effective photo-elastic coefficient.

The effective photo-elastic coefficient can be defined as follows:

$$\rho_e = \frac{n_{eff}^2}{2} [p_{12} - \nu(p_{11} + p_{12})] \quad (6.35)$$

where ν is the Poisson's ratio and p_{ij} is the silica photo-elastic tensor component.

As a reference, a fibre Bragg grating (FBG) with a Bragg wavelength of 1550 nm, exhibits a typical strain and temperature sensitivity of approximately 1.2 pm / microstrain and 13 pm / °C, respectively (Rao, 1998).

Fibre Bragg grating sensors have been used in a variety of applications relating to strain and temperature measurements (Udd, 1995; Morey et al., 1996; Lee, 2003; Kerrouche et al., 2009).

In particular fibre Bragg gratings have been extensively utilized as means of monitoring for civil structures, such as bridges (Tennyson et al., 2001; Lin et al., 2006) and reinforced concrete beams (Davis, 1997; Kalamkarov, 1999). FBG sensors have even been used in geodynamic studies (Ferraro and Natale, 2002) and marine applications (Liang et al., 2006; Majumber et al., 2008), although not as extensively. More recently FBG sensors were utilized for the analysis of the vibrational modes of propeller blades (Javdani et al., 2014).

The utilization of fibre Bragg grating sensors for acoustic emission measurements has already been explored with promising results. (Hill, 2005; Nair and Cai, 2010). The main aim of this investigation however, is to explore whether fibre Bragg gratings can be utilized as means of cavitation induced erosion monitoring, by following a similar to the piezoelectric acoustic sensors procedure and towards that direction an FBG-based acoustic sensor, for cavitation related acoustic emission measurements, was developed in City, University of London. More details will be given in the following sub-chapters.

6.12 Fibre Bragg grating sensors(FBG) – Preliminary tests

A series of preliminary tests were performed in order for the capabilities of fibre Bragg gratings in relation to cavitation erosion detection to be explored.

Fifteen fibre Bragg grating sensors were attached on a steel plate with a side length of 245 mm, a width of 145 mm and a thickness of 5mm. The length of each of the attached FBG sensors ranged from 5 to 10 mm whereas the fibre diameter was of the order of 0.25 mm.

The steel plate was placed inside a water tank, whilst cavitation was induced by means of the UIP 1000hd ultrasonic transducer by Hielscher, similarly to the other measurements. It should be noted that cavitation was induced on the opposite to the side where the fibre Bragg gratings were mounted.

The test rig as well as the instrumentation layout can be seen in Figure 6.66:

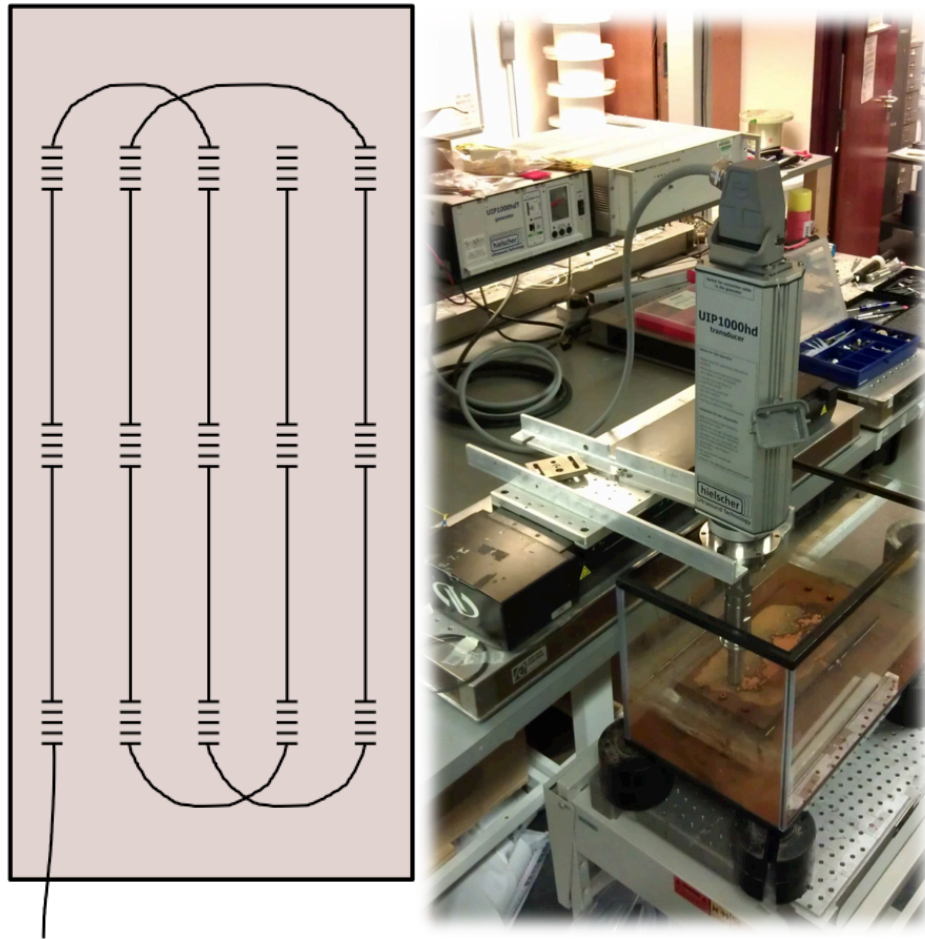


Figure 6.66: Left – Attached FBG sensors layout, Right – Test rig.

Signals from the fibre Bragg grating sensors were captured by means of the SM130 Optical Sensor Interrogator unit by Micron Optics, which is illustrated in Figure 6.67:



Figure 6.67: SM130 Optical Sensor Interrogator unit. (Source: Micron Optics, n.d.).

Signals from the fibre Bragg grating sensors were measured with regards to three different sonotrode placements (left, centre, right), with the sonotrode operating just above the steel plate surface, in the form of Bragg wavelength shifts caused by cavitation-induced stress and

strain. Those wavelength shifts were then visualized by means of the NI LabVIEW software and were plotted onto a coloured contour.

Results are presented in Figure 6.68:

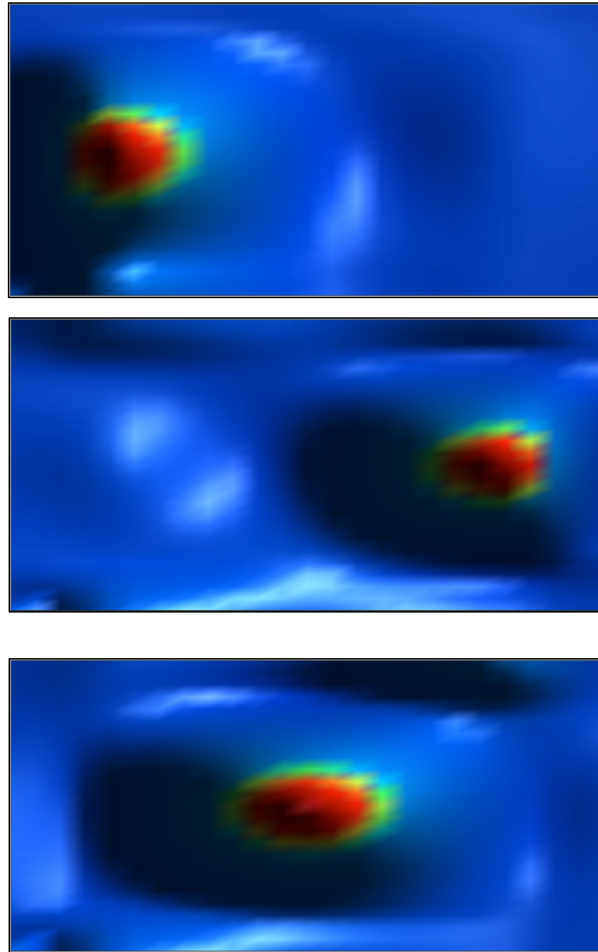


Figure 6.68: Visualised wavelength shift of the sensors for different sonotrode positions. Top (Left – Right), Bottom – Centre.

It can be seen through those figures, that cavitation activity can be successfully identified, by means of an array of multiple fibre Bragg grating acoustic sensors. In particular, the red circular areas of the contour represent the cavitation inducing sonotrode, where strain is induced and gets measured by the array of fibre Bragg grating sensors, in the form of Bragg wavelength shifts.

Results are promising and indicate that cavitation activity can at least be successfully identified and localized using fibre Bragg grating (FBG) sensors.

The use of fibre Bragg gratings as means of cavitation erosion monitoring, in a similar to the piezoelectric sensors way, is further explored in *sub-chapter 6.13*.

6.13 Fibre Bragg grating sensors (FBG) – Acoustic emission tests

In addition to cavitation localization testing based on cavitation-induced strain, the use of fibre Bragg gratings as means of acoustic emission monitoring was also explored. Towards that direction, a single fibre Bragg grating sensor was attached on the opposite to the exposed side of each specimen (grade DH36 steel), similarly to the previously tested piezoelectric sensors.

Signal interrogation was based on the optical demodulation method, where a narrow band light is reflected from the fibre Bragg grating to an optical filter. The intensity of the light, that is transmitted through the optical filter, is correlated to acoustic emission pressure on the fibre Bragg grating sensor (Perez, 2001).

The fibre Bragg grating – based acoustic emission sensing system is presented in *Figure 6.69*:

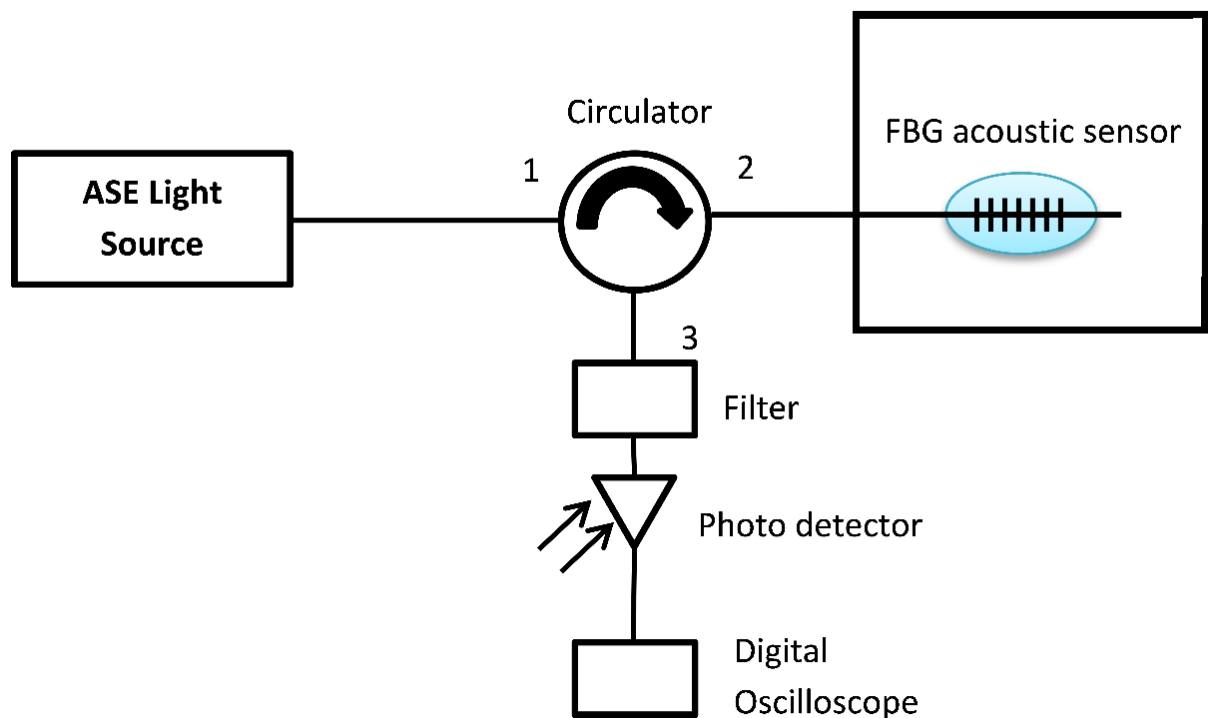


Figure 6.69: Fibre Bragg grating (FBG) – based acoustic emission sensing system.

Light is emitted from a C-Band ASE Light source, with a maximum output of 20.9 dBm, and goes through port 1 of the circulator. It is then reflected back from the fibre Bragg grating sensor subsequently through port 2 and then port 3 of the circulator to the optical filter, with a central wavelength of 1550 nm. The optical signal then enters the photo detector (PDA10CS-EC from Thorlabs), with a bandwidth of 17 MHz, and eventually gets captured by means of a

Tektronix oscilloscope. For comparison reasons, the sampling rate was identical to the measurements that were conducted on piezoelectric sensors in conjunction with the Tektronix oscilloscope, hence 31.3 MHz.

Acoustic emissions, captured through the fibre Bragg grating sensing system, were measured with regards to a variety of various test rig configurations, similarly to the previous measurements that were conducted with piezoelectric sensors. Those test rig configurations are the following:

- 4mm gap and a 5% (50W) sonotrode power output – “No erosion” after 2 hours.
- 3mm gap and a 5% (50W) sonotrode power output – Light erosion after 2 hours.
- 1mm gap and a 5% (50W) sonotrode power output – Medium erosion after 2 hours.
- 1mm gap and a 50% (500W) sonotrode power output – High erosion after 2 hours.

The average duration of each acoustic emission signal that was captured through the fibre Bragg grating - based sensing system and the Tektronix oscilloscope was 0.04s whereas the length each signal, in terms of data points, was 1250000. A fast - Fourier transform (FFT) was performed on all signals, in order for the dominant frequencies to be identified. Results for the fibre Bragg grating - based sensing system are presented in Figure 6.70:

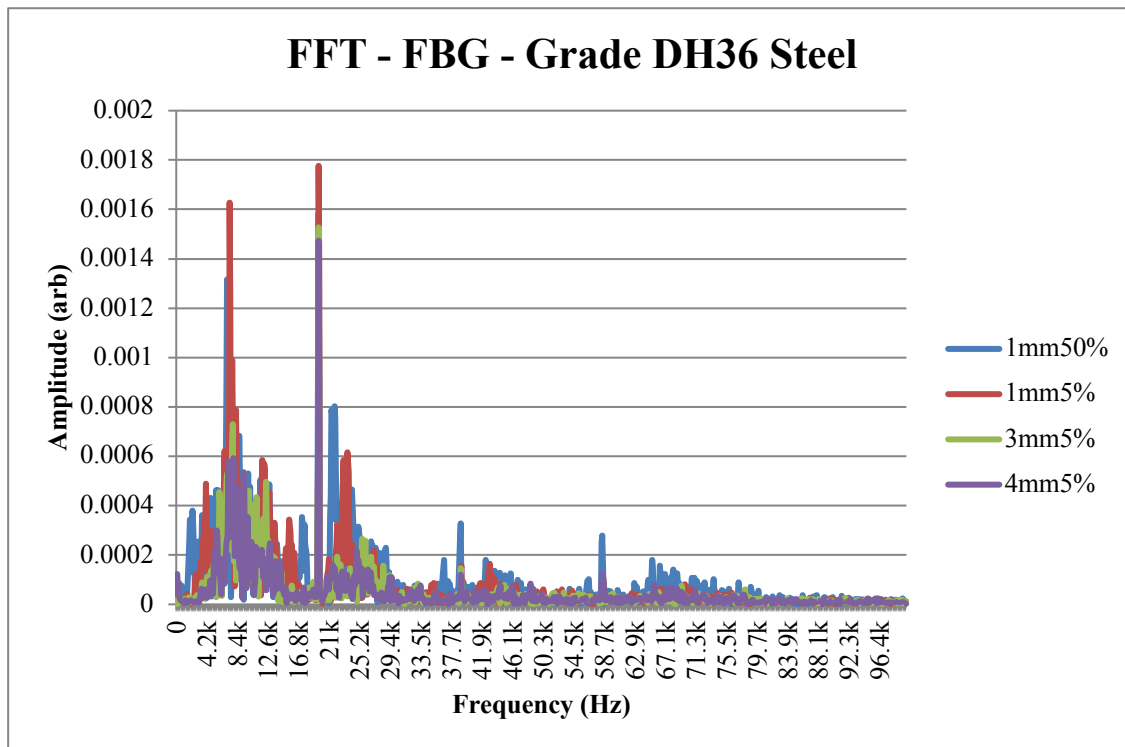


Figure 6.70: FFT – FBG sensor – DH36 steel (4mm-5%, 3mm-5%, 1mm-5%, 1mm-50%)

Interestingly, the 19.5 kHz frequency component, which perfectly matches the operating frequency of the ultrasonic transducer and is directly related to cavitation activity, is clearly apparent along with its harmonics. The amplitude of that component, however, does not appear to be changing with regards to cavitation intensity, as it was the case for the piezoelectric sensors. In particular, the difference between the ‘no erosion’ and ‘light erosion’ test rig configuration is of the order of 50 μ V (RMS) whereas with regards to the observed harmonics, these are only identifiable for the ‘high erosion’ test rig configuration. Finally, the 7 kHz frequency component was found to be related to the fibre Bragg grating sensor itself and it is only apparent when cavitation of ‘medium erosion’ intensity is induced.

It should also be noted that, at this stage, signals from fibre Bragg grating sensors could not be translated into acoustic power units (dB) and stress (MPa). This is due to the fact that the behaviour of the sensors with regards to the applied stress and the resulting signal is not linear, and in addition each one of them exhibits slightly different characteristics.

The FFT graphs of the three piezoelectric sensors are also presented in Figure 6.71, scaled accordingly in order for any common frequencies to be identified and compared:

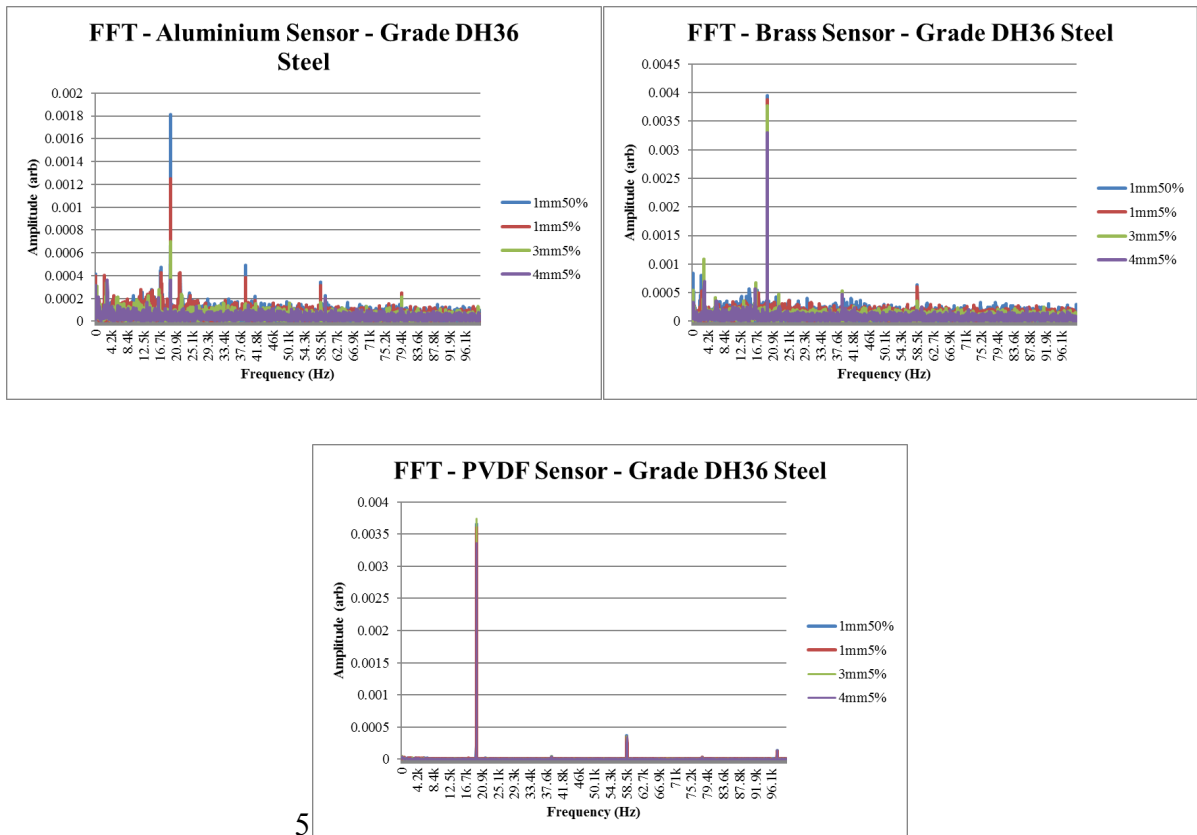


Figure 6.71: FFT comparison of different piezoelectric sensors.

It can be seen that the 19.5 kHz resonance is clearly apparent for all piezoelectric elements, similarly to the fibre Bragg grating sensor. In this case, however, the amplitude of that resonance is directly influenced by cavitation intensity, a behaviour that is more pronounced for the aluminium sensor, for which it should be noted that the resolution of different erosion levels, in terms of the resulting acoustic emission distributions, is clearer in comparison to the other piezoelectric elements and the fibre Bragg grating acoustic sensor. It should also be noted that, in the case of piezoelectric sensors, only the 19.5 kHz frequency component was apparent at this side of the spectrum, in contrast to the fibre Bragg grating sensing element.

Nevertheless, results are promising and indicate that, in addition to being able to detect cavitation in terms of the resulting strain, fibre Bragg grating acoustic sensors are also capable of detecting cavitation erosion related high frequency acoustic emissions. In this case, however, further research would be required before these signals can be accurately translated into acoustic power (dB) or stress (MPa) units.

6.14 Correlation of fracture toughness with erosion

Further to the conduction of acoustic emission measurements the parameter of fracture toughness, that was outlined in *sub – chapter 6.2*, was also explored and compared to the resulting cavitation induced erosion. Fracture toughness (K_{IC}) values for the three alloys that were examined are provided in Table 6.1 (Cambridge University Engineering Department, 2003):

	Grade DH36 steel	Stainless steel 254	Cupronickel 70-30
K_{IC} (MPa * m ^{1/2})	41 – 82	62 -280	30 - 90
Mean K_{IC}	61.5	171	60

Table 6.1: Fracture toughness values of the three examined alloys

The minimum, maximum and mean fracture toughness values for the aforementioned materials are compared to total mass loss as well as the average erosion pit depth and volume parameters.

Results are presented in Figures 6.72, 6.73 and 6.74:

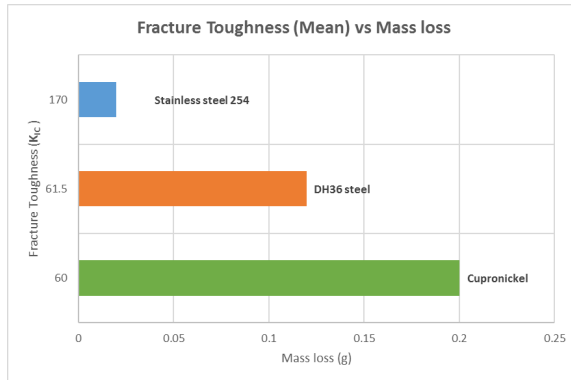
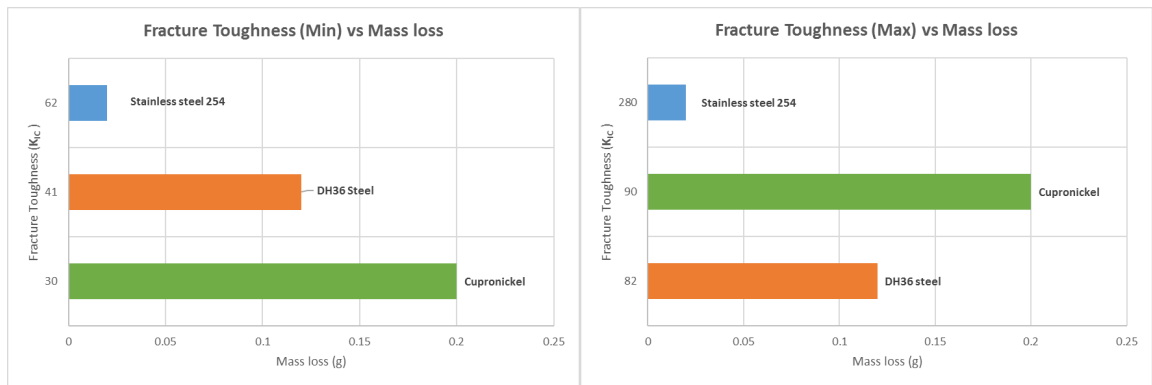


Figure 6.72: Fracture toughness vs Mass loss

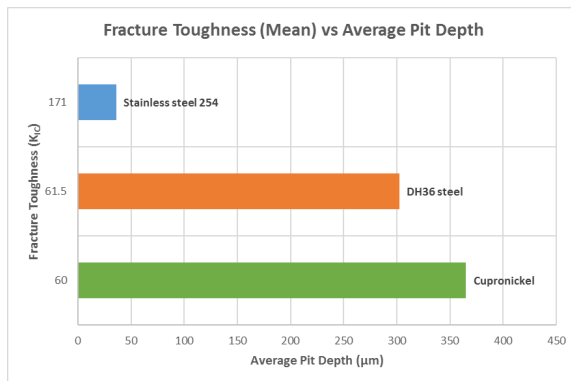
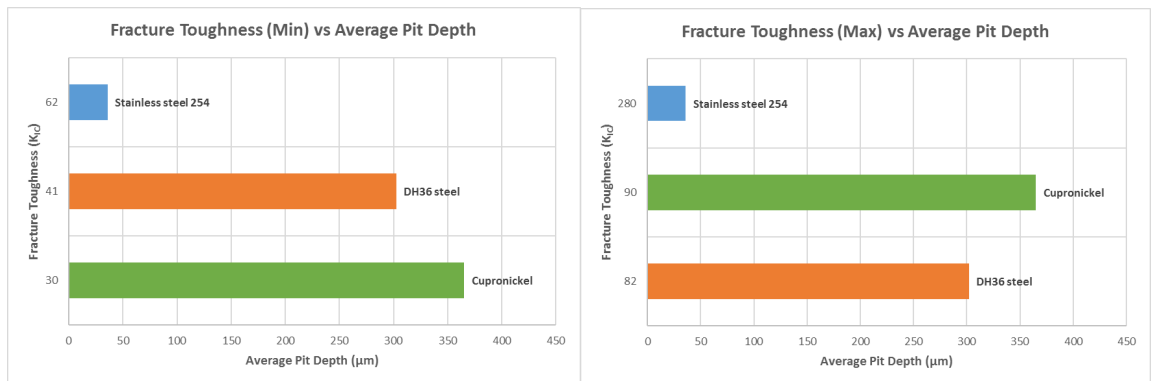


Figure 6.73: Fracture toughness vs Average pit depth

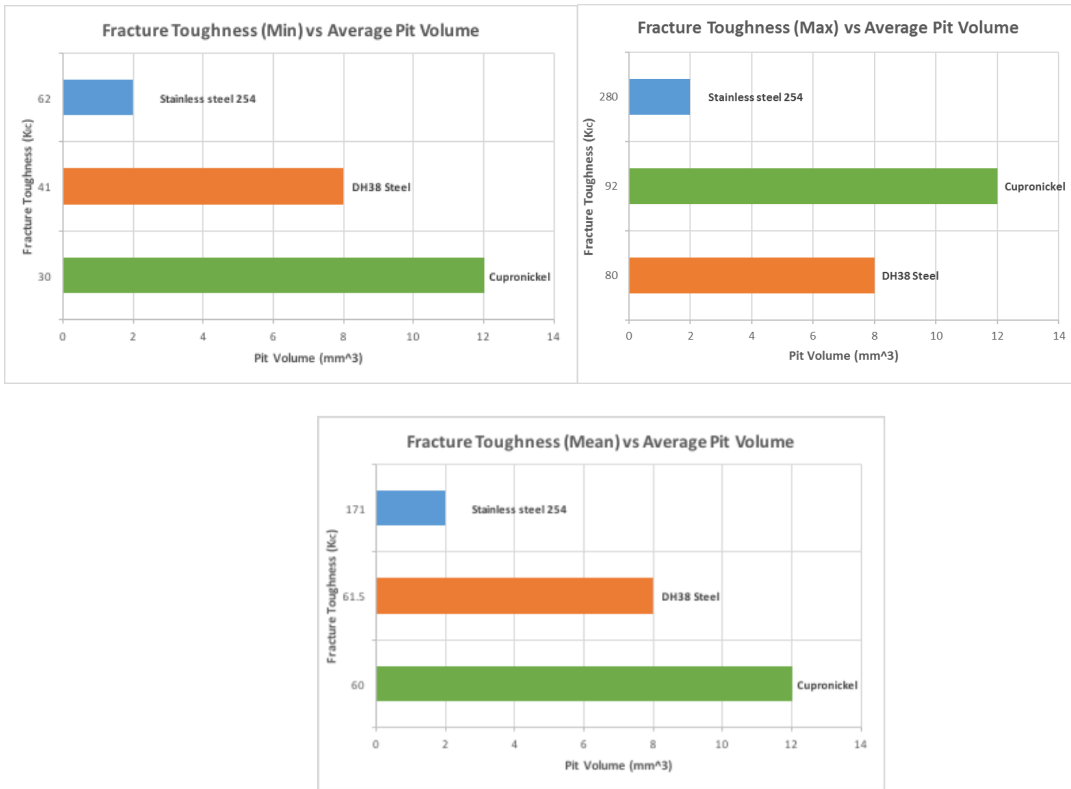


Figure 6.74: Fracture toughness vs Average pit volume

It appears from the results that the parameter of fracture toughness (K_{IC}) correlates well to the resulting mass loss. Moreover, good correlation with the average depth and volume of the resulting erosion pits was also achieved. As such, there appears to be a connection between the resulting erosion and the fracture toughness of each material, similarly to the parameters of yield and ultimate strength that also correlate well with the resulting erosion - mass loss, as it was shown in *Chapter 4* and *5*.

6.15 Summary and discussion

Tests demonstrated that cavitation erosion can be detected and cavitation activity can be distinguished between ‘non – erosive’ and erosive. It was also shown that cavitation can induce significant loading – stress onto the affected materials which will then emit elastic stress waves - acoustic emissions that can be captured, processed and interpreted, productively, by means of an appropriate procedure. The amplitude of those elastic stress waves – acoustic emissions proved to be proportional to the intensity of erosion in the sense that, when cavitation becomes increasingly ‘erosive’ they are further amplified due to the increased cavitation activity and resulting stress loading, but also due to the inception and propagation of erosion induced cracks inside the material. As such, acoustic emissions can be utilized as means of erosion monitoring in the sense that, acoustic thresholds for ‘erosive’ cavitation can be established,

supposing that the relevant amplitudes for the ‘non erosive’ conditions have also been measured.

In this context, acoustic thresholds for ultrasonically induced cavitation erosion were established for grade DH36 steel, stainless steel 254 and cupronickel 70-30. In particular, a wide range of test rig configurations were examined, leading to cavitation of varying intensity, in terms of erosion – mass loss whereas the resulting acoustic emissions, from each configuration, were then captured, converted into the appropriate units, and correlated to the corresponding erosion levels. Moreover, acoustic emission signals were further translated into stresses by means of an analytical procedure, which was based on the linear nature of the piezoelectric elements and a standardized initial calibration. Results in terms of stresses were found to be in good agreement with the mechanical properties of the material as well as the observed erosion – mass loss.

With regards to instrumentation, it appears that piezoelectric elements are more suited for those measurements, at least at this stage. Firstly, they are more studied than fibre Bragg gratings in that respect and secondly their linear behaviour is well demonstrated and of great significance with regards to the conversion of the acoustic emission signals and their subsequent correlation with the relevant erosion levels. Nevertheless, fibre Bragg gratings clearly demonstrated that they are capable of capturing acoustic emission signals related to cavitation erosion, however, more research would be required before those signals could be translated into something more useful, in a way that the sensors would be utilized for erosion monitoring purposes.

Due to promising results, it is proposed that an analogous methodology should be applied on ship rudder models in order to investigate how the method - system will perform on an object, that would resemble a ship component commonly suffering from cavitation induced erosion. In addition to acoustic emission measurements oriented towards the characterization of erosion in terms of intensity, however, tests in this case will also be conducted with regards to cavitation erosion localization whereas both piezoelectric and fibre Bragg grating sensors will be utilized in this context.

Finally, it was shown, that further to the parameters of yield and ultimate strength, the parameter of fracture toughness also correlates well to the resulting cavitation induced erosion of the examined alloys, in terms of measured mass loss as well as average erosion pit depth and volume.

Chapter 7

Acoustic Emission Measurements on Model Ship Rudders

7.1 Introduction

Further to the acoustic emission measurements that were conducted on small rectangular specimens, it was decided to deploy an analogous set of measurements and see if the method (s) could be used for detection of cavitation in ship rudders. Due to laboratory limitations, however, relating to size and weight it was decided that, measurements should be initially conducted on a smaller scale and as such a small half-rudder model was designed and manufactured, closely resembling a full size ship rudder in all aspects but size.

In addition to the evaluation of cavitation erosion severity by means of acoustic emissions similarly to previous tests conducted on small rectangular specimens, the parameter of cavitation erosion localization was also considered in that case. In particular, it was investigated whether cavitation erosion can be identified or not, in terms of location, by means of the resulting acoustic emissions and a relevant triangulation technique. Similarly to previous testing, cavitation was induced by ultrasonic means, thus an ultrasonic transducer was mounted just above the rudder's surface while with regards to instrumentation both piezoelectric and fibre Bragg grating sensors were utilized for source location purposes.

7.2 Experimental test rig

The small half-rudder model was made from grade DH36 steel, similarly to the small rectangular steel specimens that were previously tested. Moreover, it was decided that a half-rudder arrangement should be utilized for those tests as this would make the instalment of acoustic sensors inside the rudder easier without influencing the resulting acoustic emissions, considering the symmetric nature of the object.

In this context the half-rudder model is 400 mm long and 200 mm wide whereas its interior is hollow and essentially consists of a thin longitudinally positioned piece of steel acting as a reinforcing beam as well as four transversely positioned stingers. Both the reinforcing beam and the stingers are firmly joined onto the main structure of the rudder in order for, continuity with regards to the propagation of the resulting acoustic waves, to be ensured.

The exterior as well as the interior of the half-rudder model can be seen in Figure 7.1:



Figure 7.1: Half-rudder model. Top-exterior, bottom-interior.

The half-rudder model was placed into a large water tank whereas cavitation was induced by means of the Hielscher UIP1000hd 1000W ultrasonic transducer, similarly to previous tests conducted on small rectangular specimens.

With regards to source location testing, however, the portable handheld UP200Ht 200W ultrasonic transducer by Hielscher was also utilized, mainly due to its small size and portability. For instance, the vibrating tip (sonotrode) of the UP200Ht ultrasonic transducer could be conveniently positioned along the surface of the rudder by the operator, with any need for special mounting and positioning arrangements. Additionally, the diameter of the

titanium made sonotrode of the UP200Ht transducer, is only 4mm in contrast to the 22mm diameter of the larger UIP1000hd unit, thus closely positioned marked locations on the surface of the rudder could be easily tested. With regards to technical specifications, the maximum power output of the handheld unit is 200W, the operating frequency is 26 KHz and the maximum amplitude of the oscillation at the sonotrode tip is 70µm.

The UP200Ht ultrasonic transducer can be seen in Figure 7.2:



Figure 7.2: Hielscher UP200Ht ultrasonic transducer and sonotrode (Source: Hielscher - Ultrasound Technology, n.d.)

Nevertheless, with regards to the cavitation erosion severity measurements the standard UIP1000hd ultrasonic transducer along with its 22 mm titanium made sonotrode were utilized. In this case the UIP1000hd ultrasonic transducer was firmly mounted just above the rudder onto a flexible yet robust base that could be adjusted towards all directions (x, y, z).

The water tank that was used as well as the mounted UIP1000hd ultrasonic transducer unit can be seen in Figure 7.3:

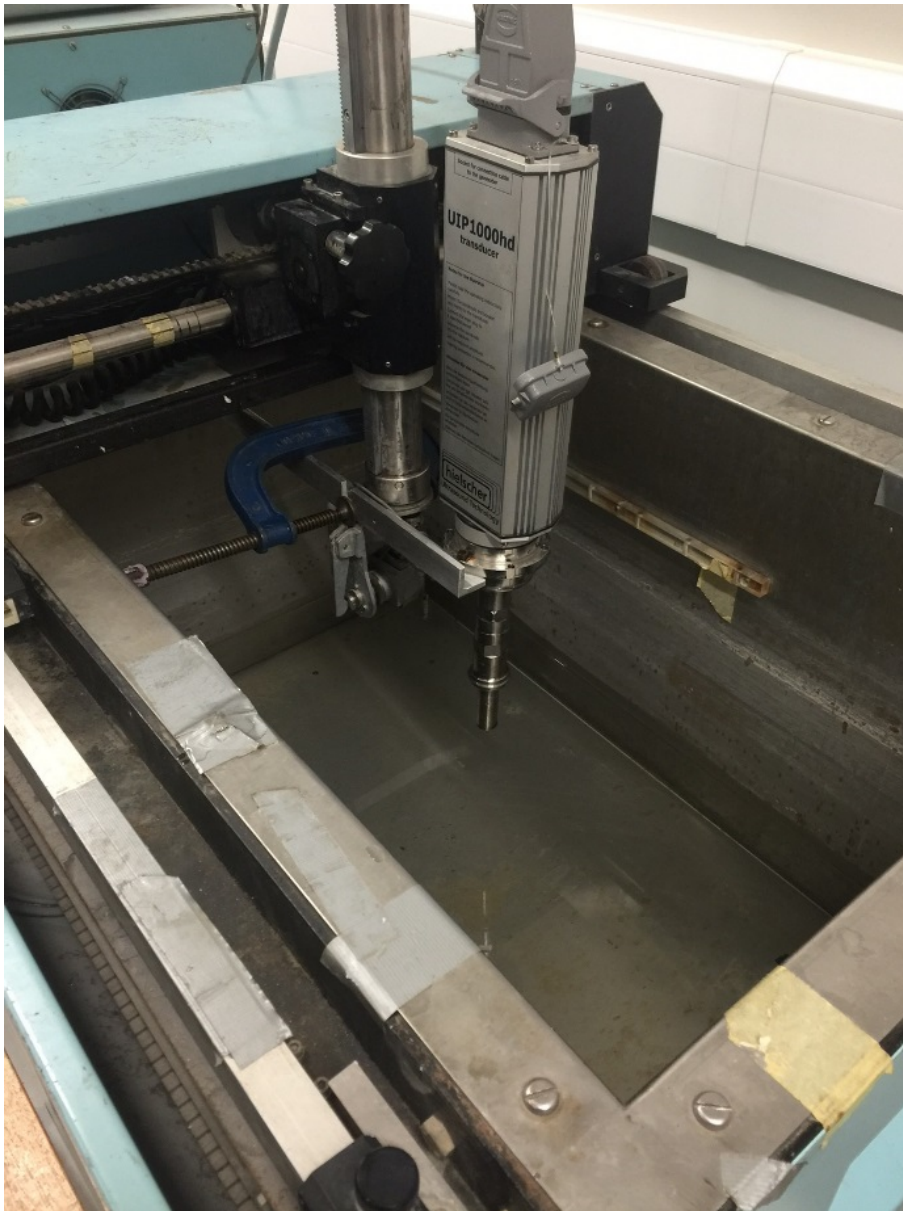


Figure 7.3: UIP1000hd ultrasonic transducer mounted onto the adjustable base inside the water tank.

In contrast the half-rudder model was not mounted but ‘hanged’ instead, by means of two elastic bands in order for the acoustic insulation of the structure to be ensured. The elastic bands, however, were supported by an aluminium bar conveniently positioned at the top of the water tank.

The ‘hanged’ half-rudder model, appropriately positioned inside the water tank, as well as the UIP1000hd ultrasonic transducer can be seen in Figure 7.4:



Figure 7.4: Half-rudder model positioned inside the water tank.

Finally, with regards to the acoustic emission sensing equipment that was utilized it consisted of both piezoelectric and fibre Bragg grating sensing elements. The operating principles, in terms of the underlying theory as well as the analytical techniques required for acoustic emission measurements, especially in relation to various cavitation erosion levels and different experimental setups, have already been discussed thoroughly in *Chapter 6* and will not be presented again.

Therefore, only outline details about procedures relating to those series of tests, such as the different test rig configurations that were examined, as well as the sensing equipment that was utilized will be given in this chapter. The same applies for the underlying principles of the source location triangulation technique.

7.3. Experimental procedure: Acoustic emission measurements and the triangulation source location technique

Acoustic emission measurements with regards to the half-rudder model can be categorized into two distinct procedures leading to different sets of experimental data. Initially, measurements were conducted with the purpose of exploring whether acoustic emissions can be correlated to various cavitation-induced erosion levels, similarly to the work that was conducted on the small rectangular specimens. Afterwards, the use of multiple sensors, either piezoelectric or fibre Bragg grating, in an arrangement dictated by a common triangulation technique, was utilized for source location purposes.

With regards to the initial acoustic emission ‘correlation’ measurements, an analogous, to the one described in *Chapter 6*, experimental procedure was followed, although in this case, only the most effective acoustic emission sensing system was utilized, based on data from the earlier tests that were conducted on small rectangular specimens. Effectiveness was essentially evaluated with regards to the appearance of the distinctive acoustic emission and stress distribution curves in relation to the various levels of cavitation erosion and the mechanical properties of the examined materials.

Under those remarks, which are more thoroughly explained in *Chapter 6*, the acoustic emission sensing system that was utilized for the initial measurements consists of the following:

- Piezoelectric sensor in aluminium case – 600 kHz nominal frequency.
- 40 dB signal attenuator
- 40 dB preamplifier with an 850 kHz high-pass filter
- Logarithmic peak detector (LPD)
- NI DAQ (data acquisition system)
- Computer

In this case, the acoustic sensor was positioned centrally on the opposite of the exposed side of the half rudder, right inside the hollow region. This position was chosen under the assumption that by placing the sensor as far as possible from the boundaries of the structure, the possible rebounds of acoustic waves could be avoided, thus the structure would be monitored more effectively. Nevertheless, due to the presence of a centrally positioned beam, the sensor was essentially positioned as centrally as possible in relation the free side of the

rudder as the other side was mostly occupied by the attached shaft. This arrangement be seen in Figure 7.5:

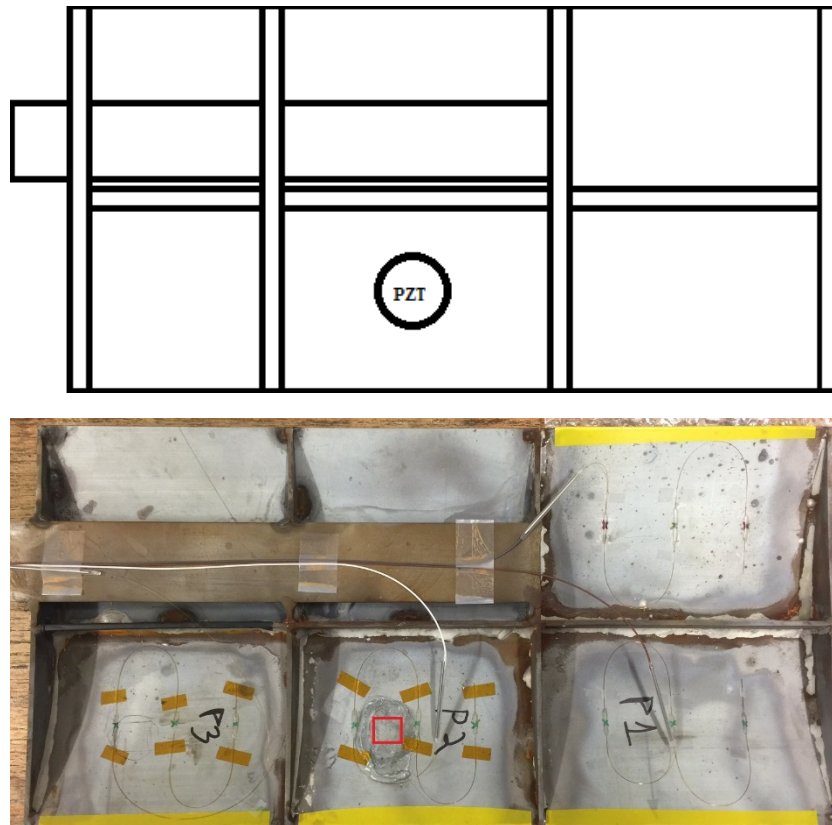


Figure 7.5: Top – Rudder with acoustic sensor (Drawing) – Rudder with acoustic sensor position marked by red square (Image).

Three distinct locations marked as P1, P2 and P3 can be seen in Figure 7.6. These essentially indicate three different sonotrode placements as it was decided that acoustic data should be captured for a variety of placements in order for the ability of the sensor to successfully monitor the whole structure, in terms of cavitation severity, to be evaluated. Those locations are represented in Figure 7.6:

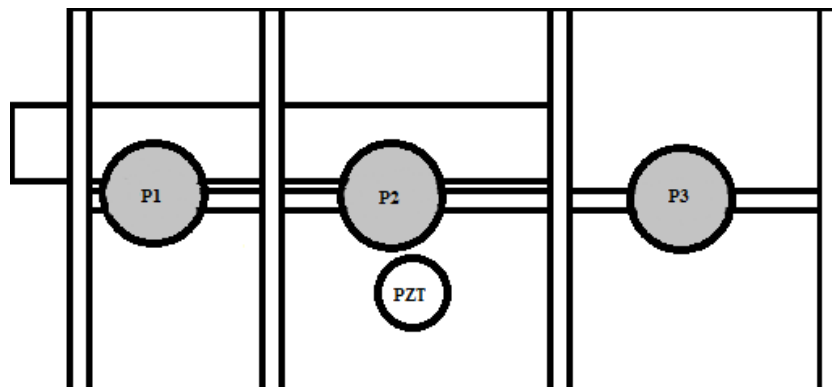


Figure 7.6: Rudder with acoustic sensor (Drawing). Different sonotrode locations (P1,P2,P3).

The main purpose of the initial ‘correlation’ measurements was to correlate acoustic emissions to the corresponding levels of cavitation-induced erosion and as such various test rig configurations were examined. Considering, however, that the half-rudder model was made from grade DH36 steel, it was decided that the test rig configurations should be analogous to the ones utilized in the case of the small rectangular grade DH36 steel specimens, earlier in this study. Under those remarks the different test rig configurations that were examined are the following:

- 4mm gap and a 5% (50W) sonotrode power output – “No erosion” after 2 hours.
- 3mm gap and a 5% (50W) sonotrode power output – Light erosion after 2 hours.
- 1mm gap and a 5% (50W) sonotrode power output – Medium erosion after 2 hours.
- 1mm gap and a 50% (500W) sonotrode power output – High erosion after 2 hours.

Acoustic emission data for all different test rig configurations – erosion levels and sonotrode positions (P1, P2, P3) were captured and translated into acoustic power and stress distributions following the procedure that is thoroughly described in *Chapter 6*.

Source location measurements on the contrary were based on the principle of triangulation essentially requiring the use of at least three and ideally four acoustic sensors. A common triangulation technique (*Tobias 1976*) was utilized in these series of measurements, the analytical aspects of which are thoroughly described in *Appendix C*, where details regarding the operating sound field are also given.

With regards to instrumentation a total of four acoustic sensors were installed on the half-rudder model, in order for the triangulation technique to be effectively applied as well as to eliminate any possible ambiguities through the utilization of a fourth acoustic sensor. Both piezoelectric and fibre Bragg grating sensors were utilized, similarly to previous experiments.

The piezoelectric sensor - based source location system, consisted of:

- Four PVDF acoustic sensors.
- Four 40dB gain preamplifiers with an 850 kHz high-pass filter
- Four 28V DC power supply units - one for each preamplifier.
- Tektronix Oscilloscope for signal capturing.
- Computer for data processing.

PVDF sensors were chosen due to their increased sensitivity as well as their ability to operate without any signal attenuators. It should be noted, however, that the other piezoelectric sensors

(aluminium, brass) could also be effectively utilized for source location purposes whereas the selection of PVDF sensors was primarily made for practical reasons. The location of the four acoustic sensors can be seen in Figure 7.7:

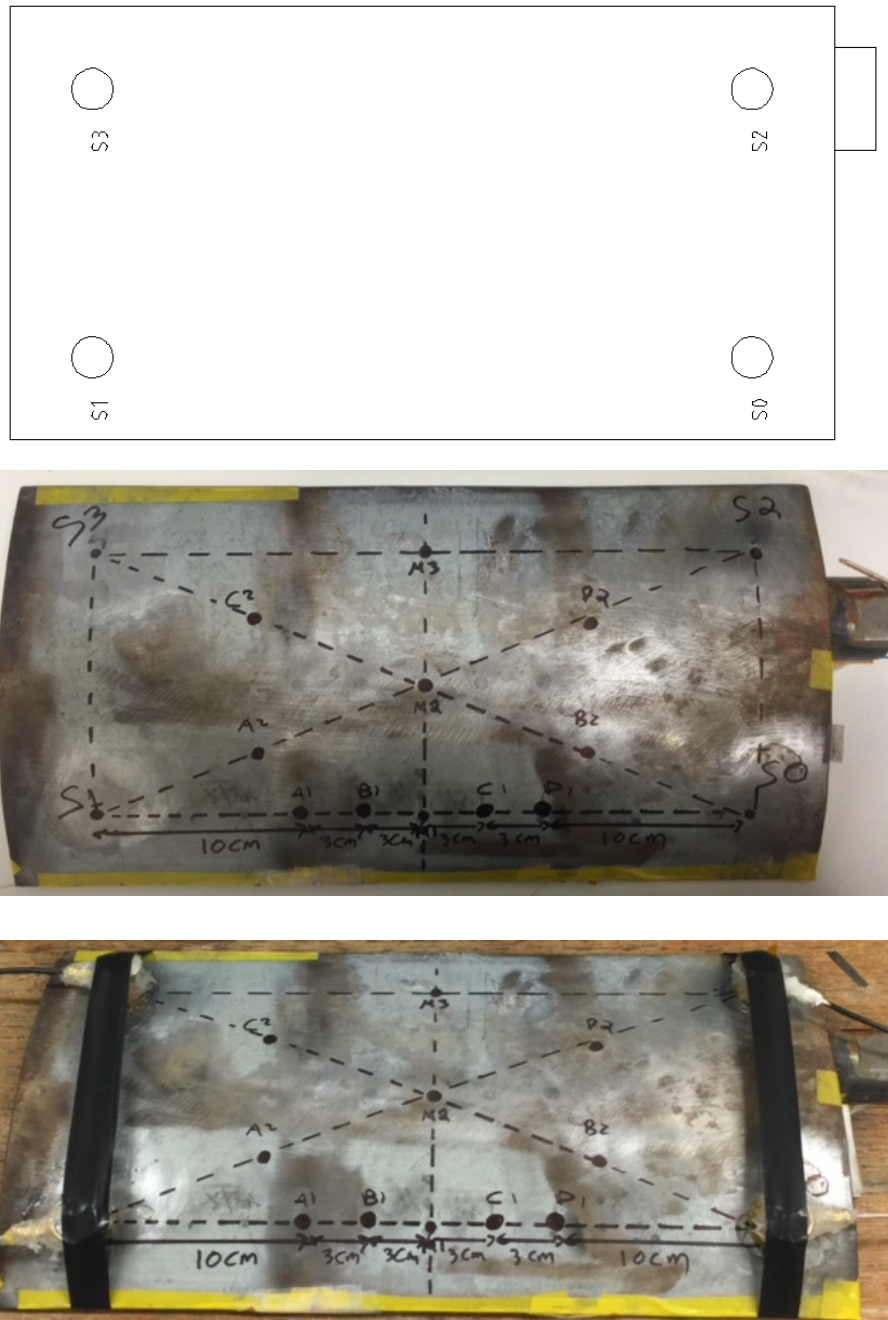


Figure 7.7: Top – Location of the four acoustic sensors (drawing). Middle – Location of the four acoustic sensors (image). Bottom – Mounted acoustic sensors (image).

An appropriated grid, that essentially formed a baseline upon which different sonotrode placements could be easily identified and the equivalent distances could be accurately measured, was designed and can be seen in the images of *Figure 7.7*.

With regards to the fibre Bragg grating - based source location system, signal capturing was based on the demodulation technique, which has been thoroughly described in *Chapter 6*. The system essentially consisted of:

- Four fibre Bragg grating sensors
- ASE Light Source.
- Four (4) circulators.
- Four (4) optical filters.
- Tektronix Oscilloscope.
- Computer for data processing.

The locations of the four fibre Bragg grating (FBG) sensors were identical to the piezoelectric sensors that were presented in Figure 7.7.

It should be noted that in both cases (piezoelectric and FBG) acoustic emission signals were captured through a digital oscilloscope and processed by means of a computer.

The triangulation technique is essentially based on the time differences between acoustic sensors with regards to the arrival of acoustic waves and makes use of an analytical method in order for source location coordinates to be derived. The required time differences between sensors were measured manually with regards to the peaks of the waveforms corresponding to the pressure pulses of the sonotrode, essentially occurring every $38\mu\text{s}$ as it was dictated by its operating frequency of 26 kHz. It should be noted that the small portable UP200Ht sonotrode was utilized for those measurements, operating at its maximum power setting (200W) and positioned at a distance of approximately 1mm from the surface of the rudder in all cases. It should be also noted that the sonotrode was allowed to operate for 2-3 minutes in order for an equilibrium to be established before any measurements were made.

Due to the complexity of the triangulation technique the rest of the required analytical calculations were made through an Excel-based software in order for the coordinates of the acoustic emission source to be derived. The calculated coordinates were then compared to the actual coordinates of the specific sonotrode placement. Considering that calculations were made in terms of coordinates, an accurate mapping of the half-rudder model was conducted, with regards to the positions of the acoustic sensors as well as the different sonotrode placements starting from sensor $S_0 (0, 0)$. Those coordinates be seen in Figure 7.8:

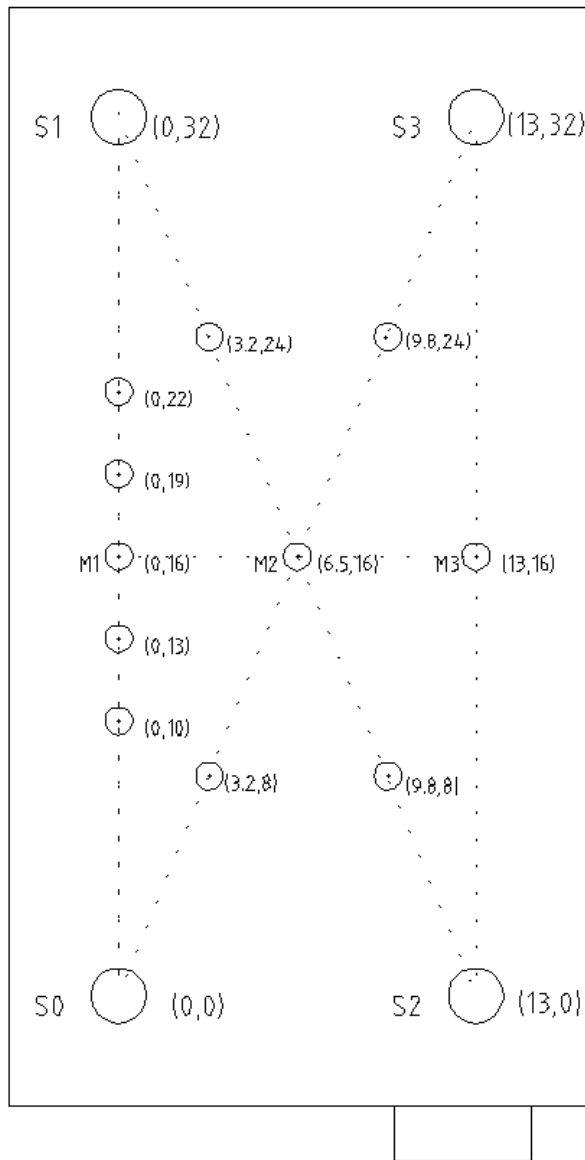


Figure 7.8: Coordinates of different sensors and sonotrode placements on the half rudder model.

More details regarding the application of the triangulation technique for source location measurements are given in *Appendix C* whereas any additional techniques that were utilized such as signal filtering will be given in the following results - oriented sub - chapters.

7.4 Acoustic emission– Cavitation erosion correlation measurements

Acoustic emission measurements were initially conducted by means of a centrally located piezoelectric sensor with the purpose of exploring whether there is any correlation between cavitation erosion and the resulting acoustic emissions. The piezoelectric sensor – based acoustic sensing system that was utilized as well as the different test rig configurations that were examined have already been presented in *sub - chapter 7.3*.

Results are presented in the form of acoustic power and stress distribution curves for various test rig configurations resulting into different levels of cavitation erosion, similarly to the results that were presented in *Chapter 6*. The process by means of which acoustic emission signals are translated into acoustic power and stress units is also identical to the one described in *Chapter 6*, the basis of which is the use of the logarithmic peak detector. In this case, however, the additional parameter of sonotrode positioning - placement is also to be considered, thus distribution curves for three different placements will be presented.

The different sonotrode placements can be seen again in Figure 7.9:

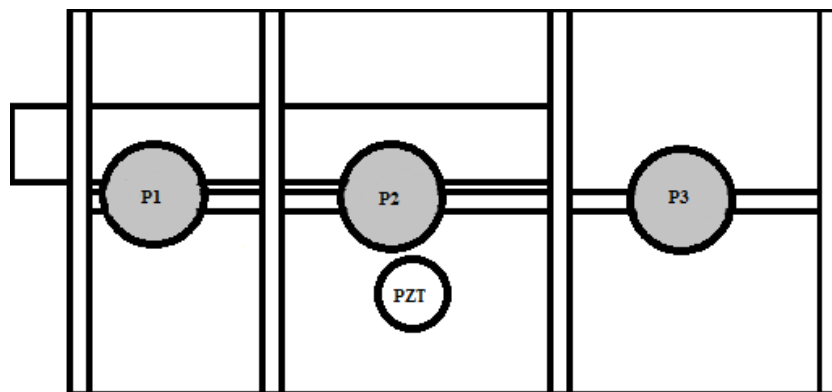


Figure 7.9: Different sonotrode placements (P1, P2, P3) and the centrally located piezoelectric sensor.

Four test rig configurations leading to different levels of erosion were examined as follows:

- 4mm gap and a 5% (50W) sonotrode power output – “No erosion” after 2 hours.
- 3mm gap and a 5% (50W) sonotrode power output – Light erosion after 2 hours.
- 1mm gap and a 5% (50W) sonotrode power output – Medium erosion after 2 hours.
- 1mm gap and a 50% (500W) sonotrode power output – High erosion after 2 hours.

Acoustic power and stress distribution curves for the rectangular grade DH36 steel specimen are also presented alongside the main rudder findings, for comparison reasons.

Acoustic power distributions can be seen in Figure 7.10:

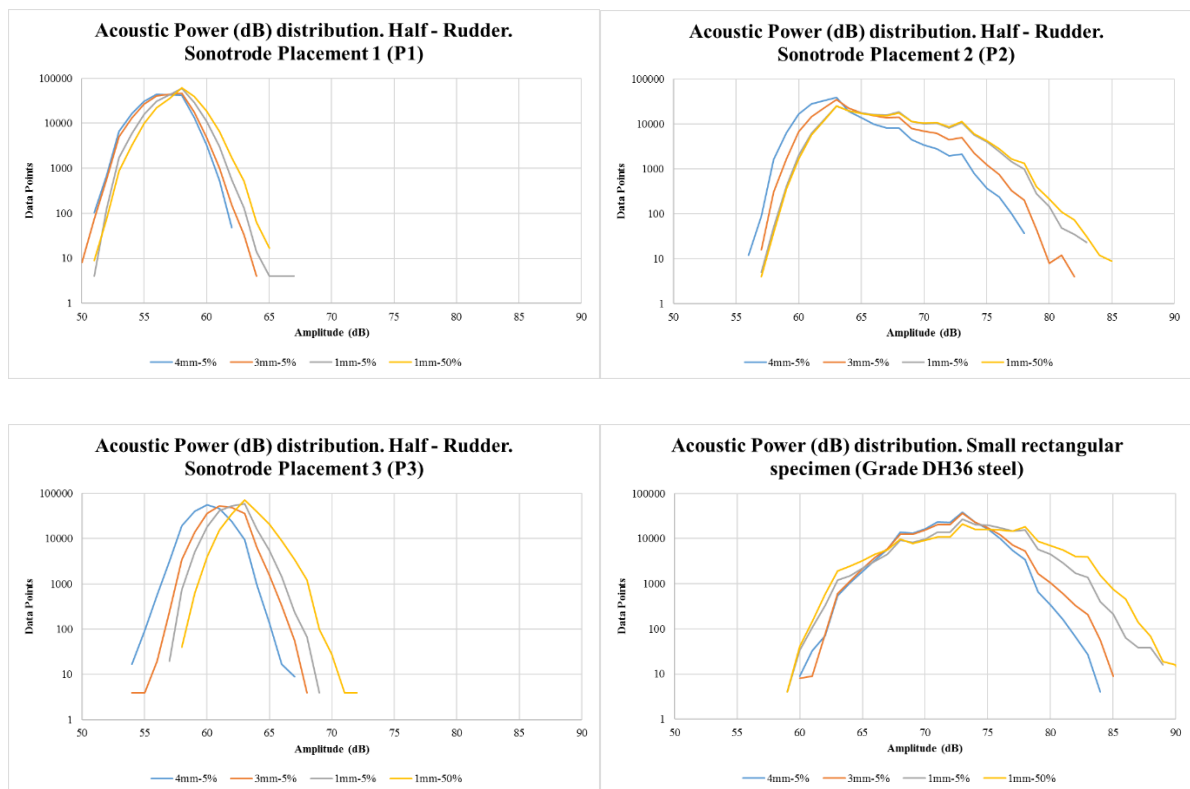


Figure 7.10: Acoustic Power (dB) distribution curves for different sonotrode placements and various test rig configurations with regards to the rudder as well as the small rectangular specimen (Grade DH36 steel).

It can be seen that acoustic emissions, in terms of acoustic power, vary significantly with regards to the sonotrode placement. This variation was essentially expected and can be attributed to the distance between the acoustic sensor and the source of cavitation (sonotrode), as acoustic waves attenuate with distance and ‘leak’ to the surrounding medium (water). In fact, the strongest signals in terms of acoustic power were obtained for P2, where the sonotrode was placed just above the acoustic sensor, followed by P3 and finally P1. It is noteworthy that the presence of a fixed shaft in P1 resulted into acoustic emissions of decreased amplitude, thereby it possibly interacted and absorbed a considerable amount of acoustic emission related energy. In contrast, acoustic emission results for P3, which was free of any thick and fixed components such as the shaft, were of higher amplitude, a fact that further enhances the aforementioned assumption. It should also be noted that, in the case of the half-rudder model the amplitudes of the resulting acoustic emissions were considerably lower in comparison to the small rectangular specimen even in the case when the sonotrode was placed above the acoustic sensor (P2). This could be explained by the nature of the dominant Lamb or Plate waves, which in the case of the small rectangular specimen were confined within its restricted boundaries, thus they preserved their energy, whereas in the case of the half-rudder model they propagated all over the structure and as a result they attenuated significantly.

Nevertheless, the transition point between ‘non-erosive’ and ‘erosive’ cavitation was identifiable in all cases with an average difference of the order of 2 dB, similarly to the small rectangular specimen, while the amplitudes of the resulting acoustic emissions varied with regards to the sonotrode placement, due to the previously mentioned reasons.

Acoustic emissions were also converted into stress units, by means of the procedure described in *Chapter 6*, and plotted onto stress distribution comparison curves. Results for different sonotrode placements (rudder) and the rectangular specimen are presented in Figure 7.11:

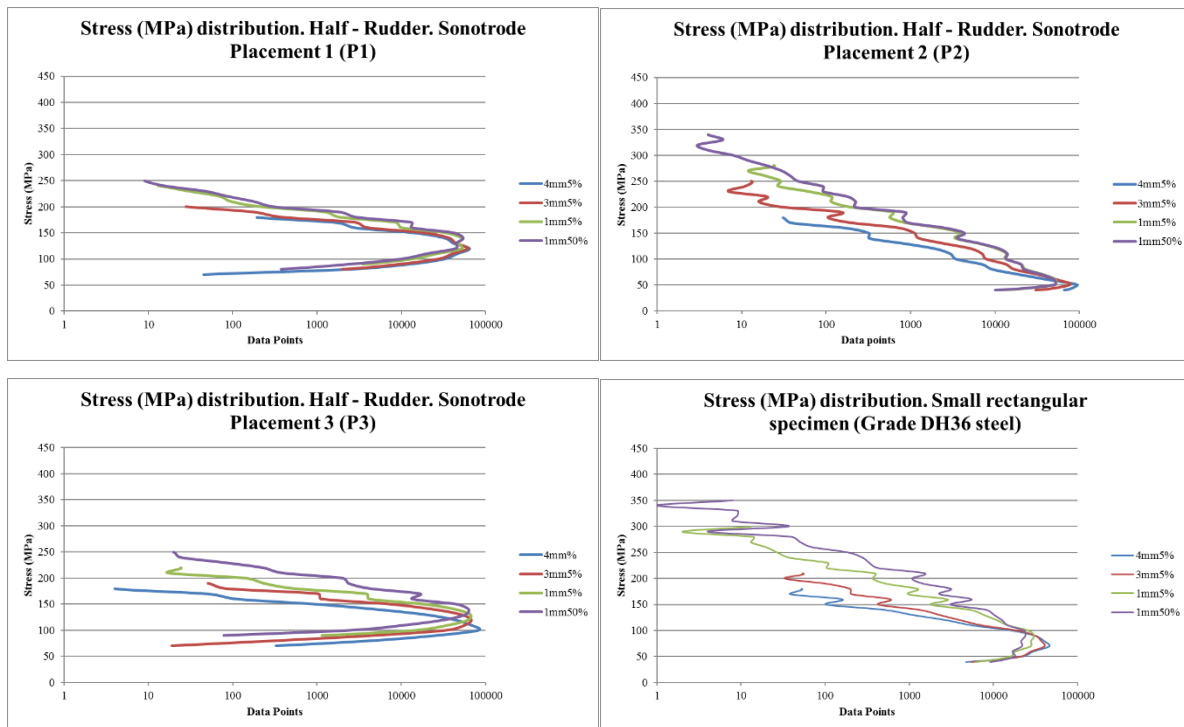


Figure 7.11: Stress (MPa) distribution curves for different sonotrode placements and test rig configurations as well as the small rectangular specimen (Grade DH36 steel).

The main difference in comparison to the acoustic power distributions is that the process of converting acoustic emissions into stress is based on an initial calibration conducted by means of a Hsu - Nielsen source. Calibration essentially allows for acoustic emission signals to be translated into stress and as such results can then be directly compared in terms of absolute values. In the case of the half-rudder model an initial calibration was conducted for each of the three sonotrode placements using the Hsu – Nielsen source and as such the resulting acoustic emission signals were converted accordingly. The immediate effect of this procedure can be seen in the resulting distribution graphs.

In particular, stress values for the ‘non-erosive’ test rig configuration were of the order of 170 MPa for all sonotrode placements along the surface of the half-rudder model as well as the

small rectangular specimen. Stress values for the ‘lightly erosive’ test rig configuration, namely the transition point between ‘non-erosive’ and ‘erosive’ cavitation, were of the order of 200-250 MPa in all cases. Those values are comparable to the endurance limit of the material (245-310 MPa). In particular, stress values of the order of 200 MPa were obtained for sonotrode placements P1 and P3 on the half-rudder model and the small rectangular specimen and 250 MPa for sonotrode placement P2 on the half – rudder model. The higher stress that was observed in the case of the P2 sonotrode placement can be attributed to some unique microscopic and macroscopic characteristics of the material in that region, acting as stress amplifiers, nevertheless it is still sensible with regards to the mechanical properties of the material and the resulting erosion in terms of mass loss.

Finally, with regards to the ‘medium-erosion’ and ‘high-erosion’ test rig configurations stress values ranging from 250 to 350 MPa were obtained for the P2 sonotrode placement on the half – rudder and the small rectangular specimen. Those values are higher than the endurance limit of the material and comparable to its yield strength (355 MPa) thus the increased observed erosion characterizing those configurations is justified in that respect. In contrast, the obtained stress values for the P1 and P2 sonotrode placements were significantly lower, ranging from 200 to 250 MPa, thus it appears that high-energy acoustic emissions related to increased erosion levels attenuated with distance. In the case of the P2 sonotrode placement and the small rectangular specimen the source of cavitation was located just above the centrally positioned acoustic sensor, whereas in all other cases it was located further apart, thus the aforementioned assumption is further enhanced.

Nevertheless, the transition point between ‘non-erosive’ and ‘erosive’ cavitation in terms of stress was in all cases identifiable and sensible with regards to the mechanical properties of the examined material whereas the high-energy acoustic emissions related to increased levels of observed erosion appeared to attenuate with distance.

7.5 Acoustic emission – Cavitation erosion source location measurements - Piezoelectric and fibre Bragg grating sensor based systems

Acoustic emission data was obtained in the form of raw waveforms from each one of the sensors before being processed into source location coordinates. As such, the surface of the half-rudder model was accurately mapped, in terms of coordinates, with regards to the location of the sensors and the different sonotrode placements as it was shown in *sub - chapter 7.3*.

All measurements were made with regards to the peaks of the incoming acoustic waves. Time - difference results as well as the relevant calculated coordinates indicate that the acoustic emission – cavitation source can be successfully identified by means of the triangulation method although not with maximum accuracy. Detailed graphs are presented in *Appendix D* while results are summarized and given in Table 1. Two sets of results, relating to the use of a fourth sensor are provided for each system.

Source location measurements – Half rudder model				
Actual Location (x, y) in cm	Piezoelectric (1) (x, y) in cm	Piezoelectric (2) (x, y) in cm	FBG (1) (x, y) in cm	FBG (2) (x, y) in cm
(0, 10)	(0.5, 10)	(2.2, 10)	(1.7, 10.6)	(2.3, 10.6)
(0, 13)	(0.8, 13)	(1.2, 13)	(1, 12.4)	(0.6, 12.4)
(0, 16)	(0.7, 16)	(1.6, 16)	(0.3, 15.7)	(1, 15.7)
(0, 19)	(0.1, 18.6)	(1, 18.5)	(0.9, 19)	(0.8, 19)
(0, 22)	(0.5, 22)	(0, 22)	(2.3, 23.2)	(0.2, 23.2)
(6.5, 16)	(6.5, 16)	(5, 16.5)	(6.5, 16)	(0, 16)
(13, 16)	(12.3, 16)	(11.5, 16)	(11.2, 16)	(11, 16)
(3.2, 8)	(3.5, 8.3)	(3.1, 8.4)	(2.3, 8.8)	(3, 8.8)
(3.2, 24)	(2.9, 24.4)	(4.2, 23.8)	(2.5, 24.1)	(4.2, 23.9)
(9.8, 8)	(9.1, 8.8)	(8.8, 8.8)	(9, 8.4)	(12, 8)
(9.8, 24)	(9.6, 23)	(10.5, 22.7)	(10, 24.6)	(10.5, 24.8)

Table 7.1: Source location measurements – Half rudder model.

That lack of maximum accuracy can be attributed to the properties of the resulting acoustic waves in conjunction with the unique geometrical characteristics of the monitored object. The produced acoustic waves are essentially Lamb waves, which propagate through the confined boundaries of a plate whereas analytical calculations regarding the various Lamb wave phases and types (symmetric and anti-symmetric) as well as their velocities are made in relation to simple semi-infinite in length plates.

In this case the main part of the half—rudder model could closely resemble a plate, however, the numerous stitches as well as the central beam and the shaft are possibly influential with regards to the propagation of the Lamb waves mainly in terms of the resulting velocity. This can explain the fact that results are more dispersed in the direction which is perpendicular to

the orientation of the attached shaft and beam. That inaccuracy is even more pronounced towards the side where the shaft is attached.

In addition, one should also consider that for the particular operating frequency of the sonotrode (26 kHz) the wavelength of the fast-symmetric mode (S0) would be of the order of 220 mm, thus larger than the vertical side of the half - rudder model and comparable to its longitudinal side (400 mm). As such size, is a contributing factor towards the appearance of strong harmonics throughout the signal. Those issues were partly resolved by means of filtering through a bandpass filter, thereby by isolating the operating frequency (26 kHz) of the sonotrode that represents the main cavitation activity. Filtering, however, can even slightly distort the signal and thus influence the accuracy of the time difference measurements. This can explain the slight differences in terms of the calculated coordinates, in comparison to the actual coordinates, although results in general indicate that the speculated inaccuracy in this case would be minimal.

Nevertheless, issues related to the size of the half-rudder model as well as the required signal filtering will be clarified by means of testing even larger rudders.

With regard to the sensing system, results indicate that the location of the cavitation source can be successfully derived both by means of fibre Bragg gratings and piezoelectric sensors, although not as accurately in the case of the former when compared to the latter. Such a behaviour was essentially expected, as the use of fibre Bragg gratings as means of acoustic sensors is currently under development thus the resulting signals will be optimized in the future. Nevertheless, this can explain why in some locations, signals were distorted to the point where the resulting coordinates could be described as inaccurate. This, however, only applies for a small number of sonotrode placements, whereas in most cases the calculated locations were accurate and directly comparable to the piezoelectric sensor – based system.

7.6 Double size model rudder– Exploration of possible scale effects

Following the initial investigation that was conducted on a small half-rudder model it was decided to explore whether any possible scale effects would be apparent or not, when one was to apply the method on an even larger rudder. Towards that direction an additional model rudder was manufactured which was identical in all aspects but size to the one that has already been tested. The exterior as well as the interior of the double size half-rudder model can be seen in Figure 7.12:



Figure 7.12: Double size half-rudder model. Top-exterior, bottom-interior.

As such the length of the double size model rudder was 800mm and its width was 400mm whereas the relevant dimensions for the small half-rudder model were 400mm and 200mm, respectively. The dimensions of the internal compartments, as these were defined by the reinforcing beam as well as the four attached stingers, were also increased accordingly. The same applies for the integrated shaft of which the dimensions also doubled.

The double size half-rudder model was accommodated in an appropriately sized water tank, similarly to the small model. As such the double size rudder was essentially ‘hanged’ into the water tank by means of two elastic belts, supported by an array of aluminium bars positioned at the top of tank. That arrangement can be seen in Figure 7.13:



Figure 7.13: Double size half-rudder model ‘hanged’ into the plastic water tank. The mounted probe of the UIP1000hd ultrasonic transducer can also be seen.

In this case cavitation was again induced by ultrasonic means, similarly to the former tests, thus the portable UP200Ht as well as the standard UIP1000hd were utilized. The latter can be seen in Figure 7.57 along with its adjustable mounting base.

The experimental procedure that was followed was identical to the earlier one, thus it consisted of both cavitation erosion correlation (severity) and source location measurements. The same applies for the relevant experimental settings and conditions that were applied as well as the equipment that was used.

With regards to the former, various test rig configurations were again examined, leading to cavitation of varying intensity, ranging from ‘non - erosive’ to ‘highly -erosive’, always in terms of the observed erosion – mass loss.

As for the latter, the same piezoelectric and fibre Bragg grating sensing systems were again utilized along with the relevant supportive elements, both in terms of hardware and software. These are thoroughly presented in *sub - chapters 7.2 and 7.3*.

As a reference, the effects of the various test rig configurations that were examined, in terms of the observed erosion – mass loss, are:

- 4mm gap and a 5% (50W) sonotrode power output – “No erosion” after 2 hours.
- 3mm gap and a 5% (50W) sonotrode power output – Light erosion after 2 hours.
- 1mm gap and a 5% (50W) sonotrode power output – Medium erosion after 2 hours.
- 1mm gap and a 50% (500W) sonotrode power output – High erosion after 2 hours.

In addition, the different sonotrode placements that were examined can be seen in Figure 7.14:

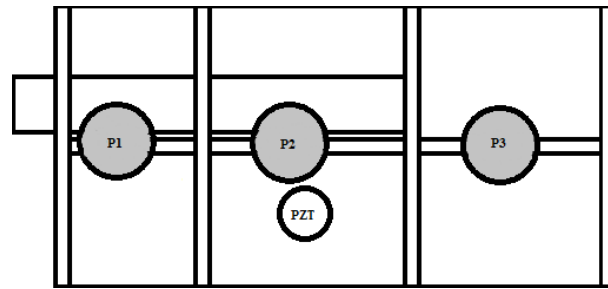


Figure 7.14: Double size rudder with acoustic sensor (Drawing). Different sonotrode locations (P1,P2,P3).

Similarly to the small rudder, the piezoelectric element was installed as centrally as possible, in order to avoid any possible interferences from the boundaries of the object while cavitation was induced in three different areas, essentially covering the whole surface of the double size rudder.

Cavitation erosion correlation (severity) results for the double size rudder, in terms of acoustic power, are presented in Figure 7.15:

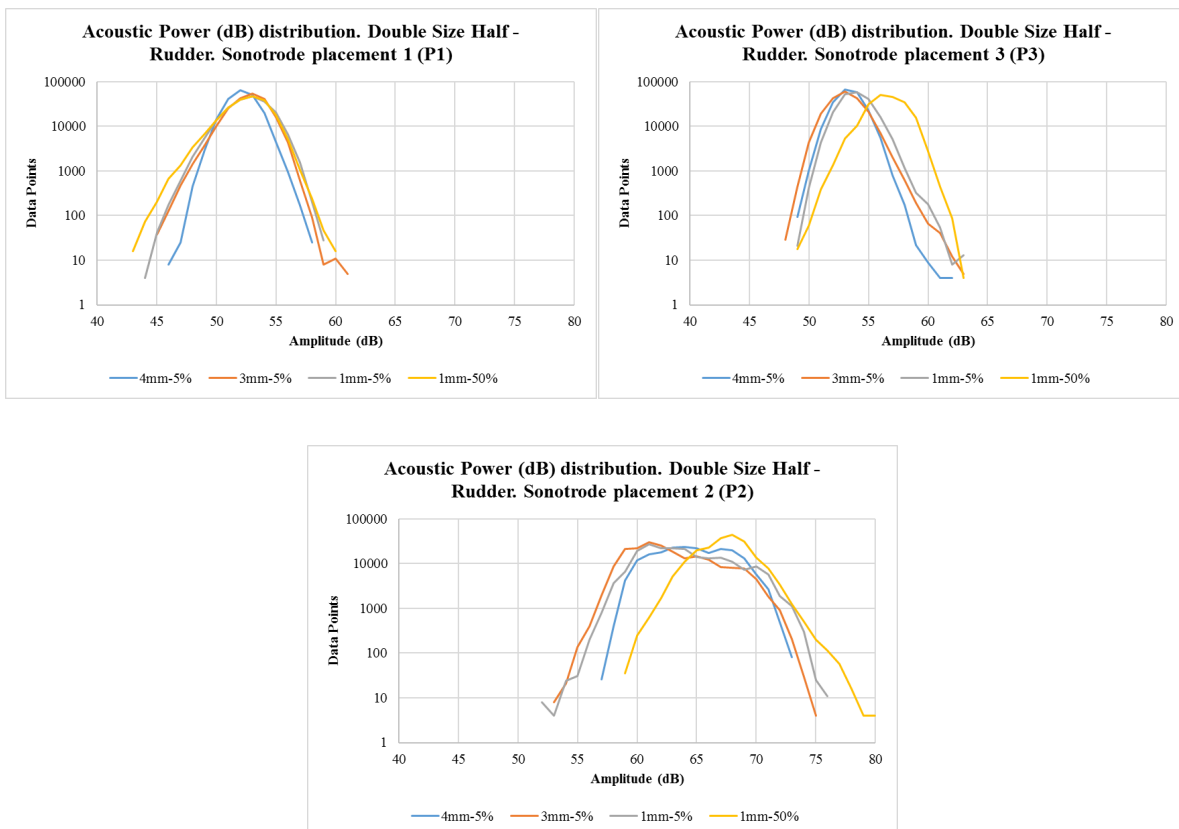


Figure 7.15: Double size rudder. Acoustic power (dB) distribution results for various sonotrode placements (P1, P2, P3) and test rig configurations.

Acoustic power distribution graphs indicate that the transition point between ‘non-erosive’ cavitation, represented by the blue lines, and ‘erosive’ cavitation, represented by the orange line, is still identifiable in all cases. In particular, the difference between the two conditions, ranges from 1 to 3 dB, which is comparable to the small rudder for which an average difference of 2 dB was observed.

It is noteworthy, that in the case of sonotrode placement P1 acoustic signals appear to attenuate more in comparison to the other placements which is similar to what was observed in the case of the small rudder. This behaviour can again be attributed to the presence of a fixed thick shaft in this area that actively interacts with the resulting acoustic waves and ‘absorbs’ a considerable amount of acoustic emission related energy. In contrast, acoustic signals were again stronger when the sonotrode was placed just above the area where the piezoelectric element was installed (P2). Finally, with regards to sonotrode placement P3, which was free of any fixed thick components, such as a shaft, signals were stronger in comparison to sonotrode placement P1 yet weaker in comparison to P2, which is sensible and identical to what was observed in the case of the small rudder.

It should be noted that, in general, the amplitudes of the resulting acoustic signals were lower in comparison to the small rudder by 4 to 5 dB. Similarly, the amplitudes of the resulting acoustic signals in the case of the small rudder were considerably lower in comparison to the small rectangular specimen, by 6 to 20 dB, depending on sonotrode placement. That implies that the parameter of size can directly influence the amplitudes of the resulting signals, in the sense that the larger the object, the more acoustic signals attenuate with distance.

What is promising at this stage is that, besides the anticipated attenuation of the resulting signals due to the increased size, the transition point between ‘non-erosive’ and ‘erosive’ cavitation can still be identified for all sonotrode placements. As such, acoustic thresholds for ultrasonically induced cavitation erosion, can be established for the double size half – rudder too, although it should be noted that these would only be valid for the particular experimental test rig and conditions. This is also the case for the other objects that were examined.

Similarly to the small rudder, acoustic signals were also converted into stress by means of the procedure described in *Chapter 6*. Results are presented in Figure 7.16:

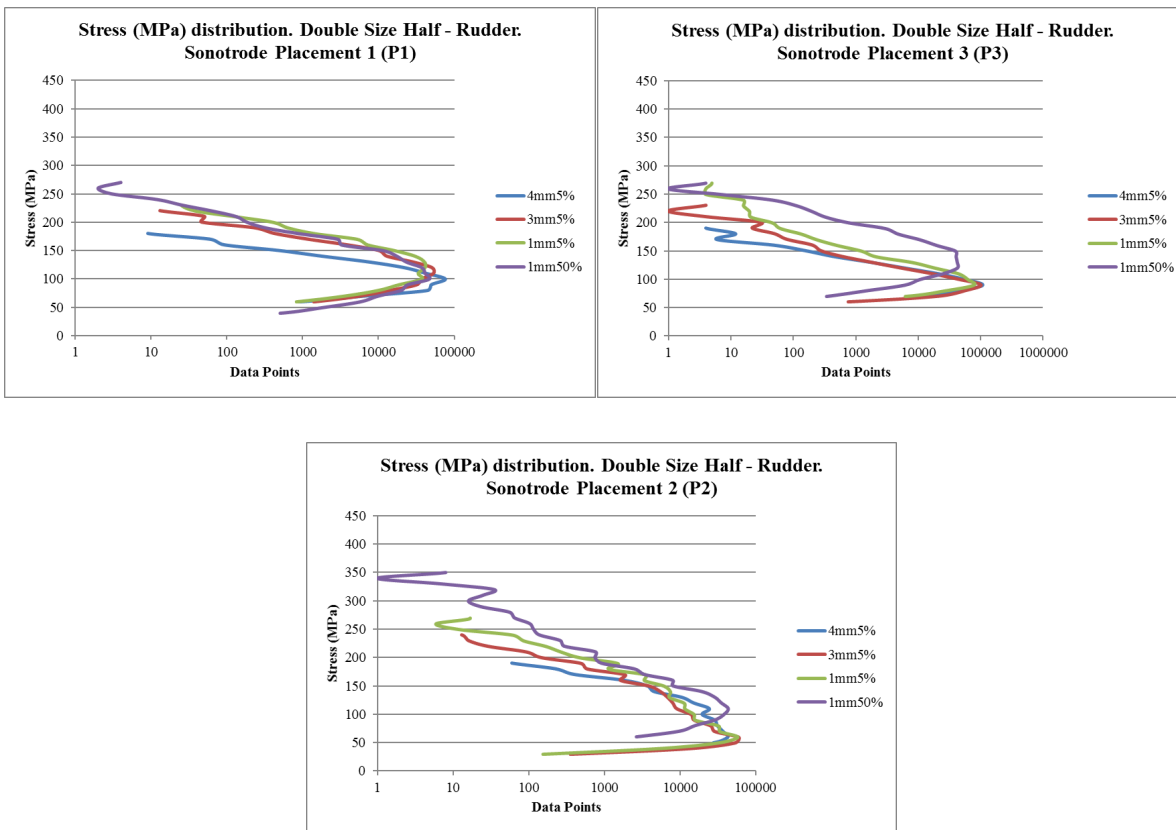


Figure 7.16: Double size rudder. Stress distribution for sonotrode placements P1, P2, P3.

The transition point between ‘non-erosive’ and ‘erosive’ cavitation is again identifiable, in terms of stress, similarly to the small rudder. In particular, stress values of the order of 170 MPa were obtained for the ‘non-erosive’ test rig configuration, whereas for the next ‘erosive’ configuration, the relevant stress values ranged from approximately 210 to 250 MPa. It should be noted that the latter are comparable to the endurance limit of the material (245-310 MPa).

The converted stress values are also comparable, in terms of amplitude, to the ones that were obtained for the small rudder. This is due to the initial calibration of the sensor that was conducted for each of the three examined positions in a way that a known force was attributed to a given response of the sensor thus acoustic signals were converted accordingly. In addition, it appears that, although the dimensions of the rudder doubled, the resulting acoustic emissions were still of sufficient amplitude to be captured by the centrally located sensor, and get converted into stress, although the raw signals were weaker in comparison to the ones obtained in the case of the small rudder. Moreover, the appearance of high energy signals is slightly less frequent in comparison to the small rudder case as it can be seen by the graphs. Attenuation in terms of frequency and amplitude in that case can be attributed to the parameter of size.

With regards to source location measurements an array of, either piezoelectric or fibre Bragg grating sensors, and the same triangulation technique that was followed in the case of the small ruder were again utilized. In that instance, however, only five sonotrode placements instead of eleven were examined, due to the operational characteristics of the ultrasonic transducer in conjunction with the size of the object and the demands of the triangulation technique.

In particular, the operating frequency of the ultrasonic transducer that was utilized for the source location measurements, namely the UIP200Ht unit, is 26 kHz corresponding to the occurrence of a pulse every 38 μ s. Results from the small rudder indicate that the maximum time difference that was measured was 32 μ s corresponding to a sonotrode placement that was 8cm off the equilibrium point between the sensors, namely the point where the time difference between the sensors would be zero. In the case of the double size rudder, however, if one was to follow a similar layout, most of the sonotrode placements would be more than 10cm off the equilibrium point, almost up to 17 cm. Distances of that sort of order would correspond to time differences comparable between the sensors, equal or larger than the 38 μ s duration of the sonotrode pulse. As such, in some cases it would be difficult to identify whether the pulses that were measured from each sensor correspond to small time differences and distances or time differences that overlap the 38 μ s operating period of the sonotrode, corresponding to equally large distances. This ambiguity could be partly resolved by means of utilizing the larger ultrasonic transducer, for which the operating period would be approximately 50 μ s, thus by incorporating more sonotrode placements that could be measured, however, in that instance results would not be as accurate due to the increased diameter of the sonotrode tip.

As such it was decided to only incorporate the sonotrode placements that can be measured without acoustic signals overlapping each other, thus the small sonotrode was utilized in this case too. In addition, an identical to the small rudder layout was followed in this case with regards to the sonotrode placements that were considered, in all aspects but distance which was doubled, for comparison reasons. These sonotrode placements can be seen in Figure 7.17:

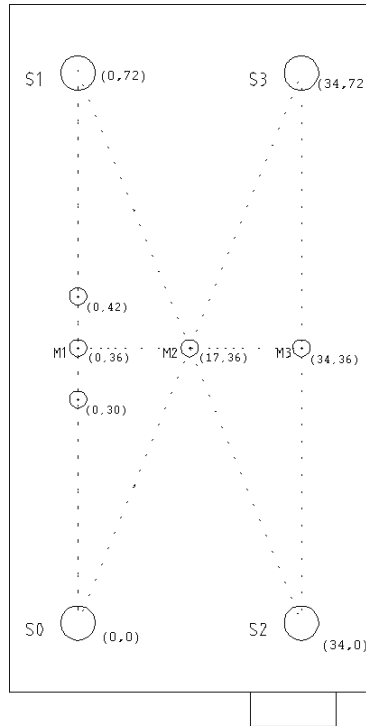


Figure 7.17: Coordinates of sensors and sonotrode placements on the double size rudder.

In this context, source location results from both piezoelectric and fibre Bragg grating arrays of sensors are summarized in Table 7.2:

Source location measurements – Double size half rudder model				
Actual Location (x, y) in cm	Piezoelectric (1) (x, y) in cm	Piezoelectric (2) (x, y) in cm	FBG (1) (x, y) in cm	FBG (2) (x, y) in cm
(0, 30)	(0.5, 30.6)	(-8, 30.6)	(1.7, 30.4)	(-6.5, 31)
(0, 36)	(2, 35)	(6.5, 35)	(3.5, 34.8)	(8, 35.1)
(0, 42)	(-1.1, 41.4)	(2.3, 41.4)	(0.8, 41)	(2.5, 41.1)
(17, 36)	(13.3, 34.4)	(10.2, 34.4)	(12, 35.2)	(13.1, 35)
(34, 36)	(29.5, 35.1)	(29.8, 35)	(28.4, 35)	(27, 35)

Table 7.2: Source location measurements – Double size half rudder model.

It is noteworthy that results are more dispersed towards the direction that is perpendicular to the beam and attached shaft of the rudder, namely the X axis. In addition, results are even more dispersed, when the fourth sensor, which is placed on the attached shaft side, is utilized. As such it appears that the presence of fixed thick components can influence the propagation

of the generated acoustic waves and influence the accuracy of the measurements, similarly to what was observed in the case of the small rudder, although to a much lesser extent.

Considering that in both cases measurements were conducted in the far field region of the sound field, it appears that the increased dispersion that was observed in the case of the double size rudder is due to scale effects, in the sense that the influence of the fixed components is further amplified.

7.7 Summary and discussion

The utilization of acoustic emissions as means of cavitation erosion monitoring for ship rudders was explored in this chapter. As such, the method was initially applied on a small half – rudder model followed by its double size counterpart.

With regards to cavitation erosion intensity, acoustic thresholds were successfully established in both cases in the sense that, the distinction between ‘non – erosive’ and ‘erosive’ cavitation, in terms of the measured acoustic emissions, was clearly identifiable all over the surface of the rudders. The same applies for the converted stress values which were sensible with regards to observed erosion and the mechanical properties of the material, although an accurate initial calibration using a known force was required in that instance.

It should be noted, however, that acoustic emissions in the case of the double size rudder were weaker in comparison to its smaller counterpart, due to size related signal attenuation. This parameter should be taken into consideration if one is to apply the method in even larger objects and it could possibly be resolved either by means of amplifying the resulting signals or using acoustic sensors of increased sensitivity.

As for the source location measurements, for which the principle of triangulation was utilized in conjunction with an array of four acoustic sensors, it was proven that ultrasonically induced cavitation can be successfully located, although some parameters must be considered. Firstly, due to the nature of the rudders that closely resemble a semi-infinite plate, the generated acoustic waves essentially consist of plate or Lamb waves, of which the propagation is guided by the boundaries of the object. As such the resulting rebounds at the boundaries of the object result into a noisier signal, which is resolved by means of filtering in order for the desired frequency to be isolated. Filtering, however, even slightly distorts the signal thus time differences are also slightly distorted. As such an amount of inaccuracy with regards to the calculated coordinates is to be expected, which was the case for both rudders.

Another parameter that should be considered is the presence of fixed components in the interior of the rudders such as the central beam and the shaft. It is noteworthy that in both cases results were more inaccurate towards the direction that is perpendicular to those components, namely the X axis, whereas the same applies for the results that were obtained from the sensor that was mounted on the shaft side. As such it appears that the propagation of the generated acoustic emissions is affected by those components in a way that they absorb a significant amount of acoustic emission energy. Considering the increased inaccuracy that was observed in the case of the double size rudder towards the direction of the shaft, in comparison to its smaller counterpart, it appears that this effect is further amplified by size.

Finally, it should be noted that due to the operating frequency of the ultrasonic transducer that was utilized for cavitation induction only a limited amount of sonotrode placements could be examined in the case of the double size rudder, due to the reasons that have already been discussed in *sub - chapter 7.7*. This condition could possibly be overcome by means of utilizing a transducer of lower operating frequency, although a minimum of 20 kHz appears to be the industry standard in that instance.

Nevertheless, results indicate that cavitation can be effectively monitored, both in terms of intensity and location, by means of the resulting acoustic emissions and the triangulation technique, whereas a distinction between erosive and non – erosive conditions can be clearly made. However, further optimization of the method, in relation to the operating frequency of the sensors to match the increased size, as well as to the induction of the appropriate adjustments to the analytical calculations and the signal filtering procedure, would be required if full scale application and even sea trials were to be considered. This prospect is within the interest of BAE Systems for the near future, in the premises of which there is a full scale rudder that is currently not in use, and could potentially be used for those tests (Figure 7.18).



Figure 7.18: Full scale ship rudder – Property of BAE Systems

Chapter 8

Conclusions & Recommendations for Future Work

8.1 Introduction

The main scope of this study related to the evaluation of the quantitative and qualitative characteristics of the cavitation induced erosion of some common shipbuilding alloys, namely grade DH36 steel, stainless steel 254 and cupronickel 70-30, with the aim of:

- Further expanding the knowledge regarding the underlying fracture mechanisms
- Exploring how this data could be utilized for erosion monitoring purposes, especially in relation to ship rudders

As such, specimens made from the aforementioned alloys were exposed to ultrasonically induced cavitation under identical experimental conditions and at the same time a series of quantitative and qualitative measurements were deployed. Initially, mass loss measurements were made in order for the effect of erosion, in terms of mass loss, to be documented and an initial evaluation regarding the resistance of the alloys to be made, always with respect to their mechanical properties. Moreover, a comparison - correlation with the 'T. O. Erosion study' was conducted, whereas the effect of cathodic protection was also examined. Afterwards, microscopic observations were conducted, by means of optical and scanning electron microscopes, in order for the underlying fracture mechanisms to be identified and evaluated with respect to the quantitative aspects of erosion. It should also be noted, that due to the interest of BAE Systems a number of protective coatings were also examined under an analogous context, although such an investigation was not within the main scope of this study. As such, these were included to the measurement file too.

Finally, acoustic emission measurements were conducted, in order for erosion to be evaluated in that respect, as well as to establish acoustic thresholds for erosive cavitation. Upon the establishment of acoustic thresholds for erosive cavitation, it was decided to deploy the aforementioned methodology for the cavitation erosion monitoring of ship rudders. As such, the potential monitoring of ship rudders, both in terms of intensity and location, was examined through experimentation on two model rudders of different size, using both piezoelectric and fibre Bragg grating sensing elements as well as a triangulation technique.

The main conclusions drawn from the aforementioned tests and measurements are presented below, whereas some recommendations for future work will be given towards the end of this chapter.

8.2 Conclusions

The main conclusions that were drawn from this study are presented below.

In relation to mass loss measurements it was shown that:

- An experimental test rig, based on the induction of cavitation by ultrasonic means, can inflict a significant amount of measurable erosion on the exposed specimens – materials. In addition, experimental conditions can be easily adjusted, thus a variety of conditions may be examined. As such a comparative investigation between different materials may be conducted through this method, although direct correlation to cavitation as it is experienced by rudders and propellers would require a more extended comparative examination between those conditions, both quantitatively and qualitatively.
- Correlation with a similar earlier was successful in the sense that analogous results were obtained in the case of grade DH36 steel. Some discrepancies with regard to the initial rate of mass loss, however, lead to the formation of a hypothesis regarding the initial surface roughness of a material and its effect on cavitation induced erosion. In particular, it was hypothesized that the higher the initial surface roughness the lower the initial resistance of a material against cavitation, a hypothesis that was confirmed through experimental measurements. This is due to the presence of notches on rough surfaces that act as stress concentrators.
- The beneficial effect of cathodic protection against cavitation induced erosion was again confirmed on grade DH36 steel, suggesting that there is an electrochemical aspect in the resulting damage. Results also showed, however, that one has to find the optimal working potential for a particular material, otherwise anodic reactions or hydrogen embrittlement would occur and as a result erosion – mass loss would increase.
- With regard to ultrasonically induced cavitation erosion, stainless steel 254 exhibited the lowest mass loss (0.02g) after five hours of exposure, followed by grade DH36 steel and cupronickel 70 - 30. Mass loss results are in good agreement with their mechanical properties in the sense that, stainless steel 254 has a yield and ultimate strength, of the order of 310 and 690 MPa, whereas the relevant values for cupronickel 70 – 30, which exhibited the highest

mass loss, are 130 and 350 MPa, respectively. Grade DH36 steel, lies between the other two alloys, with a yield and ultimate strength of, 350 and 490 MPa, respectively.

- With regard to the protective coatings, a wide range of mass loss results was obtained, ranging from a complete deterioration of the coating itself to almost negligible mass loss. It is also noteworthy, that, the uneven application of some of the coatings on the base plates, resulted into an equally uneven set of results. In any case it should be noted, the application of protective coatings, in the case of rudders and propellers, should also be examined, from a hydrodynamic as well as financial point of view.

In relation to the microscopic observations:

- Observation through the optical microscope, showed that, the depth and volume of the resulting erosion pits is analogous to the measured mass loss. For instance, the average volume of an erosion pit, in the case of cupronickel 70 – 30, which exhibited the highest mass loss, was 12 mm^3 , whereas the relevant values for grade DH36 steel and stainless steel 254, which followed, were 10 mm^3 and 2 mm^3 , respectively. The same applies for the measured depths, with average values of the order of $365.1 \text{ }\mu\text{m}$, $302.4 \text{ }\mu\text{m}$ and $36 \text{ }\mu\text{m}$, respectively. The shape and characteristics of the resulting erosion pits were unique for each material, with the pits of cupronickel 70 – 30 being characterized by asymmetrical and steep slopes, whereas analogous observations applied for grade DH36 steel, although to a lesser extent. In contrast, the erosion pits of stainless steel 254, were relatively shallow and circular in shape.
- Analogous remarks apply for the protective coatings, in the sense that the higher the mass loss, the deeper and bulkier the resulting erosion pits were found to be. In some cases, no erosion pits could be identified, although a negligible yet measurable amount of mass loss, was noted.
- Macroscopic and microscopic, through optical microscopy, observation of the eroded surfaces of the examined alloys, revealed signs of mostly brittle fracture. Further examination of the progression of erosion, however, through a scanning electron microscope, showed that erosion initiates in the form of plastic deformation (orange peeling) before progressing into ductile and eventually brittle, due to work hardening, fracture, for all alloys. The initial plastic deformation and resulting ductile fracture was more profound in the case of cupronickel 70 – 30, a behaviour that was actually expected as copper alloys are face-centred cubic (fcc) and essentially ductile in nature. This behaviour is also in good

agreement with its mechanical properties, in the sense that it has the lowest yield and ultimate strength. In addition, signs of considerable ductile fracture were even apparent, in advanced stages of erosion, despite the ongoing severe brittle, due to work hardening, fracture. This is because, being the weaker alloy, in comparison to the other two, with an ultimate strength of 350 MPa in contrast to 490 MPa and 690 MPa for grade DH36 steel and stainless steel 254, respectively, it suffered from the partial deterioration of the upper layers of its work hardened surface. As such the newly exposed layers of its surface had to go through the same ductile to brittle fracture procedure, thus signs of ductile fracture were apparent throughout the procedure. This behaviour can also be seen through its rate of mass loss, where despite the initial work hardening it remains at relatively high levels and does not decrease until the very end of the exposure. Analogous remarks apply for grade DH36 steel, although it is a body-centred cubic (bcc) alloy, thus it exhibited a ductile behaviour in the beginning of the exposure before progressing into brittle fracture, due to work hardening. Similarly, to cupronickel 70 – 30, some parts of its work – hardened surface deteriorated and had to go through the same ductile to brittle procedure, although to a much lesser extent, as it is also suggested by its properties. In particular, both its yield and ultimate strength are higher than cupronickel 70 – 30, thus suggesting a more resistant material. This is also evident in its rate of mass loss, which is relatively steady and low compared to cupronickel 70 – 30, especially past the initial work hardening stages. In contrast, stainless steel 254, which is also ductile in nature, retained the upper layers of its surface, thus it mostly suffered from brittle, due to work hardening, fracture, besides a small amount of plastic deformation and ductile fracture. This is in good agreement with its properties, which suggest that, stainless steel 254 is considerable more resistant than the other two alloys, a behaviour which was further confirmed by its measured mass loss.

- The face-centred cubic (fcc) alloys, namely stainless steel 254 and cupronickel 70 – 30, mostly exhibited intergranular fracture, which is in good agreement with theory. Moreover, they both consist of relatively larger than grade DH36 steel grains, thus they are more prone to intergranular brittle fracture, which was indeed the case. In contrast, grade DH36 steel, which is body-centred cubic, in nature, exhibited mostly transgranular brittle fracture, a behaviour which is in good agreement again with what was expected from theory. It is noteworthy that in the case of fcc alloys (stainless steel 254, cupronickel 70 – 30), the dominant intergranular fracture becomes transgranular, whereas the opposite appears to be the case for grade DH36 steel. This is due to the depletion of possible propagation paths for the former, and the presence of micro – voids in the grain boundaries for the latter.

In relation to the acoustic emission measurements:

- Acoustic emission measurements demonstrated that cavitation activity can be detected and distinguished between ‘non – erosive’ and ‘erosive’. This is because, as it appears from the results, the amplitude of the resulting acoustic emissions is analogous to the intensity of cavitation. In particular, acoustic thresholds for ultrasonically induced cavitation were established for all alloys, while acoustic emissions were further translated into stress values, by means of an analytical procedure, based on the linear behaviour of the piezoelectric elements and a standardized initial calibration. Results, in terms of stress values, were in good agreement with the mechanical properties of the alloys, as well as the resulting erosion – mass loss.
- In terms of instrumentation, piezoelectric elements are more suited for those measurements, according to the results, at least at this stage. This is mostly to their demonstrated linear behaviour, which is of great significance, if one wishes to establish acoustic thresholds for erosion. Nevertheless, fibre Bragg gratings demonstrated that they are capable of detecting acoustic emission signals due to cavitation erosion, however, more research would be required before those signals could be related to various erosion levels, for monitoring purposes. This is because their behaviour is not linear and in addition, each custom made grating, exhibits its own unique characteristics, thus extensive calibration would be required, at this stage.
- Moreover, it was shown that the K_{IC} value, namely the fracture toughness of a material, correlates well with the parameters of mass loss, average pit depth and volume for all alloys, with regard to cavitation induced erosion, similarly to the parameters of yield and ultimate strength.

Finally, with regard to the model rudder tests:

- It was shown that the utilization of acoustic emissions, for erosion monitoring purposes, in the case of rudders is viable. In particular, a distinction between ‘non – erosive’ and ‘erosive’ cavitation can be made in the case of both rudders, namely the small and double size one. In addition, it was shown that cavitation can also be located, in terms of location, through the utilization of an array of sensors in conjunction with a triangulation technique. This applies for both the piezoelectric and fibre Bragg grating sensors. Results also demonstrated that the by taking into consideration the internal structure as well as the size of the rudder the

accuracy of the monitoring system, in terms of the measured time differences and consequently the calculated source coordinates, could be further improved.

8.3 Recommendations for future work

Further to the useful information that was provided through this study it is proposed that the future researcher may:

- Examine the response of protective coatings against ultrasonically induced cavitation in more detail, considering that such an investigation was not within the main thrust of this study, and as such protective coatings were only briefly examined due to the interest of BAE Systems to the matter. Nevertheless, the increased interest of the marine industry in testing new protective coatings, demands that their behaviour against cavitation should be investigated, thus the proposed ultrasonic method, is a satisfying option.
- Examine in more detail the effect of cathodic protection, as it appears from the results that erosion is essentially a combination of mechanical and electrochemical damage. In particular, the future researcher may explore how the electrochemical parameters contributes towards the increase of total erosion and to what extent, always in respect to some commonly used shipbuilding materials, such as the ones that were examined in this study.
- Work on the development of fibre Bragg grating sensors, especially with regard to cavitation erosion monitoring through the resulting acoustic emissions. As it was previously noted their behaviour cannot be characterized as linear where each sensor exhibits slightly different characteristics. Nevertheless, they proved to be capable of detecting cavitation erosion related acoustic emissions thus in consideration of their low cost, immunity to electromagnetic interference, small size as well as chemical inertness, they may form a viable option through further development work. It is also noteworthy, that fibre Bragg gratings have shown great potential when used in an array of strain gauges for cavitation erosion monitoring purposes, thus some research could also be conducted towards that direction.
- Examine the potential use of other non – destructive techniques, such as the newly formed metal magnetic memory (MMM) method that was considered in the Appendix. Although the conclusion that was formed was not positive towards that use of that method for the evaluation of cavitation erosion, it is a fairly new method that was introduced in 1997, thus it could benefit from further research, in respect to that matter.

- Finally, the future researcher could work on the deployment of the rudder monitoring system on full – scale rudders and even conduct sea trials if possible. These prospects are indeed within the interest of BAE Systems for the near future, in the premises of which there is a full – scale rudder that is currently not in use, and could be deployed for those tests. Towards that direction, further optimization of the triangulation technique and the sensing equipment to overcome any possible issues related to size limitations could be a matter of an extended researcher work, both in hardware and software terms. This process would consist of identifying the optimal operating frequency and sampling rate conditions for the acoustic elements, and could also take into consideration of multiple arrays to cover the whole surface that is to be examined. Such a process though, would require extensive analytical calculations thus the development of the relevant software would also be part of the task. In this context, the further development of fibre Bragg gratings that was earlier proposed could also be a matter of interest towards that direction.

References

- Andrews, J (2007) *Lamb wave propagation in varying thermal environments*, M.S. Thesis, AFIT/GA/ENY/07-M01, Department of Aeronautics and Astronautics, Air Force Institute of Technology (AU), Wright Patterson, AFB, OH.
- ANTONINE EDUCATION (n.d) *Longitudinal wave*, [Drawing], Retrieved May 2017, <www.antonine-education.co.uk/Image_library/Physics_2/Waves/Wave_properties/wav_9.gif>
- Argon, A. S. (2001) ‘Mechanics and physics of brittle to ductile transitions in fracture’, *J. Eng. Mater. Technol.*, Vol. 123, pp. 1-11.
- Arndt, R. E. A. (1981) *Ann. Rev. Fluid Mech.*, Vol. 13, pp. 273-328.
- Ashworth, V., Cifuentes, L. and Procter, R. P. M. (1979) *Proc. 5th int. conf. on erosion by solid and liquid impact*, Farnborough, UK, Royal Aircraft Establishment, 66-1.
- Axdahl E. (2006), *Cavitation erosion of a watercraft propeller*, [Image], Retrieved October 2017, <https://upload.wikimedia.org/wikipedia/commons/e/e6/Cavitation_Propeller_Damage.JPG>
- Bark, G., Berchiche, N. and Grekula, M. (2004) “Application of principles for observation and analysis of eroding cavitation”, *EROCAV observation handbook*, Ed. 3.1., Chalmers University of Technology, Sweden.
- Benjamin, T.B. and Ellis, A.T. (1966) *Philos. Trans. R. Soc.*, A206, pp. 221-240.
- Benzerga, A.A. and Leblond, J.-B. (2010) ‘Ductile fracture by void growth to coalescence’, *Adv. Appl. Mech.*, Vol. 44, pp. 169-305.
- Besant, W. (1859) *Hydrostatics and Hydrodynamics*. Cambridge University Press.
- Biggs, W.D. (1960) *The brittle fracture of steel*, MacDonald and Evans, London.
- Blake, J.R. and Gibson, D.C. (1981) ‘Growth and collapse of a vapor cavity near a free surface’, *J. Fluid Mech.* 111, pp. 123-140.
- Blake, J.R. and Gibson, D.C. (1987) ‘Cavitation bubbles near boundaries’, *Ann. Rev. Fluid Mech.* 19, pp. 99-128.
- Bowden, F. P. and Field, J. E. (1964) *Proc. R. Soc.*, A282, 331.

- Bravenec, E. V. (1992) 'Intergranular fracture in carbon steel', [Fractographs], In *Handbook of Case histories in Failure Analysis*, Vol 1, K. A. Esakul, Ed, ASM International, pp. 287-290.
- Bravenec, E. V. (1992) 'Trasnggranular fracture in carbon steel', [Fractographs], In *Handbook of Case histories in Failure Analysis*, Vol 1, K. A. Esakul, Ed, ASM International, pp. 287-290.
- Briggs, L. J. (1950) 'Limiting negative pressure in water', *J. Applied Physics* 21, pp. 721-722.
- Brunton, J. H. (1970) *Proc. 3rd int. conf. on rain erosion*, Farnborough, UK, Royal Aircraft Establishment, (ed. A. A. Fyall and R. B. King) 821.
- Brunton, J. H. (1979) *Proc. 5th int. conf. on erosion by solid and liquid impact*, Farnborough, UK, Royal Aircraft Establishment, 59-1.
- Cambridge University Engineering Department (2003) *Materials Data Book*, 2003 Edition, pp. 9-13.
- Carlton, J. (2012) *Marine Propellers and Propulsion*, Third Edition, Butterworth-Heinemann.
- Carlton, J. (n.d.) *Cavitation erosion on the rudder of the Finnkraft vessel*, [Photograph], John Carlton's own private collection.
- Carlton, J. (n.d.) *CFD simulation of sonotrode operation*, [Image], John Carlton's own private collection
- Carlton, J. (n.d.) *Cloud, sheet and tip vortex cavitation* [Photograph], John Carlton's own private collection.
- Carlton, J. (n.d.) *Sheet and blade root cavitation*, [Photograph], John Carlton's own private collection.
- Chahine, G. L. (1982) 'Operating problems of pump stations and power plants', *Proc. Symp.*, International Association for Hydraulic Research, Amsterdam, Vol. 2, pp. 1-14.
- Chahine, G. L. (1982) *Appl. Sci. Res.*, 38, 187.
- Chahine, G.L. (1982) 'Experimental and asymptotic study of non-spherical bubble collapse', *Appl. Sci. Res.* 38, pp. 187-197.
- Chakrapani, D. G. (1992) 'Ductile fracture dimples in low carbon steel', [Fractograph], In *Handbook of Case histories in Failure Analysis*, Vol 1, K.A. Esakul, Ed, ASM International, pp. 168-170.

Chincholle, L. (1980) 'Hydraulic machinery in the energy related industries', International Association for Hydraulic Research, Tokyo, pp. 117-130.

Chincholle, L. and Sinomeau, R. (1982) 'Operating problems of pump stations and power plants', International Association for Hydraulic Research, Amsterdam 72-1, p. 15.

CITIMETAL CROUP CORP. (n.d.) *Quasi-cleavage fracture*, [Fractograph], Retrieved May 2017, Retrieved May 2017, < http://citimetal.com/cm/news10_files/m32.jpg >

Cottrell, A.H. (1989) 'Strengths of grain boundaries in pure metals', *Mater. Sci. Tech.*, Vol. 5, pp. 1165-1167.

Craik, D.J. and Wood, M.J. (1970) 'Magnetization changes induced by stress in a constant applied field', *J Phys D: Appl Phys* 1970, 3, pp. 1009-1061.

Cullity, B.D. and Graham, C.D. (2009) *Introduction to magnetic materials*, 2nd ed. New Jersey: John Wiley & Sons.

Curie, J. and Curie, P. (1880) 'Developpement par compression de l'electricite polaire dans le cristaux hemiedres a faces inclinees', *Bull. De la Societe Minerologique de France*, Vol. 3, pp. 90-93.

Cvetkovic M., Kompare, B. and Klemencic A.K. (2015) 'Application of hydrodynamic cavitation in ballast water treatment', *Environmental Science and Pollution Research*, Vol. 22, No. 10, pp. 7422-7438.

Dakshinamoorthy, S. (1976) MS thesis, State University of New York.

Davis, M.A., Bellemore, D.G. and Kersey, A.D. (1997) 'Distributed fiber Bragg grating strain sensing in reinforced concrete structural components', *Cem. Concr. Comp.* 19, pp. 45-57.

De, M. K. and Hammitt, F. G. (1982) 'Instrument system for monitoring cavitation noise', *J. Phys. E, Sci. Instrum.*, Vol. 15, 7, pp. 741-745.

Derendovski, A. F., Bologna, M. K. and Shalnev, K. K. (1968) *Dokl. Akad. Nauk SSSR*, 183, 1292.

Doubov, A. (1998) 'Screening of weld quality using the metal magnetic memory effect', *Welding in the World*, Vol. 41(3), pp. 196-199.

Doubov, A. and Vlasov, V.T. (2000) *Physical bases of the method of metal magnetic memory method*, ZAO "TISSO", Moscow.

- Du, B.S., Zou, Z.D. and Wang, X.H. (2008) 'In situ synthesis of TiB₂/Fe composite coating by laser cladding', *Mater. Lett.*, Vol. 62, pp. 689-691.
- Du, B.S., Zou, Z.D. and Wang, X.H. (2008) 'Laser cladding of in situ TiB₂/Fe composite coating on steel', *Appl. Surf. Sci.*, Vol. 254, pp. 6489-6494.
- Dunegan, H. et al. (1968) *Acoustic emission: A new Non-Destructive Testing Tool*, University of California, Lawrence Radiation Laboratory, UCRL-70750, p. 37.
- Eisenberg, P., Preiser, S. H. and Thiruvengadam, A. (1965) *Soc. Nav. Arch. Mar. Eng. Trans.*, 73, p. 241.
- Ellis, A. T. and Starrett, J. E. (1979) *Proc. 5th int. conf. on erosion by liquid and solid impact*, Farnborough, UK, Royal Aircraft Establishment, 57-1.
- Euler, M. (1756) 'Théorie plus complète des machines qui sont mises en mouvement par la réaction de l'eau', *L'Académie Royale des Sciences et Belles Lettres*, Berlin.
- Fanty, J.L (n.d.) MS thesis, State University Of New York.
- Farahmand, P., Frosell, T. and McGregor, M. (2015) 'Comparative study of the slurry erosion behaviour of laser clad Ni-WC coating modified by nanocrystalline WC and La₂O₃', *Int. J. Adv. Manuf. Technol.*, Vol. 79, pp. 1607-1621.
- Ferraro, P. and Natale, G. (2002) 'On the possible use of optical fibre Bragg gratings as strain sensors for geodynamical monitoring', *Opt. Laser Eng.* 37, pp. 115-130.
- Fitzgerald, E. (1966), *Particle Waves and Deformation in Crystalline solids*, Interscience Publishers, John Wiley and Sons, New York and London.
- Fontana, M. G. and Greene, N. D. (1967) *Corrosion engineering*, 91, New York, McGraw-Hill.
- Fortes-Patella, R., Reboud, J. L. and Briancon-Marjolett, L. (2004) 'A phenomenological and numerical model for scaling the flow aggressiveness in cavitation erosion', Cavitation Erosion Workshop, Val de Rueil, France.
- Fottinger, H. (1926) *Hydraulische Probleme*, Lecture Grattigen, Berlin, VDI Verlag, pp. 107-110.
- Fox, F.E. and Herzfeld, K.F. (1954) 'Gas bubbles with organic skin as cavitation nuclei', *J. Acoustic. Soc. Amer.*, Vol. 26, pp. 984-989.

- Franc, J.P. and Michel, J.M. (2004) *Fundamentals of Cavitation*, Springer Netherlands, pp. 37-39.
- Francois, D., Pineau, A. and Zaoui, A. (2013) *Mechanic Behaviour of Materials*, Fracture Mechanics and Damage, vol. II, Springer, Netherlands.
- Fujikawa, S. and Akamatsu, T. (1980) 'Effects of non-equilibrium condensation of vapour on the pressure wave produced by the collapse of a bubble in a liquid', *J. Fluid. Mech.*, Vol. 97(3), pp. 481-512.
- Gautschi, G. (2002) *Piezoelectric sensors: Force, Strain, Pressure, Acceleration and Acoustic Emission Sensors, Materials and Amplifier*, Springer.
- Gent, W. and Kooji, J. (1976) *Influence of Hull Inclination and Hull-duct Clearance on Performance Cavitation and Hull Excitation of a Ducted Propeller*, Part I, Monograph Netherlands Maritime Institute.
- Ghayal, D., Pandit, A.B. and Rathod, V.K. (2013) 'Optimization of biodiesel production in a hydrodynamic cavitation reactor using used frying oil', *Ultrason. Sonochem.*, Vol. 20, No. 1, pp. 322-328.
- Gilmore, F.R. (1952) *The growth or collapse of a spherical bubble in a viscous compressible liquid*. Cal. Inst. Techn. Hydro. Labo., Rpt 26-4.
- Gina, P.E. and Messino, C.D. (1969) *Lett. Nuovo Cimento*, 1, 305.
- Giurgiutiu, V. (2003) 'Lamb wave generation with piezoelectric wafer active sensors for structural health monitoring', *Proceedings of SPIE 5056*, pp. 111-122.
- Glikman, L.A. (1962) *Corrosion-mechanical strength of metals*, London, Butterworths.
- Goebel, J.A., Felten, E.J. and Petit, F.S. (1974) *Corrosion problems in energy conversion and generation*, (ed. C. S. Tedman), 79, Princeton, NJ, The Electrochemical society.
- Gogate, R.P. (2002) 'Cavitation: an auxiliary technique in wastewater treatment schemes', *Advances in Environmental Research*, pp. 335-358.
- Gogate, R.P. and Pandit, A.B. (2001) 'Hydrodynamic cavitation reactors: a state of the art review', *Rev. Chem. Eng.*, Vol. 17, No. 1, p. 1.
- Gould, G.C. (1970) *Proc. 3rd int. conf. on rain erosion*, Farnborough, UK, Royal Aircraft Establishment (ed. A. A. Fyall and R. B. King), 881.

Grattan, K.T.V. and Sun, T. (2000) 'Fiber optic sensor technology: An overview', *Sens. Actuators A:Phys*, Vol. 82, pp. 40-61.

Griffith, A. A. (1921) 'The Phenomena of Rupture and Flow in Solids', *Philosophical Transactions of the Royal Society A: Mathematical, Physical and Engineering Sciences*, 221 (pp. 582-593): 163.

Guth, W. (1954) *Kinematographische Aufnahmen von Wasserdampfblasen*, *Acustica*, 4, pp. 445-455.

Hackworth, J.V. (1979) *Proc. 5th int. conf. on erosion by solid and liquid impact*, Farnborough, UK, Royal Aircraft Establishment, 65-1.

Hajzargarbashi, T., Kundu, T. and Bland, S. (2011) 'An improved algorithm for detecting point of impact in anisotropic inhomogeneous plates', *Ultrasonics*, Vol. 51(3), pp. 317-324.

Hammit, F.G. and De, M.K. (1979) 'Cavitation damage prediction', *Wear*, Vol. 52(2), pp. 243-262.

Hammit, F G. (1979) 'Cavitation erosion: the state of the art and predicting capability', *Appl. Mech. Rev.*, Vol. 32(6), pp. 665-675.

Hammit, F.G., Hwang, J. B., Barber, S.A. and De, M.K. (1978) 'Predictability of prototype machine liquid cavitation and droplet impact erosion from laboratory tests', *Wear*, Vol. 46(1), pp. 127-139.

Han, J. Kong, D., Song, I.-H. and Lee, C.-S. (2001) 'Analysis of cavitating flow around the horn-type rudder in the race of a propeller', *Fourth International Symposium of Cavitation*, CAV2001:sessionB9.005, California Institute of Technology, Pasadena, USA

Han, J., Kong, D., Kim, Y. and Lew, J. (1999) 'Analysis of propeller-rudder interaction with rudder angle'. *Annual Autumn Meeting of SNAK*, Taejon, Korea, pp. 206-209.

Han, S. (2007) *Finite element analysis of lamb waves acting within a thin aluminum plate*, Thesis, AFIT/GAE/ENY/07-S02, Department of Aeronautics and Astronautics, Air Force Institute of Technology (AU).

Hansson, I. and Morch, K.A. (1978) 'The initial stage of cavitation erosion on aluminium in water flow'. *J. Phys. D: Appl. Phys.*, Vol. 11(2), pp. 147-154.

- Hansson, I. and Morch, K.A. (1979) *Proc. 5th int. conf. on erosion by solid and liquid impact*, Farnborough, UK, Royal Aircraft Establishment, 60-1.
- Hansson, I. and Morch, K.A. (1980) 'The dynamics of cavity clusters in ultrasonic (vibratory) cavitation erosion', *J. Appl. Phys.*, Vol. 51(9), pp. 4651-4658.
- Hansson, I., Kristensen, J.K. and Morch, K.A. (1978) 'A simple model for cavitation erosion on metals', *J. Phys. D, Appl. Phys.*, Vol. 11(6), pp. 891-898.
- Harrison, M. (1952) 'An experimental study of single bubble cavitation noise' *J. Acoust. Soc. Am.*, Vol. 24, pp. 776-782.
- Harvey, E.N., McElroy, W.D. and Whiteley, A.H. (1947) 'On cavity formation in water' *J. Appl. Phys.*, Vol. 18, pp. 167-172.
- He, J.G. and Hammitt, F.G. (1982) 'Velocity exponent and cavitation number for Venturi cavitation erosion of 1100-O aluminum and 1018 carbon steel', *Wear*, Vol. 80(1), pp.43-58.
- He, T., Pan, Q., Liu, Y., Liu, X. and Hu, D. (2012) 'Near-field beamforming analysis for acoustic emission source localization', *Ultrasonics*, Vol. 52(5), pp. 587-592.
- Heathcock, C.J., Protheroe, B.E. and Ball, A. (1982) 'Cavitation erosion of stainless steels', *Wear*, Vol.81(2), pp. 311-327.
- Herring, G. (1941) *Theory of the pulsations of the gas bubble produced by an underwater explosion*. OSRD, Rpt 236.
- Hickling, R. and Plesset, M.S. (1964) 'Collapse and rebound of a spherical bubble in water', *Phys. Fluids*, Vol. 7, pp. 7-14.
- Hielscher – Ultrasound Technology (n.d.) *UIP 1000hd transducer*, [Image], Retrieved May 2017, < https://www.hielscher.com/image/uiip1000hd_set_p0500.jpg >
- Hielscher – Ultrasound Technology (n.d.) *UP 200Ht transducer*, [Image], Retrieved May 2017, < https://www.hielscher.com/image/up200ht_device_p1000.jpg >
- Hill, D.J. (2005) 'DFB fibre-laser sensor developments', *Proceeding Spie*, vol. 5855, pp. 904-907.
- Hoar, T. P. and Scully, J.C. (1964) 'Mechanochemical Anodic Dissolution of Austenitic Stainless Steel in Hot Chloride Solution at Controlled Electrode Potential', *J. Electrochem. Soc.*, Vol. 111(3), pp. 348-352.

Hobbs, M.J. (1967) *Erosion by cavitation or impingement*. STP 408, 159, Philadelphia, Pa, American Society for Testing and Materials.

Hobbs, M.J. and Brunton W.C. (1965) 'Comparative erosion tests on ferrous materials, Part I: drop impact tests', Report 205, National Engineering Laboratory, East Kilbride, Glasgow.

Hong, S., Wu, Y.P. and Zhang, J.F. (2016) 'Synergistic effect of ultrasonic cavitation erosion and corrosion of WC-CoCr and FeCrSiBMn coatings prepared by HVOF spraying', *Ultrason. Sonochem.*, Vol. 31, pp. 563-569.

Hoss, V.S., Hirth, F.W., Louis, A. and Bauer, G.H. (1980) *Werkst. Korros.*, Vol. 31, pp. 1-14.

HU W. W., CLAYTON C. R. & HERMAN H. (1980) *Mater. Sci. Eng.*, 45, 263-268.

Hu, W.W., Herman, H., Clayton, C. R. and Kozubowski, J. (1980) *Ion implantation metallurgy* (ed. C. M. Preece and J. K. Hirvonen), New York, Metallurgical Society of AIME.

Huse, E. (1971) 'Propeller-Hull Vortex Cavitation', *Norw. Ship Model Exp. Tank Publ.*, No. 106, May.

Hwang, K., Mandayam, S., Udpa, S., Udpa, L., Lord, W. and Atzal, M. (2000) 'Characterization of gas pipeline inspection signals using wavelet basis function neural networks', *NDT & E Int* 2000, Vol. 33, pp. 531-545.

Ing, R.K., Quieffin, N., Catheline, S. and Fink, M. (2005) 'In solid localization of finger impacts using acoustic time-reversal process', *Applied Physics Letters*, Vol. 87 (20), 2003104

Inglis, C. E. (1913) 'Stresses in Plates Due to the Presence of Cracks and Sharp Corners', *Transactions of the Institute of Naval Architects*, Vol. 55, pp. 219-241.

Irwin, G. (1957) 'Analysis of stresses and strains near the end of a crack traversing a plate', *Journal of Applied Mechanics* 24, pp. 361-364.

Ivany, R.D. (1965) *Collapse of a cavitation bubble in viscous compressible liquid: numerical and experimental analysis*, PhD Thesis, University of Michigan.

Ivany, R.D., Hammitt, F.G. and Mitchell, T.M. (1966) 'Cavitation Bubble Collapse Observations in a Venturi', *J. Basic Eng. (Trans. ASME, D)*, Vol. 88, pp. 649-657.

Iwai, Y., Okada, T. and Hammitt, F. G (1983) 'Effect of temperature on the cavitation erosion of cast iron', *Wear*, Vol. 85(2), pp. 181-191.

- Javdani, S., Fabian, M., Arms, M., Carlton, J., Sun, T. and Grattan, K.T.V. (2014) 'Fiber Bragg Grating-Based System for 2-D Analysis of Vibrational Modes of a Steel Propeller Blade', *Journal of Lightwave Technology*, pp. 4593-4599.
- Jesnitzer, F.E., Louis, H. and Tai, P.T. (1979) *Tri. CEBEDEAU*, (427-428), pp. 255-262.
- Joel, N. and Wooster, W.A. (1961) 'On six new relations between the electric constants of crystals', *Acta Cryst.*, Vol. 15, p. 571.
- Johnson, B.D. and Cooke, R.C. (1981) 'Generation of stabilized microbubbles in seawater', *Science*, Vol. 213, pp. 209-211.
- Kaiser, J. (1950) *An investigation into the Occurrence of Noise in Tensile Tests*, Technische Hochschule, Munich, Ph.D Thesis, pp 60, [UCRL Translation – 1082 (L) June 1964]
- Kaiser, J. (1953) 'Experimental Observations and Theoretical Interpretations of Sound Measurement During Tensile Loading of Metals', *Archiv fur das Eisenhüttenwesen*, Vol. 24, No. ½, pp. 43-45, (In German).
- Kalamkarov, A.L., Fitzgerald, S.B., MacDonald, D.O. and Georgiades, A.V. (1999) 'On the processing and evaluation of pultruded smart composites', *Composites B* 30, pp. 753-763.
- Karimi, A. and Martin, J.L. (1986) 'Cavitation erosion of materials', *International Metals Reviews*, Vol. 31, pp. 1-26.
- Kashyap, M (2010) *Principles of Optical Fiber Grating Sensors*, Fiber Bragg Gratings, Second Edition, Academic Press, pp. 441-502
- Kawanami, H., Kato, H., Yamaguchi, M., Tanimura, M. and Tagaya, Y. (1997) 'Mechanism and Control of Cloud Cavitation', *J. Fluids Eng*, Vol. 119(4), pp. 788-794.
- Kelkar, M.A., Gogate, R.P. and Pandit, A.B. (2008) 'Intensification of esterification of acids for synthesis of biodiesel using acoustic and hydrodynamic cavitation', *Ultrason. Sonochem.*, Vol. 15, pp. 188-194.
- Keller, A.P. (1982) *Schlussbericht über das forschungs- vorhaben "beginnende kavitation, zugspannungen in flüssigkeiten" 2[R]*. Teil , p.15. Oskar von Miller-Institut, Germany: Technischen Universität München/Obernach.
- Kerrouche, A., Boyle, W.J.O., Sun, T., Grattan, K.T.V., Schmidt, J.W. and Taljsten, B. (2009) 'Strain measurement using embedded fiber Bragg grating sensors inside an anchored carbon fibre

polymer reinforcement prestressing rod for structural monitoring', *J. Sensors*, IEEE, 9(11), pp. 1456-1461.

Khalid, A. (1999) 'Review of the NDT market and performance of NDT companies operating in the UK', *Insight 41*, pp. 232-243.

Kinnas, S.A., Lee, H., Gu, H. and Natarajan, S. (2007) 'Prediction of sheet cavitation on a rudder subject to propeller flow', *Journal of Ship Research*, Vol. 51(1), pp. 65-75.

Kling, C.L. and Hammitt, F.G. (1972) 'A Photographic Study of Spark-Induced Cavitation Bubble Collapse', *J. Basic Eng. (Trans ASME, D)*, Vol. 94(4), pp. 825-832.

Knapp, R.T., Daily, J.W. and Hammitt, F.G. (1970) *Cavitation*, New York, McGraw-Hill.

Knott, J. (1973) *Fundamentals of Fracture Mechanics*, Butterworths, London.

Koabaz, M., Hajzargarbashi, T., Kundu, T. and Deschamps, M. (2012) 'Locating the acoustic source in an anisotropic plate', *Structural Health Monitoring: An International Journal*, Vol. 11(3), pp. 315-323.

Kooji, J. and Berg, W. (1977) *Influence of Hull Inclination and Hull-duct Clearance on Performance Cavitation and Hull Excitation of a Ducted Propeller*, Part II, Monograph Netherlands Maritime Institute.

Kornfeld, M. and Suvorov, L. (1944) 'On the destructive action of cavitation', *Journal of Applied Physics*, Vol. 15, pp. 495-506.

Kracht, A.M. (1992) *Ship-propeller-rudder interaction*, Proceedings of the 2nd International Symposium on Propeller and Cavitation, Hangzhou, China.

Krauss, G. (2000) *Steels: Heat treatment and processing principles*, ASM International.

Krenn (1949) *Elec. Rev.*, 545.

Kundu, T., Das, S., Jata, K.V. (2007) 'Point of impact prediction in isotropic and anisotropic plates from the acoustic emission data', *Journal of the Acoustical Society of America*, Vol. 122(4), pp. 2057-2066.

Lauterborn, W. and Bolle, H. (1975) 'Experimental Investigations of Cavitation-Bubble Collapse in the Neighborhood of a Solid Boundary', *J. Fluid Mech.*, Vol. 72(2), pp. 391-399.

- Laval, J. (1951) 'Elasticite des cristaux', *Compt. Rend. (Paris)*, Vol. 232, pp. 1947-1948.
- Lee, B. (2003) 'Review of the present status of optical fibre sensors', *Opt. Fibre Technol.* 9, pp. 57-79.
- LEGI Grenoble-INP (n.d.) *Orange peeling erosion pattern*, [Image], Retrieved November 2017, <<http://www.legi.grenoble-inp.fr/people/Jean-Pierre.Franc/Images/gallery2/orange%20peel.jpg>>
- Leith, W.C. and Thompson, A.L. (1960) 'Some Corrosion Effects in Accelerated Cavitation Damage', *J. Basic Eng. (Trans. ASME, D)*, Vol. 82(4), pp. 795-802.
- Lentacker, I., De Cock, I., Deckers, R., De Smedt, S.C. and Moonen C.T. (2014) 'Understanding ultrasound induced sonoporation: definitions and underlying mechanisms', *Adv. Drug Deliv. Rev.*, Vol. 72, pp. 49-64.
- Li, D.Q. (1994) *Investigation of Propeller-rudder interaction by Numerical Methods*, Ph.D. Dissertation, Chalmers University of Technology, Sweden.
- Li, S.R. (2015) 'Erosion-corrosion resistance of electroplated Co-Pd film on 316L stainless steel in a hot sulfuric acid slurry environment', *Appl. Surf. Sci.*, Vol. 331, pp. 200-209.
- Li, Z., Han, J.H. and Lu, J.J. (2015) 'Cavitation erosion behavior of Hastelloy C-276 nickel-based alloy', *J. Alloys Compd.*, Vol. 619, pp. 754-759.
- Liand, D., Yuan, S. and Liu, M. (2013) 'Distributed coordination algorithm for impact location of preciseness and real-time on composite structures', *Measurement* 46, pp. 527-536.
- Liang, R. (2006) 'Health monitoring system for offshore platform with fiber Bragg grating sensors', *J. Optical Engineering*, vol. 45 (8): Art. No.08441.
- Lin, M. (1998) *Manufacturing of Composite Structures with a Built-in Network of Piezoceramics*, Ph.D. Dissertation, Department of Mechanical Engineering, Stanford University.
- Lin, Y.B., Lai, J.S., Chang, K.C. and Li, L.S. (2006) 'Flood scour monitoring system using fiber Bragg grating sensors', *Smart Mater. Struct.* 14, pp. 1950-1959.
- Lindau, O. and Lauterborn, W. (2003) 'Cinematographic observation of the collapse and rebound of a laser-produced cavitation bubble near a wall', *J. Fluid. Mech.*, Vol. 419, pp. 327-348.
- Lippman, M.G. (1881) 'Principe de la conservation de l'electricite', *Annales de Chimie et de Physique*, Ser. 5, Vol. 24, pp. 145-178.

- Majumber, M., Gangopadhyay, T.K., Chakraborty, A.K., Dasgupta, K. and Bhattacharya, D.K. (2008) 'Fibre Bragg gratings in structural health monitoring – Present status and applications', *J. Sensors and Actuators A: Physical*, 147(1), pp. 150-164.
- Mal, A.K., Riccim, F., Gibson, S., Banerjee, S. (2003) 'Damage detection in structures from vibration and wave propagation data', *Proceedings of SPIE 5047*, pp. 202-210.
- Mal, A.K., Shih, F., Banerjee, S. (2003) 'Acoustic emission waveforms in composite laminates under low velocity impact', *Proceedings of SPIE 5047*, pp. 1-12.
- Marine Insight (2017) *Semi - Balanced Ship Rudder*, [Image], Retrieved October 2017, <<https://www.marineinsight.com/wp-content/uploads/2014/12/rudder.jpg>>
- Mathieson, R. and Hobbs, M.J. (1960) *Engineering*, Vol. 189, (4892), p. 136.
- Matthewson, M. J. (1979) *Proc. 5th int. conf. on erosion by liquid and solid impact*, Farnborough, UK, Royal Aircraft Establishment, 73-1.
- Mclaskey, G.C., Glaser, S.D., Grosse, C.U. (2010) 'Beamforming array techniques for acoustic emission monitoring of large concrete structures', *Journal of Sound and Vibration*, Vol. 329(12), pp. 2384-2394.
- Meltz, G., Morey, W.W. and Glenn, W.H. (1989) 'Formation of Bragg gratings in optical fibres by a transverse holographic method', *Opt. Lett.* 14 (15), pp. 823-825.
- MICRON OPTICS (n.d.) *SM130 Interrogator unit*, [Image], Retrieved May 2017, <micronoptics.com/wp-content/uploads/2015/12/sm130_Optical_Sensing_interrogator-500x334.jpg>
- Mihailov, S.J. (2012) 'Fiber Bragg grating sensors for harsh environments', *Sensors 2012*, Vol. 12, pp. 1898-1918.
- Mitchell, T.M. and Hammitt, F.G. (1970) *Collapse of a spherical bubble in a pressure gradient*, ASME Cavitation Forum.
- Mitchell, T.M. and Hammitt, F.G. (1973) 'Asymmetric cavitation bubble collapse', *Fluids Eng.*, Vol. 95(1), Trans. ASME J.
- Mitsubishi Heavy Industries (n.d.) *Cavitation tunnel*, [Image], Retrieved August 2017, <www.mhims.co.jp/en/products/machinery/testequipment/marineships/images/cavitationtunnel_01.jpg>

- Molland, A.F. (1981) *The free-stream characteristics of ship skeg-rudders*, PhD thesis, Department of Ship Science, University of Southampton, UK.
- Molland, A.F. and Turnock, S.R. (1991) *Wind tunnel investigation of the influence of propeller loading on ship rudder performance*, Ship Science Reports, 46, University of Southampton, UK.
- Morch, K. A. (1977) *Proc. Acoustic Cavitation meeting*, Poole, Dorset, Institute of Acoustics, London, 62.
- Morey, W.W, Ball, G.A. and Singh, H. (1996) ‘Applications of fiber grating sensors’, *Proc. SPIE* 2839, pp. 2-7.
- Moriyama, F. and Yamazaki, R. (1981) ‘On the forces acting on rudder’, *Transactions*, The West-Japan Society of Naval Architects, Vol. 62.
- Nair, A. and Cai, C. (2010) ‘Acoustic Emission monitoring of bridges: Review and case studies’, *Engineering Structures*, vol. 32, pp. 1704-1714.
- Nakatani, H., Hajzargarbashi T., Ito, K., Kundu, T., Takeda, N. (2012) *Locating point of impact on an anisotropic cylindrical surface using acoustic beamforming technique*, 4th Asia-Pacific Workshop on Structural Health Monitoring, Melbourne, Australia, December 5-7.
- Nakatani, H., Hajzargarbashi, T., Ito, K., Kundu, T. and Takeda, N. (2012) *Impact localization on a cylindrical plate by near-field beamforming analysis*, M. Tomizuka (Ed.). *Sensors and Smart Structures Technologies for Civil, Mechanical and Aerospace systems*, SPIE’s 2012 Annual International Symposium on Smart Structures and Nondestructive Evaluation, Vol. 8345, San Diego, California, March 12-15, 2012.
- NATIONAL INSTRUMENTS – NI (2016) *Fibre Bragg grating*, [Drawing], Retrieved May 2017 from < http://www.ni.com/cms/images/devzone/tut/diagram_20100726205948.jpg >
- Naude, C.F. and Elli, A.T. (1961) ‘On the mechanism of cavitation damage by nonhemispherical cavities collapse in contact with a solid boundary’, *Transactions of the ASME D: Journal of Basic Engineering*, Vol. 83, pp. 648-656.
- NDE ED (n.d.) *Crack Propagation Modes*, [Drawing], Retrieved May 2017, <www.nde-ed.org/EducationResources/CommunityCollege/Materials/Graphics/Mechanical/FractureModes.jpg>
- NDT ED (n.d) *Modes of Sound Wave Propagation*, [Drawing], Retrieved May 2017, < www.ndt-ed.org/EducationResources/CommunityCollege/Ultrasonics/Graphics/plateWaves.gif >

- NEWTON R.N. (1961) 'Influence of cavitation on propeller performance', *Int. Ship. Prog.*, 8.
- NPTEL (n.d.) *Three different fracture modes*, [Drawing], Retrieved May 2017, < http://nptel.ac.in/courses/105108072/mod01/image/lec1_clip_image004.jpg >
- Oba, R. (1994) 'The severe cavitation erosion', *Proc. 2nd Int. Symp. On Cavitation*, Tokyo (Japan), pp. 1-8.
- Oh, J., Lee, S.-H., Kim, S.-H. and Seo, D.-W. (2012) 'A numerical simulation for reduction of rudder cavitation with gap flow blocking bars', *International Journal of Naval Architecture and Ocean Engineering*, Vol. 4(2), pp. 71-82.
- Okada, T. and Hammitt, F.G. (1981) 'Cavitation erosion in vibratory and venturi facilities', *Wear*, Vol. 69, pp. 55-69.
- Okada, T., Iwai, Y. and Yamamoto, A. (1983) 'A study of cavitation erosion of cast iron', *Wear*, Vol. 84, pp. 297-312.
- Othonos, A. and Kalli, K. (1999) *Fiber Bragg Gratings: Fundamentals and Applications in Telecommunications and Sensing*, Artech House, Inc.
- Ozonek, J. (2012) *Application of Hydrodynamic Cavitation in Environmental Engineering*, CRC Press.
- Pai., A., Verma, S., Kachlwaha, S. and Maji, S. (2010) 'Biodiesel production through hydrodynamic cavitation and performance testing', *Renew Energy*, Vol. 35, pp. 619-624.
- Paik, B.G., Kim, K.Y., Ahn, J.W., Park, S., Heo, J. and Yu, B.S. (2008) 'Influence on the rudder gap cavitation by the scaling of its clearance', *Ocean Engineering*, Vol. 35, pp. 1707-1715.
- Pal, A., Verma, A., Kachhwaha, S.S. and Maji, S. (2009) 'Biodiesel production through hydrodynamic cavitation and performance testing', *Renewable Energy*, Vol. 35, No. 3, pp. 619-624.
- Pandit, A.B. and Moholkar, V.S. (1996) 'Harness cavitation to improve processing', *Chem. Eng. Prog.*, Vol. 96, p. 57.
- Parsons, C. and Cook, S. (1919) *Trans. Inst. Nav. Arch.*, Vol. 61, pp. 233-240.
- Parsons, C.A. and Cook, S.S. (1919) *Trans. Inst. Nav. Arch.*, Vol. 61, pp. 233-240.

- Paul, C.P., Mishra, S.K. and Tiwari, P. (2013) 'Solid-particle erosion behavior of WC/Ni composite clad layers with different contents of WC particles', *Opt. Laser Technol.*, Vol. 50, pp. 155-162.
- Perez, I., Cui, H.L. and Udd, E. (2001) 'Acoustic emission detection using fiber Bragg gratings', *Proceedings of SPIE 4328 Smart Structures and Materials 2001: Sensory Phenomena and Measurement Instrumentation for Smart Structures and Materials*, pp. 209-215.
- PETRACCHI G. (1949) 'On the interpretation of the corrosion process by cavitation', *Metall. Ital.*, Vol. 41, pp. 1-6.
- Philipp, A. and Lauterborn, W. (1998) 'Cavitation erosion by single laser-produced bubbles', *Journal of Fluid Mechanics*, Vol. 361, pp. 75-116.
- Pineau, A., Benzerga, A.A. and Pardoën, T. (2016) 'Failure of metals I: Brittle and ductile fracture', *Acta Materialia*, Vol. 107, pp. 424-483.
- Plesset, M.S. (1960) 'On Cathodic Protection in Cavitation Damage', *J. Basic Eng. (Trans. ASME, D)*, Vol. 82, pp. 808-820.
- Plesset, M.S. (1963) 'Bubble Dynamics', *CIT Rep. 5-23*. Calif. Institute of Technology, Pasadena.
- Plesset, M.S. and Chapman, R.B. (1969) 'Collapse of a vapor cavity in the neighborhood of a solid wall', *Caltech Report. 85-48*, California Institute of Technology, Pasadena.
- Plesset, M.S. and Chapman, R.B. (1971) 'Collapse of an initially spherical cavity in the neighborhood of a solid boundary', *J. Fluid Mech.*, Vol. 47(2), pp. 283-290.
- Plesset, M.S. and Devine, R.E. (1966) 'Effect of Exposure time on Cavitation Damage', *J. Basic Eng. (Trans. ASME, D)*, Vol. 88, pp. 691-705.
- Pohl, R., Erhard, A., Montag, H., Thomas. H. and Wustenberg, H. (2004) 'NDT techniques for railroad wheel and gauge corner inspection', *NDT & E Int. 2004*, Vol. 37(2), pp. 89-94.
- Pollock, A.A. (1968) 'Stress-wave Emission – A New Tool for Industry', *Ultrasonic*, Vol.6(2), pp. 88-92.
- Preece, C.M. (1979) *Treatise on materials science and technology*, Vol. 16, Erosion, Academic Press, New York.

- Preece, C.M. and Brunton, J. (1980) 'A comparison of liquid impact erosion and cavitation erosion', *Wear*, Vol. 60, pp. 269-284.
- Preece, C.M. and Kaufmann, E.N. (1982) 'The effect of boron implantation on the cavitation erosion resistance of copper and nickel', *Corros. Sci.*, Vol. 22(4), pp. 267-281.
- Preece, C.M. and Vyas, B. (1974) *Proc. 4th int. conf. on rain erosion and allied phenomena*, Farnborough, UK, Royal Aircraft Establishment, (ed. A. A. Fyall and R. B. King), 811.
- Protevin, A. and Le Chatelier, F. (1923) *Compte. Rendu.*, 176, pp. 507-510.
- PRRC (n.d.) *Transgranular and Intergranular fracture*, [Drawing], Retrieved July 2017, < <http://octane.nmt.edu/waterquality/corrosion/envinduced.aspx> >
- Qu, C.C., Li, J. and Bai, L.L. (2015) 'Effects of the thickness of the pre-placed layer on microstructural evolution and mechanical properties of the laser-clad coatings', *J. Alloys. Compd.*, Vol. 644, pp. 450-463.
- Rao, Y.J. (1998) 'Fibre Bragg grating sensors: principles and applications', in: K.T.V. Grattan, B.T. Meggitt (Eds.), *Optical Fibre Sensor Technology*, vol. 2, Chapman & Hall, London, 355-389.
- Rayleigh, L. (1917) 'The pressure developed in a liquid during the collapse of a spherical cavity', *Phil. Mag*, 34.
- Rayleigh, L. (1917) 'The pressure developed in a liquid during the collapse of a spherical cavity', *Phil. Mag*. 34.
- Reisman, G.E., Wang, Y-C and Brennen, C.E. (1998) 'Observations of Shock Waves in Cloud Cavitation', *Journal of Fluid Mechanics*, Vol. 335, pp. 255-285.
- Ren, J., Song, K., Wu, G. and Lin, J. (2001) 'Mechanism study of metal magnetic memory testing', *Proceedings of the 10th Asia-Pacific Conference on Non-Destructive Testing*, Brisbane, Australia.
- Reynolds, O. (1873) 'The causes of the racing of the engines of screw steamers investigated theoretically and by experiment', *Trans. INA*.
- Rhee, S.H. and Kim, H. (2008) 'A suggestion of gap flow control devices for the suppression of rudder cavitation', *Journal of Marine Science and Technology*, Vol. 13(4), pp. 356-370.

- Ribay, G., Catheline, S., Clorenec, D., Ing, R.K., Quieffin, N. and Fink, M. (2007) 'Acoustic impact localization in plates: properties and stability to temperature variation', *IEEE Transactions on Ultrasonics, Ferroelectrics and Frequency Control*, Vol. 54(2), pp. 378-385.
- Rogers, L. M. (2001) *Structural and Engineering Monitoring by Acoustic Emission Methods – Fundamentals and Applications*, Lloyd's Register, Technical Investigation Department, p. 5
- Rose J.L. (1999) *Ultrasonic Waves in Solid Media*, Cambridge University Press: Cambridge, MA.
- Roskosz, M. and Gawrilenko, P. (2008) 'Analysis of changes in residual magnetic field in loaded notched samples', *NDT & E Int.* 2008, Vol. 41, pp. 570-576.
- Saada, A. S. (1993) *Elasticity Theory and Applications*, Krieger Publishing Company: Malabar, Florida.
- Sachse, W. and Sancar, S. (1986) *Acoustic Emission Source Location on Plate-Like Structures Using a Small Array of Transducers*, U.S. Patent No. 4,592,034.
- Sass, W., Dreyer, HP, Kettermann, S. and Seifert, J. (1992) 'The role of cavitation activity in fragmentation processes by lithotripters', *J. Stone Dis.*, Vol. 4, pp. 193-207.
- Schofield, H. (1958) *Acoustic Emission Under Applied Stress*, U.S.A.F., Wright Air Development Centre, WADC-TR-58-194, NTIS Accession No. AD 155674.
- Schroter, H. (1932) *Z. Ver. Deut. Ing.*, 76, pp. 511-512.
- Scruby, C. B. (1984) *Quantitative Acoustic Emission Techniques*, Materials Physics and Metallurgy Division, Atomic Energy Research Establishment, Harwell, U. K., Report No. AERE-R-11262.
- Seah, M.P. (1980) 'Absorption – induced interface decohesion', *Acta Mater*, Vol. 28, pp. 955-962.
- Shank, M.E. (1954) 'A critical survey of brittle failure in carbon plate steel structures other than ships', *Weld Res Council*, Bull 17.
- Shannon, R., Braithwaite, I. and Morgan, L., (1988) 'Flux-leakage vehicles pass tests for pipeline inspection', *Oil Gas J*, 1988;86(32), pp. 47-59.
- Sharma, S. (2012) 'Wear study of Ni-WC composite coating modified with CeO₂', *Int. J. Adv. Manuf. Technol.*, Vol. 61, pp. 889-900.

Shen, Y., Chen, W. and Remmers, D. (1997) 'A Twisted Rudder for Reduced Cavitation', *Journal of Ship Research*, Vol. 41(4), pp. 260-272.

Shen, Y., Remmers, K. and Jiang, C.W. (1997) 'Effects of ship hull and propeller on rudder cavitation', *Journal of Ship Research*, Vol. 41(3), pp. 172-180.

Shima, A., Takayama, K., Tomita, Y. and Miura, N. (1981) 'An Experimental Study on Effects of a Solid Wall on the Method of Bubbles and Shock Waves in Bubble Collapse', *Acustica*, Vol. 48, pp. 293-301.

Shutler, N.D. and Mesler, R.B. (1965) 'A photographic study of the dynamics and damage capabilities of bubbles collapsing near solid boundaries', *J. Basic Eng. (Trans. ASME, D)*, Vol. 87, pp. 511-517.

Simoneau, R., Filhey, J. L. and Roberge, R. (1981) *Cavitation erosion in fluid systems*. (ed. W. L. Swift and R. E. A. Arndt), 71-82, New York, McGraw-Hill.

Stierman, E. (1989) 'The influence of the rudder on propulsive performance – Part I', *International Shipbuilding Progress*, Vol. 36, pp. 303-334.

Sutton, G.W. (1957) 'A photoelastic study of strain-waves caused by cavitation', *J. Appl. Mech. (Trans. ASME)*, Vol. 24(3), pp. 340-348.

SVA Potsdam GmbH (n.d.) *Cavitating Propeller*, [Image], Retrieved October 2017, <https://www.sva-potsdam.de/wp-content/uploads/2015/12/PropUKavi_Leistungen_header.jpg>

SVA Potsdam GmbH (n.d.) *Rudder – Propeller interaction*, [Image], Retrieved October 2017, <https://www.sva-potsdam.de/wp-content/uploads/2016/04/Prop_n_Cav_Highspeed_Video-473x325.png>

Tamashima, M., Matsui, S., Yang, J., Mori, K. and Yamazaki, R. (1993) 'The method for predicting the performance of propeller-rudder system with rudder angles and its application to the rudder design'. *Transaction of the West-Japan Society of Naval Architects*, Vol. 86, pp. 53-76 (in Japanese).

Taylor, I. (1979) *Treatise on materials science and technology*, Vol. 16, 373, New York, Academic Press.

- Tennyson, R.C., Mufti, A.A., Rizkalla, S., Tadros, G. and Benmokrane, B. (2001) 'Structural health monitoring of innovative bridges in Canada with fiber optic sensors', *Smart Mater. Struct.* 10, pp. 560-573.
- Thiruvengadam, A. and Preiser, H. (1964) 'On Testing Materials for Cavitation Damage Resistance' *J. Ship. Res.*, Vol. 8(3).
- Thomas, G.P. and Brunton, J.H. (1970) 'Drop Impingement Erosion of Metals', *Proc. R. Soc.*, Vol. 314, pp. 549-565.
- Timoshenko, S., and Goodier, J. (1970) *Theory of Elasticity*, McGraw-Hill, New York, N.Y, pp. 433-441.
- Tobias A. (1976) 'Acoustic-emission source location in two dimensions by an array of three sensors', *Nondestr. Test.* 9, pp. 9-12.
- Tomita, Y. and Shima, A. (1986) 'Mechanisms of impulsive pressure generation and damage pit formation by bubble collapse', *Journal of Fluid Mechanics*, Vol. 169, pp. 535-564.
- Tracy, M. and Chang, F.K. (1996) 'Identifying impact load in composite plates based on distributed piezo-sensors', *The Proceedings of SPIE Smart Structures and Materials Conference*, San Diego, CA.
- Trilling, L. (1952) 'The collapse and rebound of a gas bubble', *J. Appl. Phys*, Vol. 23, p. 14.
- Tsakonas, S., Jacobs, W.R. and Ali, M.R. (1975) 'Propeller-rudder interaction due to loading and thickness effects', *Journal of Ship Research*, Vol. 19(2), pp. 99-117.
- Tulin, M.P. (1969) *Problems of hydrodynamics and continuum mechanics*, Society for Industrial and Applied Mathematics, Philadelphia, Pa, 725.
- Tyne & Wear Museums (n.d.) *Turbinia vessel at speed in 1894*, [Photograph], Retrieved August 2017, < <http://www.tynebuiltships.co.uk/T-Ships/Turbinia-1894.jpg>>
- Udd, E. (1995) *Fiber Optic Smart Structures*, John Wiley & Sons, Inc., New York.
- University of Southampton (n.d.) *Brittle failure*, [Image], Retrieved May 2017, < http://www.southampton.ac.uk/~doctor/QS_4_files/image016.gif>
- University of Southampton (n.d.) *Ductile failure*, [Image], Retrieved May 2017, < http://www.southampton.ac.uk/~doctor/QS_4_files/image008.gif>

- Vaidya, S. and Preece, C.M. (1978) 'Cavitation erosion of age-hardenable aluminum alloys', *Metall. Trans.*, Vol. 9A, pp. 299-307.
- Van Wijngaarden L. (1964) *Proc. 11th int. cong. of applied mechanics*, Munich, (ed. H. Gortler), Berlin, Springer, pp. 854-861.
- Vogel, A., Lauterborn, W. and Timm, R. (1989) 'Optical and acoustic investigations of the dynamics of laser-produced cavitation bubbles near a solid boundary', *Journal of Fluid Mechanics*, Vol. 206, pp. 299-338.
- Voigt, W. (1890) 'Al gemeine Theorie der piezo- und pyroelectrischer Erscheinungen an Krystallen', *Abhandlungen der Koniglichen Gesellschaft der Wissenschaften zu Gottingen*, Vol. 36, pp. 1-99.
- Von Altof, F. C., Buhl, H. and Voight, H. (1973) *Werkst. Korros.*, 24, (1020), pp. 606-673.
- Votava, E. and Jav, P. (1979) *Inspection of Nuclear Reactors by Means of Acoustic Emission During Hydro-test*, Kraftwerk Union A.G., Erlangen, Germany.
- Vyas, B. and Preece, C. M. (1976) 'Stress produced in a solid by cavitation', *J. Appl. Phys.*, Vol. 47(12), pp. 5133-5138.
- Vyas, B. and Preece, C. M. (1974) *Erosion, wear and interface with corrosion*, (ed. A. Thiruvengadam), STP 567, 77, Philadelphia, Pa, American Society for Testing and Materials.
- Wade, E.H.R. and Preece, C.M. (1978) 'Cavitation erosion of iron and steel', *Metall. Trans.*, Vol. 9A, pp. 1299-1310.
- Wang, Z., Deng, B. and Yao, K. (2011) 'Physical model of plastic deformation on magnetization in ferromagnetic materials', *J Phys D: Appl. Phys.* 2011, 109:083928.
- Wang, Z., Liu, J.W. and Kang, N. (2016) 'Cavitation erosion of plasma-sprayed CoMoCrSi coatings', *Tribol. Ini.*, Vol. 102, pp. 429-435.
- Wells, A.A (1956) 'The brittle fracture strengths of welded steel plates', *Trans Royal Inst Naval Architects*, 98:296.
- Westergaard, H. M. (1939) 'Bearing pressures and cracks', *Journal of Applied Mechanics* 6, pp. A49-A53.
- Wheeler, W.H. (1960) 'Indentation of metals by cavitation', *ASME trans.*, Series D, 82.

- Wijngaarden E. (2012), *Cavitating Propellers, Vibration vs. Hydrodynamic Performance*, Ship Noise & Vibration Seminar, Lloyds Maritime Academy, London.
- Williams, R.A., Delius, M., Miller, D.L. and Schwarze, W. (1989) 'Investigation of cavitation in flowing media by lithotripter shock waves both in vitro and in vivo', *Ultrasound in Med. & Biol.*, Vol. 15, No. 1, pp. 53-60.
- Wright, R.N. and Mikkola, D.E. (1976) 'Cavitation-induced erosion of ordered and disordered Cu₃Au', *Mater. Sci. Eng.*, Vol. 26, pp. 263-268.
- Wu, J. Pepe, J. and Rincon, M. (2006) 'Sonoporation, anti-cancer drug and antibody delivery using ultrasound', *Ultrasonics*, Vol. 44, Suppl. 1, pp. e21-e25.
- Yount, D.E. (1979) 'Skins of varying permeability: a stabilization mechanism for gas cavitation nuclei', *J. Acoust. Soc. Am.*, Vol.65, pp.1429-1439.
- Yount, D.E. (1982) 'On the evolution, generation and regeneration of gas cavitation nuclei', *J. Acoust. Soc. Am.*, Vol. 71., pp. 1473-1481.
- Zhang, S., Wu, C.L. and Yi, J.Z. (2015) 'Synthesis and characterization of FeCoCrAlCu high-entropy alloy coating by laser surface alloying', *Surf. Coat. Technol.*, Vol. 262, pp. 64-69.
- Zhang, S., Wu, C.L. and Zhang, C.H. (2015) 'Phase evolution characteristics of FeCoCrAlCuVxNi high entropy alloy coatings by laser high-entropy allowing', *Mater. Lett.*, Vol. 141, pp. 7-9.
- Zhao, W.M., Wang, C. and Zhang, T.M. (2016) 'Effects of laser surface melting on erosion-corrosion of X65 steel in liquid-solid jet impingement conditions', *Wear*, Vol. 362-363, pp. 39-52.
- Zheng, Q., Durben, D.J. and Wolf, G.H. (1991) 'Liquids at large negative pressures: Water at the homogeneous nucleation limit', *Science*, Vol. 254, pp. 829-832.
- Zhong, P., Cioanta, I., Cocks, FH and Preminger, GM (1997) 'Inertial cavitation and associated acoustic emission produced during electrohydraulic shock wave lithotripsy', *J. Acoust. Soc. Am.*, Vol. 101, pp. 2940-2950.
- Zhu, S., Cocks, FH, Preminger, GM and Zhong, P. (2002) 'The roll of stress waves and cavitation in stone comminution in shock wave lithotripsy', *Ultrasound Med. Biol.*, Vol. 28, pp. 661-671.
- Zhu, Z-L and Dong, S-T (1986) *A theoretical method for predicting the hydrodynamic performances of propeller-rudder interaction*, International Symposium on Propeller and Cavitation, Wuxi, China.

Appendix A

A.1 Case study: Acoustic emission (AE) hull structural monitoring

The application of acoustic emissions as means of non-destructive hull structural monitoring on a high endurance cutter is presented in Appendix A. It should be noted that only brief details regarding the procedure and findings will be given due to the confidential nature of the work and the fact that the ship serves as a maritime law enforcement unit.

The procedure can be divided into two parts as follows:

- The volumetric measurements requiring the use of multiple acoustic sensors and a triangulation technique for the detection of cracks throughout the structure.
- Strains measurements for fatigue estimation purposes requiring the use of gauge length strain extensometers.

A.2 Procedure and equipment

A total of sixteen acoustic sensors with nominal frequencies ranging from 75 to 150 kHz were installed at crucial points of the ship structure with the purpose of detecting the presence as well as the inception of cracks. An equal number of band pass preamplifiers with frequencies ranging from 50 to 200 kHz were also installed in conjunction with the acoustic sensors. Signals from all sensors were captured by a BALRUE Data Acquisition Unit and Dongle and further processed by means of the relevant software package installed in a laptop computer, both conveniently installed and located in a protected yet easily accessible area.

With regards to the analytical procedure regarding the volumetric measurements, the method was based on a simple triangulation technique and as such the acoustic sensors were divided into four groups each one containing the required four sensors. Time delays between the sensors of each group, when processed by means of the triangulation analytical technique could indicate the presence as well as the inception of cracks in terms of spatial coordinates. The theory behind this method as well as the governing equations are thoroughly described in Appendix C.

Results regarding the ship structure as well as the presence of cracks will not be given due to the confidential nature of the work. The instalment of a number of acoustic sensors and their corresponding preamplifiers however, at crucial points of the structure, as well as the BALRUE Data Acquisition Unit and the Laptop computer, can be seen in Figure A1.



Figure A1: Top -Two acoustic sensors along with their preamplifiers installed at crucial points of the ship structure. Bottom – BALRUE Data Acquisition Unit and Laptop.

In addition to the volumetric measurements a series of strain measurements also took place for fatigue estimation purposes. A total of six gauge length strain extensometers were installed

at crucial points of the ship structure. Signals were captured by means of a strain conditioning unit and further processed through the relevant software installed on an additional laptop computer. The strain conditioning unit as well as the laptop can also be seen in *Figure A1* alongside the BALRUE Data Acquisition Unit and its dedicated laptop computer. The instalment of two gauge length strain extensometers can be seen in *Figure A2*.

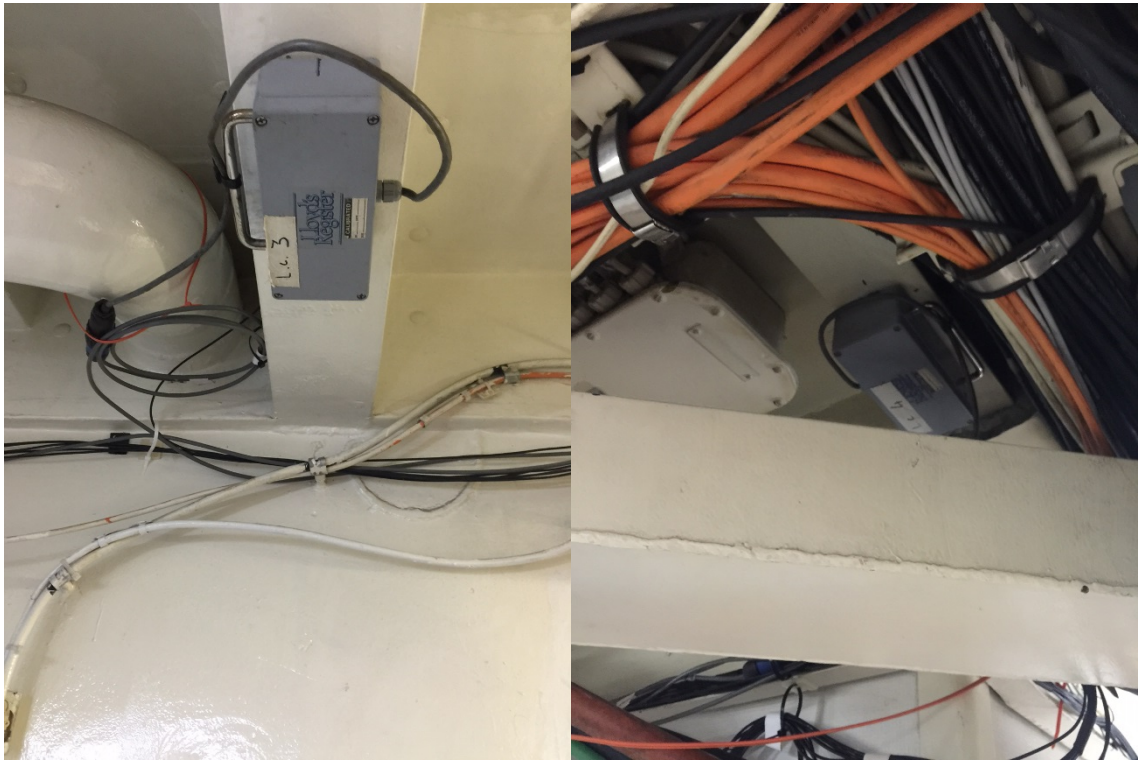


Figure A2: Gauge length strain extensometers installed at crucial points of the ship structure.

With regards to the underlying analytical procedure, the obtained signals, in terms of voltage, were initially converted into strain values and were then translated into stresses following a similar to the one described in *Chapter 6* procedure. Stress data was then plotted onto comparative graphs.

A.3 Indicative results

Although accurate results regarding strain measurements will again not be given due to the confidential nature of the work, the response of four gauge length strain extensometers during a sea trial is shown in *Figure A3*. It should be noted that stress data was further processed by means of statistical tools in order for incidents related to the operation of the ship to be highlighted, as a consequence of the high frequency with which they occurred.

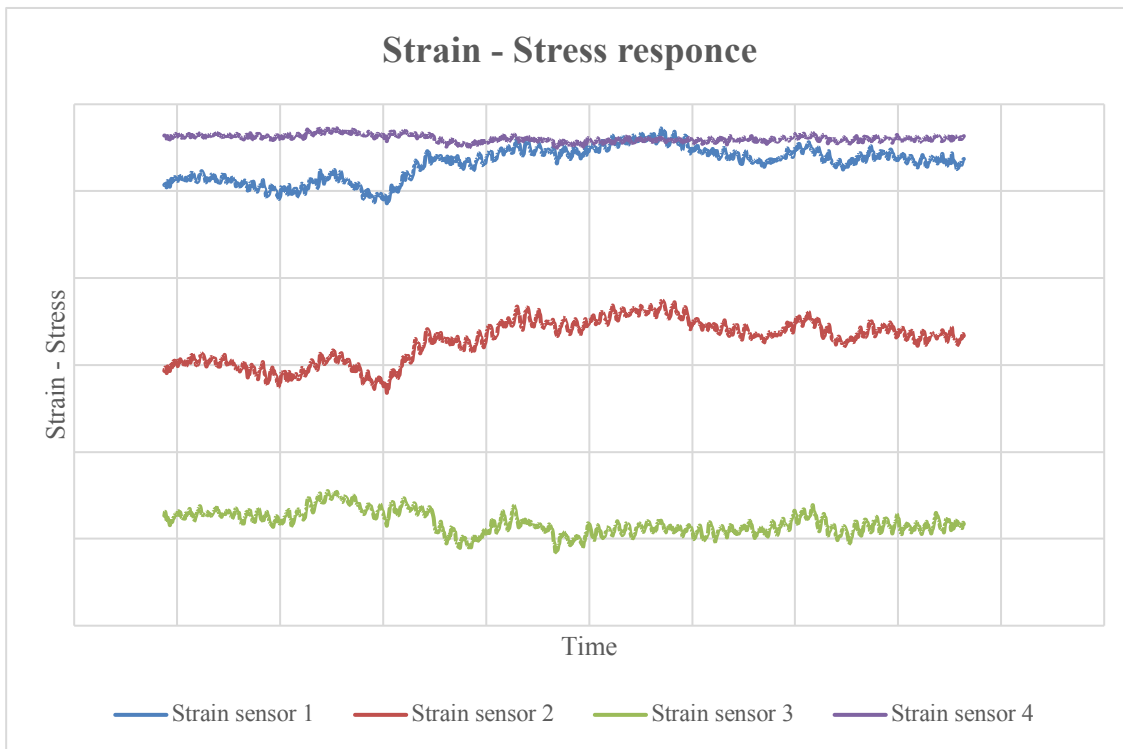


Figure A3: Strain – Stress response of four gauge length strain extensometers during sea trials.

The measured variations, with regards to the response of the gauge length strain extensometers in terms of strain – stress at the monitored areas, that can be seen in Figure A3 can be attributed to the operating conditions of the examined vessel (speed, direction, weather).

Appendix B

B.1 The metal magnetic memory (MMM) method

The residual magnetic field (RMF) of a ferromagnetic material can be influenced by various physical processes such as:

- The magneto-mechanical effect or inverse magneto-strictive effect, which is the change of the magnetic field of a material when subjected to mechanical stress.
- The magnetic field leakage effect caused by discontinuities and structural defects of the material.
- The interaction of external magnetic fields with discontinuities inside the material.

Traditional magnetic flux leakage (MFL) methods rely on strong artificial magnetic fields and have been used extensively for the detection of macro-defects in pipelines and other steel structures. The main disadvantage of these methods is that the strong artificial magnetic field tends to re-orient the magnetic field of the examined material, thus all information related to micro-defects and internal stresses which would normally influence the residual magnetic field is eliminated.

The metal magnetic memory method (MMM) is based on the magneto-mechanical effect in ferromagnetic materials. It was first introduced in 1997 as a new passive non-destructive testing method (NDT). In contrast to MFL methods the metal magnetic memory (MMM) method takes advantage of Earth's own magnetic field instead of an artificial one, thus changes of the residual magnetic field of the material due to mechanical degradation can be directly identified. Additionally, changes of the residual magnetic field of a material due to external loads and subsequently internal micro-damage is permanent, thus the exposed structures can be inspected even when the load is removed.

The metal magnetic memory (MMM) is a fairly new non-destructive testing (NDT) and as a result the underlying physical mechanisms are not yet fully understood. The method is at the moment orientated in the elastic deformation stage, where the residual magnetic field (RMF) exhibits a linear behaviour thus it is mostly effective as an early damage inspection tool. Plastic deformation however, affects the residual magnetic field of the examined material in a non-linear and complex way and requires further study. Similarly, the relation between the RMF

signals and specific defects (micro-cracks, macro-cracks etc.) should be investigated more thoroughly. Many related studies are moving towards that direction at the moment.

B.2 Experimental procedure and testing

The metal magnetic memory method is a non-destructive testing (NDT) method based on the recording of the residual magnetic field of the examined material. Earth's own magnetic field is used as the stimulus source (about 40 A/m). During the MMM testing the distribution of the residual magnetic field (H) is identified along the surface of the examined material and its gradient is calculated. In fact, external loading of sufficient magnitude, can create internal dislocations that can significantly influence the material's residual magnetic field in those areas. In particular, when slip bands are formed, the vector of the magnetic field in those areas follows the direction of the slip planes and not the direction of the external magnetic field.

An important parameter of the method is the line of polarity change of the magnetic field that is created when the material is subjected to external loading. The value of the normal component H_n in the line of polarity change is $H_n=0$ whereas the tangential component H_t shows its maximum value. The underlying physical mechanisms behind the creation of the line are not yet fully understood, however it is thought that is related to the direction of the slip bands inside the material. The quantitative evaluation of the stress concentration areas lies on the calculation of the gradient K :

$$K_i = |\Delta H_i|/2\lambda_k \quad (B1)$$

In this equation:

ΔH_i is the difference between two values of either the normal component H_n or the tangential component H_t at two inspection points positioned at a distance of λ_k from both sides of the line of polarity change ($H_n=0$). The value of K_i is proportional to the intensity of magnetic field changes and subsequently of the internal stresses at the inspection areas at least for damage related to elastic deformation.

Perpendicular and longitudinal scanning of the examined surface is conducted by means of the MMM instrument and the values of the gradient K_i of the components of the magnetic field (normal and tangential) across the surface are identified. Results are then plotted on Position-Gradient (K_i) graphs on which stress concentration areas are identified. The highest K values are related to areas of maximum stress concentration. It is necessary that the material has been scanned before any loading is applied in order for possible defects and unique characteristics

to be identified and not be confused with actual loading damage. This can also be performed on a load-free area of the material.

B.3 Cavitation erosion evaluation by means of the metal magnetic memory (MMM) method

The metal magnetic memory method has exhibited promising results especially in cases of elastic deformation whereas the relation between stresses and the change of the magnetic field is linear. The relation between plastic deformation and the change of the magnetic field though has not been fully understood yet. On this note, the very early stages of cavitation related erosion could be possibly detected, just before plastic deformation and eventually brittle fracture takes place. Fatigue in exposed components could also be identified due to the presence of related stresses in the material.

On the other hand, application of the metal magnetic memory method is possible only in materials with ferromagnetic behaviour. Metals with ferromagnetic properties include iron, cobalt and nickel as well as most of their alloys. Mechanical components exposed to cavitation however, such as ship propellers and rudders are sometimes manufactured by non-ferromagnetic materials such as copper and its alloys and should be examined by means of an alternative NDT method. Results from different NDT methods though, are not always comparable thus a common inspection method would be preferable in complex structures that are exposed to cavitation and are made of different types of metals such as ship propulsion systems.

Moreover, the dependence of the MMM method to the Earth's magnetic field and the absence of any other magnetic interference makes it inapplicable for complex structures such as ships and their propulsion systems. Interference from the extensive machinery and electrical networks, will possibly interfere with the MMM sensor and the detected magnetic field of the examined component. Components would have to be removed in order to be examined, which is not always possible, especially in operating ships, thus a different type of NDT testing would be preferred such as an acoustic emissions or strain monitoring system.

It appears that cavitation related erosion in exposed components cannot be effectively monitored and inspected by the MMM method for the moment. Nevertheless, one has to take into account that the MMM is a fairly new method that was first presented in 1997, thus the underlying physics are not well understood yet, especially in cases of plastic deformation.

Related studies are working towards that direction, as well as with the development and application of the method in more complex structures.

Appendix C

C.1 The triangulation technique by Tobias – The operating sound field

The basis of the described triangulation technique lies on an array of three acoustic sensors, located at points $S_0 (0, 0)$, $S_1 (x_1, y_1)$ and $S_2 (x_2, y_2)$ as well as an acoustic emission source located at $P (x, y)$ at a distance r from S_0 . An acoustic emission event would then lead to a set of time differences δ_1 and δ_2 :

$$\delta_1 = PS_1 - PS_0 = t_1xc \tag{C1}$$

$$\delta_2 = PS_2 - PS_0 = t_2xc$$

where c is the velocity with which sound propagates in the material and t_1 and t_2 the measured time difference with regards to the arrival of the sound waves for the pairs of sensors $S_1 - S_0$ and $S_2 - S_0$, respectively.

The acoustic emission source $P (x, y)$ would be located at the intersection of three circles with a radius of r , $r + \delta_1$ and $r + \delta_2$ whereas the centre of those circles would be located at the points $S_0 (0, 0)$, $S_1 (x_1, y_1)$ and $S_2 (x_2, y_2)$, respectively. This technique, applied on the half – rudder model is graphically illustrated in Figure C1:

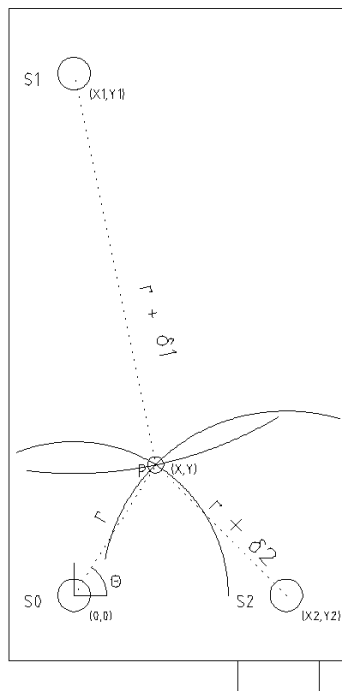


Figure C1: Acoustic emission source location at the intersection of three circles. Rudder.

The three circles would be described in analytical terms as follows:

$$x^2 + y^2 = r^2 \quad (C2)$$

$$(x - x_1)^2 + (y - y_1)^2 = (r + \delta_1)^2$$

$$(x - x_2)^2 + (y - y_2)^2 = (r + \delta_2)^2$$

Combining the equations describing the three circles and switching to polar coordinates would lead to:

$$r = \frac{A_1}{2(x_1 \cos\theta + y_1 \sin\theta + \delta_1)} = \frac{A_2}{2(x_2 \cos\theta + y_2 \sin\theta + \delta_2)} \quad (C3)$$

where

$$A_1 = x_1^2 + y_1^2 - \delta_1^2 \quad (C4)$$

$$A_2 = x_2^2 + y_2^2 - \delta_2^2$$

Equation (C3) can be rewritten as follows:

$$(A_1 x_2 - A_2 x_1) \cos\theta + (A_1 y_2 - A_2 y_1) \sin\theta = A_2 \delta_1 - A_1 \delta_2 \quad (C5)$$

Further expansion of equation (C5) by means of dividing with the term:

$$[(A_1 x_2 - A_2 x_1)^2 + (A_1 y_2 - A_2 y_1)^2]^{\frac{1}{2}}$$

leads to:

$$\begin{aligned} & \frac{(A_1 x_2 - A_2 x_1) \cos\theta}{[(A_1 x_2 - A_2 x_1)^2 + (A_1 y_2 - A_2 y_1)^2]^{\frac{1}{2}}} \\ & + \frac{(A_1 y_2 - A_2 y_1) \sin\theta}{[(A_1 x_2 - A_2 x_1)^2 + (A_1 y_2 - A_2 y_1)^2]^{\frac{1}{2}}} = \frac{A_2 \delta_1 - A_1 \delta_2}{[(A_1 x_2 - A_2 x_1)^2 + (A_1 y_2 - A_2 y_1)^2]^{\frac{1}{2}}} \end{aligned} \quad (C6)$$

Considering that the coefficients of $\cos\theta$ and $\sin\theta$ are less than unity, equation (C6) can be rewritten in the form

$$\cos(\theta - \varphi) = K \quad (C7)$$

where:

$$K = \frac{(A_2\delta_1 - A_1\delta_2)}{[(A_1x_2 - A_2x_1)^2 + (A_1y_2 - A_2y_1)^2]^{\frac{1}{2}}} \quad (C8)$$

and:

$$\tan\varphi = \frac{(A_1y_2 - A_2y_1)}{(A_1x_2 - A_2x_1)} \quad (C9)$$

Therefore, the angle φ can be derived by equation (C9) in the range of $-\pi$ to $+\pi$ as follows:

$$\varphi = a + 2m\pi \quad (C10)$$

for $m=0, \pm 1, \pm 2$.

As for the term K and considering that its denominator is positive by definition whereas its numerator can be derived from the known locations of sensors $S_1 (x_1, y_1)$ and $S_2 (x_2, y_2)$ this would lead to a solution of the form:

$$\beta = \cos^{-1}|K| \quad (C11)$$

As such equation (C7) could be transformed and rewritten as follows:

$$(\theta - \varphi) = \beta + 2n\pi \quad (C12)$$

Or

$$(\theta - \varphi) = -\beta + 2n\pi$$

for $n=0, \pm 1, \pm 2$.

It should be noted that there are two solutions for the equation $\cos(\theta-\varphi) = K$ in the range $-\pi$ to $+\pi$ as it can be seen in equation (C12).

Combination of equations (C7), (C10), (C11) and (C12) would lead to:

$$\theta = (a + \beta) + 2n\pi \quad (C13)$$

$$\theta = (a - \beta) + 2n\pi$$

It can be seen that similarly to the term $(\theta-\varphi)$ there are two solutions for the angle θ in the range $-\pi$ to $+\pi$.

Eventually once the two solutions for angle θ are calculated, the radius r can be calculated by means of equation (C3) and as such the acoustic emission source location $P(x, y)$ can be derived through the set of equations (C2).

It should be noted, however, that a solution of θ must lead to a positive value of r in order to be valid. This is the case for the majority of measurements where only one value of θ is valid for a given pair of time differences δ_1 and δ_2 . Nevertheless, the rare ambiguity of having two valid solutions of θ is resolved by using a fourth acoustic sensor $S_3(x_3, y_3)$ and through comparison between the measured time difference for sensors $S_3 - S_0$ and the resulting time difference when the calculated position of the acoustic emission source is taken into account.

Finally, with regards to the operating sound field it should be noted that there are significant fluctuations near an ultrasonic transducer due to the constructive or destructive interference of multiple acoustic waves. As such, the conduction of accurate measurements within that region is considered to be extremely difficult, thus the far field region where acoustic waves form a uniform front is much preferred. The length of that near field region, where these phenomena occur, can be calculated by means of equation (C14):

$$N = \frac{D_t^2 f}{4c} \quad (C14)$$

where N is the near field length, f is the frequency of the transducer, D_t is the diameter of the transducer and c the speed of sound in the material.

In this context the near field length, in the case of the half-rudder models, ranges from 0.05 mm to 0.41 mm, depending on the ultrasonic transducer that was utilized. As such, and by considering the dimensions and thickness of the rudders, all acoustic measurements, both in terms of intensity and location, were conducted in the far field region.

Appendix D

D.1 The triangulation technique – Source location measurements – Piezoelectric sensors

Results are presented in the form of graphs containing the relevant time differences, with regards to the arrival of the acoustic waves to each one of the piezoelectric sensors, and the calculated source location positions, respectively. It should be noted that all acoustic waveforms were processed through an appropriate band pass filter in order for the 26 kHz operating frequency of the sonotrode to be isolated. In addition, graphs are arranged in an order corresponding to the positions of the sensors, as these are presented in the mapping graphs, while the time scale of the X axis is adjusted accordingly in order for time differences to be distinguishable. Finally, it should be noted that the starting - reference point for all measurements, was the sensor that was closer to the source of cavitation.

Sonotrode Placement (0, 10)

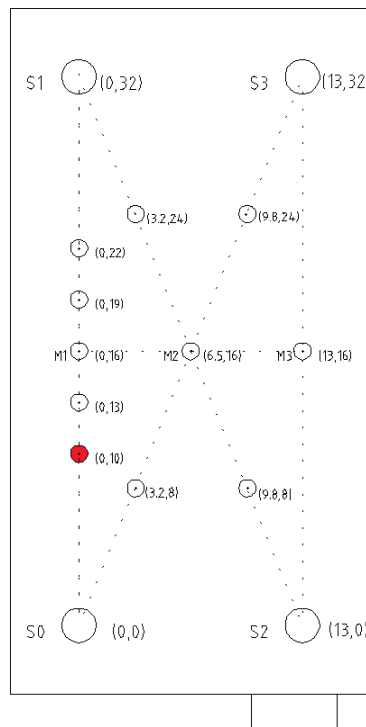


Figure D1: Sonotrode placement (0, 10) – Piezoelectric sensor based system

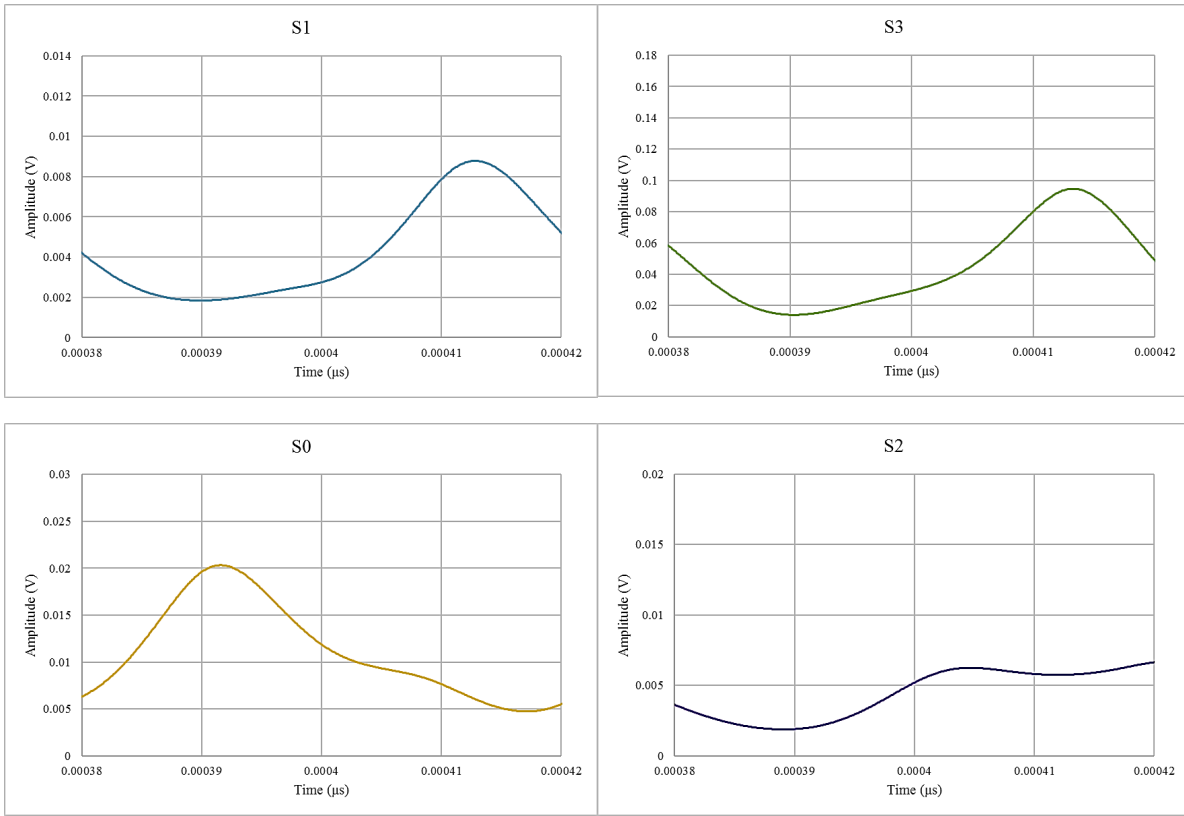


Figure D2: Filtered waveforms from all piezoelectric sensors (0, 10)

$t_1 (S_0 - S_1)$	21 μs
$t_2 (S_0 - S_2)$	10 μs
$t_3 (S_0 - S_3)$	23 μs
<i>Calculated location from S_0, S_1, S_2</i>	(x, y) = (0.5, 10)
<i>Calculated location from S_0, S_1, S_3</i>	(x, y) = (2.2, 10)
<i>Actual Location</i>	(x, y) = (0, 10)

Table D1: Results chart (0, 10) – Piezoelectric sensor based system

Sonotrode Placement (0, 13)

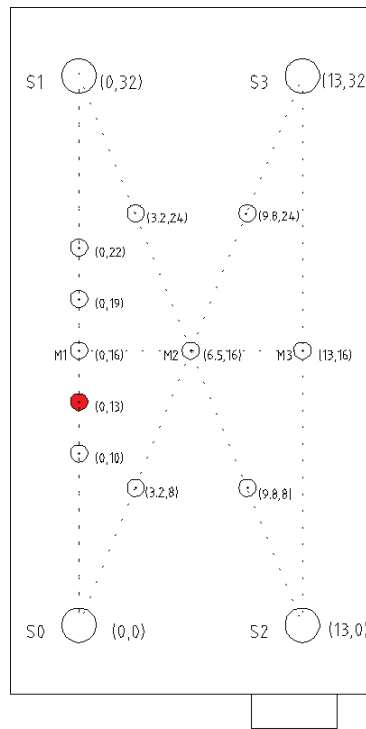


Figure D3: Sonotrode placement (0, 13) – Piezoelectric sensor based system

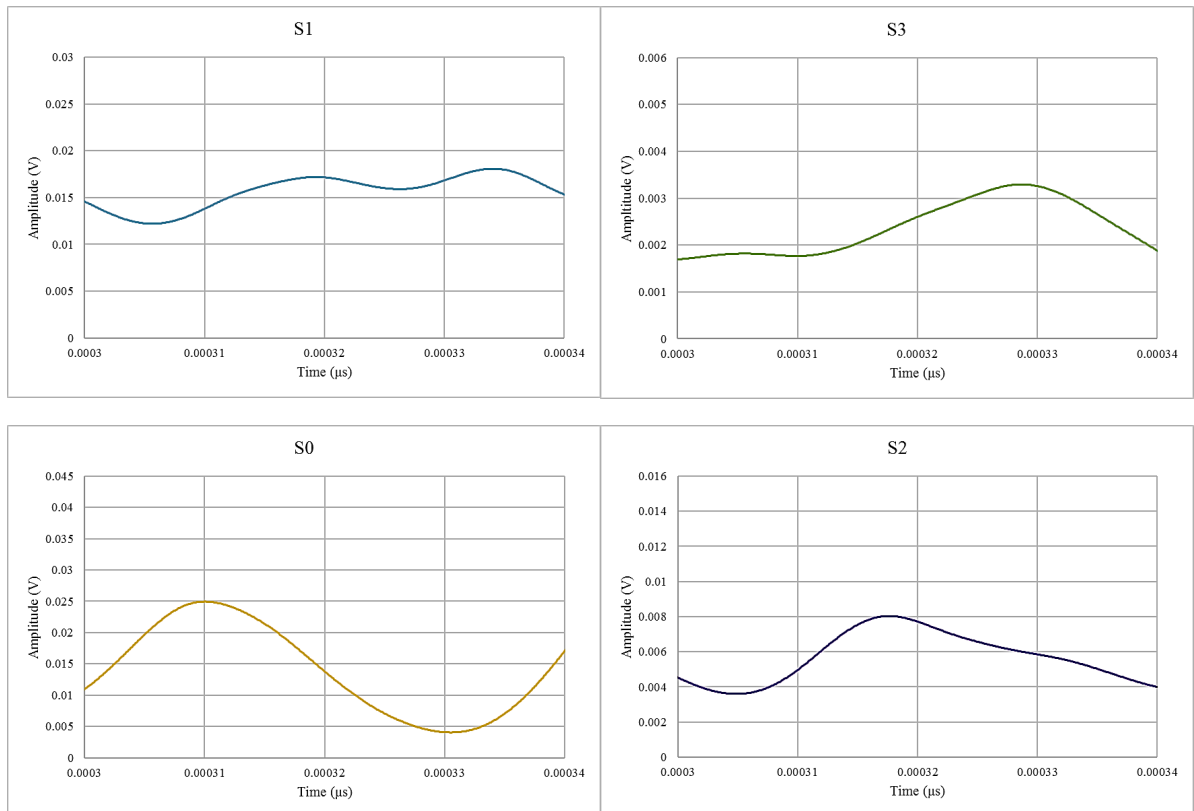


Figure D4: Filtered waveforms from all piezoelectric sensors (0, 13)

$t_1 (S_0 - S_1)$	10 μs
$t_2 (S_0 - S_2)$	8 μs
$t_3 (S_0 - S_3)$	18 μs
<i>Calculated location from S_0, S_1, S_2</i>	(x, y) = (0.8, 13)
<i>Calculated location from S_0, S_1, S_3</i>	(x, y) = (1.2, 13)
<i>Actual Location</i>	(x, y) = (0, 13)

Table D2: Results chart (0, 13) – Piezoelectric sensor based system

Sonotrode Placement (0, 16)

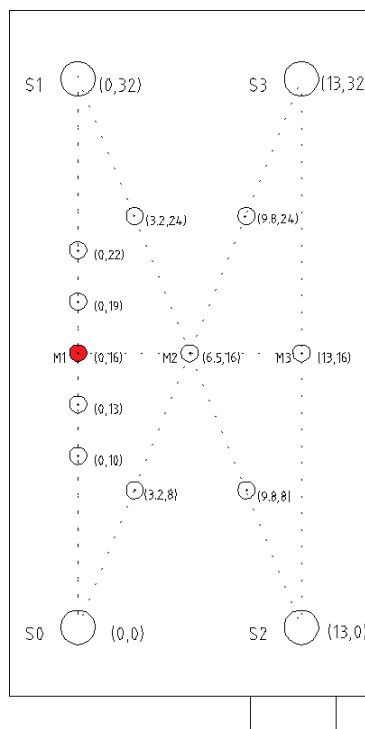


Figure D5: Sonotrode placement (0, 16) – Piezoelectric sensor based system

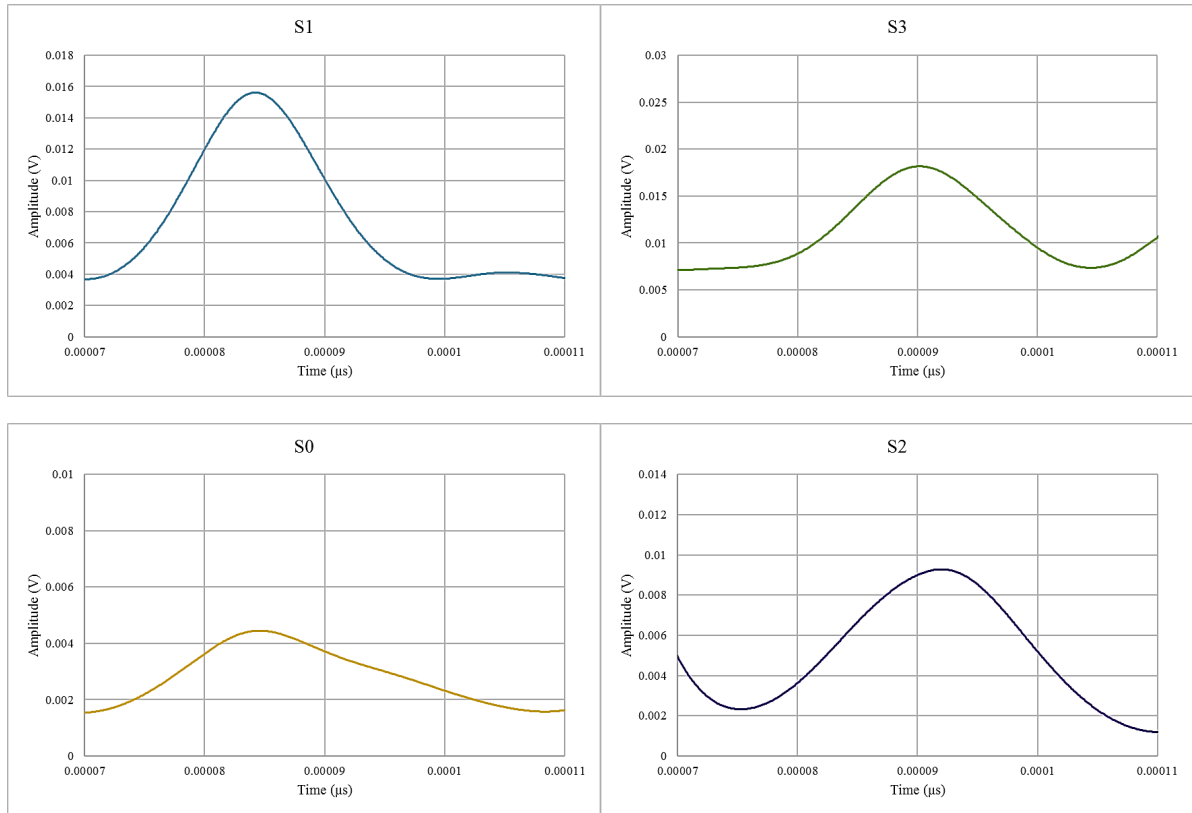


Figure D6: Filtered waveforms from all piezoelectric sensors (0, 16).

$\delta_1 (S_0 - S_1)$	0 μs
$\delta_2 (S_0 - S_2)$	7 μs
$\delta_3 (S_0 - S_3)$	6 μs
<i>Calculated location from S_0, S_1, S_2</i>	(x, y) = (0.7, 16)
<i>Calculated location from S_0, S_1, S_3</i>	(x, y) = (1.6, 16)
<i>Actual Location</i>	(x, y) = (0, 16)

Table D3: Results chart (0, 16) – Piezoelectric sensor based system

Sonotrode Placement (0, 19)

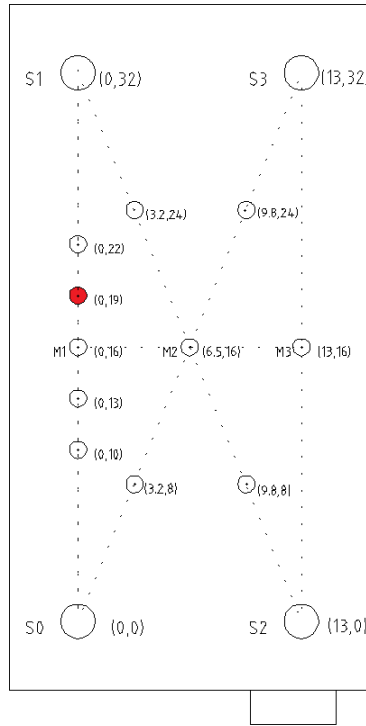


Figure D7: Sonotrode placement (0, 19) – Piezoelectric sensor based system

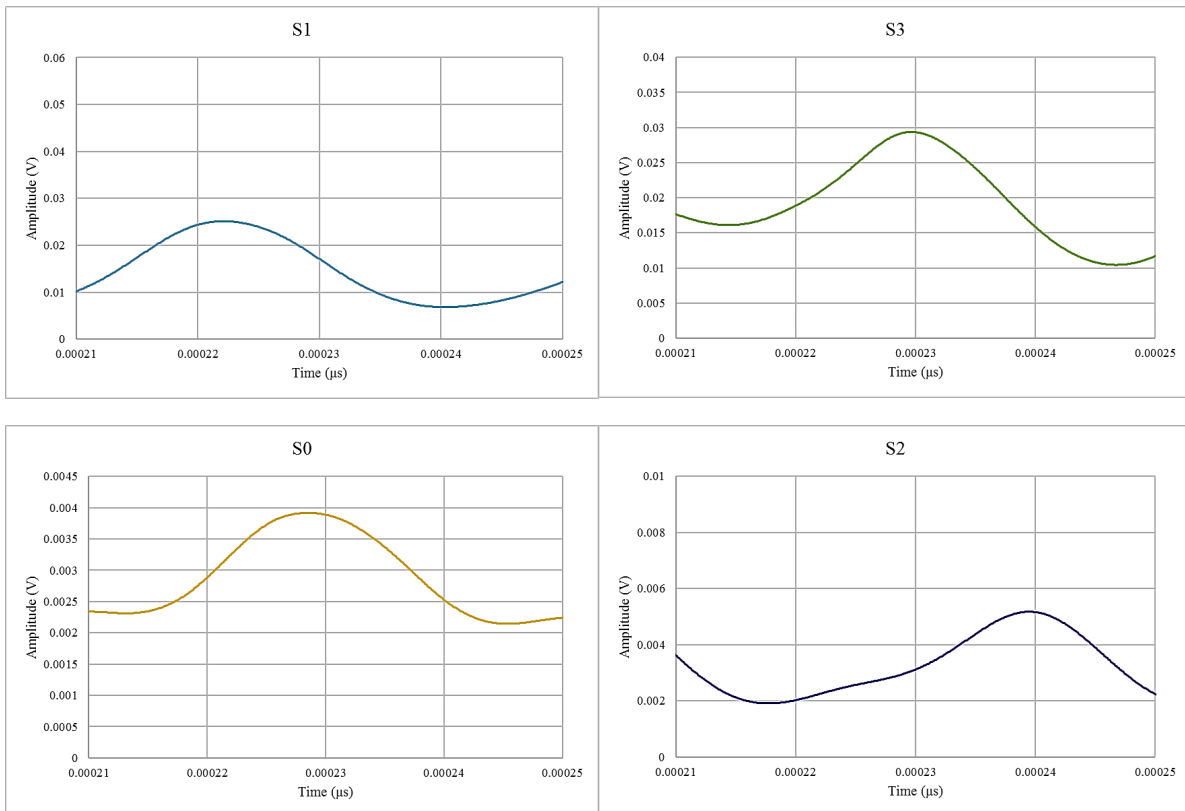


Figure D8: Filtered waveforms from all piezoelectric sensors (0, 19).

$\delta_1 (S_1 - S_0)$	8 μ s
$\delta_2 (S_1 - S_3)$	9 μ s
$\delta_3 (S_1 - S_2)$	16 μ s
<i>Calculated location from S_0, S_1, S_3</i>	(x, y) = (0.1, 18.6)
<i>Calculated location from S_0, S_1, S_2</i>	(x, y) = (1, 18.5)
<i>Actual Location</i>	(x, y) = (0, 19)

Table D4: Results chart (0, 19) – Piezoelectric sensor based system

Sonotrode Placement (0, 22)

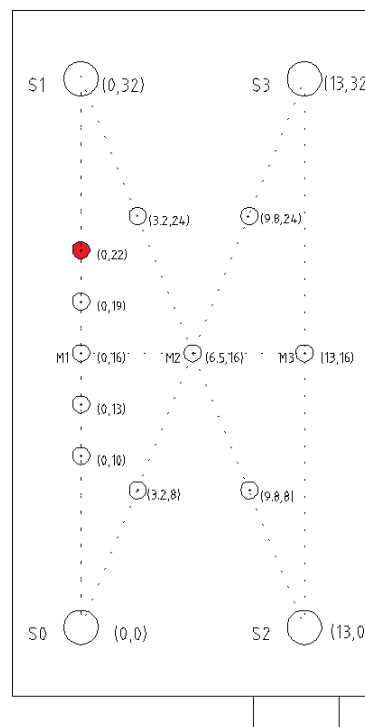


Figure D9: Sonotrode placement (0, 22) – Piezoelectric sensor based system

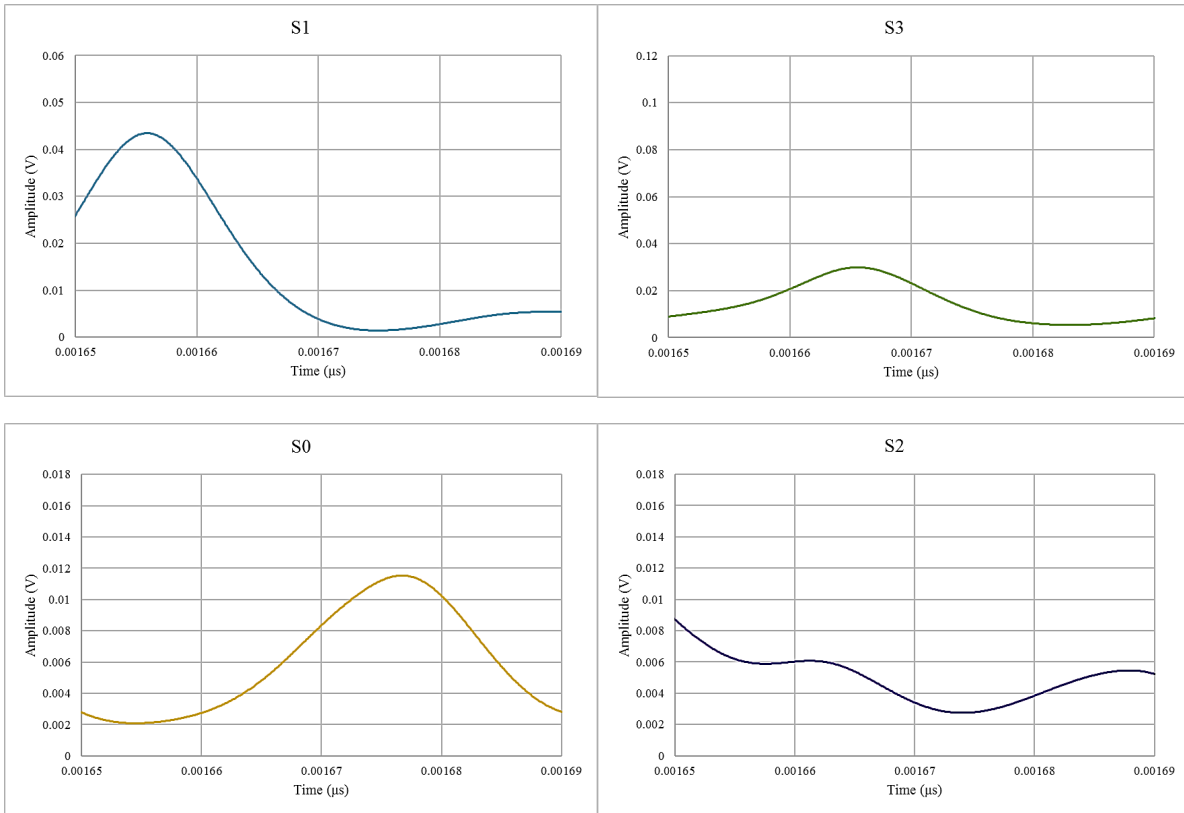


Figure D10: Filtered waveforms from all piezoelectric sensors (0, 22)

$\delta_1 (S_1 - S_0)$	20 μs
$\delta_2 (S_1 - S_3)$	10 μs
$\delta_3 (S_1 - S_2)$	28 μs
<i>Calculated location from S_0, S_1, S_3</i>	$(x, y) = (0.5, 22)$
<i>Calculated location from S_0, S_1, S_2</i>	$(x, y) = (0, 22)$
<i>Actual Location</i>	$(x, y) = (0, 22)$

Table D5: Results chart (0, 22) – Piezoelectric sensor based system

Sonotrode Placement (6.5, 16)

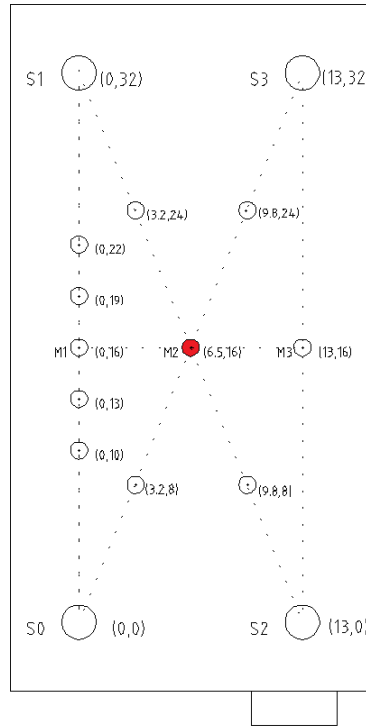


Figure D11: Sonotrode placement (6.5, 16) – Piezoelectric sensor based system

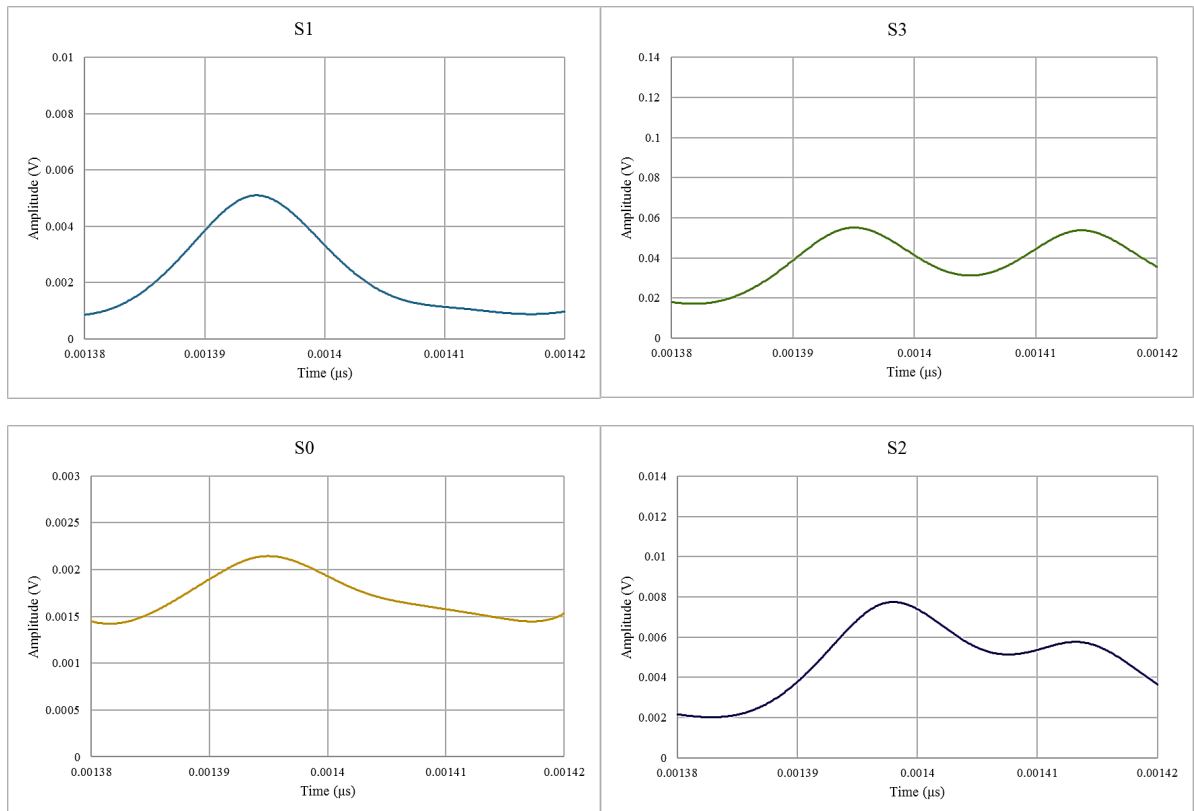


Figure D12: Filtered waveforms from all piezoelectric sensors (6.5, 16)

$\delta_1 (S_1 - S_0)$	0 μs
$\delta_2 (S_1 - S_3)$	0 μs
$\delta_3 (S_1 - S_2)$	2 μs
<i>Calculated location from S_0, S_1, S_3</i>	(x, y) = (6.5, 16)
<i>Calculated location from S_0, S_1, S_2</i>	(x, y) = (5, 16.5)
<i>Actual Location</i>	(x, y) = (6.5, 16)

Table D6: Results chart (6.5, 16) – Piezoelectric sensor based system

Sonotrode Placement (13, 16)

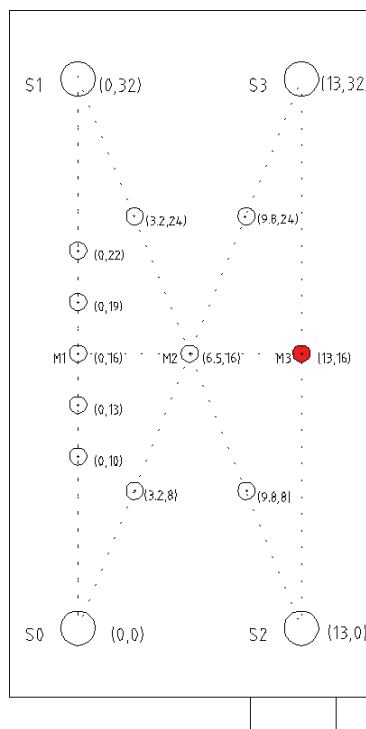


Figure D13: Sonotrode placement (13, 16) – Piezoelectric sensor based system

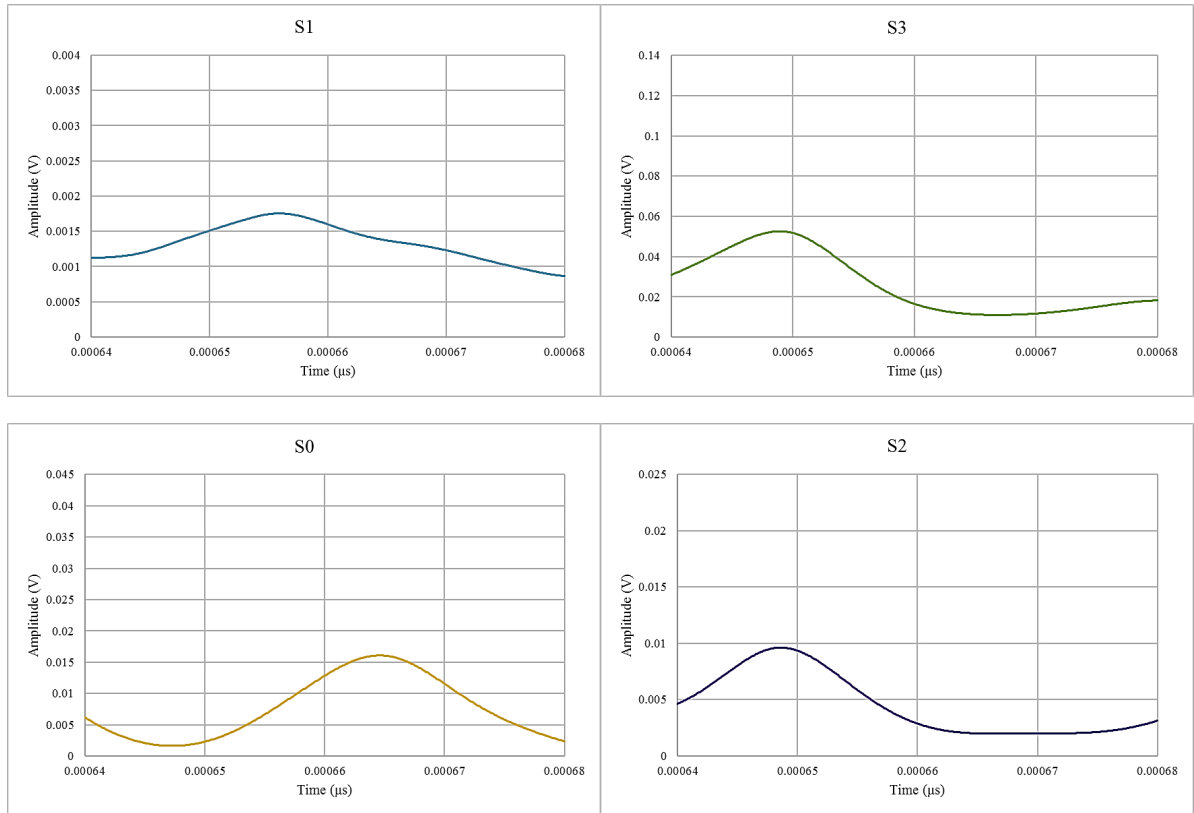


Figure D14: Filtered waveforms from all piezoelectric sensors (13, 16)

$\delta_1 (S_2 - S_3)$	0 μs
$\delta_2 (S_2 - S_1)$	7 μs
$\delta_3 (S_2 - S_0)$	14 μs
<i>Calculated location from S_1, S_2, S_3</i>	(x, y) = (12.3, 16)
<i>Calculated location from S_0, S_2, S_3</i>	(x, y) = (11.5, 16)
<i>Actual Location</i>	(x, y) = (13, 16)

Table D7: Results chart (13, 16) – Piezoelectric sensor based system

Sonotrode Placement (3.2, 8)

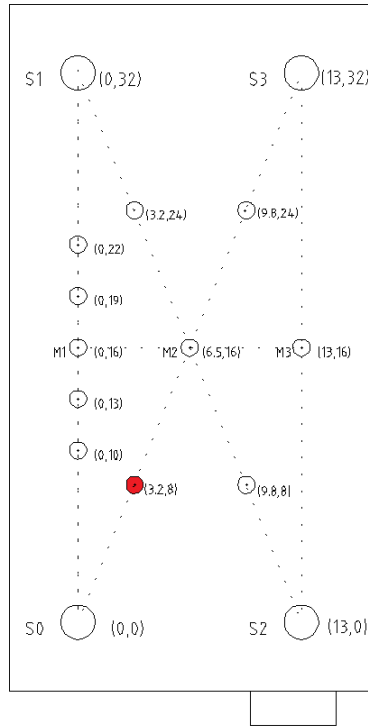


Figure D15: Sonotrode placement (3.2, 8) – Piezoelectric sensor based system

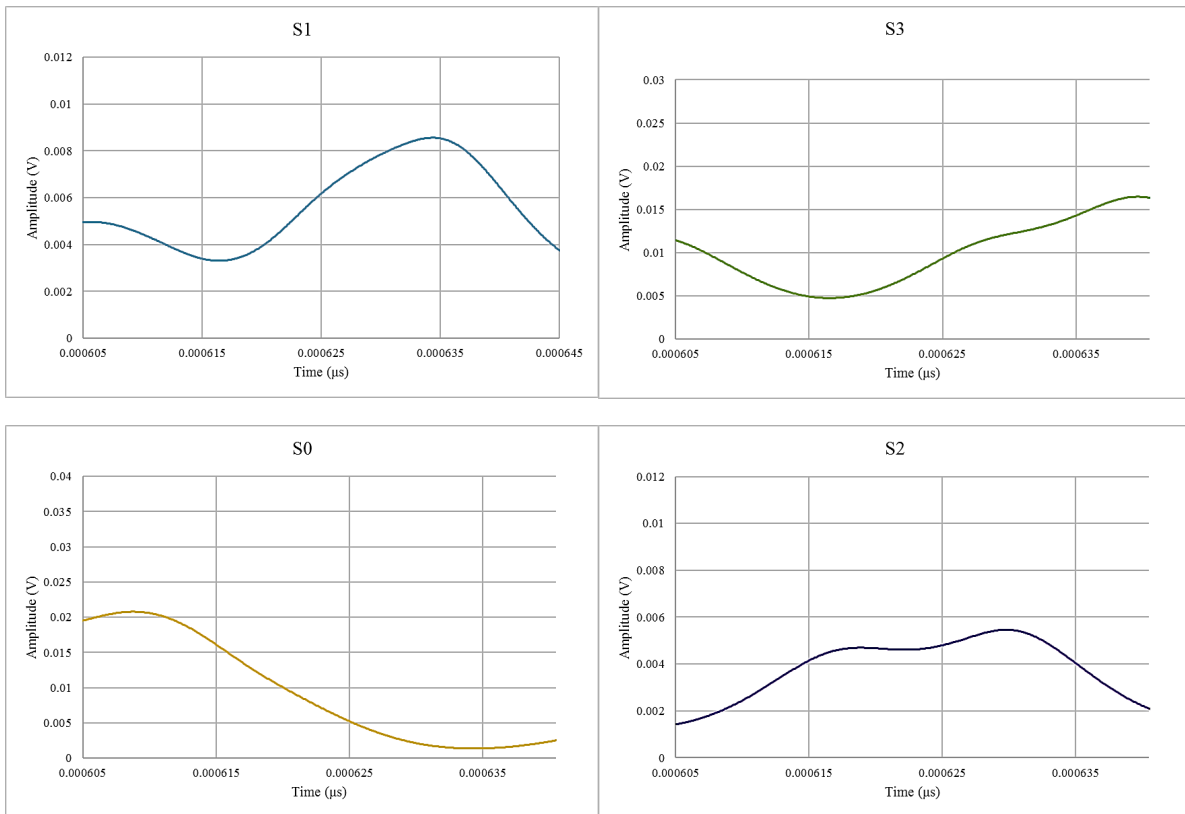


Figure D16: Filtered waveforms from all piezoelectric sensors (3.2, 8)

$t_1 (S_0 - S_1)$	25 μ s
$t_2 (S_0 - S_2)$	8 μ s
$t_3 (S_0 - S_3)$	28 μ s
<i>Calculated location from S_0, S_1, S_2</i>	(x, y) = (3.5, 8.3)
<i>Calculated location from S_0, S_1, S_3</i>	(x, y) = (3.1, 8.4)
<i>Actual Location</i>	(x, y) = (3.2, 8)

Table D8: Results chart (3.2, 8) – Piezoelectric sensor based system

Sonotrode Placement (3.2, 24)

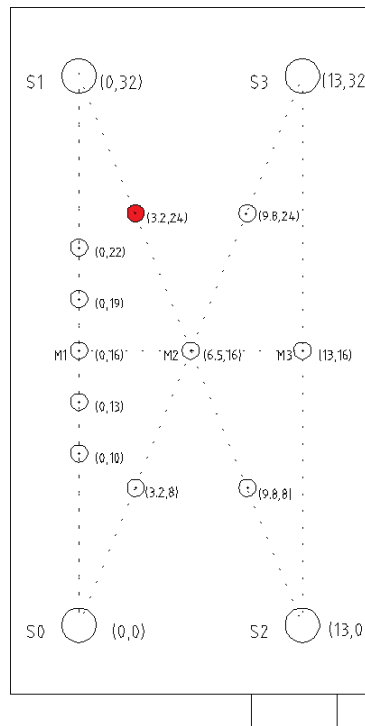


Figure D17: Sonotrode placement (3.2, 24) – Piezoelectric sensor based system

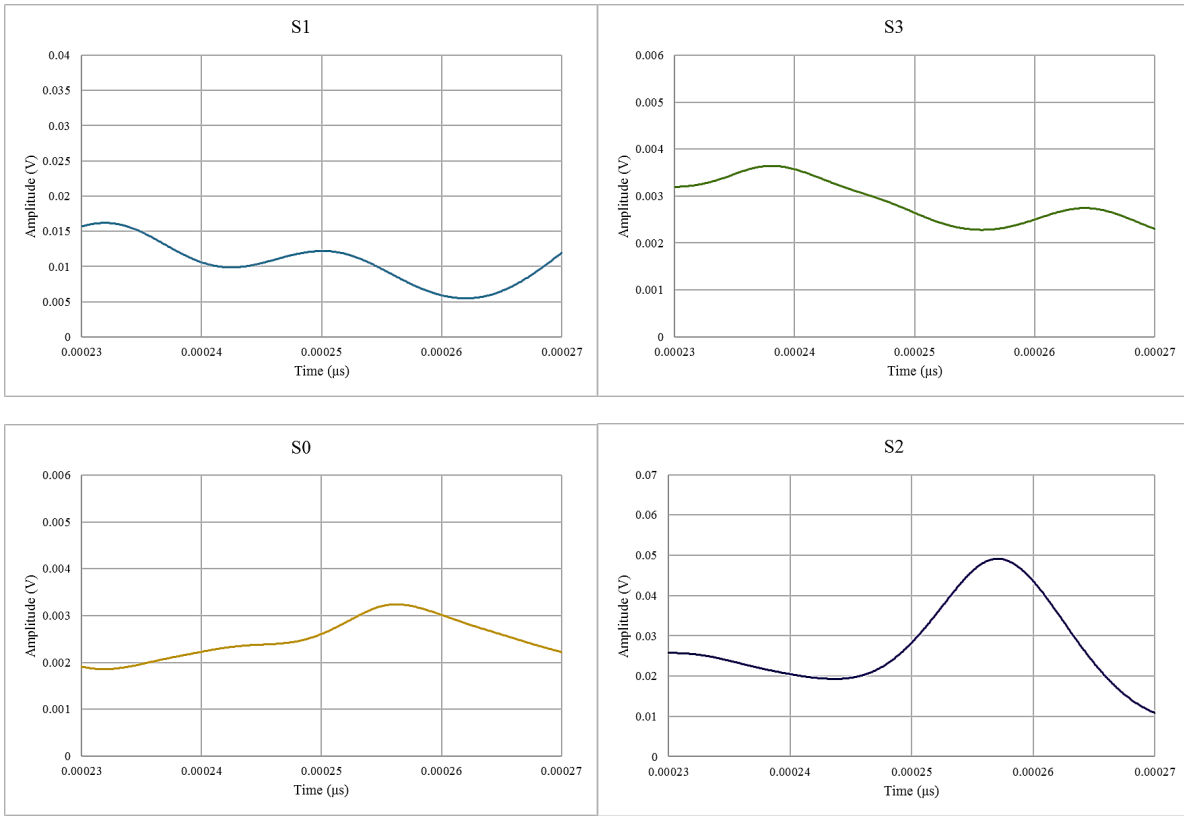


Figure D18: Filtered waveforms from all piezoelectric sensors (3.2, 24)

$\delta_1 (S_1 - S_0)$	24 μs
$\delta_2 (S_1 - S_3)$	7 μs
$\delta_3 (S_1 - S_2)$	26 μs
<i>Calculated location from S_0, S_1, S_3</i>	(x, y) = (2.9, 24.4)
<i>Calculated location from S_0, S_1, S_2</i>	(x, y) = (4.2, 23.8)
<i>Actual Location</i>	(x, y) = (3.2, 24)

Table D9: Results chart (3.2, 24) – Piezoelectric sensor based system

Sonotrode Placement (9.8, 8)

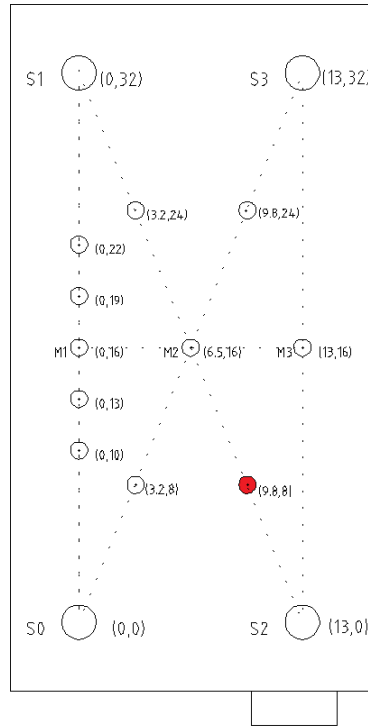


Figure D19: Sonotrode placement (9.8, 8) – Piezoelectric sensor based system

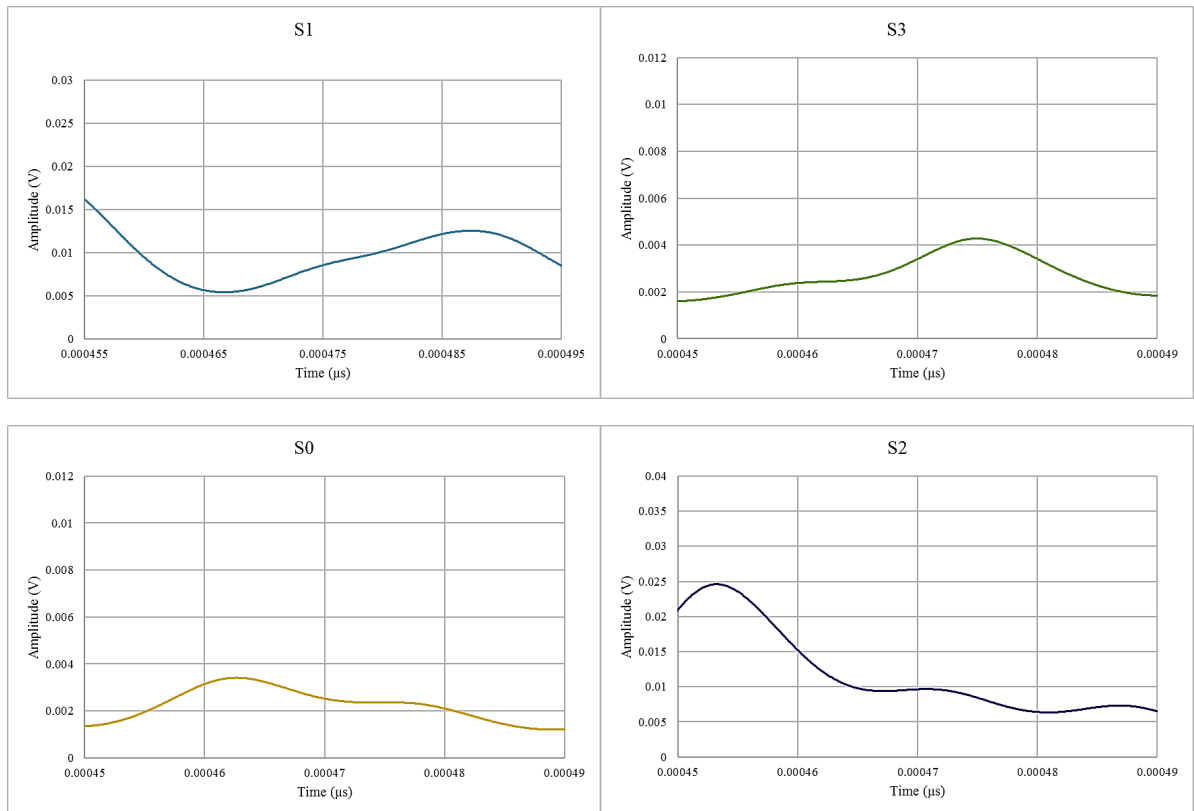


Figure D20: Filtered waveforms from all piezoelectric sensors (9.8, 8)

$\delta_1 (S_2 - S_0)$	8 μs
$\delta_2 (S_2 - S_3)$	24 μs
$\delta_3 (S_2 - S_1)$	28 μs
<i>Calculated location from S_0, S_2, S_3</i>	(x, y) = (9.1, 8.8)
<i>Calculated location from S_1, S_2, S_3</i>	(x, y) = (8.8, 8.8)
<i>Actual Location</i>	(x, y) = (9.8, 8)

Table D10: Results chart (9.8, 8) – Piezoelectric sensor based system

Sonotrode Placement (9.8, 24)

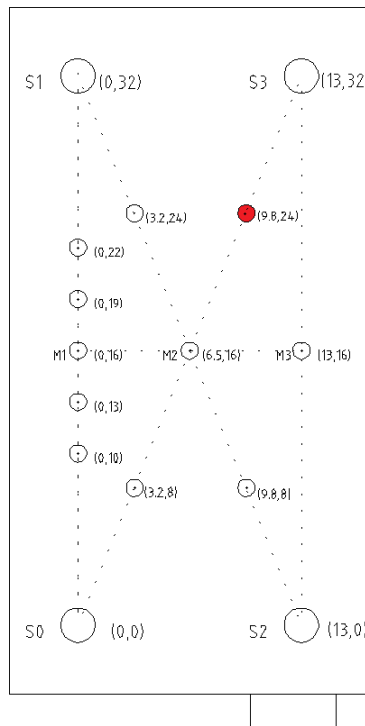


Figure D21: Sonotrode placement (9.8, 24) – Piezoelectric sensor based system

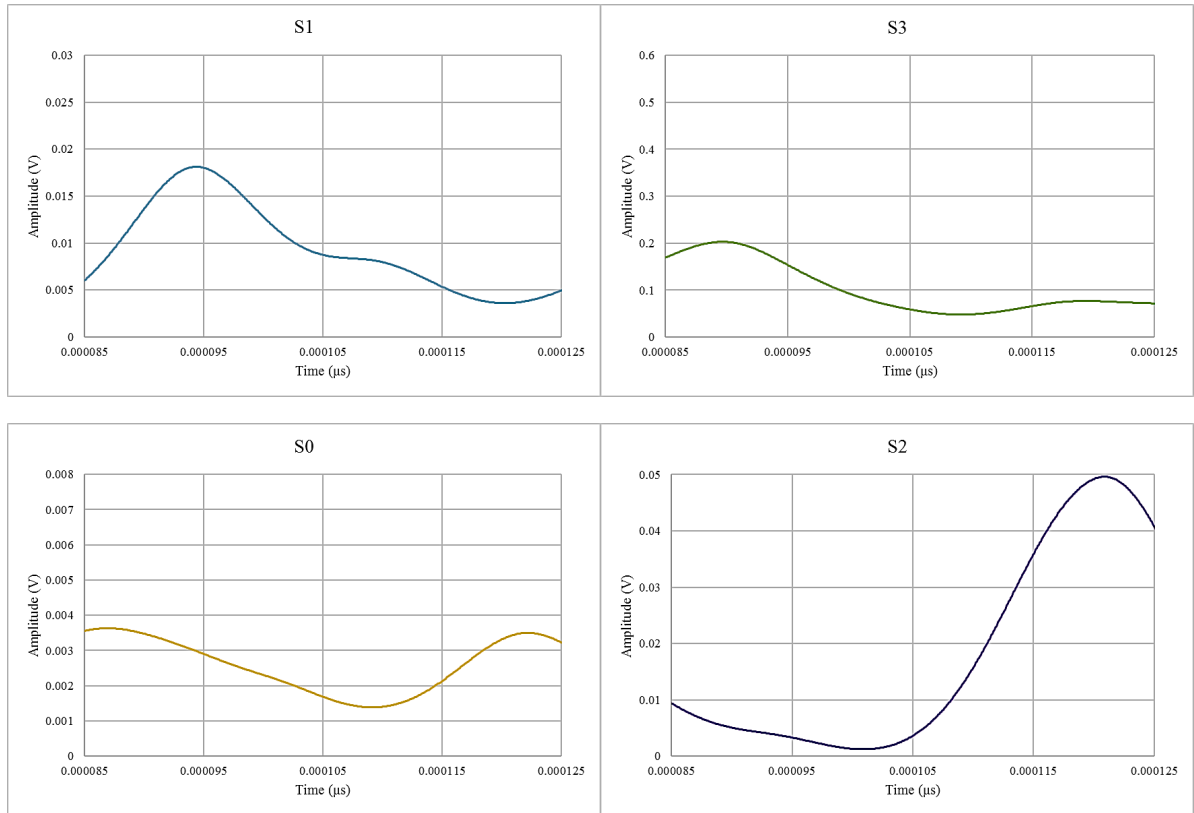


Figure D22: Filtered waveforms from all piezoelectric sensors (9.8, 24)

$\delta_1 (S_3 - S_2)$	30 μs
$\delta_2 (S_3 - S_1)$	6 μs
$\delta_3 (S_3 - S_0)$	32 μs
<i>Calculated location from S_1, S_2, S_3</i>	(x, y) = (9.6, 23)
<i>Calculated location from S_0, S_2, S_3</i>	(x, y) = (10.5, 22.7)
<i>Actual Location</i>	(x, y) = (9.8, 24)

Table D11: Results chart (9.8, 24) – Piezoelectric sensor based system

D.2 The triangulation technique– Source location measurements– Fibre Bragg grating sensors

Source location measurements were also conducted by means of a fibre Bragg grating sensor – based system, through a similar to the one described in *sub-chapter 7.5*, experimental and data processing procedure. As such, raw acoustic data from all sensors and different sonotrode placements were processed through a band pass filter in order for the 26 kHz operating frequency of the sonotrode to be isolated. Time differences between sensors were then measured, with regards to the peaks of the acoustic waves – pulses, and location coordinates were eventually derived by means of the analytic triangulation technique.

Acoustic data is presented in the form of graphs arranged in an order similar to the actual positions of the sensors, for comparison reasons. In addition, all graphs are appropriately scaled with regards to the X axis (time) in order for the time differences between different sensors to be distinguishable.

Sonotrode Placement (0, 10)

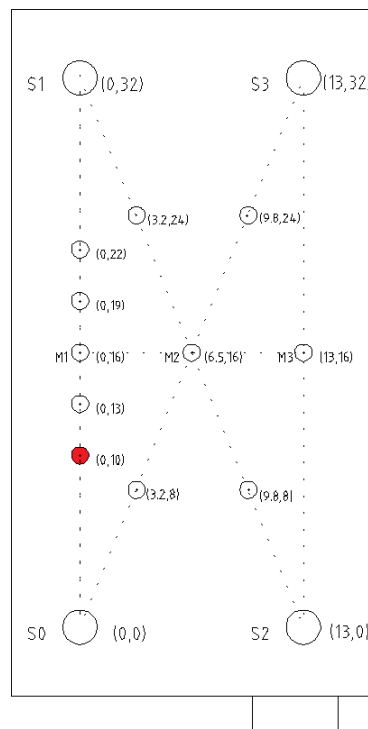


Figure D23: Sonotrode placement (0, 10) – FBG sensor based system

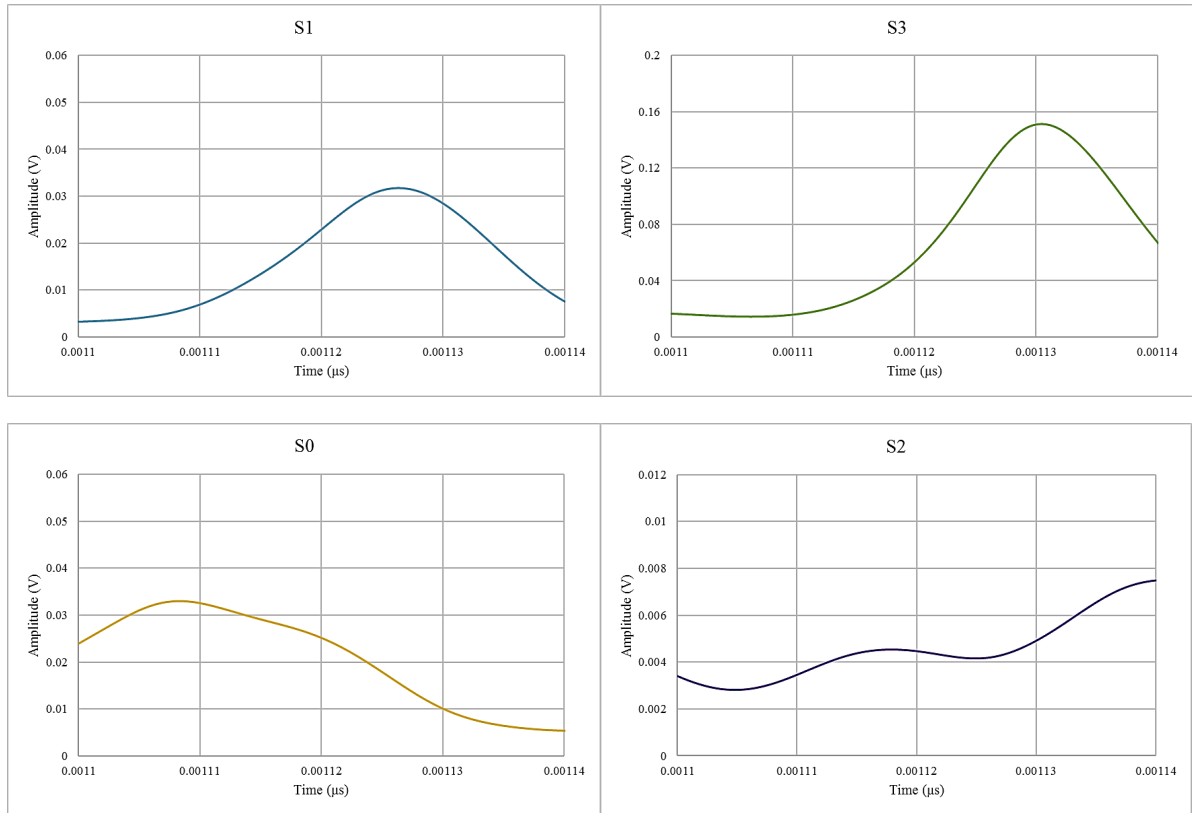


Figure D24: Filtered waveforms from all FBG sensors (0, 10)

$t_1 (S_0 - S_1)$	18 μs
$t_2 (S_0 - S_2)$	8 μs
$t_3 (S_0 - S_3)$	22 μs
<i>Calculated location from S_0, S_1, S_2</i>	$(x, y) = (1.7, 10.6)$
<i>Calculated location from S_0, S_1, S_3</i>	$(x, y) = (2.3, 10.6)$
<i>Actual Location</i>	$(x, y) = (0, 10)$

Table D12: Results chart (0, 10) – FBG sensor based system

Sonotrode Placement (0, 13)

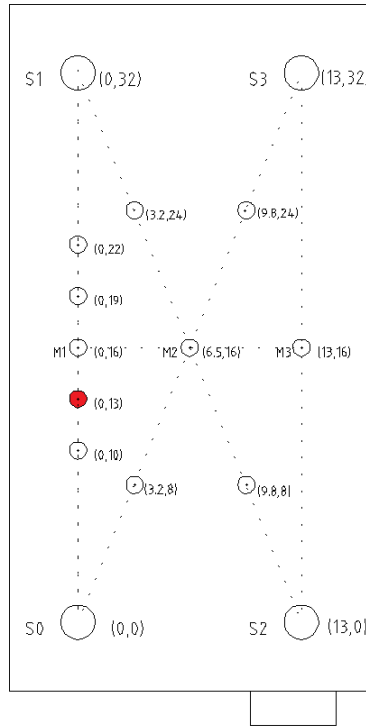


Figure D25: Sonotrode placement (0, 13) – FBG sensor based system.

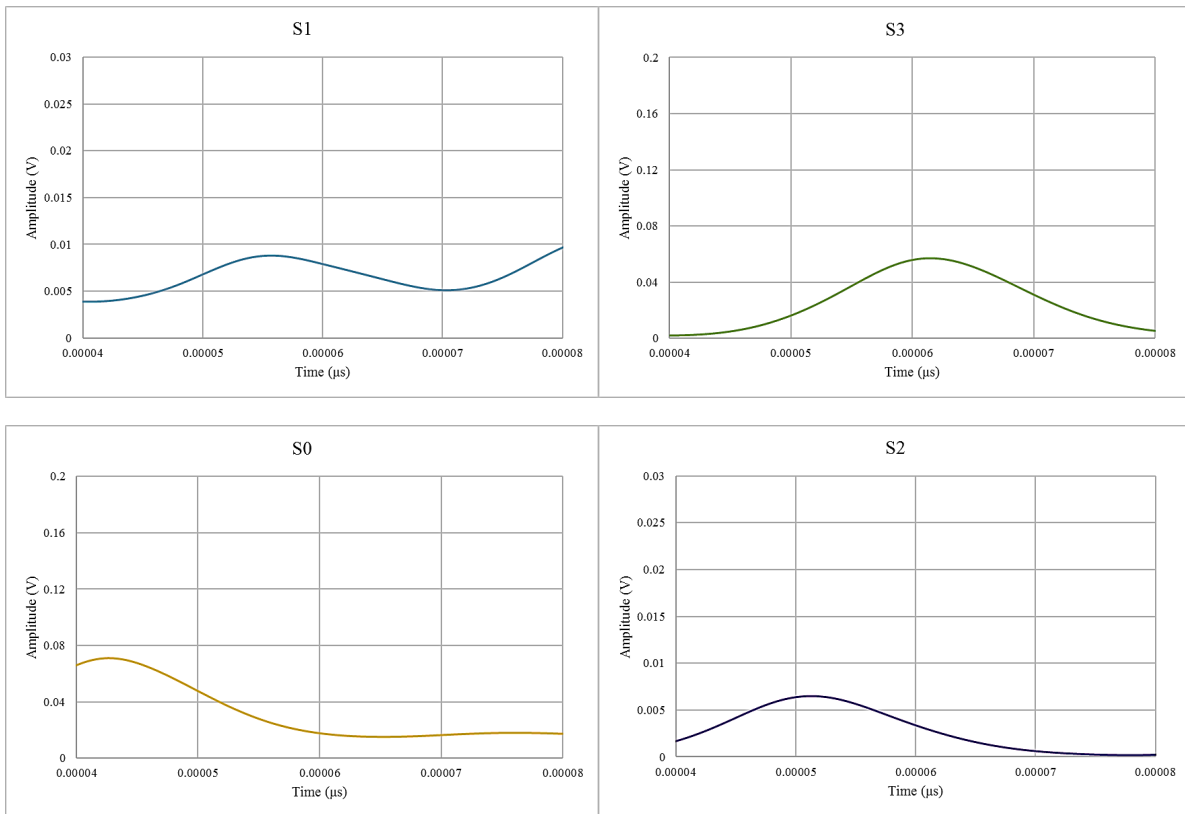


Figure D26: Filtered waveforms from all FBG sensors (0, 13)

$t_1 (S_0 - S_1)$	12 μs
$t_2 (S_0 - S_2)$	8 μs
$t_3 (S_0 - S_3)$	18 μs
<i>Calculated location from S_0, S_1, S_2</i>	$(x, y) = (1, 12.4)$
<i>Calculated location from S_0, S_1, S_3</i>	$(x, y) = (0.6, 12.4)$
<i>Actual Location</i>	$(x, y) = (0, 13)$

Table D13: Results chart (0, 13) – FBG sensor based system.

Sonotrode Placement (0, 16)

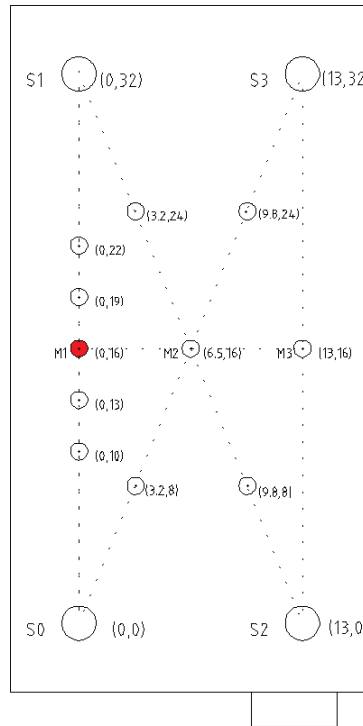


Figure D27: Sonotrode placement (0, 16) – FBG sensor based system

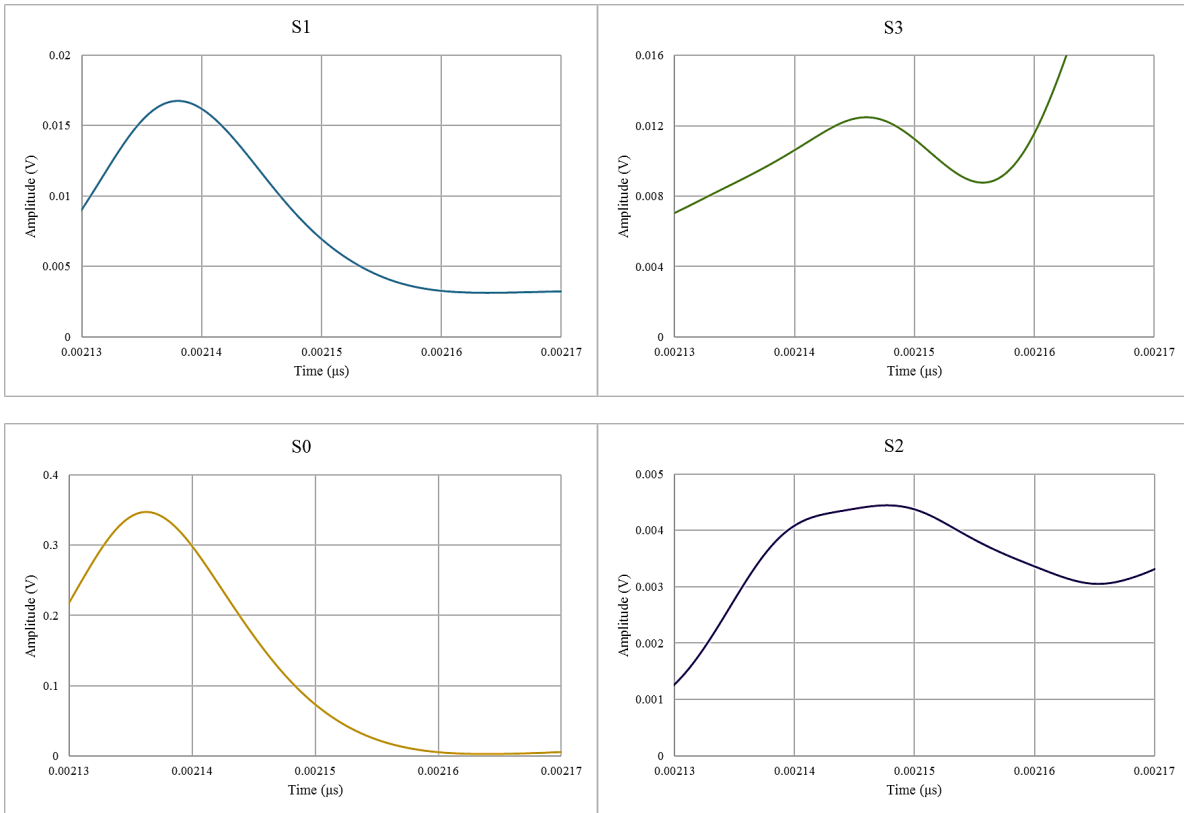


Figure D28: Filtered waveforms from all FBG sensors (0, 16)

$t_1 (S_0 - S_1)$	1 μs
$t_2 (S_0 - S_2)$	9 μs
$t_3 (S_0 - S_3)$	8 μs
<i>Calculated location from S_0, S_1, S_2</i>	$(x, y) = (0.3, 15.7)$
<i>Calculated location from S_0, S_1, S_3</i>	$(x, y) = (1, 15.7)$
<i>Actual Location</i>	$(x, y) = (0, 16)$

Table D14: Results chart (0, 16) – FBG sensor based system

Sonotrode Placement (0, 19)

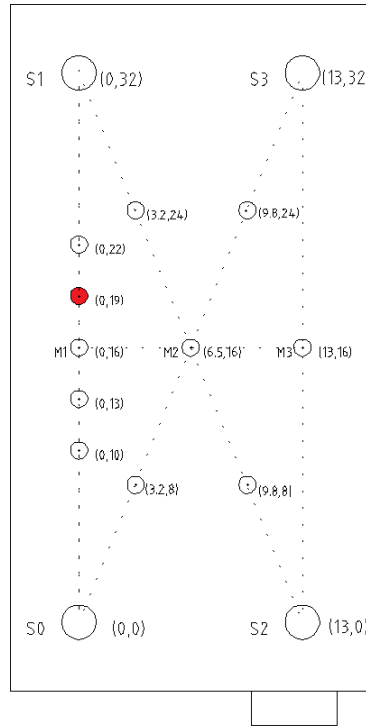


Figure D29: Sonotrode placement (0, 19) – FBG sensor based system

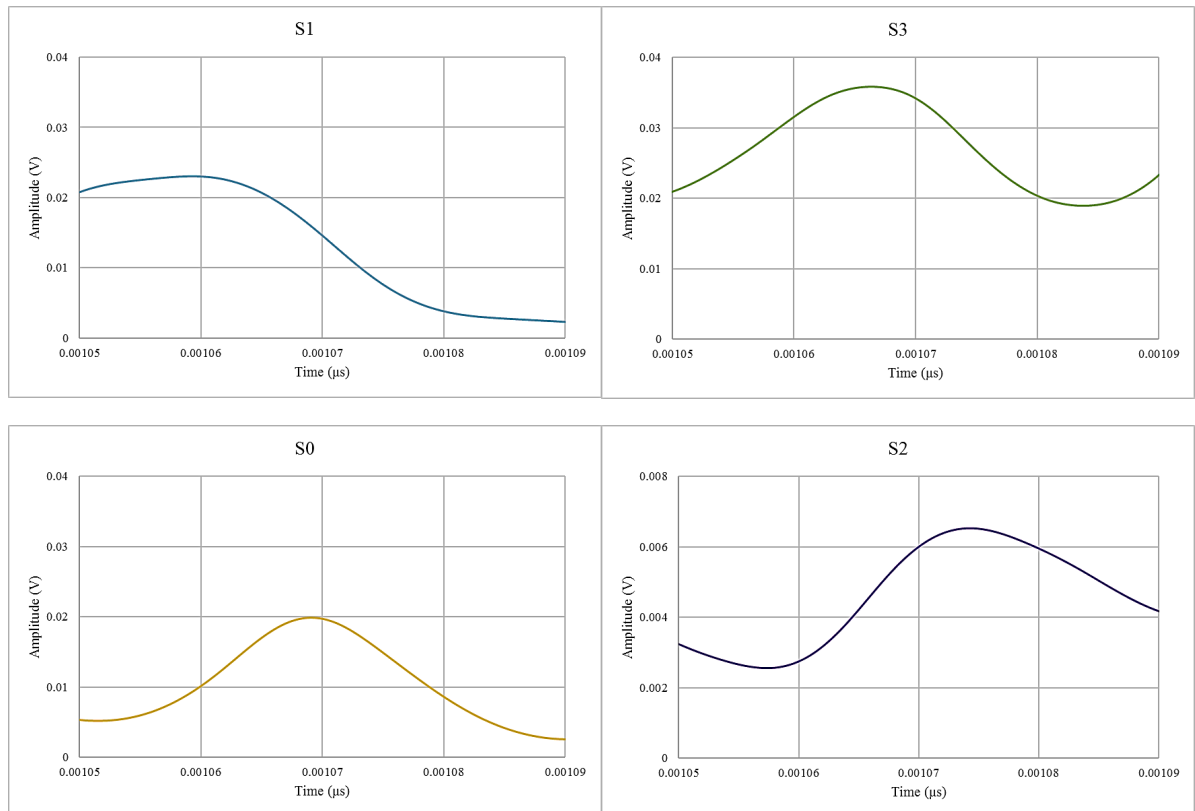


Figure D30: Filtered waveforms from all FBG sensors (0, 19)

$\delta_1 (S_1 - S_0)$	10 μs
$\delta_2 (S_1 - S_3)$	8 μs
$\delta_3 (S_1 - S_2)$	16 μs
<i>Calculated location from S_0, S_1, S_3</i>	(x, y) = (0.9, 19)
<i>Calculated location from S_0, S_1, S_2</i>	(x, y) = (0.8, 19)
<i>Actual Location</i>	(x, y) = (0, 19)

Table D15: Results chart (0, 19) – FBG sensor based system

Sonotrode Placement (0, 22)

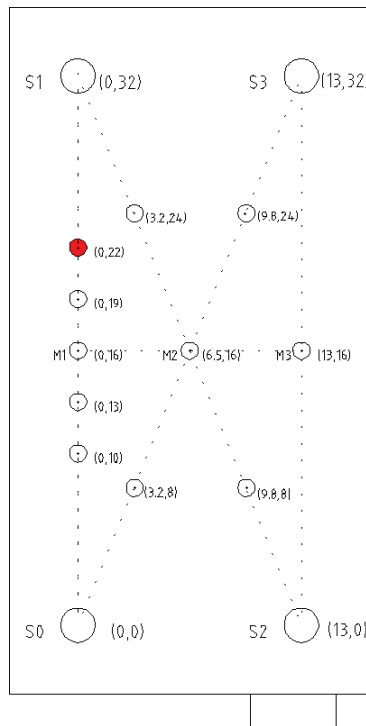


Figure D31: Sonotrode placement (0, 22) – FBG sensor based system

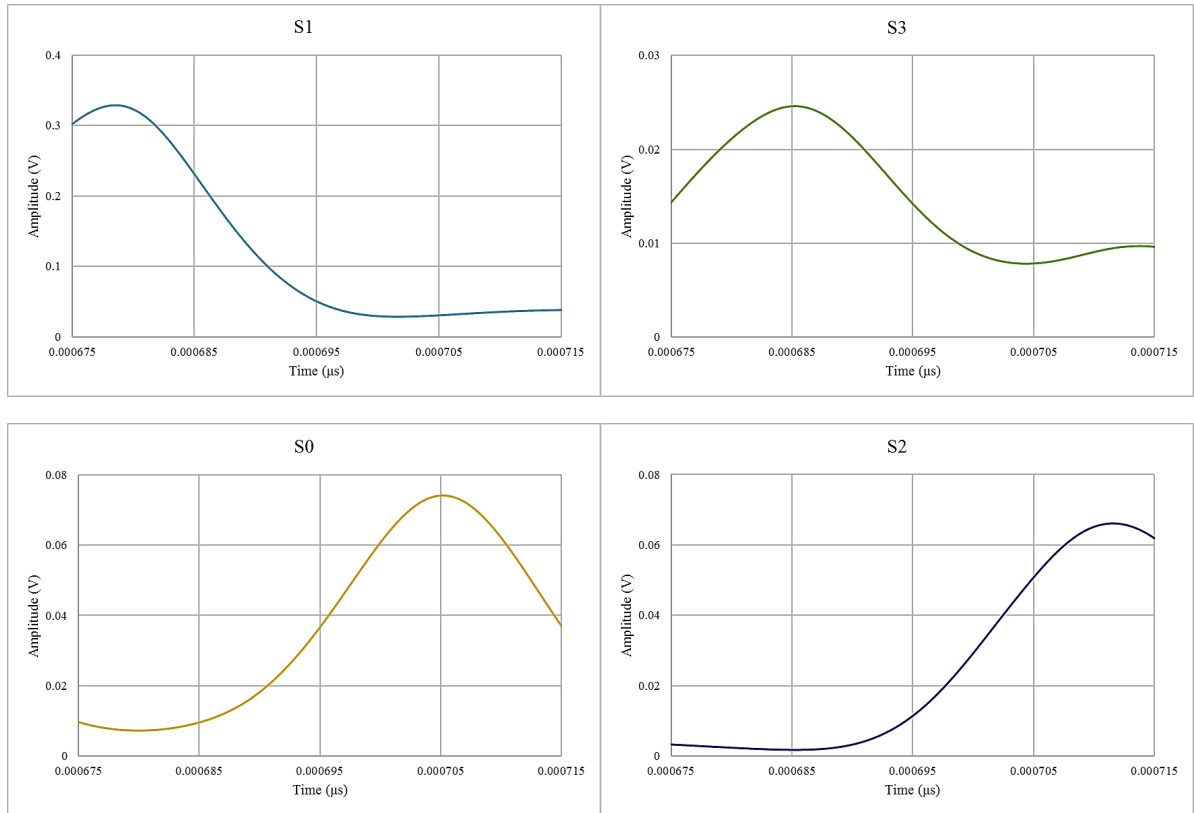


Figure D32: Filtered waveforms from all FBG sensors (0, 22)

$\delta_1 (S_1 - S_0)$	24 μs
$\delta_2 (S_1 - S_3)$	8 μs
$\delta_3 (S_1 - S_2)$	29 μs
<i>Calculated location from S_0, S_1, S_3</i>	$(x, y) = (2.3, 23.2)$
<i>Calculated location from S_0, S_1, S_2</i>	$(x, y) = (0.2, 23.2)$
<i>Actual Location</i>	$(x, y) = (0, 22)$

Table D16: Results chart (0, 22) – FBG sensor based system

Sonotrode Placement (6.5, 16)

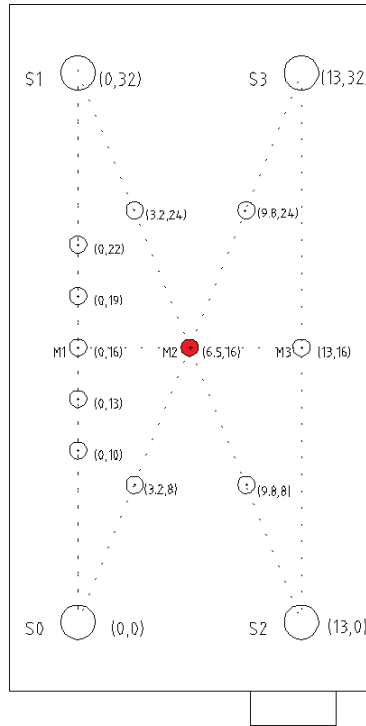


Figure D33: Sonotrode placement (6.5, 16) – FBG sensor based system

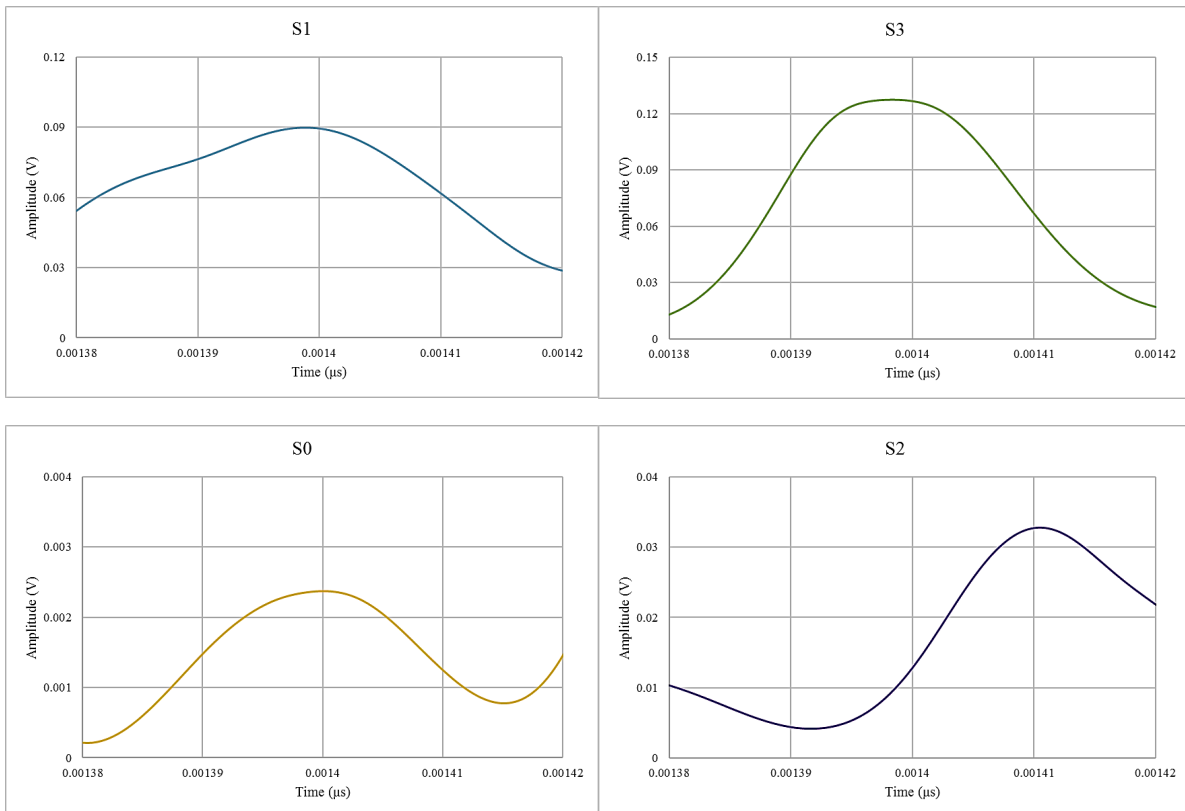


Figure D34: Filtered waveforms from all FBG sensors (6.5, 16)

$\delta_1 (S_1 - S_0)$	0 μ s
$\delta_2 (S_1 - S_3)$	0 μ s
$\delta_3 (S_1 - S_2)$	10 μ s
<i>Calculated location from S_0, S_1, S_3</i>	(x, y) = (6.5, 16)
<i>Calculated location from S_0, S_1, S_2</i>	(x, y) = (0, 16)
<i>Actual Location</i>	(x, y) = (6.5, 16)

Table D17: Results chart (6.5, 16) – FBG sensor based system

Sonotrode Placement (13, 16)

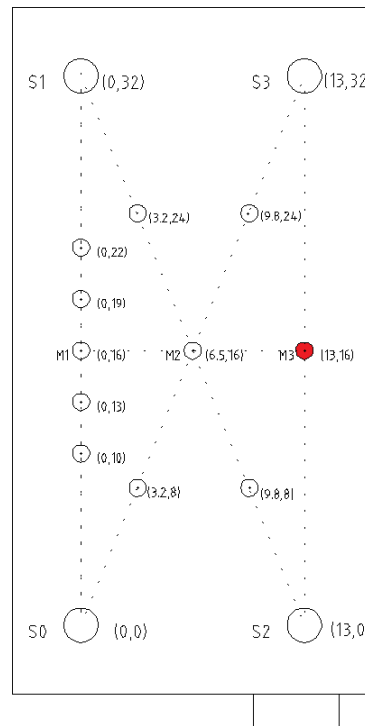


Figure D35: Sonotrode placement (13, 16) – FBG sensor based system

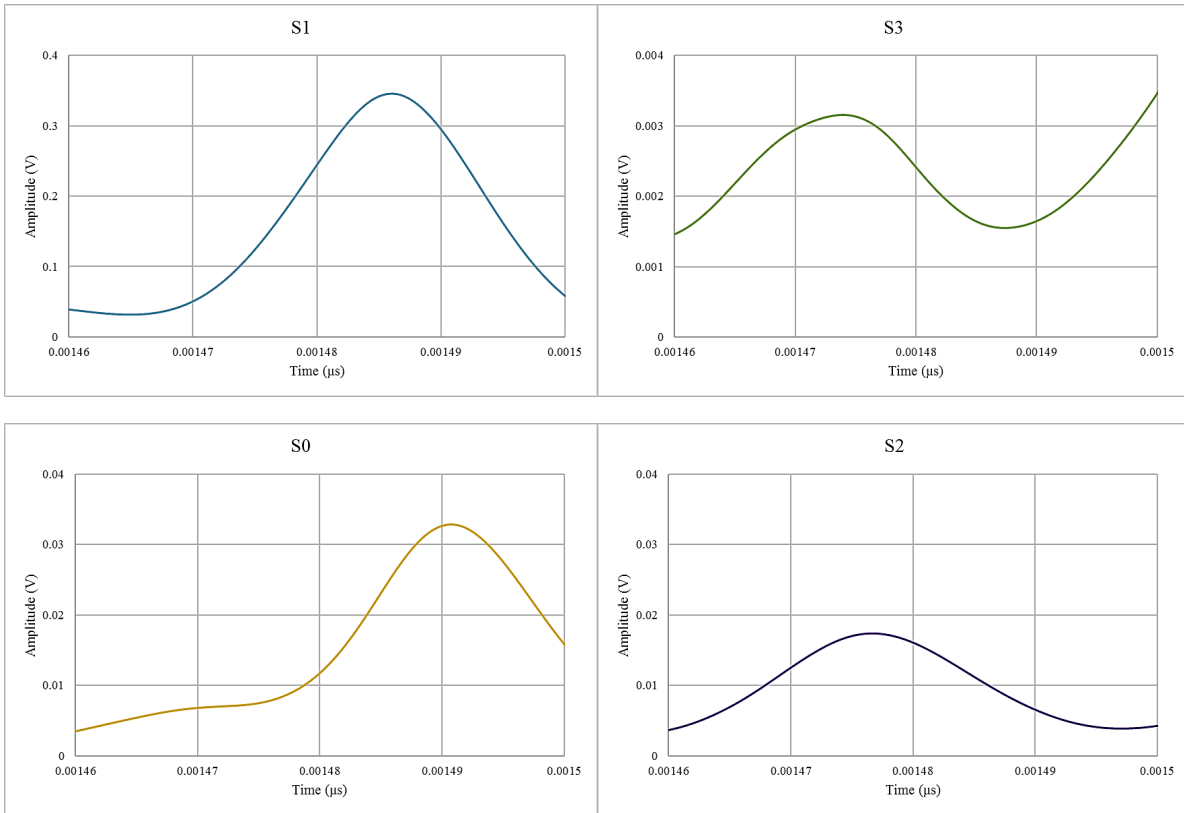


Figure D36: Filtered waveforms from all FBG sensors (13, 16)

$\delta_1 (S_2 - S_3)$	0 μs
$\delta_2 (S_2 - S_1)$	8 μs
$\delta_3 (S_2 - S_0)$	12 μs
<i>Calculated location from S_1, S_2, S_3</i>	(x, y) = (11.2, 16)
<i>Calculated location from S_0, S_2, S_3</i>	(x, y) = (11, 16)
<i>Actual Location</i>	(x, y) = (13, 16)

Table D18: Results chart (13, 16) – FBG sensor based system

Sonotrode Placement (3.2, 8)

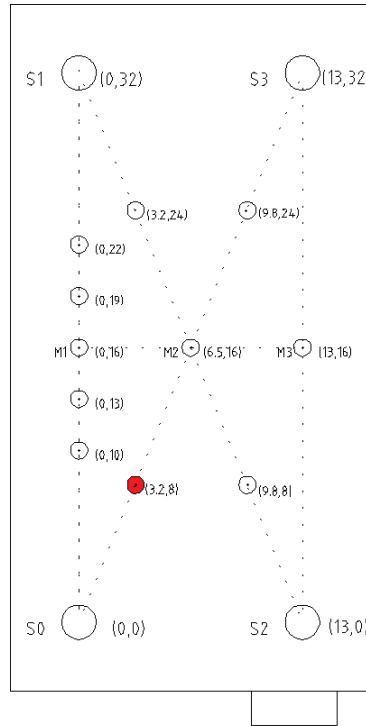


Figure D37: Sonotrode placement (3.2, 8) – FBG sensor based system

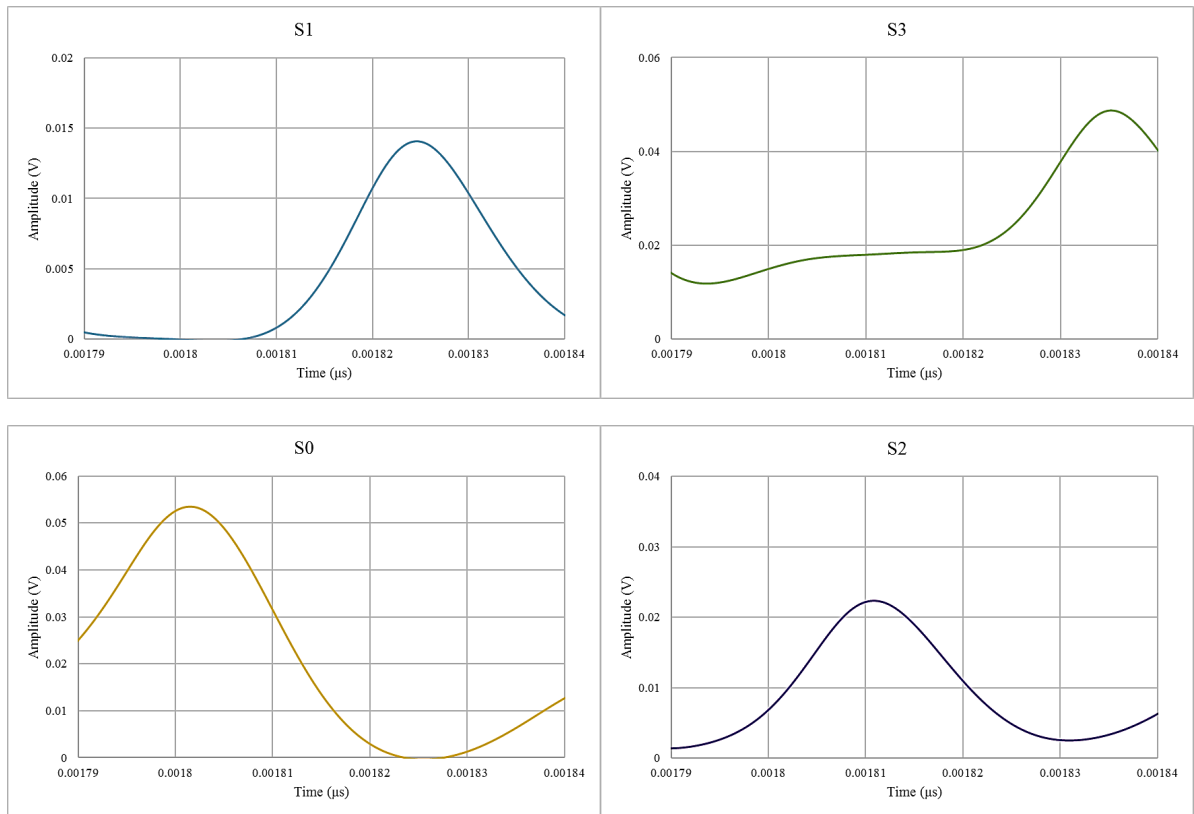


Figure D38: Filtered waveforms from all FBG sensors (3.2, 8)

$t_1 (S_0 - S_1)$	23 μ s
$t_2 (S_0 - S_2)$	8 μ s
$t_3 (S_0 - S_3)$	30 μ s
<i>Calculated location from S_0, S_1, S_2</i>	$(x, y) = (2.3, 8.8)$
<i>Calculated location from S_0, S_1, S_3</i>	$(x, y) = (3, 8.8)$
<i>Actual Location</i>	$(x, y) = (3.2, 8)$

Table D19: Results chart (3.2, 8) – FBG sensor based system

Sonotrode Placement (3.2, 24)

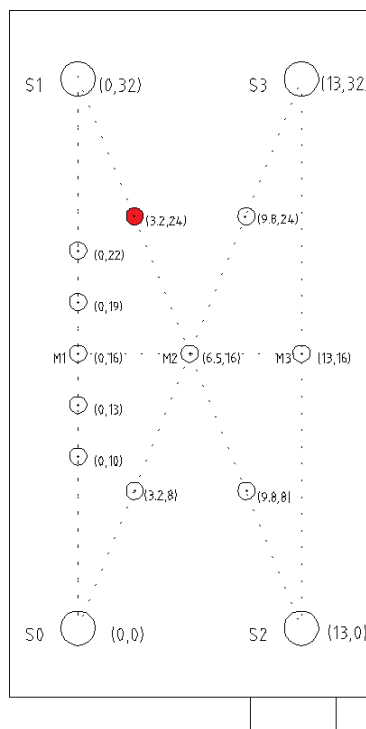


Figure D39: Sonotrode placement (3.2, 24) – FBG sensor based system

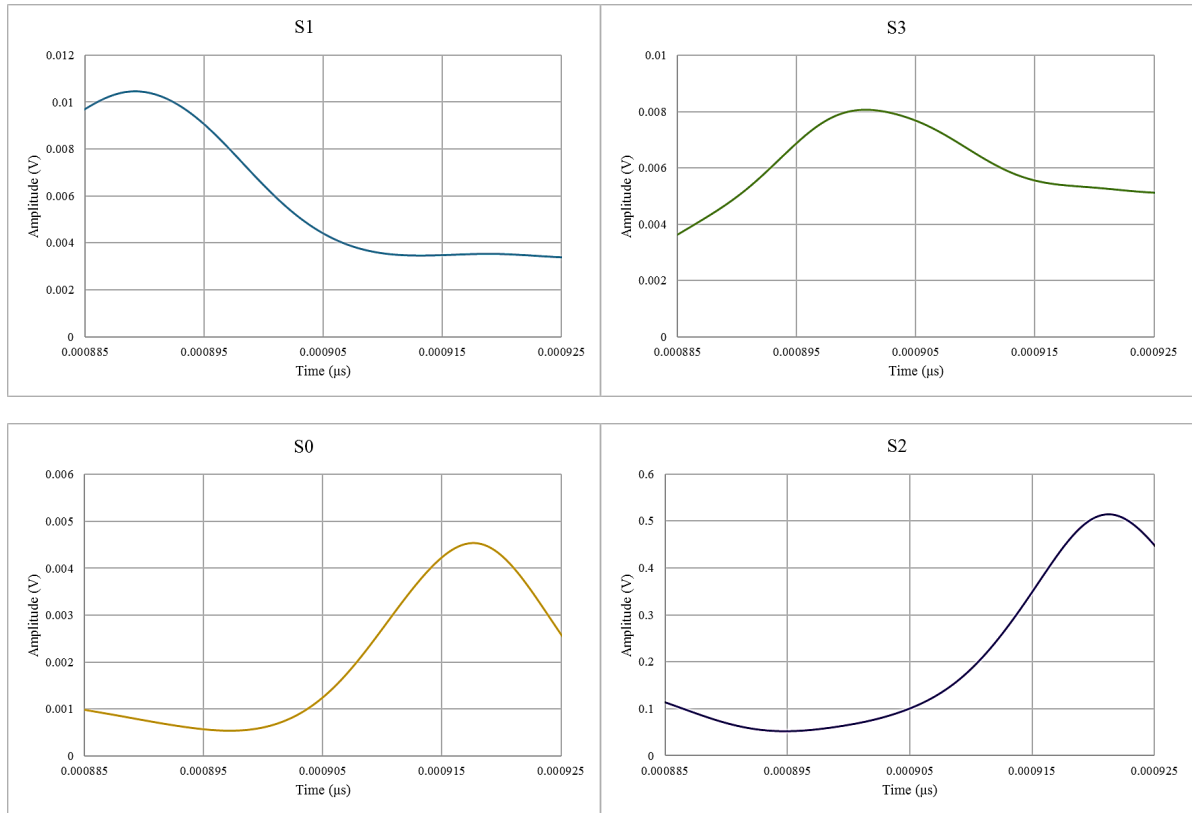


Figure D40: Filtered waveforms from all FBG sensors (3.2, 24)

$\delta_1 (S_1 - S_0)$	26 μs
$\delta_2 (S_1 - S_3)$	10 μs
$\delta_3 (S_1 - S_2)$	28 μs
<i>Calculated location from S_0, S_1, S_3</i>	$(x, y) = (2.5, 24.1)$
<i>Calculated location from S_0, S_1, S_2</i>	$(x, y) = (4.2, 23.9)$
<i>Actual Location</i>	$(x, y) = (3.2, 24)$

Table D20: Results chart (3.2, 24) – FBG sensor based system.

Sonotrode Placement (9.8, 8)

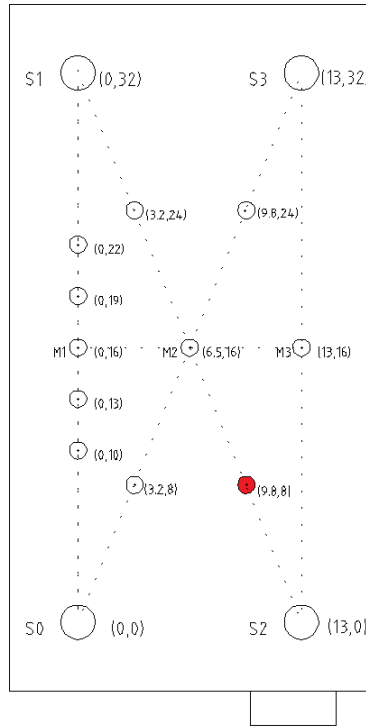


Figure D41: Sonotrode placement (9.8, 8) – FBG sensor based system

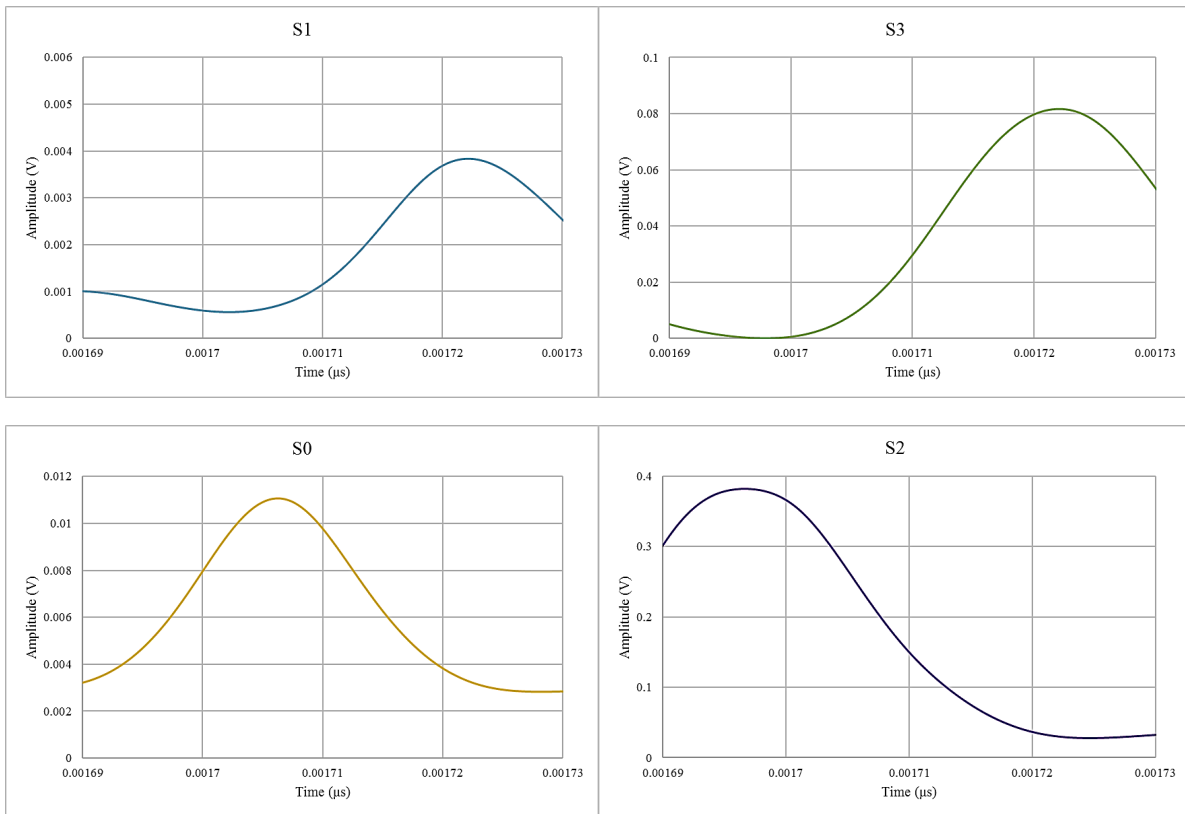


Figure D42: Filtered waveforms from all FBG sensors (9.8, 8)

$\delta_1 (S_2 - S_0)$	8 μ s
$\delta_2 (S_2 - S_3)$	25 μ s
$\delta_3 (S_2 - S_1)$	26 μ s
<i>Calculated location from S_0, S_2, S_3</i>	$(x, y) = (9, 8.4)$
<i>Calculated location from S_1, S_2, S_3</i>	$(x, y) = (12, 8)$
<i>Actual Location</i>	$(x, y) = (9.8, 8)$

Table D21: Results chart (9.8, 8) – FBG sensor based system

Sonotrode Placement (9.8, 24)

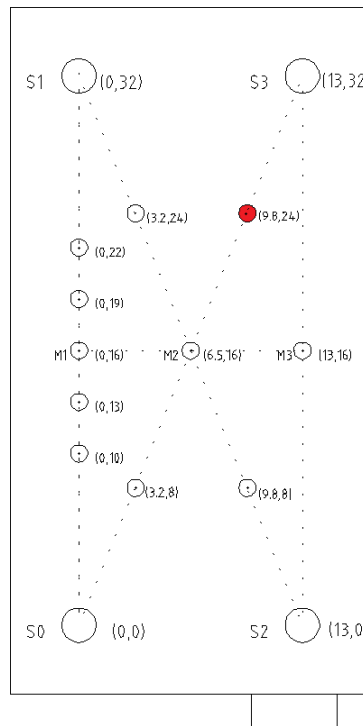


Figure D43: Sonotrode placement (9.8, 24) – FBG sensor based system

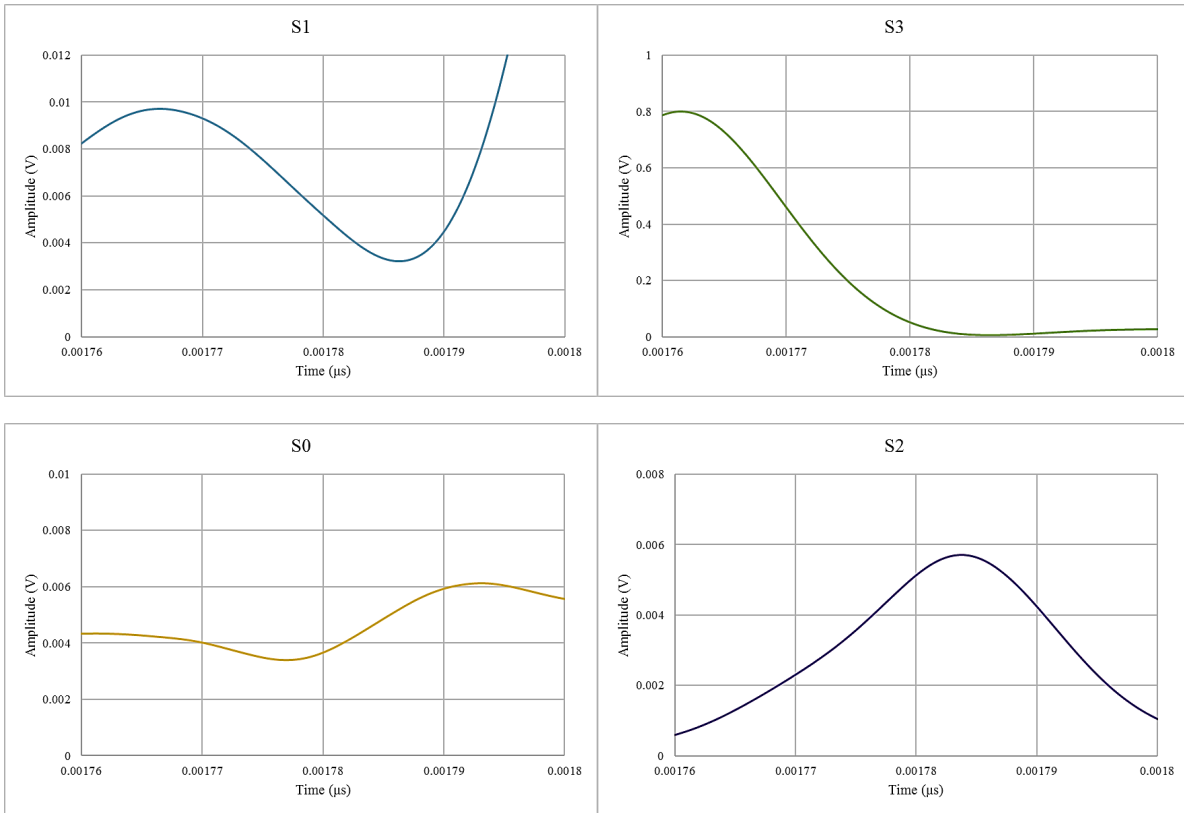


Figure D44: Filtered waveforms from all FBG sensors (9.8, 24)

$\delta_1 (S_3 - S_2)$	24 μs
$\delta_2 (S_3 - S_1)$	6 μs
$\delta_3 (S_3 - S_0)$	28 μs
<i>Calculated location from S_1, S_2, S_3</i>	(x, y) = (10, 24.6)
<i>Calculated location from S_0, S_2, S_3</i>	(x, y) = (10.5, 24.8)
<i>Actual Location</i>	(x, y) = (9.8, 24)

Table D22: Results chart (9.8, 24) – FBG sensor based system

Appendix E

E.1 Case study: Cavitation erosion and impact testing on the Metaline 785 protective coating

The erosion resistance of an elastomeric semi-soft protective coating (**MetaLine 785**), against ultrasonically induced cavitation, was examined. Samples were exposed to cavitation, initially for a period of 5h and eventually to 25h and their mass loss was periodically measured every 30 min. Erosion images of the examined surfaces were taken in order for any signs of erosion to be identified. Towards that direction, samples were also examined by means of optical and scanning electron microscopy.

In addition, an impact test was also conducted by means of a steel ball of known weight. It should be noted that, in both cases (erosion and impact testing) a comparison with the best performing coatings that were tested through this PhD study was conducted.

E.2 Experimental procedure and conditions - Erosion

The **MetaLine 785** coating was applied on the top surface of a mild steel plate (50x50x5mm) similarly to coatings from another supplier. The thickness of the coating was 3.5 mm. The steel plate was placed at the bottom of a small tank filled with tap water and cavitation was induced just above the coated surface.

Cavitation was generated by means of a Hielscher UIP 1000hd ultrasonic transducer. The titanium made transducer (22mm diameter at the tip), oscillates at a frequency of 19.5 KHz and up to an amplitude of 114 μm . The power output of the transducer is adjustable and directly affects cavitation intensity. Similarly, the gap between the ultrasonic transducer and the exposed sample can also effect cavitation intensity and the erosion rate.

The experimental setup can be seen in Figure E1:

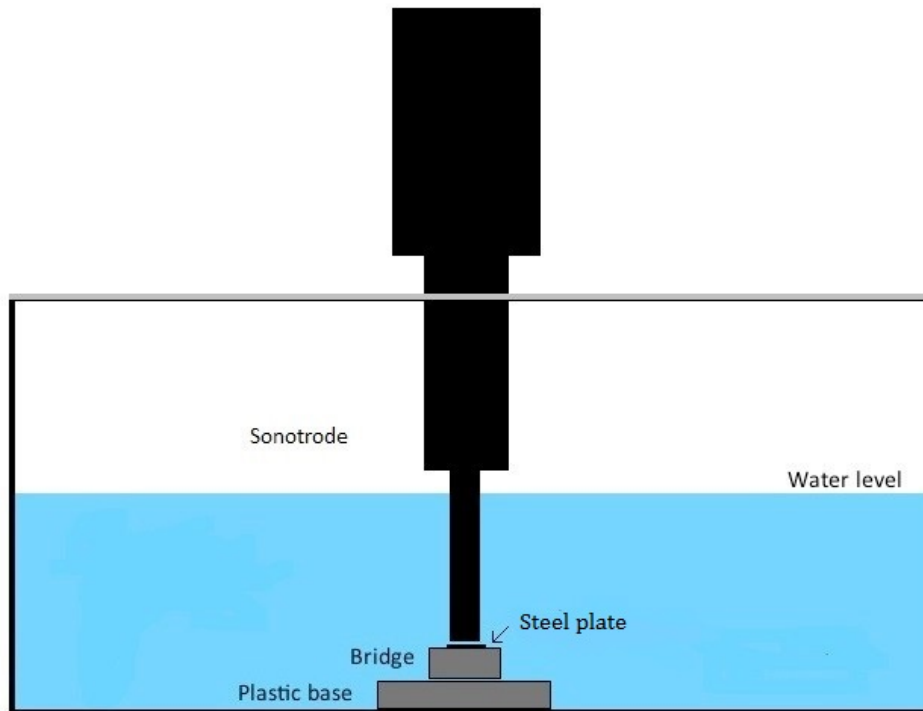


Figure E1: Test rig and water recirculation system

The ultrasonic transducer was positioned just above the coating surface at a distance of 1mm and its power output was set at 750W, similarly to the tests on other coatings. These settings had been previously found to induce cavitation of sufficient intensity without excessively eroding the tip of the transducer.

Samples were exposed for a period of 5h which was eventually extended to 25h due to promising results. Mass loss measurements were taken every 30 min as well as images of the exposed surface.

E.3 Results and discussion - Erosion

A total of 5 **MetaLine 785** steel samples were examined. Mass loss through the 5h exposure period was negligible (non-measurable) for all **MetaLine 785** samples, in contrast to the other coatings that have been tested so far. This can be seen in Figure E2 and E3:

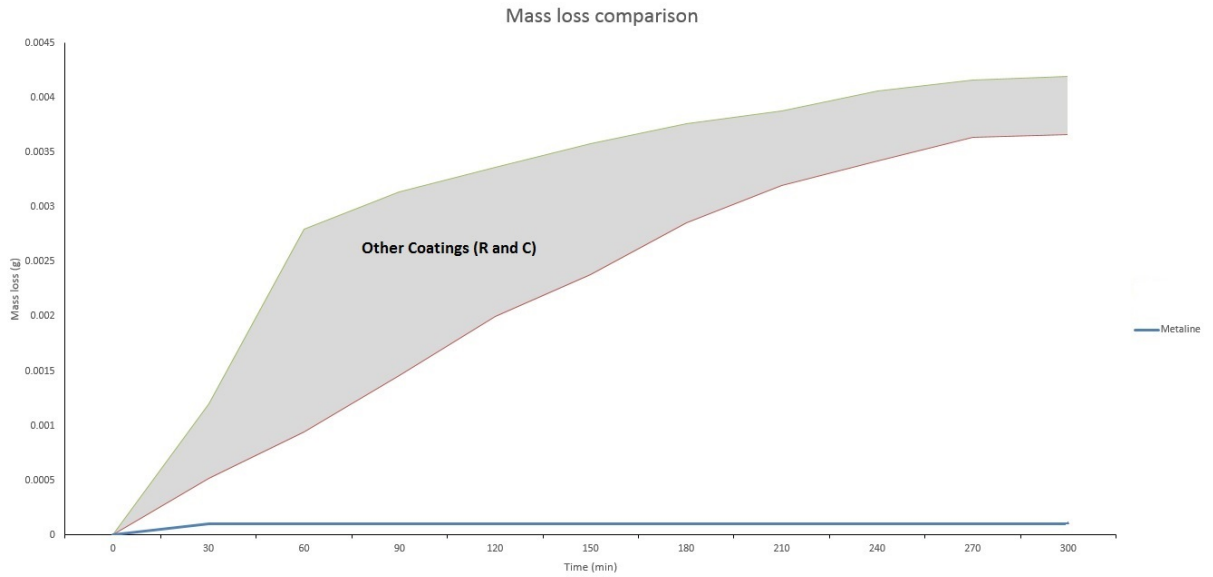


Figure E2: Mass loss comparison between the MetaLine 785 and coatings from another supplier – Best coatings

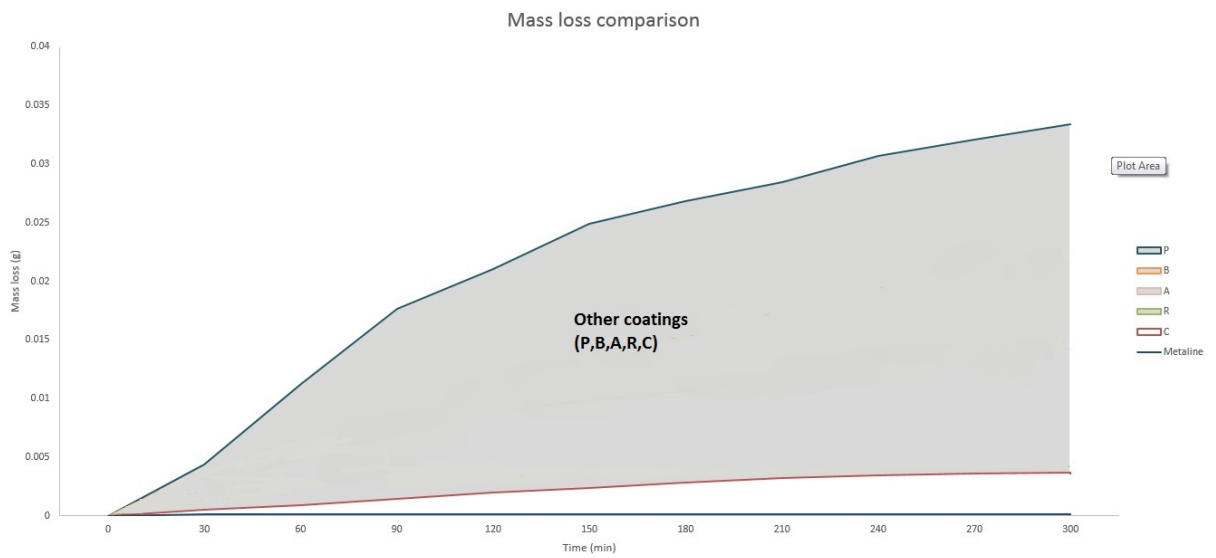


Figure E3: Mass loss comparison between the MetaLine 785 and coatings from another supplier – All coatings

The appearance of the exposed surface through the 5h period can be seen in Figure E4:

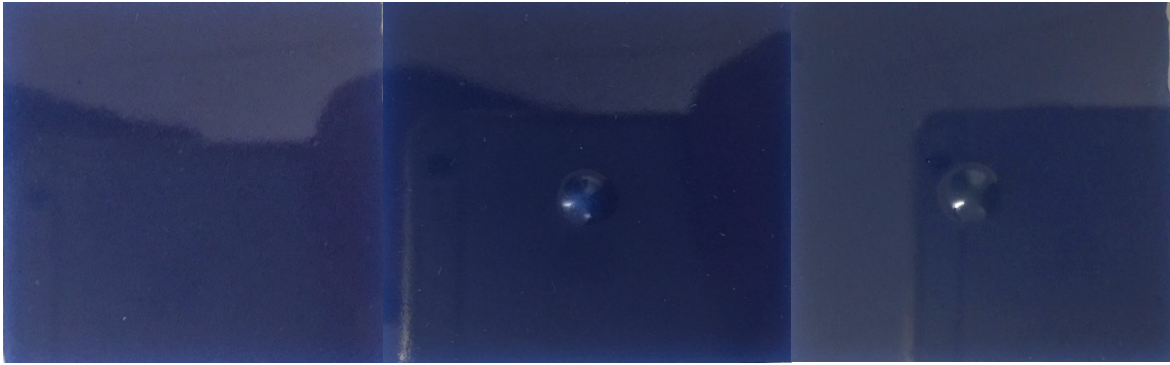


Figure E4: Erosion progress. From left to right: 0h-2h-5h

No erosion pits could be identified macroscopically apart from the appearance of a very distinctive bump, possibly due to local temperature effects. This was the case for all the **MetaLine 785** samples that were tested. Microscopic examination of the distinctive bump revealed a single erosion pit, in one of the examined samples. The contribution of that erosion pit to the total mass loss was negligible (non-measurable). The erosion pit can be seen in Figure E5:

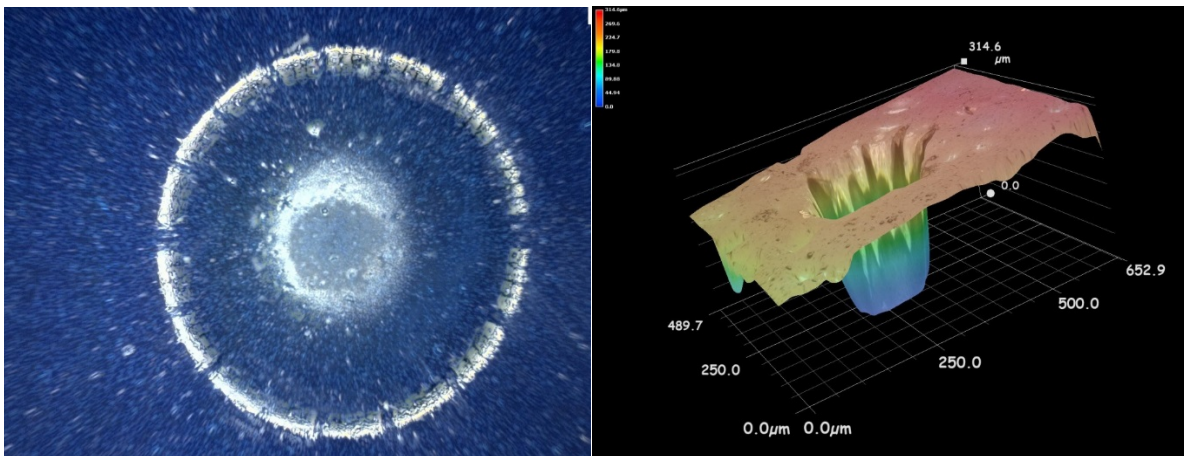


Figure E5: Distinctive bump at 100x (Left)-3D representation of the identified erosion pit on the bump at x500(Right)-Optical Microscopy

For comparison reasons the microscopic appearance of the other coatings that have been tested is presented in Figure E6:

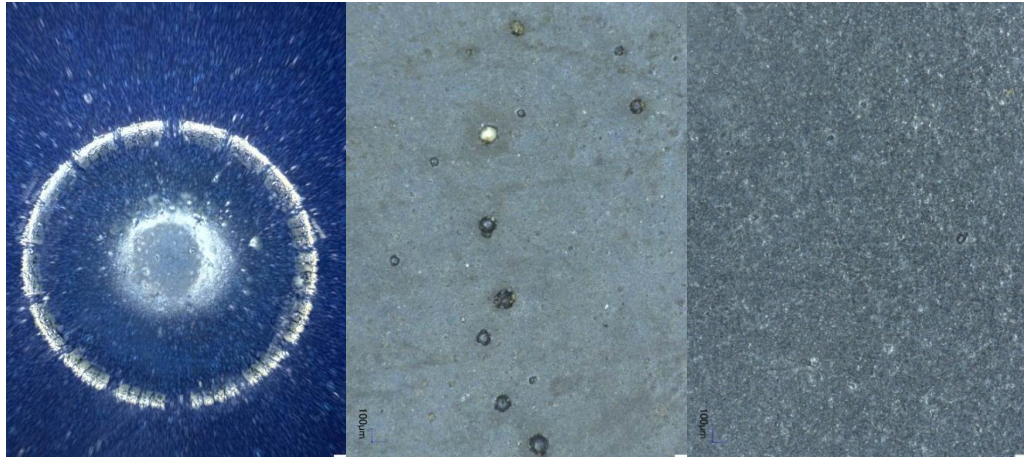


Figure E6: Erosion pattern after 5h of cavitation at 100x. From left to right: Metaline-A-B. Optical microscopy

Several erosion pits could be identified on the surfaces of the A and B coatings, leading to a measurable amount of mass loss.

Examination by means of scanning electron microscopy (SEM) of the **MetaLine 785** sample revealed another interesting, cross shaped, feature positioned at the top of the distinctive bump. This could be due to excessive stress concentration at the top of the bump. Again, its contribution to the total mass loss was negligible (non-measurable). The cross-like feature can be seen in Figure E7:

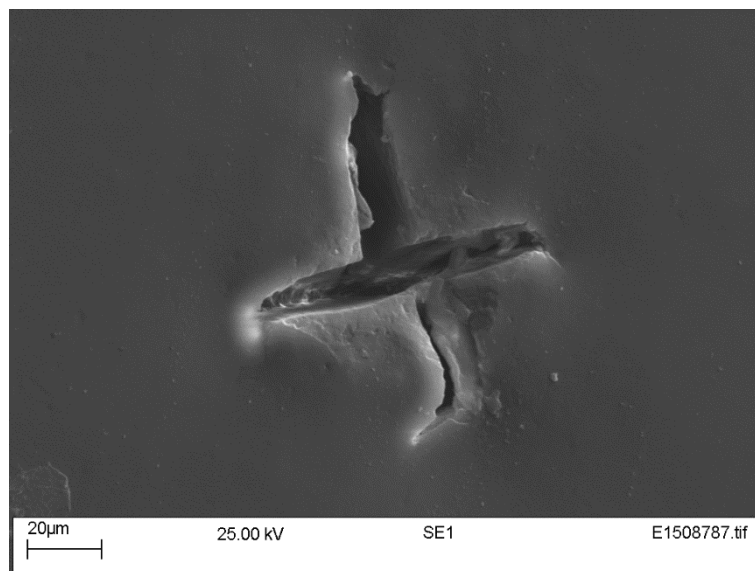


Figure E7: Cross-like feature at the top of the distinctive bump

Finally, due to promising results, it was decided to extend the exposure period up to a maximum of 25 hours, for one of the already eroded samples. Again, mass loss measurements

were taken every 30 min as well as macroscopic images of the exposed surface. Figure E8 shows the appearance of the eroded surface through this extended period:

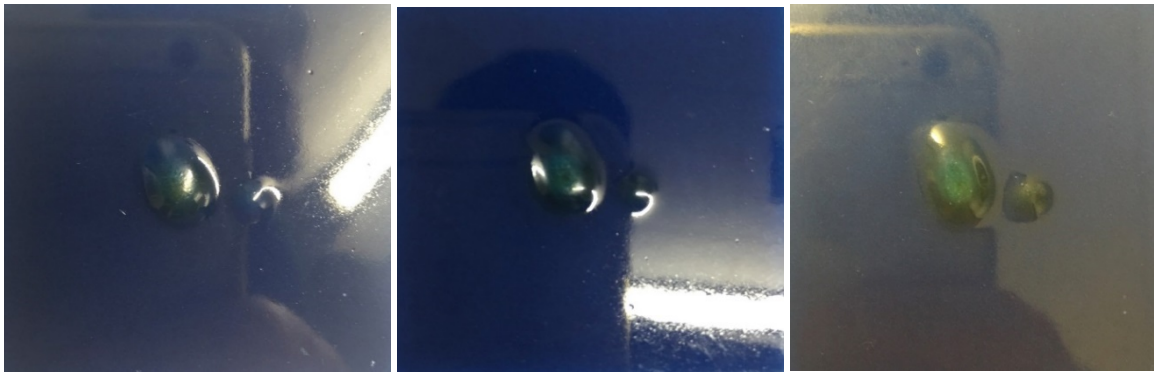


Figure E8: Erosion progress during the extended exposure. From left to right: 7h-15h-25h

Any mass loss was again negligible (non-measurable). The second bump appeared after approximately 2h of cavitation exposure (total exposure-7h), similarly to the appearance of the first one during the first 5h, possible due to local temperature effects. It is also noteworthy that apart from a slight initial inflation, the shape and volume of the first bump didn't change significantly during the extended exposure period (5h-25).

E.4 Conclusion - Erosion

The **MetaLine 785** protective coating exhibited a very resistant nature against ultrasonically induced cavitation, especially when compared to the other coatings that have been tested so far. Mass loss through the initial (5h) and the extended (25h) exposure period was negligible (non-measurable). This was also represented by the lack of any distinctive erosion pits even after 25h of continuous exposure. More specifically, only a single pit could be identified on the 'erosion bump' of one of the samples however its contribution to the total mass loss was negligible.

On the other hand, the cross-like feature on the top of the bump implies that the coating will eventually rupture at some point. The appearance of those bumps however is possibly related to temperature effects that can affect and weaken the coating locally. This could be due to the operation of the ultrasonic transducer as it has been observed in a similar coating from a different supplier.

E.5 Impact testing

A ball drop test was conducted on the R and C coatings supplied by BAE Systems as well as on the Metaline 785 protective coating. The aim of this test was to simulate and explore how the coatings would react when hit by a moving object.

In this case the moving object was simulated by a carbon steel ball of a diameter of **6.35 cm (2.5 inches)** and a mass of approximately **1 kg**. When dropped from a height of **4 m** above the examined coating the ball at the time of impact would have a speed of **8.85 m/s** equal to about **17 Knots**. At this speed the **1 kg** steel ball would have a kinetic energy of **39.2 J**.

The steel ball as well as the three examined coatings can be seen in Figure E9:

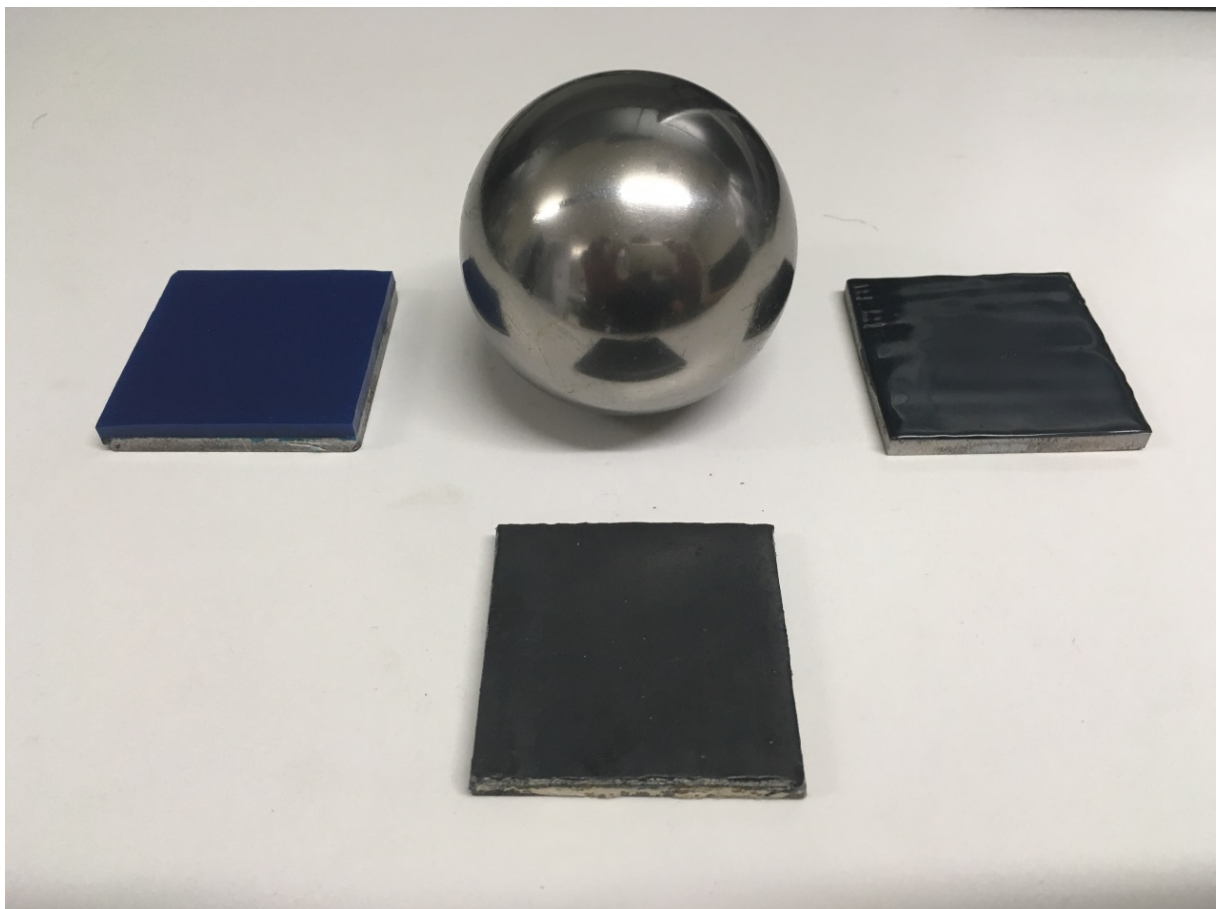


Figure E9: 1Kg steel ball and the three coatings – From left to right- Metaline, R and C

E.6 Impact testing - Results

The appearance of the surface of each of the three coatings just before impact can be seen in Figure E10:



Figure E10: From left to right – Metaline, R and C coatings before impact.

The appearance of their surface just after the steel ball impact is presented in Figure E11:



Figure E11: From left to right – Metaline, R and C coatings after impact.

A very characteristic dent can be identified on the right side of the C coating which is the area of impact. Similar dents were observed on both the Metaline and R coating although they don't appear to be as severe as the one on the C coating. Microscopic images of the damaged areas are presented in Figure E12:



Figure E12: From left to right – Metaline, R and C coatings after impact (20x)

Optical microscopic images confirm that the C coating has suffered the greater damage as its deep dent implies followed by the Metaline and R coating with much thinner dents. Further details about those dents can be provided by the 3D images presented in Figure E13:

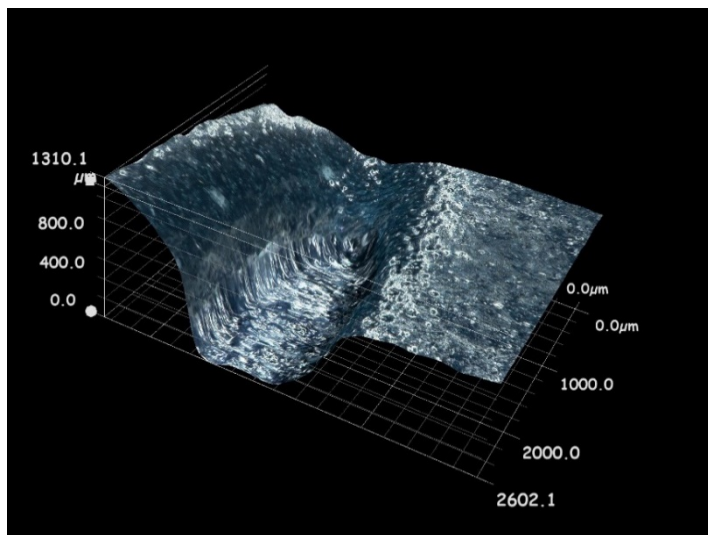
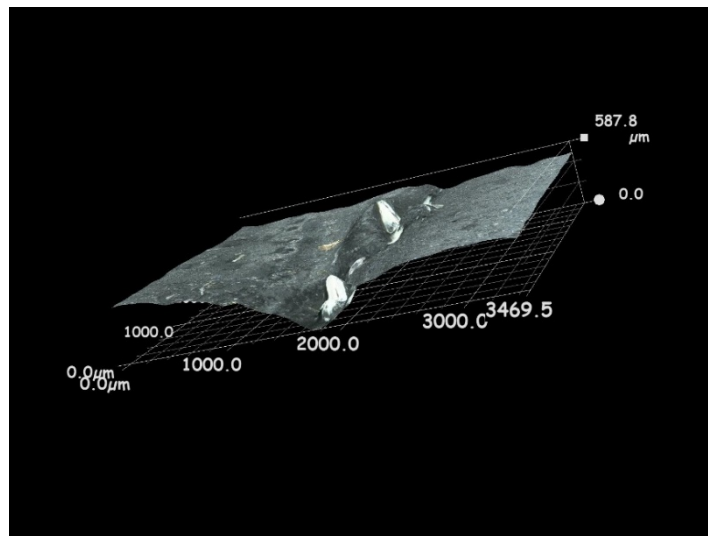
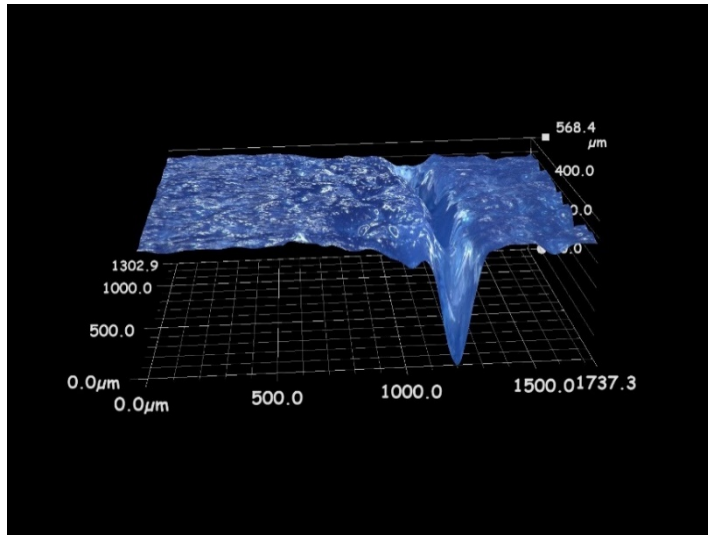


Figure E13: From top to bottom – Metaline, R and C coatings after impact (3D)

The 3D images confirmed that the C coating has suffered the greater damage, as it is implied by the depth of its dent (**1.3101 mm**) followed by Metaline and R coatings with similar dents depths (**568.3 μm** and **587.8 μm** , respectively). Interestingly, there was a measurable amount of mass loss due to the ball impact as it can be seen in Figure E14:

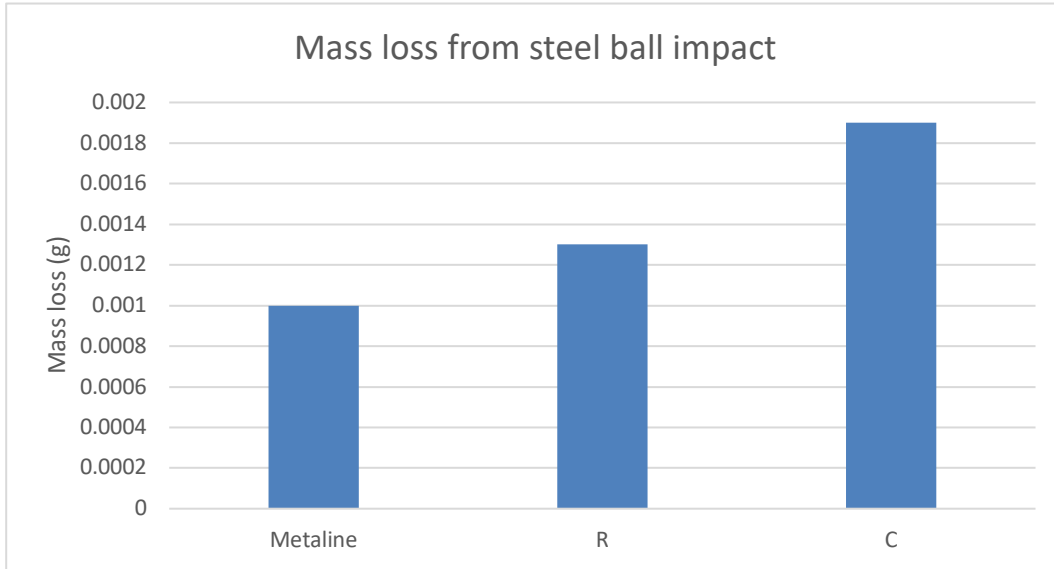


Figure E14: Mass loss due to steel ball impact

The greater mass loss was experienced by C coating followed by R and Metaline). Results match macroscopic and optical microscopic observations with regards to the damage experienced by the coatings. Finally, a comparison between the mass loss caused by the steel ball impact and ultrasonically induced cavitation is presented in Figure E15:

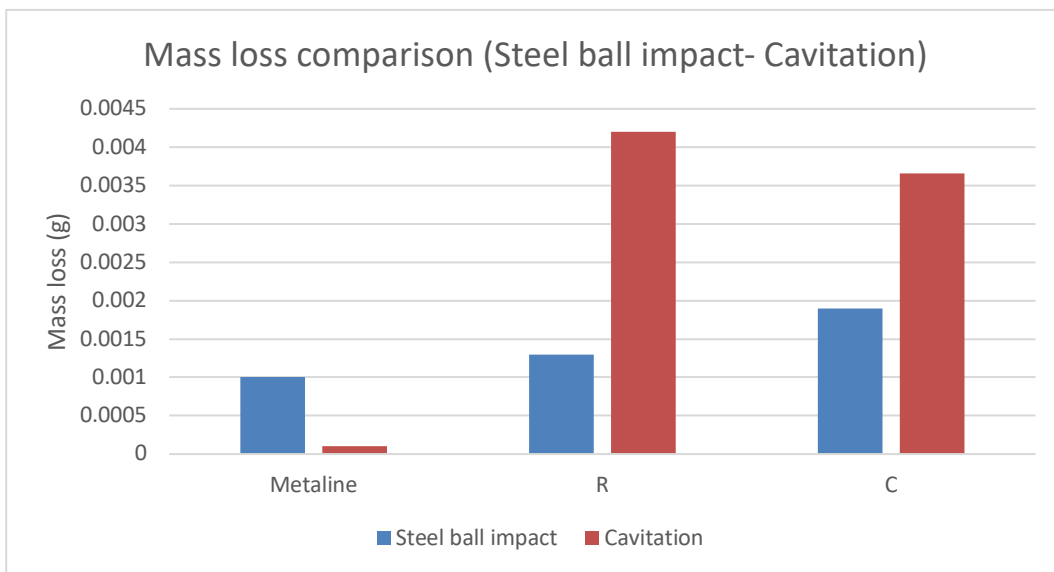


Figure E15: Mass loss comparison. Steel ball impact – Cavitation

Appendix F

F.1 Three dimensional microscopic images of cavitation erosion pits

Grade DH36 Steel

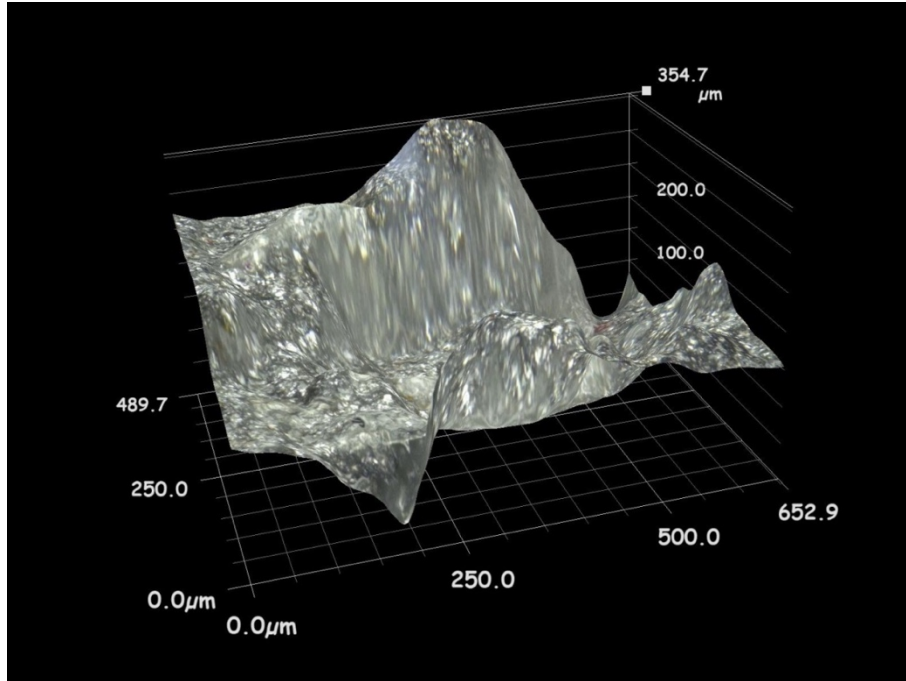


Figure F1: 3D illustration of erosion pit (2). Grade DH36 steel.

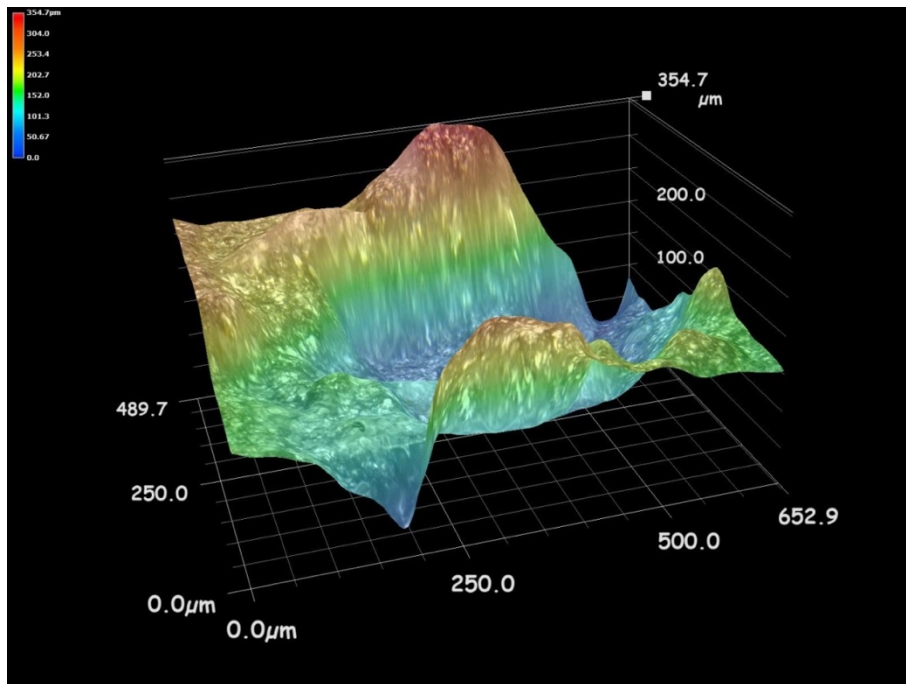


Figure F2: 3D illustration of erosion pit (2). Grade DH36 steel – Colour contour.

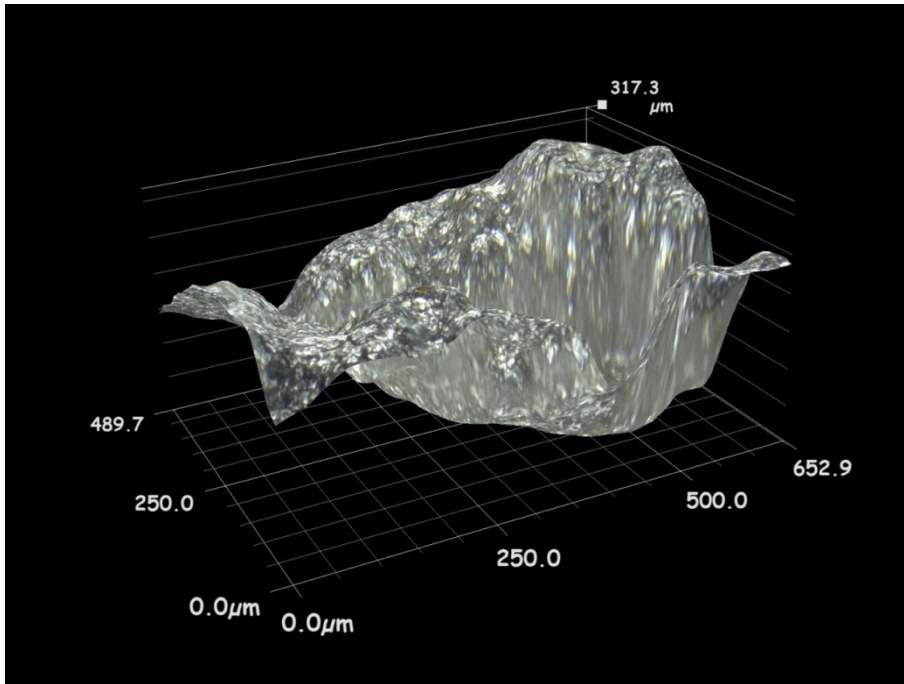


Figure F3: 3D illustration of erosion pit (3). Grade DH36 steel.

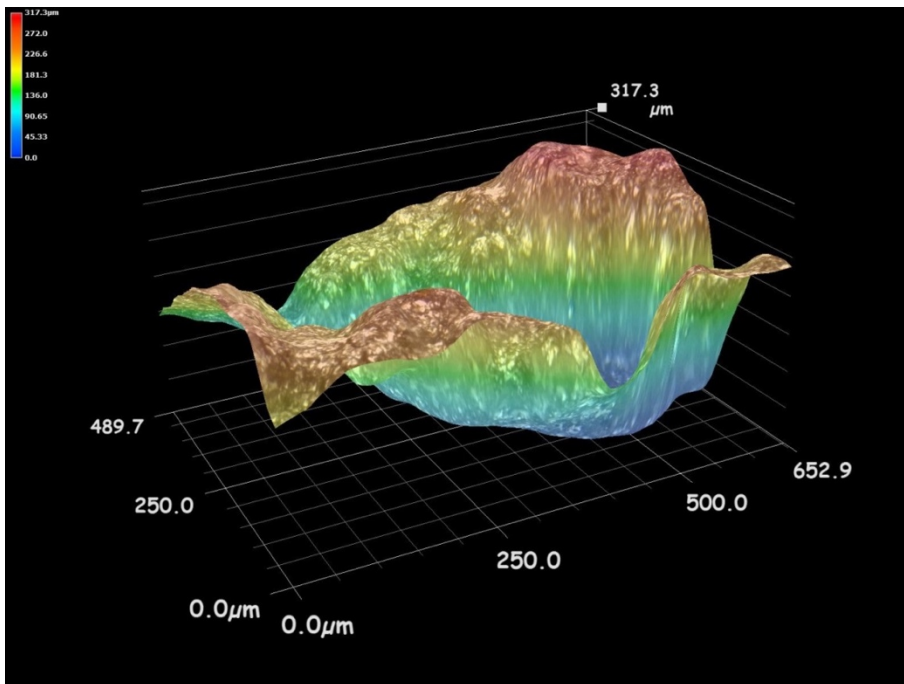


Figure F4: 3D illustration of erosion pit (3). Grade DH36 steel – Colour contour.

Stainless steel 254

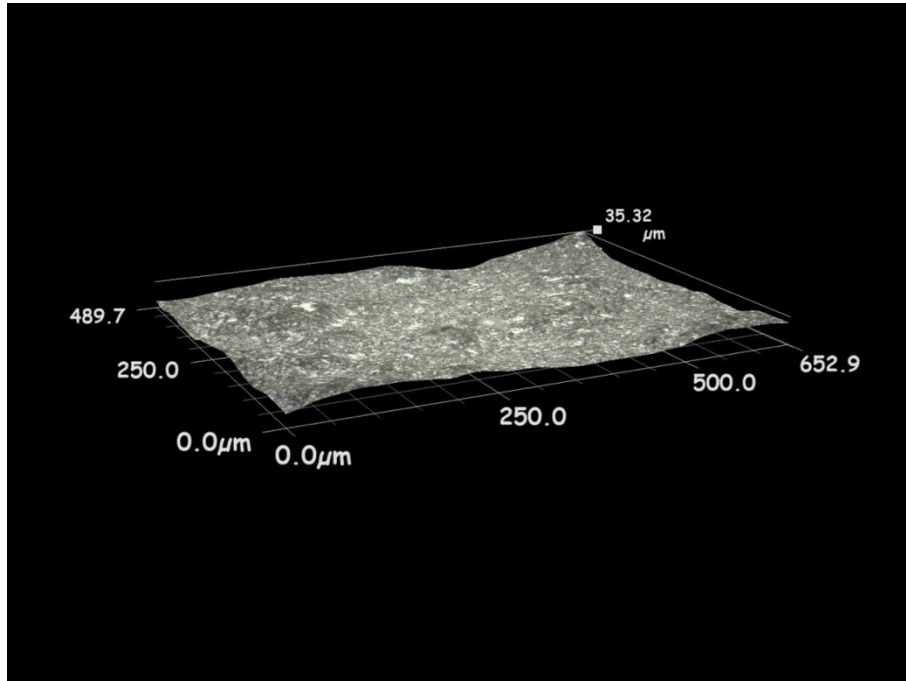


Figure F5: 3D illustration of erosion pit (2). Stainless steel 254.

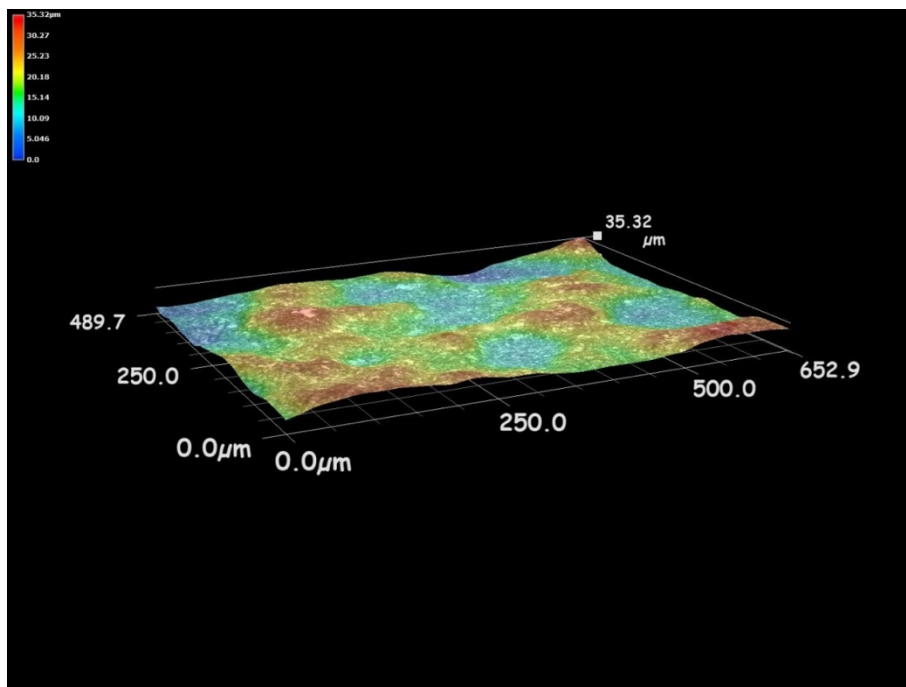


Figure F6: 3D illustration of erosion pit (2). Stainless steel 254 – Colour contour.

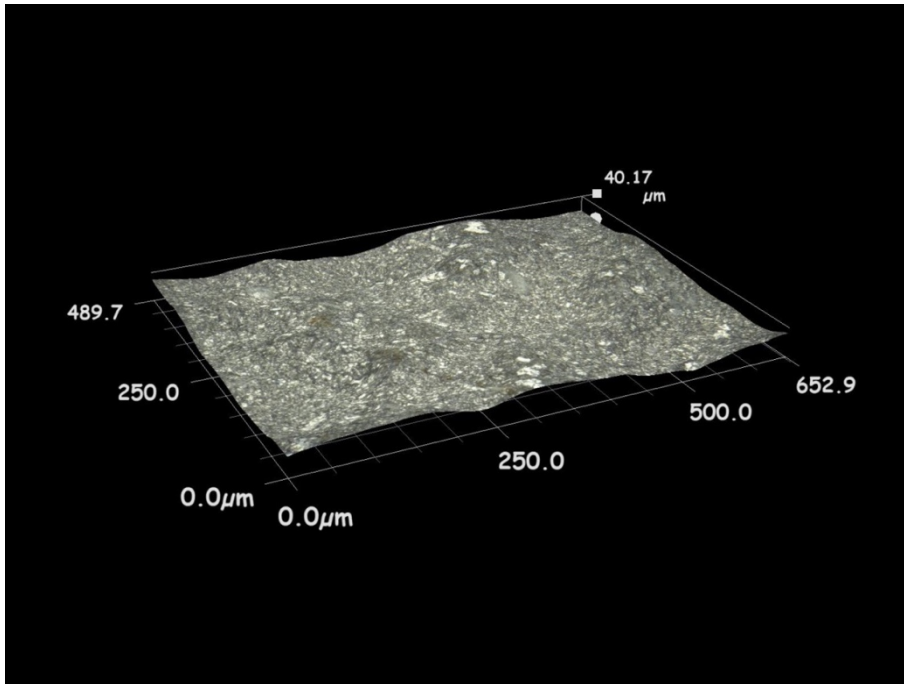


Figure F7: 3D illustration of erosion pit (3). Stainless steel 254.

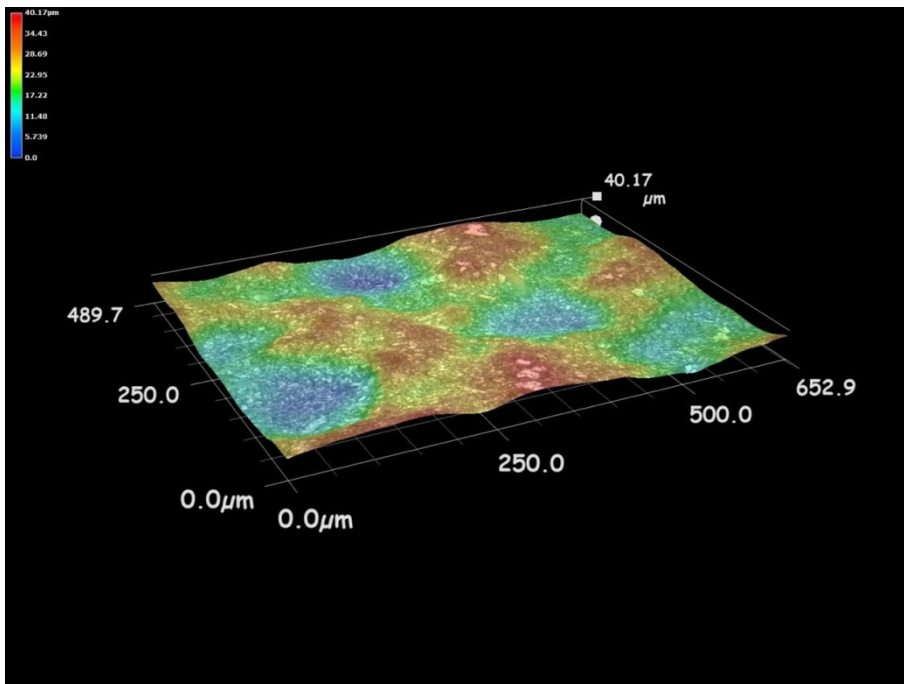


Figure F8: 3D illustration of erosion pit (3). Stainless steel 254 – Colour contour.

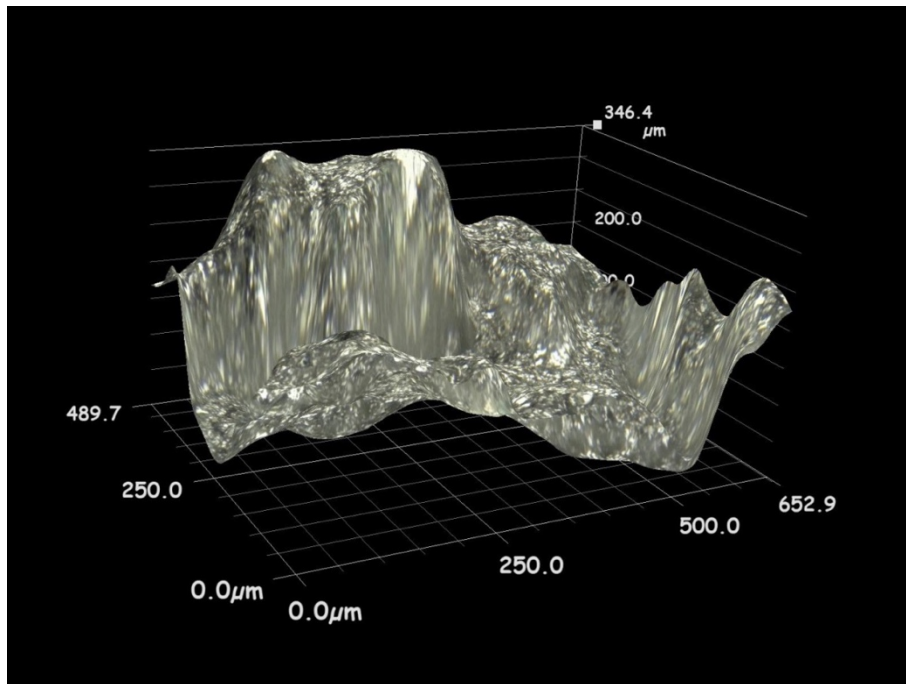


Figure F9: 3D illustration of erosion pit (2). Cupronickel 70-30.

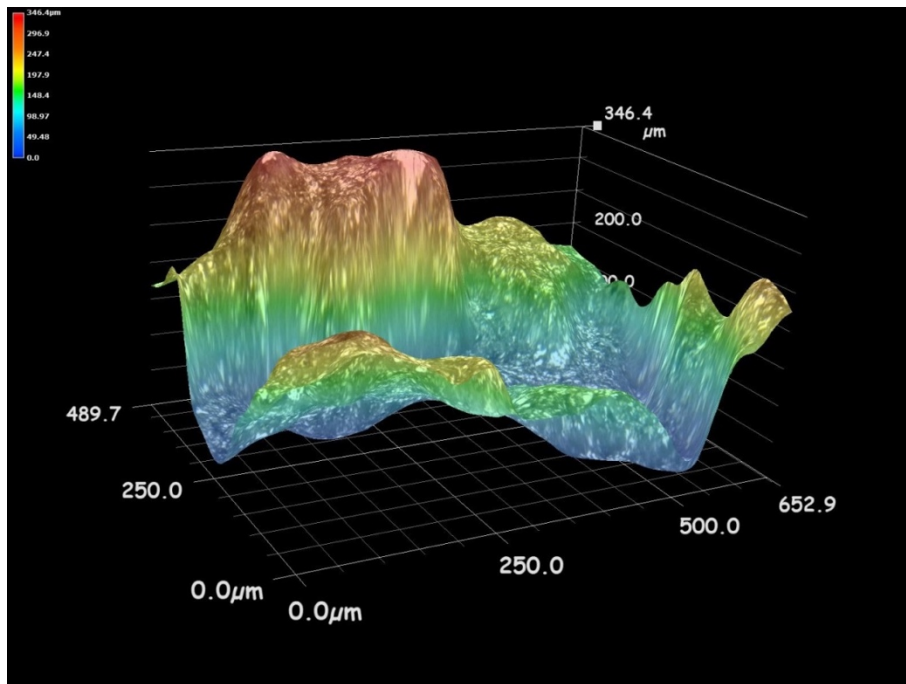


Figure F10: 3D illustration of erosion pit (2). Cupronickel 70-30 – Colour contour.

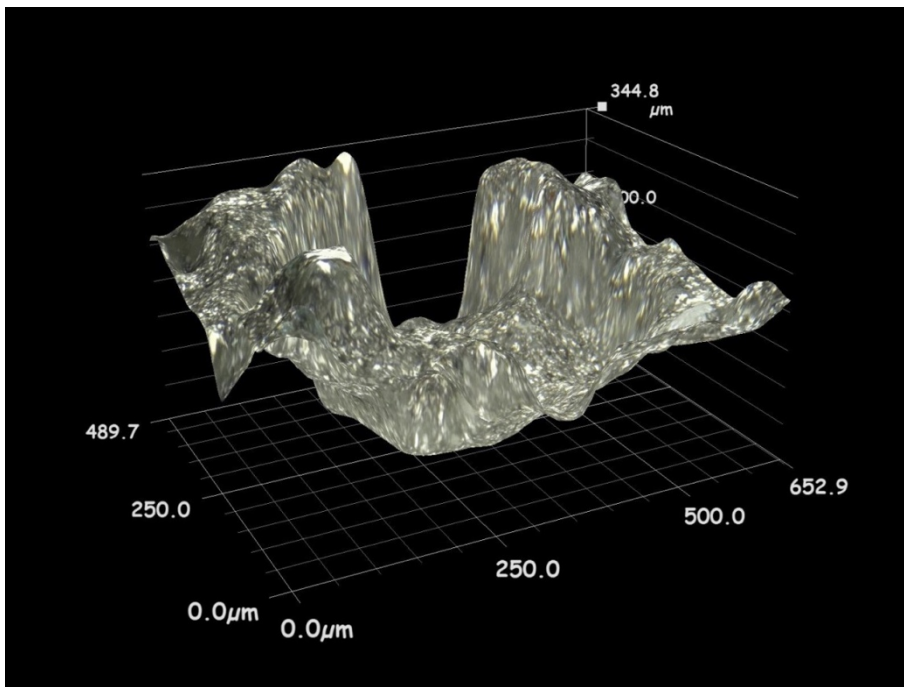


Figure F11: 3D illustration of erosion pit (3). Cupronickel 70-30.

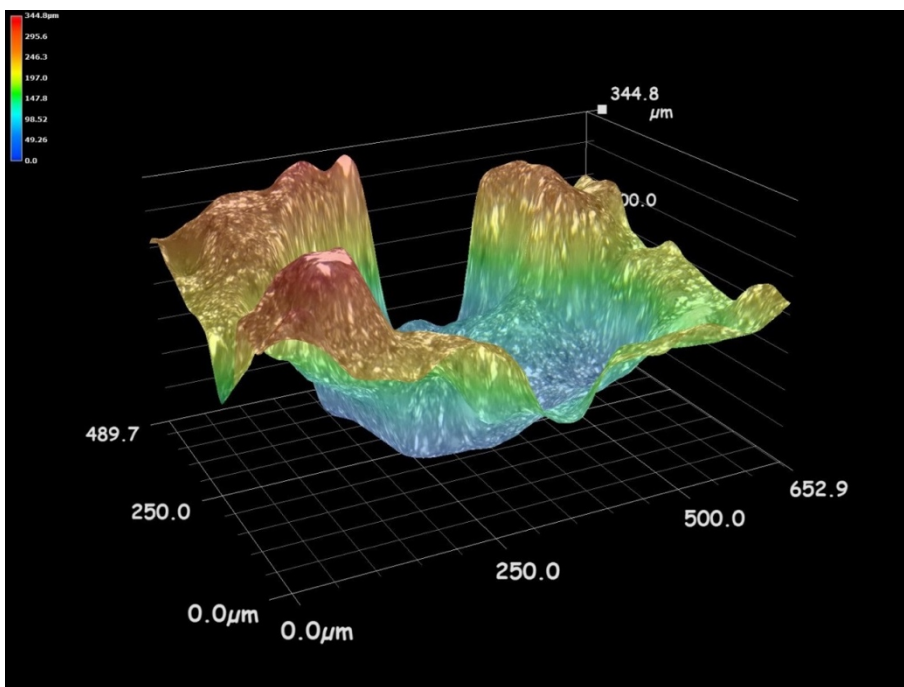


Figure F12: 3D illustration of erosion pit (3). Cupronickel 70-30 – Colour contour.

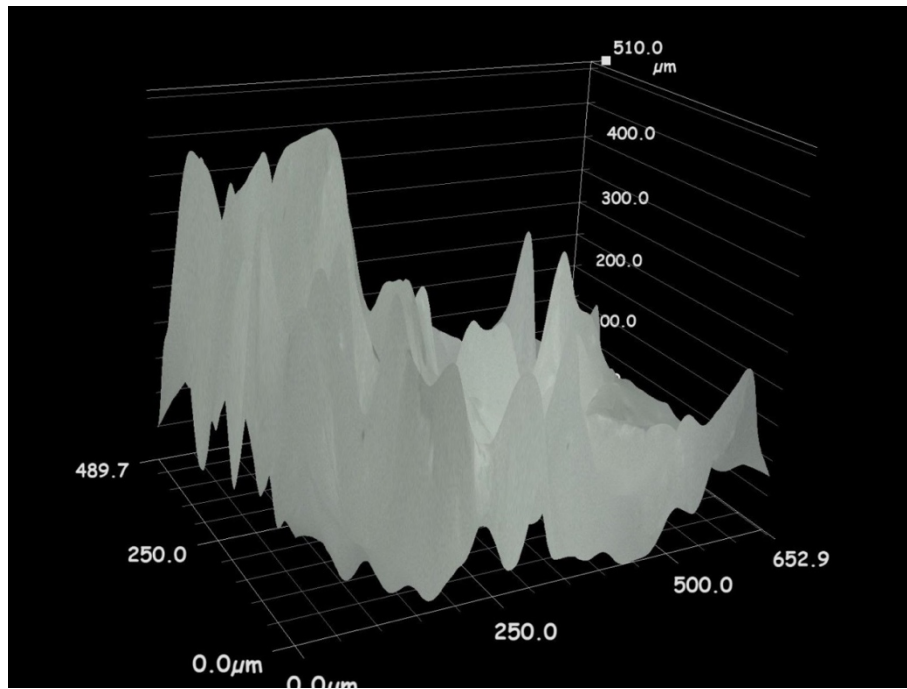


Figure F13: 3D illustration of erosion pit (2). I coating.

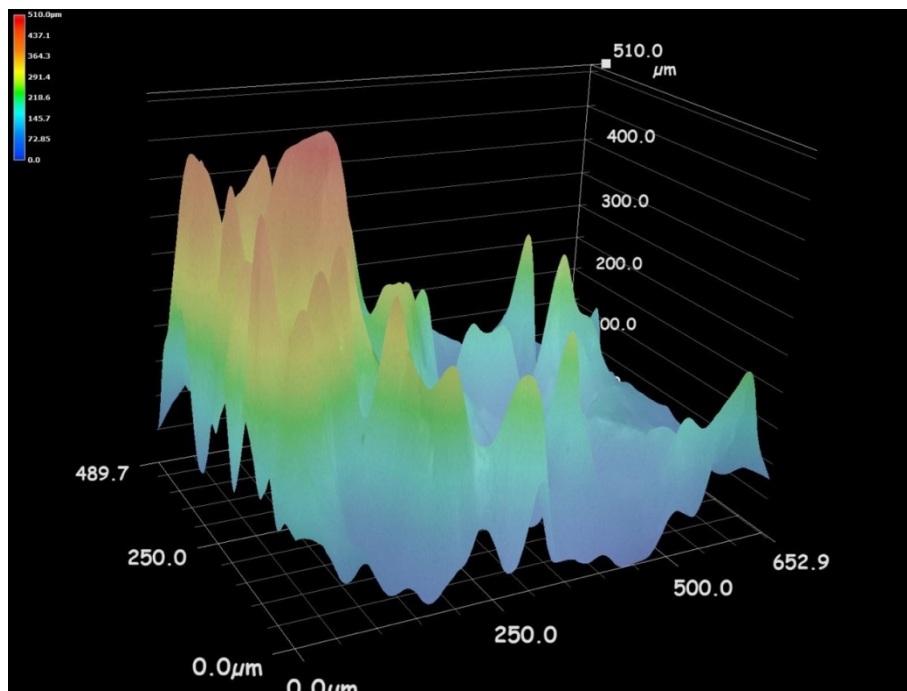


Figure F14: 3D illustration of erosion pit (2). I coating – Colour contour.

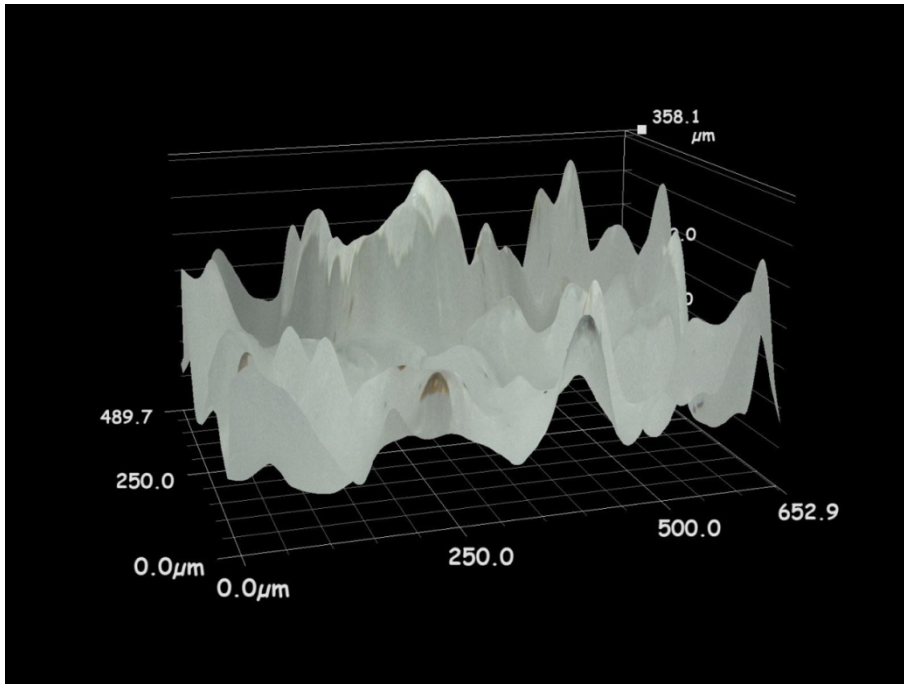


Figure F15: 3D illustration of erosion pit (3). I coating.

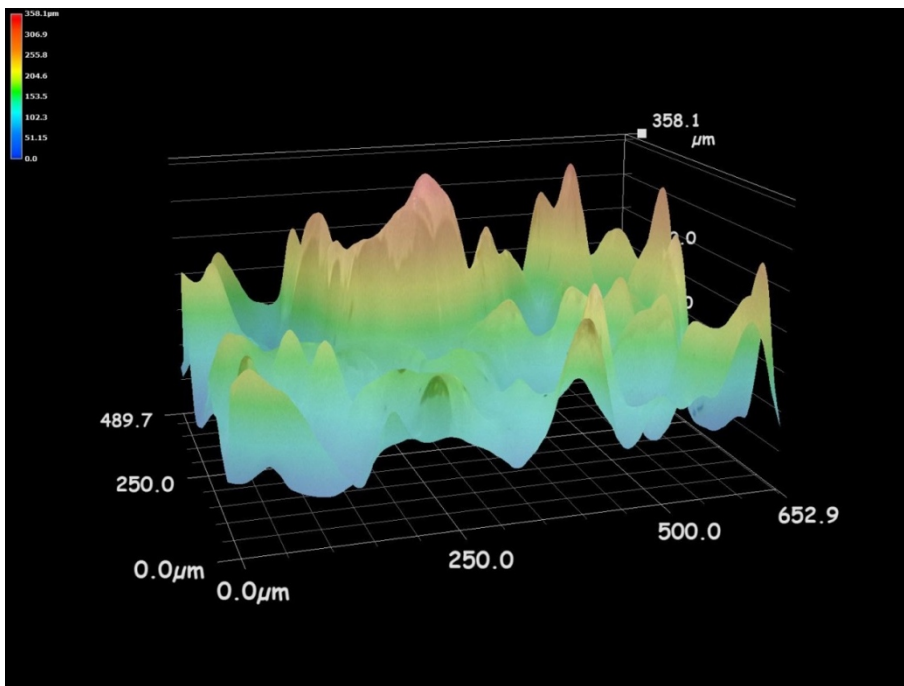


Figure F16: 3D illustration of erosion pit (3). I coating – Colour contour.

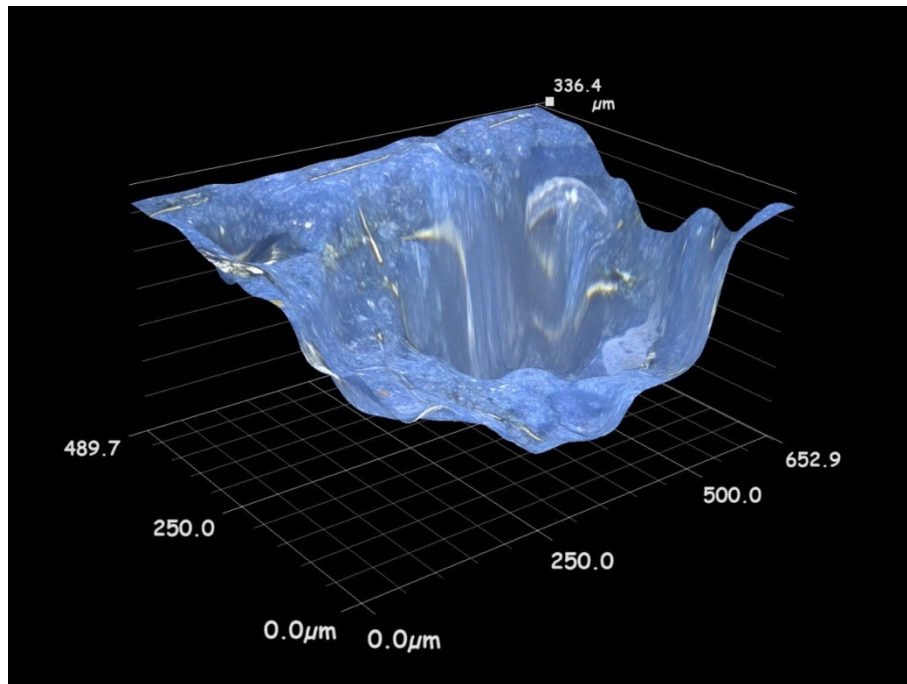


Figure F17: 3D illustration of erosion pit (2). P coating.

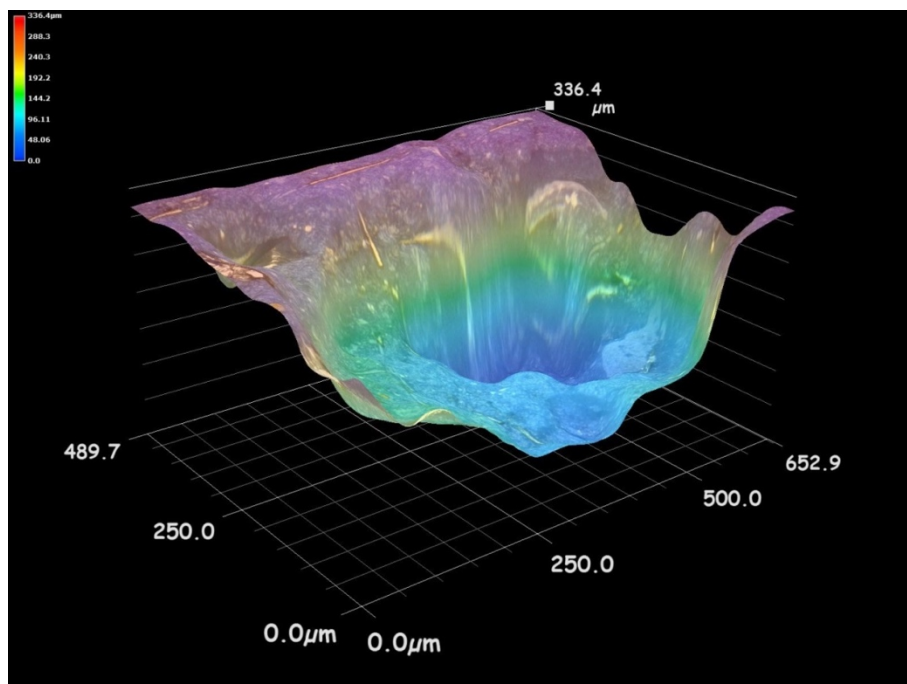


Figure F18: 3D illustration of erosion pit (2). P coating – Colour contour.

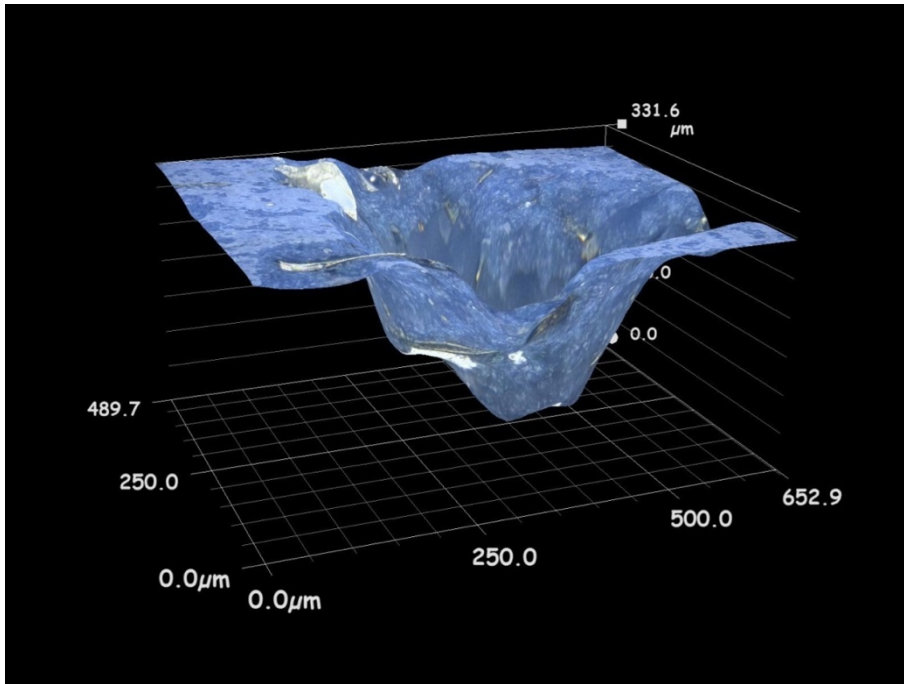


Figure F19: 3D illustration of erosion pit (3). P coating.

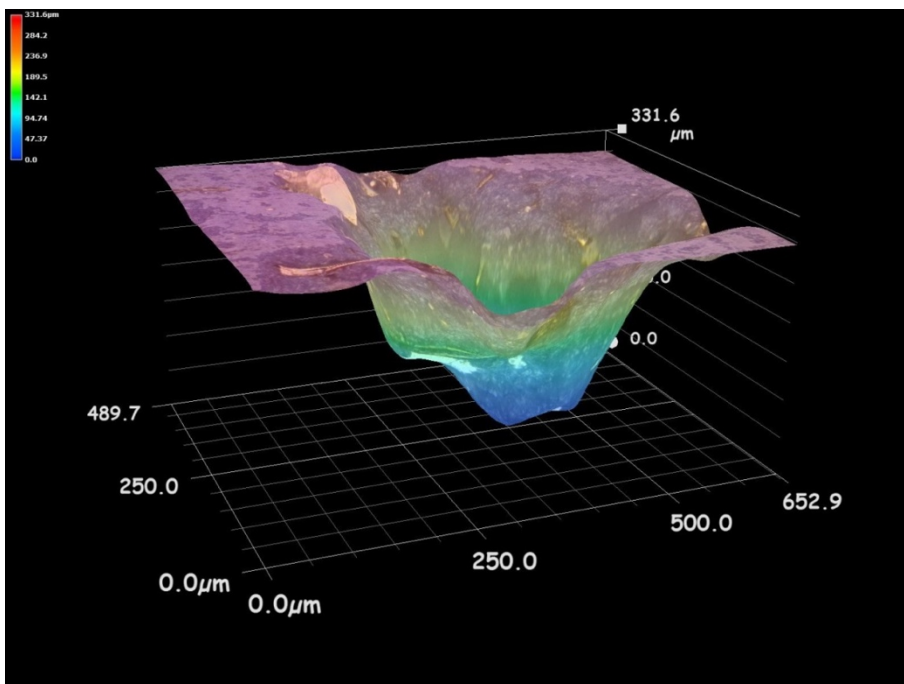


Figure F20: 3D illustration of erosion pit (3). P coating – Colour contour.

A coating

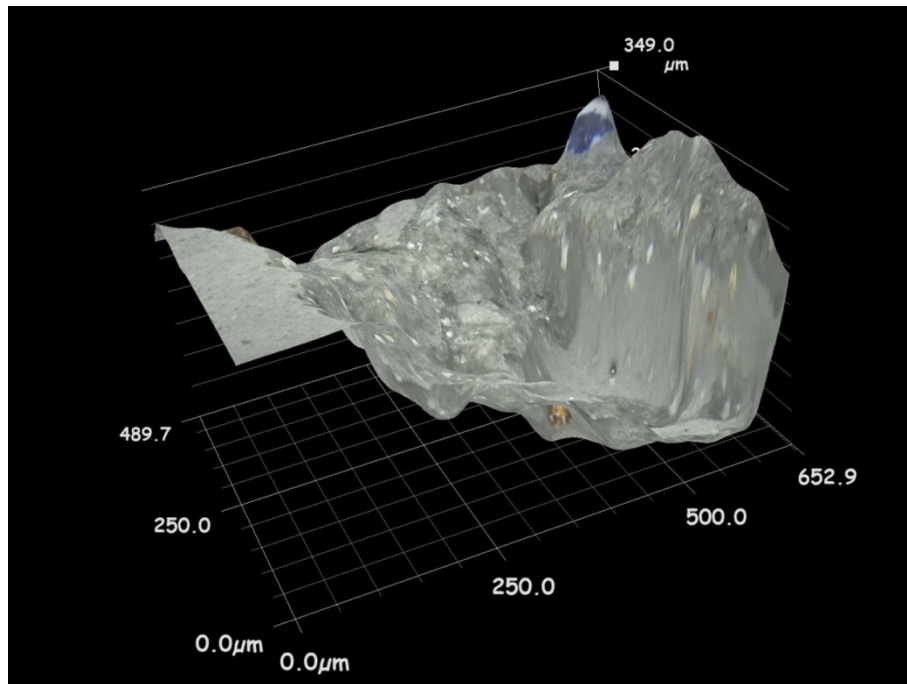


Figure F21: 3D illustration of erosion pit (2). A coating.

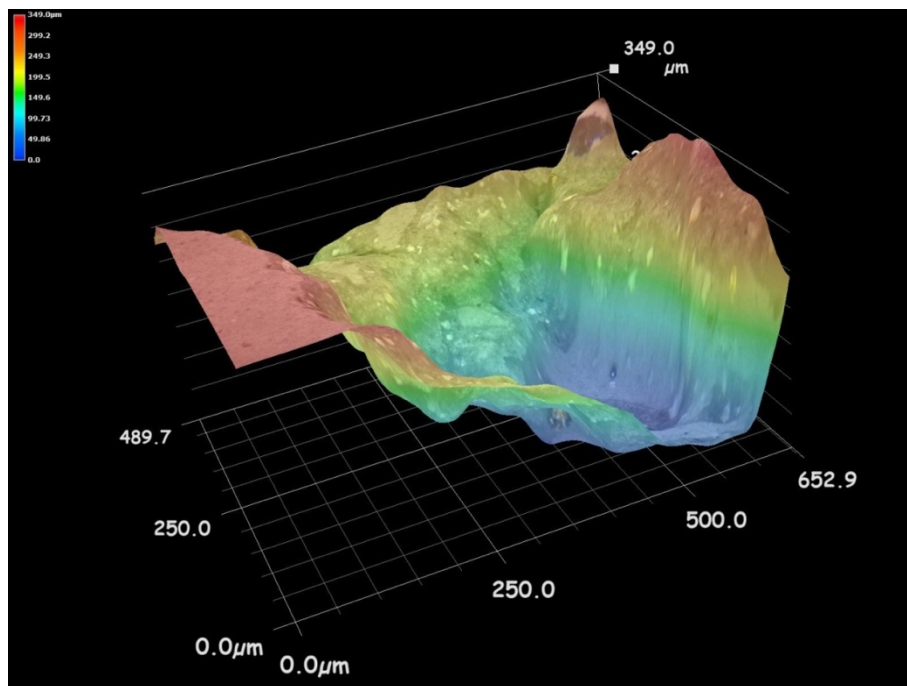


Figure F22: 3D illustration of erosion pit (2). A coating – Colour contour.

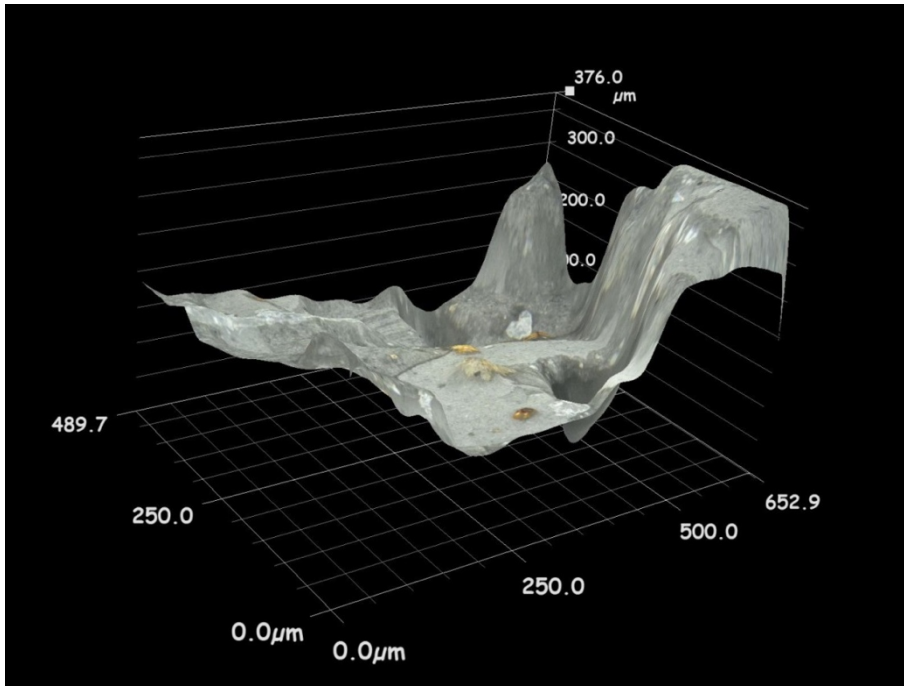


Figure F23: 3D illustration of erosion pit (3). A coating.

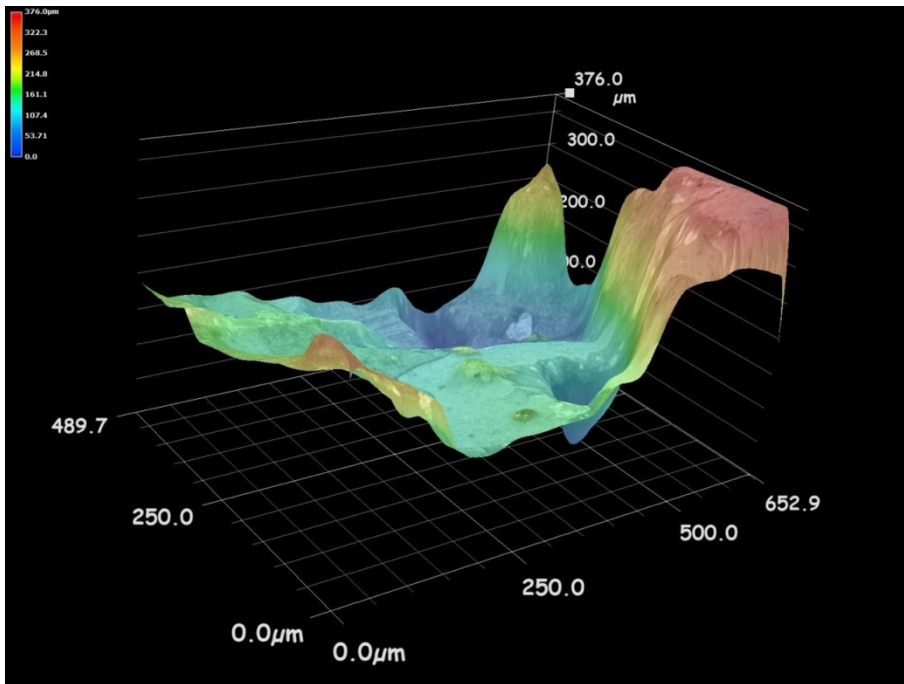


Figure F24: 3D illustration of erosion pit (3). A coating – Colour contour.

Double coating

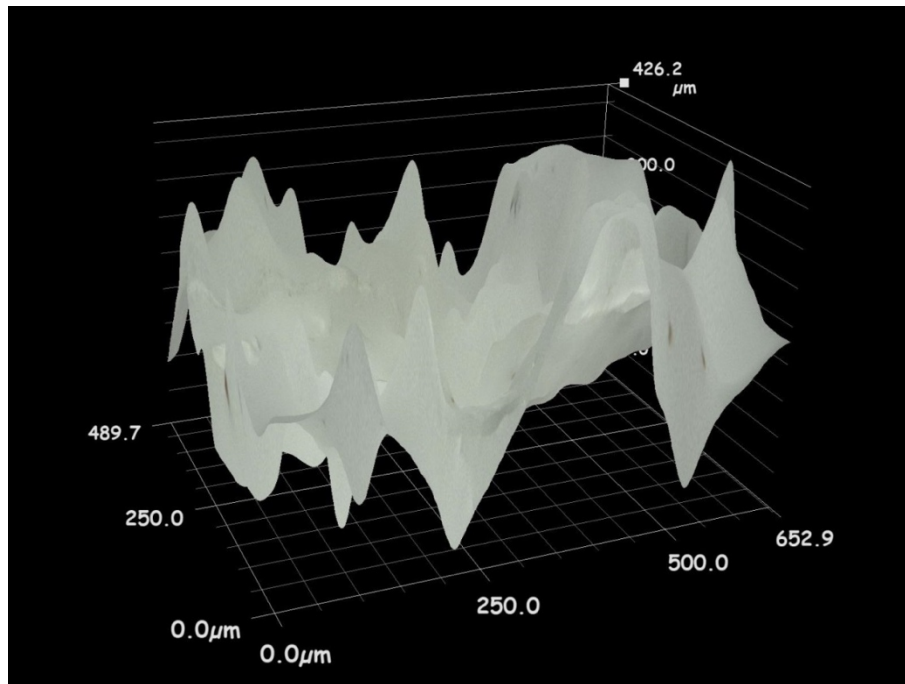


Figure F25: 3D illustration of erosion pit (2). Double coating.

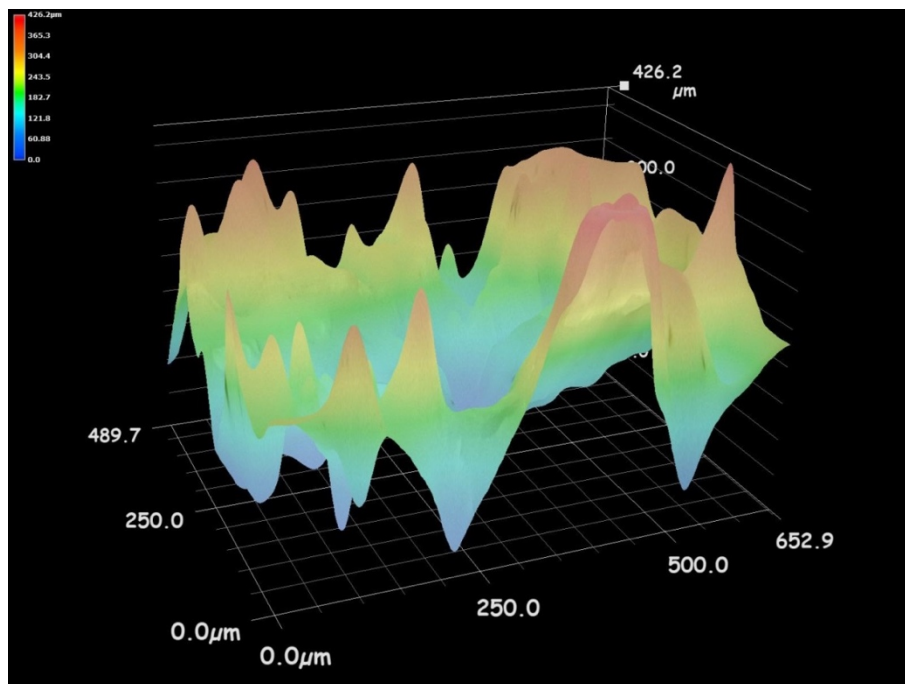


Figure F26: 3D illustration of erosion pit (2). Double coating – Colour contour.

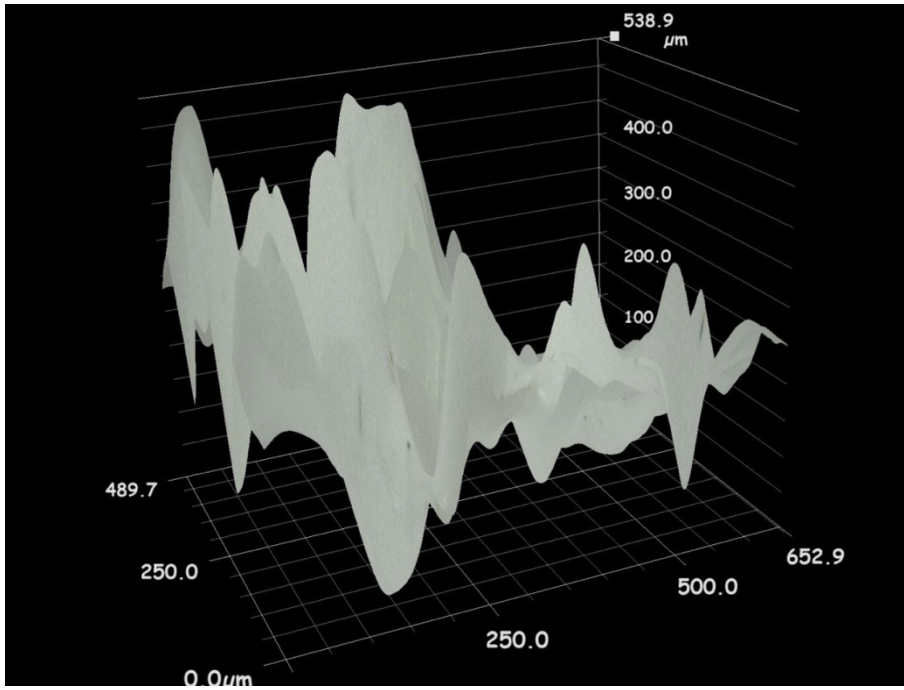


Figure F27: 3D illustration of erosion pit (3). Double coating.

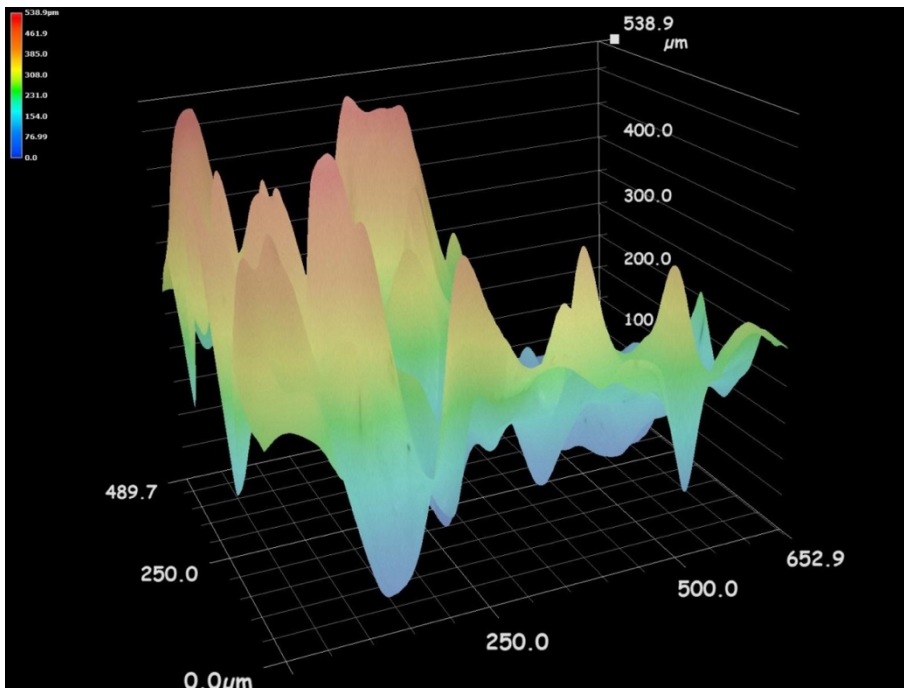


Figure F28: 3D illustration of erosion pit (3). Double coating – Colour contour.

R coating

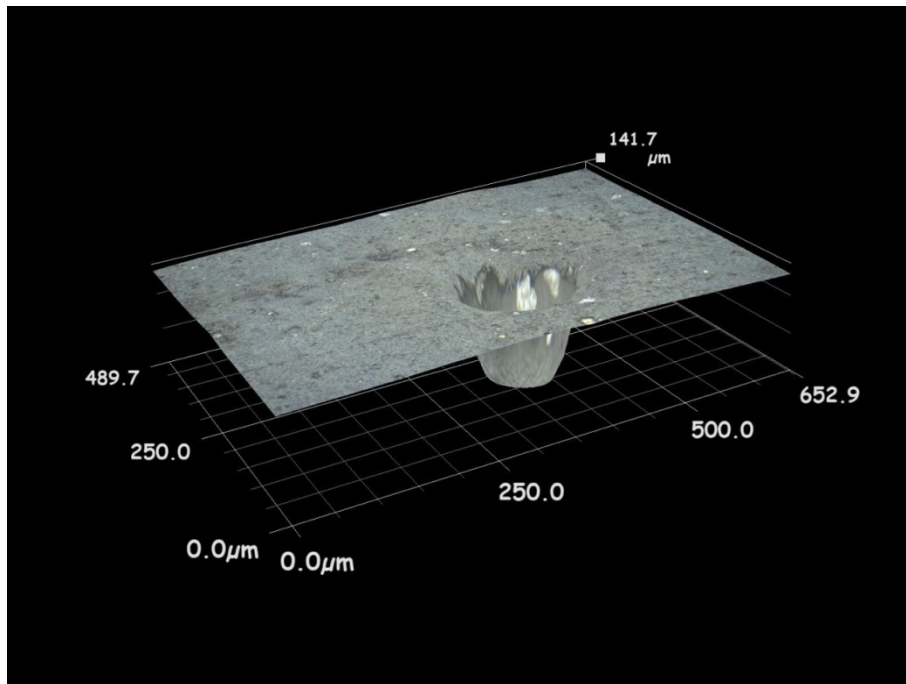


Figure F29: 3D illustration of erosion pit (2). R coating.

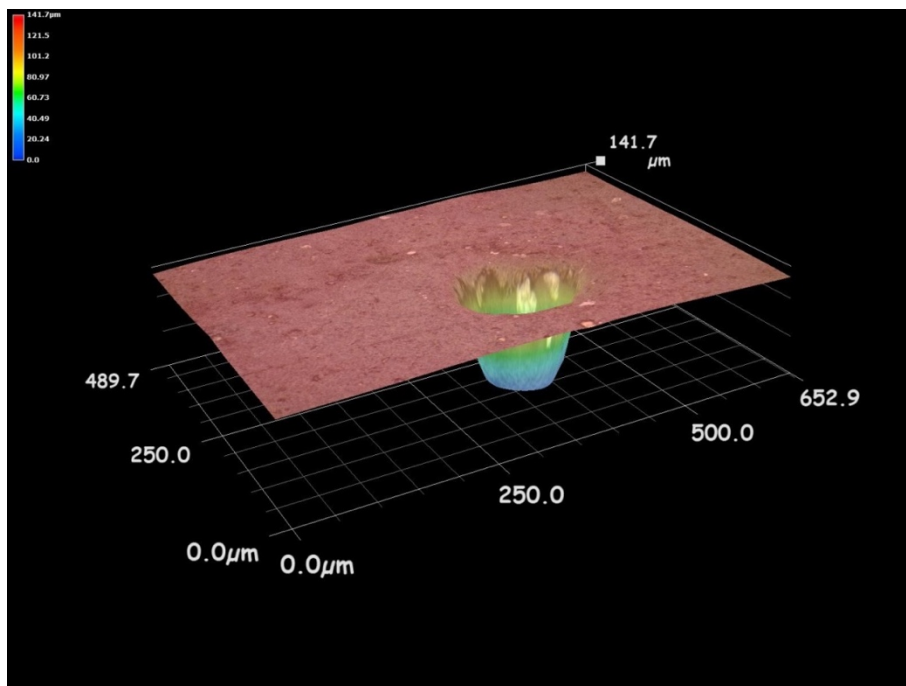


Figure F30: 3D illustration of erosion pit (2). R coating – Colour contour.

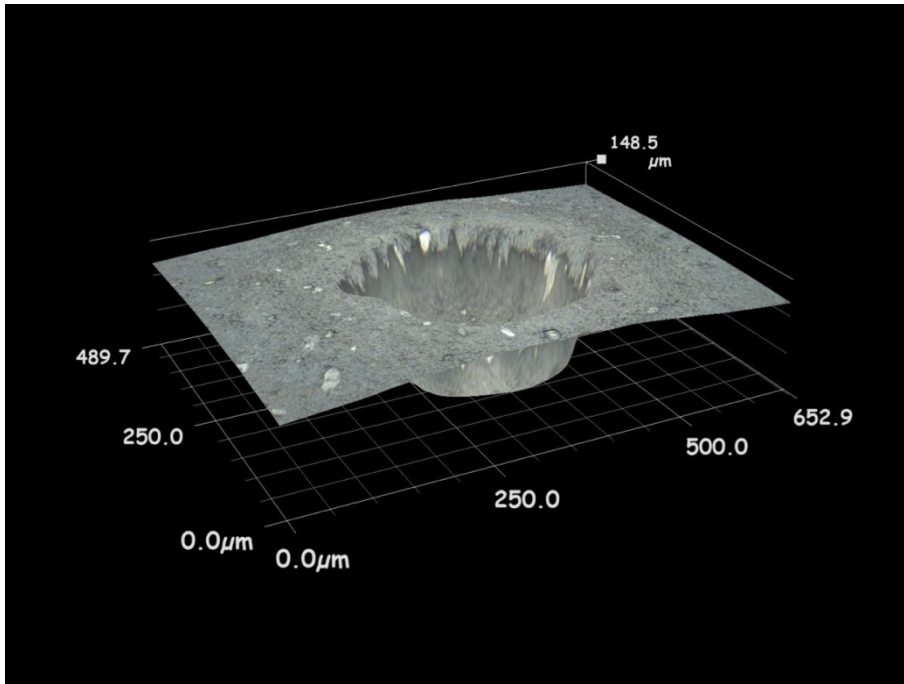


Figure F31: 3D illustration of erosion pit (3). R coating.

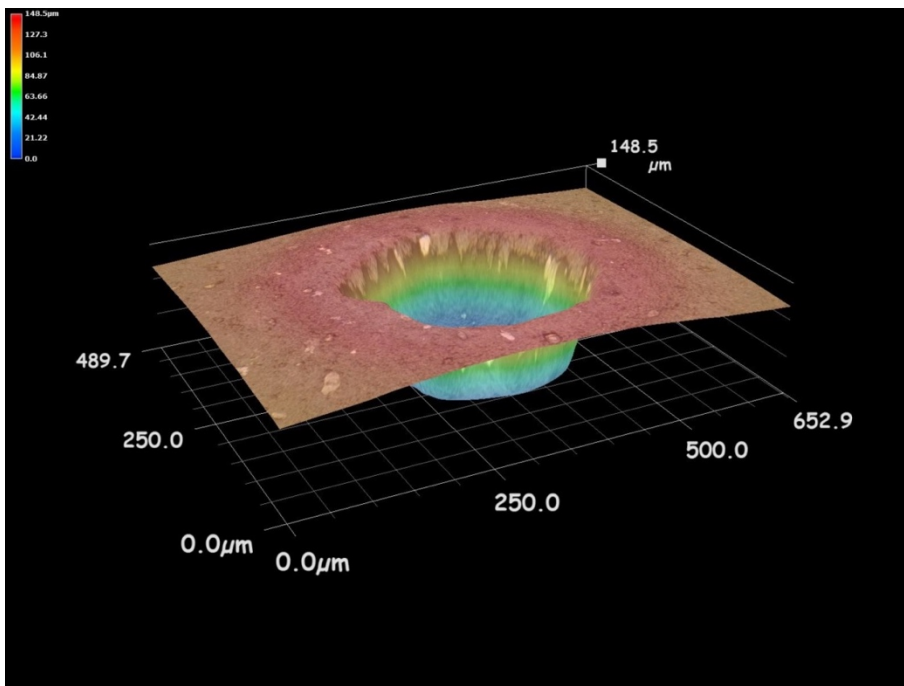


Figure F32: 3D illustration of erosion pit (3). R coating – Colour contour.

B coating

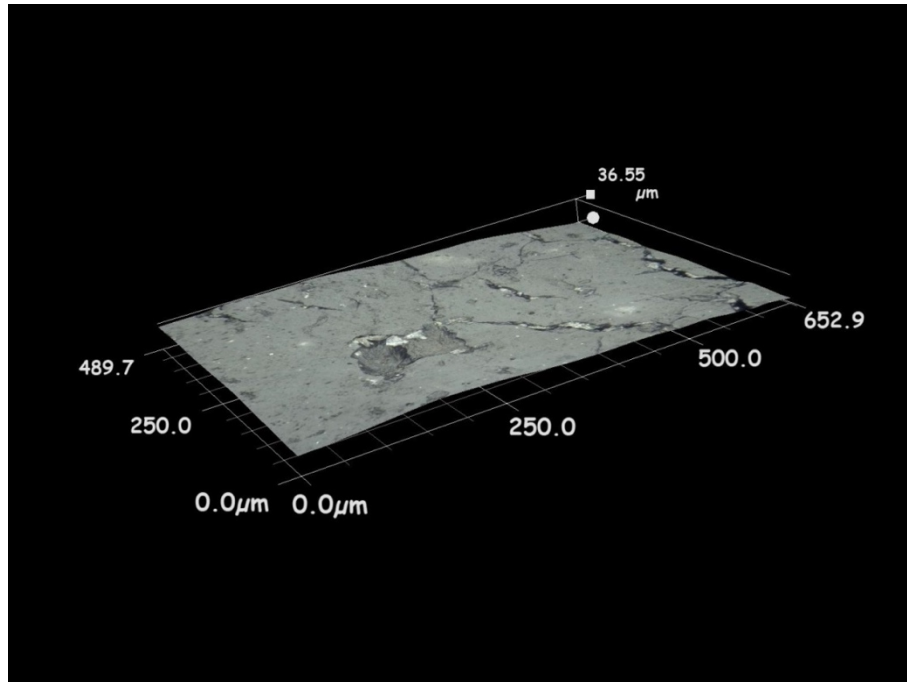


Figure F33: 3D illustration of erosion pit (2). B coating.

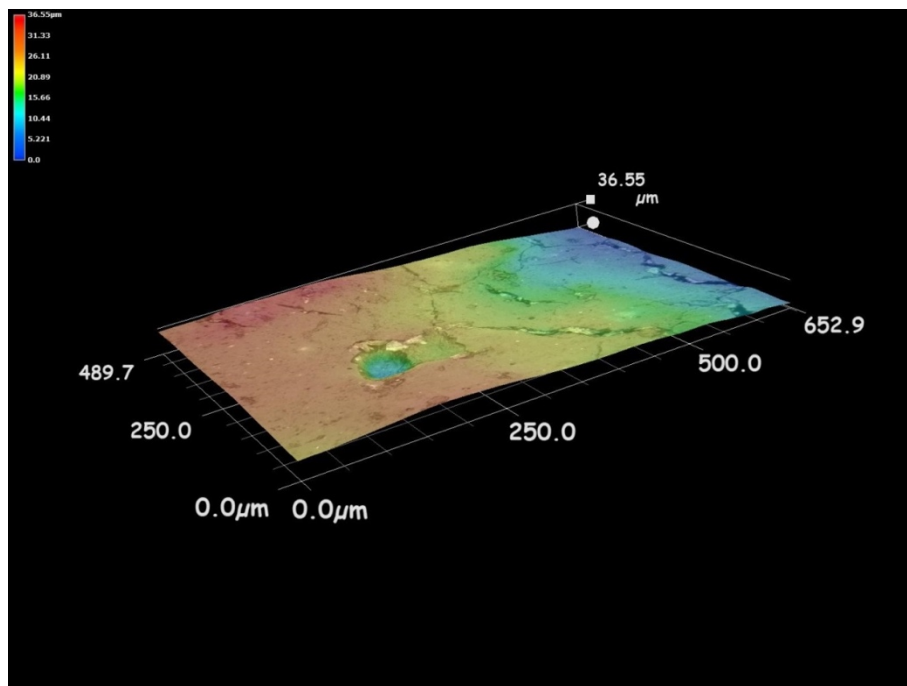


Figure F34: 3D illustration of erosion pit (2). B coating – Colour contour.

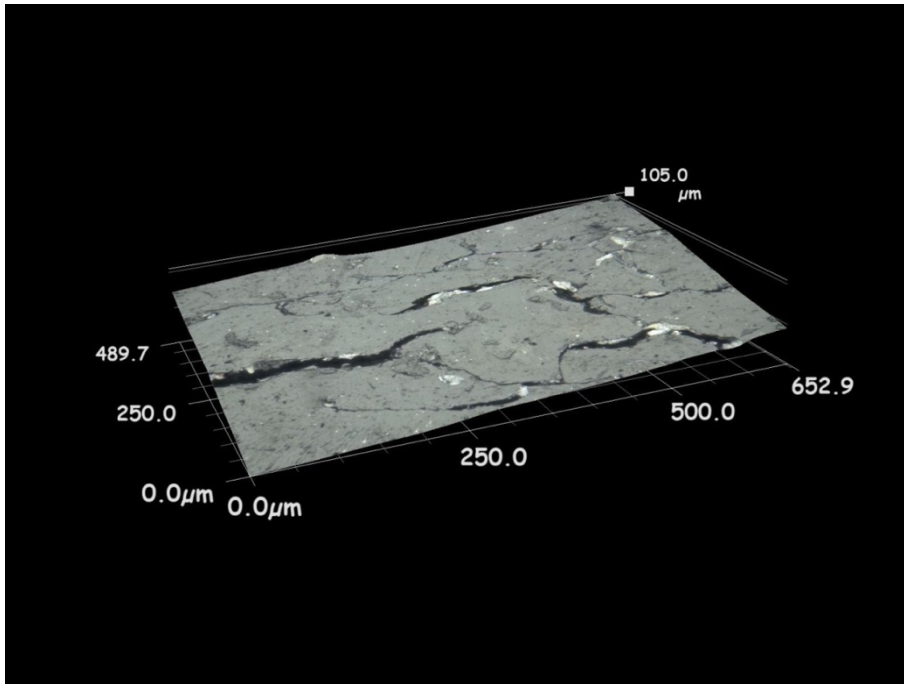


Figure F35: 3D illustration of erosion pit (3). B coating.

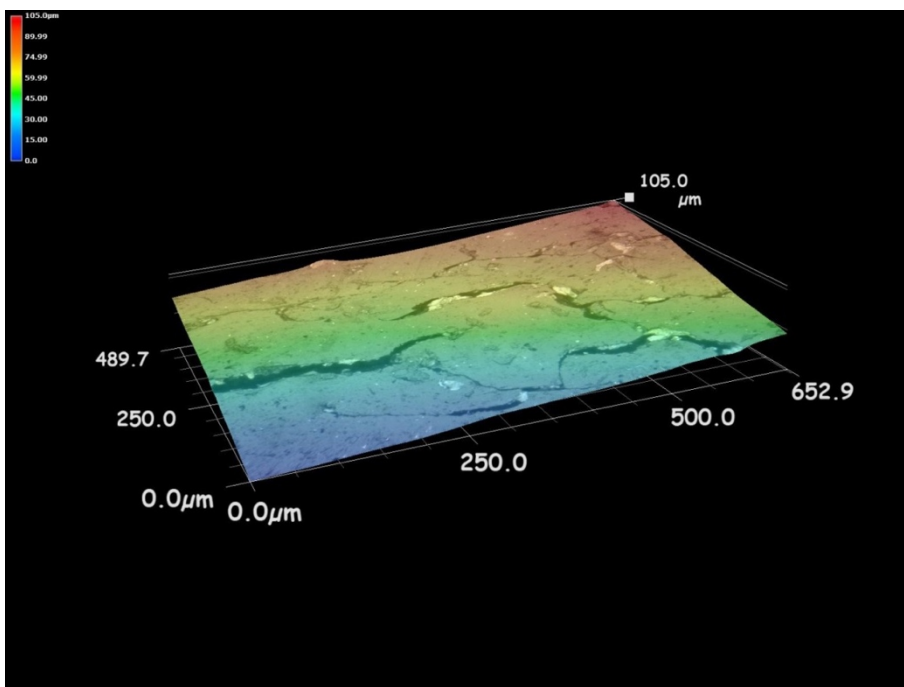


Figure F36: 3D illustration of erosion pit (3). B coating – Colour contour.

C coating

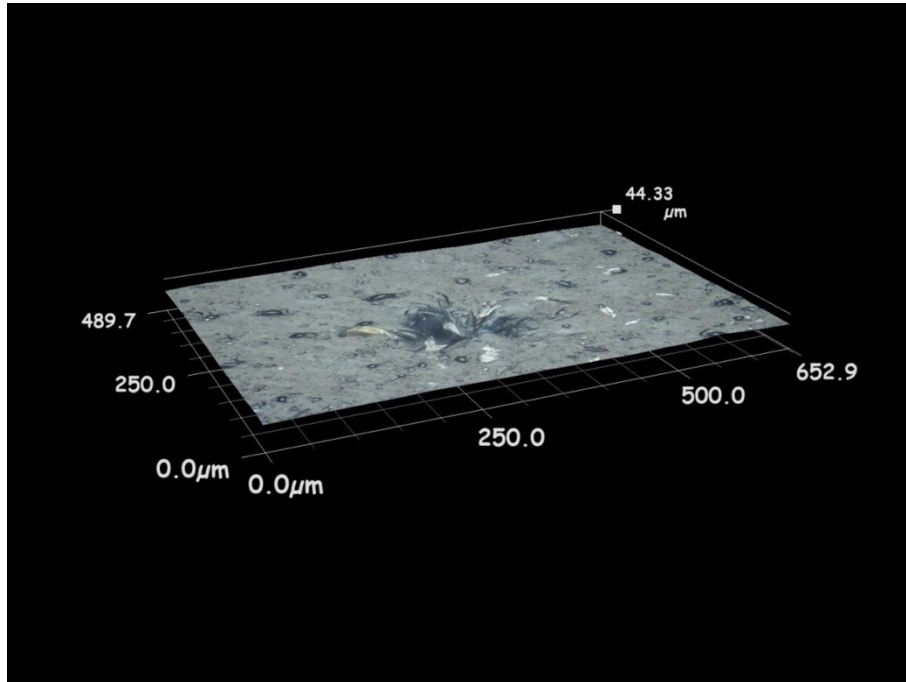


Figure F37: 3D illustration of erosion pit (2). C coating.

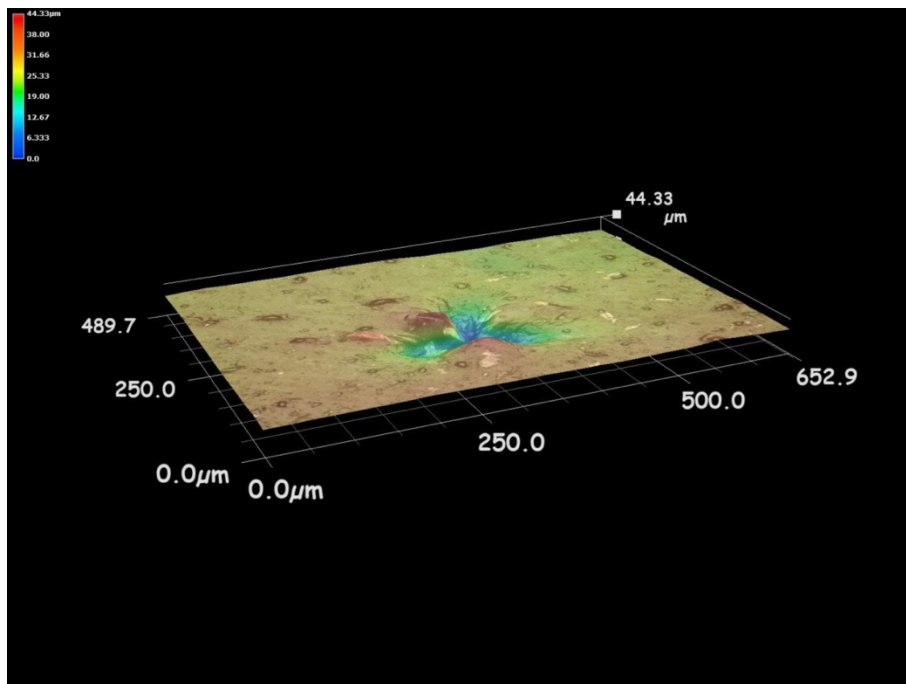


Figure F38: 3D illustration of erosion pit (2). C coating – Colour contour.

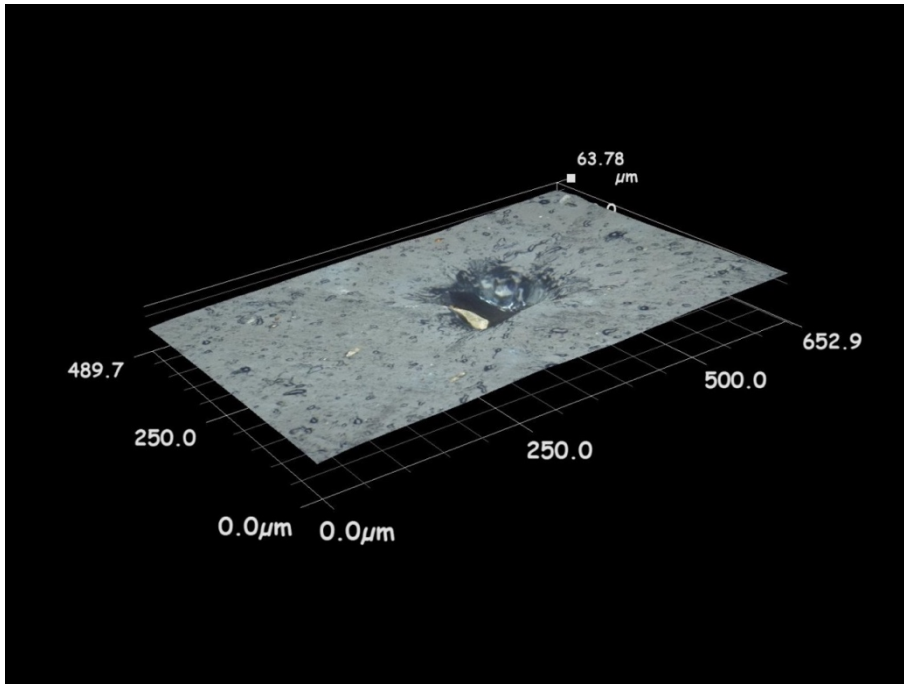


Figure F39: 3D illustration of erosion pit (3). C coating.

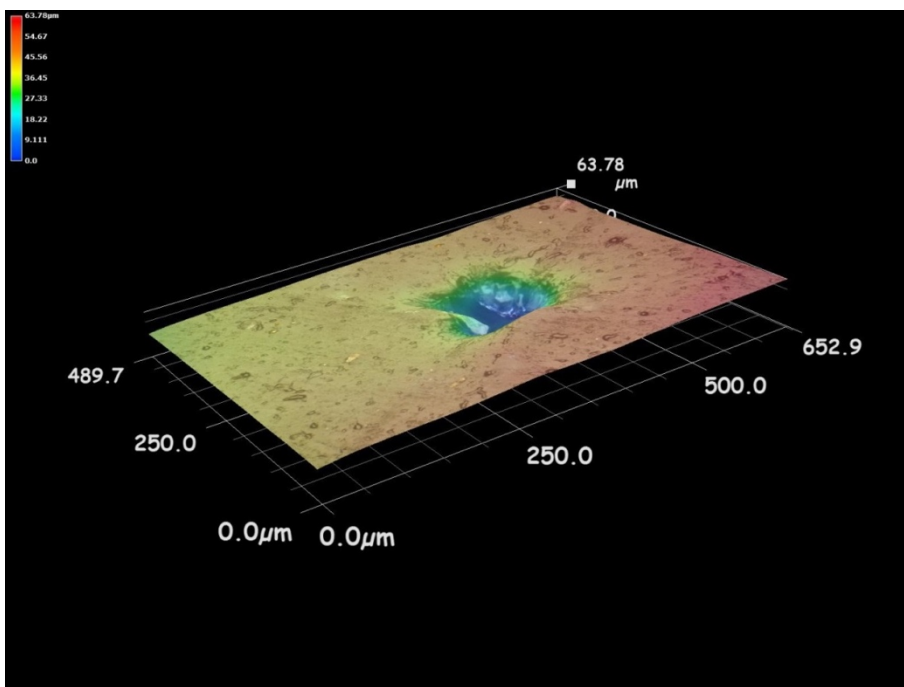


Figure F40: 3D illustration of erosion pit (3). C coating – Colour contour.

Appendix G

G.1 Measurement uncertainty analysis

This study essentially consisted of both quantitative and qualitative elements. The former consisted of mass loss and acoustic emission measurements, for which a measurement uncertainty analysis was undertaken, in order to ensure, that the different results that were obtained for various conditions, are actually accurate, and not the result of measurement uncertainty.

Due to the fact that large sets of data were recorded for both series of measurements, a Type A estimate of uncertainty was selected, which consists of initially calculating the mean value and the standard deviation of a set of data, before eventually calculating the estimated standard uncertainty. This process can be expressed mathematically through the following set of equations (G1).

$$s = \sqrt{\sum_{i=1}^n \frac{(x_i - \bar{x})^2}{(n - 1)}} \quad (\text{G1})$$

$$u = \frac{s}{\sqrt{n}}$$

where x_i stands for the result of the i measurement, \bar{x} for the arithmetic mean of all measurements, n for the number of the results and s for the calculated standard deviation. In addition, u stands for the estimated standard uncertainty of a set of data.

In the case of mass loss tests a series of twenty measurements, using a known weight were initially taken, using the weight balance that was to be used for this study, giving a mean value \bar{x} of 19.4993g and a standard deviation s of 0.00005g. As such the estimated standard uncertainty u would be 0.00001 g. For $k=2$ (95% confidence level) the measurement uncertainty would be ± 0.00002 g. Considering that the mass loss differences that were recorded for the three alloys, were of the order of the 2nd decimal and in many cases of the 1st, it was assumed that measurement uncertainty was not going to influence the recorded results.

Mass loss measurements for the protective coatings, had differences of the order of the 4th to the 2nd decimal, thus measurement uncertainty, was not likely to influence them either,

although not to the same extent as of the alloys. Nevertheless these measurements were recorded due to the interest of BAE Systems to the matter, and were not within the main scope of this study, which was oriented towards the three basic alloys.

It should also be noted that the weight balance was properly calibrated throughout this study, whereas an average of three measurements was taken before a mass loss value was recorded, in order for any mistakes relating to the operator of the measurements to be taken into account. In addition the cavitation inducing ultrasonic transducer, was operating through a fully automated software, which could offer accurate reproducibility of testing conditions, as well as indications on when a consumable part had to be changed. However, all consumable parts were replaced prior to the software indicating the need for replacement, as a preventive measure. It should also be noted that an average of five specimens were tested for each material, whereas the average of those sets was calculated and evaluated, in order for the effects of a slightly different composition, within the material standard, to be eliminated.

With regard to acoustic emission measurements an analogous procedure was utilized by means of a standardized procedure known as the Hsu – Nielsen calibration. This consists of breaking a 2H graphite pencil lead, with a 0.5 mm tip diameter, on the surface of the examined material or sensor, at a 45° angle. This event will produce a standard 1N force which will then induce strain on the crystal of the piezoelectric sensor, and consequently a specific electric signal. This procedure is often being used for the calibration of acoustic sensors, either directly or indirectly through the material they are installed on to. It should be noted that this is the procedure that was utilized in this study, with regard to the conversion of electric signals into acoustic power (dB) and stress (MPa) units, as it is referred in *Chapter 6*.

As such a series of twenty measurements was taken for each of the examined sensors, in order for the mean values, standard deviation, estimated standard uncertainty and measurement uncertainty for a 95% confidence level, to be calculated. Results are presented below:

- Aluminium sensor: $\bar{x} = 0.1225 \text{ V}$, $s = 0.0022 \text{ V}$, $u = 0.0005 \text{ V}$, measurement uncertainty = $\pm 0.001 \text{ V}$ (95% confidence level)
- Brass sensor: $\bar{x} = 0.1225 \text{ V}$, $s = 0.0022 \text{ V}$, $u = 0.0009 \text{ V}$, measurement uncertainty = $\pm 0.0018 \text{ V}$
- PVDF sensor: $\bar{x} = 0.00612 \text{ V}$, $s = 0.00011 \text{ V}$, $u = 0.0001 \text{ V}$, measurement uncertainty = $\pm 0.0002 \text{ V}$

As such, for the aluminium sensor, in terms of acoustic power (dB), and for the values that were recorded, a measurement uncertainty of the order of ± 0.007 dB (95% confidence level) would be expected. This is minor compared to the measured differences of 2-3 dB. Similarly for the brass and PVDF sensor the measurement uncertainty would be of the order of, ± 0.001 dB and ± 0.016 dB, respectively.

In terms of stress, and for the order of values that were recorded, an uncertainty of ± 0.4 , ± 0.06 and ± 1.6 MPa, would be expected, for the aluminium, brass and PVDF sensor, respectively. This uncertainty is again considered to be minor, considering that differences of the order of hundreds of MPa were measured, for different test rig configurations.